NUMERICAL SIMULATION AND ANALYSIS OF THE PROPAGATION OF A PREFRONTAL SQUALL LINE

Jennifer M. Cram

Colorado State University

DEPARTMENT OF ATMOSPHERIC SCIENCE

PAPER NO. 471

NUMERICAL SIMULATION AND ANALYSIS OF THE PROPAGATION OF A PREFRONTAL SQUALL LINE

Jennifer M. Cram

Department of Atmospheric Science
Colorado State University
Fort Collins, Colorado
Fall, 1990

Atmospheric Science Paper No. 471

ABSTRACT

NUMERICAL SIMULATION AND ANALYSIS OF THE PROPAGATION OF A PREFRONTAL SQUALL LINE

An observational and numerical study of the squall line that occurred on 17-18 June 1978 is described. This squall line was initially triggered by the strong surface convergence along a cold front, and stretched from Illinois to the Texas panhandle. The squall line was aligned with the surface front during its initial development (at 0000 UTC 18 June 1978), but then propagated faster than the front, resulting in a separation of approximately 200 km by 0300 UTC and 300-400 km by 0600 UTC.

The CSU RAMS model is used to model the squall line development and propagation. Several sensitivity experiments were completed to test the sensitivity of the results to the use of the Kuo-type cumulus parameterization scheme and grid-scale microphysical processes. The simulations that included the cumulus parameterization scheme and grid scale latent heating or condensation effects accurately modelled the initial development of the squall line and its subsequent movement away from the front. The effects of the grid-scale microphysical processes (versus the more simple grid-scale condensation and latent heat release) were minor in these simulations. A simulation to test the effects of varying the initial specification of roughness length z_0, soil texture, and soil moisture was also completed. The results were very similar to the results with a non-varying specification of z_0 and soil texture, especially in the region of the squall line. Greater differences were found to the east of the squall line where the convection was not as strongly forced by the dynamics.

The propagation of the squall line in the model is shown to be due to the propagation of a deep tropospheric internal gravity wave, in a wave-CISK-like process. The thermal and

dynamic perturbations associated with the hypothesized wave are shown to be consistent with gravity wave theory, and the characteristics of the wave are compared to similar results from wave-CISK studies. The wave is forced by the heating profile associated with the convection and propagates southeastward at 18 m s^{-1} with a horizontal wavelength of ~200 km and a vertical wavelength of 10 km. The wave maintains its coherence and energy through the quasi-resonant effects of reflection from the stability discontinuity at the tropopause and a low-level layer in which the Scorer parameter is very small. The wave dissipates when the heating maximum associated with the wave forcing widens and rises so that the resonant effect is diminished. A critical layer also develops in the upper atmosphere at about the same time, which acts to absorb the wave energy.

The propagation of the squall line as an internal gravity wave is discussed in relation to other studies. The current literature favors the mechanism of gust front convergence to explain squall line propagation, although there are a few other modelling studies that show specific instances of squall line propagation as being due to internal gravity waves. It is suggested that a spectrum of scales of forcing may exist and be responsible for squall line propagation, but many models and observations may be able to detect only the gust-front-type processes. The 17-18 June 1978 squall line probably did not propagate solely as the result of any one mechanism, but instead as the product of several active mechanisms. The dominant mechanism in these modelling simulations was an internal gravity wave, and it seems reasonable that the gravity wave was at least one of the mechanisms responsible for the actual propagation of the 17-18 June 1978 squall line.

Jennifer M. Cram
Department of Atmospheric Science
Colorado State University
Fort Collins, Colorado 80523
Fall, 1990

ACKNOWLEDGEMENTS

I would first like to thank my Committee members, Professors Roger A. Pielke, William R. Cotton, Richard H. Johnson, and Faculty Affiliate Dr. Gary M. Johnson for their help and many suggestions over the course of this work. Professor Roger Pielke was my advisor and is thanked for his support and many helpful suggestions. Professor William Cotton is especially thanked for his helpful advice on many of the convection and cloud-modelling-related aspects of this work, and his thorough review of this manuscript. Professor Richard Johnson provided advice on the observational aspects of this study. Dr. Gary Johnson's help in obtaining computer time on several different systems is especially appreciated.

I was supported as a graduate student in the Department of Atmospheric Science at Colorado State University for 5 years by a NASA Training Grant Fellowship (NASA Grant NGT-06-002-802). This fellowship was first administered by Dr. Gary M. Johnson, and then subsequently by Drs. Patrick J. Burns and David W. Zachmann. All are thanked for their conscientious work in maintaining the fellowship program over the past 5 years. Colorado State University provided support on their CYBER 205 computer in association with the fellowship, which was very much appreciated.

The modelling simulations described were mostly completed on the CRAY X-MP computer at the National Center for Atmospheric Research (NCAR) (under National Science Foundation grant ATM-8814913) and on a CRAY Y-MP computer at the San Diego Supercomputing Center. The National Center for Atmospheric Research is sponsored by the National Science Foundation. Data obtained from the NCAR data archives were used to initialize the model simulations and for verification analyses. Most of the preliminary work for this study, including extensive model debugging, was completed on the CYBER

205 computer at Colorado State University. Mr. John Cooley and the other consultants at the Colorado State University Computer Center are thanked for their time and help in solving many problems, and continuously increasing the limits of my computer accounts.

Drs. Craig Tremback and Bob Walko answered many model-related questions over the course of this work, and their help is appreciated. Mike Moran is thanked for his advice on several topics, especially the deformation-K-based turbulence parameterization scheme, and Jerry Schmidt is thanked for several very helpful discussions about gravity waves. Dr. Mel Nicholls provided a very helpful review of this manuscript. Duane Steigler, from Dr. T.T. Fujita's project at the University of Chicago, supplied the satellite pictures included in Chapter 3. Ray Zehr is thanked for advice in interpreting the satellite pictures. Dr. Thomas Matejka, of the National Severe Storms Laboratory in Boulder, is especially thanked for providing his personal observations of the 17-18 June 1978 squall line.

Finally, Dallas McDonald is thanked for her part in the typing of this manuscript, for answering hundreds of questions about word processing, and for her thorough review of the manuscript. Her expertise in organizing the word processing aspects of the manuscript was invaluable. Bryan Critchfield and Tony Smith are also thanked for their share of the typing. Judy Sorbie-Dunn drafted several of the figures.

TABLE OF CONTENTS

LIST OF FIGURES

LIST OF TABLES

Chapter 1

INTRODUCTION

Squall lines are most simply defined as lines of convection. These lines can be only 100 km long, or near 1000 km long. There is a distinct linear structure to squall lines (as compared to individual thunderstorm cells or systems), although the lines do not necessarily propagate or translate in a direction perpendicular to their length. As Bluestein and Jain (1985) point out, squall lines may be oriented along a front for part or all of their lifetimes, or not at all. Bluestein and Jain's general definition of a squall line as a line-oriented mesoscale convective system (Maddox, 1980) will be adopted in this study. It is assumed that the squall line convection is "deep tropospheric", or mature at some point, although it is not necessary that an anvil or region of stratiform precipitation develop.

The numerical modelling of squall lines has only recently been extended to three dimensions from two dimensions because of a relaxation of computer memory and speed limitations. The linear shape of squall lines has implied that they may perhaps be adequately modelled in only two dimensions. However, the interactions between synoptic scale features (such as frontal forcing) and mesoscale features (such as a squall line and gravity waves) cannot be properly modelled in only two dimensions, and with model initializations from only one sounding. Even with current computer power, it is difficult to have a large enough domain (several thousands kilometers) with a small enough resolution (tens of kilometers or even smaller) to adequately resolve the meso-β and meso-γ scale processes internal to, and in the vicinity of, a squall line, and at the same time also properly simulate the synoptic and meso-α scale processes that may have initially forced the squall line. There are several different scales of motion that can be responsible for forcing squall line development and propagation and it is impossible to correctly model

all of these scales with current computer power. As a result, the modelling of squall lines seems to have split into two widely separate "camps". One group approaches the problem with the finest resolutions possible, but then has to neglect larger scale processes. The other group approaches the problem with synoptic and meso-α scale resolutions but then has to neglect or parameterize the smaller scale processes. The former (small scale resolution) group has done most of the work in recent years on determining squall line development and propagation mechanisms with the resulting emphasis in the literature on gust front propagation. Such studies are unable to address the possibility that several scales of motion may be forcing squall line propagation, as only the smallest scales are properly simulated in their models.

Most higher resolution squall line modelling studies (with grid spacings from 500 m to 5 km) have been two-dimensional and initialized in a "horizontally-homogeneous" manner, i.e. from one sounding and an initial forcing of some sort such as a warm bubble or convergent circulation (Hane, 1973; Moncrieff and Miller, 1976; Thorpe *et al.*, 1982; Hane *et al.*, 1987; Nicholls, 1987, Nicholls and Weissbluth, 1988; Nicholls *et al.*, 1988; Rotunno *et al.*, 1988; Lafore and Moncrieff, 1989; Tripoli and Cotton, 1989a,b; Schmidt and Cotton, 1990). Such studies are needed for investigating the internal cloud-scale squall line dynamics and convective heating effects, and the cloud-scale influence on the meso-β scale aspects of squall line propagation and maintenance (such as the importance of strong downdrafts and the gust front). However, they are unable to take three-dimensional and synoptic scale variations into account or interactions with other mesoscale features (such as fronts) that may have initially forced the squall line. For instance, many of the more recent squall line modelling studies have concluded that cold downdrafts and resulting gust front motion are mainly responsible for squall line propagation (Hane *et al.*, 1987; Nicholls *et al.*, 1988; Rotunno *et al.*, 1988). However, some squall lines have been observed whose propagation is definitely not only due to gust front convergence (Bluestein and Jain, 1985; Srivastava *et al.*, 1986; Crook and Moncrieff, 1988; Carbone *et al.*, 1990). In such instances either larger scale processes or other motions not resolved by such models are responsible for the squall line propagation.

The larger scale studies that have been initialized with synoptic data generally have grid spacings on the order of 25-100 km and concentrate on the synoptic (> 2000 km) and meso α (200-2000 km) scale aspects of squall line propagation and maintenance (Chang *et al.*, 1981; Orlanski and Ross, 1984, 1986; Zhang and Fritsch, 1986, 1987, 1988a,b; Zhang *et al.*, 1988, 1989; Zhang and Gao, 1989). However, these studies are generally unable to resolve the meso-β and meso-γ scale processes which may be important in the development and propagation of squall lines. An additional problem with larger scale studies is their need to rely on parameterizations of subgrid scale processes. In some instances these parameterizations may incorrectly force grid-scale motions or mechanisms. For instance, Tripoli and Cotton (1989b) noted that the inclusion of a convective parameterization incorrectly coupled convective activity with the motion of a large scale gravity wave. A smaller scale simulation with explicit convective processes did not couple the convective activity and the gravity wave motion.

Recently, more attention has been focussed on the possible interactions of mesoscale internal gravity waves with convection, and their potential importance to the propagation and development of squall lines (Ley and Peltier, 1978; Raymond, 1984; Xu and Clark, 1984; Nehrkorn, 1986; Zhang and Fritsch, 1988b; Tripoli and Cotton, 1989a,b; Crook *et al.*, 1990; Schmidt and Cotton, 1990). The numerical simulation of gravity waves also requires model grid spacings on the order of 20 km or finer. There have been two different approaches to the idea of frontal-squall line interactions and gravity waves. The first approach, which includes wave-CISK (Conditional Instability of the Second Kind) theories, is that the squall line is a solitary, propagating mode initiated by, or propagating faster than, the front (Raymond, 1984; Xu and Clark, 1984). The second approach looks at gravity waves as smaller scale features interacting between the front and squall line, or propagating outward from the squall line and initiating new convection (Ley and Peltier, 1978; Zhang and Fritsch, 1988b, Crook *et al.*, 1990). Both approaches require models able to resolve gravity waves with wavelengths on the order of 20 to 100 km, which require horizontal grid increments on the order of 5 to 25 km, respectively.

The purpose of this study is to investigate the development and propagation of a particular prefrontal squall line. The case that has been chosen is that of a mid-latitude

squall line that developed on 17 June 1978. This case was observed during project NIMROD (Northern Illinois Meteorological Research On Downbursts; Fujita, 1979, 1981) and was used for a Doppler radar study by Srivastava *et al.* (1986). This is a case with reasonably strong synoptic-scale forcing that produced a very long, but narrow, prefrontal squall line. The squall line initially developed along the front but then moved out ahead and away from it. Several investigators have speculated that gravity waves may have played a role in the squall line propagation (Srivastava *et al.*, 1978; Thomas Matejka, personal communication).

A nested grid numerical model was used to simulate the development of the squall line across several scales, from the synoptic scale down to meso-β scales. A coarse grid (80 km grid spacing) is used to properly simulate the synoptic scale dynamics and frontal forcing. Finer mesh grids (20 km and 5 km grid spacings) are needed to properly represent the separation of the squall line from the front. It will be shown that the squall line initially developed along the strong surface frontal convergence line, but then moved out ahead of the front as a propagating internal gravity wave in the 20 km grid spacing simulations. The speed of the propagating wave was greater than that of the front, resulting in the separation with time of the front and squall line, and the "prefrontal" character of the squall line. The gravity wave and squall line appear to be manifestations of a wave-CISK type process. The 20 km spacing is not fine enough to resolve smaller scale processes that were undoubtedly important in the squall line structure and maintenance. However, it is hypothesized that several scales of motion were responsible for the squall line propagation and maintenance, and that the 20 km grid spacing simulations show one of the dominant scales. Gust front processes not resolved by that scale undoubtedly played a role in the squall line propagation and initiation, but were not entirely responsible for the propagation, as evidenced by the observations of discrete propagation ahead of the gust front.

A review of previous squall line research is provided in Chapter 2 of this study. Both observational and theoretical/modelling studies will be discussed. In addition, a brief theoretical review of internal gravity waves is provided, as well as a review of several wave-CISK studies. Observational studies involving meso-α scale gravity waves are also discussed.

The observational analysis of the squall line is presented in Chapter 3. Satellite photographs, radar summary charts, and upper air and surface analyses will be discussed, in addition to the one other paper that has been written on this case (Srivastava *et al.*, 1986). Several personal observations provided to this author by Thomas Matejka will also be discussed.

Chapter 4 is a description of the numerical methods and data used in the simulations described in this study. The model initial analysis scheme will be described, along with the various data sets used in the analyses. The particular version of the Colorado State University (CSU) Regional Atmospheric Modelling System (RAMS) model that was used for the simulations is also described.

Results from model simulations with 80 km and 20 km grid spacings are discussed and compared to the observational data in Chapter 5. Several sensitivity studies that were completed to investigate the importance of the parameterized and grid-resolved convection, latent heat release, and microphysical processes are discussed in this chapter, and the hypothesized mechanism of the squall line propagation as an internal gravity wave is introduced. A comparison of the model results with similar results from a wave-CISK study is made, and the characteristics of the internal gravity wave are discussed. In Chapter 6 the results from a set of simulations with varying initial surface characteristics (surface roughness, soil type, and soil wetness) are presented.

The results from simulations with a horizontal grid spacing of 5 km are presented in Chapter 7. These simulations were completed in an attempt to explicitly resolve the convective processes that were parameterized in the coarser resolution simulations. Several problems were encountered in the simulations on this scale, however, and will be discussed in that chapter.

Finally, Chapter 8 is a summary of the results in this study. A discussion is presented of some of the modelling problems encountered in the simulations on these scales, and suggestions for future research are provided.

Chapter 2

LITERATURE REVIEW

A review of previous squall line studies will be presented in this chapter. The first section will discuss observational studies, starting with those of Newton and Tepper in the 1950s, and proceeding on to more recent comparisons of tropical and mid-latitude squall lines. The second section will review the many theoretical and modelling studies of squall lines, starting with the work of Hane in the early 1970s. The results and comparisons of a wide range of two- and three-dimensional modelling studies, with horizontal grid spacings ranging from 1 to 100 km, will be discussed.

A brief review of gravity wave theory and observations of meso-α scale gravity waves is also presented in this chapter. Section 2.3 is a brief review of simple gravity wave theory which will be referred to in later chapters. Wave-CISK theory and studies are reviewed in Section 2.4, and a survey of observational studies of gravity waves is provided in Section 2.5.

2.1 Observational Studies of Squall Lines

2.1.1 Early studies

One of the earliest observational studies of extra-tropical squall lines is by Newton (1950). Newton used rawinsonde data from the Thunderstorm Project to analyze the prefrontal squall line of 29 May 1947. He noted that the passage of the squall line was associated with a large temperature drop and smaller dewpoint drop, and a windshift. He referred to the "squall sector" as that sector of air between the cold front and squall line. As the southern end of the squall line is often aligned with the southern end of the cold front, the "squall sector" can be a completely bounded sector of air. Newton also

outlined the importance of vertical momentum transports: transfer of higher momentum from aloft to low levels behind the squall line helps maintain low-level convergence while upward transfer of low-level, low momentum results in horizontal divergence aloft and the maintenance of the surface low pressure trough. He also showed that the squall line must move faster than the cold front because it derives its forward momentum from higher levels than those of the cold front, although the squall line did initially develop as a result of cold-frontal lifting. Finally, Newton noted other observations of rapidly moving pressure falls in advance of squall lines, but found no evidence to associate these troughs with squall line formation.

Tepper (1950) analyzed surface data for the squall line case of 16-17 May 1948. Among the features analyzed with the squall line passage were a strong average pressure jump of 2.3 mb over 5 minutes, a wind speed maximum, and a temperature fall. The temperature fall and precipitation persisted long after the pressure leveled off and started to fall. Tepper does not seem to have observed a significant, or separate, pressure trough ahead of the jump. Tepper proposed that the squall line developed as a pressure jump line, initiated by the cold front and propagating along the warm sector inversion as a gravitational wave, independent of the precipitation process initiated by the wave. Tepper's hypothesized gravity wave is an example of a bore (Section 2.3) or a wave propagating along a density discontinuity, as opposed to an internal gravity wave in a continuously stratified fluid. In contrast, Newton noted that his theory for the propagation of the squall line was dependent upon the interactions and existence of convection and precipitation.

Fujita (1955) also analyzed surface data for several squall lines. He further defined the pressure trace through the squall line to include the initial pressure surge, a thunderstorm high, a pressure drop, and a wake depression (Fig. 2.1). He hypothesized that the wake depression was dynamically induced as a result of flow around the main thunderstorm high. Later studies attributed the wake depression to subsidence warming associated with a rear-to-front mid-level jet (Zipser, 1977; Brown, 1979; LeMone, 1983; LeMone *et al.*, 1984; Smull and Houze, 1987; Johnson and Hamilton, 1988).

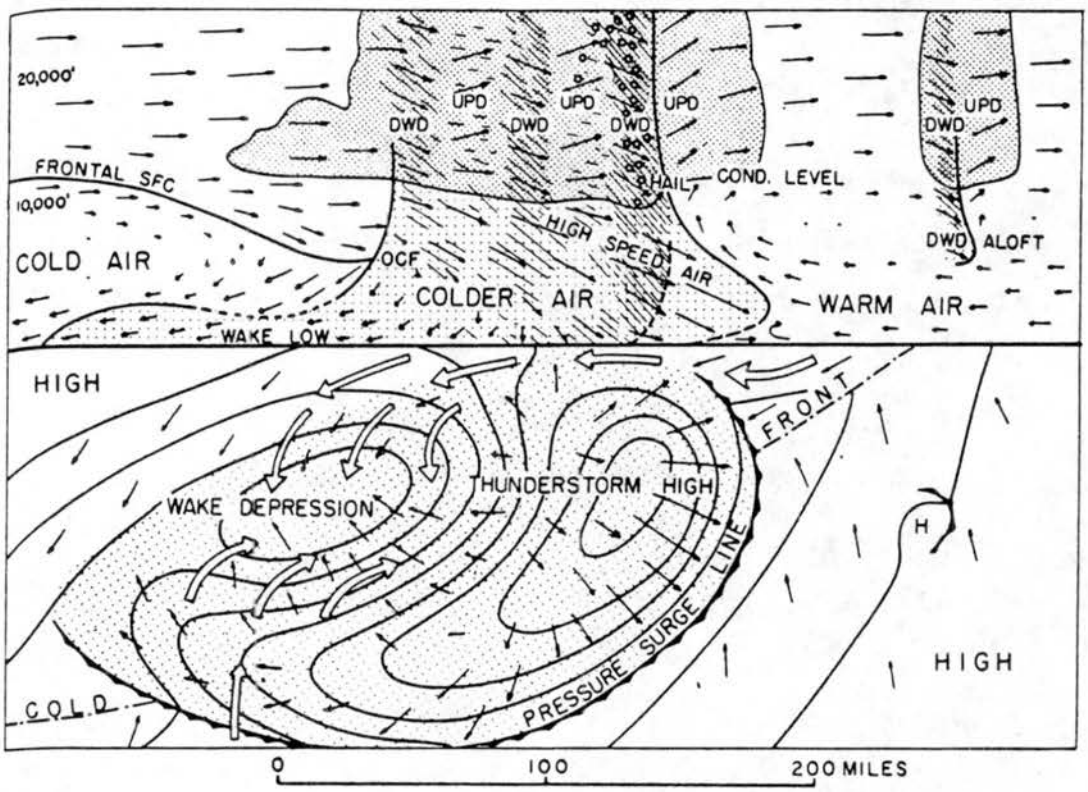

Figure 2.1: Schematic section through a squall-line thunderstorm and illustration of the wake depression (from Fujita, 1955).

2.1.2 Tropical squall lines

Tropical squall lines often differ from mid-latitude squall lines in that they occur in weak shear, weak convective instability environments. As a result of the weak shear, storm-relative flow is from front-to-rear at all levels at the leading edge. Roux (1988) provides a concise description of tropical squall lines:

> "The leading line consists of discrete cumulonimbus towers which form ahead of the line and weaken to the rear (this region is referred to as the "convective region"). The trailing anvil region shows a horizontal stratification with a pronounced bright-band characteristic of a melting layer (this region is referred to as the "stratiform region"). The convective scale and mesoscale vertical air motions are both important components of the squall line system. The buoyant convective updrafts are fed by the unstable presquall boundary layer while convective downdrafts, initiated by the liquid water loading and sustained by evaporation, are fed by mid-level air entering the squall line between the cells. In the stratiform region a mesoscale downdraft, supported by the cooling effect of evaporation and melting, occurs below the base of the anvil cloud. Within the cloud, observational and modeling evidence suggests the presence of a mesoscale updraft probably maintained by the latent heat released from the transition from water to ice saturation and by the increase of the effective buoyancy through the fallout of precipitation. The squall line propagation is generally faster than the presquall environmental wind at any altitude, but its origin remains an open question, although various mechanisms have been proposed: release of kinetic energy; density current; internal solitary wave; constructive interference of normal modes; and wave-CISK."

Although the forcing may be different for tropical and mid-latitude squall lines, the internal dynamics and structure have many similarities. Several studies of tropical squall lines will be briefly outlined below.

Houze (1977) analyzed a GATE squall line from 4-5 September 1974. Figure 2.2 shows his schematic cross section through the squall line. Storm-relative inflow occurred at all levels ahead of the storm and at mid-levels from the rear. Outflow occurred to the rear at upper and lower levels. Houze distinguished a mesoscale downdraft area below the trailing anvil and a convective-scale downdraft from the heavy rain zone just behind the leading edge. The convective-scale downdrafts spread forward, producing the gust front, and rearward in a layer at the surface only 200-400 m thick. Zipser (1977) also distinguished between convective and mesoscale downdrafts in a separate case (18 August

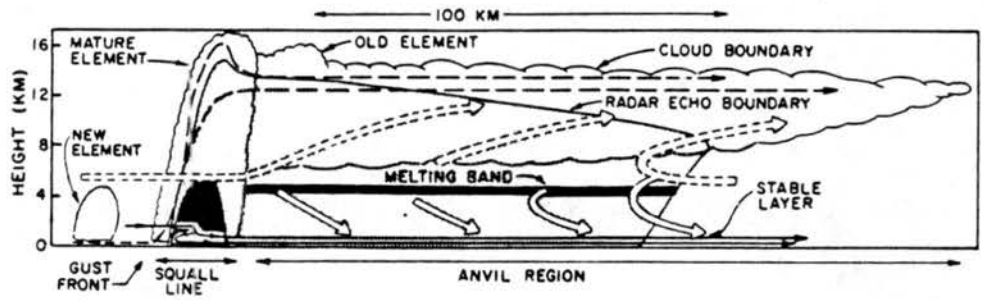

Figure 2.2: Schematic cross section through squall-line. Streamlines show flow relative to the squall line. Dashed streamlines show updraft circulation, thin solid streamlines show convective-scale downdraft circulation associated with mature squall-line element, and wide arrows show mesoscale downdraft below the base of the anvil cloud. Dark shading shows strong radar echo in the melting band and in the heavy precipitation zone of the mature squall-line element. Light shading shows weaker radar echoes. Scalloped line indicates visible cloud boundaries (from Houze, 1977).

1968) that was observed during a field program near Barbados (Garstang *et al.*, 1970). Zipser developed a squall line schematic very similar to Houze's, with inflow ahead of the storm at all levels and at mid-levels from the rear. Houze also emphasized the discrete nature of the squall line propagation by discrete cores of convection, termed squall line elements. At any time several different elements existed, in different stages of development. As an element weakened new elements formed ahead of it, discretely propagating the squall line. In general, the new elements seemed to be triggered by the downdrafts spreading forward from the mature, older elements.

Gamache and Houze (1982) confirmed the presence of a mesoscale updraft in the anvil. They calculated horizontal divergences along pressure slabs and integrated upwards to obtain vertical motion. Figure 2.3 shows the vertical profile of average divergence and vertical motion in the squall line and anvil regions. They developed a squall line schematic that showed the anvil ascent and mid-level front-to-rear flow through the squall line.

Barnes and Seickman (1984) compared the environments of fast and slow-moving tropical convective lines. They found that the fast moving lines had a more pronounced minimum of θ_e at mid-levels (Fig. 2.4). and that the low-level vertical shear (in the lowest 4 km) of the horizontal wind was mostly normal to the direction of movement for the fast

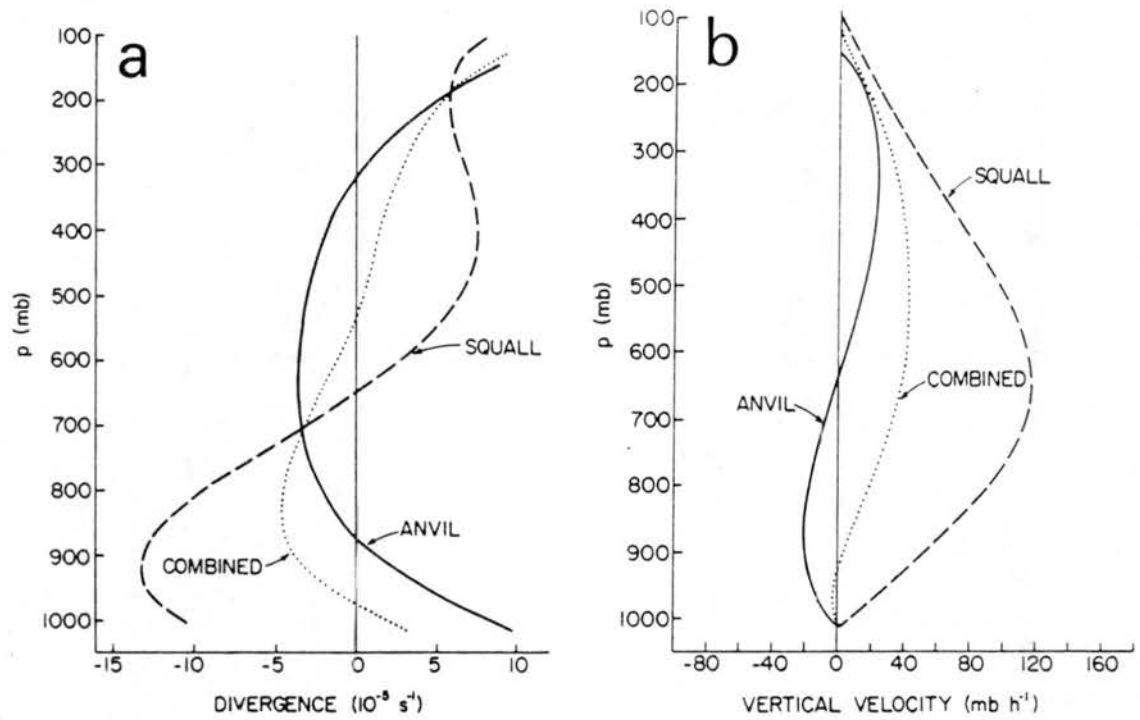

Figure 2.3: Vertical profiles of (a) average divergence (10^{-5} s^{-1}); and (b) vertical velocity (mb h^{-1}) in the squall line, anvil, and combined regions (from Gamache and Houze, 1982).

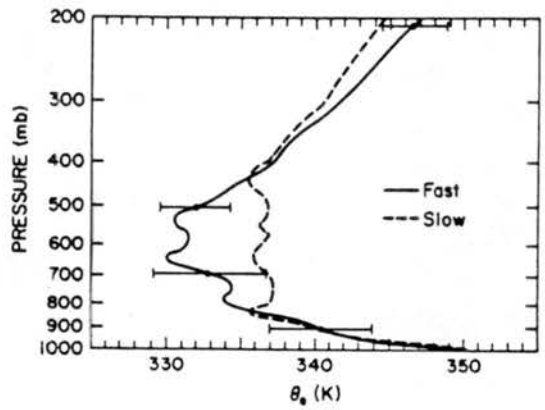

Figure 2.4: Profiles of equivalent potential temperature θ_e of the environment for fast (solid) and slow-moving (dashed) cloud line composites. Bars indicate typical standard deviations for the squall line at selected levels (from Barnes and Seickman, 1984).

lines and parallel to the direction of movement for the slow lines (Figs. 2.5 and 2.6). The lower minimum of θ_e for the fast moving lines may be an indication of stronger downdrafts and thus a stronger forward-moving gust front.

Roux (1988) analyzed a west African squall line from 23 June 1981 observed during the COnvection Profonde Tropicale (COPT) experiment. This squall line was of the discretely propagating class, with new cells forming ahead of the older cells, and convective downdrafts between and behind the cells. He found that a cold low-level frontward flow across the convective region (induced by convective downdrafts) induced a dynamic pressure high in front of the line. The resulting vertical pressure gradient forced the lifting of the initially weakly or negatively buoyant air parcels to a level where buoyancy alone could maintain the upward motion. The dry mid-level air further reinforced the formation of strong downdrafts and the low-level forward moving cold pool. Roux also found that the vertical flux of the component of horizontal momentum normal to the line was up-gradient while the flux of the parallel component was down-gradient. This is in agreement with the findings of LeMone (1983) and LeMone *et al.* (1984). Roux attributes the up-gradient momentum flux to pressure gradient acceleration and the two-dimensionality of the line.

2.1.3 Mid-latitude squall lines

Mid-latitude squall lines differ from their tropical counterparts in that the storm relative flow is not always front-to-rear, and they may exist in an environment of more variable and stronger wind shear. Mid-latitude squall lines can also be more intense than tropical squall lines (if they are of the type that is a line of supercells). However, many mid-latitude squall lines have tropical squall line characteristics. A brief discussion of a study of a South China Sea cold surge is also provided in this section because of its similarity to the propagation of prefrontal squall lines.

Ogura and Liou (1980) analyzed the meso-β and meso-α scale structure of a mature-to-decaying squall line that occurred on 22 May 1976. This squall line was associated with a dry line, rather than a cold front, and with weak vertical shear and weak convective instability. They used a composite analysis of 81 soundings from 9 different Oklahoma

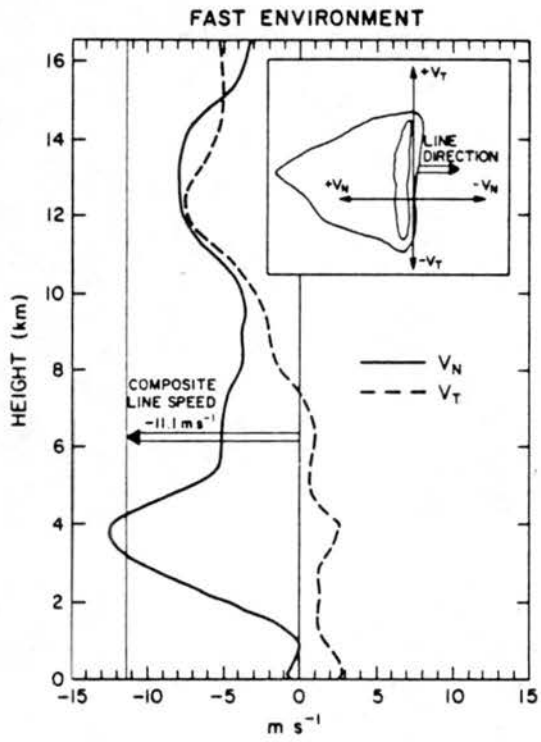

Figure 2.5: Composite profile of the wind environment normal (solid) and parallel (dashed) to the leading edge of a fast-moving squall line for the environment. The mean line speed is shown by a thin vertical line (from Barnes and Seickman, 1984).

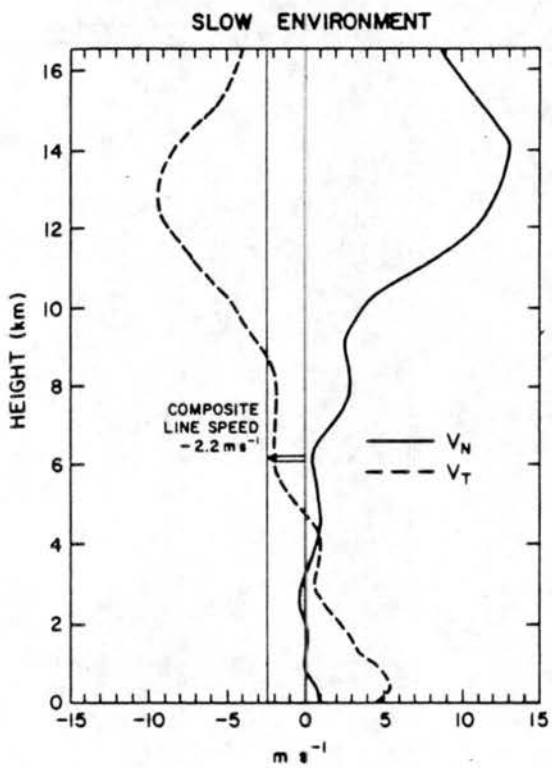

Figure 2.6: Composite profile of the wind environment normal (solid) and parallel (dashed) to the leading edge of a slow-moving squall line for the environment. The mean line speed is shown by a thin vertical line (from Barnes and Seickman, 1984).

stations. One of the many features they found was a definite upshear tilt; the axis of low-level convergence/upper-level divergence tilted 70 km horizontally from the surface to 200 mb. They noted equally strong squall-line-relative low-level inflow and outflow (15 m s^{-1}) and upper-level outflow >10 m s^{-1} ahead of the squall line at 200 mb. Mid-level air entered from the rear between 500 and 600 mb. Strong convection occurred at the low-level leading edge of the squall line with divergence in the rain area behind the leading edge. The two updraft maximums were located at 700 mb approximately 20 km behind the leading edge and at 400 mb about 130 km beyond the leading edge. The maximum updraft was -30 μ b s^{-1}. Figures 2.7 and 2.8 show the streamlines derived from the u

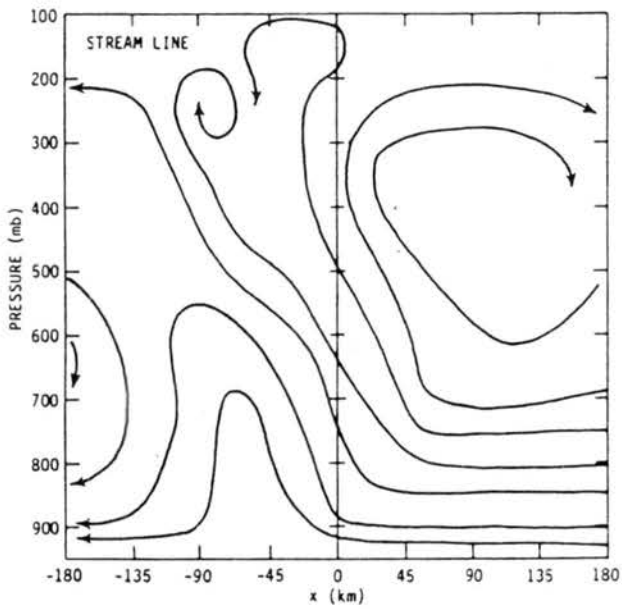

Figure 2.7: Streamlines relative to the moving squall line in an east-west vertical cross section. x is the distance ahead of the leading edge of the squall line (from Ogura and Liou, 1980).

and w wind components and the equivalent potential temperature distribution. High θ_e air is found ahead of the squall line at low-levels with lower θ_e air at mid-levels ahead and low-to-mid levels behind the squall line. Finally, Ogura and Liou noted the similarity of this squall line to tropical squall lines, in similar weak shear and weak convective inability environments.

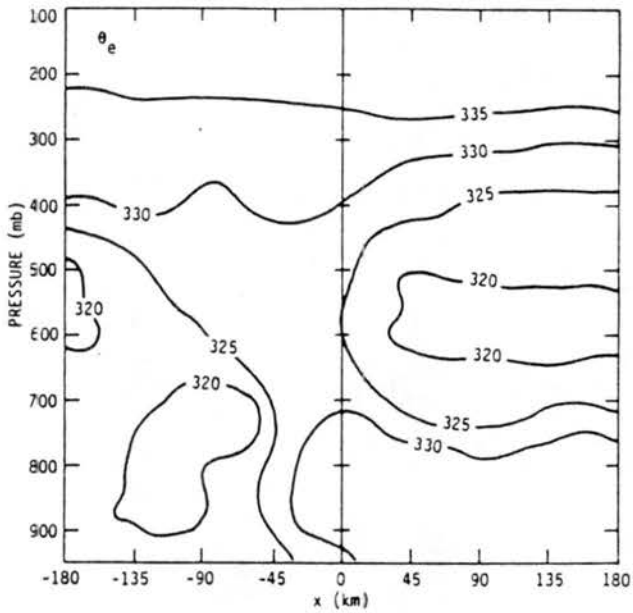

Figure 2.8: Equivalent potential temperature in an east-west cross section. x is the distance ahead of the leading edge of the squall line (from Ogura and Liou, 1980).

Chang *et al.* (1983) investigated cold surges over the South China Sea observed during the Winter Monsoon Experiment (MONEX). The surges usually occurred in two stages with the first stage characterized by a pressure rise, followed several hours to a day later by the second stage, characterized by a decrease in dew point temperature. The second stage was associated with frontal passage, and the first stage was hypothesized to be due to a propagating gravity wave. The front moved at 10 m s^{-1} while the wave moved at 40 m s^{-1}, significantly faster than the strongest winds at that level (25 m s^{-1}). Lim and Chang (1981) used a simple analytical model to investigate the temporal and spatial scales of the various wave responses to a mid-latitude forcing, such as the cold front. Similar to Ley and Peltier (1978), they found a transient motion response to the pressure-wind imbalance, i.e. dispersive gravity waves moving away from the front. The group velocity of their simulated inertia-gravity waves was 22 m s^{-1}, less than the observed 40 m s^{-1}, but calculated using a very simple model.

Koch (1984) and Dorian *et al.* (1988) investigated cases where an ageostrophic frontogenetically-forced circulation resulted in the formation of a clear zone (CZ) behind the front and the subsequent development of line convection (LC) or a squall line at the leading edge of the clear zone. A thermally direct frontogenetic circulation developed transverse to the cold front and generated the LC and CZ. The frontogenetically-forced circulation was diagnosed by a form of the Sawyer-Eliassen equation. Figure 2.9 is a schematic showing the development of the initial frontogenetically-forced circulation and then the CZ and LC.

Smull and Houze (1985) also examined the 22 May 1976 case (same case as Ogura and Liou, 1980), concentrating on the analysis of Doppler radar data. They found that air entered the front of the storm through a deep layer and continued rearward, dominating the internal circulation. There was not a strong rear-to-front mid-level flow. They speculated that acceleration of air parcels into a mesolow associated with the trailing stratiform region might be responsible for the strong front-to-rear flow. Figure 2.10 shows their schematic of the flow for this storm.

Smull and Houze (1987) further examined the structure of the squall line rear inflow on the 22 May 1976 case and several other cases. They developed mean horizontal wind profiles for "strong rear inflow" and "stagnation zone" cases (Fig. 2.11). The "strong rear inflow" cases had stronger front-to-rear flow above and below the rear inflow level. The axis of strongest rear inflow sloped downward to the front of the storm, resulting in the lowering of θ_w values. The convergence of this rear inflow air with the outflow from the convective downdrafts was an important element in the feedback and maintenance of the squall line convection. They also found a convergence of the rear inflow with the mid-to-upper level front-to-rear flow in the stratiform rain area. They speculated that two separate mechanisms were responsible for the development of the rear inflow. A hydrostatic pressure minimum under and behind the warm convective updrafts resulted in rear-to-front low-level acceleration just behind the convective zone. Similar accelerations were diagnosed by LeMone (1983) and LeMone *et al.* (1984) in tropical cumulonimbus

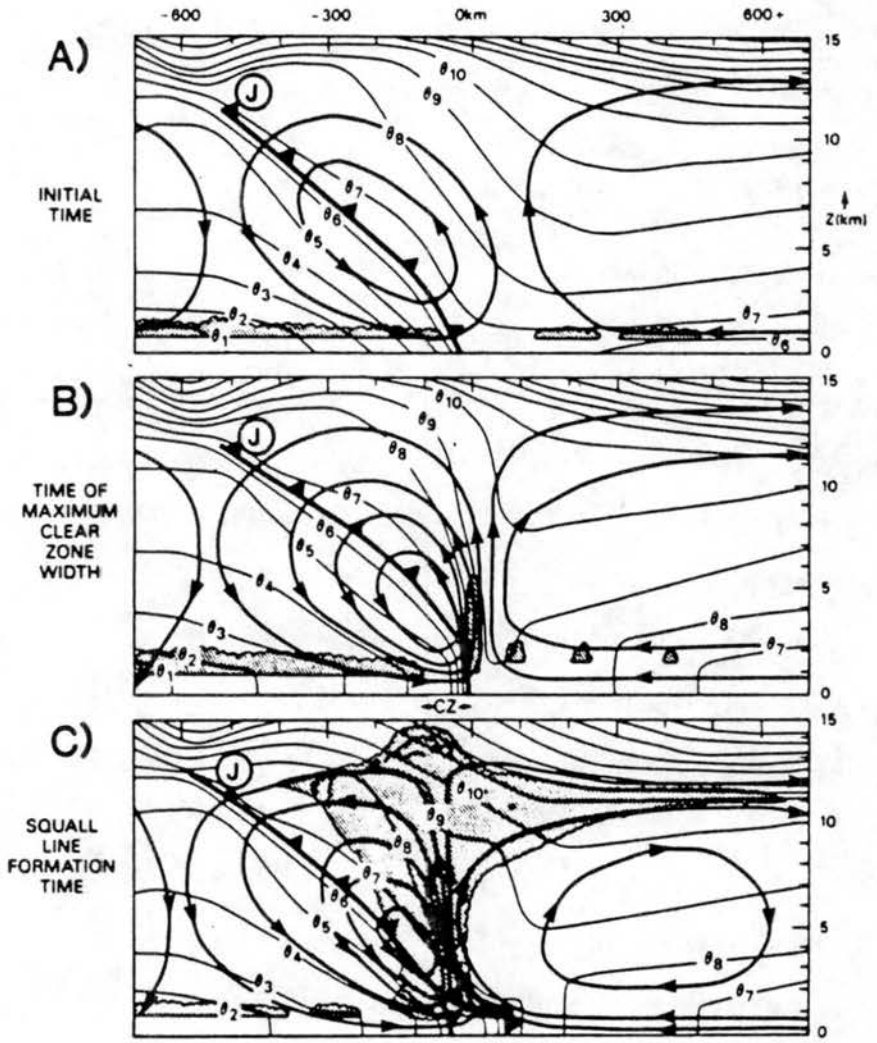

Figure 2.9: Schematic illustration of the hypothesized ageostrophic circulation transverse to an intensifying, two-dimensional front. The abcissa represents the distance relative to the surface cold front. Isentropes and streamlines are depicted by thin and solid lines respectively, Isentrope interval is 5 K. Streamline spacing is inversely proportional to speed. Location of upper level jet core is shown by "J". Clear zone is found immediately behind frontal line convection in middle panel, and results from erosion of leading edge of stratocumulus deck seen in top panel. Gust front produced by squall line is shown slightly ahead of cold front (from Dorian *et al.*, 1988).

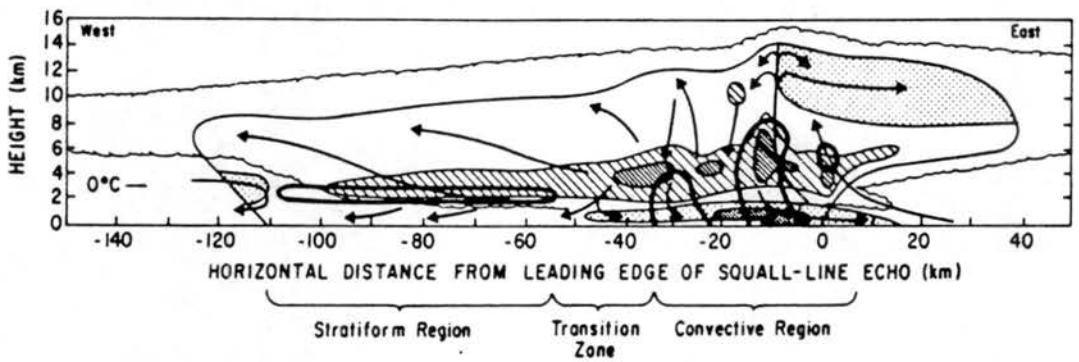

Figure 2.10: Conceptual model of the mature 22 May 1976 Oklahoma squall line system viewed in a vertical cross section oriented normal to the convective line. System motion is from left to right at 15 m s^{-1}. Scalloped line marks extent of cloud. Outermost solid contour marks boundary of detectable precipitation echo, while heavy solid lines enclose more intense echo features. Stippling indicates regions of system-relative horizontal wind directed from rear to front (left to right); darker stippling represents stronger flow. Elsewhere within the echo, relative flow is from front to rear (right to left). Maximum front-to-rear flow at middle and upper levels is shown by hatching; darker hatching denotes embedded speed maxima. Thin streamlines show two-dimensional projection of relative flow determined from the dual-Doppler analysis and the composite rawinsonde analysis of Ogura and Liou (1980). The 0°C level in the trailing stratiform region is indicated at the rear of the echo (from Smull and House, 1985).

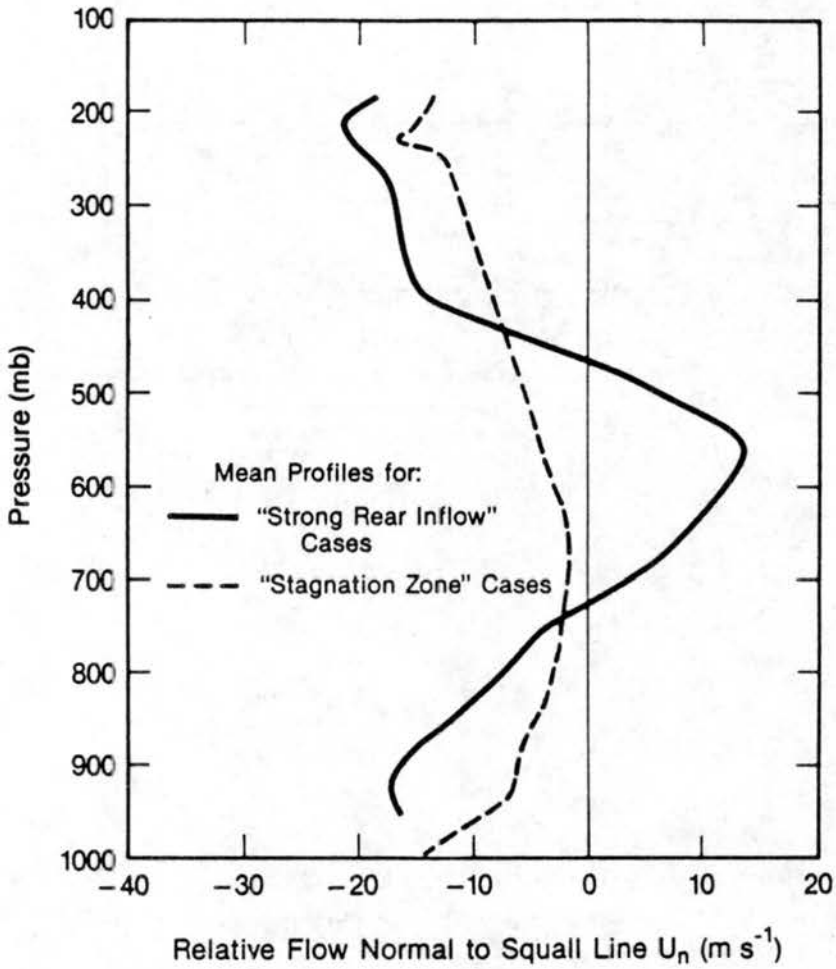

Figure 2.11: Mean profiles of system-relative wind component normal to the convective line for strong rear inflow and stagnation zone cases (from Smull and Houze, 1987).

lines. They also speculated that the mid-level rear-to-front accelerations at the back edge of the stratiform region were due to acceleration into a mid-level mesolow, a result of the effects of latent heat release aloft and evaporative cooling below, as in Brown (1979).

Heymsfield and Schotz (1985) analyzed the structure and development of the squall line of 2 May 1979. The squall line seemed to develop from convection that formed along the leading edge of a surface cold front. The squall line was composed of discrete convective cells, although the cells themselves propagated by continuous regeneration, similar to supercells, rather than discretely. Although the development of this squall line was associated with a front, it did not seem to develop or move ahead of the front as the typical prefrontal squall lines of Newton (1950).

Bluestein and Jain (1985) analyzed 11 years of radar data from the National Severe Storm Laboratory (NSSL) in Norman, Oklahoma and came up with four types of convective line developments: broken line, back-building, broken areal, and embedded areal (Fig. 2.12). The broken line was typical of the narrow cold-front type of squall lines, and most similar to the squall line in this study (17-18 June 1978). The environment of the broken lines consisted of weak vertical shear, large convective available potential energy (CAPE) and large bulk Richardson numbers. This type of line seemed to be the result of frontogenetically-forced multicells. Back-building lines were of the continuous propagation type (vs. discrete) and were more likely to consist of supercells and in an environment with strong vertical shear and small bulk Richardson numbers. Broken areal formations existed in environments with low CAPE and seemed to result from the interactions of outflow boundaries and embedded areal lines (embedded within a stratiform region), or were possibly due to some sort of hydrodynamic instability or ducted gravity wave mechanisms. All of the squall lines, however, formed in environments with relatively strong vertical shear at low levels and much weaker shear aloft.

Srivastava *et al.* (1986) did a Doppler radar study of the prefrontal squall line of 17-18 June 1978 (the case modelled and discussed in this study). The squall line formed along a slow-moving cold front and extended over 2000 km from the Great Lakes to the Texas

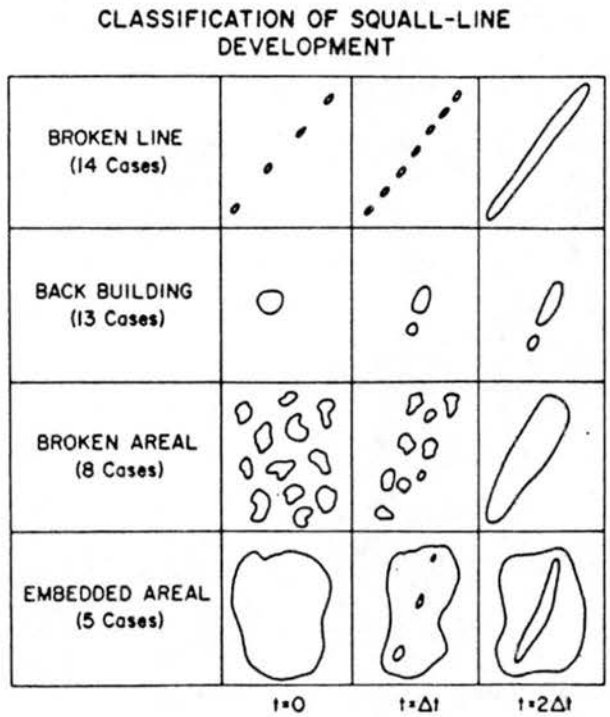

Figure 2.12: Idealized depiction of squall-line formation (from Bluestein and Jain, 1985).

Panhandle. The squall line moved southeastward at approximately 15 m s^{-1}, separating from the slower moving cold front. The squall line formed in a zone where warm air advection occurred below 700 mb and cold air advection above. The line propagated discretely with new convective elements forming up to 25 km ahead of the line. Most of the vertical wind shear was at low levels (Fig. 2.13). An interesting result from their analyses of divergence was a banded structure in the divergence fields, in the stratiform anvil region, especially pronounced at the 7 km height. The bands were angled north to south whereas the squall line was oriented northeast to southwest. They speculated that these bands could be manifestations of internal gravity waves. Srivastava *et al.* also derived cross sections through the squall line of transverse wind speed that showed a mid-level, rear-to-front, descending flow with rearward outflow above and below. The Srivastava *et al.* results are discussed more thoroughly in Section 3.1.

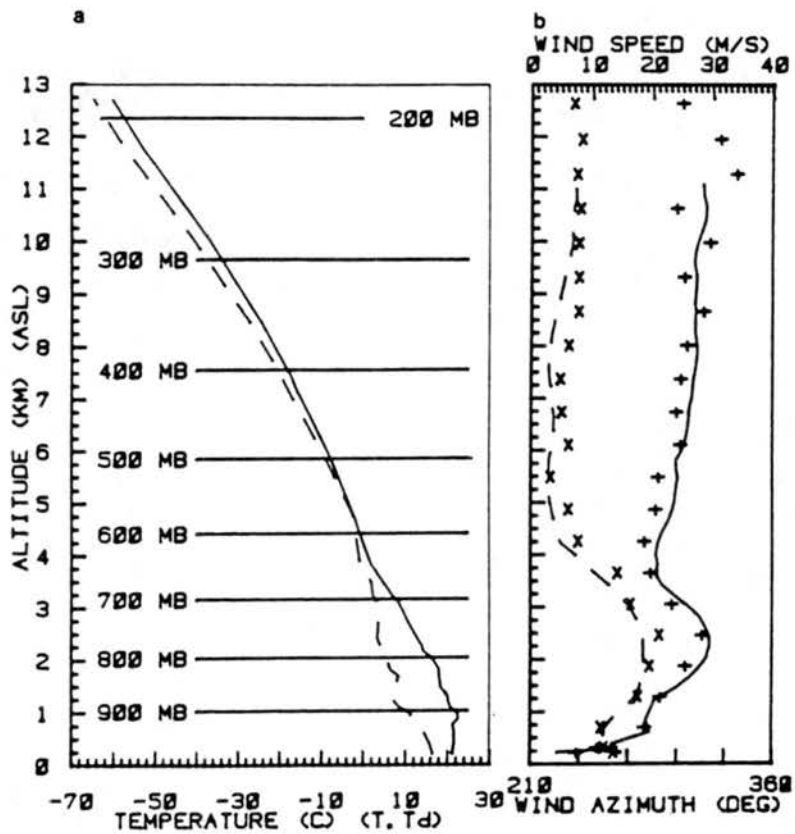

Figure 2.13: (a) Vertical profile of temperature (solid line) and dewpoint temperature (dashed line) from the rawinsonde released from the CP3 radar site (at Yorkville, Illinois) at 2356 CDT. (b) Vertical profiles of wind speed (solid line) and wind direction (dashed) from the extended velocity azimuth display (EVAD) analysis. The wind direction ($\times$) and speed ($+$) from the rawinsonde ascent are also shown. The vertical scale is altitude above sea level. The ground at CP3 radar site is at 226 m asl (from Srivastava *et al.*, 1986).

Kessinger *et al.* (1987) studied a severe squall line that occurred on 19 May 1977 in Oklahoma. They developed a conceptual model of the squall line based on a multiple Doppler analysis (Fig. 2.14) and identified four major regions of the system: preline con-

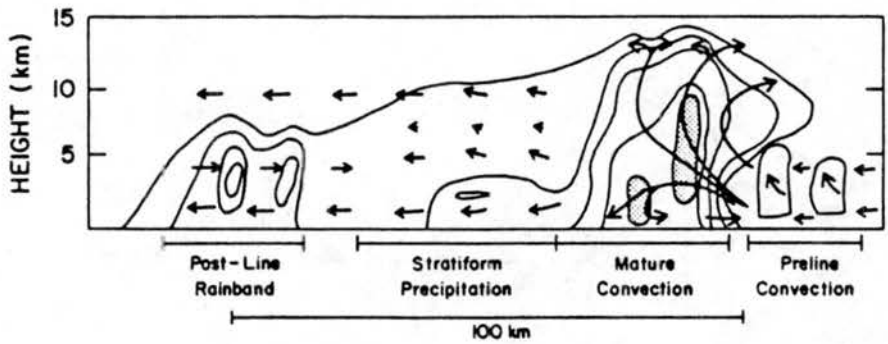

Figure 2.14: Schematic of the preline convective region, mature convective region, trailing precipitation area, and the postline rainband of the 19 May 1977 squall line. This is valid for areas near mature convection within the squall line. The four regions of this squall line are labeled. Streamlines trace the wind flow. Solid lines are reflectivity (from Kessinger *et al.*, 1987).

vection, mature convection, stratiform precipitation, and a postline rainband. The preline convection region consisted of new cells ahead of the squall line that gradually flowed back (relative to the squall line motion) into the main squall line. The mature convection region was about 35 km wide and consisted of both strong updrafts and downdrafts. The updrafts tilt westward (against the environmental shear) in low and mid-levels, and towards the east at higher levels. The stratiform precipitation region was about 35 km wide and mesoscale ascent occurred above 5 km, with descent below 5 km. Weak rear inflow occurred at mid-levels. The postline rainband was observed approximately 30 km to the rear of the stratiform region. Hane *et al.* (1987) also did a numerical modelling study of this case, discussed in Section 2.2.

Johnson and Hamilton (1988) did a detailed observational analysis of a squall line that occurred during the Oklahoma-Kansas Preliminary Regional Experiment for STORM-Central (OK PRE-STORM). They analyzed the surface pressure perturbations associated

with the storm (the presquall mesolow, squall mesohigh, and the wake low) and a rear inflow jet. They determined that subsidence warming in the descending rear inflow jet in the anvil region caused the wake low. The surface pressure in the wake low region was at a minimum where there was not yet enough evaporative cooling to offset the warming. Figure 2.15 is their schematic of the wake low region and also of the surface pressure perturbations associated with the wake low.

Schmidt and Cotton (1989) analyzed a northern plains squall line from the 1981 Cooperative Convective Precipitation Experiment (CCOPE). They developed a three-dimensional schematic of the storm flow (Fig. 2.16), and emphasized the inaccuracies of a two-dimensional flow assumption. They found that the three-dimensional trajectories were quite different from what might be assumed from a two-dimensional cross section. For example, a rear inflow jet appeared to descend to the leading convective line in two-dimensional cross sections but with three-dimensional trajectories it was apparent that this air turned and exited to the rear of the system. They also found that the strong winds behind the convective band of the system were a result of acceleration caused by a mesohigh-mesolow pressure couplet. This was also a case in which the surface air was very stable (similar to Carbone *et al.*, 1990), which may have been a factor in the different behavior of this system.

Carbone *et al.* (1990) investigated the initiation and forcing of a nocturnal squall line. The nocturnal squall line actually developed as secondary convection when a southward propagating outflow boundary from earlier convection collided with a separate northward propagating boundary. The southward moving gust front seemed to propagate initially as a gravity current until it collided with a deeper stable boundary layer to the east of a dryline. Carbone *et al.* hypothesized that the gust front propagated as an internal undular bore beyond that point (Fig. 2.17), until it collided with the northward moving boundary and forced the new convection.

Briefly summarizing the observational studies of squall lines, many investigators have diagnosed a rearward-tilting main convective updraft (Ogura and Liou, 1980; Smull and

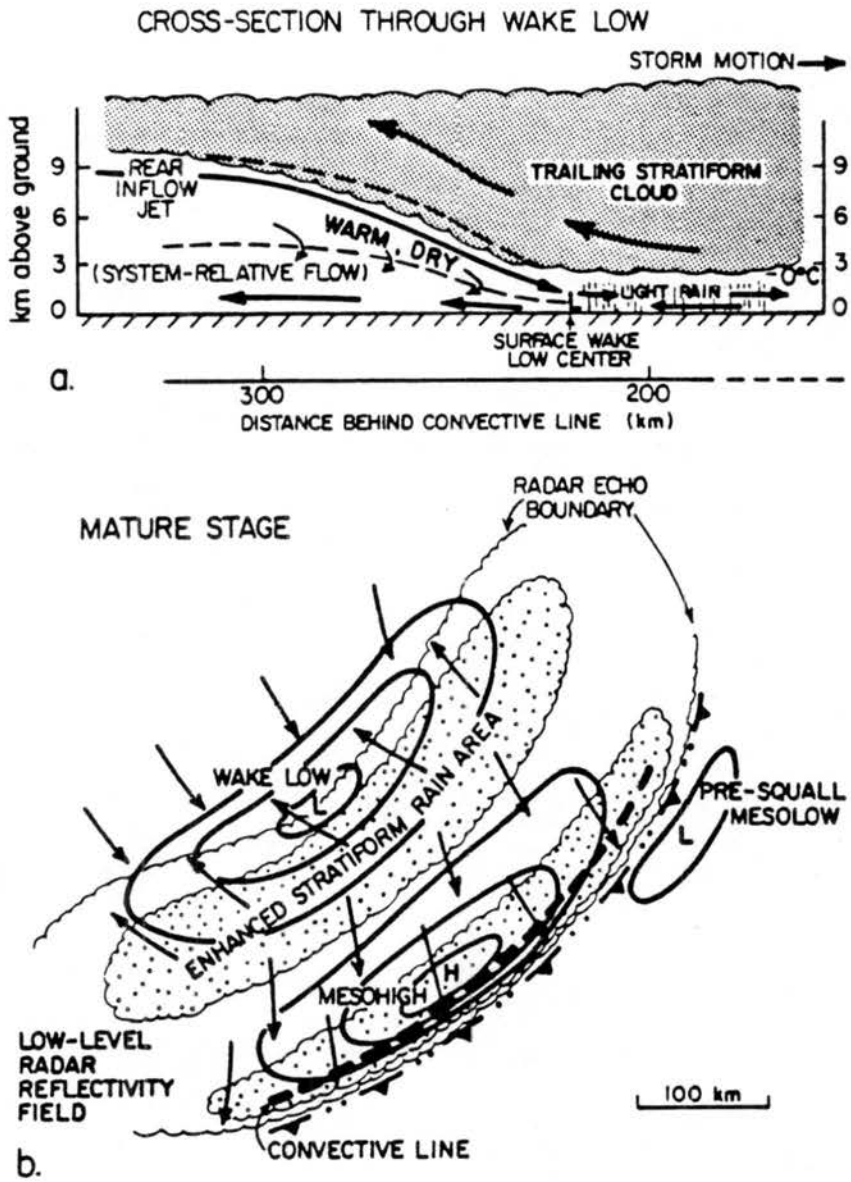

Figure 2.15: Schematic cross section through (a) wake low; and (b) surface pressure and wind fields and precipitation distribution during squall line mature stage. Winds in (a) are system-relative with the dashed line denoting zero relative wind. Arrows indicate streamlines, not trajectories, with those in (b) representing actual winds. Note that horizontal scales differ in the two schematics (from Johnson and Hamilton, 1988).

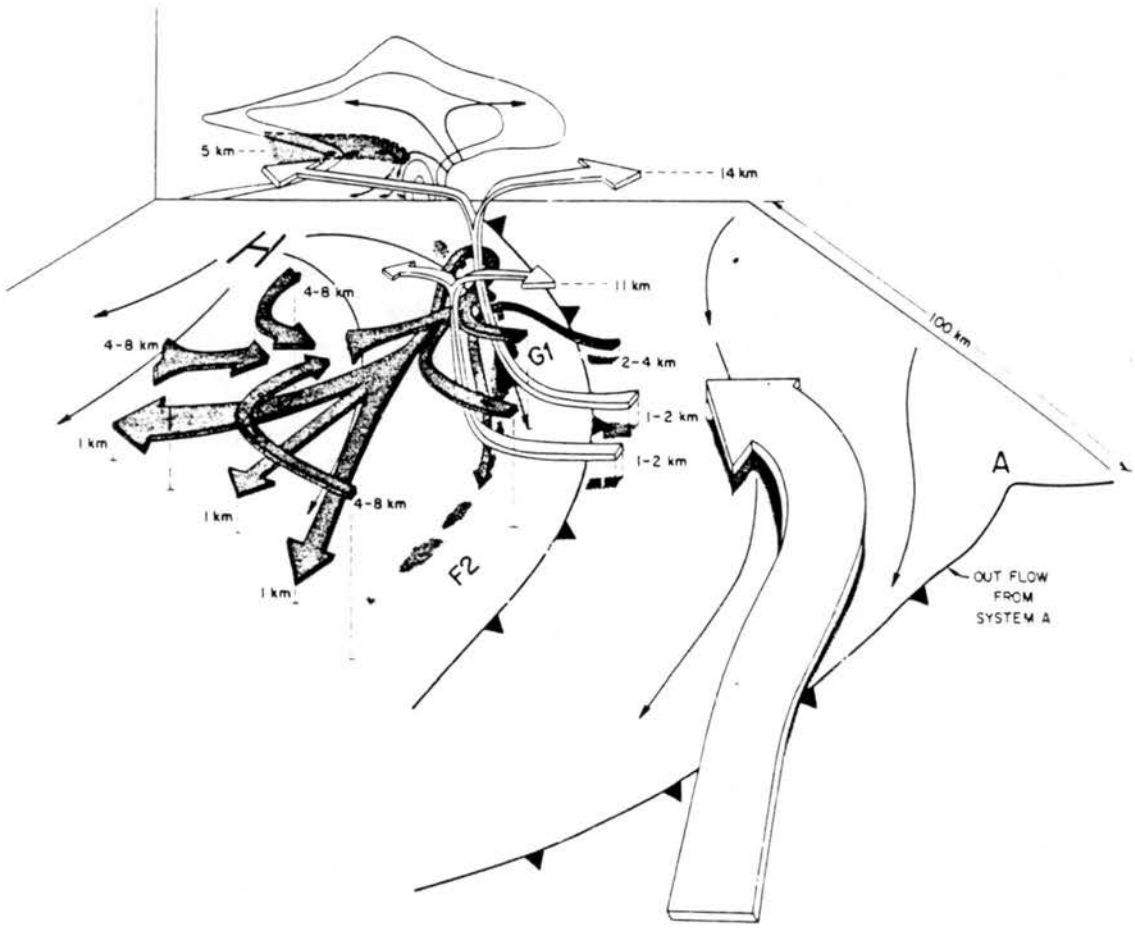

Figure 2.16: Schematic depiction summarizing the 2-D and 3-D flow features for the 2 August 1981 CCOPE squall line showing mesoscale outflow boundaries, surface streamlines (thin arrows), convective reflectivity structure (stippled), overriding flow (bold arrow), and storm relative flow (thin ribbons). The vertical cross section corresponds to a representative depiction of the storm core G1 and shows reflectivity (thin sold lines), schematic storm relative flow (thin arrows) and location of the middle-level upshear inflow (shaded). G1 and F2 represent the cell groups along the squall line and the bold H represents the location of the surface mesohigh. Labeling of the storm relative flow ribbons refers to height AGL (from Schmidt and Cotton, 1989).

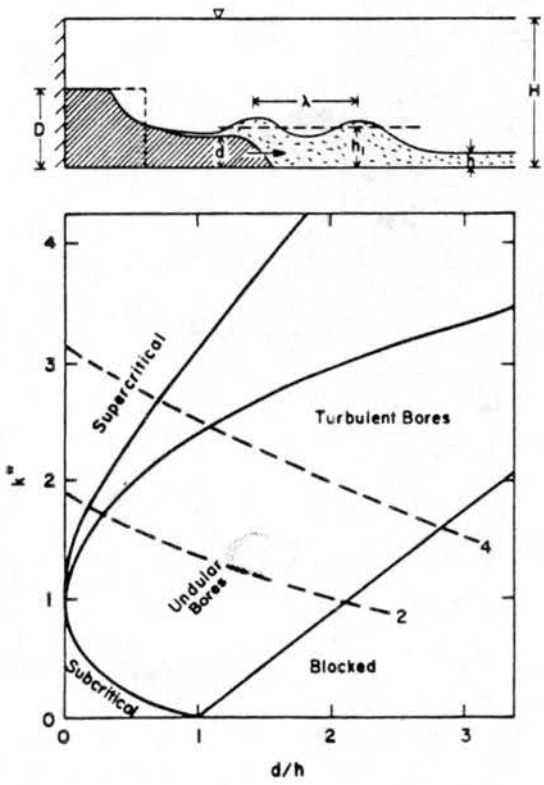

Figure 2.17: Speed of internal bores generated by gravity currents in the laboratory. Speed is nondimensionalized as the internal Froude number $k^* = U/(g'h)^{-0.5}$ where g' is $g(\Delta\rho/\rho$; d is depth of the gravity current and h is the depth of the undisturbed dense layer. Dashed lines refer to undular bore magnitude. Conditions for this case study are shown by the shaded area (from Carbone *et al.*, 1990).

Houze, 1985, 1987; Kessinger *et al.*, 1987). Mesoscale surface features associated with squall lines include a presquall mesolow, the squall mesohigh, and a wake low. The wake low seems to be caused by subsiding air in the rear-inflow jet (Johnson and Hamilton, 1988) while the presquall mesolow and squall mesohigh are thought to be caused by preline subsidence (adiabatic warming) and mesoscale ascent (adiabatic cooling), respectively. The environment of many squall lines (as opposed to supercell-type storms) exhibits weak vertical shear, with most of the shear concentrated in lower levels (Bluestein and Jain, 1985).

2.2 Modelling and Theoretical Studies of Squall Lines

Various modeling and theoretical studies of squall lines will be reviewed and discussed in this section. Both two- and three-dimensional models have been used to simulate squall lines, and the validity of two versus three dimensions in the modelling of squall lines has been debated by several investigators. Several different scales of squall line development have been studied (from the synoptic scale to the meso γ scale), and several different theoretical approaches have been employed (gust front forcing, wave-CISK, solitary waves). Finally, numerous sensitivity studies have been completed on the effects of varying atmospheric stabilities and vertical wind profiles to squall line development and propagation.

Takeda (1971) was one of the first to attempt to numerically model convection. He used a two-dimensional model with a domain size of 50 km and a grid spacing of 1 km. Cloud physical processes were included in the model through prognostic equations for seven size distributions of water drops, and included condensation, evaporation, coagulation, breaking, and terminal fall velocity of the water drops. Ice processes were not included. The effects of different vertical shear profiles on convection were investigated. In weak shear environments, new convection formed due to cold downdrafts and outflow from previous convection. In environments of strong constant vertical shear the convection leaned downshear and was short-lived. The formation of long-lived convection resulted from strong shear in a low layer, opposite in direction to that aloft. The convection then

leaned in the direction of the low level shear, and the downdraft and inflow air were on opposite sides of the cloud and thus did not interfere with each other.

Hane (1973) used a two-dimensional model with a 400 m grid spacing in both the vertical and horizontal directions, and explicit prediction of water vapor, cloud water, and liquid water mixing ratios. Radiative and surface processes were not included in the model. The purpose of his experiments was to test the effect of various shear profiles on the maintenance and propagation of the squall line. In general, Hane found that stronger shear resulted in faster-moving, more intense, and longer lasting systems. He interpreted this as because the stronger shear systems propagated faster and thus had a stronger relative inflow of low-level warm, moist air. The simulated updraft tilted upshear, except in the stronger shear cases where they tilted downshear at the top. Hane initiated the simulations with a "well-developed thunderstorm-like" circulation, and never was able to develop a sustained steady-state updraft. He attributed the pulsing, or lack of steady-state, to the two-dimensional aspect of the simulations: 1) the downdraft air is forced in his simulations to spread forward or back, not sideways at all; 2) the upper level rear-to-front flow is all forced to go through the cloud (not around it at all) because of the two-dimensionality; and 3) the downdrafts are forced to balance the updrafts in the two-dimensional cloud planes, alone.

Moncrieff and Miller (1976) developed both analytical and numerical models of a tropical cumulonimbus in an attempt to calculate propagation speed and outflow characteristics of a tropical squall line. They developed a schematic of a tropical cumulonimbus (Fig. 2.18) and noted that the flow must be three-dimensional. Despite the limited domain of their numerical model (only 30×30×9 points) Moncrieff and Miller were able to simulate a discretely propagating series of cells. As each cell decayed it produced a strong downdraft and density current, which in turn generated convergence and new cells. They found that the propagation speed of the cells was a function of the convective available potential energy (CAPE), where CAPE is a measure of the difference between the potential temperature profile of the rising parcel and the undisturbed environment.

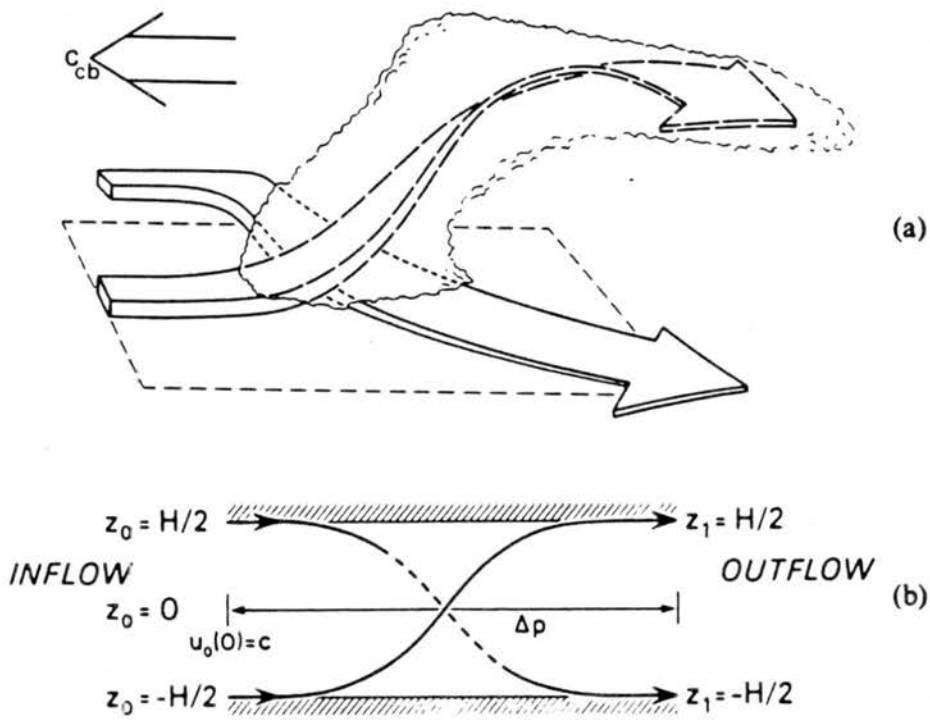

Figure 2.18: (a) Schematic of a propagating cumulonimbus. (b) Limiting relative streamlines in the analytic model. On inflow, the velocity profile $U_0 = u_0 - c$, the static stability, and the parcel lapse rate are specified as a function of the inflow level z_0 but c is calculated. On outflow, for each streamline passing through z_0, the values of $z_1(z_0), U_1(z_0)$ and $\phi_1(z_0)$ are calculated, where $-H/2 \leq z_0 \leq H/2$ (from Moncrieff and Miller, 1976).

Ley and Peltier (1978) used an analytic model to investigate the idea that a packet of internal gravity waves could be generated by a cold front, and then produce a pressure minima and region of horizontal convergence approximately 75 – 100 km ahead of the cold front. They hypothesized that such a wave packet could be responsible for the initiation and propagation of a prefrontal squall line. They found that gravity waves could be emitted as a result of the geostrophic adjustment process along a strengthening front. The waves emitted by the front in their analytic model had a group velocity of 6 m s^{-1}, significantly less than similarly observed wave speeds of 13 m s^{-1}. However, their simple model assumed cross-front geostrophic balance and had a very simple temperature structure. They note that the thermodynamic structure and the possibility of wave ducting can have a significant effect on the propagation speeds of internal gravity waves.

Thorpe, Miller, and Moncrieff (1982) (TMM) used a two-dimensional model to investigate squall line development and propagation. They noted that while tropical squall lines and cumulonimbus were inherently three-dimensional, as in Moncrieff and Miller's (1976) schematic, their mid-latitude counterparts may be more two-dimensional. In order to maintain steady convection in two dimensions, TMM found that both non-constant shear and a shallow (vs. deep) downdraft were required. Figure 2.19 is an idealized schematic of their modelled flow. The non-constant shear (most of the shear in low levels) forced the shallower downdraft, and allowed the system to tilt upshear, thus allowing constructive interference of the updrafts and downdrafts. Constant shear and a deep downshaft resulted in a downshear-tilting updraft which was consequently cut off by the downdraft air. The use of non-constant shear allowed mid level air to enter the storm and feed the downdraft. Tropical cumulonimbi and squall lines typically only have air entering from the forward side and with constant shear. This implies that these storms must be three-dimensional if they are to reach any sort of steady state, as noted by both Moncrieff and Miller (1976) and TMM (1982).

Chang *et al.* (1981) used a three-dimensional numerical model to simulate the 6 May 1975 Omaha squall line with grid spacings of 140 and 35 km. This squall line developed

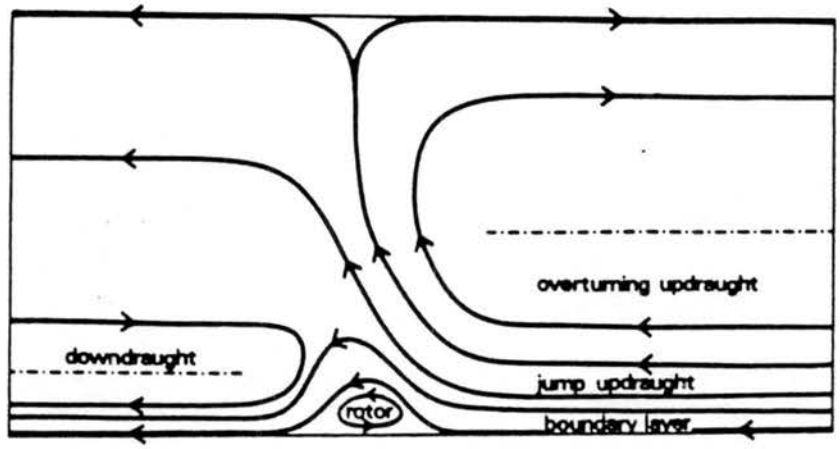

Figure 2.19: Conceptual model of squall line with individual flows labelled (from Thorpe *et al.*, 1982).

from convergence into a northward extending tongue of warm, moist air and, both in their numerical simulations and in reality, was relatively short-lived as it quickly used up its available supply of warm, moist air. At the same time the latent heat release in the upper troposphere stabilized the lower troposphere and decreased the mesoscale ascent and convergence. The emphasis for this study was on the large-scale forcing and characteristics of the squall line. Aspects such as internal dynamics and updraft tilt were not addressed.

Seitter and Kuo (1983) were interested specifically in the development of the upshear-tilting updraft in extra-tropical squall line type thunderstorms. As they point out, the idea that the upshear tilt was caused by conservation of horizontal momentum has not been verified in numerical models. Many numerical models had been unable to develop or sustain an upshear-tilting updraft. Seitter and Kuo proposed that an upshear-tilted updraft was maintained by differential erosion of the downdraft side of the updraft. The erosion occurred at the interface of the downdraft and updraft, and was greater at lower levels because of the larger concentrations of liquid water. A stable balance is eventually established for a certain updraft slope between the water loading mechanism and the environmental shear. They were able to simulate this effect in a two-dimensional model

with constant vertical shear, although it is not clear whether their simulated systems were quasi-steady at all. They attribute the non-steadiness to the two-dimensionality of the model. However, they also attribute part of the subsidence upshear of the updraft to the blocking effect of the updraft, which may again be a result of the two-dimensionality of their model.

Raymond (1984) used a wave-CISK model to simulate both tropical and mid-latitude squall lines. An initial advecting mode (moving at the environmental wind speed) produces a region of convection. The collapse of this initial convection forces two oppositely-moving propagating modes. The rightward moving mode moves downshear, as normally seen with squall lines. The streamlines associated with this mode are reasonable and agree well with the diagnosed streamlines of Ogura and Liou (1980) (Fig. 2.20). Raymond hypothesizes

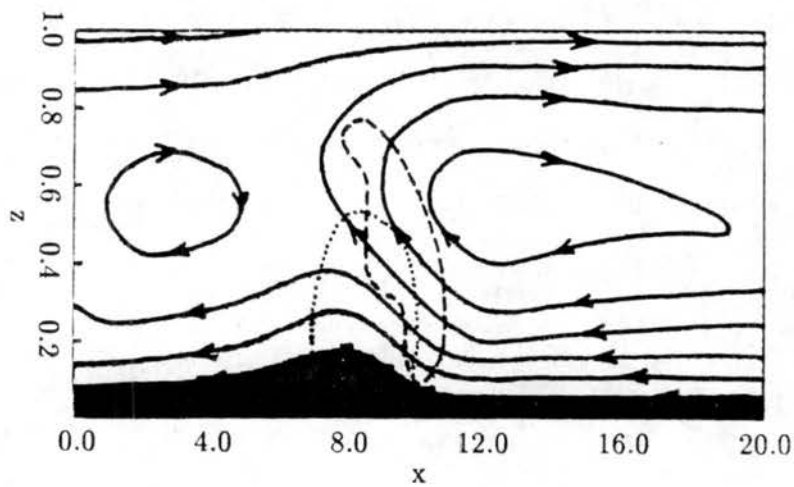

Figure 2.20: Streamlines for the rightward moving disturbance at $t = 100$. The streamfunction is calculated relative to the disturbance, which is assumed to move at a dimensionless speed of 0.1. The dashed and dotted lines, respectively, show the 30% contours of updraft and downdraft mass flux. The downdraft is clearly fed from the front, or right side of the squall line (from Raymond, 1984).

that the spurious left-ward moving mode is maintained in his model because of the inability of the wave-CISK convective parameterization to include mid-level ventilation effects. These effects would tend to destroy the left-ward, up-stream moving mode. Raymond's work, and that of other wave-CISK investigators, is reviewed more thoroughly in Section 2.4.

Orlanski and Ross (1977, 1984, 1986) and Ross and Orlanski (1982) have used a three-dimensional numerical model and simple analytic two-layer model to investigate the evolution of fronts and squall lines. They studied a case where a squall line developed intermittently parallel to, and ahead of, a springtime cold front over the southeastern United States. Their simulated squall line developed along the front; it is not clear from their paper whether the squall line then moved out ahead of the front, or the front and squall line remained together. They described the squall line as a solitary wave, which develops from a gravitational mode in an unstable layer. The initial convective cell excites a gravity wave in a lower stable layer. This gravity wave speed must match the phase speed of the unstable cell in the upper layer for the squall line to persist. The convective region must also have the physical structure and propagation speed of a solitary wave in the surrounding stable environment. This means that the speed of the system must be similar to the group velocity of a solitary wave, and secondly, that the aspect ratio should indicate a non-dispersive wave. If the wavelength is too short, or too long, it will be dispersive. Orlanski and Ross define these aspect ratio limits as

$$\frac{f}{N} << \frac{H}{L} << 1$$

where $N^2 = \frac{g}{\theta}\frac{\partial \theta}{\partial z}$, f is the coriolis force, H is the wave amplitude, and L is the wavelength. A typical height H for a convective system of 10 km, and f and N of 10^{-4} and 10^{-2} s^{-1} yield

$$10 \text{ km} << L << 1000 \text{ km}$$

Bolton (1984) also developed a simple linear model of the development of a squall line as the constructive interferences of normal modes of an unstably stratified shear flow. The results with a mid-level wind speed maximum (a jet) are similar to the tropical squall lines in that the convection moves slightly faster than the maximum flow speed. The results with unidirectional shear are similar to mid-latitude squall lines in that the line of cells moves at the mid-level mean flow speed.

Hane *et al.* (1987) did a modelling study of the squall line analyzed by Kessinger *et al.* (1987). They used a numerical model with a horizontal grid spacing of 400 m and found that the preline cells (as described by Kessinger *et al.*, 1987) formed in a region of enhanced convergence at the head of the gust front, with periodic surges of vertical motion traveling westward (back towards the main line) above the cold outflow air. They hypothesized that these perturbations could be Kelvin-Helmholtz billows propagating back along the upshear-propagating (upshear in the low levels) gust front outflow air.

Nicholls (1987), Nicholls and Weissbluth (1988), and Nicholls *et al.* (1988) have done several numerical modelling studies of tropical squall lines. Nicholls (1987) used a two-dimensional version of the CSU RAMS model with a 500 m horizontal grid spacing. He noted that shallow clouds frequently formed a considerable distance ahead of the density current head, and were subsequently uplifted when the gust front reached them. The formation of these shallow clouds seem to be caused by faster-moving gravity waves moving ahead of the system. Nicholls developed a simple schematic to illustrate the response of the atmosphere to a warm system caused by latent heat release (Fig. 2.21). The mid-

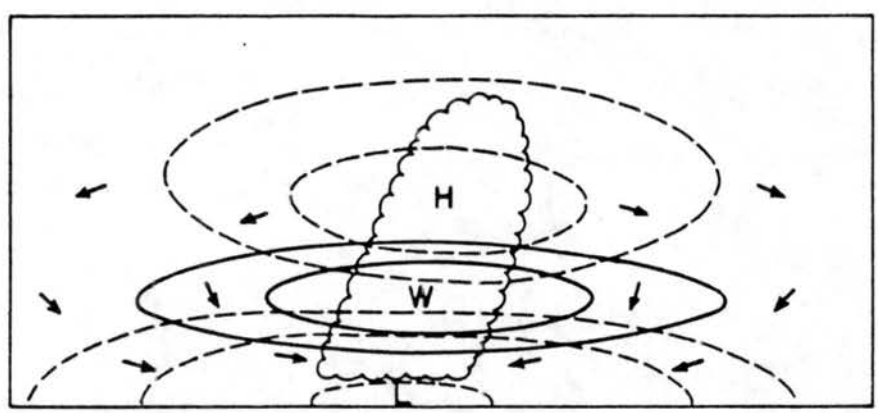

Figure 2.21: A schematic illustrating the temperature, pressure, and accelerations due to latent heat release (from Nicholls, 1987).

level warming caused higher pressures aloft and lower pressures below, and the required compensating subsidence circulation both ahead and behind the squall line. Nicholls and

Weissbluth (1988) compared two- and three-dimensional simulations of a tropical squall line. They did not find any major differences between the two- and three-dimensional simulations, concluding that two-dimensional simulations of tropical squall lines were an economical and realistic alternative. They did note several differences between their simulations and the two and three-dimensional simulations of Rotunno *et al.* (1988). Nicholls and Weissbluth found that they were unable to replicate the discretely propagating cell process and oscillating growth/decay mode as was simulated by Rotunno *et al.* They speculate that the differences could be due to initial sounding and wind profile differences. Nicholls *et al.* (1988) did a series of two-dimensional numerical simulations of squall lines with varying initial wind and thermodynamic profiles. They found that an increase in total buoyancy produced a stronger cold pool and gust front, and a resulting greater tilt to the updraft. The development of an upshear tilt to the main updraft, and the consequent strength and longevity of the system is closely related to the development of the cold pool.

Rotunno *et al.* (1988) investigated the issue of whether a squall line is a system of long-lived super-cells or a long-lived system of short-lived ordinary cells. They found that shallow shear oriented perpendicular to the squall line resulted in a system of short-lived cells, while deep shear at an angle to the line resulted in a line of supercells. Their shallow-shear result is similar to the conclusion from TMM that low-level shear perpendicular to the squall line promotes a long-lived system. Rotunno *et al.* argued that it was the interaction of the vorticity produced by the low-level wind shear, and that produced by the spreading of the cold pool that sustained a cell (Fig. 2.22). Contrary to the conclusions of many previous investigators, they maintained that the tilt of the updraft is not important to the longevity of the squall line. However, recent observational radar studies have shown rearward-tilting updrafts in squall lines, especially in the low-to-mid levels (Smull and Houze, 1985, 1987; Kessinger *et al.*, 1987). Rotunno *et al.* maintain that upshear tilt is more important to the longevity of a single-cell system which is a supercell. The interaction of the cold pool and a specific optimum value of low-level shear can result in an "optimal" erect updraft. This cell weakens as the cold pool becomes

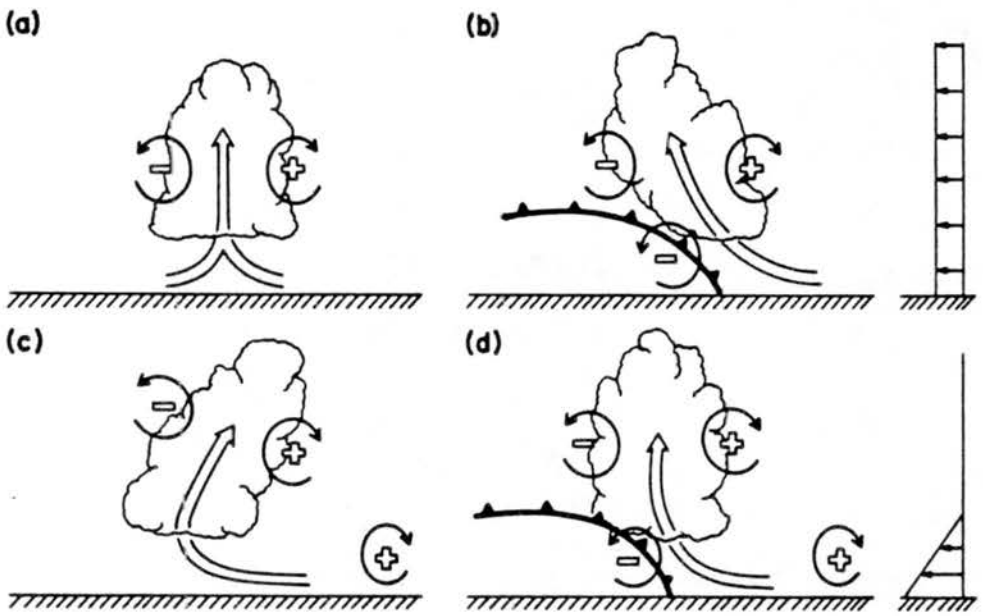

Figure 2.22: Schematic diagram showing how a buoyant updraft may be influenced by wind shear and/or a cold pool. (a) With no shear and no cold pool, the axis of the updraft produced by the thermally created, symmetric vorticity distribution is vertical. (b) With a cold pool, the distribution is biased by the negative vorticity of the underlying cold pool and causes the updraft to lean upshear. (c) With shear, the distribution is biased toward positive vorticity and this causes the updraft to lean back over the cold pool. (d) With both a cold pool and shear, the two effects may negate each other and allow an erect updraft (from Rotunno *et al.*, 1988).

stronger and no longer balances the low-level shear. The updraft then tilts downshear over the cold pool and weakens. New updrafts are initiated along the leading edge of the cold pool, resulting in a discretely propagating system. Pielke *et al.* (1990) found a similar mechanism of discrete propagation, or the formation of secondary convection, from the convergence forced by the generation of a cooler boundary layer from downdrafts under cumulonimbus.

Crook and Moncrieff (1988) maintained that large scale convergence was one of the most important factors in generating and maintaining squall line-like convection, in contrast to others' emphases on the importance of the cold pool (Thorpe *et al.*, 1982; Nicholls *et al.*, 1988; Rotunno *et al.*, 1988). Two-dimensional numerical simulations with a horizontal grid spacing of 1 km established the sensitivity of the convection to both the intensity and scale of preexisting large-scale convergence. The large-scale convergence served to bring the convective environment to a state of conditional instability, close to saturation. New convection formed ahead of the main squall line convection as a result of transient features propagating out ahead of the convection in the conditionally unstable environment, not as a result of a propagating gust front/density current. Crook and Moncrieff emphasize that the mechanisms important to the generation, maintenance, and propagation of convection in an environment of large-scale convergence can be very different than the mechanisms in an environment where the large-scale vertical motion does not exist and the convection is initiated by the warm bubble technique. This idea is also applicable to the difference between the upscale generation of convection from very small scales in horizontally-homogeneous fine resolution (grid spacings on the order of 1 km) numerical models (such as by a warm bubble) and the downscale generation (due to convergence) of convection in coarser resolution (grid spacings on the order of 20 km or larger) models with horizontally-varying initial fields. Crook and Moncrieff also state that the convective intensity is sensitive to the scale of the large-scale convergence.

Investigators at Pennsylvania State University (PSU) and the National Center for Atmospheric Research (NCAR) have published several papers on modeling studies using

the PSU-NCAR model that apply to this work. Their work is especially pertinent to this study because: a) they have also been interested in the model development of meso-β scale features from meso-α or longer scale initial conditions, b) they have simulated at least two different squall lines cases with their model, and c) they have used their model to do some of the finest resolution, nested grid, meso-α scale simulations in the literature.

Zhang and Fritsch (1986) used the PSU model to study the 1977 Johnstown Flood case. They used a coarse grid spacing of 75 km and a fine-grid spacing of 25 km. The model included the Fritsch and Chappell (1980a) and Anthes/Kuo (Anthes and Keyser, 1979) cumulus parameterization schemes (Fritsch-Chappell on the fine grid, Anthes-Kuo on the coarse grid) as well as grid scale precipitation process. Their model was initialized using the National Meteorological Center's (NMC) spectral model analyses as a first guess, enhanced with available soundings. The model simulated many of the observed meso-β scale features of the case, including the surface pressure perturbations associated with the development and movement of the mesoscale convective complex (MCC) and squall line. In their case the squall line seemed to separate from the MCC and moved eastward. They note that the convection was initiated some distance behind the trough axis, and speculate that it may have been excited by internal gravity waves emanating from the squall line. Overall, their results were very encouraging because of their success in simulating many meso-β scale features from a much larger scale initial analysis.

Zhang and Fritsch (1987, 1988a,b) further used the PSU-NCAR model to investigate the Johnstown flood case. An important conclusion from the latter two papers was the importance of the grid-resolvable precipitation processes to the system development, as well as the parameterized convective processes. They found that resolvable-scale condensation resulted in approximately 30-40% of the predicted precipitation for this case. However, they emphasized that the parameterized convection, and its higher level heating, is instrumental in creating the dynamic and thermodynamic conditions to force the lower-level, grid-resolvable condensation. They found that the deep convection helped generate a near-saturated, moist adiabatic atmosphere that then resulted in a positive

feedback between the lower (mid-to-low levels) grid-resolvable condensational heating and the low-level mass and moisture convergences (i.e., a CISK-like process).

Zhang *et al.* (1988) further investigated the importance of grid resolvable, or explicit, condensation and precipitation vs. parameterized convection, or implicit, processes. Basically, they found that both explicit and implicit processes were needed for a successful simulation, even on scales down to 10 km. In the Johnstown flood case convective processes appear to be responsible for the development of the squall line while the grid-resolvable, larger scale ascent processes are responsible for the development of the meso-vortex and stratiform rainfall. It is worrisome that they found that a convective parameterization scheme is necessary even with grid spacings on the order of 10 km, as most convective parameterization schemes are generally designed with grid scales of 50-400 km in mind. The problem is that a 10 km grid spacing is still too large to explicitly model convective motions, but it is also small enough that a 10 km square box will represent only a part of the system (such as the strong updrafts, or part of the anvil region) and thus may not be well represented by a general convective parameterization scheme.

Zhang and Fritsch (1988b) studied the interaction between a model-simulated squall line and internal gravity waves, again with the Johnstown flood case. Their observations show a wave front (pressure wave) moving ahead of, and faster than the squall line (outflow boundary) (Fig. 2.23). They suggested that the squall line and gravity wave may have evolved simultaneously, but as the gravity wave propagated farther ahead of the squall line it eventually reached a destructive interference position and contributed to the weakening and dissipation of the squall line. They analyze an internal gravity wave in their simulation with a wavelength of 250-300 km and a speed of 25-30 m s^{-1}, propagating outward from a warm core mesovortex. The orientation of the gravity waves troughs and ridges constructively interferes with the northern part of the simulated squall line but destructively interferes with the southern part of the squall line. This coincides with the dissipation of the southern end of the squall line. They suggest that the subsidence warming by the propagating gravity wave is responsible for the generation of the pressure

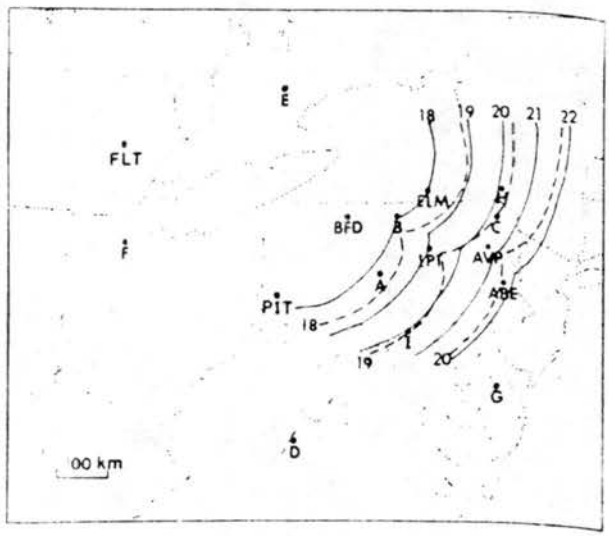

Figure 2.23: Hourly (UTC) position of the outflow boundary (solid lines) associated with the squall line, and the analyzed wave front (dashed lines). Large dots indicate locations of surface stations (standard three-letter code) and model grid points (single letters) (from Zhang and Fritsch, 1988b).

trough ahead of the squall line. Overall, they concluded that both the "locked phase" aspect of the speed of the convection and gravity wave propagation, and the necessity of the similar time scales for the gravity wave forcing and initial convective triggering are important for an overall constructive interference of convection and gravity waves.

Finally, Zhang *et al.* (1989) and Zhang and Gao (1989) used the PSU-NCAR model to simulate a PRE-STORM squall line case. They used the NMC 2.5° gridded analyses enhanced with the standard rawinsonde soundings and available surface data. As in previous studies, they used a coarse grid spacing of 75 km and a fine grid spacing of 25 km. Starting from these meso-α and larger scale initial conditions, they were able to reproduce many of the meso-β scale features associated with the squall line, including the presquall mesolow, the squall mesohigh, and the wake low, as analyzed by Johnson and Hamilton (1988). Zhang and Gao (1989) extensively analyzed the descending rear-inflow jet and the related wake low. Their results were very encouraging in that they were apparently able to simulate many of the complex meso-β scale features of the squall

line system starting from relatively coarse initial conditions. Anthes *et al.* (1982) had questioned whether a mesoscale model would be capable of developing mesoscale and sub-synoptic scale features from initial conditions estimated only from synoptic scale data. Their results however, and those from Zhang *et al.* and Zhang and Gao indicate that, at least in certain conditions, the sub-synoptic scale features can be accurately simulated when only larger scale data is available for the initial conditions.

Lafore and Moncrieff (1989) did a series of two-dimensional numerical simulations of tropical squall lines. They developed a schematic of the squall line (Fig. 2.24) with primarily front-to-rear flow. They emphasized that the squall longevity was dependent upon the larger scale interactions of the convective and stratiform regions, not just the convective scale interactions of the cold pool and low-level shear (the latter hypothesized by Thorpe *et al.*, 1982 and Rotunno *et al.*, 1988). Lafore and Moncrieff (1990) and Schmidt and Cotton (1990) point out that the low-level shear ahead of the gust front may be modified by the squall line, and thus that this modified shear should be considered when determining the balance of the vorticities produced by the low-level shear and cold pool.

Tripoli and Cotton (1989a,b) used a numerical model to study the development and propagation of an orographically-forced line of convection. The convection (a north-south oriented line of convection) initially developed over the foothills just east of the Rocky Mountains in Colorado and moved eastward. It initially weakened as it moved out over the plains and then redeveloped. As it moved farther eastward new convection developed ahead of it and the convection evolved from the linear structure to a more classical MCC shape. They used a two-dimensional model with a very fine resolution (1.08 km horizontal grid spacing) to try to resolve the different scales important to the development and propagation of the squall line. In their simulation the deep convection initially developed in the upward branch of the mountain-plains solenoid. The system intensified and drifted eastward. The convection was suppressed and collapsed as it moved across the region where the topography slope changed from the mountains to the plains. This change in

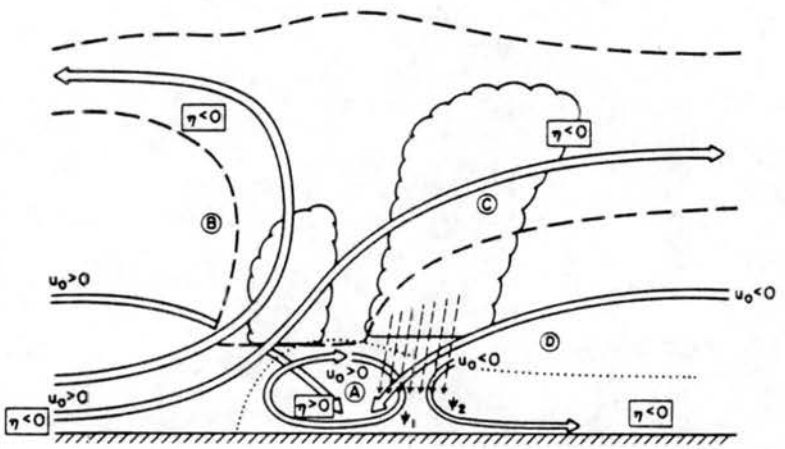

Figure 2.24: Schematic of the relative flow and vorticity in a squall line system consisting of an unsteady convective region and a quasi-steady mesoscale region. Region A: the rotor with predominately positive vorticity and positive vorticity generation; region B: the overturning updraft; region C: the propagating updraft; region D: the mesoscale descent. The unsteady inflow to the downdraft, the rotor, and the rearward-moving convective-scale downdraft outflow are maintained by evaporative cooling and water-loading. The outlines of convective cells are shown by scalloped lines, the envelope of the cell aggregate representing the mesoscale system by the broken lines and the outline of the density current by the dotted lines, respectively (from Lafore and Moncrieff, 1989).

slope results in a downward branch of the mountain-plains solenoid which suppresses the convection (Dirks, 1969). As the convection moves further eastward it reintensifies, but seems to collapse and redevelop every two hours. Every time that the convection collapses, oppositely propagating gravity waves (oppositely propagating in the east-west plane) are generated which move outward and upward. The convection moves eastward as the western edge of the low-level capping inversion is progressively eroded by the solenoidally-forced convection. Tripoli and Cotton speculate that, without the inversion, the system would probably move eastward more rapidly as the gravity waves initiated new convection, and would also probably retain less of its mesoscale, line-like organization. After sunset the anvil top cools radiatively, resulting in an initial growth of the updraft followed by a breakdown as the surface cools. A very interesting result was that the destabilization of the anvil resulted in the trapping and horizontal ducting of the gravity waves emitted by the collapsing system. As the gravity waves were forced horizontally they initiated new convection in a much larger area. This stage may represent the transition from the line-like structure to the more classical MCC structure. The outward-moving gravity waves had wavelengths on the order of 160 – 240 km and speeds of approximately 30 m s^{-1}. This speed corresponds to that of the deepest internal wave in the modelled troposphere.

Tripoli and Cotton (1989a,b) also investigated the effects of the use of coarser resolutions and the use of a convective parameterization in the numerical simulation. The convective parameterization seemed to improperly couple the convection to the meso-β scale propagating gravity waves. However, that may have been due to an improper choice of the "threshold" vertical motion used to initiate the cumulus parameterization. In the original simulation the convection was confined to the meso-α scale solenoidal updraft and the low-level inversion prevented the transient meso-β scale waves from initiating convection. The squall line simulated in this study (17-18 June 1978) displayed several observational characteristics of gravity wave propagation, although in this case (as contrasted to the Tripoli and Cotton case) the convection does appear to be linked to the gravity wave propagation.

Schmidt and Cotton (1990) also linked gravity wave propagation to squall line structure and maintenance. They used a two-dimensional numerical model, with a horizontal grid spacing of 2 km, and experimented with the effects of various soundings on the development and maintenance of a squall line. Their model atmosphere had three distinct layers in the vertical: a low-level stable boundary layer; a mid-tropospheric, nearly dry-adiabatic layer; and an upper tropospheric layer of intermediate stability. The winds varied from east-northeasterly within the stable boundary layer to westerly aloft. This was a case with strong shear throughout the troposphere, above very stable surface air. The squall line was initialized with a warm bubble. Basically they found that the bubble initiated outward-propagating gravity waves in the low-level boundary layer and also in the upper stable layer. With no atmospheric winds, the lower level waves had speeds of ± 19 m s^{-1} while the upper waves had speeds of ± 30 m s^{-1}. The addition of vertical wind shear altered the phase speed and magnitudes of the four waves, and a particular shear (close to that observed) resulted in the super-position of the rightward moving lower wave and the leftward moving upper wave. The trapping of gravity waves is a function of both low-level static stability and vertical shear. The middle layer of low stability only partially traps the upward propagation of the lower layer waves and the downward propagation of the upper layer waves. The increase in shear further increases the trapping, especially for the lower layer waves. The upper layer waves are still free to propagate upward and away. In this case the gravity wave propagation was tied to the convective propagation. This was not the case in Tripoli and Cotton (1989a,b), although outward propagating gravity waves were also evident in their simulations. Schmidt and Cotton also hypothesized that the air parcels in the rear-to-front mid-level jet were influenced by the squall-line-caused temperature and pressure perturbations in the upper troposphere and lower stratosphere. A cold perturbation at the tropopause and in the lower stratosphere hydrostatically resulted in a pressure high in the upper troposphere, and had a downward and forward channeling effect on the upper level rear inflow. Schmidt and Cotton also noted that the squall line

can produce perturbations to the environmental shear and thermodynamic profiles that significantly alter the environmental characteristics.

Crook *et al.* (1990) used a numerical model to more closely examine the mechanisms behind the development of the nocturnal squall line discussed by Carbone *et al.* (1990). The squall line seemed to develop as a result of the collision of two outflow boundaries from earlier convection. Carbone *et al.* had hypothesized that the southward moving outflow boundary or gust front propagated as an internal undular bore after it crossed a dryline and encountered a deeper, more stable boundary layer. Crook *et al.* investigated three possible mechanisms that could have caused the regeneration of the convection (the squall line generation) along the old outflow boundary: an increase in low-level moisture, an increase in low-level wind shear, and a mesoscale oscillation forced by the first system (Fig. 2.25). As the gust front encountered a region of higher low-level moisture content, the level of free convection (LFC) was effectively lowered, resulting in a greater likelihood of convection. Likewise, an increase in low-level shear (also observed by Carbone *et al.*) would also result in an increased likelihood of convection. This mechanism is similar to that proposed by Rotunno *et al.* (1988) where the shear component of vorticity balances the buoyancy-generated component of vorticity. The third mechanism was the result of a mesoscale oscillation in the 600-800 mb layer with a period of approximately 7 hours, similar to that numerically simulated by Tripoli and Cotton (1989a,b). The mesoscale oscillation in Tripoli and Cotton was due to the eastward advection of the mountain-plains solenoid. In their simulations, Crook *et al.* found that the first two mechanisms had the strongest effect on the convective regeneration, although the third mechanism was probably important in determining the exact timing of the regeneration.

Many different modelling studies of squall lines have been reviewed in this section encompassing many different aspects and scales of squall line development and maintenance. Some studies have indicated that squall lines propagate due to gust front convergence (Takeda, 1971; Moncrieff and Miller, 1976; Thorpe *et al.*, 1982; Nicholls *et al.*, 1988; Rotunno *et al.*, 1988; Zhang *et al.*, 1989;), while others have shown several scales

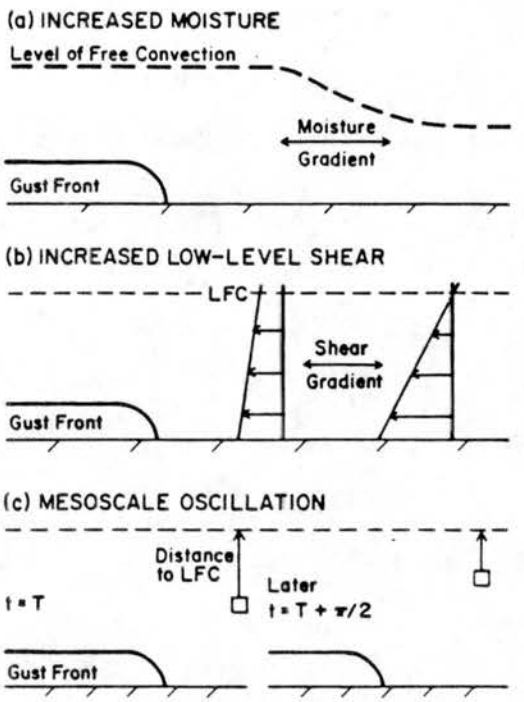

Figure 2.25: Schematic illustration of the three convective regeneration mechanisms. In (c), even though the mesoscale oscillation undoubtedly affects the LFC, it is shown at a fixed position at the two times, T and $T + \pi/2$. The important aspect of this mechanism is that the distance below the LFC changes with time (from Crook *et al.*, 1990).

of gravity wave mechanisms (Ley and Peltier, 1978; Raymond, 1984; Ross and Orlanski, 1982; Orlanski and Ross , 1984, 1986; Hane *et al.*, 1987; Zhang and Fritsch, 1986, 1988b; Schmidt and Cotton, 1990). The squall line in this study (17-18 June 1978) is hypothesized to propagate as an internal gravity wave. Gravity wave and wave-CISK theory will be briefly reviewed in the next two sections.

2.3 Review of Gravity Wave Theory

A brief review of simple gravity wave theory is presented in this section to provide a basis for the discussion of model results in Chapter 5. There seems to be a lot of confusion in terminology in the literature between gravity waves, gravity currents, solitary waves, and bores. Carbone *et al.* (1990) make the distinction between gravity currents, bores, and solitary waves as follows:

> "When low-level stratification is present, then an evolution of phenomena from gravity currents, to turbulent bores, to undular bores, to solitary waves is possible. At the outset, gravity currents represent essentially pure mass transport excepting a small amount of potential energy stored in the elevated wave-like "head" region. Bores and solitons are gravity waves "of elevation" at low-level inversions. These may be induced by lifting from cold pools of the gravity current type. Undular bores retain some of the mass transport characteristics of gravity currents in addition to energy transport by means of wave excitation. Solitary waves, while similar to undular bores, transfer little, if any mass. Solitary waves tend to be identified as distinct entities when farther removed from a source of initial elevation such as cold pools. In a stratified environment, one may view the gravity current-undular bore-solitary wave family as a temporal sequence rooted in gravity current dissipation and energy dispersion."

Simpson (1987) further notes the difference between internal bores and solitary waves as observed at the surface. An internal bore may be characterized by a sudden pressure jump, and then steady pressure, but increased over that previous to the bore so there is a net pressure rise. A solitary wave passage is characterized by a pressure jump (or dip) but there is no net pressure change.

The basic properties of internal gravity waves can be described using a two-dimensional linearized version of the incompressible, Boussinesq equations:

$$\left(\frac{\partial}{\partial t} + U_o\frac{\partial}{\partial x}\right)u' + w'\frac{\partial}{\partial z}U_o + \frac{1}{\rho_o}\frac{\partial}{\partial x}p' = 0 \tag{2.1}$$

$$\left(\frac{\partial}{\partial t} + U_o\frac{\partial}{\partial x}\right)w' + \frac{1}{\rho_o}\frac{\partial}{\partial z}p' + g\frac{\rho'}{\rho_o} = 0 \tag{2.2}$$

$$\frac{\partial}{\partial x}u' + \frac{\partial}{\partial z}w' = 0 \tag{2.3}$$

$$\left(\frac{\partial}{\partial t} + U_o\frac{\partial}{\partial x}\right)\rho' + w'\frac{\partial}{\partial z}\rho_o = 0 \tag{2.4}$$

where u' and w' are the perturbation velocities in the horizontal and vertical, ρ' and p' are the perturbation density and pressure, $\rho_o(z)$ is the mean density and $U_o(z)$ is the mean horizontal velocity. The Brúnt Väisälä frequency is defined as $N^2 = \frac{-g}{\rho_o}\frac{\partial \rho_o}{\partial z}$. Solutions are assumed of the form:

$$\begin{pmatrix} u' \\ w' \\ p' \\ \rho' \end{pmatrix} = \begin{pmatrix} u(z) \\ w(z) \\ p(z) \\ \rho(z) \end{pmatrix} e^{ik(x-ct)} \tag{2.5}$$

where $k = \frac{2\pi}{L_x}$ is the horizontal wave number and c is the wave speed. The vertical wave number for the disturbance is found in the definition for $w(z)$.

It is possible to derive the polarization equations, or relations of the four variables u, w, p, and ρ, from the previous equations. If the solutions in Eq. (2.5) are substituted into Eqs. (2.1) – (2.4), then the following equations relating the variables can be found:

$$u = \frac{-i}{k}\frac{\partial w}{\partial z} \tag{2.6}$$

$$p = (U_o - c)\rho_o u \tag{2.7}$$

$$\rho = \frac{i}{k(U_o - c)}\frac{\partial p_o}{\partial z}w \tag{2.8}$$

These equations relate the areas of relative motion, high and low pressures, and warming and cooling as shown in Fig. 2.26.

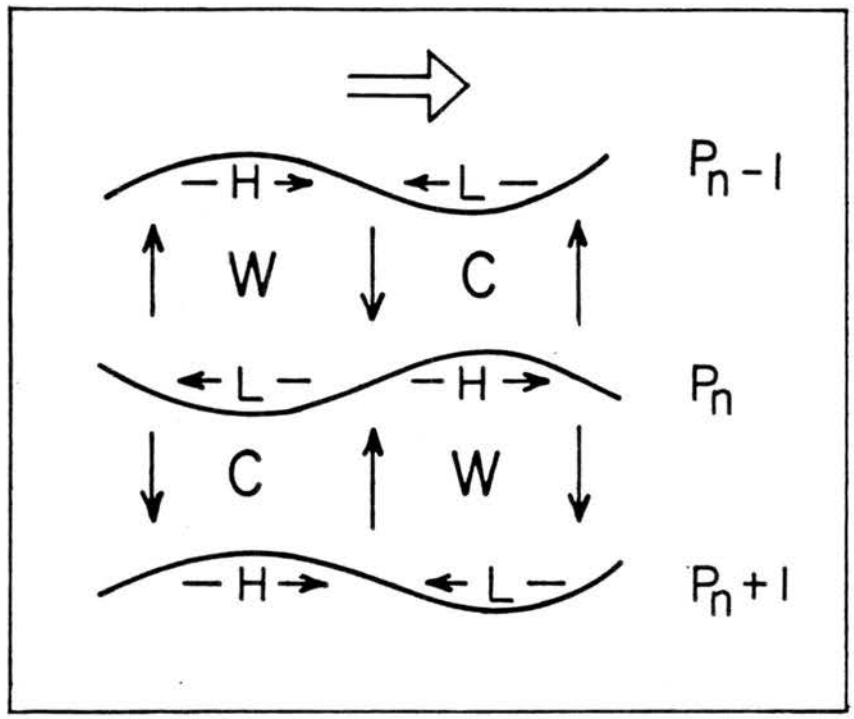

Figure 2.26: Vertical cross section of the relative motion, pressure and temperature perturbations in a propagating internal gravity wave. The wave is propagating to the right. The arrows are drawn in the region of maximum velocity in that direction. C and W are cold and warm, and H and L are high and low pressure. The lines are isobaric surfaces.

Using the solution form of Eq. (2.5) it is also easy to derive the Taylor-Goldstein equation:

$$\frac{\partial^2}{\partial z^2} w + \left[\frac{N^2}{(U_o - c)^2} - \frac{\frac{\partial^2}{\partial z^2} U_o}{(U_o - c)} - k^2 \right] w = 0 \tag{2.9}$$

where $l^2 = \frac{N^2}{(U_o - c)^2} - \frac{\frac{\partial^2}{\partial z^2} U_o}{(U_o - c)}$ is the Scorer parameter. Waves are evanescent (trapped) in the vertical if $l^2 < k^2$. This situation is most likely to occur if N^2 is small or negative (low stability), $U_o - c$ is large (strong shear), or $\frac{\partial^2}{\partial z^2} U_o$ is large (a sharp jet). Lindzen and Tung (1976), Crook (1988), and Lin and Goff (1988) have reviewed specific criteria necessary

for the ducting of gravity waves. Lindzen and Tung summarize the properties necessary for a duct as:

1. The duct has to be statically stable, i.e. N^2 has to be positive in the duct.

2. The duct has to be sufficiently thick so that it can accommodate a quarter of the vertical wavelength corresponding to the observed phase speed. This is defined by:

$$C_{D,n} \approx \frac{NH}{\pi(\frac{1}{2}+n)}, \quad n = 0, 1, 2... \tag{2.10}$$

$$L_n \approx 2\pi \frac{C_{D,n}}{N} \tag{2.11}$$

where n is the mode, H is the depth of the layer, $C_{D,n}$ is the phase speed for a particular mode, and L_n is the approximate horizontal wavelength for long (mesoscale) waves. The fastest mode is the $n = 0$ mode, thus:

$$C_{D,0} = \frac{2NH}{\pi} \tag{2.12}$$

3. The duct has to be topped above by a good reflector, i.e. the Scorer parameter must approach zero in the reflecting layer. This could occur if the wind speed in that layer equals the phase speed of the wave, a strong jet occurs in that layer (so the curvature term is very large), or N^2 is very small in that layer. It is not necessary, however, that the Scorer parameter be exactly zero. Waves can be partially trapped and still travel horizontally for a few cycles before losing most of their energy.

4. The wind speed in the duct cannot equal the phase speed of the wave. In that case the wave energy would be totally absorbed.

Lindzen and Tung (1976) also point out that the duct, or layer within which the wave is traveling, selects the phase speed of the wave, but does not specify any horizontal scale. If

the wave exists in a convectionally unstable environment, they suggest that the horizontal scale of the wave could be forced by the scale of the instabilities. If τ_i is a characteristic time scale for the instability, then they hypothesize that the convection would force a wave with

$$L_x = c \times 2\pi\tau_i \ . \tag{2.13}$$

For example, τ_i could also be a time scale associated with the flow over a mountain. Such a wavelength applies when the convection or a time-scale-forced instability is forcing the wave, not, for instance, when the wave is forced by vertical shear instability.

Many possible mechanisms exist for the generation of gravity waves, such as shear instability (Lalas and Einaudi, 1976; Chimonas and Grant, 1984), convection (Clark *et al.*, 1986; Lin and Smith, 1986; Lin and Goff, 1988; Lin and Li, 1988; Bretherton, 1988), wave-CISK (Hayashi, 1970; Davies, 1979; Emanuel, 1982), topographical forcing (Smith, 1979), and geostrophic adjustment (Blumen, 1972; Uccellini and Koch, 1987). The mechanisms of geostrophic adjustment and shearing instability are very briefly discussed below. Wave-CISK is reviewed more extensively in Section 2.4, as it is hypothesized to be the propagation mechanism of the squall line discussed in this study.

Uccellini and Koch (1987) briefly review geostrophic adjustment as a gravity wave source mechanism, and suggest that a wave that is forced by geostrophic adjustment processes will have a wavelength of the Rossby radius of deformation, λ_R (Rossby, 1938; Cahn, 1945). The Rossby radius of deformation for a stratified atmosphere is defined by Blumen (1972) as:

$$\lambda_R \sim \frac{NH}{2\pi f} \tag{2.14}$$

where H is the atmospheric scale height and f is the Coriolis parameter.

Shearing instability can also force gravity waves, and provide a continuing energy source to the waves when $R_i < 0.25$, where R_i is the Richardson number. R_i is defined

as $\frac{N^2}{\left(\frac{\partial U_g}{\partial z}\right)^2}$. Uccellini and Koch (1987) and Lalas and Einaudi (1976) provide reviews of theory of the interaction of shear and gravity waves.

2.4 Review of Wave-CISK Theory and Studies

The concept of wave-CISK was first introduced by Hayashi (1970). Conventional CISK (Convective Instability of the Second Kind) is mostly associated with theories of tropical cyclone development (Charney and Eliassen, 1964), where the low-level, friction-induced convergence forces upward motion, condensational heating, and pressure falls which in turn force more convergence. In contrast, the mechanism of wave-CISK is that the convergence is caused by gravity wave motions. The basic assumptions in wave-CISK theory are that:

1. The convection is always phase-locked with the wave-induced, low-level convergence, and

2. The interactions between the waves and convection can be basically modelled with linear theory.

The phase-lock, or coupling of the gravity wave and convection implies that either the gravity wave or convection must be initially forced by some other mechanism. In the case modelled for this study, the convection is initially forced by the strong frontal convergence, and then excites the gravity wave and propagates with it. Clark *et al.* (1986), Tripoli and Cotton (1989a,b), and Schmidt and Cotton (1990) have all shown that convection can excite many different scales of gravity waves, none of which will necessarily phase-lock with the convection. The coupling of the gravity wave and convection can apparently only occur in specific circumstances.

A problem in many wave-CISK models has been an apparent lack of scale selection for the most unstable modes; the shortest resolvable waves are always the most unstable. Davies (1979) describes this as due to the quasi-equilibrium assumption, that the convection and latent heat release are instantaneously forced by the convergence and always in phase with the convergence. The quasi-equilibrium assumption is valid for conventional

CISK where the convection is relatively stationary, steady, and long-lived. However, in mid-latitude, mesoscale convective systems the time scale of the "cloud" (or time lag from initial convergence to latent heat release) is not negligible compared to the time scale of the system or the time scale of the mesoscale motions (the time scale of the gravity wave). Davies (1979) introduced the concept of phase-lagged wave-CISK, where a time lag is introduced between the low-level convergence and latent heat release. The time lag then forces a scale selection for the most unstable gravity wave. Bolton (1980) also showed that unstable propagating solutions can only occur when the heating is out of phase with the vertical velocity, which is consistent with the structure of the propagating gravity wave shown in Fig. 2.26. Using various time-lag modifications, Davies (1979), Xu and Clark (1984), and Raymond (1983, 1984) have all been able to simulate reasonable horizontal scale selections in wave-CISK models.

Raymond (1975, 1976, 1983, 1984) has done extensive work with wave-CISK modelling of convective systems and squall lines. Figure 2.27 is Raymond's (1975) schematic of the hypothesized relation between the gravity wave-forced convergence and the convective system. As discussed previously in this chapter, Raymond (1984) used a wave-CISK model to simulate the propagation of both tropical and mid-latitude squall lines. His simulations showed the initial growth of an advecting mode (moving at the environmental wind speed) associated with the convection. The collapse of this initial convection forced outward-propagating modes. The down-stream moving mode moved faster than the environmental wind and was thus associated with the squall line propagation. The streamlines for this mode were shown in Fig. 2.20. The initial advecting mode in Raymond's simulation was found to be very sensitive to the incorporation of downdraft effects in the cumulus parameterization (Raymond, 1983). The growth rate of the advecting mode was nearly independent of wavelength and much larger than that of the propagating mode. Raymond (1983, 1984) hypothesizes that the advecting mode corresponds to air-mass-type thunderstorms while the propagating modes may correspond to faster-moving squall lines. Raymond also found that the advecting mode was relatively insensitive to the vertical

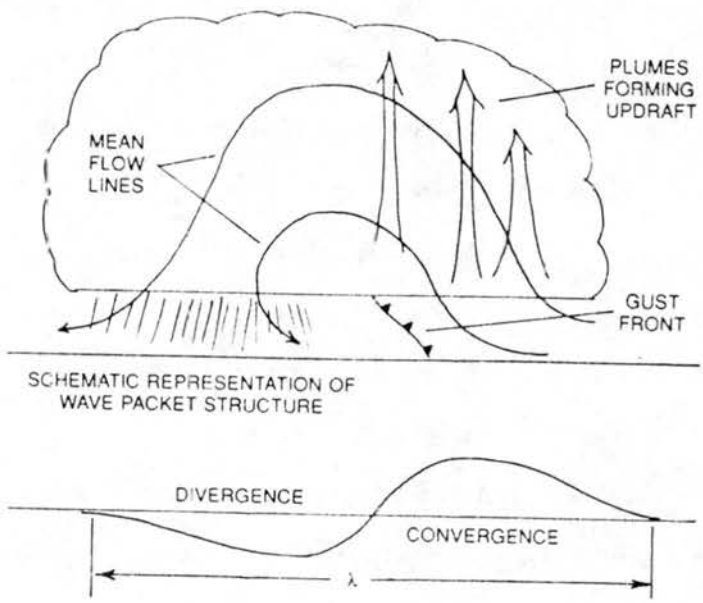

Figure 2.27: Schematic diagram of the hypothesized relationship between a packet of gravity waves and the associated convective storm, subject to the limitations of a two-dimensional drawing. The wave packet consists of one convergent and one divergent region with a dominant wavelength λ comparable to the diameter of the storm. Convective plumes develop in the convergent region, passing into the divergent region as they decay and produce rain (from Raymond, 1975).

shear specification, although the propagating modes are suppressed by stronger shears. Aside from the effects of the cumulus parameterization, the circulations in Raymond's model were assumed dry and thus no anvil circulations were produced.

Xu and Clark (1984) developed a wave-CISK model with time-dependent effects in the cloud model to provide the phase-lag. They used a simple sinusoidal profile (Fig. 2.28) to specify the heating function in the cloud model, but point out that this simple function is still realistic. Figure 2.29 shows the growth rate as a function of the horizontal wavenumber k, and z_c the cloud base level. The most unstable growth rate in their model is at $k =$

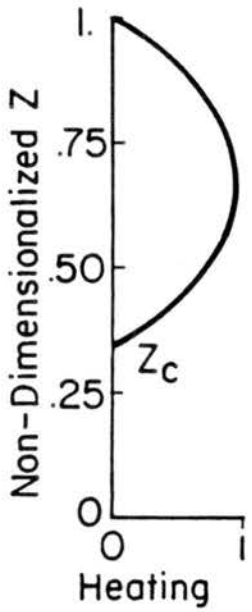

Figure 2.28: Normalized heating profile of cloud model in Xu and Clark (1984) wave-CISK model.

5.5 and $z_c = .34$, which corresponds to a wavelength of 114 km and a wave speed of 16.7 m s^{-1} in their case. Figure 2.30 shows the relative insensitivity of the phase speeds and vertical wavelengths to variations in z_c and k. The vertical wavelength is close to 2π and the phase speed is close to 16 m s^{-1}, even as k and z_c vary. The vertical wavelength of 2π corresponds to the $n = 2$ mode, and is forced by the $n = 2$ mode structure of the vertical heating function (heating at upper levels, relative cooling at lower levels). Figure 2.31 shows the streamfunction and potential temperature perturbations for the most unstable

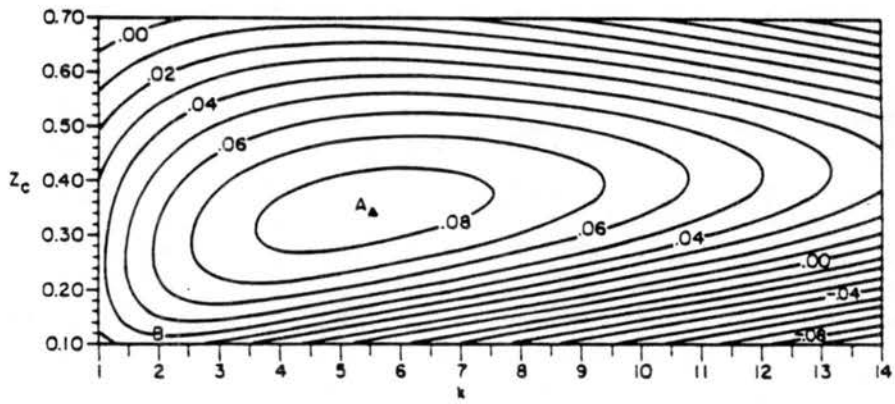

Figure 2.29: Growth rates $\omega_i(z_c, k)$ for the typical external parameters where z_c and k are nondimensional cloud base height and horizontal wavenumber. Point A lies at the peak of growth rates where the most unstable wave has a phase speed of 16.7 m s^{-1} and a wavelength of 114 km (from Xu and Clark, 1984).

wave in Fig. 2.29 (at point A). The correlations of the horizontal and vertical motions and temperature perturbations are consistent with gravity wave motions. Xu and Clark also found that the vertical structure of the resultant waves was insensitive to minor changes in the heating profile. The waves in Fig. 2.31 are propagating to the right but also extend to infinity at the right because of the Fourier decomposition of the structure. In reality, only one horizontal cell at a time would be forced by the heating over cooling profile, and the wave structure would be that of a solitary wave. Xu and Clark also found that if the stability in the stratosphere is increased relative to that in the troposphere, the most unstable waves shift to shorter horizontal wavelengths, and there is less sensitivity to changes in z_c. The higher the stability difference across the tropopause, the more the waves resemble free internal hydrostatic waves of mode $n = 2$ between two rigid boundaries. Emanuel (1982) found a similar dependence of wavelength on the relative stratification.

The question still remains as to how the waves are maintained in the Xu and Clark model. They are continuously forced by the upper level heating, but Xu and Clark also

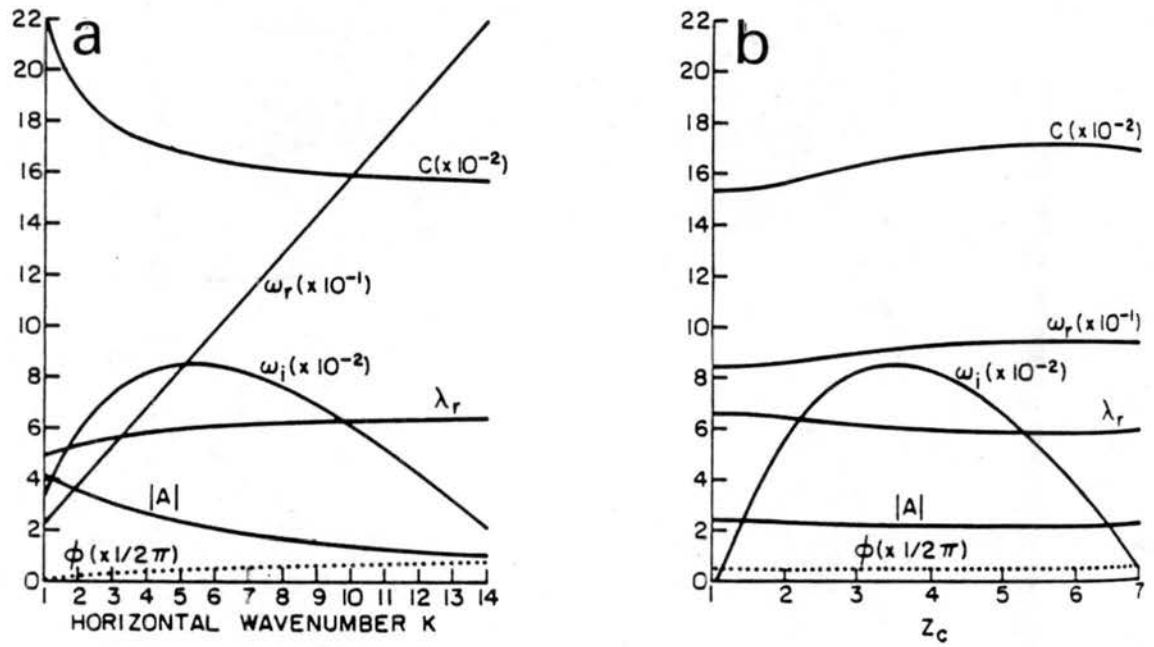

Figure 2.30: Plots of $\omega_i, \omega_r, \lambda_r, C, A_0$, and ϕ for (a) fixed $z_c = 0.34$; and (b) fixed $k = 5.5$ (from Xu and Clark, 1984). ω_i is the unstable growth rate (s^{-1}) (or e-folding time $\frac{1}{\omega_i}$), ω_r is the intrinsic frequency of the system (s^{-1}, and $C = \frac{\omega_r}{k}$), λ_r is the vertical wavelength (radians), C is the wave speed (m s^{-1}), A_0 is the amplitude of the cloud mass flux, and ϕ is the phase lag (radians) of the cloud mass flux to the initial forcing.

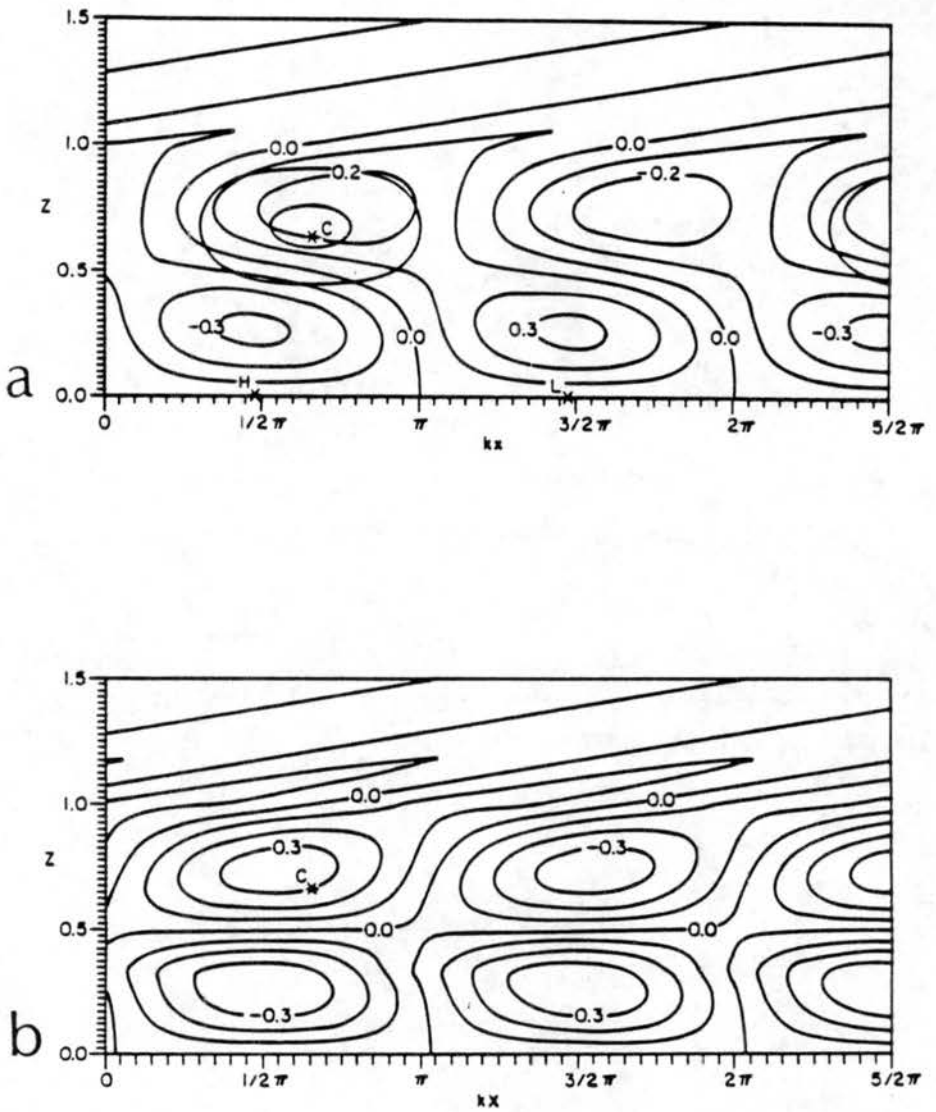

Figure 2.31: Fields in non-dimensional space for the most unstable wave in Fig. 2.29 (point A) of (a) streamfunction; and (b) potential temperature perturbation (from Xu and Clark, 1984). Motion is clockwise around the positive streamfunction perturbation and counter-clockwise around the negative perturbation.

argue that an over-reflection or quasi-resonance effect occurs. A resonant or reinforcing reflection effect will occur when the source and boundary are an odd integral number of quarter wavelengths apart (Gill, 1982; Crook, 1988). In Xu and Clark's model, there is one-quarter wavelength from the cloud heating maximum to the stratification discontinuity at the tropopause, and three-quarters of a wavelength from the heating maximum to the ground, which in both cases will result in the most efficient reflection. However, the reflection is far from perfect. Lindzen and Tung (1976) showed that a discontinuity in stability is not a particularly good reflector. The reflection coefficient that they calculated for a doubling of stability between the troposphere and stratosphere was only 0.33. Xu and Clark calculated the reflection coefficient for a wave packet incident on the tropopause from below as

$$r = \left| \frac{1 - S}{1 + S} \right| \tag{2.15}$$

where $S = N_s/N_t$, and N_s and N_t are the stratospheric and tropospheric Brúnt Väisälä frequencies respectively. If $S = 3$, then $r = 0.5$, and if $S = 5$, then $r = 0.66$. Xu and Clark used $S = 2.5$ which was apparently sufficient to maintain the wave. To summarize Xu and Clark's (1984) paper, a time-lagged wave-CISK model produced waves with the vertical structure highly dependent on the mode $n = 2$ heating profile, and with horizontal wavelengths and speeds on the order of 100-150 km and 16 m s^{-1}. The waves were maintained by the cloud heating and a quasi-resonant effect that resulted in constructive reflection from the tropopause and from the ground. Specific aspects of the Xu and Clark results will be compared to the simulation results in Chapter 5.

Nehrkorn (1986) developed a wave-CISK model with a baroclinic base state (constant vertical wind shear) and compared the results to squall line observations. He investigated the effects of the vertical heating profile and environmental specifications on the wavelength of maximum growth rate and the orientation of the disturbance axis relative to the shear vector. Nehrkorn found that the horizontal wavenumber of the maximum growth rate only decreased from $l = 14$ to $l = 10$ as the non-dimensional level of maximum heating

was raised from 0.5 to 0.8. The wavenumbers of l = 14 and 10 correspond to wavelengths of 450 and 630 km respectively. Xu and Clark (1984) also found a relative insensitivity of the most unstable wavelength to the vertical heating function, although their most unstable wavelengths were on the order of 100-200 km. Nehrkorn notes that his longer horizontal wavelengths may be a result of his parameterization of cumulus heating in which the effects of convection are spread laterally over a large part of the wave, including areas of descent. Similar to Xu and Clark's results, Nehrkorn found that the vertical structure of the most unstable wave was closely related to the vertical heating profile, and that the wavelength of maximum instability decreased as the stability difference between the stratosphere and troposphere increased. The vertical structure of the wave with z_m=0.8 (convective heating maximum at 0.8 of the tropospheric scale height) was very similar to Xu and Clark's mode n=2 wave and Raymond's (1984) propagating mode, with the updraft sloping rearward with height.

Nehrkorn also examined the sensitivity of the phase speed and orientation angle of the propagating mode with respect to the shear vector. His calculated phase speeds were on the order of 2-5 times too large, although he notes that his model assumes constant vertical wind shear while the environment of squall lines often has the most shear only in low-levels (Bluestein and Jain, 1985). The assumption of constant vertical wind shear may have also affected the selection of the most unstable horizontal wavelength. Nehrkorn found that the squall line orientation angles varied from 0 to $-30°$ (the angle of the squall line axis relative to the axis of the wind shear vector) as z_m decreased from 0.8 to 0.5. Nehrkorn compared his model-predicted parameters to two climatological studies of squall lines and found that his results did not agree with the observed orientation angles and phase speeds. However, he only compared his results to climatological averages, not specific cases, and he assumed constant vertical wind shear, which was not a characteristic of the climatological data sets.

To summarize, wave-CISK studies have found varying degrees of sensitivity to the cumulus parameterization schemes used, and the structure of their heating functions. As

Raymond (1983) noted, "parameterization continues to be the Achilles' heel of wave-CISK." However, when realistic heating profiles are chosen (with heating maxima in the upper troposphere), the various studies generally show similar vertical wave structure (as Xu and Clark's mode $n = 2$ wave) and rearward tilt of the updraft, and relative insensitivities to small perturbations in the heating profile. The problem of horizontal scale selection is also sensitive to the cumulus parameterization. Realistic values of horizontal wavelength seem to be obtained when some form of a phase-lag between the low-level convergence and convective heating is introduced. Unfortunately, the phase-lag (and cumulus parameterization schemes in general) is determined by somewhat arbitrary, yet hopefully realistic, parameters. Aspects of wave-CISK models also seem to be sensitive to the downdraft cooling and wind shear specifications, although these effects are secondary to those of the heating profile. Although there is much disparity between studies, many wave-CISK models have predicted realistic horizontal wavelengths, phase speeds, and vertical structures for propagating squall line systems.

2.5 Observational and Modelling Studies of Gravity Waves

A review of several specific observational and modelling studies of gravity waves is presented in this section. The emphasis is on meso-α scale waves, with wavelengths on the order of hundreds of kilometers and phase speeds of 10-50 m s^{-1}.

As noted previously, Tepper (1950) was one of the first to link squall lines (or convection) and gravity wave activity. Tepper's theory was that the prefrontal squall line was a manifestation of a gravity wave moving along an inversion in the warm sector, initially forced by the cold front (Fig. 2.32). Although he didn't describe it as such, his theoretical wave appears to be a solitary wave of elevation. Tepper (1951) also documented an example of a traveling wave of depression that could be seen in both the surface pressure traces and in a cloud layer at approximately 3 km. The wave traveled at approximately 20-34 m s^{-1}.

Bosart and Cussen (1973) studied a gravity wave over the southeastern United States that occurred on 3 December 1968. The wave traveled at 10-15 m s^{-1} and seemed to

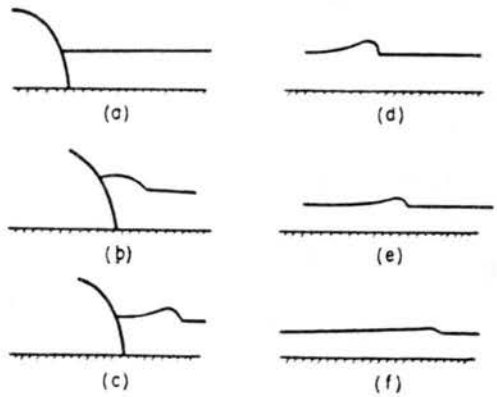

Figure 2.32: Life history of a squall line (idealized). (a) Initial position of the cold front and the inversion in the warm sector; (b) the cold front accelerates inducing a pressure jump on the inversion; (c) the cold front decelerates while the jump moves out ahead with the rarefaction wave following; (d), (e), and (f) successive illustrations of the pressure jump being overtaken by the rarefaction wave (from Tepper, 1950).

propagate as a wave of depression along a low-level temperature inversion. Pressure drops as high as 7 mb occurred at the surface with the passage of the wave. The wave appeared to develop as the result of thunderstorm activity, although the relation between the propagating wave and convection is not clear.

Eom (1975) analyzed surface observations of a rapidly propagating disturbance. The disturbance traveled to the north with a speed of approximately 50 m s^{-1} and with a wavelength of 500 km. The width of the disturbance (distance perpendicular to the direction of propagation) was only 200 km. The correlations of the low-level wind speed and direction changes with the pressure changes and deduced vertical motions (from cloud cover changes) indicated that the disturbance was indeed a low-level gravity wave. The atmosphere in this situation had a nearly isothermal low-level stable layer from the surface to 700 or 800 mb, with a more unstable layer above that. Eom used a simple linear analytic model of a two-layer atmosphere to show that an internal gravity wave with phase speeds close to that observed could exist in the atmosphere.

Uccellini (1975) related gravity wave activity to the initiation or intensification of convection for a case in May 1971. After filtering the surface pressure traces from 130

midwest surface stations, a northeastward moving gravity train was apparent. The waves had speeds ranging from 35-45 m s^{-1} and wavelengths from 300 to 450 km. The wave amplitudes at the surface ranged up to 2 mb. As in Eom's (1975) case, these waves also had a very limited horizontal extent (200-300 km). Uccellini also used a simple linear analytic model to confirm that the wind and pressure relations of the observed waves were consistent with those of internal gravity waves.

Hoxit *et al.* (1976) have studied several cases where troughs or mesolows formed ahead of convection. They attribute the troughs to subsidence warming ahead of the convection although they appear similar to gravity wave activity. The areas of subsidence that they identified had widths of 20-80 km, which would imply wavelengths on the order of 40-160 km. Fankhauser (1974) similarly diagnosed a mid-tropospheric area of subsidence about 40 km in width ahead of a squall line (Fig. 2.33). The vertical motion was calculated kinematically using wind data from a mesoscale rawinsonde network. Again, Fankhauser does not identify the motions as gravity wave activity, but they do bear similarities to such activity.

Gedzelman and Rilling (1978) studied the properties of short-period atmospheric gravity waves observed at Palisades, New York. The waves that they observed were generally much shorter and of higher frequency than those observed by Bosart and Cussen (1973), Eom (1975), and Uccellini (1975), with periods on the order of 10 minutes and wavelengths on the order of 20 km. Gedzelman hypothesized that most of the waves were generated by shear instability as they usually occurred directly under an upper level wind maximum and in an environment with low-level stable stratification.

Miller and Sanders (1980) analyzed surface observations from 3 April 1974 and found signals of 10 different gravity wave packets. One packet in particular consisted of a wave trough leading an area of convection, traveling at approximately 15 m s^{-1}. This packet was linked to the convection for more than 20 hours. Miller and Sanders suggest that this was an example of a wave-CISK mechanism. Several of the other packets that they observed seemed to form as a result of specific convection or within areas of preexisting

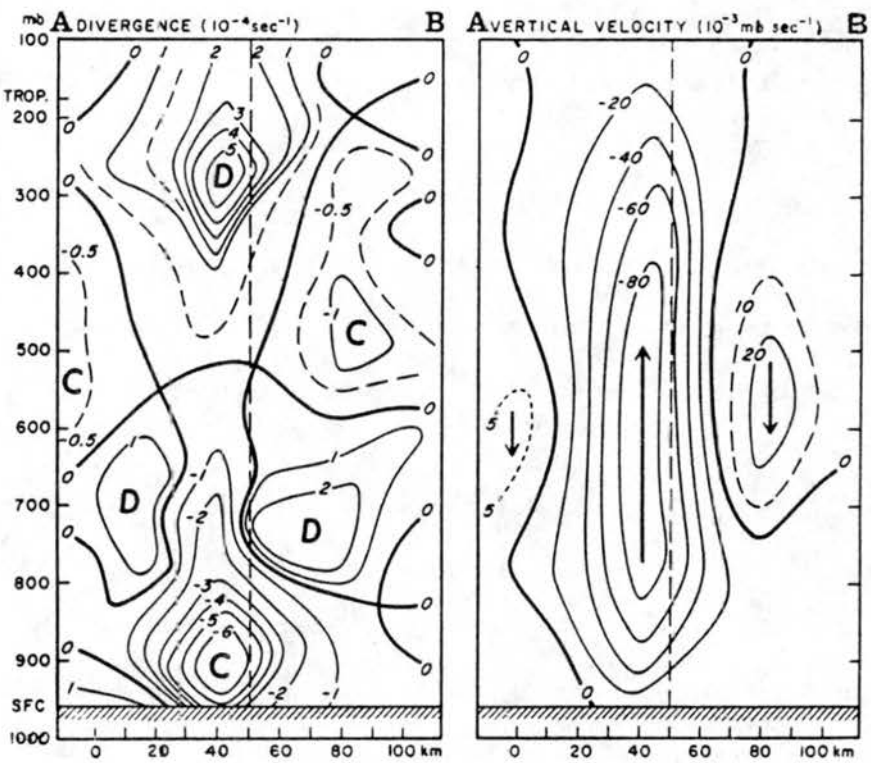

Figure 2.33: Cross sections of divergence and vertical velocity through squall line. (10^{-3} mb sec^{-1} $\approx$ 1.5 cm sec^{-1} at 500 mb; from Fankhauser, 1974).

convective activity. They did not find any indication of the initialization of convection by preexisting gravity waves, although preexisting convection was modified and reorganized by the gravity waves.

Stobie *et al.* (1983) also analyzed the relation between propagating internal gravity waves and the initialization of convection for the 9 May 1979 case. They analyzed two different sets of waves with phase speeds of 30 and 20 m s^{-1}, and wavelengths of 265 and 240 km respectively. These waves existed within bands only 300 km wide. They also did a theoretical analysis of the waves and suggested that the shear provided by a propagating upper level jet helped to both initiate the wave and provide a continuing mechanism for the wave to extract energy from the environment, and acted as a wave guide (critical level) to help reduce upwards leakage of wave energy. There also seemed to be a positive feedback mechanism between the convection and gravity waves, similar to a wave-CISK mechanism.

Pecnick and Young (1984) studied a case with a very strong deep tropospheric gravity wave. They called this a "wave of depression" although it seems to fit within the class of internal gravity waves (vs. solitary waves). The case that they studied occurred on 27 March 1975 and showed up at the surface as a solitary wave of depression with an amplitude of approximately 7 mb and a propagation speed of 32 m s^{-1}. The width of the perturbation (distance parallel to propagation direction) was 60-100 km and its length (distance perpendicular to propagation direction) was 500 km. The existence of the wave in the upper tropcsphere was confirmed using satellite imagery. Based on the surface and upper air (approximately 300 mb) data, they analyzed the wave as tilting upstream with height and hypothesized that the wave was maintained by interaction with the synoptic shear flow. Pecnick and Young also tied the initiation of the wave to an upper level jet streak, similar to Stobie *et al.* (1983) and Uccellini (1975).

Bosart and Sanders (1986) studied a propagating gravity wave that occurred on 11-12 February 1983. The wave appeared to be a depression followed by an elevation and then another depression, traveling at 15-25 m s^{-1}, and existed in an environment suitable for

wave ducting, as described by Lindzen and Tung (1976). The scale of this wave packet ranged from 100 to 400 km. The relation between the wave and accompanying convection was again unclear.

Uccellini and Koch (1987) reviewed 13 cases of apparent gravity wave activity. They analyzed waves with wavelengths of 50-500 km and horizontal phase speeds of 13-50 m s^{-1}. They did not find a correlation between wave amplitude and the presence of convection and thus concluded that the convection was probably not the source of the waves. Most of the waves existed in environments that exhibited wave trapping characteristics. Uccellini and Koch correlated the existence of jet streaks with the source regions for the waves and speculated that the waves were excited by shearing instability or geostrophic adjustment processes.

Einaudi *et al.* (1987) analyzed in detail four gravity wave events that occurred over northeast Colorado in July 1983. Unlike most previous studies that only had surface data available, they were able to use wind profiler data to investigate the vertical structure of the waves. Two of the wave trains that they studied seemed to be maintained by shear instability and two of the events were termed "nonsingular neutral modes". The first two waves existed in an environment with an upper level jet streak and with a critical level, and the authors concluded that those waves were maintained by shear instability. Those waves had speeds of near 14 m s^{-1} and wavelengths near 90 km. Einaudi *et al.* also hypothesized that convection was important in choosing the scales of these waves, although the convection did not always move with the waves. The other two waves propagated faster than the wind at all levels, and also faster than the convection. These latter waves had speeds of approximately 18 m s^{-1} and wavelengths of 92-144 km. Convection did exist with these latter two waves, but it moved more slowly, and the relationship between the waves and convection was again unclear.

In the first of a series of 3 papers, Koch and Golus (1988) identified two wave episodes that occurred during the Cooperative Convective Precipitation Experiment (CCOPE) in Montana. They used various detailed spectral analyses and filters to analyze the gravity

waves and confirm that the phase relations of pressure, horizontal motion, and vertical motion were consistent with those found in gravity waves. The waves that they identified had wavelengths of 70 and 160 km and phase speeds of close to 20 m s^{-1}. In Part II of the series, Koch *et al.* (1988) investigated the relationship between the gravity waves and convection. They found that none of the waves in this case were excited by convection, although there did exist a positive feedback between the convection and waves in several cases. In Part III of the series, Koch and Dorian (1988) further investigated the possible wave source mechanisms and maintenance. They concluded that geostrophic adjustment processes in the vicinity of an upper level jet streak were the primary source mechanism, with shear instability and wave ducting contributing to the maintenance of the waves.

Bosart and Seimon (1988) analyzed a strong surface gravity wave that occurred on 27 February 1984. The wave had a wavelength of 100-150 km and propagated at about 15 m s^{-1}. The wave was a wave of depression following a squall line, with maximum pressure falls of 10 mb. Similarities existed between this depression and the subsidence-induced clear zone trailing a line of convection described by Dorian *et al.* (1988) and Koch (1984), although the subsidence in the latter two investigations was hypothesized to be due to frontogenetically-forced circulations. Bosart and Seimon demonstrate that a sufficient ducting mechanism did occur in the wave environment.

Lin and Goff (1988) identified a solitary wave of depression from barograph traces that occurred on 6 March 1969. The wave moved towards the northeast at approximately 55 m s^{-1} with a wavelength of 185 km. They hypothesized that the wave initially developed as a result of deep convective activity and then propagated along a mid-level inversion (at approximately 500 mb) beneath a weakly stratified layer. The development of light precipitation, but not deep convection, was associated with the passage of the wave.

Chapter 3

CASE DESCRIPTION

The case that was chosen for this study is that of a mid-latitude squall line that developed on 17 June 1978. This case was observed during project NIMROD (Northern Illinois Meteorological Research On Downbursts; Fujita, 1979, 1981) and was used for a Doppler radar study by Srivastava *et al.* (1986). The squall line convection initially developed along a very long, well-defined cold front, and then moved out ahead of, and away from, the front, thus giving the squall line its "prefrontal" character. At its peak, a very narrow line of convection extended all the way from Illinois to the Texas panhandle.

The only paper that has been written on this case is that of Srivastava *et al.* (1986). That paper, and several personal observations provided by Thomas Matejka, will be described in the first two sections of this chapter. The remaining sections will discuss the various types of observational data and analyses available for this case: satellite data, radar summary charts, upper air analyses, surface analyses, and individual rawinsonde soundings. All of the times referred to in the following sections will be in UTC hours. The difference between Central Standard Time (CST) and UTC is 6 hours, so 1200 UTC corresponds to 6 a.m. CST and 0000 UTC is 6 p.m. CST.

3.1 Review of Srivastava et al. (1986) Paper

Srivastava *et al.* (1986) did a Doppler radar study of a portion of the trailing anvil region associated with the squall line. The data for the Srivastava *et al.* study was collected during project NIMROD. There were 3 Doppler radars arrayed in a triangle about a network of 27 automated surface stations in Northern Illinois (Fig. 3.1). The surface stations had a spacing of approximately 10-20 km while the 3 radars were situated

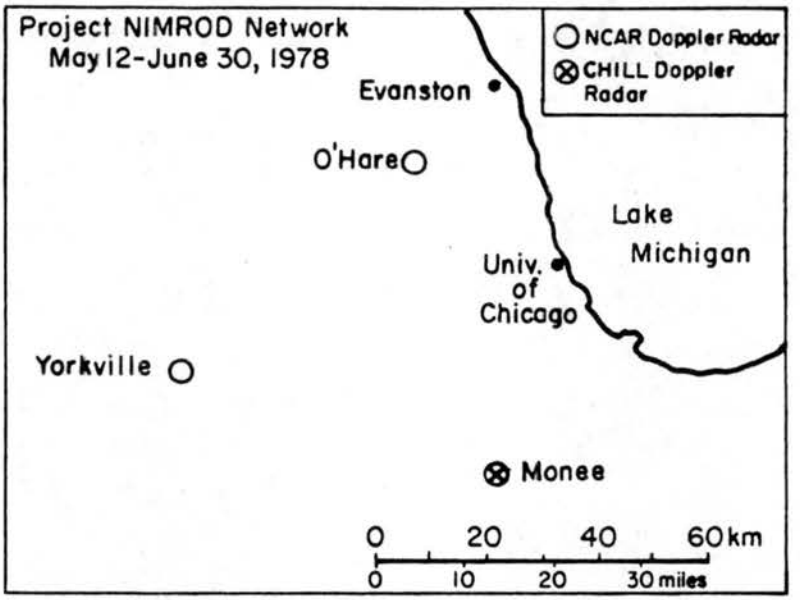

Figure 3.1: Doppler radar locations for project NIMROD (adapted from Srivastava *et al.*, 1986).

about 60 km apart. Both single-Doppler and multiple-Doppler analyses of the data were completed.

Srivastava *et al.* (1986) describe the synoptic situation as consisting of low-level warm advection from the southwest at 850 mb with cold advection aloft at 700 and 500 mb. From radar reflectivity pictures they determined that individual cores in the squall line had lifetimes of 30 to 40 minutes and moved northeastward, while the line itself moved southeastward as new convective elements formed up to 25 km ahead of the line. Srivastava *et al.* note that the squall line began to intensify rapidly at 2130 UTC and by 0100 UTC had formed a continuous cloud band stretching 2000 km from Wisconsin to Texas, with widths ranging from 70 to 200 km. The squall line moved southeastward through northern Illinois at approximately 15 m s^{-1}, "considerably faster than the motion of the cold front". According to their observations, the squall line passed through their network between 0200 UTC 17 June and 0800 UTC 18 June, while the cold front did not pass through until 1200 UTC 18 June. However, they do not state how they defined "cold front passage".

The squall line entered the NIMROD network at about 0300 UTC 17 June. At that time it was observed that the stratiform precipitation to the rear of the active convection was just starting to become extensive. By 0445 UTC the convection had weakened and the area of stratiform precipitation extended 140 km behind the line. At that time they observed that a new line of convection formed about 20 km ahead of, and detached from, the old decaying leading edge. However, the stratiform precipitation region behind the old leading edge continued for approximately two more hours. Srivastava *et al.* did their Doppler radar study with data collected over a 9 separate minute intervals from 0445-0545 UTC on that stratiform precipitation region of the storm. They speculated that the new line became detached from the old line because the gust front extended far ahead of the old line, due to an accumulation of the colder, denser air from the convective downdrafts. Compensating subsidence associated with the new convection served to further delineate the old and new convective regions.

From their analysis of particle fall speeds in the anvil region, Srivastava *et al.* determined that snow was falling from 11 km down to 6.5 km, with particle growth probably occurring by deposition, riming, and aggregation. Between 6.5 and 4.2 km the particle fall speeds did not increase. They speculate that this occurred because large aggregates had already formed by 6.5 km, and the fall speed of aggregates is only very weakly mass-dependent. The top of the melting level was at about 4.2 km and the fall speeds increased from 2 to 9 m s^{-1} in that region and then decreased below that to 7.5 – 8 m s^{-1}. They deduced that there was substantial particle aggregation above the melting level, and significant particle break-up below that level.

Figures 3.2 and 3.3 show the divergence and vertical wind profiles in the anvil region deduced by Srivastava *et al.* in their Doppler radar analysis. Apart from the surface, their largest convergence occurred at 3.5 km, in the melting region. They do not consider their results above 11 km to be reliable. However, based on a multiple Doppler analysis and surface data, they do consider the strong convergence near the ground to be reliable. Figure 3.3 shows the vertical velocity obtained by integration of the anelastic continuity equation with the horizontal divergences in Fig. 3.2. The three different curves in Fig. 3.3 are due to the use of three separate boundary conditions; they consider curve C to be the most reliable. They note that their results are qualitatively similar to other studies, with upward motion above 6 km and downward motion below that. Their calculation of weak ascending motion near the surface has not been corroborated by other studies, although it is consistent with several independent data sources in their analyses.

Srivastava *et al.* (1986) used their multiple Doppler analysis to calculate the wind speeds transverse and relative to the squall line (Fig. 3.4). The 0 point on the abcissa is the radar location. The corresponding reflectivity cross section in Fig. 3.5 shows the structure of the precipitation in the anvil region. Their wind analysis shows rear inflow into the trailing anvil between 3 and 6.5 km, with outflow above and below that. The cross section also suggests that the rear-inflow air descends towards the surface as it approaches the front of the storm. Srivastava *et al.* calculated that the air would descend in this

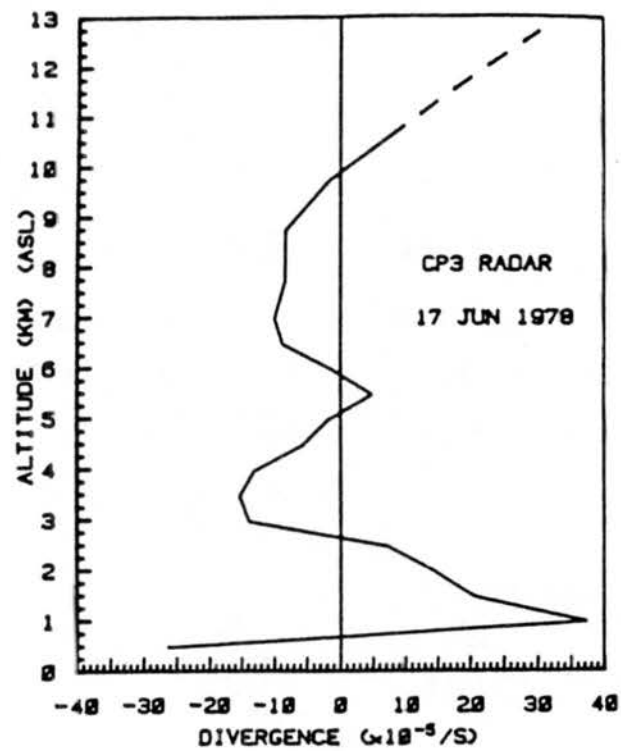

Figure 3.2: Deduced divergence profiles (from Srivastava *et al.*, 1986).

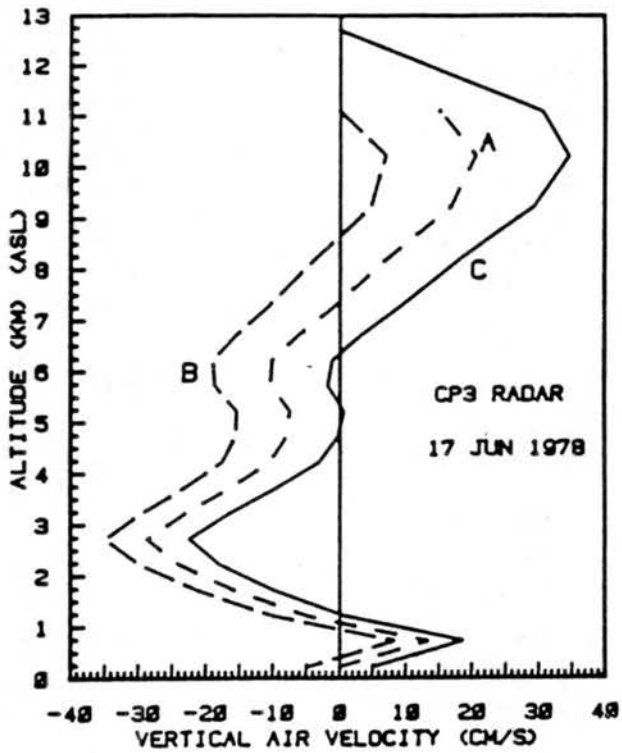

Figure 3.3: Deduced vertical velocity w profiles from integration of the divergence in Fig. 3.2. Curve A assumes $w = 0$ at the ground. Curves B and C assume $w = 0$ at the radar and satellite-estimated cloud tops, respectively. Curve B uses the solid divergence curve in Fig. 3.2, while curve C also uses the dashed extrapolation in Fig. 3.2 (from Srivastava *et al.*, 1986).

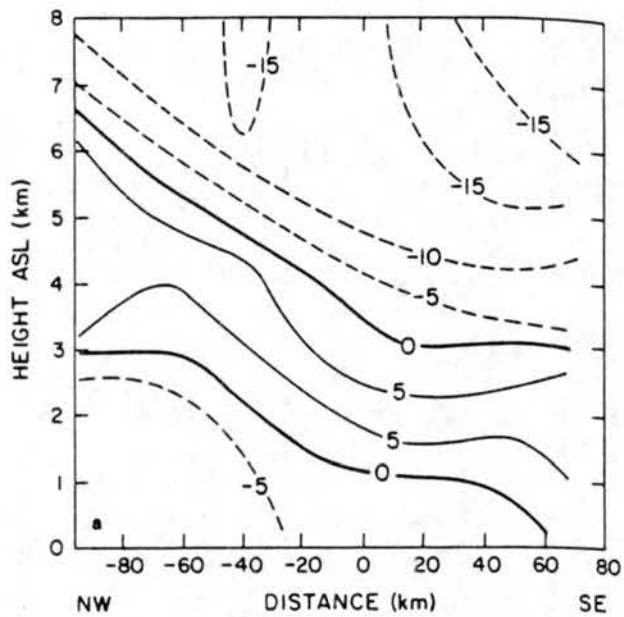

Figure 3.4: Wind speeds transverse and relative to the squall line (m s^{-1}). Positive numbers indicate winds towards the southeast. The CP3 radar (at Yorkville, Illinois) is located at point 0. The leading edge of the squall line is at +90 km (from Srivastava *et al.*, 1986).

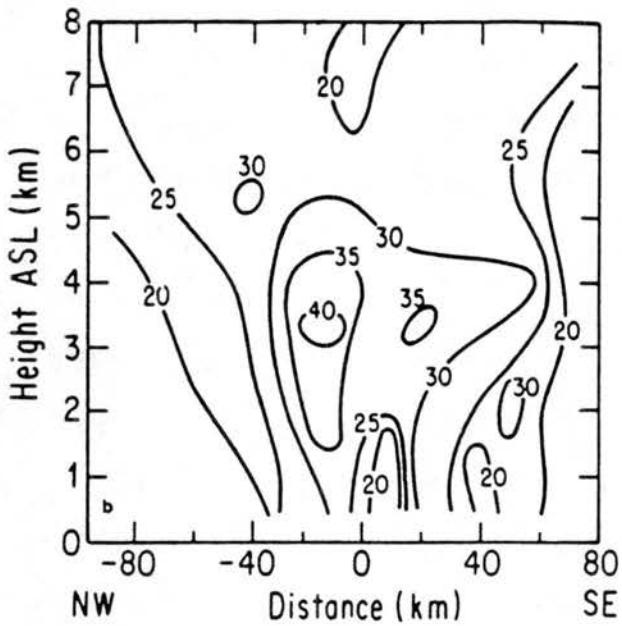

Figure 3.5: Radar reflectivity factor (dBZ) cross section through the squall line. Positive numbers indicate winds towards the southeast. The CP3 radar (at Yorkville, Illinois) is located at point 0. The leading edge of the squall line is at +90 km (from Srivastava *et al.*, 1986).

region at about 30 cm s^{-1}. However, it should be noted that the leading edge convective region associated with this anvil had dissipated and reformed 20 km ahead by this time.

An interesting result from the multiple Doppler analyses was that a banded pattern in the divergence fields was evident at mid-to-upper levels, with the bands oriented north-south (the squall line was oriented northeast-southwest). The bands had a wavelength of approximately 60 km and were most pronounced at about 7 km. Srivastava *et al.* speculated that these bands may be due to internal gravity waves.

Several points need to be noted on the relation of the Srivastava *et al.* (1986) study to this work. First of all, the Srivastava *et al.* study mainly concentrated on the trailing anvil part of the squall line, while most of the emphasis in this work is on the leading convective region of the squall line, and its propagation. It is also not known (nor addressed by Srivastava *et al.*) to what extent the observations at the northern edge of the squall line, where the NIMROD network was situated, are representative of the entire length of the squall line. This squall line stretched from Illinois to the Texas panhandle, and the NIMROD field project was only situated in northern Illinois, at the very northern end of the squall line. The northern end of the squall line convection seemed to merge with a large, non-linear in shape, mesoscale convective system, so it is not clear whether the mechanisms operating in that region apply to the full length of the squall line. Finally, although their observations are generally consistent with other studies, it is also not clear whether the "detached", yet semi-steady-state, anvil studied by Srivastava *et al.* is representative of other squall line stratiform anvils. It is, however, similar to those studied by Smull and Houze (1987), Rutledge *et al.* (1988), and Johnson and Hamilton (1988).

3.2 Comments From Thomas Matejka

Thomas Matejka participated in the field project that observed this squall line in Northern Illinois and is one of the authors of the Srivastava *et al.* (1986) paper. He provided several personal observations of the squall line to this author which will be briefly summarized in this section.

First of all, Matejka has emphasized the discrete nature of the propagation of the squall line. He noted that new thunderstorms formed 20 to 35 km ahead of the forward edge of the gust front, and that the actual passage of the gust front was associated with dissipating elements of the squall line.

Secondly, Matejka noted that the squall line initially formed along the front, and only subsequently moved out ahead of it. In northern Illinois, he observed the frontal passage approximately four hours after the passage of the rear edge of the trailing stratiform precipitation.

Matejka's third observation was of a much larger discrete jump of the squall line. He observed that the squall line dissipated in northern Illinois before reaching the Yorkville field site, and then reformed 100 km ahead of the old position. He noted that the radar data showed that the squall line seemed to consist of "large segments, 100 to 200 km long, that marched along in phase, occasionally jumping forward but eventually getting back in step with adjacent segments." It will be shown later that some of the aspects that Matejka described have been successfully replicated in the model simulations.

3.3 Satellite Imagery

The satellite imagery available for this case will be discussed in this section. Unfortunately, the available area of coverage is limited and does not encompass the entire squall line. The areal coverage for most of these pictures only encompasses the northeastern two-thirds of the squall line.

Figures 3.6a-i show the enhanced IR satellite photographs from 1200 through 2330 UTC 17 June 1978, and at 0100 and 0430 UTC 18 June 1978. The latter two photographs are from Srivastava *et al.* (1986). The squall line did not start to develop until after 1800 UTC so the photographs are shown at three-hourly intervals up to that time (1200, 1500, and 1800 UTC) and then at one-hourly intervals through 2300 UTC. Figures 3.6j-k are from Srivastava *et al.* (1986) and were the only satellite photographs available after 0000 UTC.

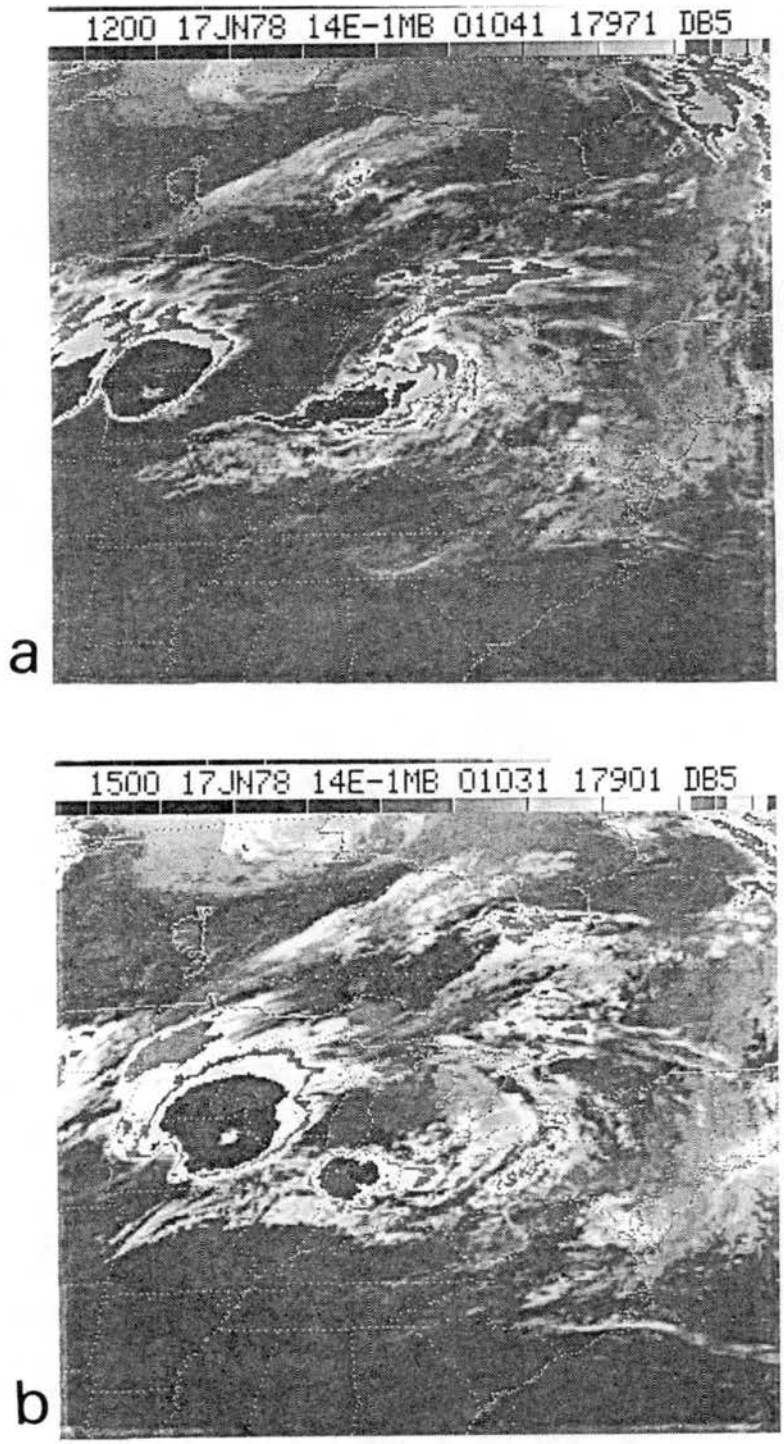

Figure 3.6: Enhanced IR satellite photographs from 1200 – 2330 UTC 17 June 1978, and at 0100 and 0400 UTC 18 June 1978: (a) 1200 UTC; and (b) 1500 UTC.

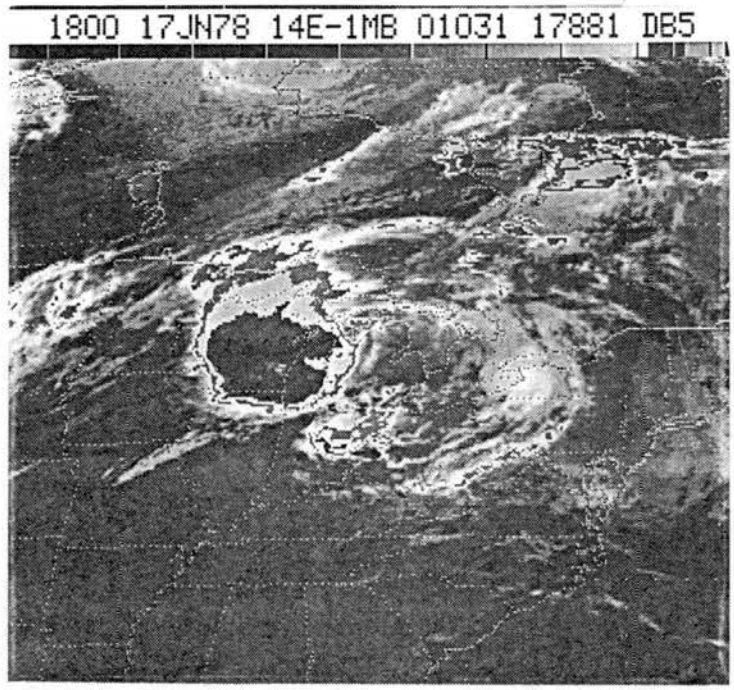

c

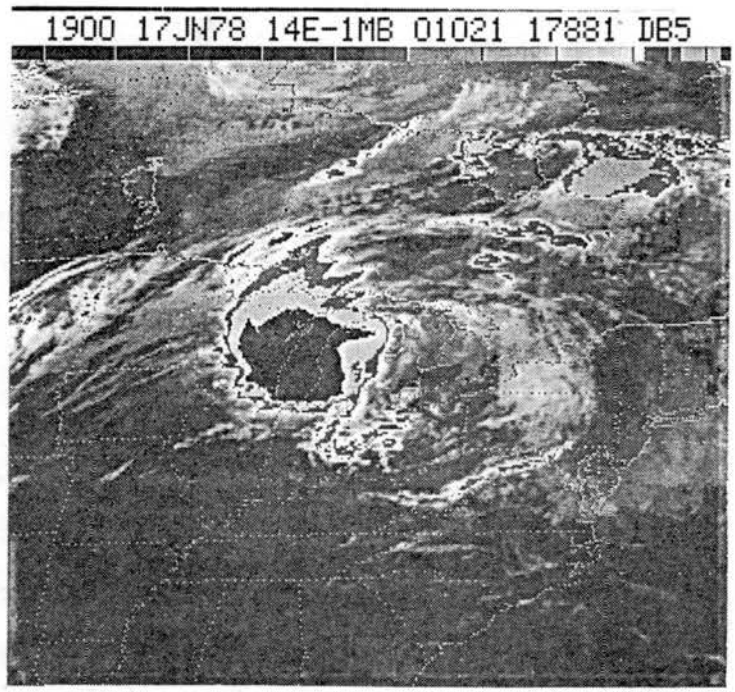

d

Figure 3.6: Continued: (c) 1800 UTC; and (d) 1900 UTC.

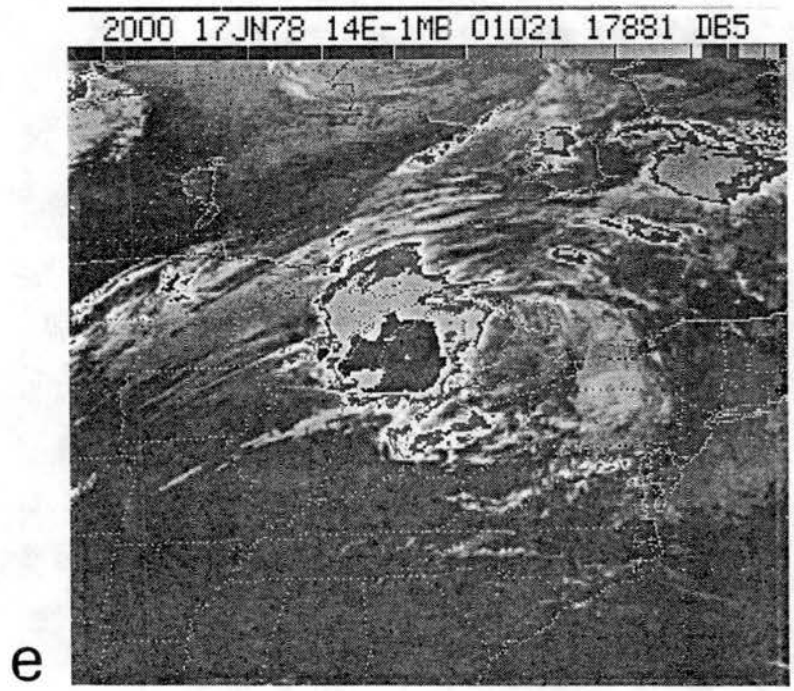

e

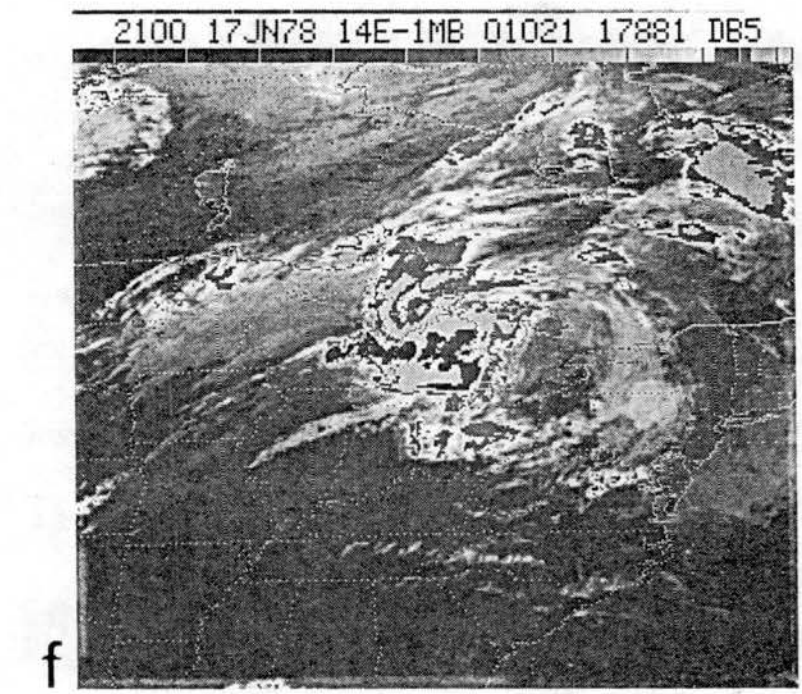

f

Figure 3.6: Continued: (e) 2000 UTC; and (f) 2100 UTC.

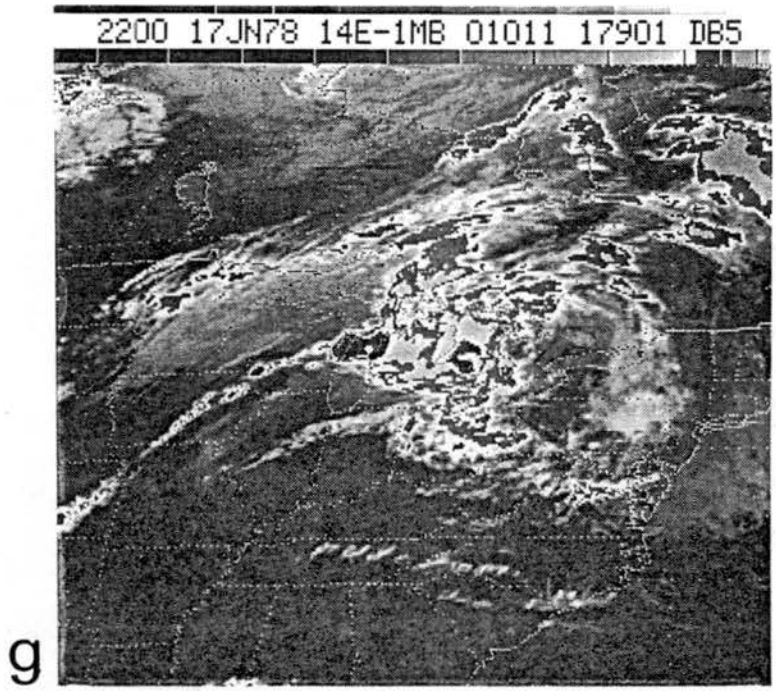

g

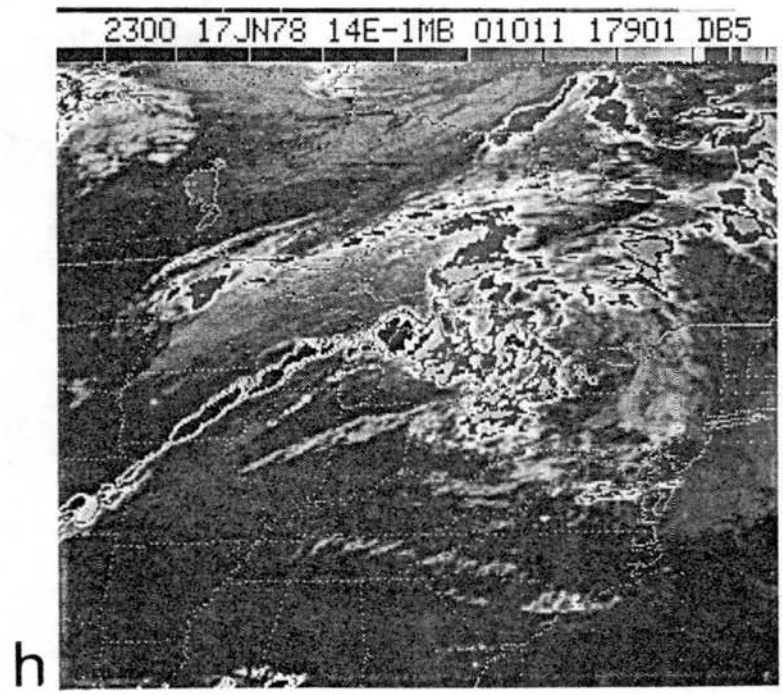

h

Figure 3.6: Continued: (g) 2200 UTC; and (h) 2300 UTC.

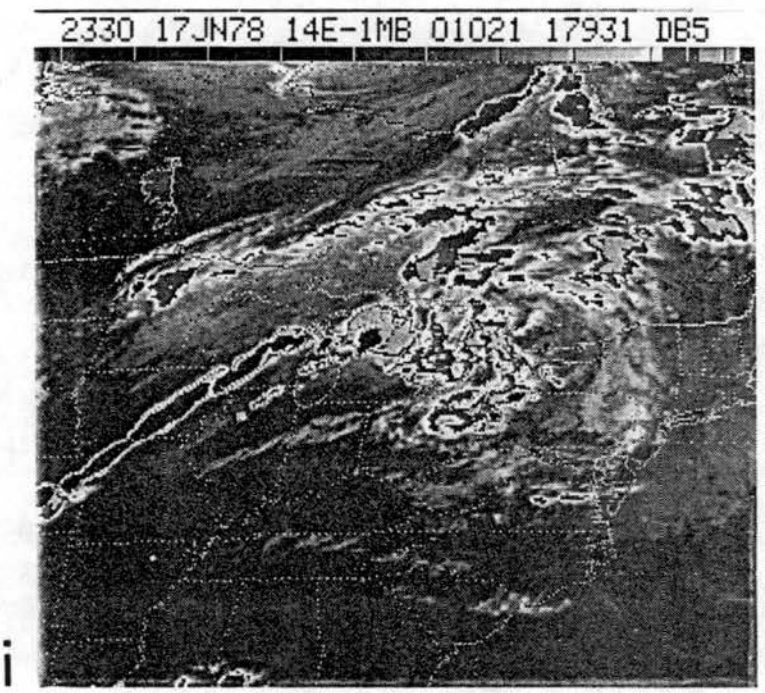

i

Figure 3.6: Continued: (i) 2330 UTC.

j

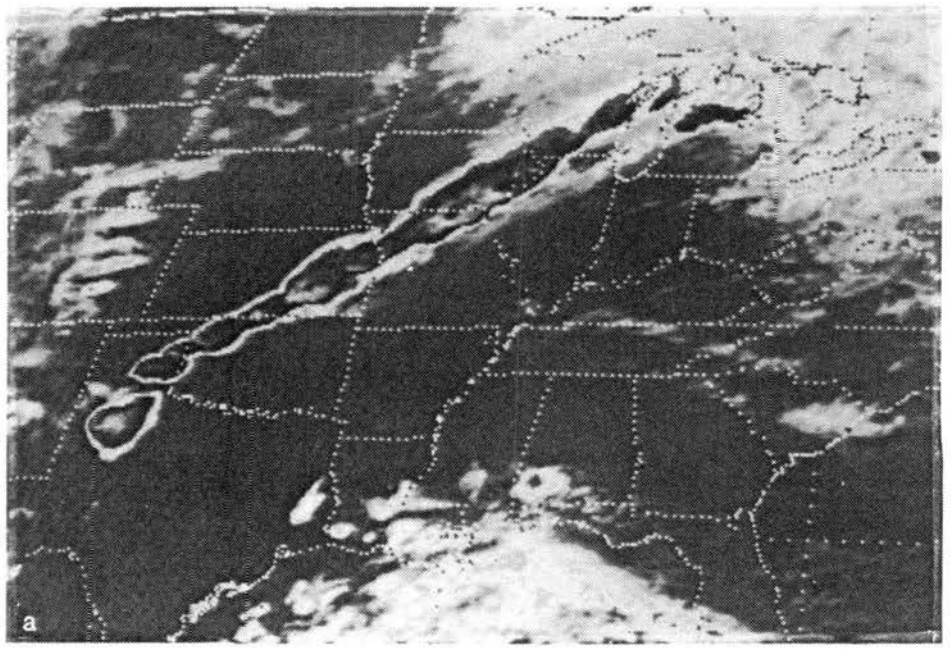

k

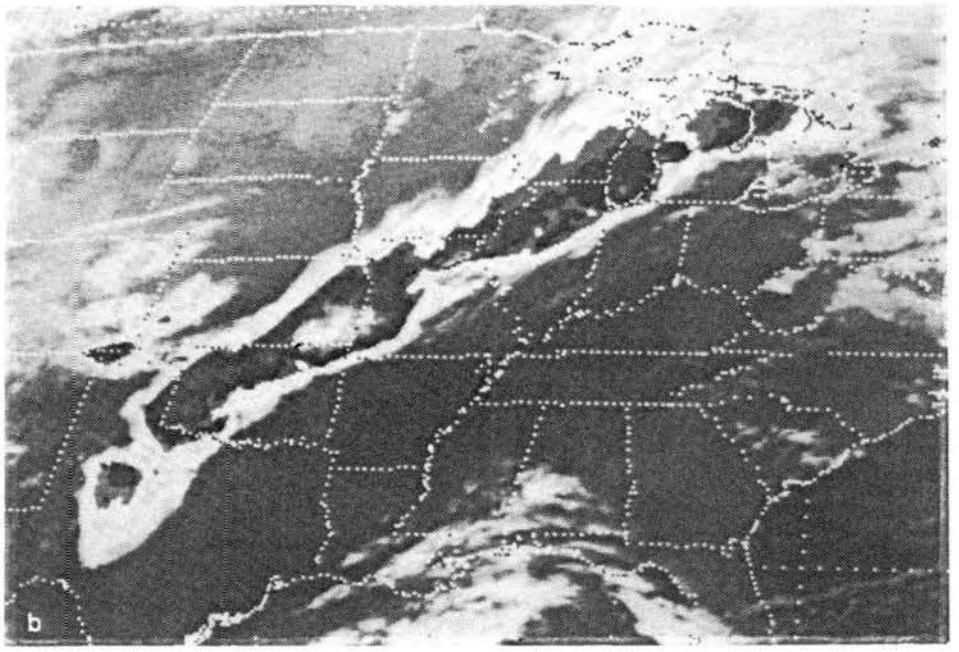

Figure 3.6: Continued: (j) 0100 UTC; and (k) 0430 UTC. (j) and (k) are from Srivastava *et al.* (1986).

The rapid northeastward movement of a large mesoscale convective complex (MCC) from northern Iowa to southern Wisconsin can be seen in Figs. 3.6a-c. The convection associated with the squall line is first just barely visible at 1800 UTC (Fig. 3.6c) in the northwestern section of Kansas. The line of convection extending southwestward from the MCC centered over Wisconsin is not associated with the squall line.

The line of convection in northeastern Kansas grows stronger and can be seen developing from 1900 – 2100 UTC (Figs. 3.6d-f), but the squall line convection farther northeast (in Missouri and Iowa) does not seem to start developing until 2100 UTC. By this time the MCC has moved eastward to over Michigan and is starting to dissipate.

Between 2100 and 2330 UTC the squall line develops explosively (Figs. 3.6f-i). A very narrow but continuous band of very cold cloud tops is visible at 2300 and 2330 UTC, associated with the squall line anvils. The width of the cloud tops is only about 100 km but the line extends more than 1000 km continuously.

Also, in Figs. 3.6g-i (2200 – 2330 UTC), a short segment of convection has developed approximately 100 km ahead of the original squall line. The segment extends from northern Illinois northeastward across Lake Michigan. It is not clear whether this segment is in some way associated with the overall squall line dynamics. The convection associated with the northern end of the squall line is first visible in southern Wisconsin at 2000 UTC (Fig. 3.6e) but does not show up as enhanced cloud tops (very cold and very high) until 2200 UTC. This is the same time that the new segment of convection has first become visible. Closer examination of the satellite photographs in that region reveals that there may be a moisture boundary oriented along where the new segment develops. There is a slight gradation in the shading, indicating a moisture gradient or boundary between clear air and a fair-weather-cumulus field. Also the new segment is oriented parallel to, but behind, the line of convection that extends southwestward from the MCC. Again, it is not clear whether the squall line is the primary forcing mechanism for the new convection in that region. Although the development of the new segments of convection approximately 100 km ahead of the original squall line is consistent with Matejka's observations

(discussed previously in Section 3.2), no other such segments can be seen in these satellite photographs. Figures 3.6j-k show the squall line at 0100 and 0430 UTC. At 0100 UTC the squall line has widened to almost 200 km, and at 0430 UTC is more than 300 km wide.

The explosive development of the squall line and its very narrow, yet very long and continuous, development have been shown in this section. It is clear from the photographs that the northern end is not necessarily representative of the rest of the squall line. A large area of MCC-related convection moved through northern Illinois and Wisconsin less than 6 hours prior to the squall line development in that region. In addition a second segment of convection appeared to develop approximately 100 km ahead of the original squall line in that region, but only slightly after the original development. Such discrete segments are not visible along any other parts of the squall line shown in the photographs (from Kansas northeastward) at any of the available times (through 2330 UTC). However, as will be noted in the next section, strong development of the squall line convection continued through at least 0300 UTC 18 June 1978.

3.4 Radar Summary charts

The National Weather Service (NWS) radar summary charts covering the period of the squall line will be discussed in this section. Figure 3.7 shows the hourly radar summary charts from the National Weather Service from 1235 UTC 17 June through 0935 UTC 18 June (the charts from 2135 and 2335 UTC 17 June were unavailable, and the chart from 1835 UTC 17 June had most stations reported as NA-not available).

Figures 3.7a-c show the convection associated with the MCC depicted in the satellite photographs extending from Nebraska to Illinois and Wisconsin. Several cells are evident at 1235 UTC but they have consolidated by 1935 UTC into one large MCC centered over southern Wisconsin. The convection associated with the line extending southwestward from the MCC (described in Section 3 previously) is visible over northeastern Missouri at 1535 UTC. However, no convection directly associated with the squall line is visible yet at 1735 UTC (not shown). The 1835 UTC map is not shown as most stations reported NA (not available) at that time.

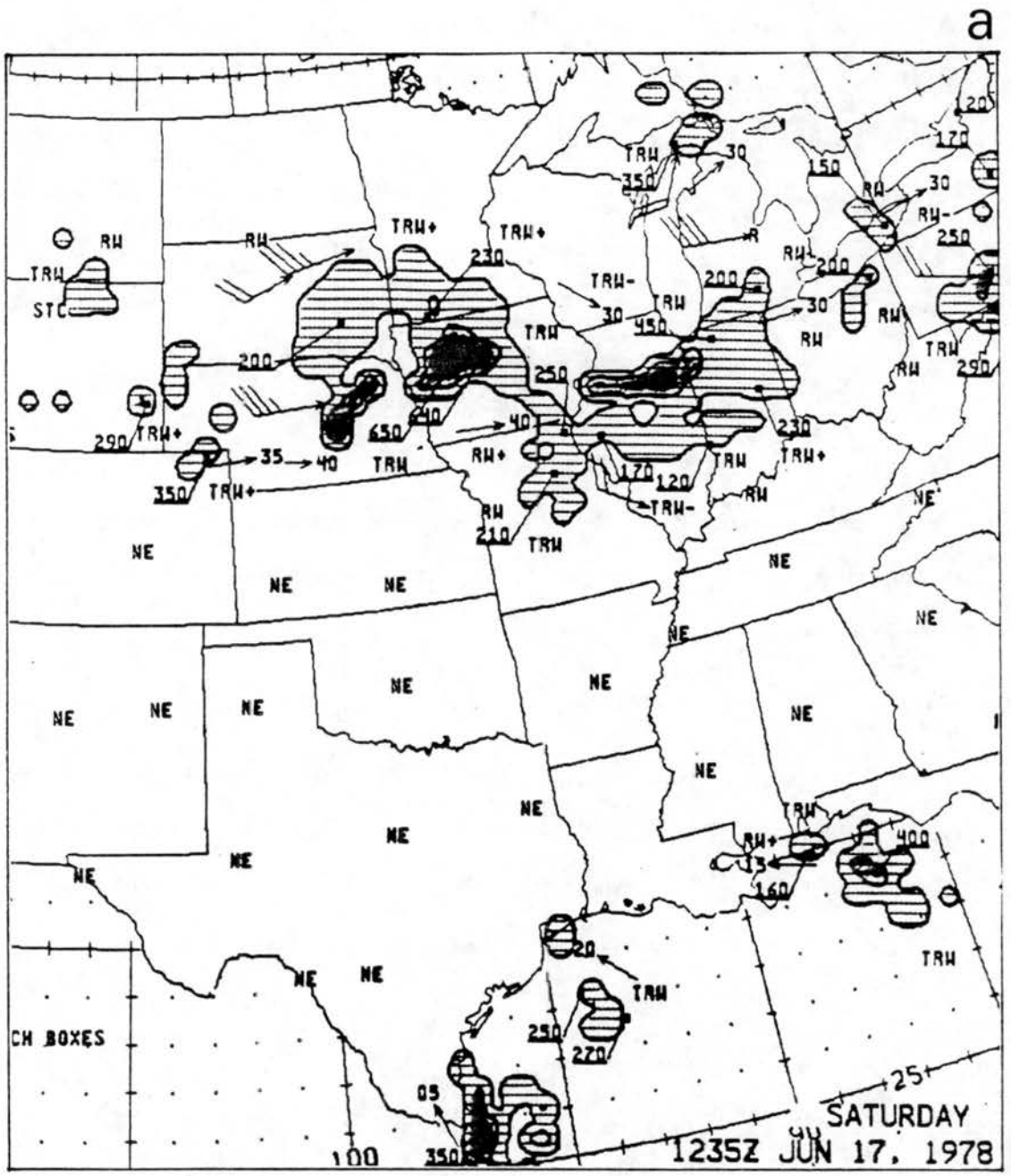

Figure 3.7: Radar summary charts from 1235 UTC 17 June 1978 through 0935 UTC 18 June 1978: (a) 1235 UTC.

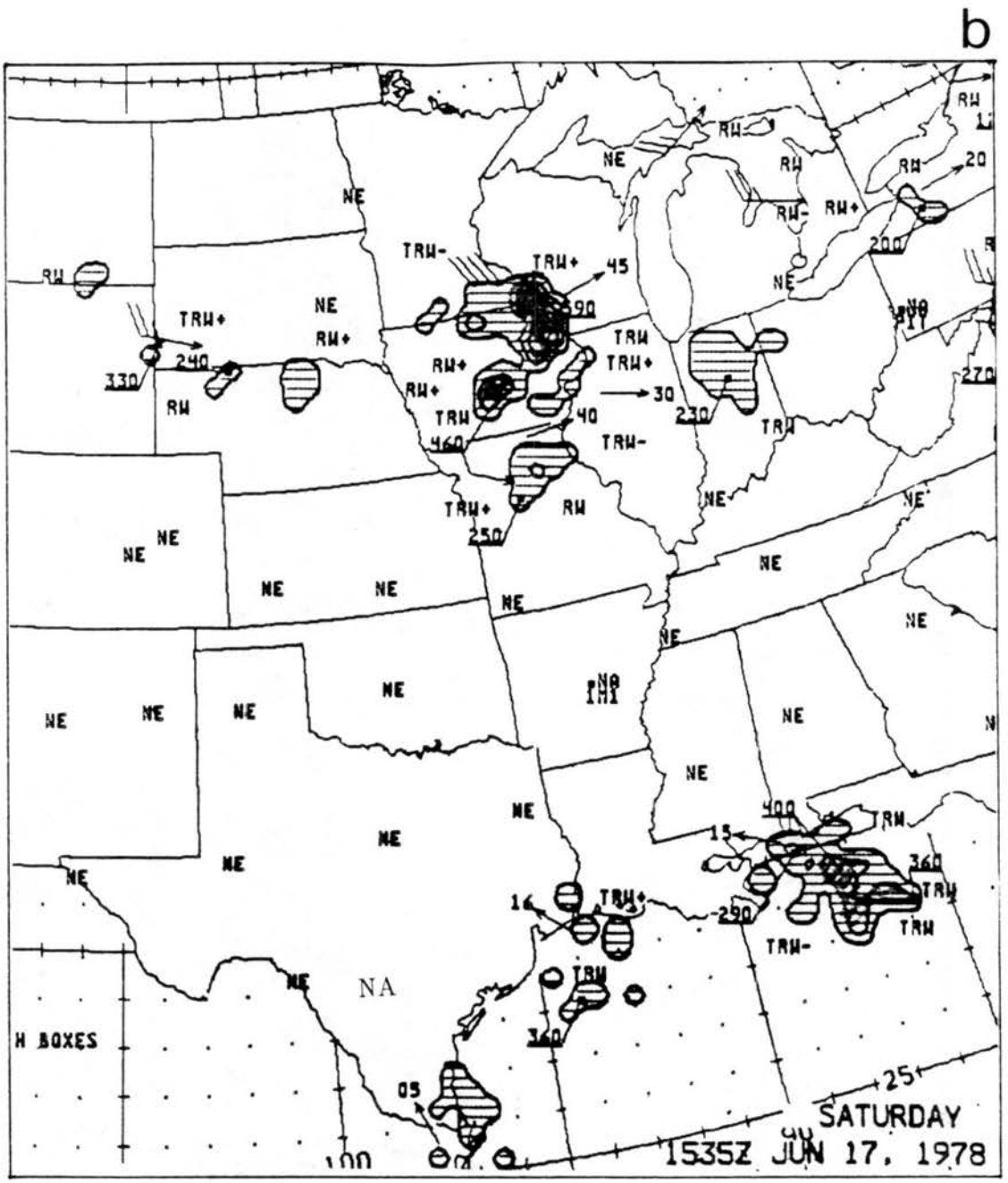

Figure 3.7: Continued: (b) 1535 UTC.

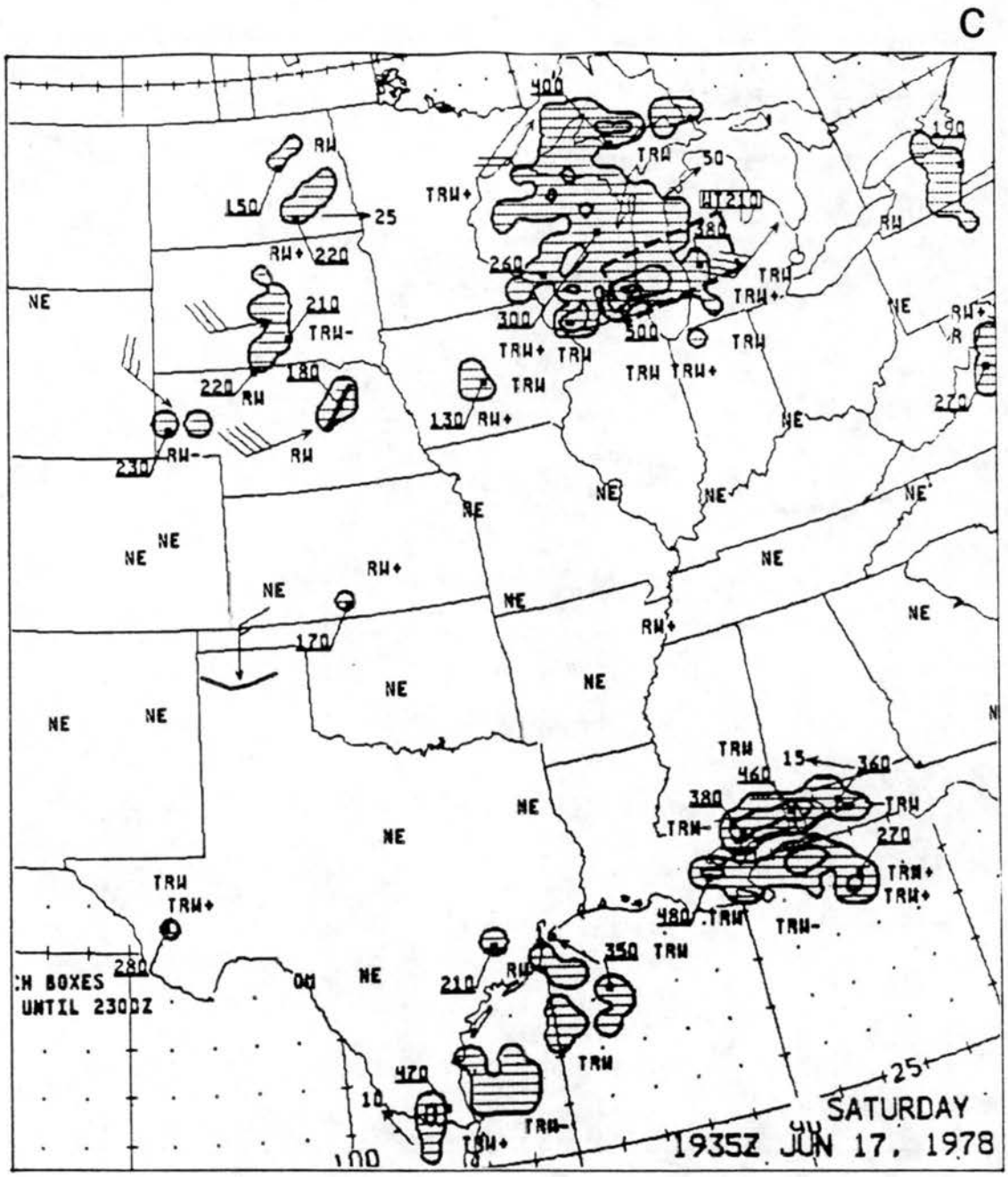

Figure 3.7: Continued: (c) 1935 UTC.

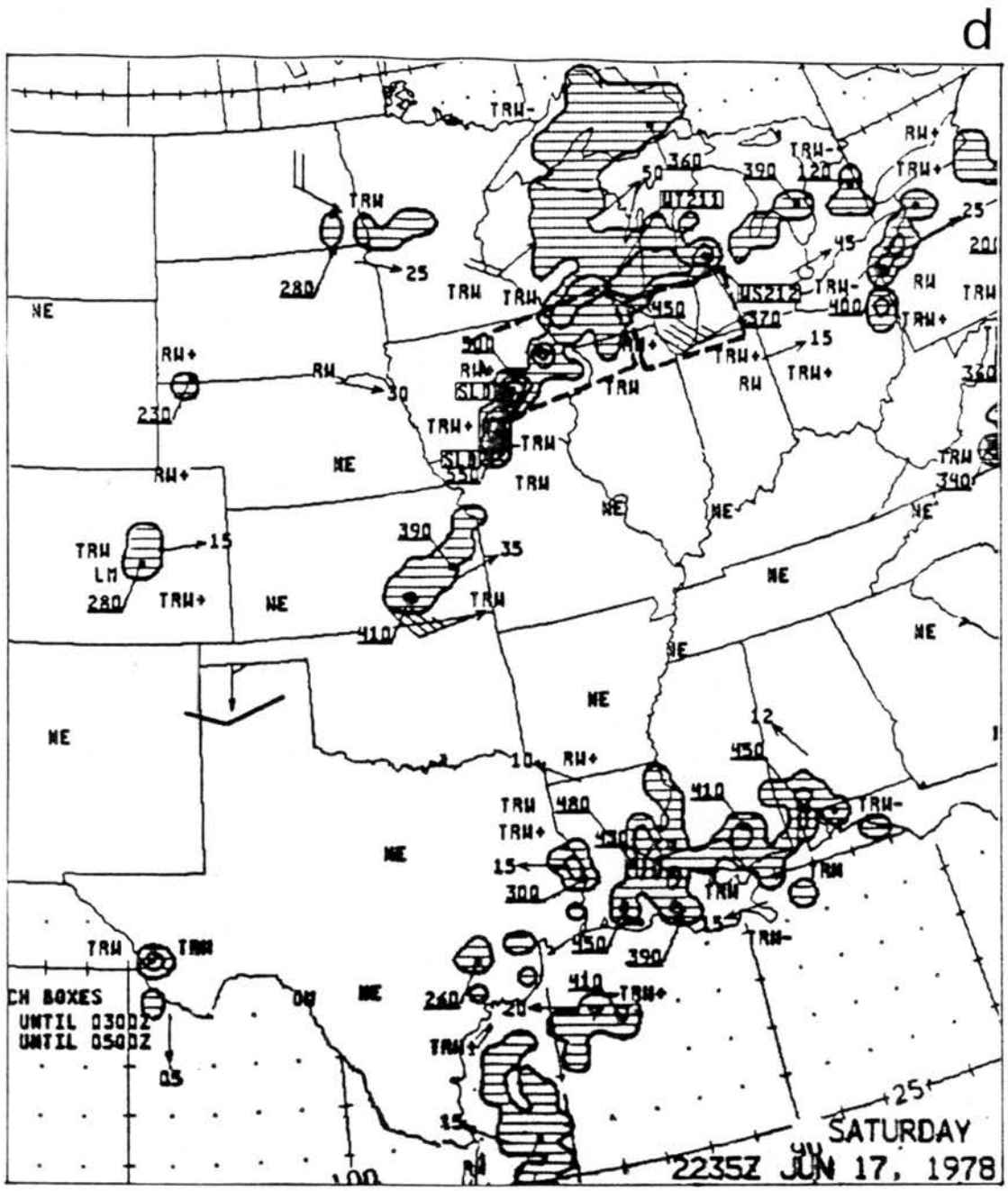

Figure 3.7: Continued: (d) 2235 UTC.

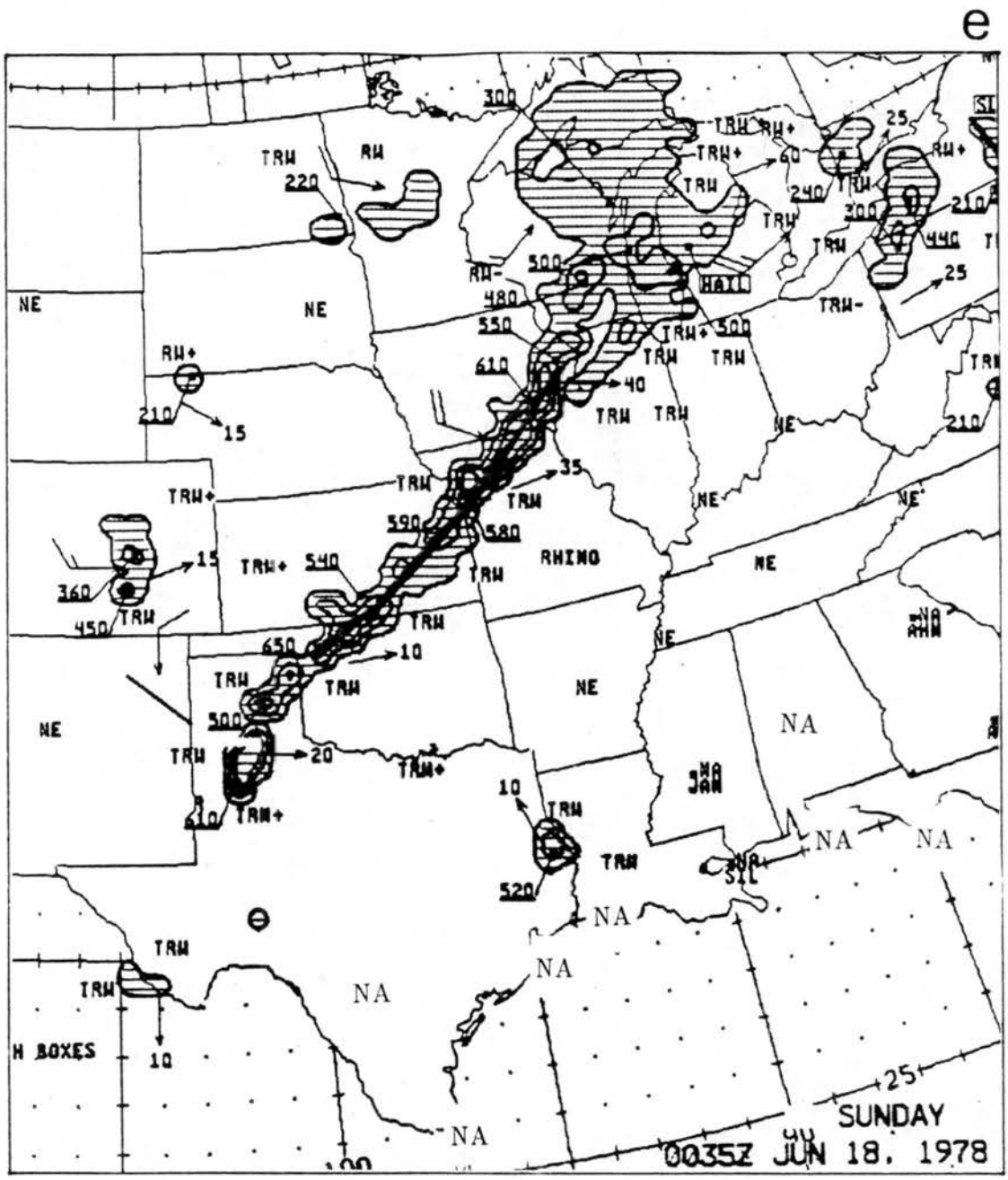

Figure 3.7: Continued: (e) 0035 UTC.

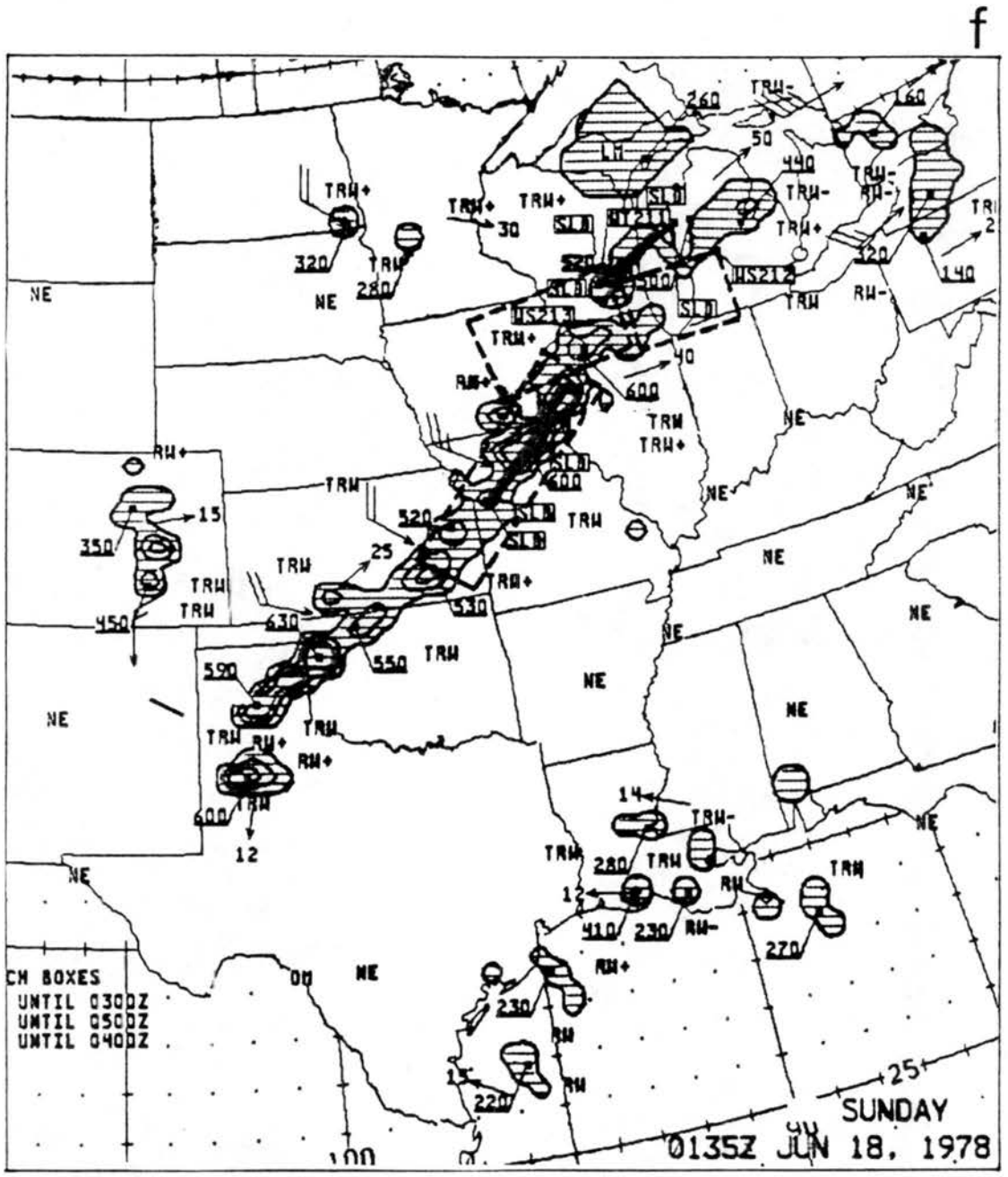

Figure 3.7: Continued: (f) 0135 UTC.

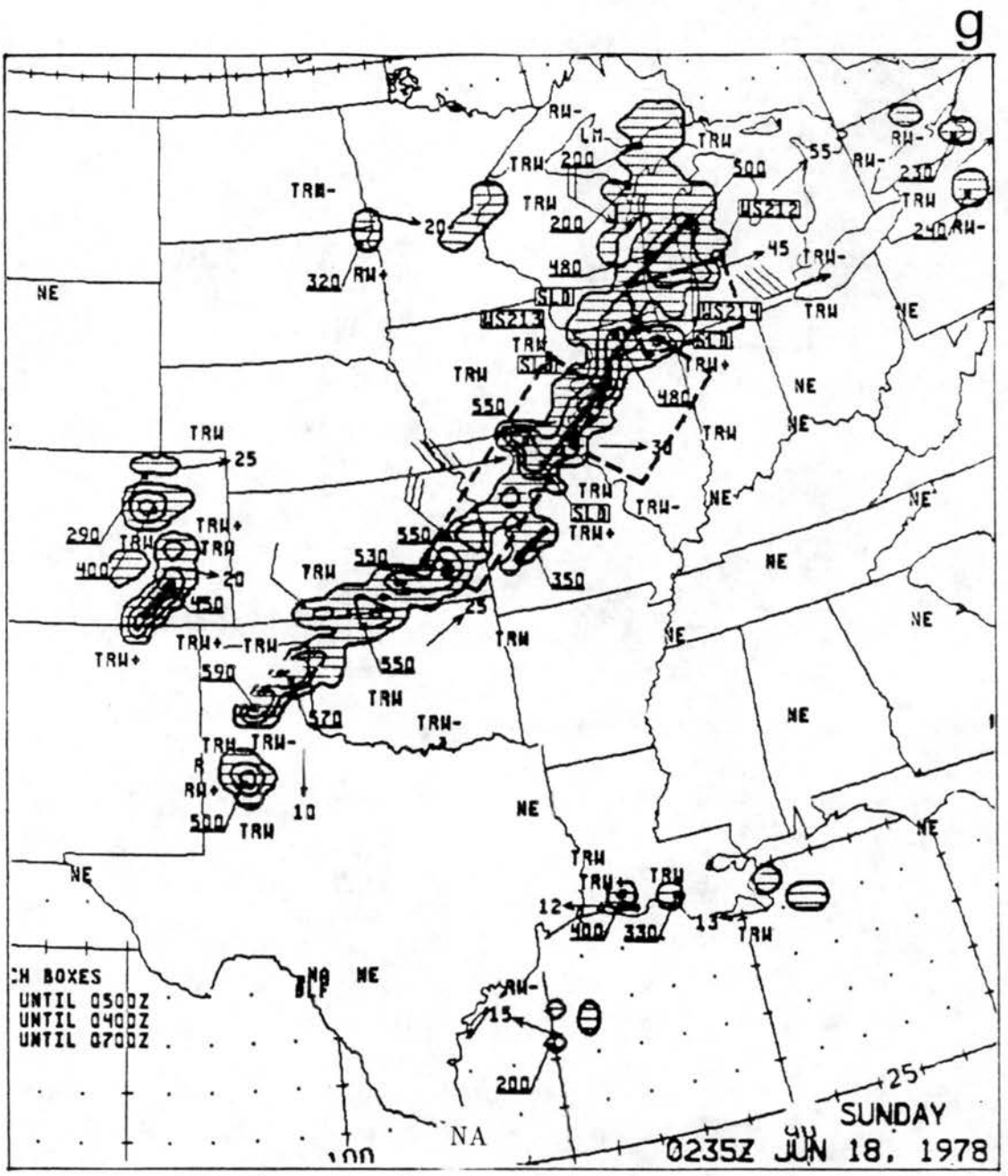

Figure 3.7: Continued: (g) 0235 UTC.

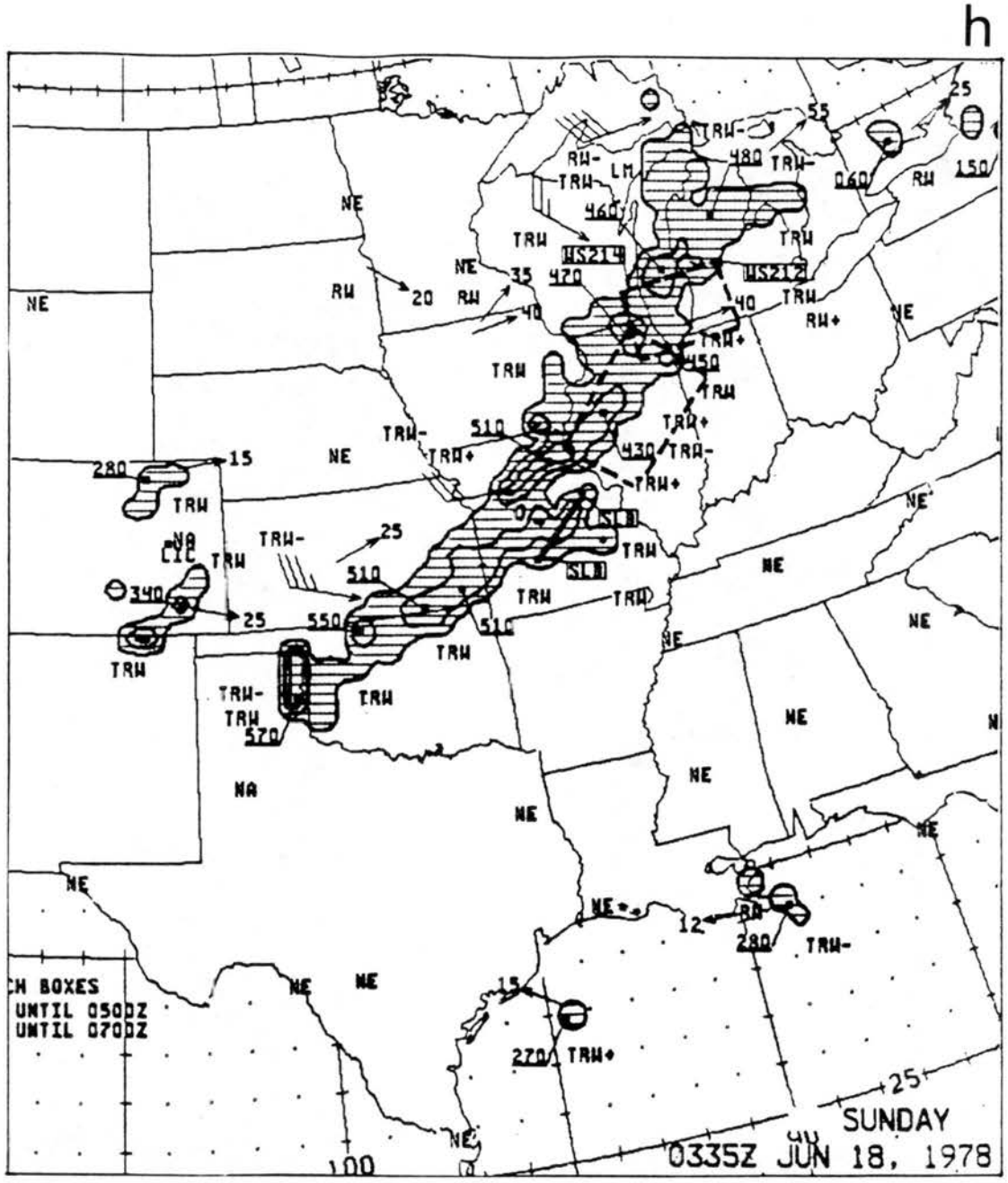

Figure 3.7: Continued: (h) 0335 UTC.

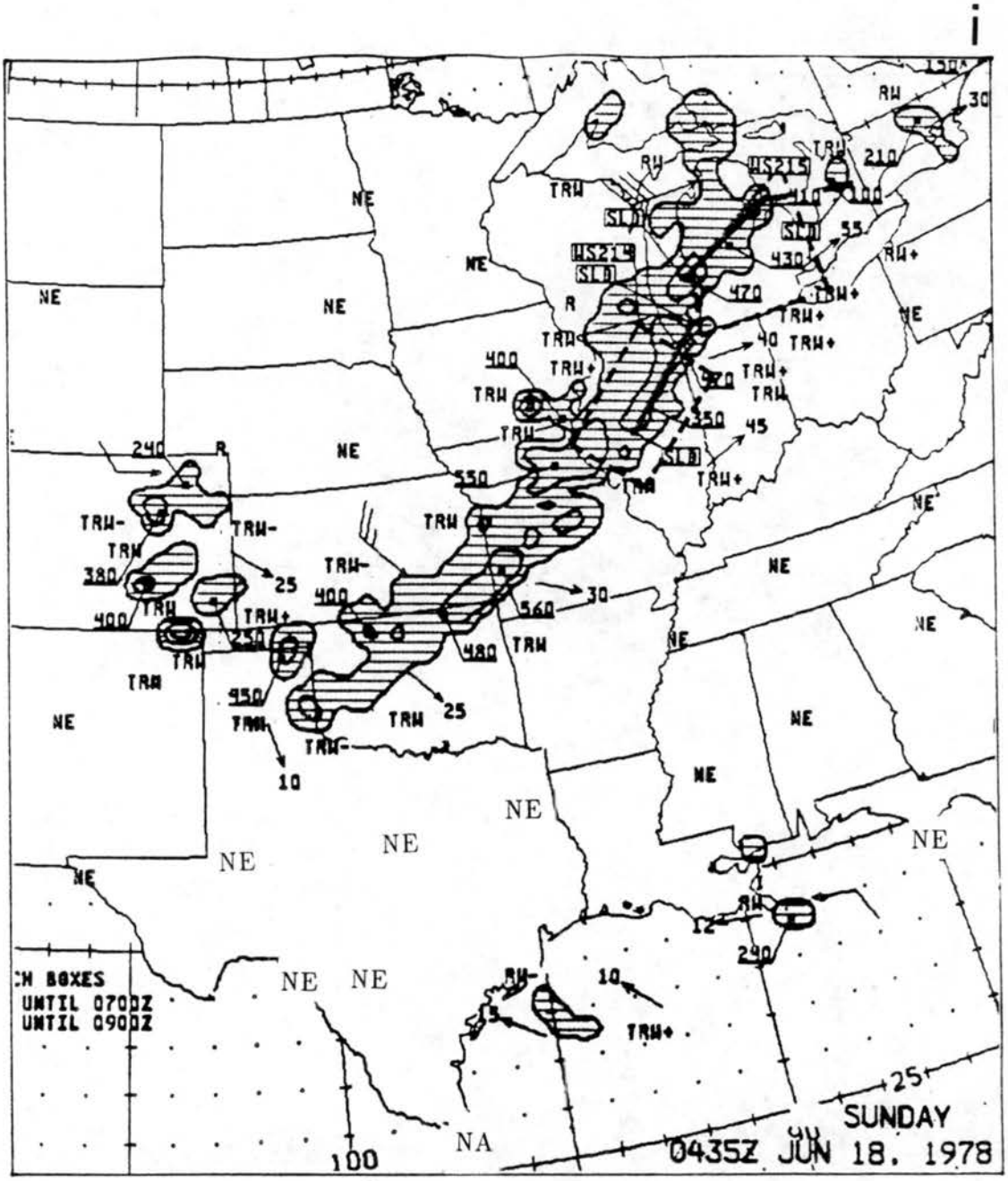

Figure 3.7: Continued: (i) 0435 UTC.

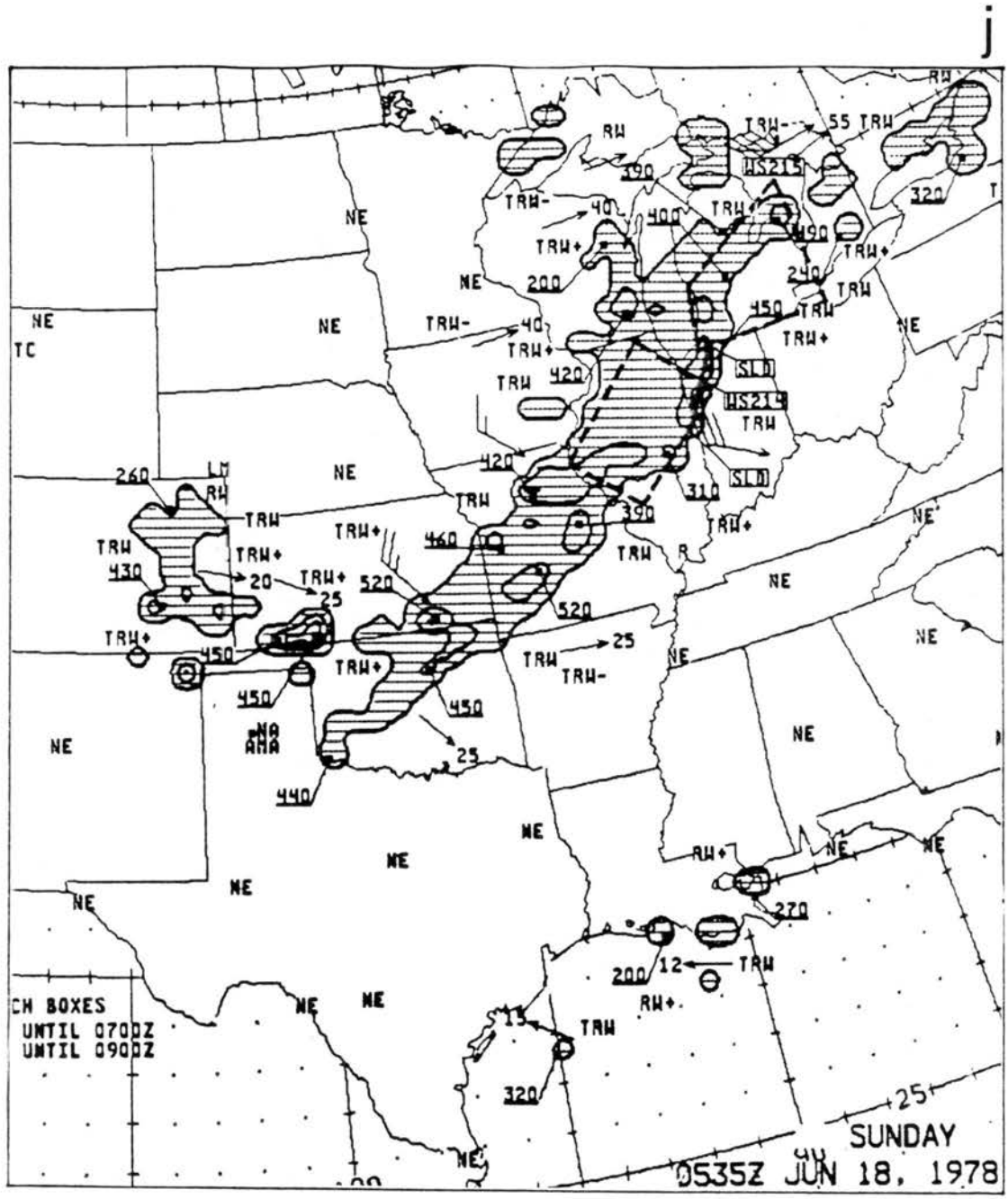

Figure 3.7: Continued: (j) 0535 UTC.

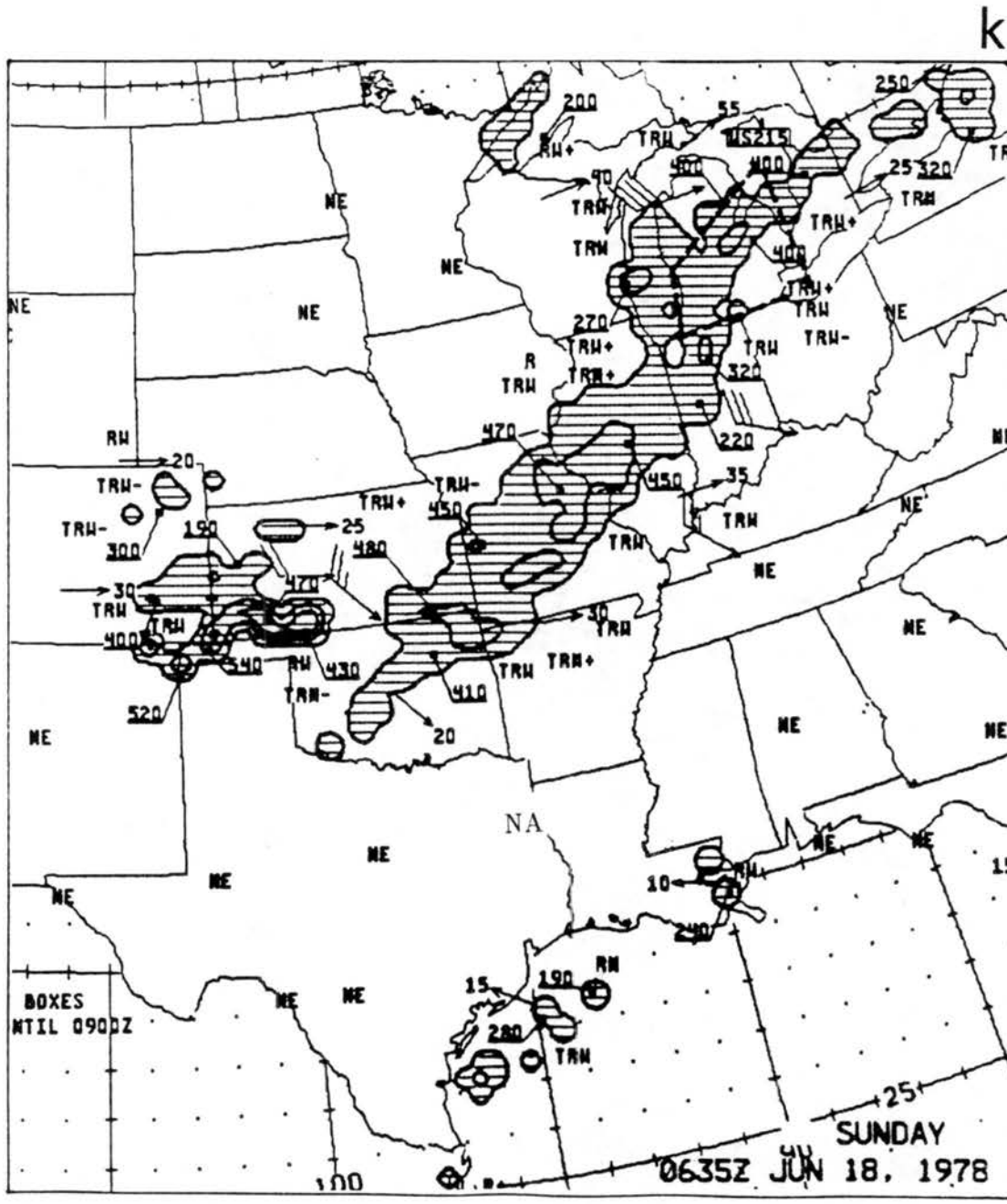

Figure 3.7: Continued: (k) 0635 UTC.

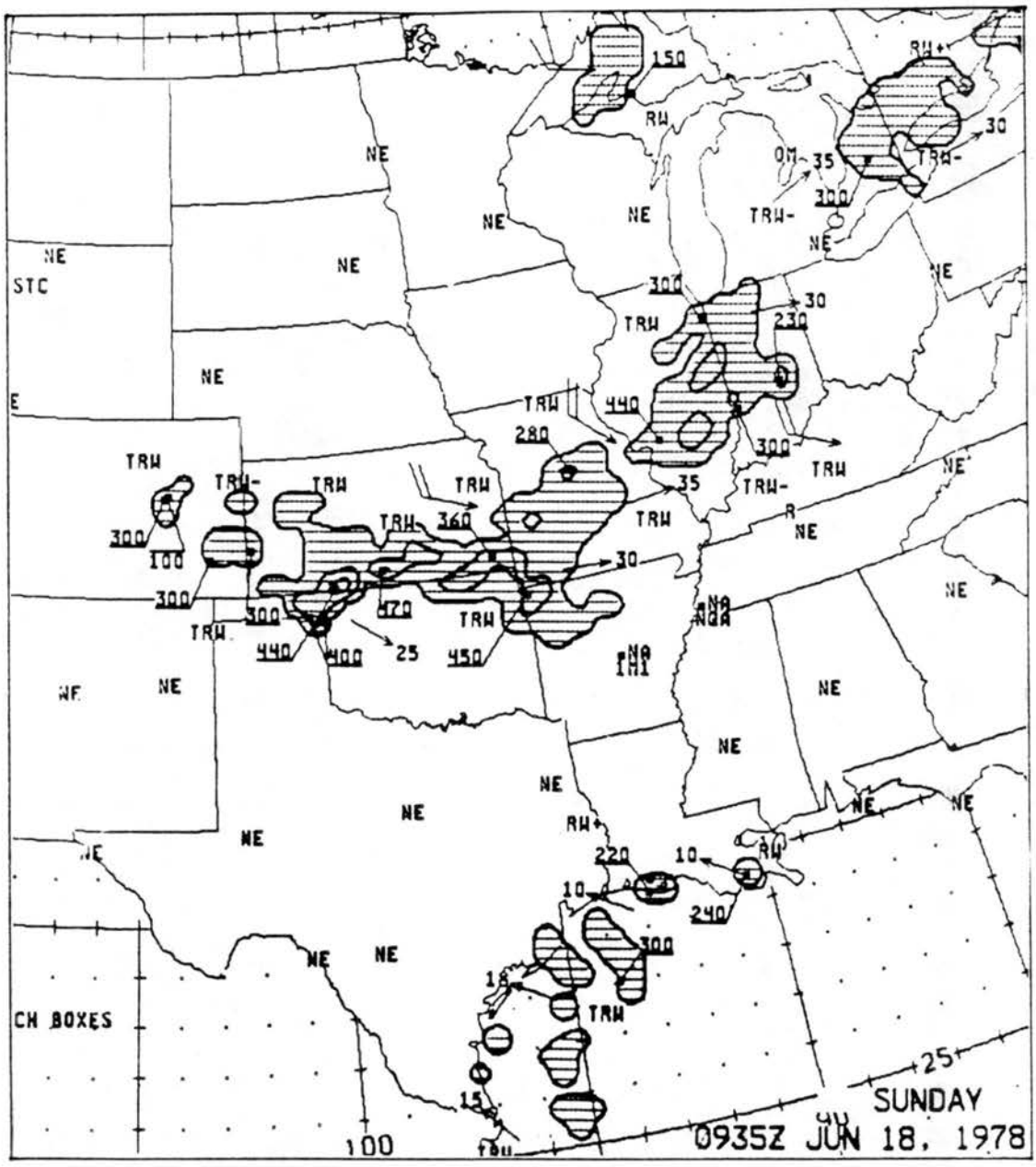

Figure 3.7: Continued: (l) 0935 UTC.

The first echoes associated with the squall line are visible at 1935 UTC (Fig. 3.7c). A small echo over southern Kansas and another over central Iowa are the first indications of the developing squall line. By 0035 UTC (Fig. 3.7e) the line of radar echoes is continuous from the Texas panhandle through northern Illinois. The maximum tops reported at that time are all near 60,000 feet (18 km) although one top in the Texas panhandle extends to 65,000 feet (almost 20 km). The movements of individual cells along the line range from 10-40 knots (5-20 m s^{-1}) and are generally eastward. At 0035 UTC the line appears to be fairly straight and continuous; there is no evidence on that scale of a discrete or segment-like propagation.

From 0035 through 0235 UTC (Figs. 3.7e-g) the line translates approximately 30 – 50 km southeastward. Individual cellular movements along the front of the line vary from 25 to 40 knots (13-20 m s^{-1}) and are eastward through northeastward. Evidence of the discrete propagation of the line is visible at 0235 UTC. A segment of convection approximately 150 km long appears to have developed approximately 50 km ahead of the original line over central Missouri. The large area of convection associated with the MCC decreases over this period, and by 0235 UTC the squall line and remaining MCC activity form a continuous and fairly straight line of radar echoes from the Texas panhandle to the northern edge of Lake Michigan. Several cells also develop over eastern Colorado during this period.

Between 0235 and 0635 UTC, the radar echoes associated with the squall line widen and weaken. The segment of convection that developed ahead of the original line over Missouri is still visible at 0335 UTC (Fig. 3.7h) and is still ahead of the rest of the line-associated echoes. The width of the squall line echo region widens from approximately 100 km at 0235 UTC (Fig. 3.7g) to 150 km at 0335 UTC (Fig. 3.7h), and to 200 km at 0635 UTC (Fig. 3.7k). The individual echoes move at speeds from 25 – 30 knots eastward through southeastward during this period. The convection from eastern Colorado moves southeastward and consolidates over southwestern Kansas by 0635 UTC. The tops of the echoes range from 41,000 – 48,000 feet (12.5 – 14.5 km) at 0635 UTC.

From 0635 – 0935 UTC (Figs. 3.7k-l) the squall line continues to weaken. The newer and stronger convection over southwestern Kansas merges with the remains of the squall line over southern Kansas, and the echoes lose their distinct, long-line shape.

The radar summary maps have shown that the squall line developed most strongly and explosively between 2235 and 0035 UTC. At its peak in terms of radar echo intensity, 0035 – 0235 UTC (6:35 p.m. – 8:35 p.m. CST), the squall line extended from Illinois through the Texas panhandle, although the radar echo region was only about 100 km wide and tops were on the order of 60,000 feet (18 km). Although there is evidence from the radar summary maps of at least one area of discrete, segment-like propagation, the line of radar echoes generally appears to be fairly straight and continuous. However, these are only hourly snapshots of the line, and of the radar-resolvable precipitation.

3.5 Surface Analyses

Analyses of the hourly surface data were created for verification purposes. The data set used for these analyses (NCAR data set 472.0) is described in Section 4.1.1. The analysis scheme is described in Section 4.1.3. Surface analyses of winds, temperature, mean-sea-level pressure (MSLP), and dewpoint temperature are shown in Figs. 3.8-3.20 for selected times from 1200 UTC 17 June through 0600 UTC 18 June.

Figures 3.8-3.10 show the surface analyses at 1200, 1500, and 1800 UTC, before the squall line convection developed. In all of these figures the wind shift line is aligned almost exactly along the center of the pressure trough, and there is a strong temperature gradient to the northwest of the line. The wind shift line is also aligned along the leading edge of a gradient in dewpoint temperature. The cold front is clearly defined by the wind shift line at these times.

Hourly analyses from 1900 UTC 17 June through 0300 UTC 18 June are shown in Figs. 3.11-19. The squall line convection first started to show up in the radar and satellite imagery between 1900 and 2100 UTC, and the line was continuous by 2300 – 0000 UTC. The first evidence of the convection shows up in the surface analyses at 2000 UTC (Fig. 3.12) where there is a perturbation in the surface dewpoint temperatures in

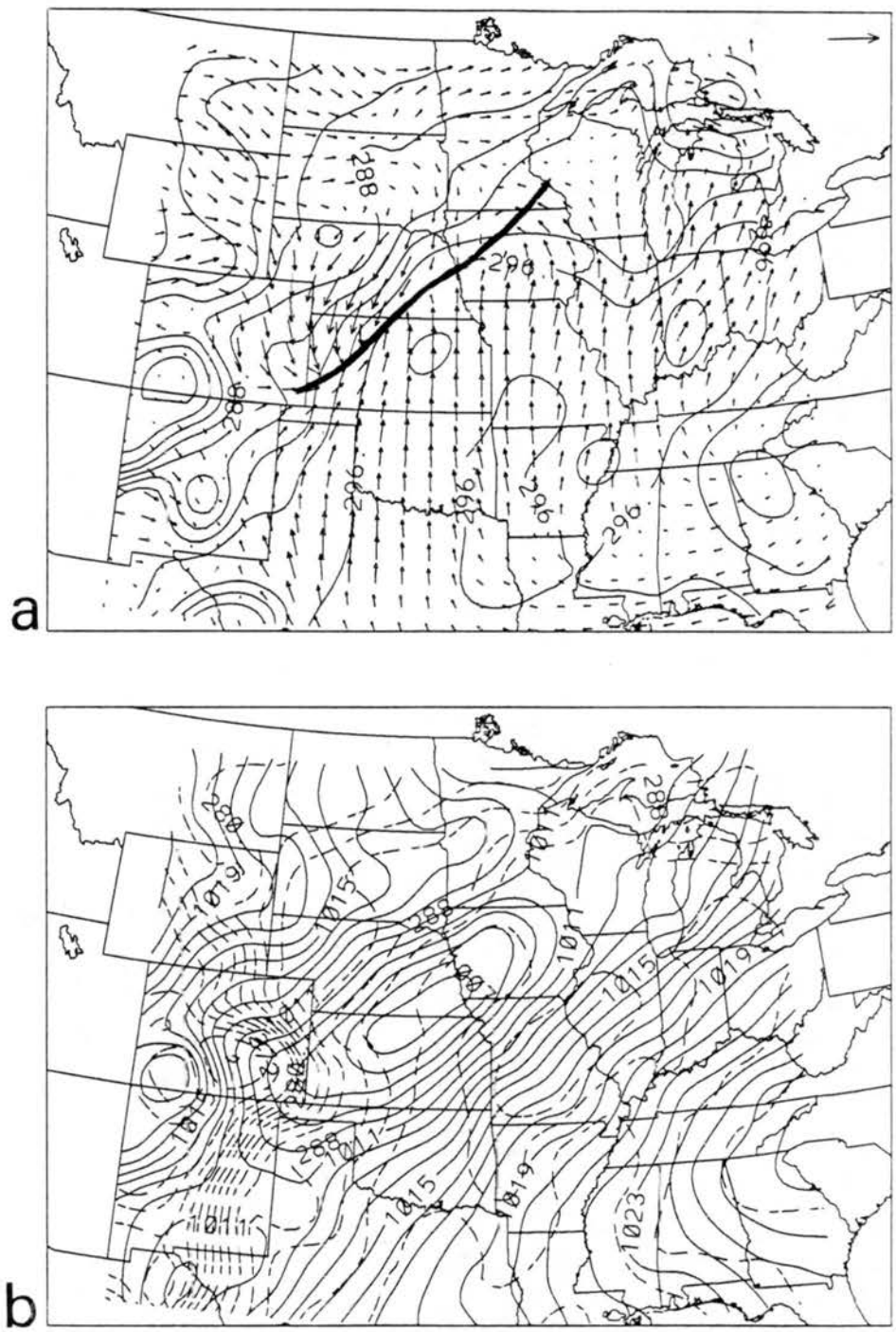

Figure 3.8: Surface analyses at 1200 UTC 17 June 1978 for (a) wind vectors and temperature (K); and (b) MSLP (solid lines, mb) and dewpoint temperature (dashed lines, K). The vector lengths are scaled by speed: the single vector in the upper-right corner of (a) represents 15 m s^{-1}. The maximum windspeeds in (a) are 11 m s^{-1}. The solid line superimposed on (a) is the frontal position.

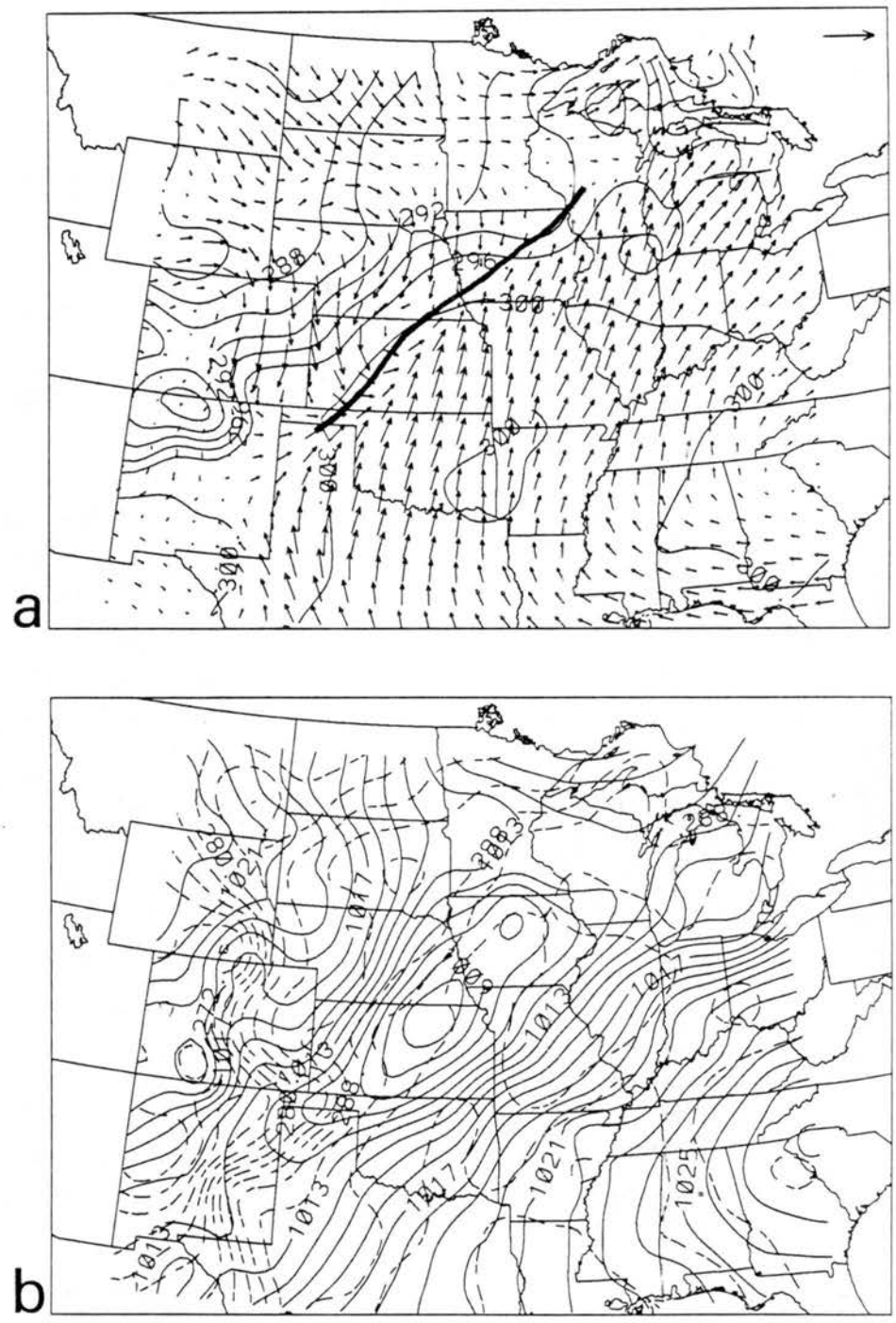

Figure 3.9: Surface analyses at 1500 UTC 17 June 1978 for (a) wind vectors and temperature (K); and (b) MSLP (solid lines, mb) and dewpoint temperature (dashed lines, K). The vector lengths are scaled by speed: the single vector in the upper-right corner of (a) represents 15 m s^{-1}. The maximum windspeeds in (a) are 10 m s^{-1}. The solid line superimposed on (a) is the frontal position.

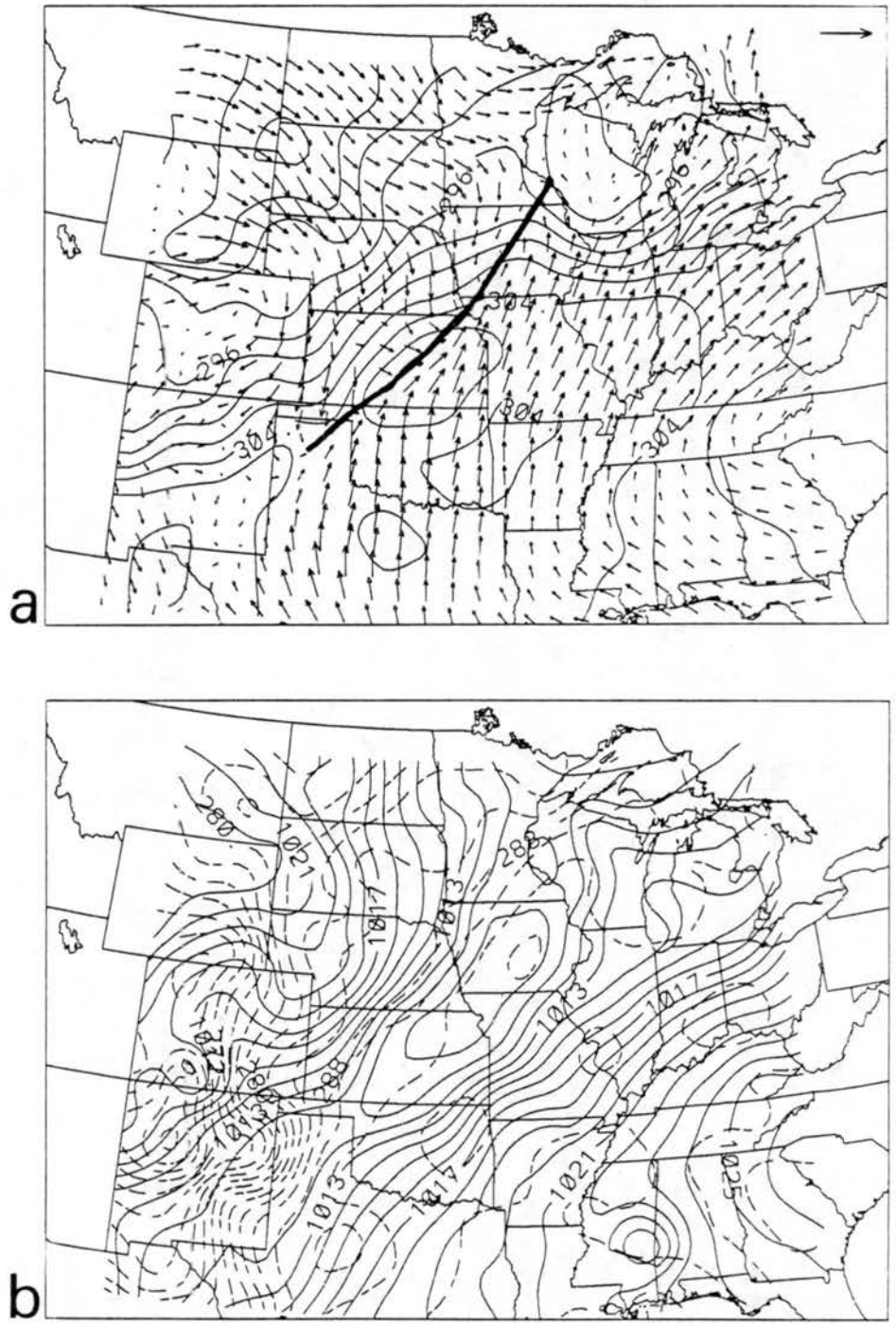

Figure 3.10: Surface analyses at 1800 UTC 17 June 1978 for (a) wind vectors and temperature (K); and (b) MSLP (solid lines, mb) and dewpoint temperature (dashed lines, K). The vector lengths are scaled by speed: the single vector in the upper-right corner of (a) represents 15 m s^{-1}. The maximum windspeeds in (a) are 10 m s^{-1}. The solid line superimposed on (a) is the frontal position.

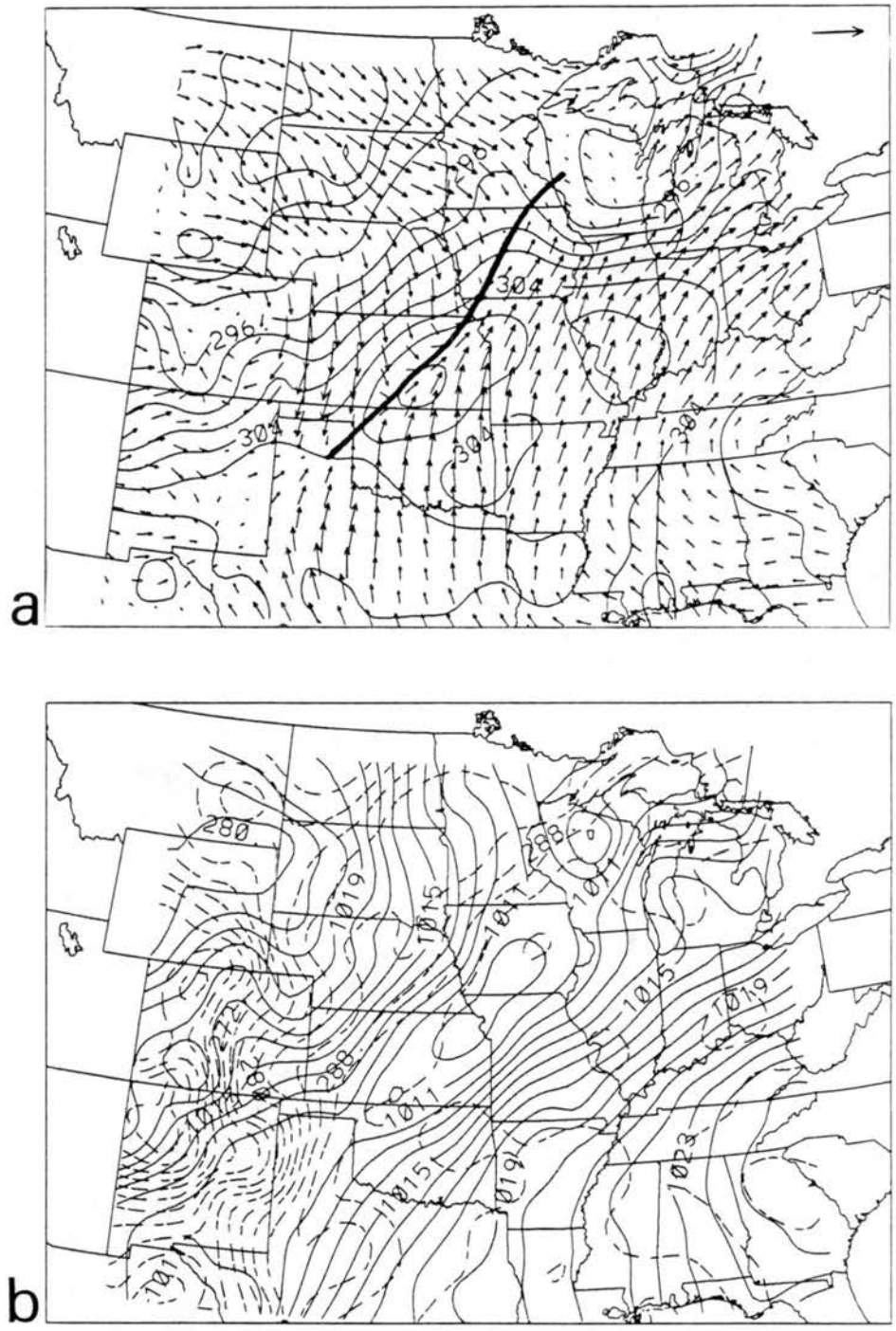

Figure 3.11: Surface analyses at 1900 UTC 17 June 1978 for (a) wind vectors and temperature (K); and (b) MSLP (solid lines, mb) and dewpoint temperature (dashed lines, K). The vector lengths are scaled by speed: the single vector in the upper-right corner of (a) represents 15 m s^{-1}. The maximum windspeeds in (a) are 11 m s^{-1}. The solid line superimposed on (a) is the frontal position.

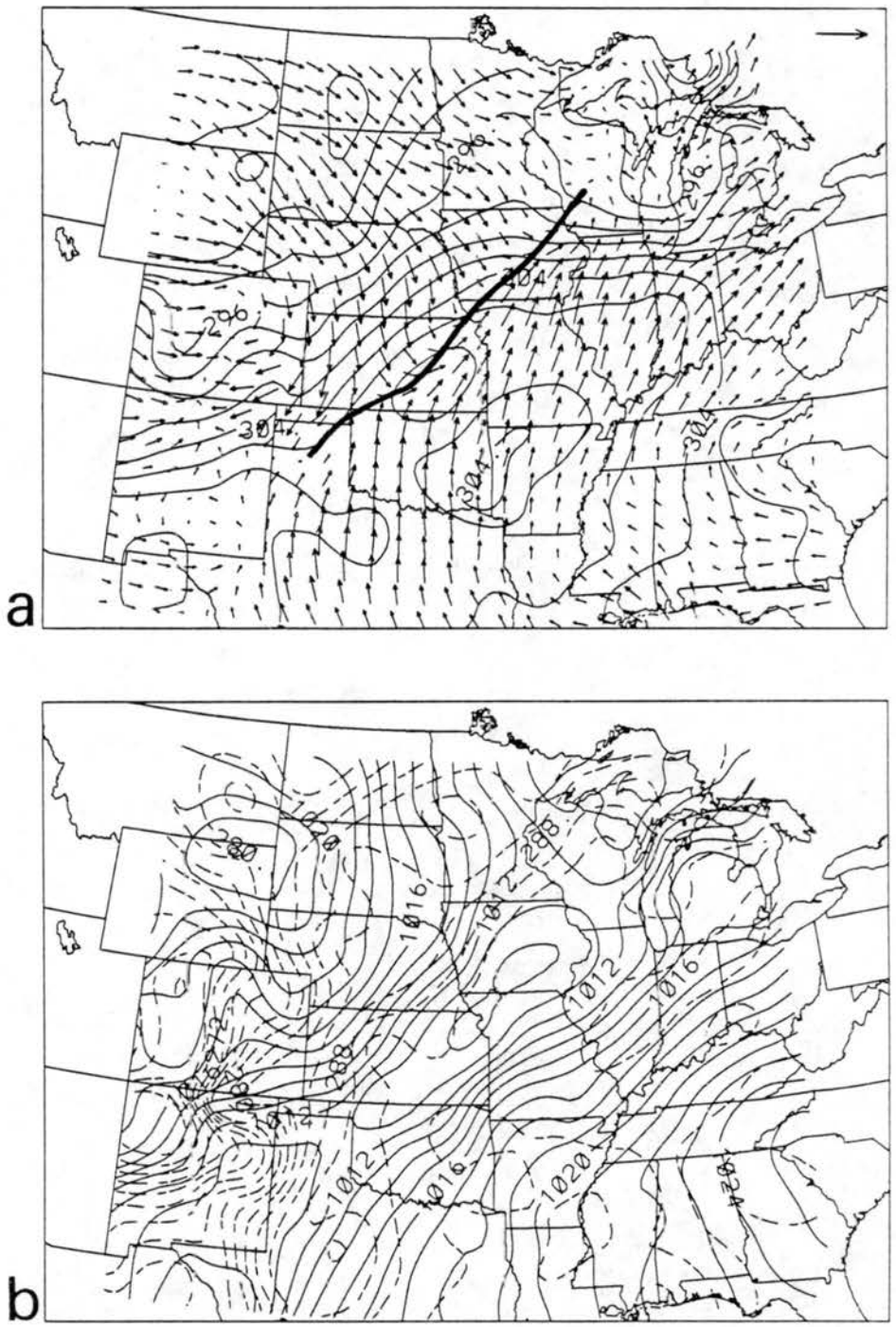

Figure 3.12: Surface analyses at 2000 UTC 17 June 1978 for (a) wind vectors and temperature (K); and (b) MSLP (solid lines, mb) and dewpoint temperature (dashed lines, K). The vector lengths are scaled by speed: the single vector in the upper-right corner of (a) represents 15 m s^{-1}. The maximum windspeeds in (a) are 10 m s^{-1}. The solid line superimposed on (a) is the frontal position.

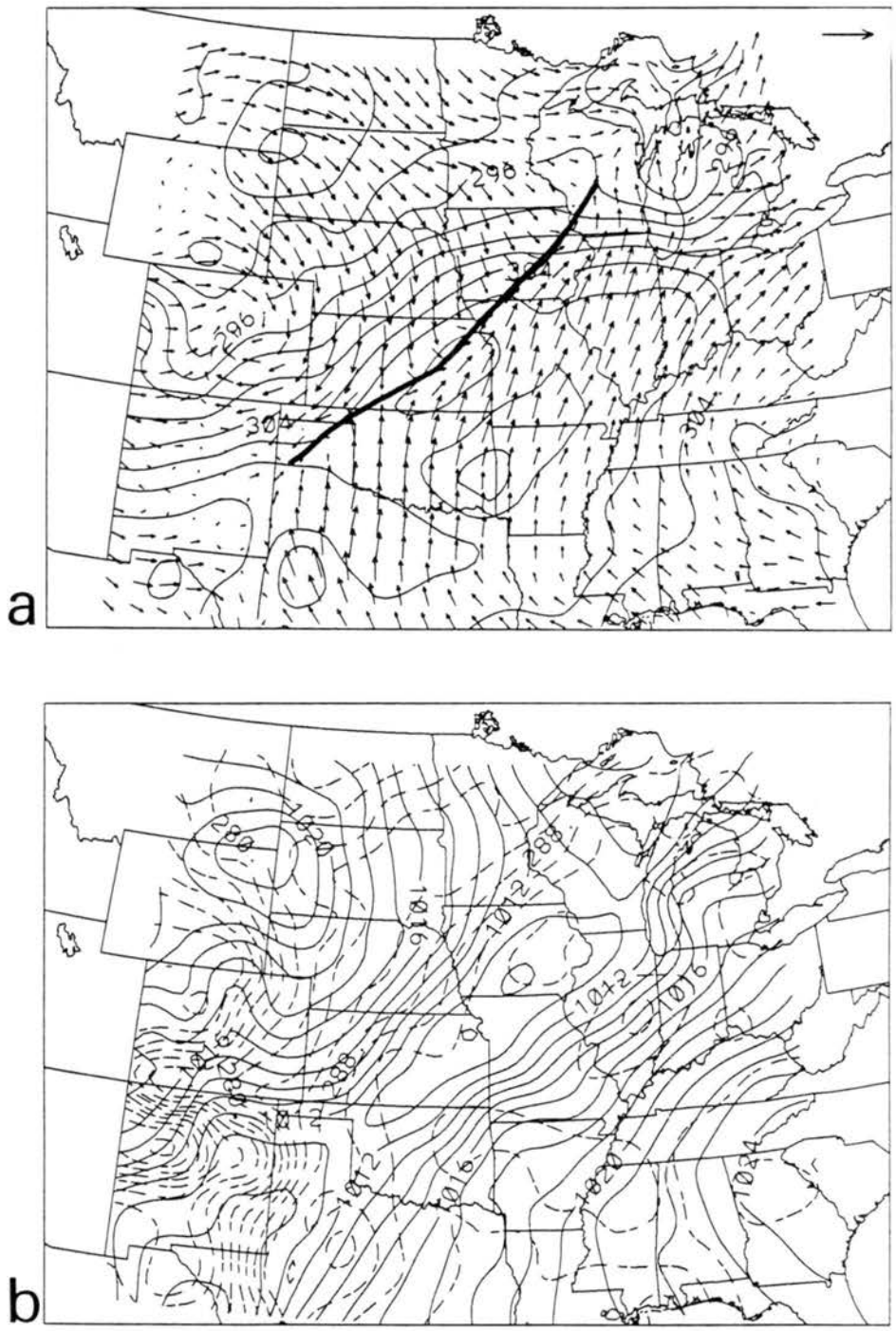

Figure 3.13: Surface analyses at 2100 UTC 17 June 1978 for (a) wind vectors and temperature (K); and (b) MSLP (solid lines, mb) and dewpoint temperature (dashed lines, K). The vector lengths are scaled by speed: the single vector in the upper-right corner of (a) represents 15 m s^{-1}. The maximum windspeeds in (a) are 10 m s^{-1}. The solid line superimposed on (a) is the frontal position.

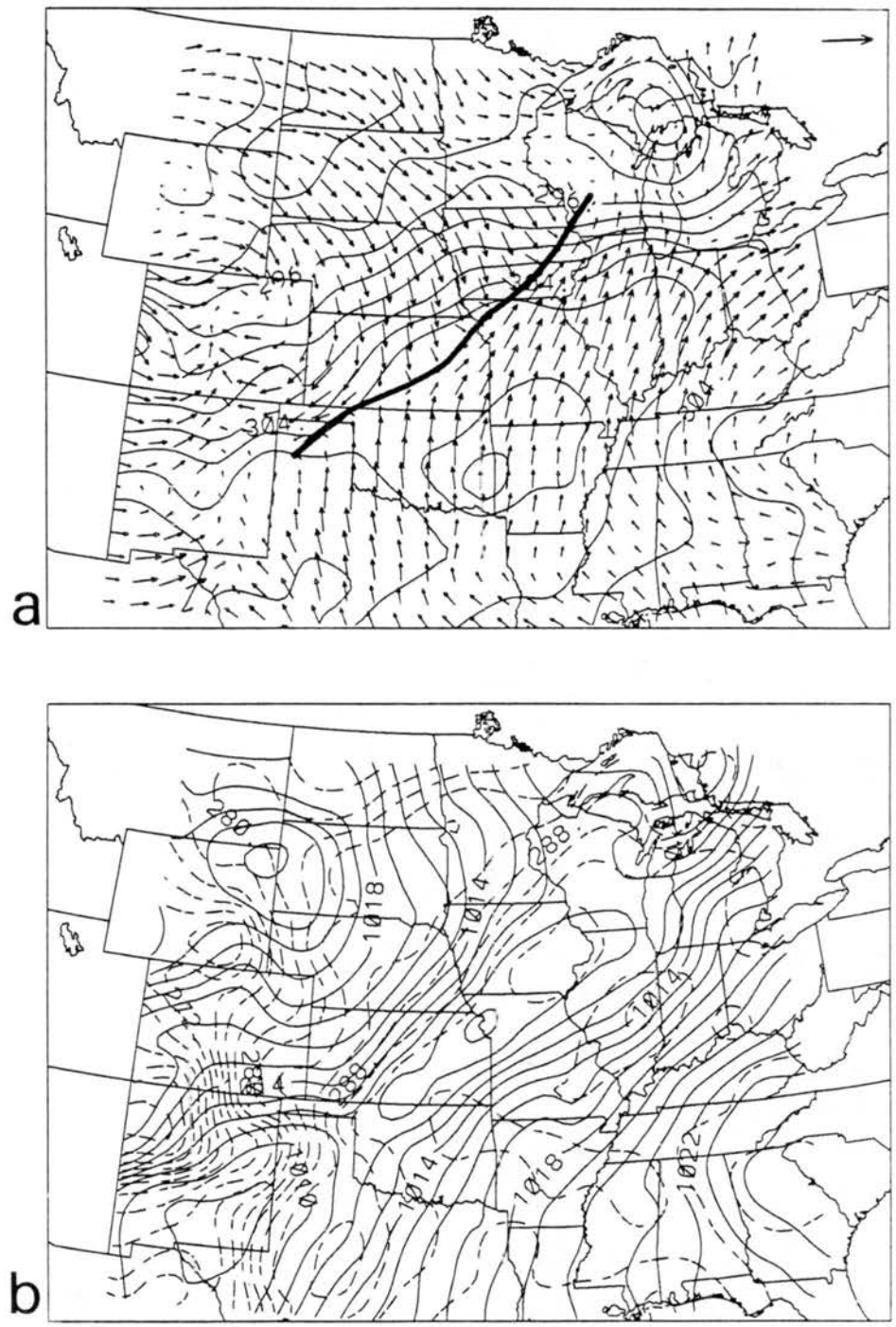

Figure 3.14: Surface analyses at 2200 UTC 17 June 1978 for (a) wind vectors and temperature (K); and (b) MSLP (solid lines, mb) and dewpoint temperature (dashed lines, K). The vector lengths are scaled by speed: the single vector in the upper-right corner of (a) represents 15 m s^{-1}. The maximum windspeeds in (a) are 10 m s^{-1}. The solid line superimposed on (a) is the frontal position.

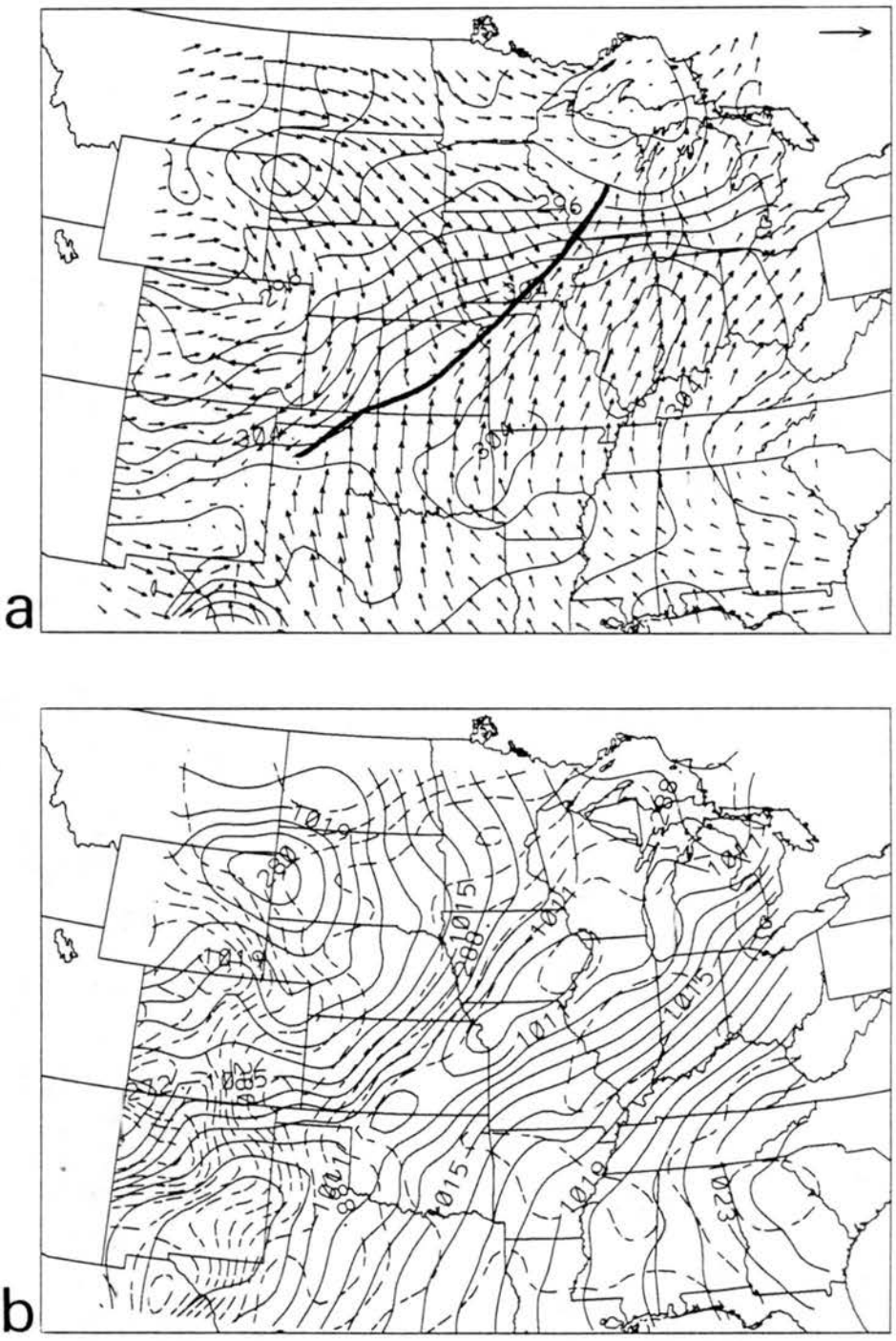

Figure 3.15: Surface analyses at 2300 UTC 17 June 1978 for (a) wind vectors and temperature (K); and (b) MSLP (solid lines, mb) and dewpoint temperature (dashed lines, K). The vector lengths are scaled by speed: the single vector in the upper-right corner of (a) represents 15 m s^{-1}. The maximum windspeeds in (a) are 9 m s^{-1}. The solid line superimposed on (a) is the frontal position.

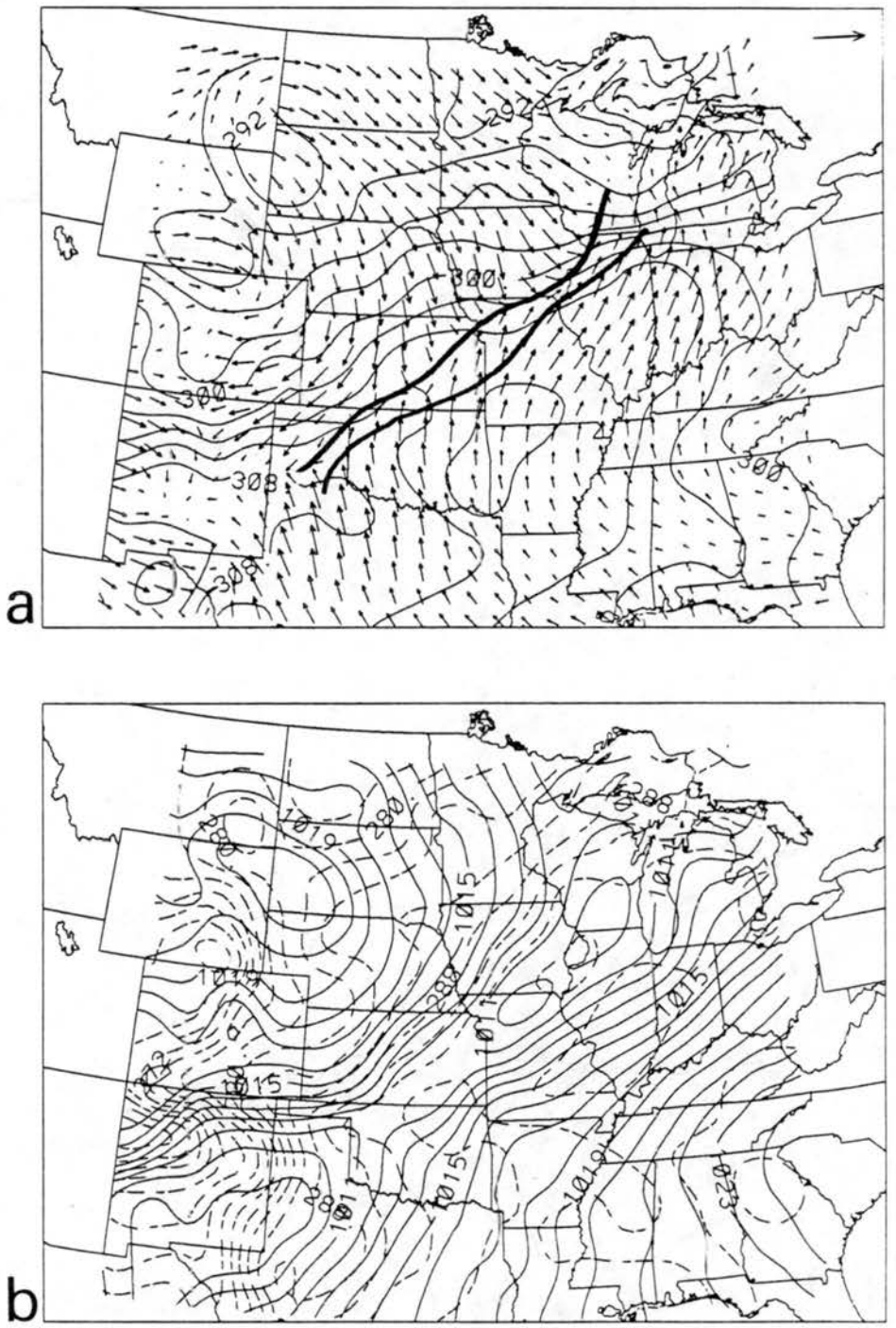

Figure 3.16: Surface analyses at 0000 UTC 18 June 1978 for (a) wind vectors and temperature (K); and (b) MSLP (solid lines, mb) and dewpoint temperature (dashed lines, K). The vector lengths are scaled by speed: the single vector in the upper-right corner of (a) represents 15 m s^{-1}. The maximum windspeeds in (a) are 9 m s^{-1}. The solid lines superimposed on (a) are the frontal position (farther northwest) and the leading edge of the radar echoes at 0035 UTC 18 June (farther southeast).

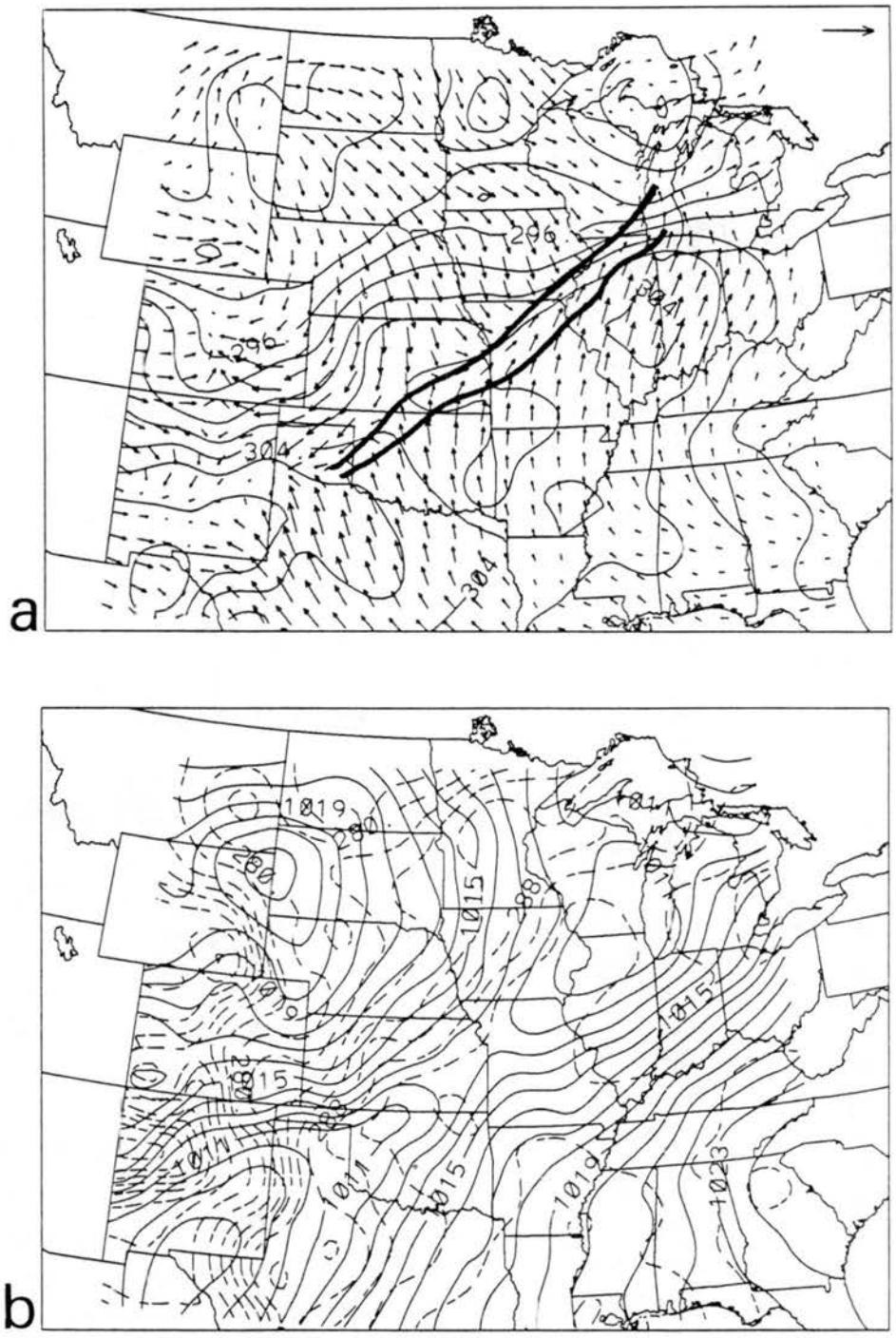

Figure 3.17: Surface analyses at 0100 UTC 18 June 1978 for (a) wind vectors and temperature (K); and (b) MSLP (solid lines, mb) and dewpoint temperature (dashed lines, K). The vector lengths are scaled by speed: the single vector in the upper-right corner of (a) represents 15 m s^{-1}. The maximum windspeeds in (a) are 10 m s^{-1}. The solid lines superimposed on (a) are the frontal position (farther northwest) and the leading edge of the radar echoes at 0135 UTC 18 June (farther southeast).

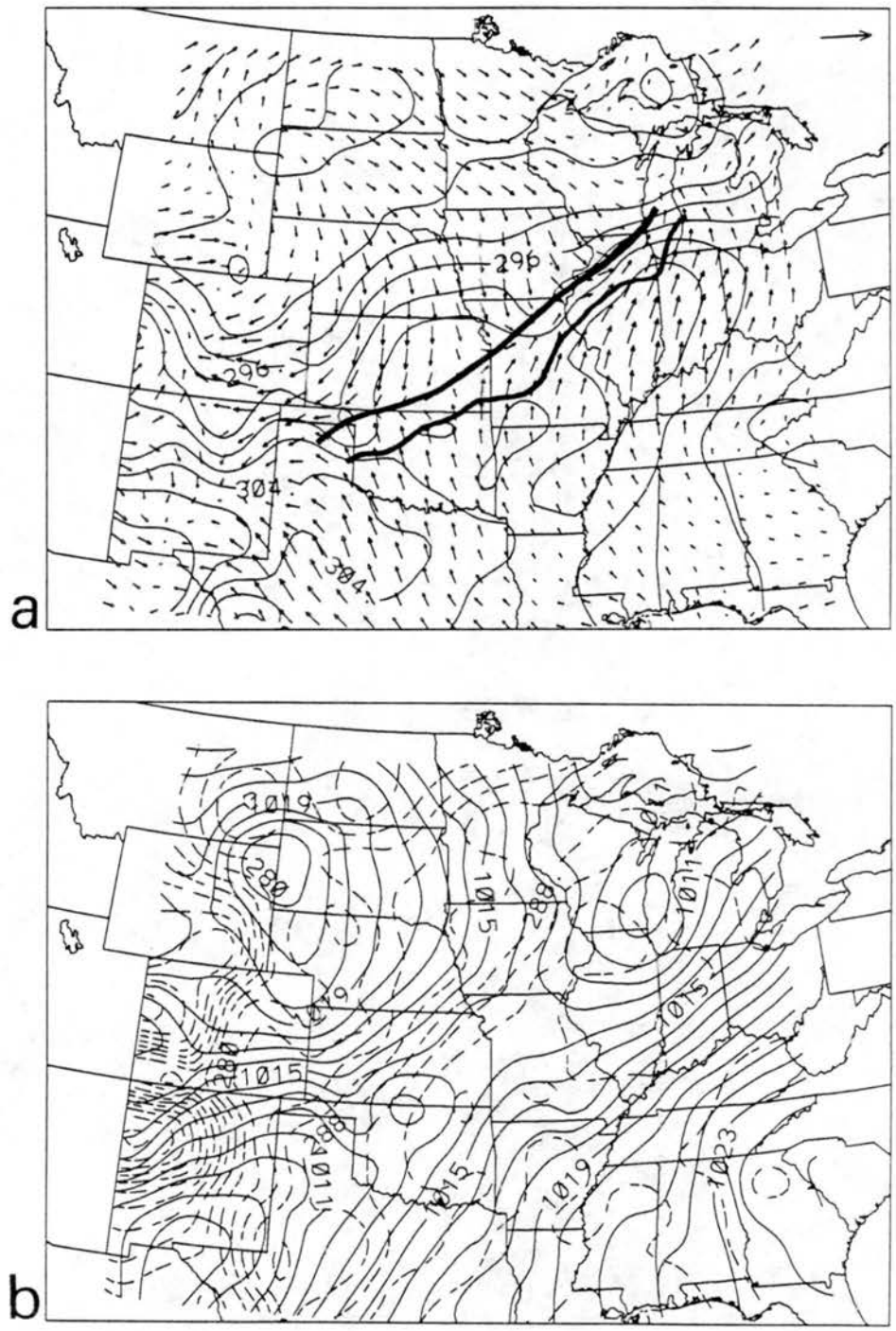

Figure 3.18: Surface analyses at 0200 UTC 18 June 1978 for (a) wind vectors and temperature (K); and (b) MSLP (solid lines, mb) and dewpoint temperature (dashed lines, K). The vector lengths are scaled by speed: the single vector in the upper-right corner of (a) represents 15 m s^{-1}. The maximum windspeeds in (a) are 9 m s^{-1}. The solid lines superimposed on (a) are the frontal position (farther northwest) and the leading edge of the radar echoes at 0235 UTC 18 June (farther southeast).

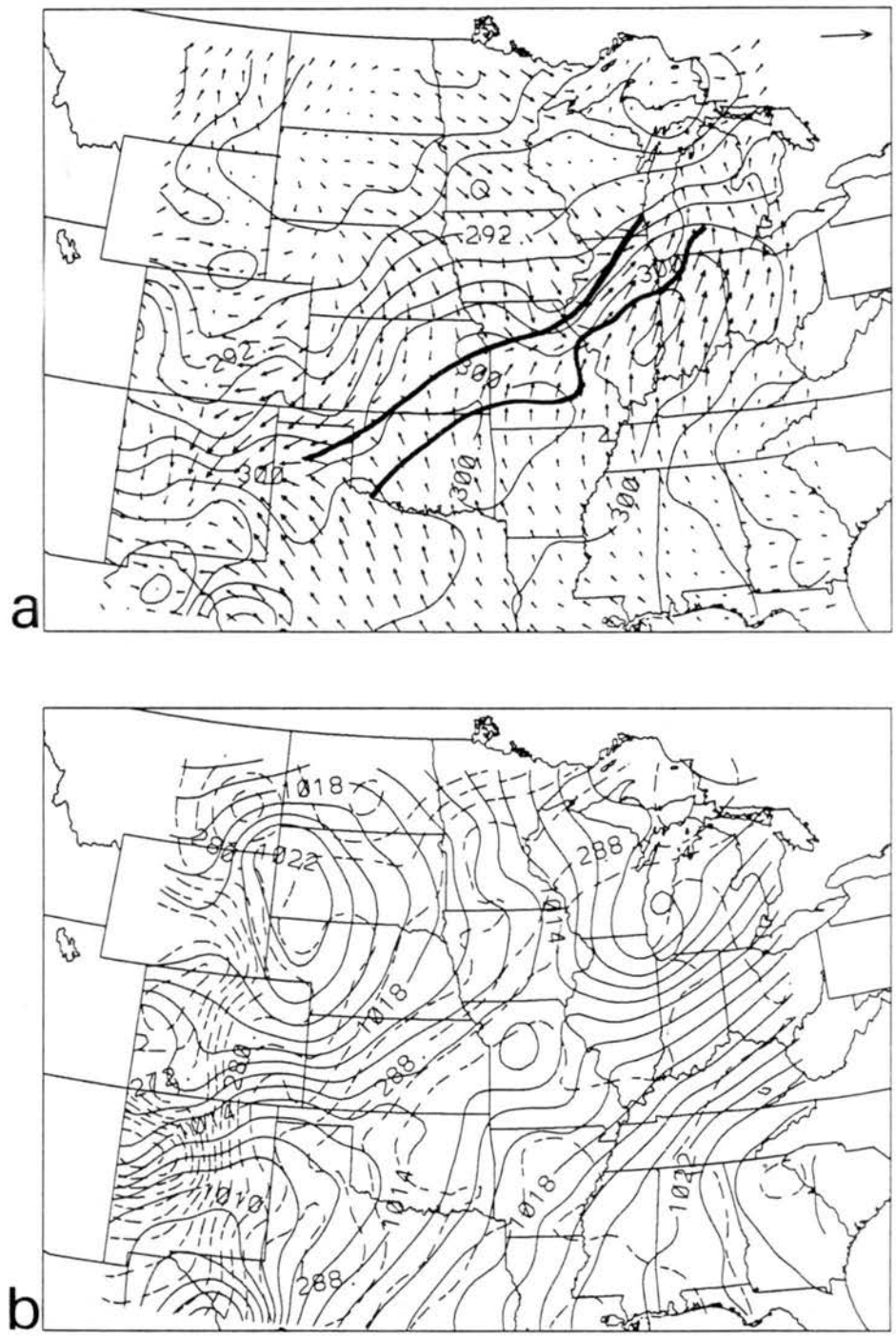

Figure 3.19: Surface analyses at 0300 UTC 18 June 1978 for (a) wind vectors and temperature (K); and (b) MSLP (solid lines, mb) and dewpoint temperature (dashed lines, K). The vector lengths are scaled by speed: the single vector in the upper-right corner of (a) represents 15 m s^{-1}. The maximum windspeeds in (a) are 9 m s^{-1}. The solid lines superimposed on (a) are the frontal position (farther northwest) and the leading edge of the radar echoes at 0335 UTC 18 June (farther southeast).

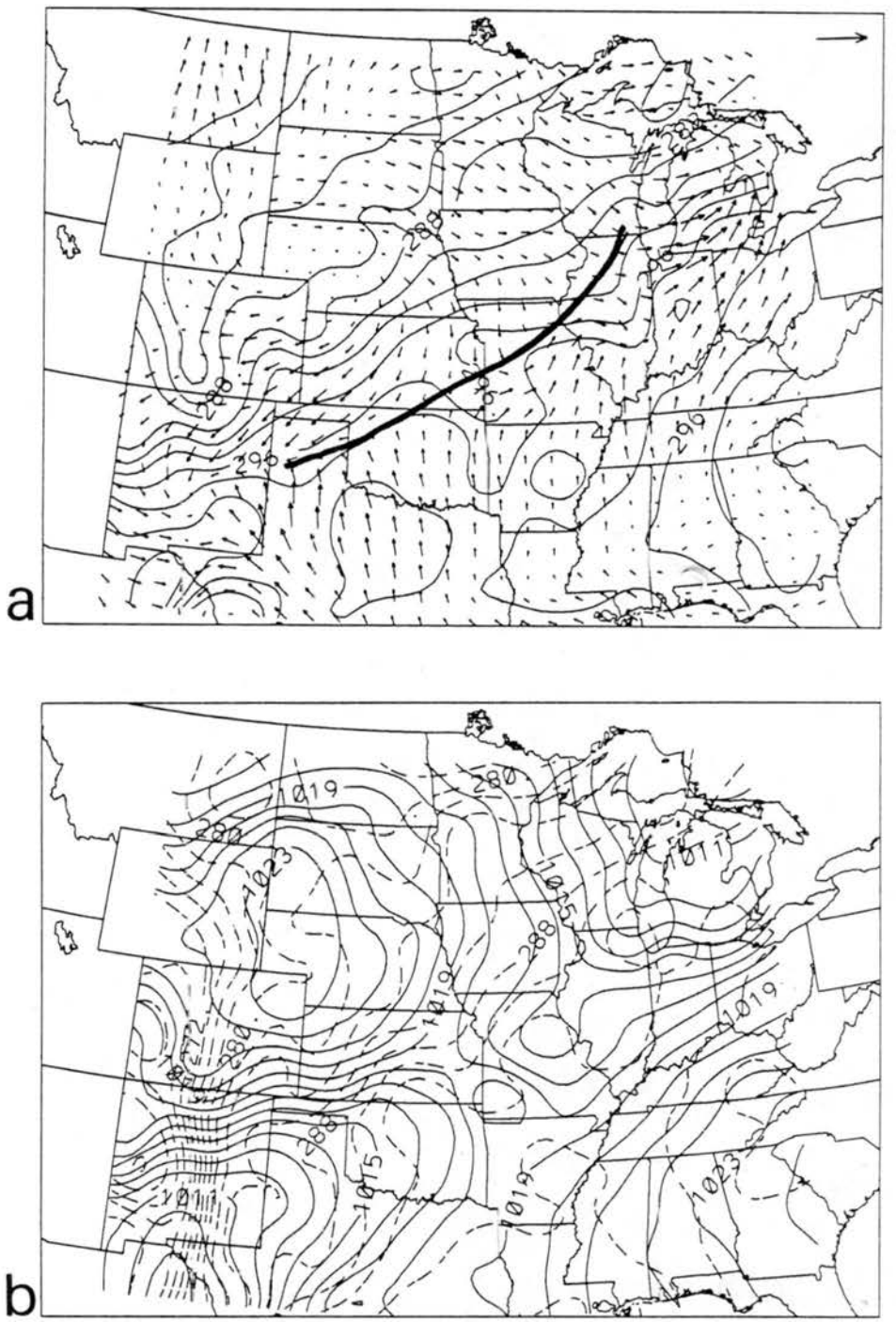

Figure 3.20: Surface analyses at 0600 UTC 18 June 1978 for (a) wind vectors and temperature (K); and (b) MSLP (solid lines, mb) and dewpoint temperature (dashed lines, K). The vector lengths are scaled by speed: the single vector in the upper-right corner of (a) represents 15 m s^{-1}. The maximum windspeeds in (a) are 8 m s^{-1}. The solid line superimposed on (a) is the frontal position.

central Kansas along the wind shift line. This perturbation is associated with the first cells that developed along the squall line in Kansas and were visible in the radar summary charts at 1935 UTC (Fig. 3.7c). The convection cannot be traced exactly by these surface analyses, but the perturbations do become stronger and more widespread along the frontal zone from 2000 UTC 17 June through 0300 UTC 18 June.

The leading edge of the echoes on the radar summary chart for 0035 UTC is superimposed on the surface analyses at 0000 UTC. The leading edge of the echoes is just barely in front of the wind shift line at these times. The corresponding echo lines are also superimposed on the surface analyses from 0100 through 0300 UTC. There is a widening separation between the wind shift line and the leading edge of the squall line convection. By 0300 UTC it becomes increasingly difficult to define the frontal position from the surface wind and temperature analyses because of the convective-related perturbations.

Some insight into the relative positions of the front and squall line convection can be gained by more closely analyzing the MSL pressure analyses. Looking at the MSL pressure analyses and dewpoint temperature analyses, the front appears to be consistently aligned along the back edge of the surface pressure trough. Although there are transient perturbations in the surface temperature analyses, the frontal temperature gradient also seems to be most consistently aligned along the back edge of the trough. Before the squall line convection has significantly developed (before 2300 UTC 17 June) the surface pressure trough remains relatively narrow and well-defined. The wind shift line is aligned along the center of the trough throughout this period. Between 1200 and 1800 UTC the pressures in the center of the trough increase from approximately 1005 mb to 1009 mb, and then stay at that level through 0000 UTC. Between 0000 and 0300 UTC the trough widens and the pressures increase to 1014 mb. The pressures continue to increase and the trough widens through 0600 UTC. At times beyond 0000 UTC the leading edge of the squall line convection lines up along the front edge of the trough, and the most consistent analysis of the frontal position appears to be along the back edge of the trough. By 0300 UTC this results in a separation distance between the front and the leading edge of the squall line

of approximately 200 km. By 0600 UTC this gap appears to be approximately 250 - 300 km, although the squall line convection is not very active at this time.

To summarize, the widening and filling of the trough is associated with the convectively-modified air (surface mesohigh region) produced by the squall line. The squall line, front, and surface trough are all initially aligned at 0000 UTC 18 June. As the squall line translates southeastward it moves faster than the front and leaves in its wake a zone of convectively-modified air. This convectively-modified air between the front and the squall line is reflected in the MSL surface pressure analyses.

Figure 3.21 shows the surface analyses of 12 hour precipitation at 0000 and 1200 UTC 18 June 1978. There is not any precipitation associated with the squall line at 0000 UTC, although the precipitation analyses were based on a much more limited number of stations than the other surface data analyses.

The analyses shown in this section have helped to establish that a separation between the front and leading edge of the squall line did occur. The frontal position is consistently aligned along the trough and wind shift line in the preconvective stage. Once the squall line has developed (0000 UTC) the front is most consistently aligned along the back edge of the trough. The convection results in an overall widening and weakening of the trough, with the squall line aligned along the front edge of the trough. By 0300 UTC there is a separation of approximately 200 km between the leading edges of the squall line and front.

3.6 Upper-Level Analyses

The NMC spectral model analyses (2.5° grid spacing) at 1200 UTC 17 June and 0000 and 1200 UTC 18 June 1978 will be briefly discussed in this section. These are not the final analyses used for the model simulations (discussed in Section 5.2). The horizontal cross sections shown are on constant height surfaces, although the actual NMC fields are initially available only on the standard pressure surfaces. They have been interpolated to the terrain-following model grid and then back to the specified surfaces, so some "noise" is evident over areas of high terrain (Fig. 3.22), especially when the interpolation is to a surface below ground level.

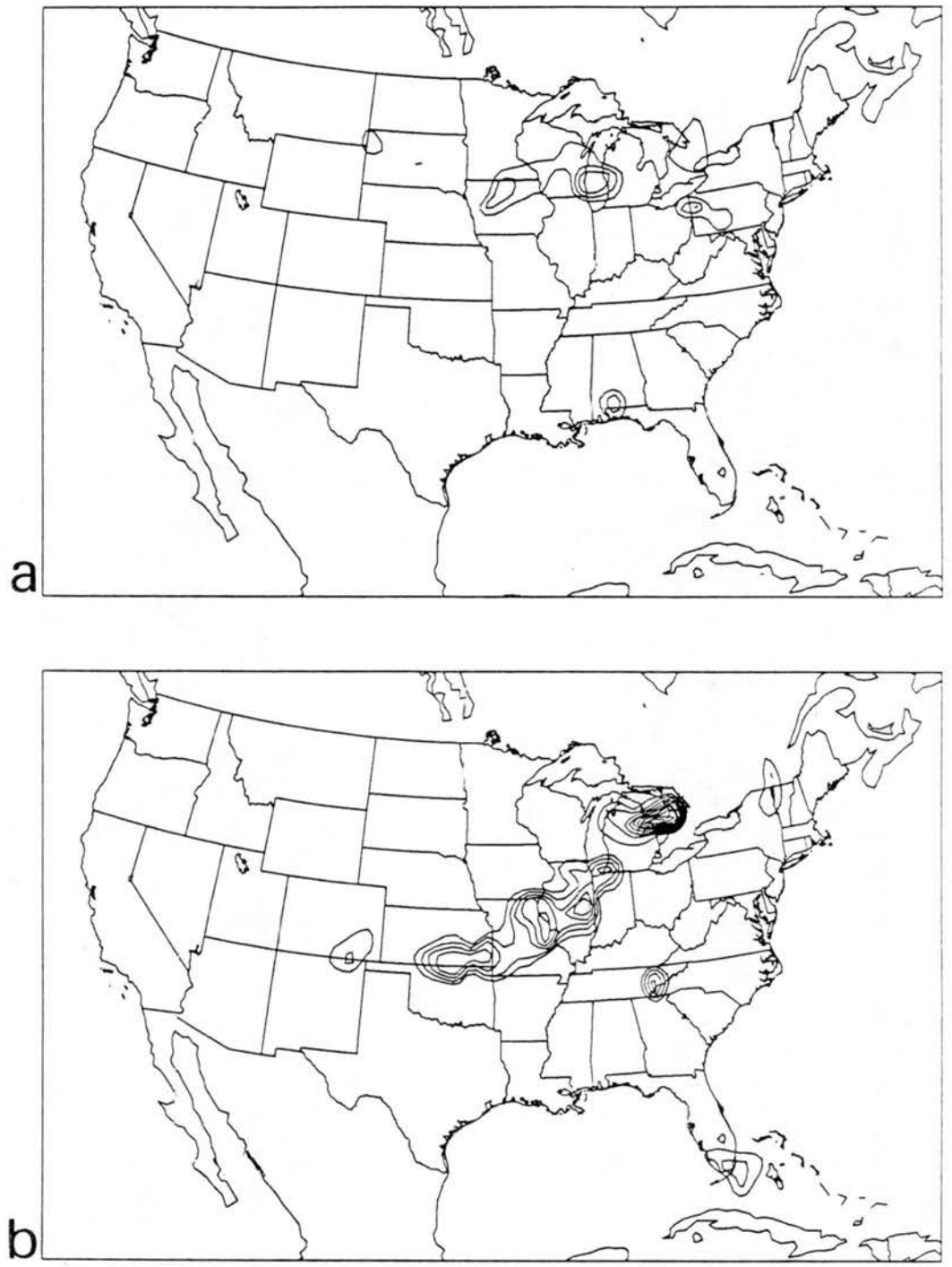

Figure 3.21: Surface analyses of 12 hour precipitation (cm, contour interval is 0.5 cm) at (a) 0000 UTC 18 June; and (b) 1200 UTC 18 June 1978.

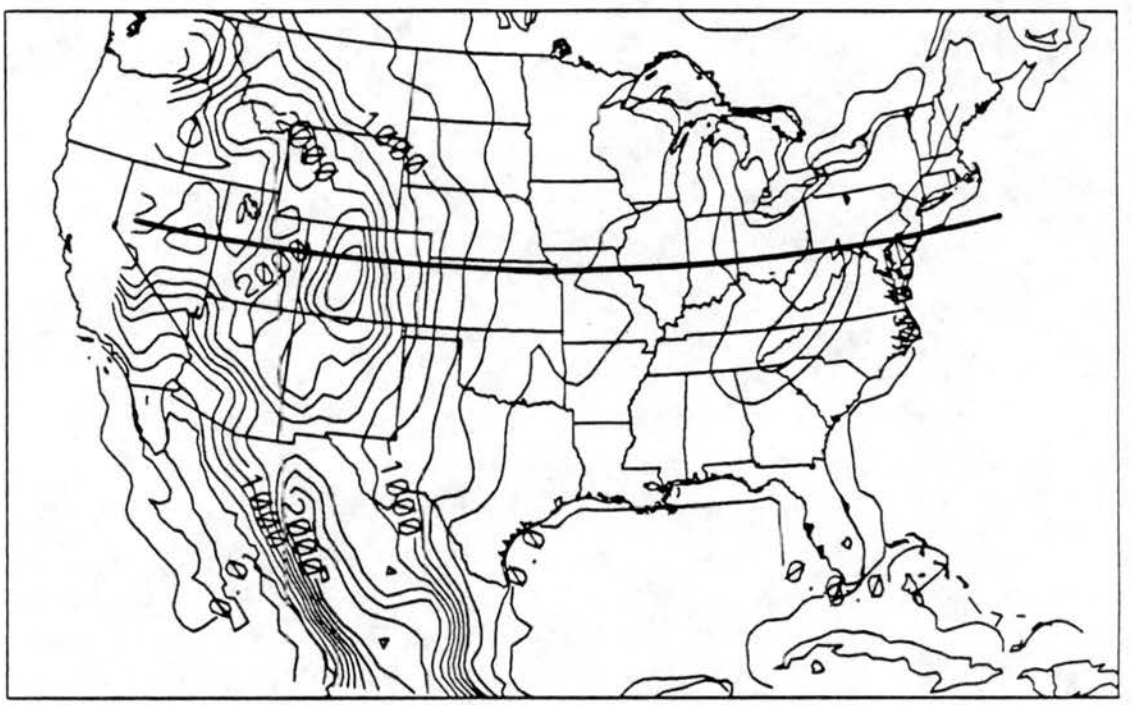

Figure 3.22: Surface terrain (m, contour interval is 250 m) for NMC data analyses. Cross section location for Fig. 3.27 is horizontal line.

Figures 3.23-3.25 show the pressure and temperature analyses at 3.1, 5.0, and 10.5 km for each of the three synoptic times surrounding the squall line development. A short wave trough with strong warm air advection ahead of it is evident at 1200 UTC 17 June at 3.1 km, with the surface front oriented just ahead of the trough line. The trough lifts out over the next 24 hours with very little temperature advection at 3.1 km by 1200 UTC 18 June. A similar pattern is evident at 5.0 km with a large scale trough with strong temperature advection ahead of it at 1200 UTC 17 June, which lifts out over the next 24 hours. At 10.5 km the flow is primarily barotropic and with a more westerly component than at the surface levels. A short wave moves into the domain between 0000 and 1200 UTC 18 June at 10.5 km, but to the west of the area of interest for this case.

Figure 3.26 shows the vertical cross sections (cross section location shown in Fig. 3.22) of equivalent potential temperature through the domain. At 1200 UTC 17 June the surface front is located at about 99°W at the latitude of the cross section, at about 95°W at 0000 UTC 18 June, and at about 91°W at 1200 UTC 18 June. A low-level stable layer is evident to the east of the front at 1200 UTC 17 June but has destabilized by 12 hours later. However, these are very coarse analyses and interpolated at low levels from the 1000, 850, and 700 mb NMC analyses, so the low-level structure is not necessarily accurate. The rawinsonde soundings discussed in Section 3.7 show a low-level stable layer in the prefrontal region at all three synoptic times. It will also be shown in Chapter 5 that the model simulations retained a low-level stable layer ahead of the front throughout the entire simulation period.

The analyses shown in this section have established that the surface front was oriented just ahead of a low-level trough, with strong warm advection occurring ahead of the trough all the way up to 5.0 km. The flow above that level was generally barotropic and with a more westerly component. There were not any significant upper level jets resolved by the NMC spectral data along or through the frontal zone.

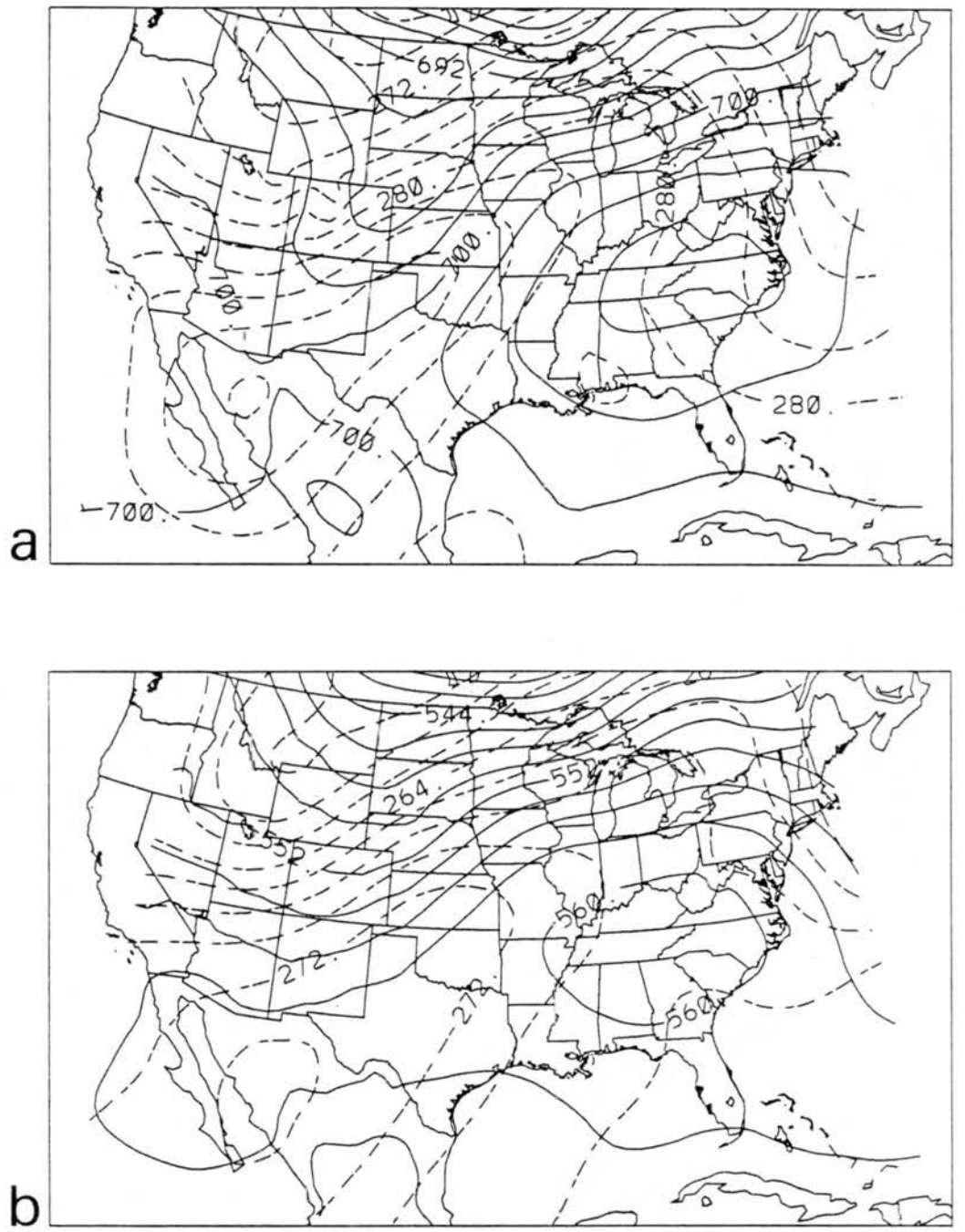

Figure 3.23: Upper air analyses analyses from NMC spectral model data at 1200 UTC 17 June 1978: (a) 3.1 km pressure (mb, solid lines, contour interval is 2 mb) and temperature (K, dashed lines, contour interval is 2 K); and (b) 5.0 km pressure (mb, solid lines, contour interval is 2 mb) and temperature (K, dashed lines, contour interval is 2 K).

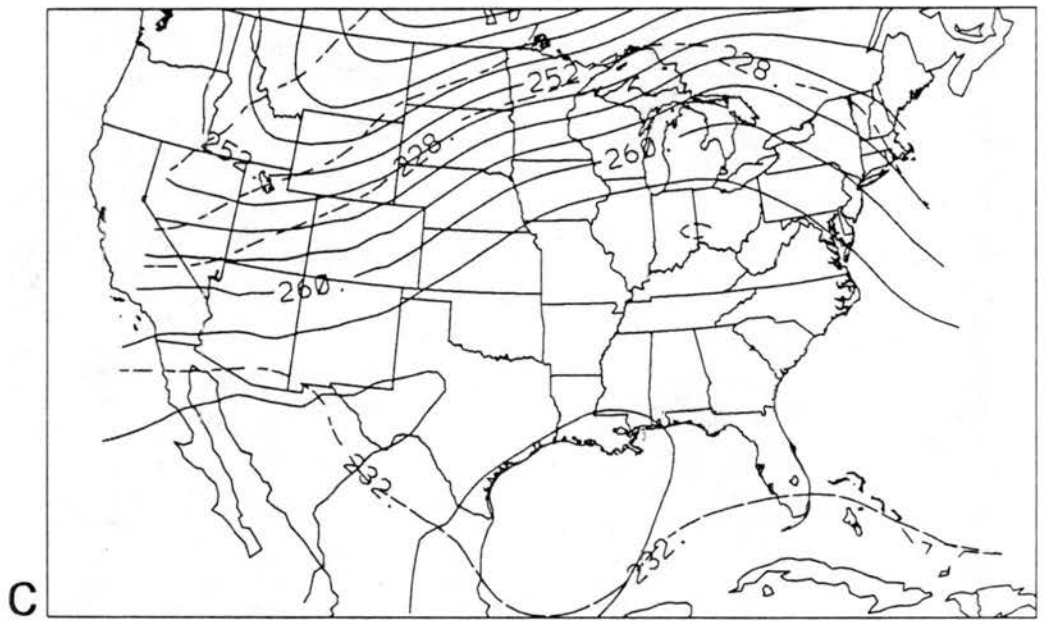

Figure 3.23: Continued: (c) 10.5 km pressure (mb, solid lines, contour interval is 2 mb) and temperature (K, dashed lines, contour interval is 2 K).

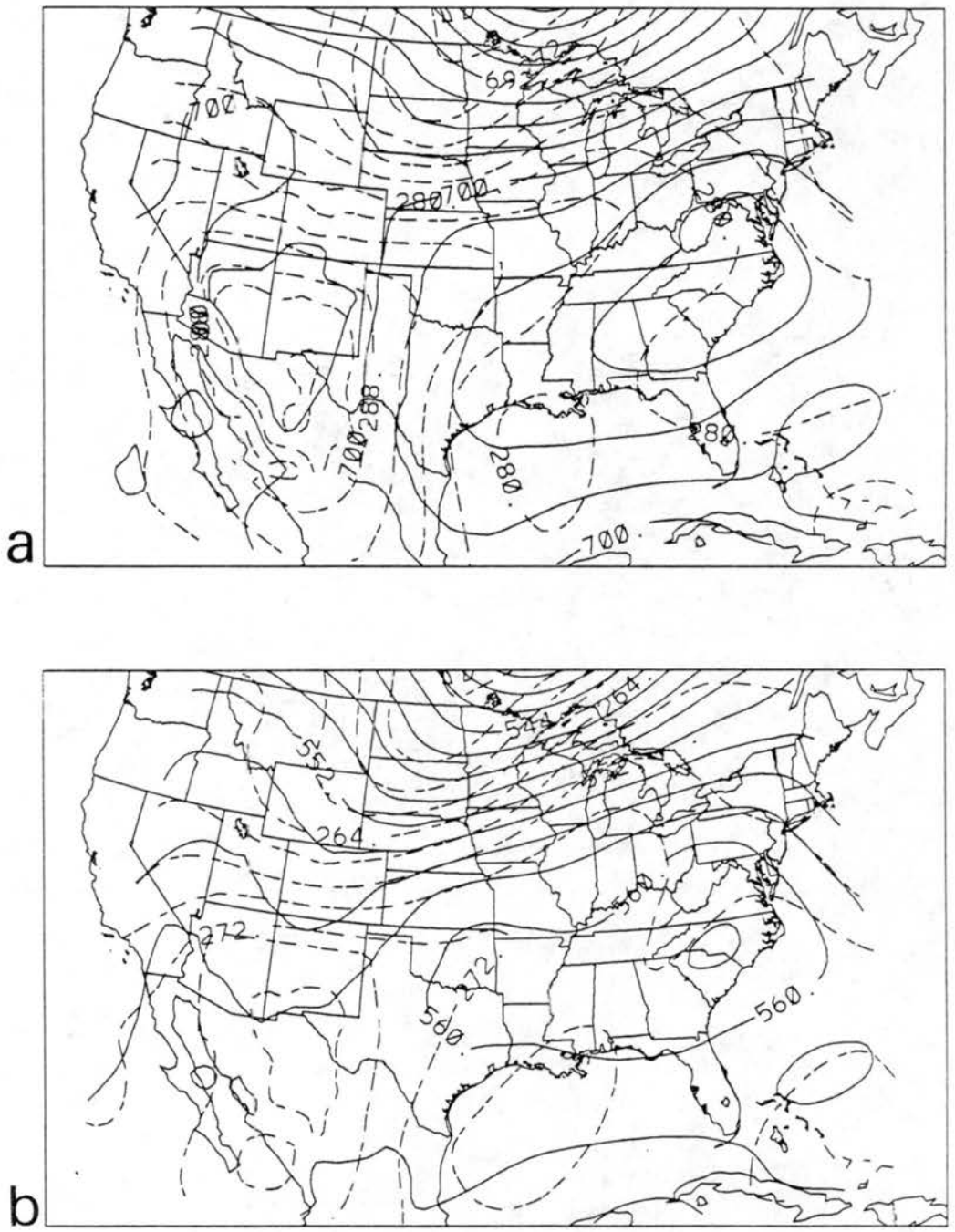

Figure 3.24: Upper air analyses analyses from NMC spectral model data at 0000 UTC 18 June 1978: (a) 3.1 km pressure (mb, solid lines, contour interval is 2 mb) and temperature (K, dashed lines, contour interval is 2 K); and (b) 5.0 km pressure (mb, solid lines, contour interval is 2 mb) and temperature (K, dashed lines, contour interval is 2 K).

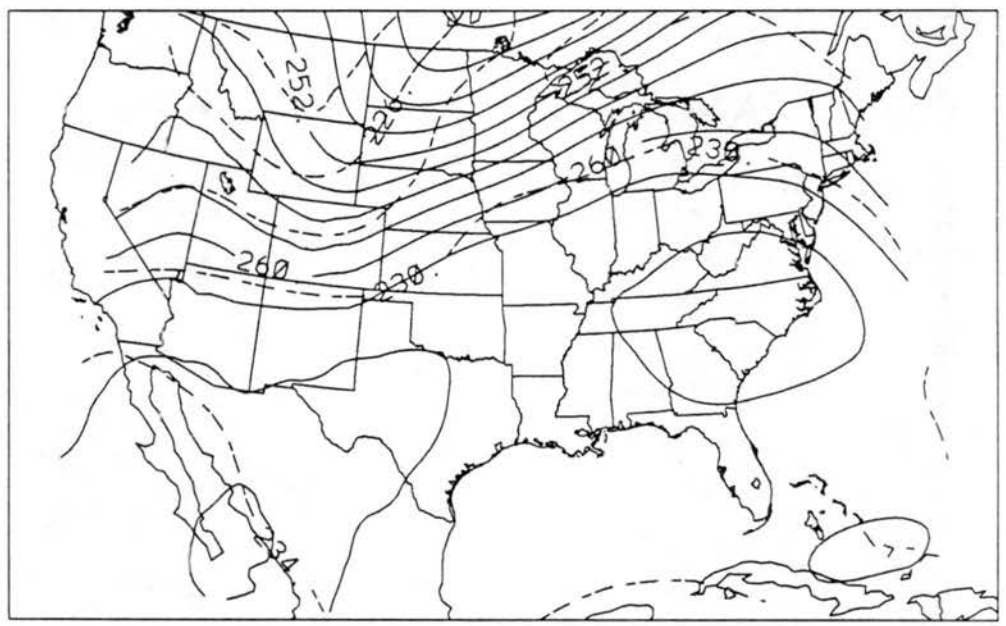

Figure 3.24: Continued: (c) 10.5 km pressure (mb, solid lines, contour interval is 2 mb) and temperature (K, dashed lines, contour interval is 2 K).

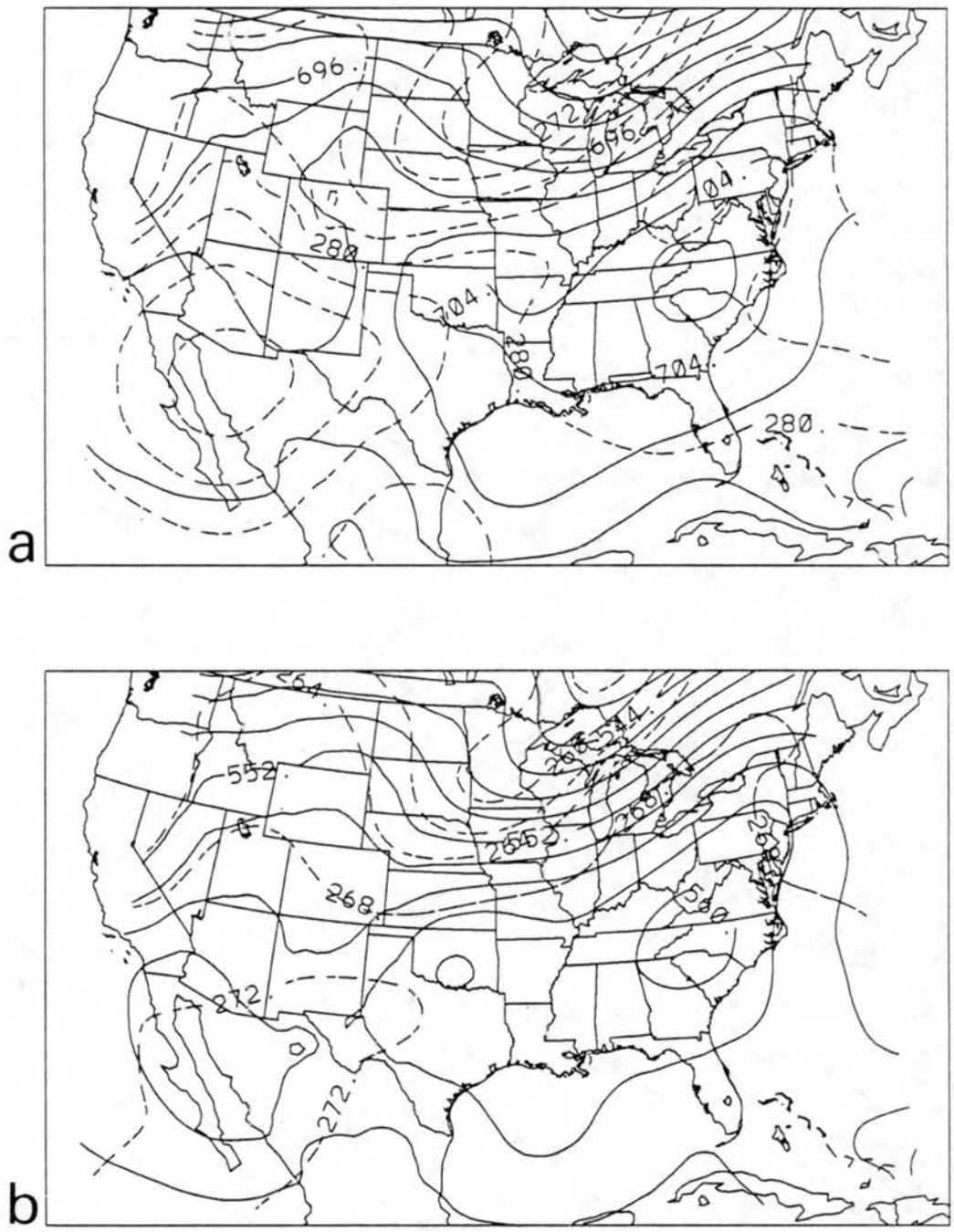

Figure 3.25: Upper air analyses analyses from NMC spectral model data at 1200 UTC 18 June 1978: (a) 3.1 km pressure (mb, solid lines, contour interval is 2 mb) and temperature (K, dashed lines, contour interval is 2 K); and (b) 5.0 km pressure (mb, solid lines, contour interval is 2 mb) and temperature (K, dashed lines, contour interval is 2 K).

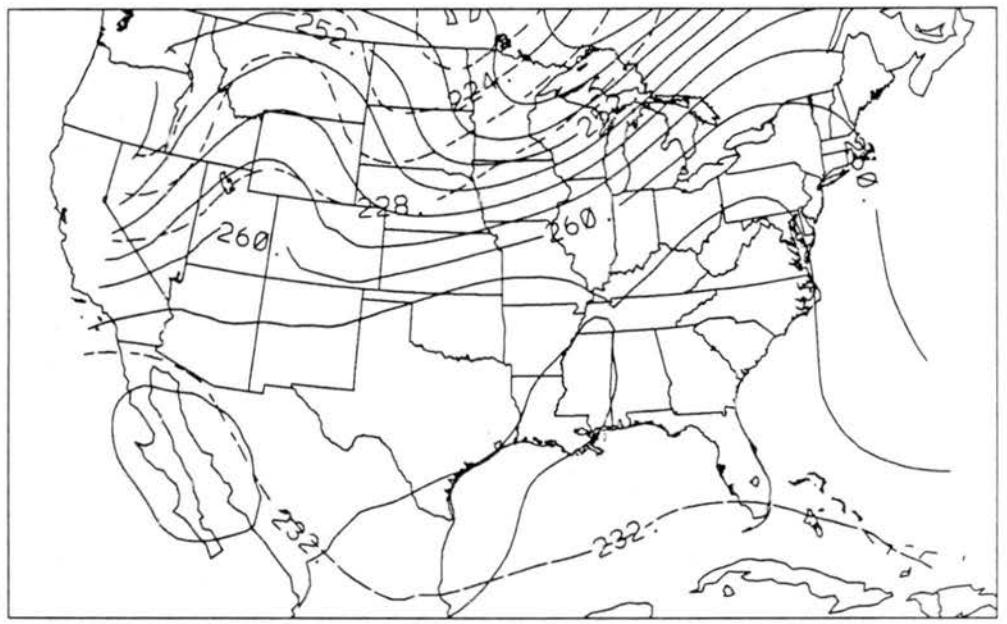

Figure 3.25: Continued: (c) 10.5 km pressure (mb, solid lines, contour interval is 2 mb) and temperature (K, dashed lines, contour interval is 2 K).

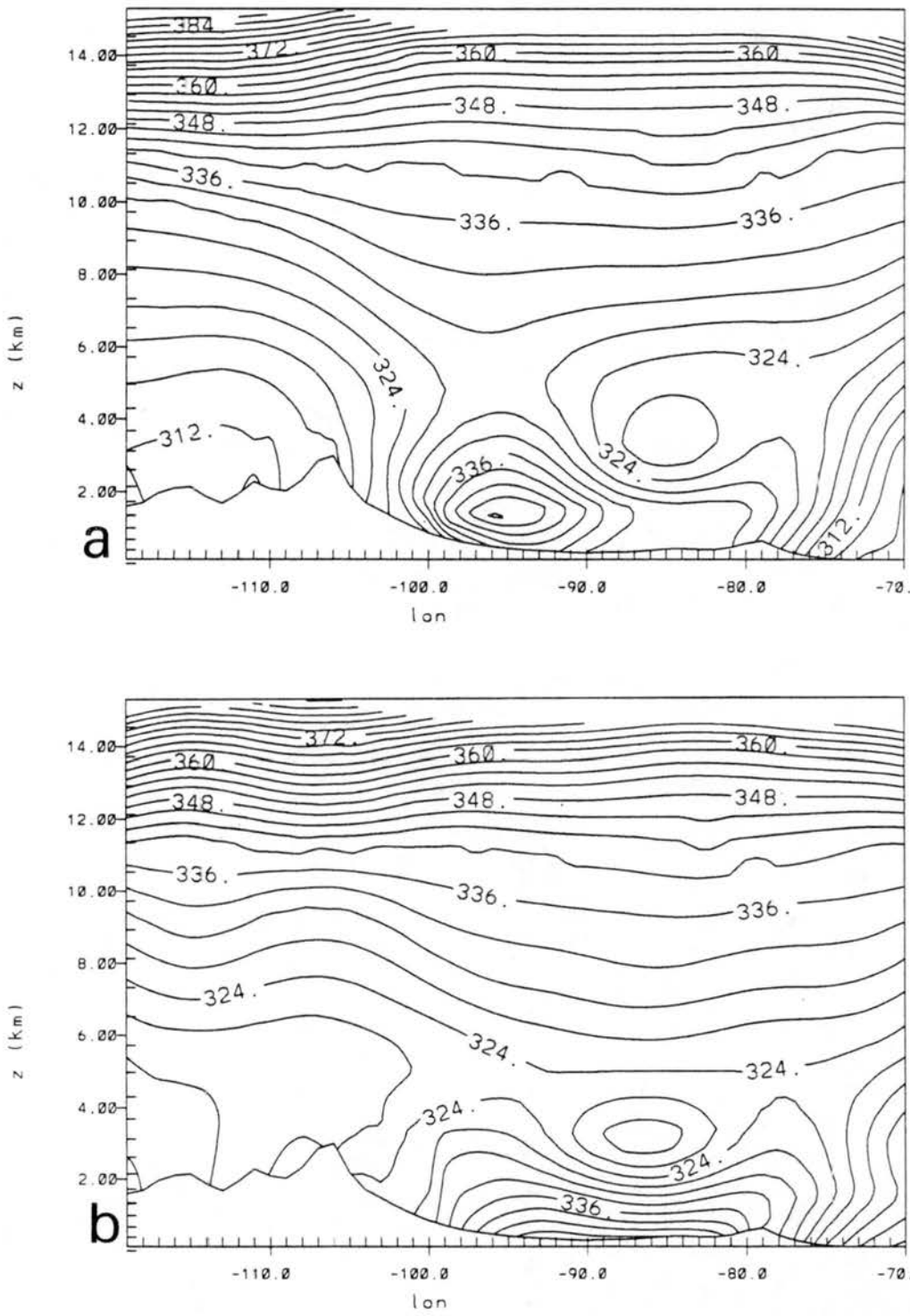

Figure 3.26: Vertical cross sections of equivalent potential temperature θ_e (K) from NMC spectral analyses at a) 1200 UTC 17 June; and b) 0000 UTC 18 June.

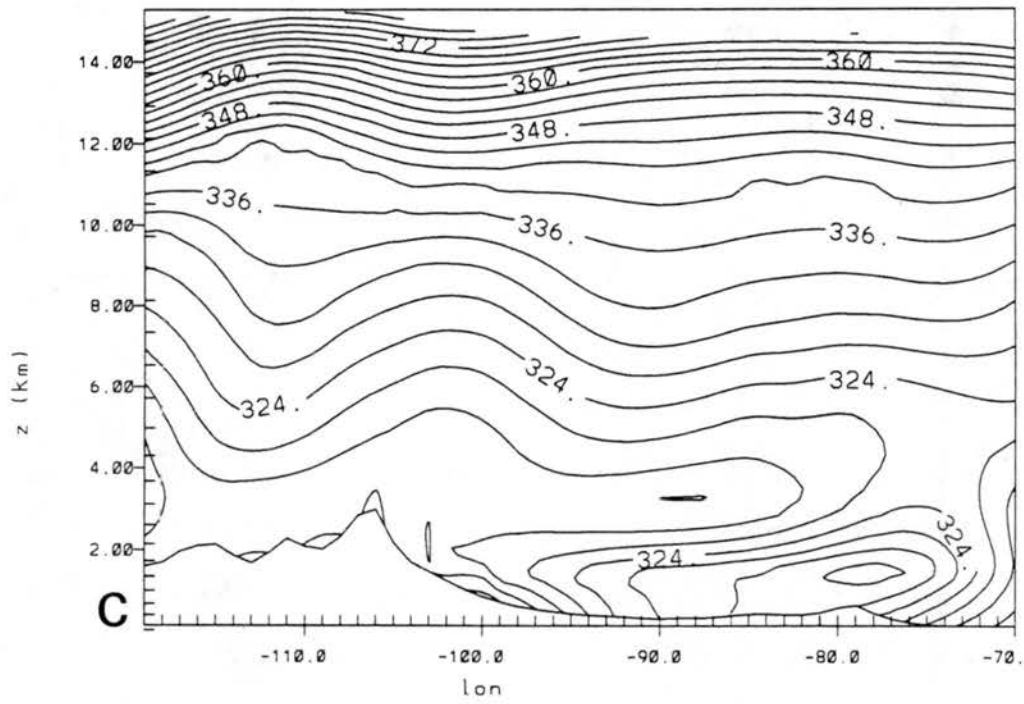

Figure 3.26: Continued: c) 1200 UTC 18 June.

3.7 Sounding Data

Rawinsonde sounding data from 4 stations (locations shown in Fig. 3.27) are shown in Figs. 3.28-3.35 at 1200 UTC 17 June and 0000 UTC 18 June 1978. The frontal positions at 1200 UTC 17 June and 0000 UTC 18 June, and the squall line positions at 0035 and 0635 UTC 18 June are superimposed on Fig. 3.27. At 1200 UTC 17 June the squall line had not yet developed and all 4 stations were still ahead of the surface front. At 0000 UTC 18 June OKC and UNM were still ahead of the squall line, TOP was behind the leading edge of the squall line, and PIA was just at the leading edge of the squall line. The PIA sounding is included because it is closest to the location of the NIMROD network (location of observations and study in Sections 3.1 and 3.2), but it is least similar to the other three shown. It is in a location that has been influenced by other convection previous to and concurrent with the squall line development (see Sections 3.3 and 3.4).

UNM and OKC are probably most representative of the presquall environment. Both of these soundings have low-level stable layers extending from the surface to 750-800 mb at both 1200 UTC 17 June and 0000 UTC 18 June, and then deep layers of conditional instability above that. The soundings are most unstable, close to dry adiabatic, between 300 and 400 mb. There is very little wind shear, except in a layer below 700 mb. In both locations, the surface wind are approximately 10-20 m s^{-1} from 220° while the 700 mb winds are from approximately 5-10 m s^{-1} from 280°. Above 700 mb there is much less speed and directional shear.

The existence of weak vertical shear is consistent with Bluestein and Jain's (1985) "broken-line" squall line composite. In their study, the broken-line classification is that associated with frontal-type squall lines, and most closely represents the squall line in this study. They point out that this sort of weakly sheared environment for squall lines is indicative of strong external forcing for the squall line, such as by frontal convergence.

The vertical shear in the UNM and OKC soundings is also consistent with the shear required by the Rotunno *et al.* (1988) model of a long-lived squall line. They maintain that the vorticity produced by the low-level shear balances that of the cold pool. The surface

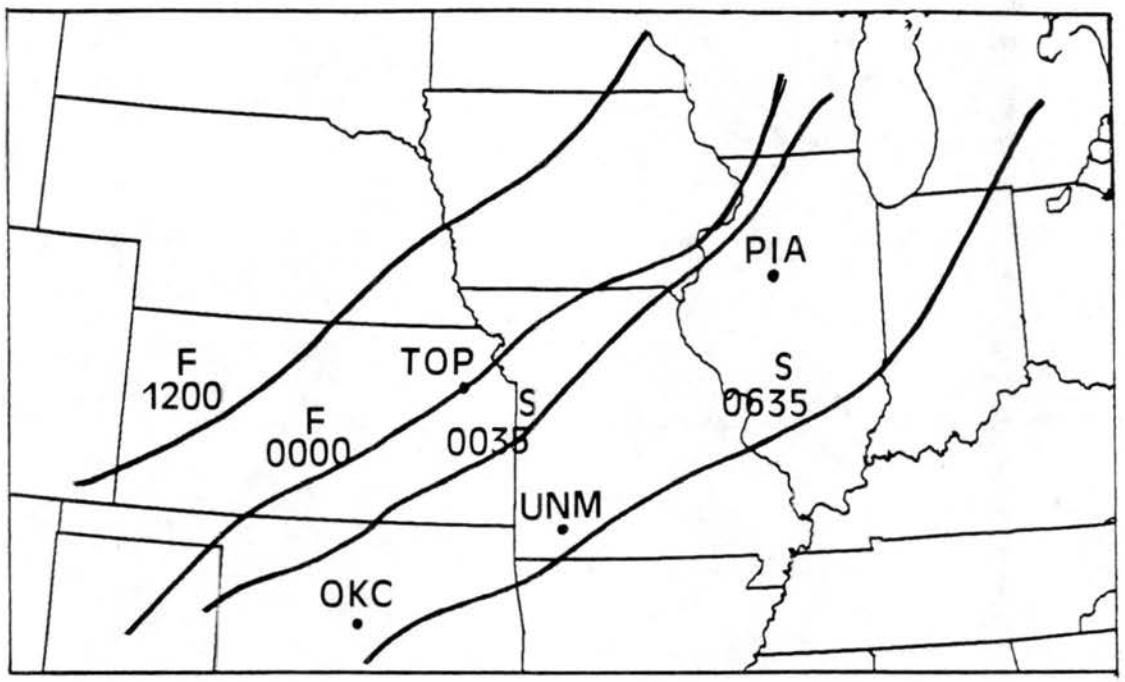

Figure 3.27: Rawinsonde sounding locations. The observed frontal locations at 1200 UTC 17 June and 0000 UTC 18 June, and the leading edge of the radar echoes at 0035 and 0635 UTC 18 June are superimposed on the figure.

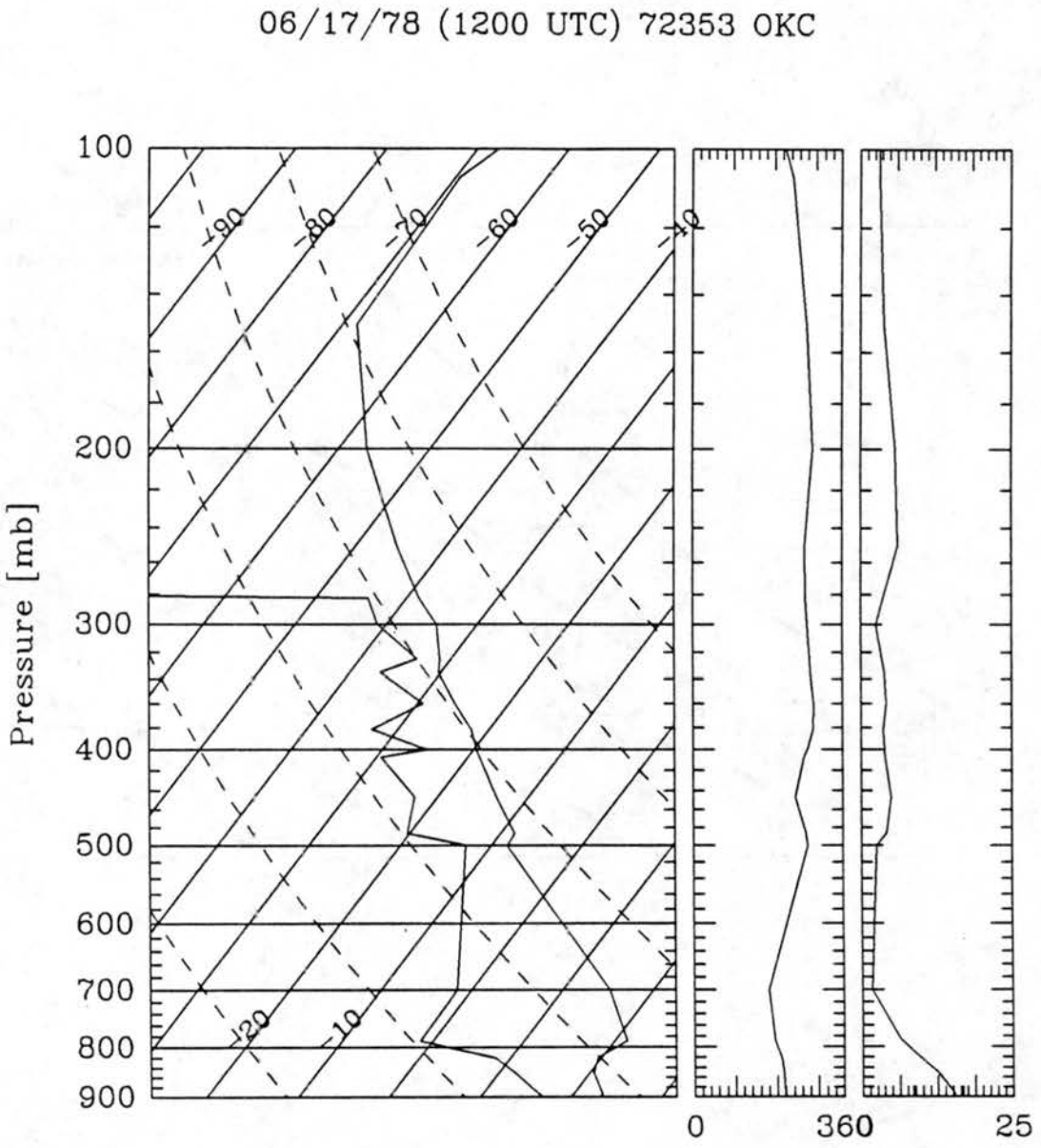

Figure 3.28: OKC rawinsonde sounding at 1200 UTC 17 June 1978. Temperature and dewpoint are shown on the left panel, and wind direction (direction wind is blowing from, in degrees) and speed (m s^{-1}) are shown in the two farthest right panels.

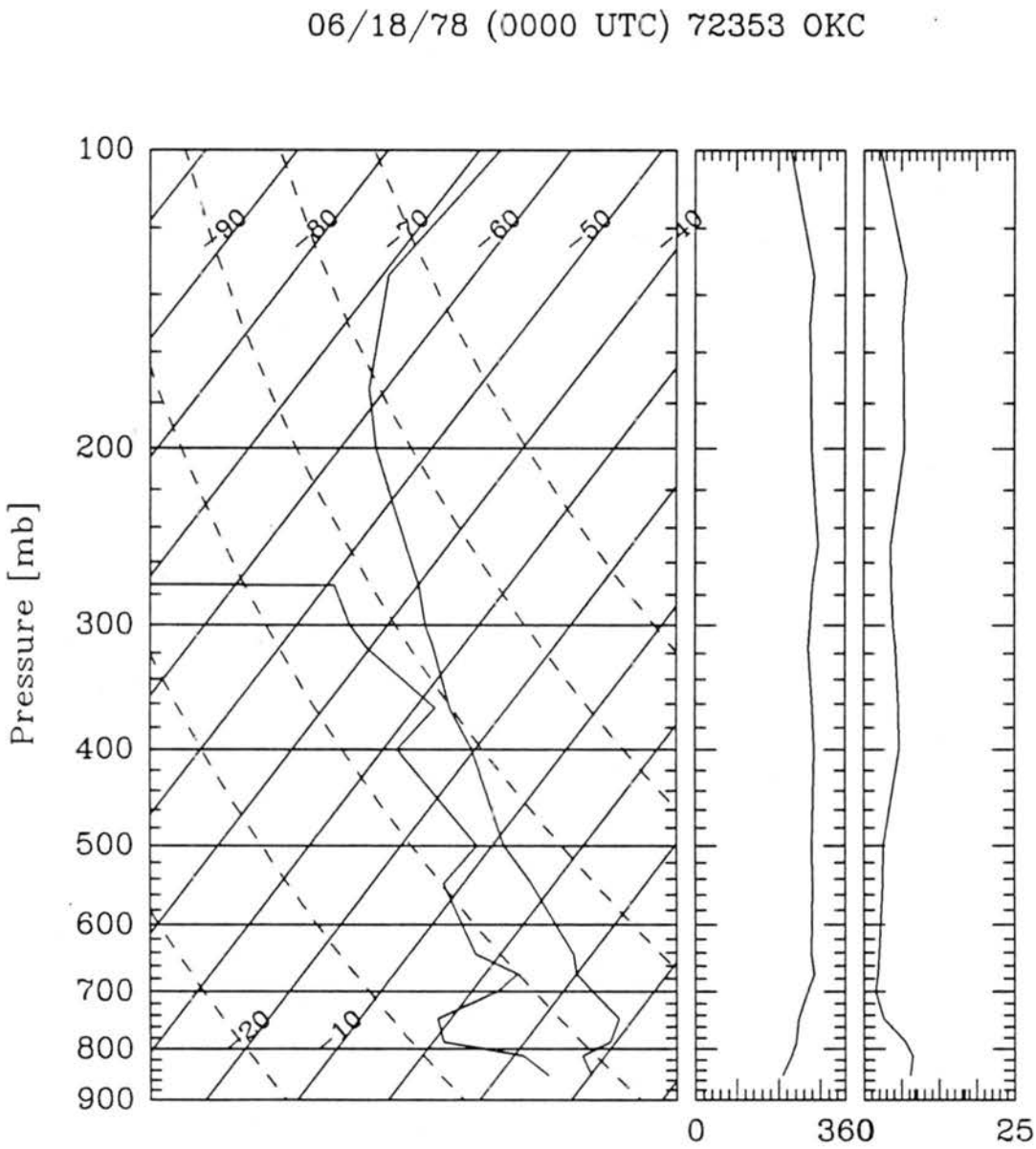

Figure 3.29: OKC rawinsonde sounding at 0000 UTC 18 June 1978. Temperature and dewpoint are shown on the left panel, and wind direction (direction wind is blowing from, in degrees) and speed (m s^{-1}) are shown in the two farthest right panels.

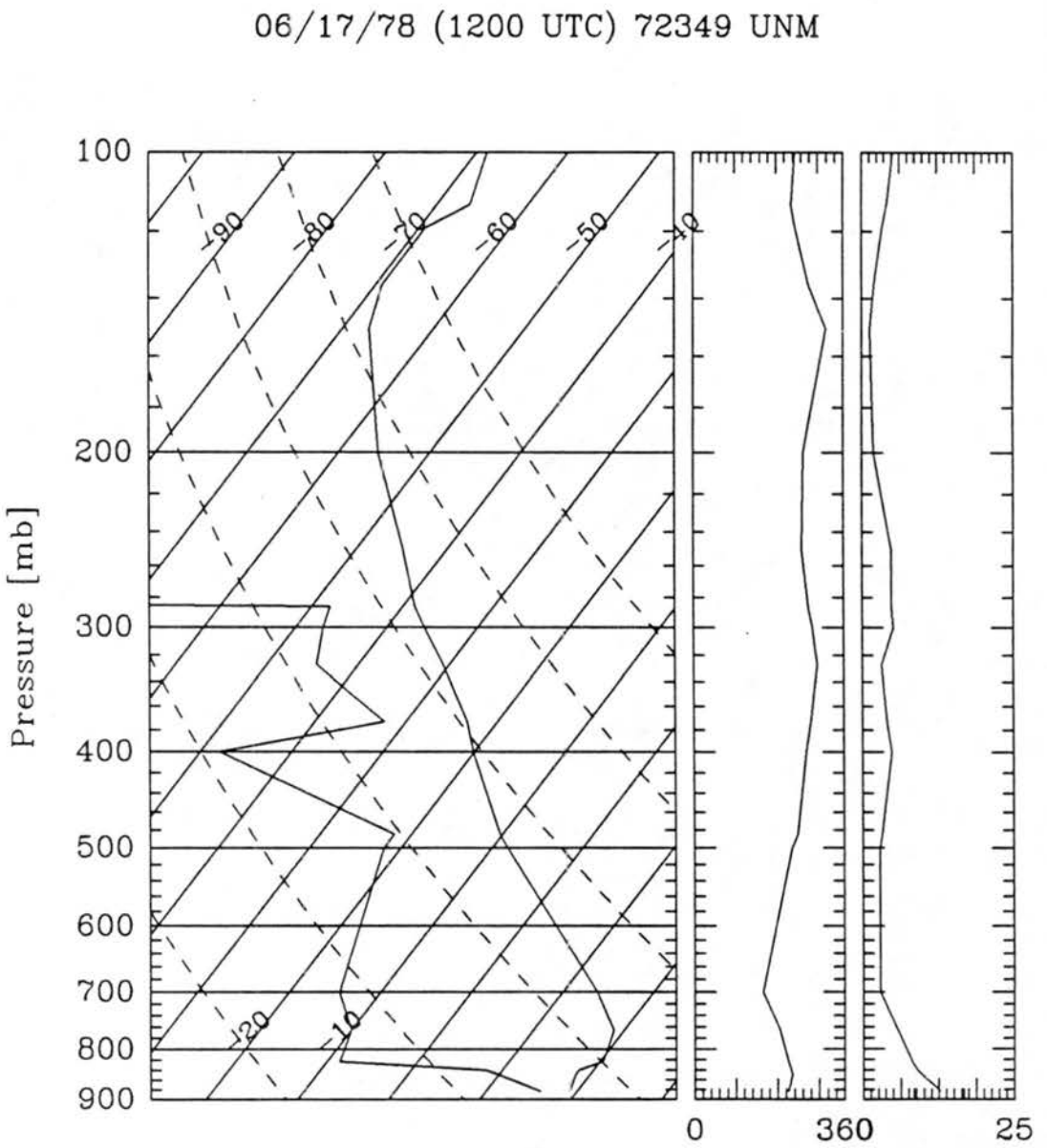

Figure 3.30: UNM rawinsonde sounding at 1200 UTC 17 June 1978. Temperature and dewpoint are shown on the left panel, and wind direction (direction wind is blowing from, in degrees) and speed (m s^{-1}) are shown in the two farthest right panels.

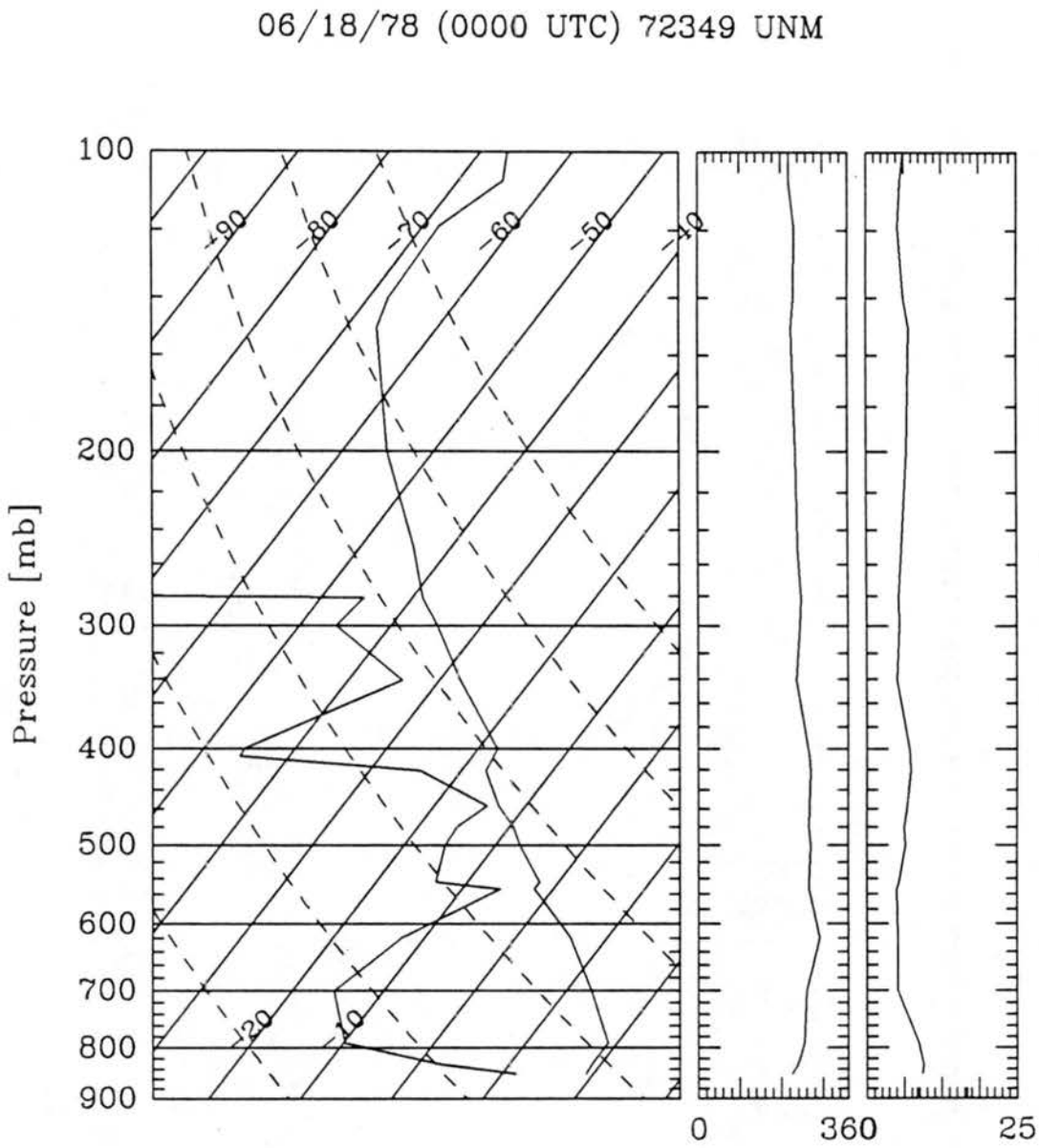

Figure 3.31: UNM rawinsonde sounding at 0000 UTC 18 June 1978. Temperature and dewpoint are shown on the left panel, and wind direction (direction wind is blowing from, in degrees) and speed (m s^{-1}) are shown in the two farthest right panels.

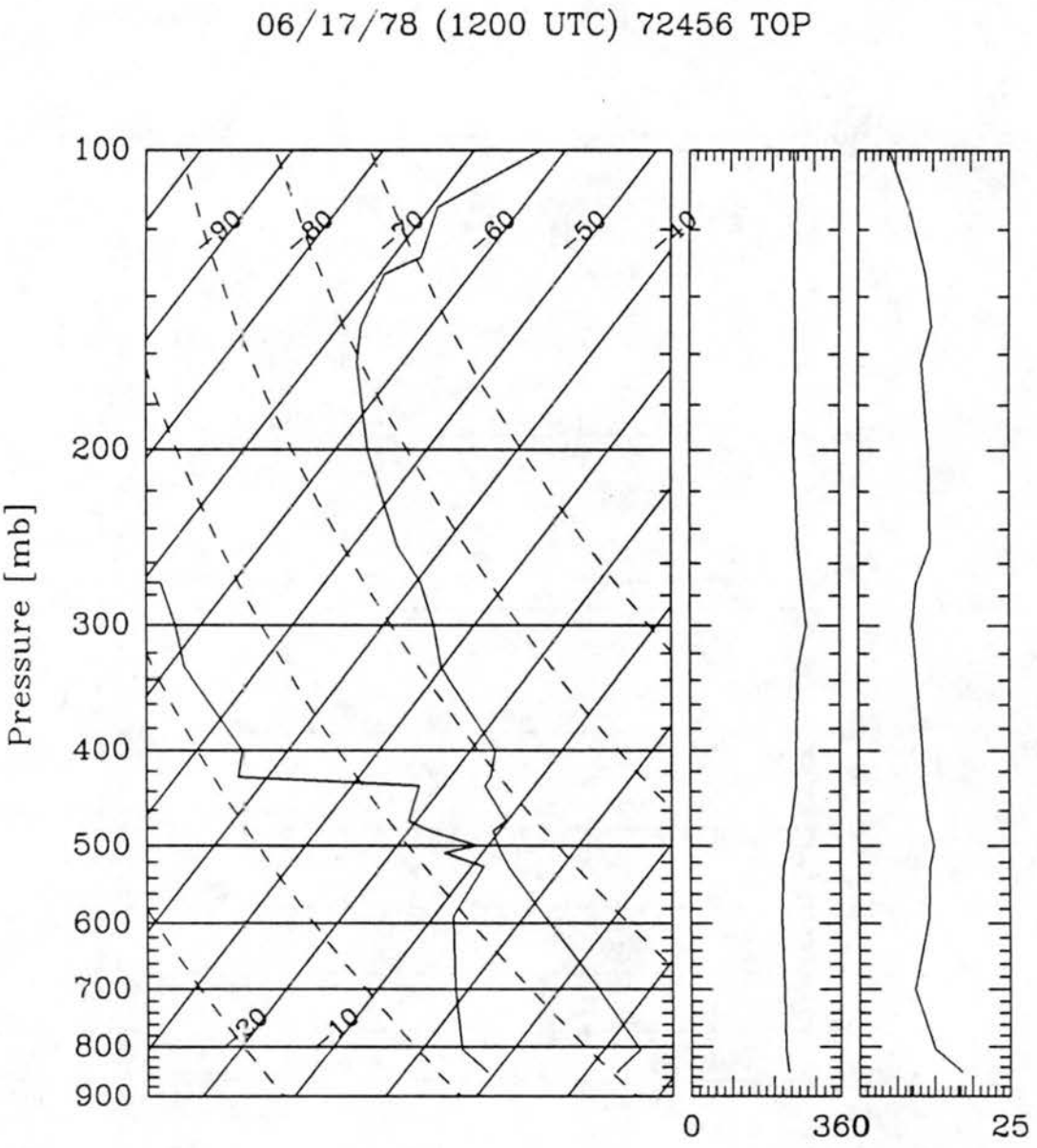

Figure 3.32: TOP rawinsonde sounding at 1200 UTC 17 June 1978. Temperature and dewpoint are shown on the left panel, and wind direction (direction wind is blowing from, in degrees) and speed (m s^{-1}) are shown in the two farthest right panels.

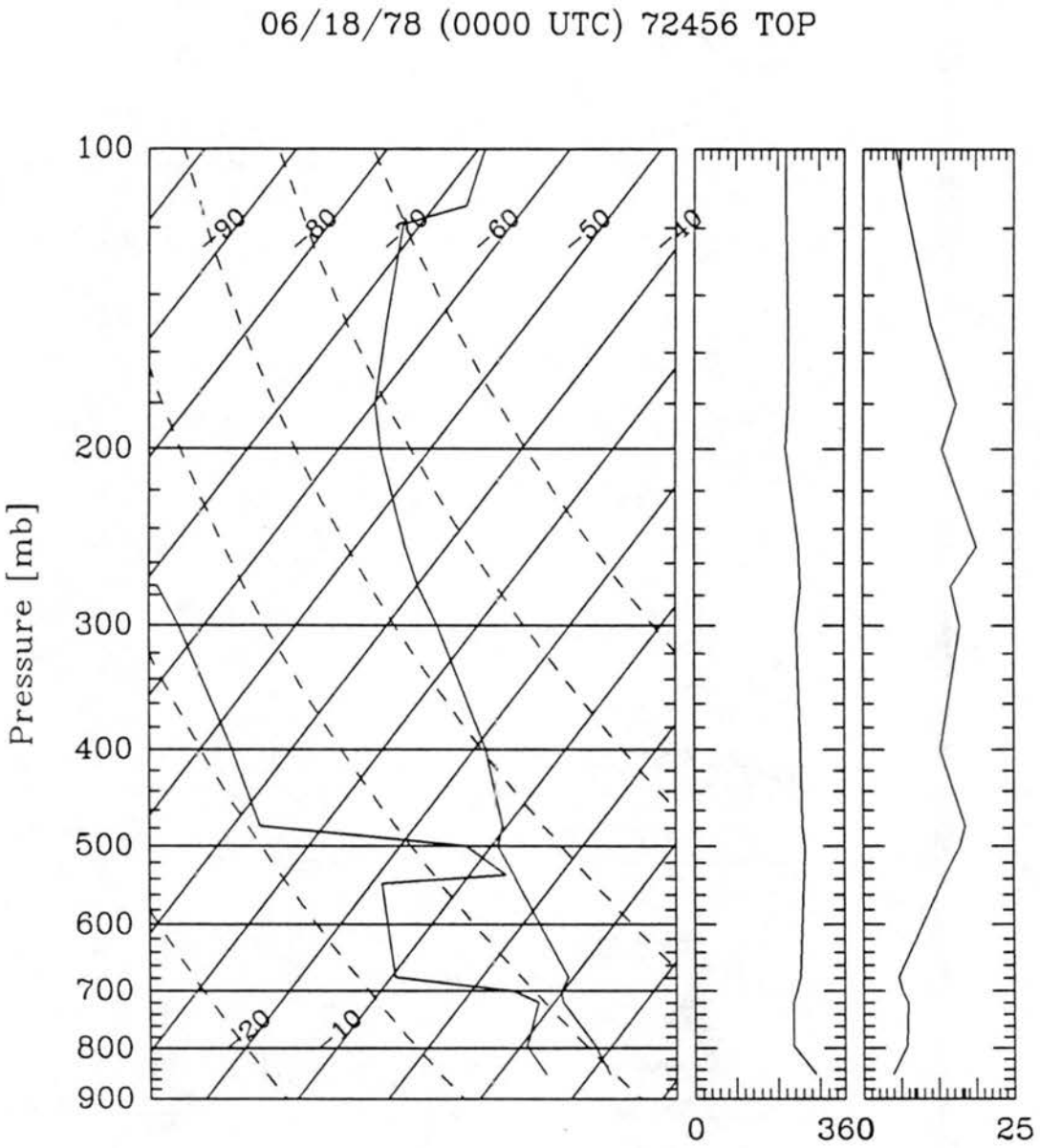

Figure 3.33: TOP rawinsonde sounding at 0000 UTC 18 June 1978. Temperature and dewpoint are shown on the left panel, and wind direction (direction wind is blowing from, in degrees) and speed (m s^{-1}) are shown in the two farthest right panels.

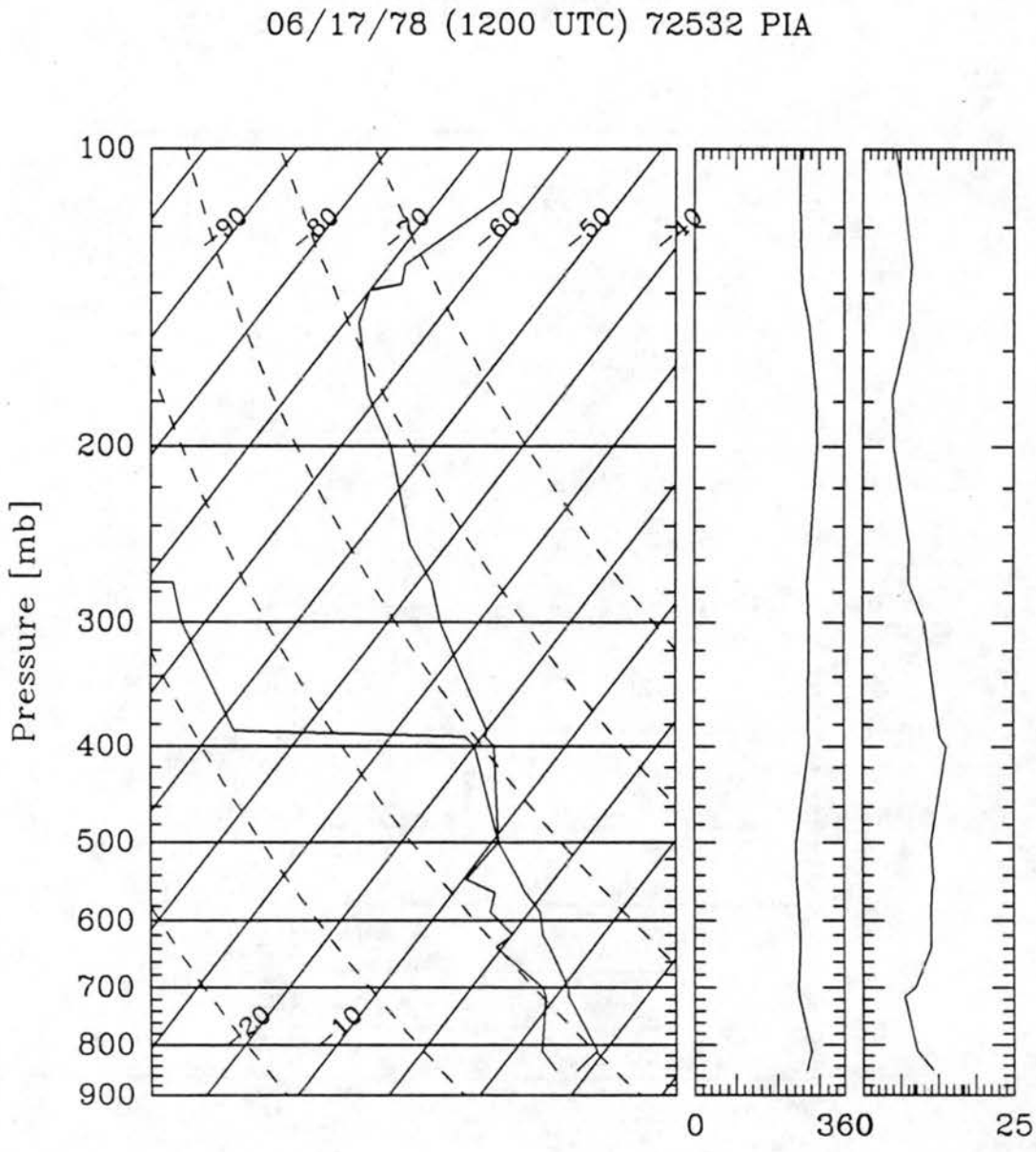

Figure 3.34: PIA rawinsonde sounding at 1200 UTC 17 June 1978. Temperature and dewpoint are shown on the left panel, and wind direction (direction wind is blowing from, in degrees) and speed (m s^{-1}) are shown in the two farthest right panels.

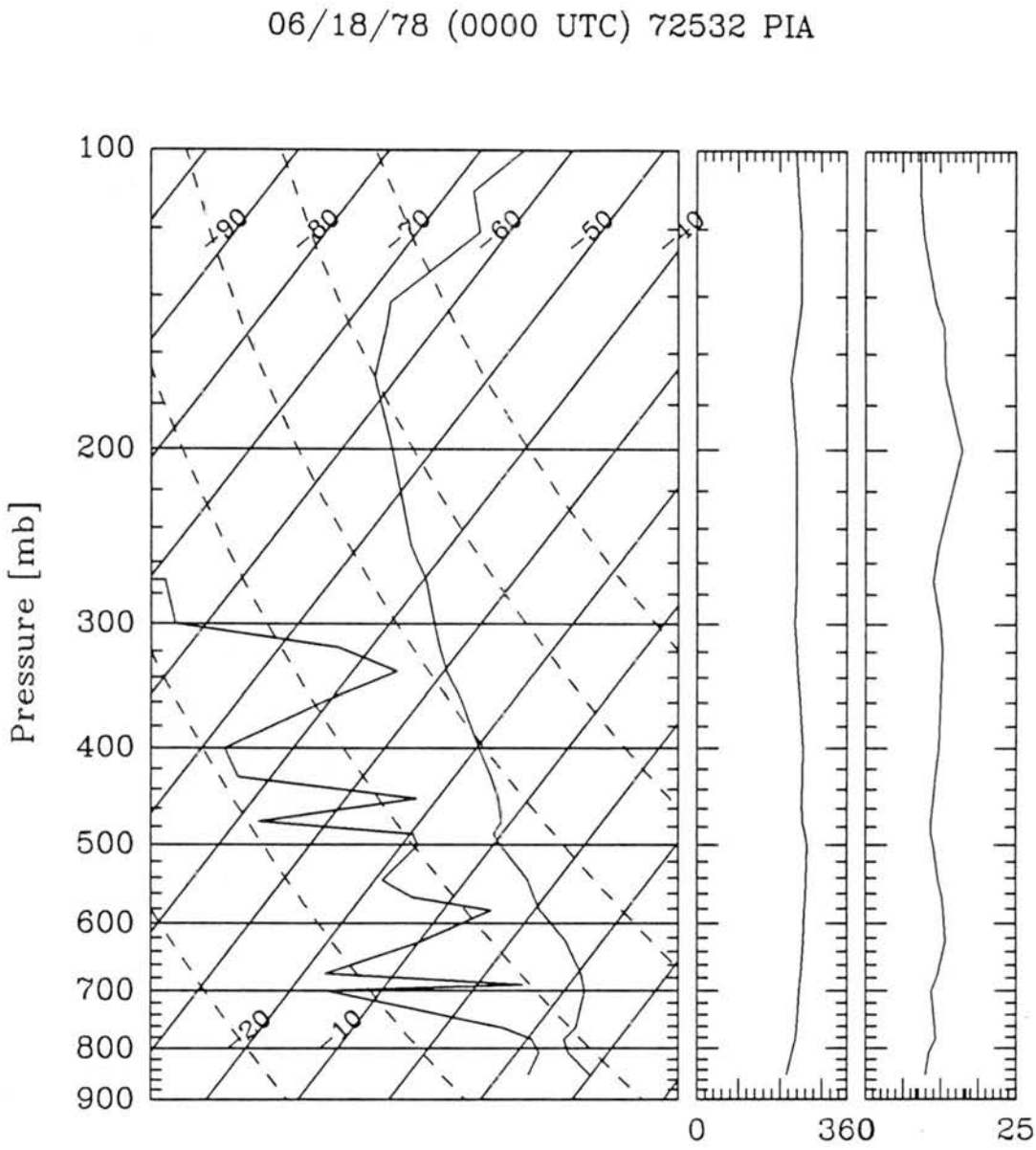

Figure 3.35: PIA rawinsonde sounding at 0000 UTC 18 June 1978. Temperature and dewpoint are shown on the left panel, and wind direction (direction wind is blowing from, in degrees) and speed (m s^{-1}) are shown in the two farthest right panels.

winds at UNM and OKC ahead of the squall line are strongest and have components both toward and parallel to the squall line. By 700 mb the winds have weakened to much less than the speed of the squall line (approximately 15 m s^{-1}) and are blowing in the direction of the squall line propagation (towards the southeast or from the northwest).

The existence of the low-level stable layer below 800 mb is important in inhibiting the convection until the frontal forcing becomes strong. The representation of the low-level stable layer in the model initial analyses was found to be critical to the proper development of the convection along the front. The stable layer also indicates the potential for trapping of internal gravity waves and their propagation along the interface between the stable and unstable layers (Lindzen and Tung, 1976; Crook, 1988). Internal gravity waves have been suggested as a possible mechanism for the sort of discrete propagation of the squall line observed by Thomas Matejka in this case (Section 3.2).

The PIA sounding has almost no directional shear, but some speed shear aloft. This sounding is more indicative of the strong upper-level winds in an MCC-type environment or isolated supercell (Browning, 1964; Klemp and Wilhelmson, 1978a,b; Maddox, 1980), and is in fact very close to the MCC to the north. The TOP sounding at 1200 UTC 17 June (before the squall line has passed) is similar to the OKC and UNM soundings, but by 0000 UTC 18 June has been modified by the squall line convection. The increase in wind speeds in the layer from 500 to 200 mb is perhaps due to convective effects.

3.8 Summary

The observed development and lifetime of the 17-18 June 1978 squall line has been described in this chapter. The radar summary charts and satellite pictures best show the explosive development of the squall line between 2100 and 0000 UTC. The upper air and surface analyses show that the squall line was primarily forced by strong surface frontal convergence, with very weak flow aloft. The soundings indicate the squall line developed in a conditionally unstable environment with a low-level stable area ahead of the front which probably helped to inhibit convection ahead of the front and squall line. The vertical wind profiles in the presquall environment are similar to those described by Bluestein and Jain

(1985), and Rotunno *et al.* (1988) for strong, prefrontal-type squall lines. The hourly surface analyses show that the squall line initially developed along the front, but by 0300 UTC had moved almost 200 km ahead of the front. The active convection in the squall line appears to have lasted from approximately 2100 UTC 17 June to between 0300 and 0600 UTC 18 June, with mostly anvil remaining at 0600 UTC.

Chapter 4

DATA ANALYSIS/MODEL DESCRIPTION

The data sets, analysis methods, and model used for the modelling simulations will be described in this chapter. The model used in this study was the CSU Regional Atmospheric Modelling System (RAMS) (Tremback *et al.*, 1986; Cotton *et al.*, 1988). This model is a completely new code that is the merger of a non-hydrostatic cloud model (Cotton *et al.*, 1982; Tripoli and Cotton, 1980, 1982, 1989a,b) and two hydrostatic mesoscale models (Pielke, 1974; Mahrer and Pielke, 1977; McNider and Pielke, 1981; McCumber and Pielke, 1981; Tremback *et al.*, 1985). The options used in these simulations included two-way interactive nesting, non-hydrostatic, time-splitting, a cumulus parameterization scheme, warm-rain and ice-phase microphysics, a surface parameterization, a radiation parameterization, and time-dependent lateral boundary conditions. These options are described more fully in Section 4.2 of this chapter. The National Meteorological Center (NMC) spectral model analyses, and rawinsonde and surface data available on the NCAR data archives were used for the initial fields and time-dependent lateral boundary conditions. The model initial analysis package is described in Section 4.1 of this chapter. The horizontal grid intervals used in the simulations described in this study ranged from 80 km at larger scales to 20 and 5 km within the nested regions. The specific model domains and resolutions used for the different experiments will be described in Chapter 5.

4.1 Data Sets, Objective Analyses

The objective analysis and initialization package is used to create the analyses from real data used for the initial and lateral boundary conditions when "variable initialization" is used. (RAMS has two basic initialization options: variable initialization and horizon-

tally homogeneous. All of the studies described in this paper used variable initialization.) The initial analysis package was first developed by Tremback (1990), although many modifications and additions have been added by other users, including this author. A brief overview of the package is provided in this section. The package has been developed to access standard data sets archived at the National Center for Atmospheric Research (NCAR). These data sets, and others used in this study, will be described. A package was also developed to analyze hourly surface observations for verification purposes. That package is also described briefly.

4.1.1 Data sets

The standard data sets used in the data analysis package are all available on, or derived from, the NCAR data archives. These include the NMC spectral model analyses, the NMC observational upper air data set, the NMC observational surface data set (three-hourly), 30′ resolved terrain and land versus water data, and 1° resolved sea surface temperature data. Special data sets used in this work also included hourly surface data, soil classification, and land cover classification. These data sets are all described briefly. Many other special-purpose data sets (other soil characteristics, higher resolution terrain, etc.) are available on the NCAR data archives and have been adapted and used by specific users, but are not a part of the standard RAMS initial analysis package. These data sets are all briefly described in the NCAR memo "Data availability at NCAR" (Jenne, 1987).

Standard data sets

The NMC spectral data set is the NCAR-archived analyses from the NMC spectral model (NCAR data set 082.0). These analyses are available for 0000 and 1200 UTC daily, from July 1976 onwards. The analyses are global with a 2.5° horizontal grid interval. The vertical levels available (and used in this study) include 1000, 850, 700, 500, 400, 300, 250, 200, 150, 100, 70, and 50 mb. The variables available are height, temperature, relative humidity, and u and v wind components. The data is archived in NMC's "packed data" format (NMC ON 84, 1979), and read using standard NMC access routines available at

NCAR. The NMC spectral analyses are a combination of a model first-guess, analysis data, and various adjustment/initialization procedures. The first-guess analyses, the data used, the type of analysis scheme, and the adjustments have all changed many times since 1976; there are several informal memos from NCAR (Jenne, personal communication) and NMC references (Kistler and Parrish, 1982; Dey *et al.*, 1985) detailing these changes.

The NMC operational upper air data set (NCAR data set 353.4) includes the global network of rawinsonde observations. These are available at 0000 and 1200 GMT from January 1973 onwards. The rawinsonde data is available at both mandatory and significant levels, and includes pressure, height, temperature, dew point depression, and wind speed and direction. Figure 4.1 shows the sites of the rawinsonde observations used in the initial analyses for the model simulations described in this study.

The NMC operational surface data set (NCAR data set 464.0) includes the global network of surface observations. These are available at three-hour intervals from July 1976 onwards. The data used in the analysis package include surface temperatures, pressures, relative humidities, wind speed and wind direction. Figure 4.2 shows the sites of the surface stations from this three-hourly data set that were used in the initial analyses for the model simulations.

The terrain data set is derived from the United States Air Force (USAF) global 1° and 30′ average elevation data set (NCAR data set 755.0). The 30′ data is used where available, with the 1° data used elsewhere. The 30′ data is not available over some areas of the globe (Australia for example). This data set also includes land vs. water information for each 1° or 30′ square. Figure 4.3 shows the terrain analysis used for the simulations described in this paper.

The sea surface temperature (SST) data is a 1° interval data set compiled by the Rand corporation (Alexander and Mobley, 1974) (NCAR data set 270.2). This data set was compiled from two other data sets: the NCAR global SST data set with 2.5° spacings, and the Fleet Numerical Weather Central (FNWC) data set (125 × 125 rectangular grid covering the entire Northern Hemisphere). Thus, the final 1° data set is not actually

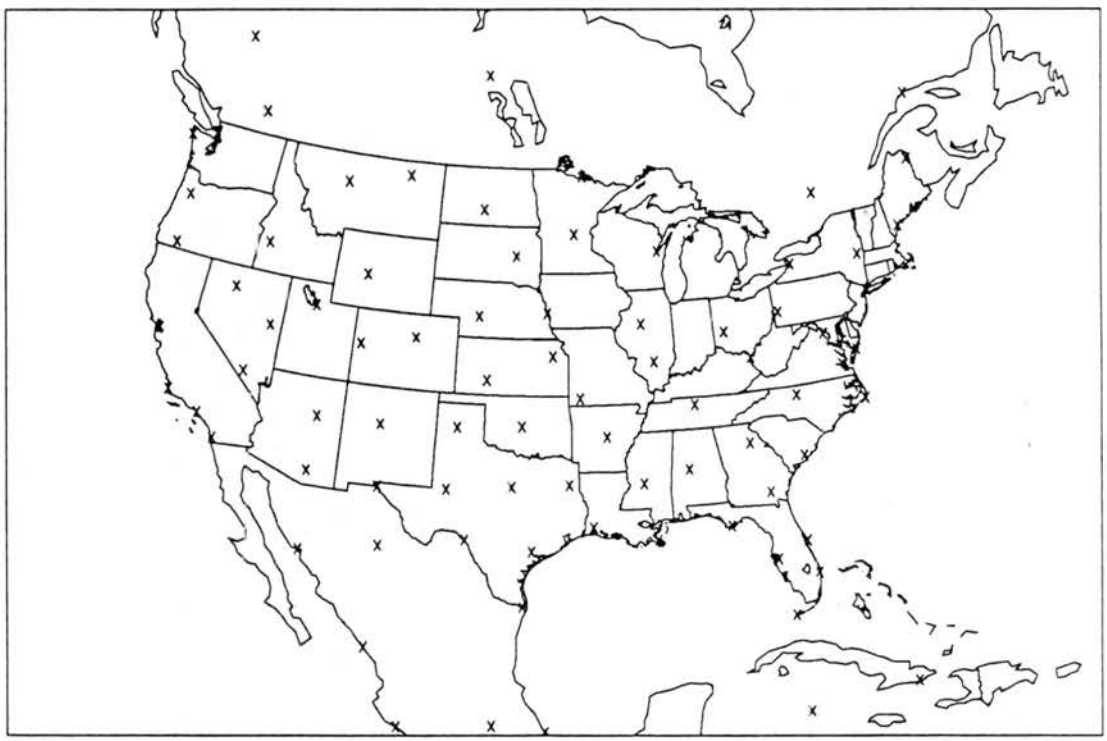

Figure 4.1: Locations of rawinsonde observations used in analyses.

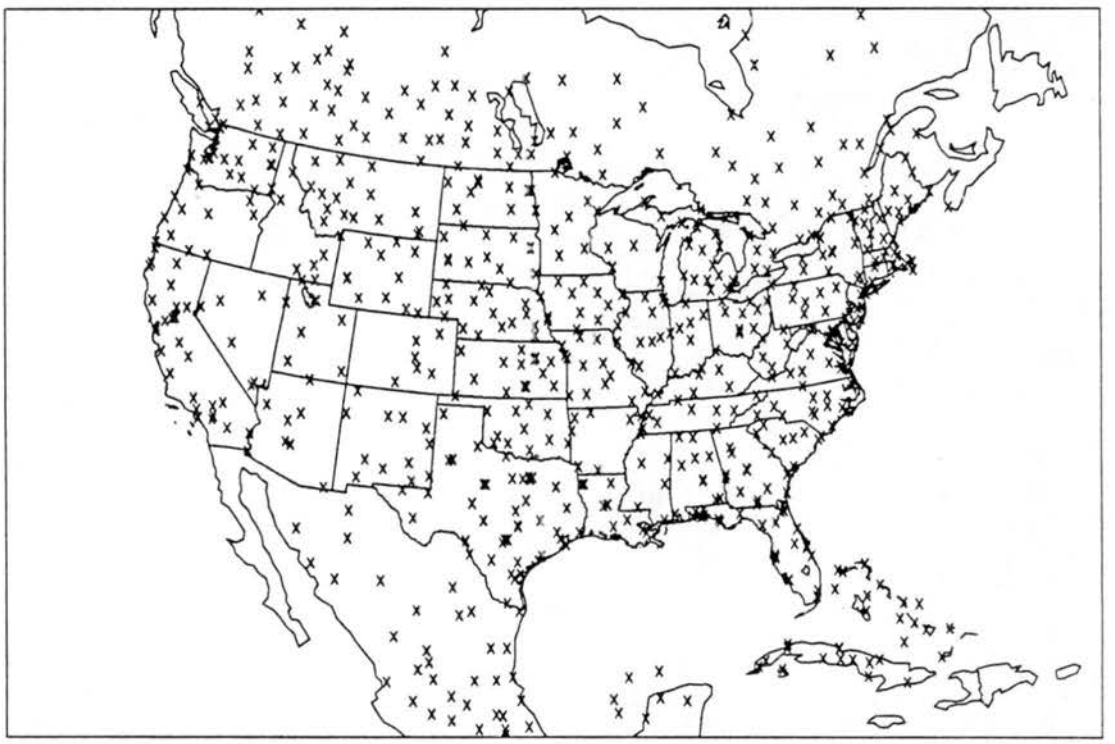

Figure 4.2: Locations of surface stations used in model initial analyses.

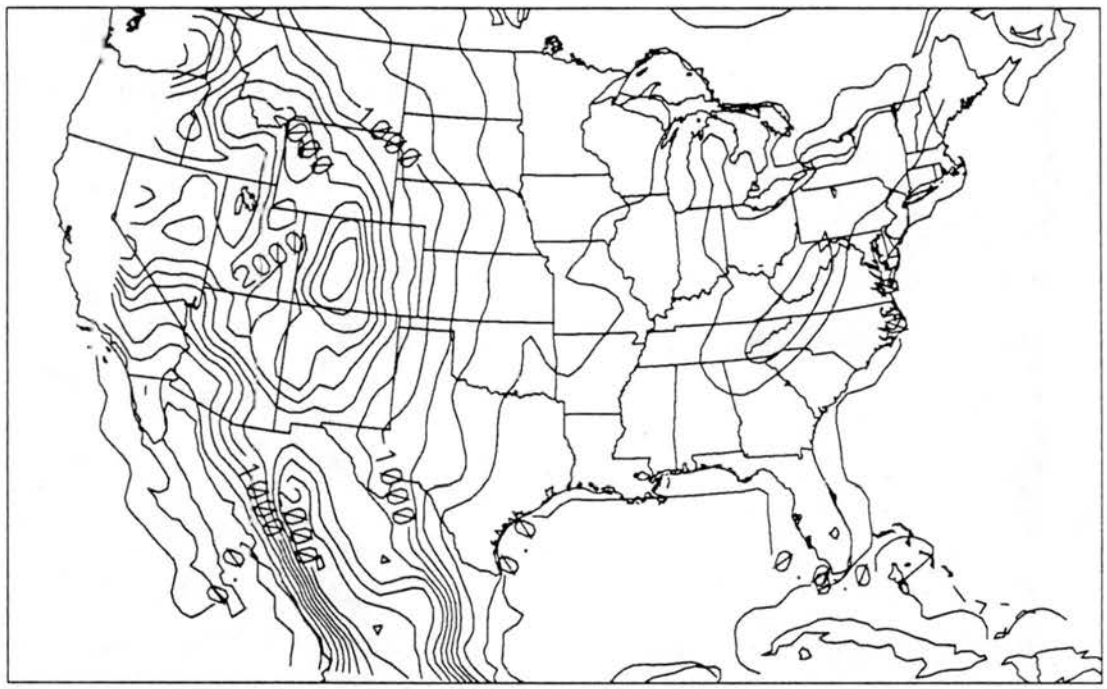

Figure 4.3: Terrain analyses (m) used in model simulations. Contour interval is 100 m.

compiled entirely from 1° spaced SST observations. There is a data set of the average SSTs for each month. The appropriate monthly data set is used in the RAMS initial analysis package (June in this case).

Special-use data sets

The NMC three-hourly surface data (NCAR data set 464.0) was sufficient for the initial data analyses needed for model initialization and time-dependent lateral boundary conditions (needed at 12-hourly intervals). However, another NCAR data set was used for the hourly surface analyses needed for verification of the model simulation. The data set used for these analyses was NCAR data set 472.0, with the hourly surface observations. The variables used in the verification analyses included temperature, dew point, wind speed and direction, 12-hour precipitation amount, and sea-level-pressure. Figure 4.4 shows the locations of the stations used in the verification analyses.

Most of the simulations described in this study used a constant soil type and surface roughness, and an initial soil moisture specification based on the atmospheric relative humidity (described in Section 4.2.8). However, one experiment was done to test the effects of using a nonconstant initialization of these variables. The data set used for the soil type and surface roughness initialization was NCAR data set 767.0. This data set includes 1° interval arrays of soil properties and land cover classes compiled by Henderson-Sellers of the University of Liverpool. This data set is described in Wilson and Henderson-Sellers (1985), and Henderson-Sellers *et al.* (1986). Tables 4.1 and 4.2 show the classes of land cover and soil information available in this data set. Figures 4.5 and 4.6 show the distribution of these classes over the domain used in the model simulations. The types of variables available in this data set do not correspond exactly to the types of variables used in the model, so transitions had to be devised. The RAMS model uses the 12 United States Department of Agriculture (USDA) soil classes shown in Table 4.3. A transition from Henderson-Sellers soil classes to the USDA soil classes was devised based on the soil-texture triangle that the USDA soil classes are based on (Fig. 4.7 from Kohnke, 1968) and

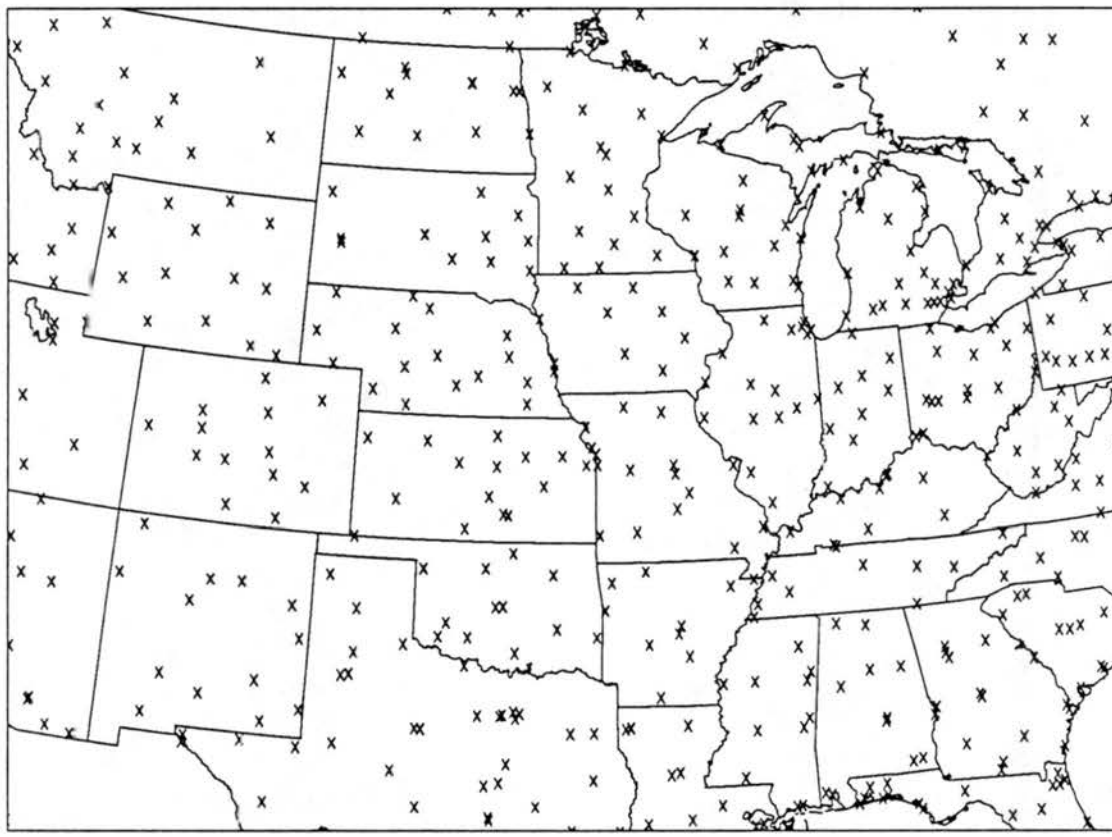

Figure 4.4: Locations of surface stations used for verification analyses.

Table 4.1: Henderson-Sellers land-cover classes.

Code	Type
00	Open water
01	Inland water
02	Bog or marsh
03	Ice
04	Paddy rice
05	Mangrove
10	Dense needleleaf evergreen forest
11	Open needleleaf evergreen woodland
12	Dense mixed forest
13	Open mixed woodland
14	Evergreen broadleaf woodland
15	Evergreen broadleaf cropland
16	Evergreen broadleaf shrub
17	Open deciduous needleleaf woodland
18	Dense deciduous needleleaf forest
19	Dense evergreen broadleaf forest
20	Dense deciduous broadleaf forest
21	Open deciduous broadleaf woodland
22	Deciduous tree crop
23	Open tropical woodland
24	Woodland plus shrub
25	Dense drought deciduous forest
26	Open drought deciduous woodland
27	Deciduous shrub
28	Thorn shrub
30	Temperate meadow and permanent pasture
31	Temperate rough grazing
32	Tropical grassland plus shrub
33	Tropical pasture
34	Rough grazing plus shrub
35	Pasture plus tree
36	Semi-arid rough grazing
37	Tropical savanna
39	Pasture plus shrub
40	Arable cropland
41	Dry farm arable
42	Nursery and market gardening
43	Cane sugar

Table 4.1: Continued.

Code	Type
44	Maize
45	Cotton
46	Coffee
47	Vineyard
48	Irrigated cropland
49	Tea
50	Equatorial rainforest
51	Equatorial tree crop
52	Tropical broadleaf forest
61	Tundra
62	Dwarf shrub
70	Sand desert and barren land
71	Scrub desert and semidesert
73	Semidesert and scattered trees
80	Urban

Table 4.2: Henderson-Sellers soil classes.

Code	Color	Texture	Drainage
11	light	coarse	free
12	light	intermediate	free
14	light	coarse	impeded
15	light	intermediate	impeded
16	light	fine	impeded
17	medium	coarse	free
18	medium	intermediate	free
19	medium	fine	free
20	medium	coarse	impeded
21	medium	intermediate	impeded
22	medium	fine	impeded
23	dark	coarse	free
24	dark	intermediate	free
25	dark	fine	free
32	dark	coarse	impeded
27	dark	intermediate	impeded
28	dark	fine	impeded
29	light	–	poor
30	medium	–	poor
31	dark	–	poor
34	ice	–	–

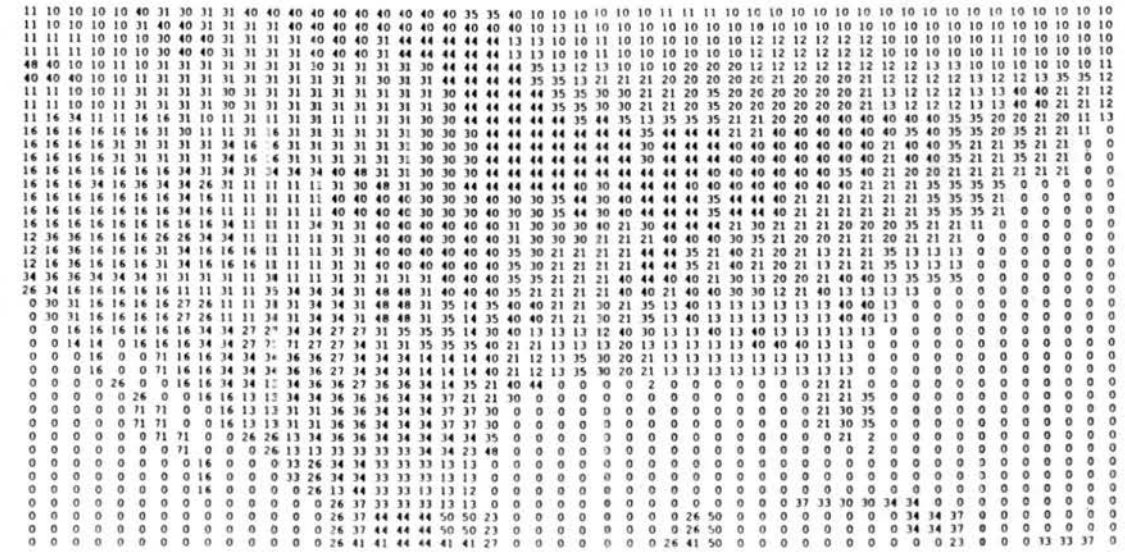

Figure 4.5: Distribution of Henderson-Sellers land-cover classes over the model domain (classes described in Table 4.1.) Each number represents a 1.0° longitude × 0.75° latitude box. The southwest corner of the domain is at 119°W and 21°N.

Table 4.3: USDA soil classes.

Sand
Loamy sand
Sandy loam
Silt loam
Loam
Sandy clay loam
Silty clay loam
Clay loam
Sandy clay
Silty clay
Clay
Peat

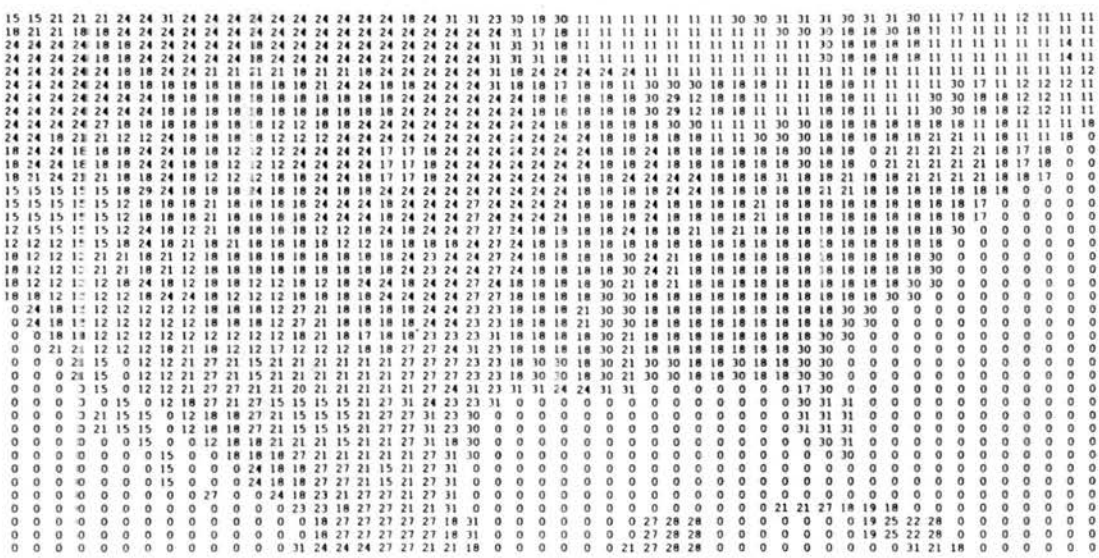

Figure 4.6: Distribution of Henderson-Sellers soil classes (classes described in Table 4.2) over the model domain. Each number represents a 1.0° longitude × 0.75° latitude box. The southwest corner of the domain is at 119°W and 21°N.

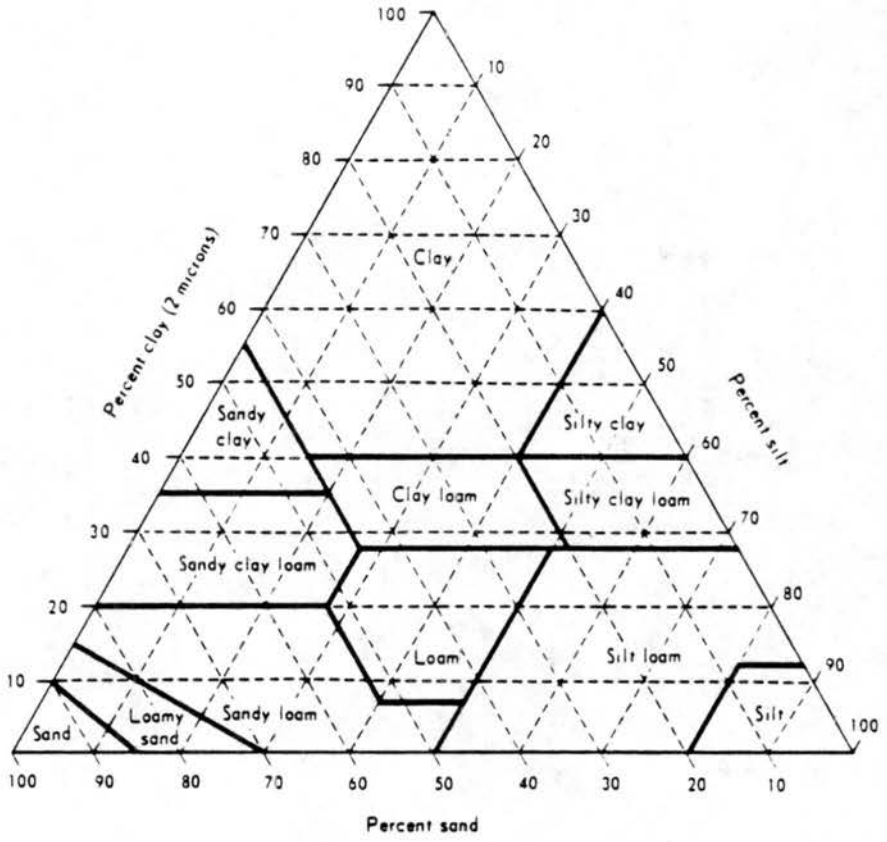

Figure 4.7: USDA soil triangle (from Kohnke, 1968).

Table 4.4 (also from Kohnke, 1968). The transition relations from the Henderson-Sellers soil classes to the USDA soil classes that were devised are shown in Table 4.5.

Table 4.4: Description of soil classes (from Kohnke, 1968).

Coarse-Textured Soils	1. Sands and loamy sands	Sand, Loamy sand
Medium-Textured Soils	2. Sandy loam	Sandy loam, Fine sandy loam
	3. Loamy soils	Very fine sandy loam, Loam, Silt loam, Silt
	4. Moderately heavy soils	Sandy clay loam, Clay loam, Silty clay loam
Fine-Textured Soils	5. Clays and silty clays	Sandy clay, Silty clay, Clay

The resulting domain map of USDA soil classes is shown in Fig. 4.8. The RAMS model also uses a surface roughness length variable. A transition from the Henderson-Sellers land classes to surface roughness was devised based on Table 4.6 (from Henderson-Sellers *et al.*, 1986).

The resulting domain map of roughness lengths is shown in Fig. 4.9. The initialization of soil moisture for that one simulation was based on an analysis of the previous 24 hours of precipitation data available in NCAR data set 472.0 (described previously). The analysis method is described in Section 4.1.3. Other specifics of the model initialization for this experiment will be described in Section 5.5.

4.1.2 Formulation of RAMS initial analysis package

The initial analysis package has been developed to use the standard data sets available from the NCAR data archives (data sets described previously). The analysis is hydrostatic and completed on isentropic surfaces. The analysis package is divided into five basic stages: Stage 1 is the access of the NMC spectral analyses on pressure levels; Stage 2 is the conversion of that data to isentropic surfaces; Stage 3 is the objective analysis and enhancement of the isentropic data to include rawinsonde and surface observations; Stage

Table 4.5: Transition from Henderson-Sellers to USDA soil classes.

Henderson-Sellers Soil Classes	USDA Soil Classes	
11	2	loamy sand
12	5	loam
14	3	sandy loam
15	6	sandy clay loam
16	10	silty clay
17	2	loamy sand
18	5	loam
19	9	sandy clay
20	3	sandy loam
21	6	sandy clay loam
22	10	silty clay
23	2	loamy sand
24	5	loam
25	9	sandy clay
32	3	sandy loam
27	3	sandy loam
28	6	sandy clay loam
29	11	clay
30	11	clay
31	11	clay

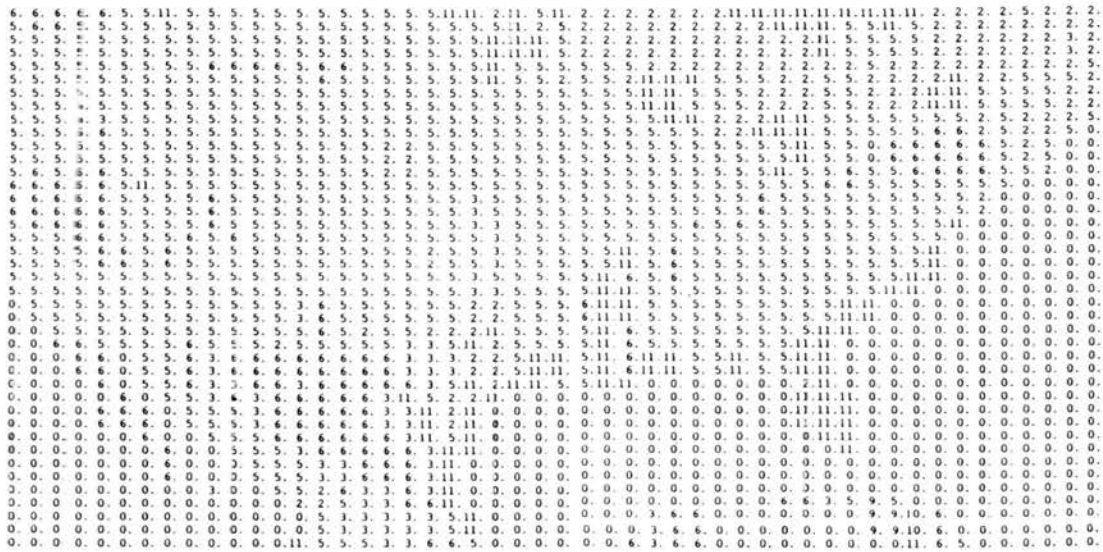

Figure 4.8: Distribution of USDA soil classes over model domain. Each number represents a 1.0° longitude × 0.75° latitude box. The southwest corner of the domain is at 119°W and 21°N.

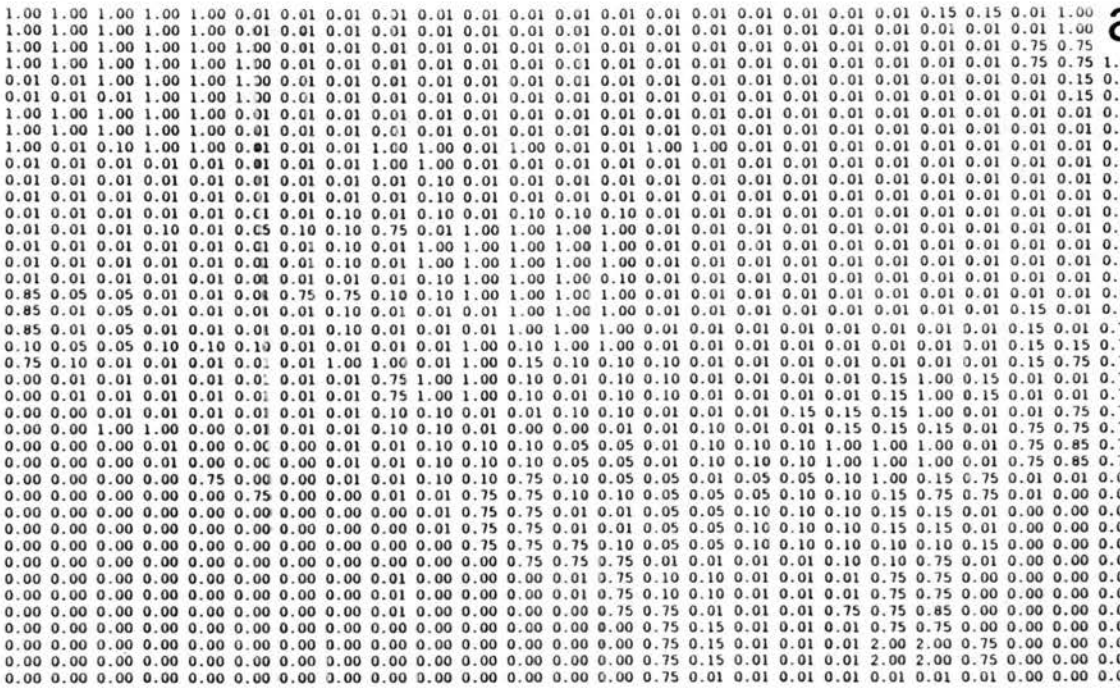

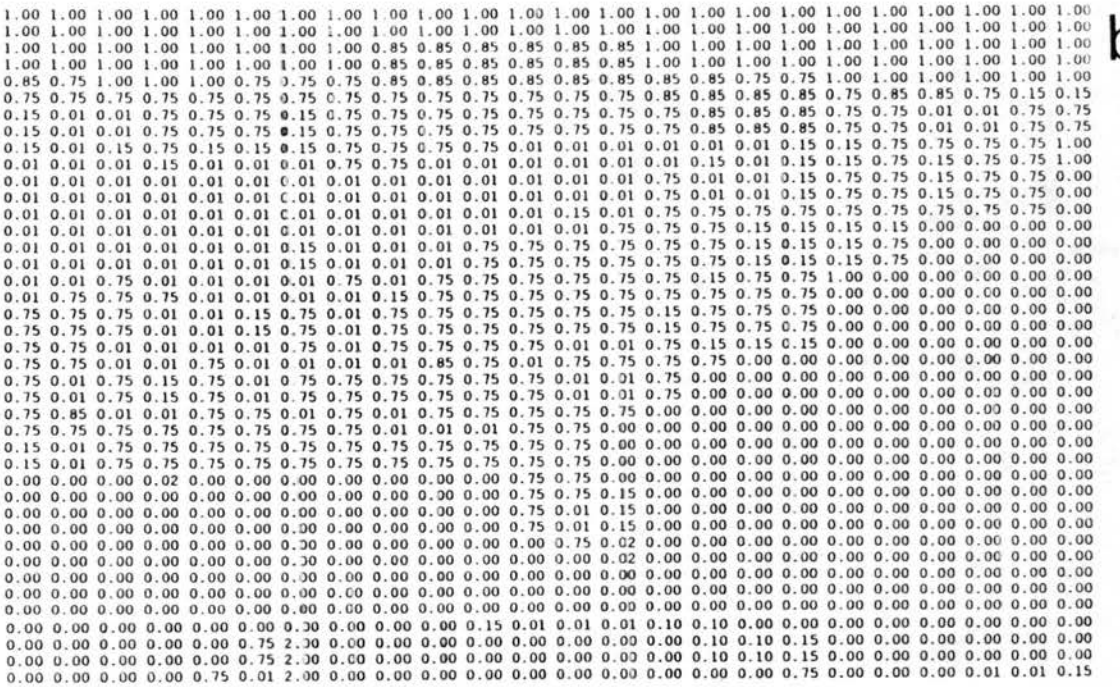

Figure 4.9: Distribution of roughness lengths over domain. Each number represents a 1.0° longitude × 0.75° latitude box. The southern edge of the domain is at 21°N. (a) is from 119°W to 95°W, and (b) is from 94°W to 70°W.

Table 4.6: Transition from Henderson-Sellers land-cover to roughness length (from Henderson-Sellers *et al.*, 1986).

Henderson-Sellers Land-Cover Classes	Simple Vegetation Classes	Roughness z_0 (cm)
01 Inland water	11 Bog or marsh	2.0
02 Bog or marsh	11 Bog or marsh	2.0
03 Ice	9 Ice	0.5
04 Paddy rice	10,11 Cultivation, Bog or marsh	1.5
05 Mangrove	08 Rainforest	200
10 Dense needleleaf evergreen forest	07 Evergreen forest	100
11 Open needleleaf evergreen woodland	07 Evergreen forest	100
12 Dense mixed forest	6,7 Deciduous forest, Evergreen forest	85
13 Open mixed woodland	6,7 Deciduous forest, Evergreen forest	85
14 Evergreen broadleaf woodland	07 Evergreen forest	100
15 Evergreen broadleaf cropland	07 Evergreen forest	100
16 Evergreen broadleaf shrub	03 Grassland	1.0
17 Open deciduous needleleaf woodland	06 Deciduous forest	75
18 Dense deciduous needleleaf forest	06 Deciduous forest	75
19 Dense evergreen broadleaf forest	07 Evergreen forest	100
20 Dense deciduous broadleaf forest	06 Deciduous forest	75
21 Open deciduous broadleaf woodland	06 Deciduous forest	75
23 Open tropical woodland	06 Deciduous forest	75
24 Woodland plus shrub	06 Deciduous forest	75
25 Dense drought deciduous forest	06 Deciduous forest	75
26 Open drought deciduous woodland	06 Deciduous forest	75
27 Deciduous shrub	03 Grassland	1.0
28 Thorn shrub	04 Grassland with shrub cover	10
30 Temperate meadow and pasture	03 Grassland	1.0
31 Temperate rough grazing	03 Grassland	1.0
32 Tropical grassland plus shrub	04 Grassland with shrub cover	10
33 Tropical pasture	03 Grassland	1.0
34 Rough grazing plus shrub	04 Grassland with shrub cover	10
35 Pasture plus tree	05 Grassland with tree cover	15
36 Semi-arid rough grazing	01 Desert	0.2
37 Tropical savanna	05 Grassland with tree cover	15
39 Pasture plus shrub	03 Grassland	1.0
40 Arable cropland	10 Cultivation	1.0
41 Dry farm arable	10 Cultivation	1.0
42 Nursery and market gardening	10 Cultivation	1.0
43 Cane sugar	10 Cultivation	1.0
45 Cotton	04 Grassland with shrub cover	10
46 Coffee	04 Grassland with shrub cover	10
47 Vineyard	05 Grassland with tree cover	15

Table 4.6: Continued.

Henderson-Sellers Land-Cover Classes	Simple Vegetation Classes	Roughness z_0 (cm)
48 Irrigated cropland	10 Grassland with tree cover	1.0
49 Tea	04 Grassland with shrub cover	10
50 Equatorial rainforest	08 Rainforest	200
51 Equatorial tree crop	08 Rainforest	200
52 Tropical broadleaf forest	08 Rainforest	200
61 Tundra	02 Tundra	2.0
62 Dwarf shrub	2,4 Tundra, Grassland with shrub cover	6.0
70 Sand desert and barren land	01 Desert	0.2
71 Scrub desert and semi-desert	01 Desert	0.2
73 Semi-desert and scattered trees	01 Desert	0.2
80 Urban	04 Grassland with tree cover	10

4 is plotting; and Stage 5 is the interpolation of the analyses to the model grid. Each stage will be briefly described in this section. As with the model, a configuration file sets up the array dimension maxima and the common blocks. The namelist specifies general parameters such as file names and dates, and specific parameters for each stage.

Stage 1 is the access of the NMC spectral model analyses on pressure surfaces. This data set has a 2.5° global grid spacing and the user specifies the subset area and vertical levels to be accessed. The output from this stage is gridded arrays of u and v wind components, height, temperature, and relative humidity on pressure surfaces. The NMC data accessed for this study included all levels from 1000 mb to 50 mb (see NMC spectral data description). The domain of the Stage 1 analyses for this experiment is shown in Fig. 4.10 (box A).

Stage 2 is the vertical interpolation of the pressure level data to isentropic surfaces and the access of the terrain, land vs. water, and SST data. The user can specify the isentropic levels to be used, or pick one of two options to have the levels automatically specified. The levels chosen for this case were at 4 K intervals from the lowest isentropic surface to 360 K, and then at 10 K intervals to the highest isentropic surface. The u and v wind components and relative humidity are interpolated vertically linearly with respect to θ. Pressure and Montgomery streamfunction ($c_pT + gz$) are interpolated vertically

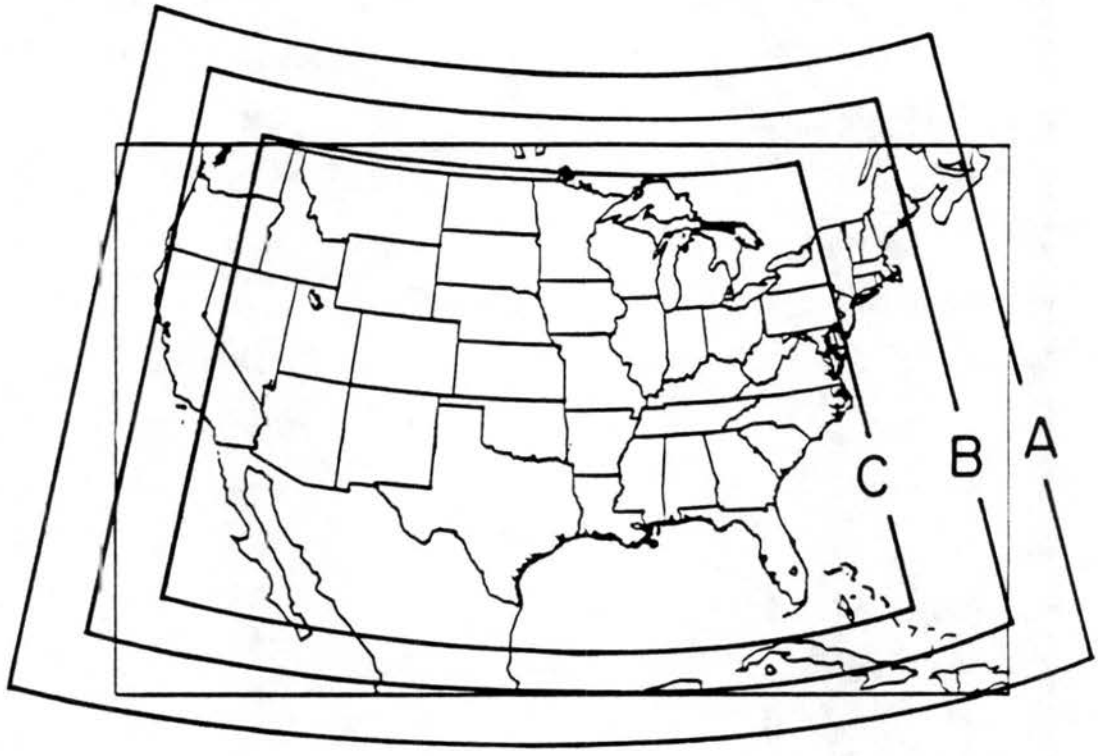

Figure 4.10: Domain of Stages 1-5 analyses and model simulation domain. Box A is the domain for Stages 1 and 2, box B is the domain for Stage 3, and box C is the domain for Stage 5 and the model simulation.

hydrostatically. Any winds above 100 mb are calculated geostrophically. The terrain, land vs. water, and SST arrays are accessed and interpolated to the horizontal grid using the overlapping polynomial technique of Bleck and Haagenson (1968). Surface values of u and v wind component, relative humidity, and θ are interpolated to the terrain heights linearly with respect to height. Surface pressure and Montgomery streamfunction are interpolated hydrostatically. The output from this stage is gridded fields (on isentropic surfaces and at the surface) of u and v wind components, relative humidity, pressure, and Montgomery streamfunction.

Stage 3 includes the horizontal interpolation of the Stage 2 data to a "fine grid" and the reanalysis of the data to include the upper air and surface observations. The user specifies the fine grid boundaries and resolution. The horizontal resolution used for the output analyses from this stage was a 1° grid spacing. The Stage 3 domain used in this study is also shown in Fig. 4.10 (box B). There are options in the package to just interpolate the Stage 2 data horizontally, or to reanalyze the Stage 2 data to include various combinations of that data and the observations. The horizontal interpolations all use the overlapping polynomial technique. The option chosen for the analyses in this study was to reanalyze the Stage 2 data to also include the rawinsonde data and the surface data. The Stage 2 analyzed fields are treated as a set of "observations" in the analysis procedure, and the "Stage 2 observation" at a point is thrown out if a rawinsonde observation is within 2.0° of the "Stage 2 observation". Parameters can also be specified to exclude certain observations from the analysis, or to exclude an observation based on its proximity to a Stage 2 data point. A Barnes (1964, 1973) objective analysis scheme is used and the user can input parameters that will determine the characteristics of the response function for the scheme. The response function used in these analyses is shown in Fig. 4.11. Terrain, land vs. water, and SST data are all interpolated to the fine grid in this stage. The terrain can be interpolated using the overlapping polynomial technique or by using the Barnes analysis and adjusting the response function to act as a filter. The latter option was chosen for this study, with the response function for the terrain analyses

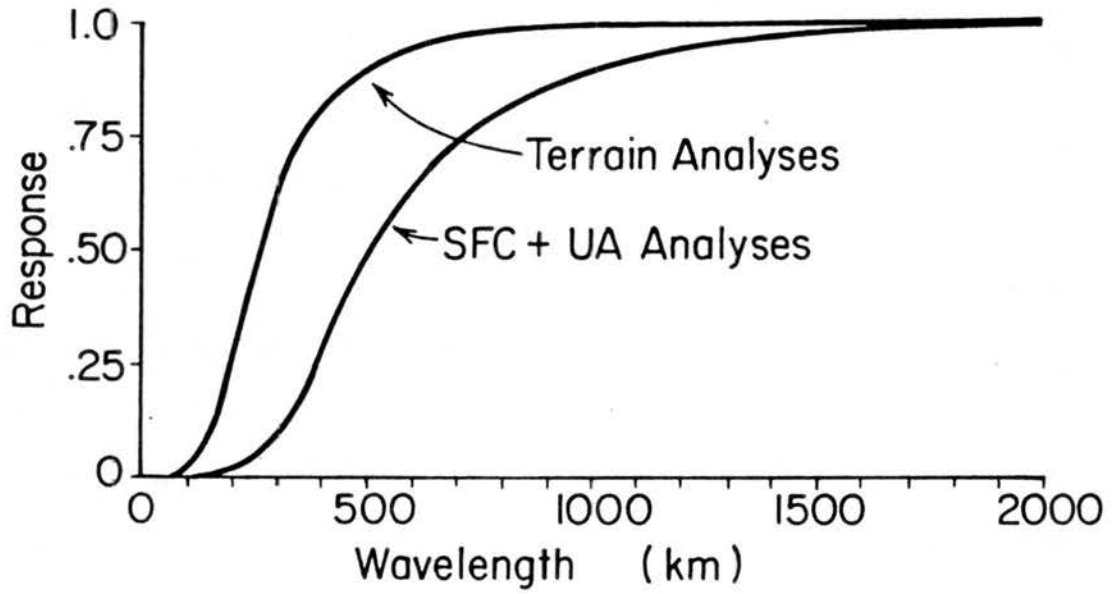

Figure 4.11: Response functions used in Stage 3 for the upper air and surface analyses, and the terrain analysis.

also shown in Fig. 4.11. The analyzed terrain was shown in Fig. 4.3. Pressures are recalculated hydrostatically in this stage (upwards and downwards) from a user-specified θ level (360 K in this case). The output arrays from this stage are the upper air (on isentropic surfaces) and surface values of u and v wind components, relative humidity, pressure, and Montgomery streamfunction.

Stage 4 is the calculation and plotting of certain fields from Stages 1 through 3. Available cross sections include Stage 1 fields on pressure surfaces, and Stage 2 and 3 fields on isentropic surfaces. Fields that can be plotted include variables such the u and v wind components, relative humidity, Montgomery streamfunction, pressure, and theta, and diagnosed fields such as divergence, vorticity, and reduced sea level pressure.

Stage 5 is the final interpolation of the Stage 3 output fields to the model grid. The user specifies the horizontal grid and vertical, terrain-following, coordinate levels in the namelist. The grid domain shown for this stage (same as the model coarse grid) is shown in Fig. 4.10 (box C). Options are also included to smooth the terrain in this stage and to calculate geostrophic winds. Neither of those options were used in this study. Horizontal interpolations are computed using the overlapping polynomial technique. Vertical interpolations of the u and v wind components , θ, and relative humidity are done linearly with respect to height. Relative humidity is converted to mixing ratio. The Exner function, π, is calculated hydrostatically from a middle level. The fields output from this stage are used directly as input to the model for the initial analyses, and also to calculate the time dependent boundary conditions. For this study, analyses were completed for 1200 UTC 17 June 1978, and 0000 and 1200 UTC 18 June 1978.

4.1.3 Verification analyses

A version of the Stage 3 initial analysis package described previously was modified to perform analyses of surface data for verification purposes. This analysis was also a Barnes (1964, 1973) analysis, with the response function shown in Fig. 4.12. The surface data used in the verification analyses came from the NCAR hourly surface observational data set (described in Section 4.1.1). Figure 4.12 also shows the response function used for the

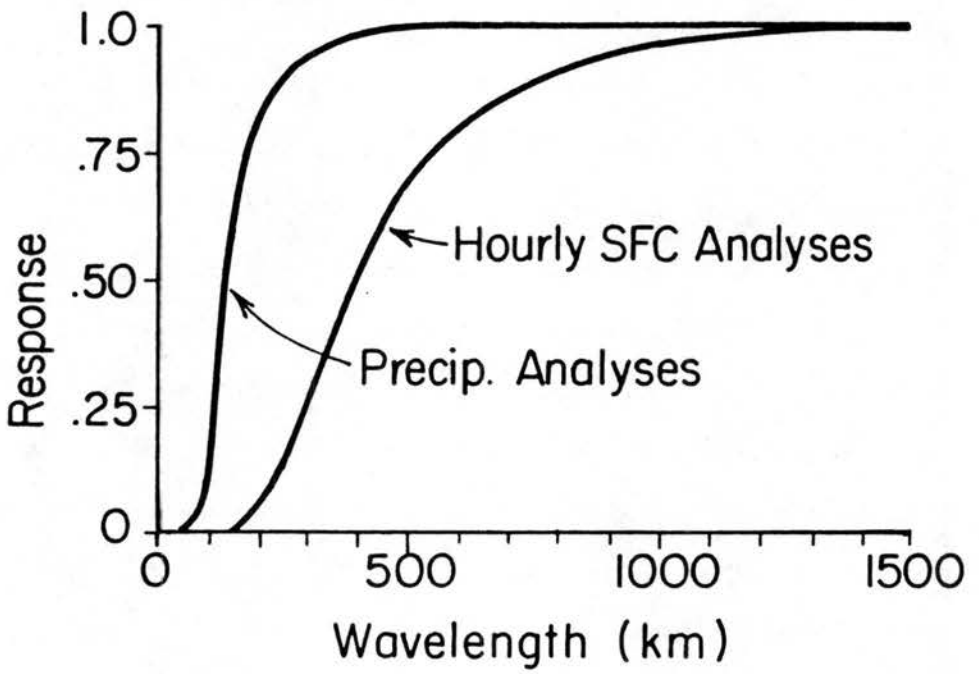

Figure 4.12: Response functions used for hourly surface data verification analyses and 12 hour precipitation analyses.

precipitation analyses discussed in Sections 4.1.1 and 5.5. Figure 4.4 showed the locations of the surface stations used in the analyses.

4.2 Model Formulation/Options

The basic formulation of the RAMS model used in this study will be described in this section. The specific version of the model used was 2A. There are other options available in RAMS than those that are described here; only options pertinent to these simulations are described. The reader is referred to Tremback *et al.* (1986) and Cotton *et al.* (1988) for a more general overview of RAMS. As stated previously, this model is a merger of a non-hydrostatic cloud model (Cotton *et al.*, 1982; Tripoli and Cotton, 1980, 1982, 1989a,b) and two hydrostatic mesoscale models (Pielke, 1974; Mahrer and Pielke, 1977; McNider and Pielke, 1981; McCumber and Pielke, 1981; Tremback *et al.*, 1985).

A unique feature of RAMS is its extreme modularity and machine portability. The model is divided into 19 basic model modules and 15 library modules. The library modules are all system-independent (except one) and model-run-independent, i.e. they are self-sufficient, standard Fortran subroutines. The one system-dependent library module has all the system-dependent calls (such as file OPENs) for different computers. A model preprocessor picks out the calls needed for the specific machine being used. In addition, the preprocessor adds the model-run-dependent COMMON blocks and array size information into each basic model module. The extreme modularity allows different aspects of the model (such as advective processes, surface processes, turbulence parameterization) to be isolated and thus more easily utilized, and modified, by the user. In addition, the modules can be mix-and-matched, depending on the options desired for the simulation, and the code for all possible options does not have to be compiled.

Another unique feature of RAMS is its explicit I/O (Input/Output) scheme. This is a scheme that was developed in the model to do I/O out to disk files, and thus enable the user to run simulations with larger grids than could be core-contained. This is especially useful when nested grids are being used, and was used in all the nested grid simulations described in this work.

Some of the specific options and model characteristics used in these simulations are briefly described in the following sections. As stated before, this is not a comprehensive description of RAMS, or even of the specific version of RAMS used in these simulations.

4.2.1 Basic model variables

The basic variables used in RAMS are potential temperature θ, u and v wind components, Exner function $\pi(\pi = (\frac{p}{p_0})^{\frac{R}{c_p}})$, and mixing ratio. Different types of mixing ratio are predicted depending on the choice of microphysical sophistication (described in Section 4.2.7). The model actually predicts perturbation Exner function, where the perturbation is based on the difference from an initial "base state".

4.2.2 Grid structure/coordinate system

The grid used in RAMS is a standard C grid (Arakawa and Lamb, 1981). This grid is staggered in both the horizontal and vertical directions

The horizontal coordinates used in this study were latitude-longitude. The variation in the length of a longitude increment with latitude is taken into account in this version of the model, but map factors are not included in the equations, and the equations used are those for cartesian coordinates, so the convergence of v-momentum with latitude is not accounted for. These inconsistencies have been corrected in a later version of RAMS, although they would be expected to have an insignificant effect on the conclusions of this study. The latitude and longitude increments do not have to be equal.

The vertical coordinate used in the model is a terrain following σ_z system, with the coordinate transformation described in Gal-Chen and Somerville (1975a,b), and Clark (1977). The vertical grid resolution can vary. For example, the vertical grid spacings used in this study ranged from 250 m at the surface to 500 - 800 m at the model top.

4.2.3 Non-hydrostatic

RAMS includes both hydrostatic and non-hydrostatic options. The non-hydrostatic version of the model was chosen for this study because of the potential importance of gravity wave ducting and propagation, and the differing properties of internal gravity

waves in hydrostatic versus non-hydrostatic atmospheres (Tapp and White, 1976). The horizontal grid spacings in the model varied from 80 km down to 5 km. Although the motions simulated with the 80 and 20 km grid lengths are certainly hydrostatic, it is not so certain that they will be hydrostatic with the 5 km grid lengths.

4.2.4 Numerics

The numerics of the non-hydrostatic model are best described in Tripoli and Cotton (1982), and Tripoli (1988). The time-differencing operator is a leapfrog scheme. A time-split scheme is used so that a long time-step can be used for advective processes and a shorter time-step for gravity-wave processes. An Asselin filter is applied after each long timestep to suppress the computational mode (Cotton and Tripoli, 1978). An anelastic form of the continuity equation is used.

RAMS includes options for either second or fourth-order advection schemes. The second-order scheme was chosen after comparisons of simulations showed negligible differences at the scales in this study. The second order scheme is also computationally less expensive.

4.2.5 Two-way interactive nesting

The nesting procedure used in RAMS is that of Clark and Farley (1984). The coarse mesh grid provides the initial interpolated fields to the fine grid, and then lateral boundary conditions at each time step. The fine grid variables are averaged back up to the coarser grid at each time step to provide the two-way interaction.

4.2.6 Cumulus parameterization scheme

The convective parameterization is a modified form of the Kuo-type parameterizations of Kuo (1965, 1974) and Molinari (1985), developed by Tremback (1990). This is a scheme that uses a simple one-dimensional cloud model to calculate the convective heating and moistening. The source level for the convective air, its LCL, and cloud top are calculated based on the grid-scale moisture convergence and vertical motion. A simple downdraft calculation is also included by assuming that the downdraft starts at the level of the θ_e

minimum, and is 2°C colder at cloud base and 5°C colder at the ground. The downdraft area is weighted relative to the updraft by assuming that the downdraft area varies from zero at the θ_e minimum to one-half of the updraft at cloud base, and to the area of the cloud-base-updraft at the ground. The total convective heating and moistening profiles are then calculated. The b parameter, or the moisture partitioning parameter of Kuo, is a measure of the fraction of the moisture convergence used to heat the column. The remainder of the moisture, $1 - b$, is precipitated and the latent heat warms the column. As Tremback points out, $1 - b$ can also be interpreted as precipitation efficiency. Thus he calculates the quantity $1 - b$ based on the precipitation efficiency formula in Fritsch and Chappell (1980a). The final model-scale heating and moistening rates are then calculated.

Because of its simplicity, this convective parameterization scheme depends on several arbitrary parameters (the downdraft parameters for instance). In this study a value of 5 cm s^{-1} was used as the minimum upward motion needed at cloud base to initiate convection.

4.2.7 Explicit microphysics

Three different levels of microphysics were used in the simulations described in this work. The simplest level involved simple advection of mixing ratio, with no condensation or latent heating. The second level allowed condensation and latent heating, and the production of cloud water. The third level of microphysics used the parameterizations described by Flatau *et al.* (1989), and Cotton *et al.* (1982, 1988) to handle the "grid-scale-resolved" condensation and precipitation processes. Mixing ratios and concentrations of rain, pristine crystals, snow, aggregates, and graupel are prognosed and diagnosed at each timestep. All five species of water were allowed to occur in these simulations. The default options in the model were used for the diagnosis of species concentration and are shown in Table 4.7 (from Flatau *et al.*, 1989).

4.2.8 Surface/soil parameterization

The surface layer and soil model is that described in Tremback and Kessler (1985). This scheme is a modification of the schemes described by Mahrer and Pielke (1977),

Table 4.7: Default microphysics parameters in the model (from Flatau *et al.*, 1989).

Category	Parameter	Value
Cloud	Concentration	300
Rain	Diameter	.054
Pristine Ice	Concentration	min $(10^{-8}, 10^{-8} \exp[0.6T_s])$
Snow	Diameter	0.1
Aggregates	Diameter	0.33
Graupel	Diameter	0.1

and McCumber and Pielke (1981). A surface energy budget is calculated which includes shortwave and longwave radiative fluxes, latent and sensible heat fluxes, and conduction to and from the soil. A prognostic soil model predicts soil temperature, and soil drying and moistening from precipitation and dew.

Although the initial u, v, r, θ, and π fields are all three-dimensional and determined from the objective analysis/initialization package, the initial surface and soil characteristics are automatically set unless otherwise specified. The surface roughness z_0 and choice of USDA soil textural class (Table 4.3) are usually set to be horizontally homogeneous. For most of the simulations described in this study, z_0 was defined as 5 cm and the soil textural class was set to sandy clay loam. One experiment, described in Chapter 6, used a horizontally-varying initialization of soil texture, roughness length, and soil moisture. The data sets used to define the soil texture, roughness length, and soil moisture were described in Section 4.1.1. The soil temperature is currently set initially to vary from 4°C colder than the air at the surface to 3°C warmer than the air at a depth of 20 cm. The soil relative humidity is set equal to the atmosphere relative humidity at the surface. The soil moisture doubles from the surface to a depth of 20 cm, although it is limited at the surface to 0.75 of saturation. None of the saturations were greater than 0.75 in the nested grid domain of the simulations described in this work.

4.2.9 Turbulence/diffusion parameterizations

The turbulence parameterization used in this study is a deformation K closure type scheme. The scheme is described in Tremback (1990), and Tripoli and Cotton (1982).

This scheme is similar to that of Smagorinsky (1963), with modifications by Hill (1974) and Lilly (1962). The vertical scale length is set equal to the vertical grid spacing and the three-dimensional deformation is used to calculate the vertical exchange coefficients. A Richardson number/stability-dependent factor is used to decrease the vertical exchange coefficients (and effects of vertical mixing) in stable regions. The horizontal scale length is set equal to the square-root of $\Delta x \times \Delta y$ and only the horizontal components of deformation are used in calculating the horizontal exchange coefficients.

A fourth-order filter is also applied every 600 seconds to remove two Δx noise.

4.2.10 Radiation parameterization

The radiation parameterization scheme used in the simulations, unless otherwise noted, is that of Mahrer and Pielke (1977). This parameterization includes the calculation of both long-wave and short-wave radiation fluxes as a function of the vertical temperature and water vapor structures in the model. "Clouds" in the model thus only influence the radiation fluxes as levels of high water vapor content. The solar (short-wave radiation) varies longitudinally across the domain and with time, and the downward short-wave flux at the surface is adjusted to account for topography slope.

A second radiation parameterization was used for one of the sensitivity studies described in Chapter 5. That scheme was developed by Chen and Cotton (1983a,b) and includes the radiative effects of condensate, water vapor, ozone, and carbon dioxide.

4.2.11 Lateral boundary conditions

An important aspect of variable initialization simulations is the choice of lateral boundary conditions. There are two choices in RAMS 2A for the lateral boundary conditions: a Perkey and Kreitzberg (1976) sponge or a Davies (1976) relaxation. In both cases data at two times (the output from the objective analysis package at the initial time and 12 hours later, for example) are used by the model to force the boundary values of the variable tendencies. The Davies boundary condition was chosen for these simulations based on a set of sensitivity experiments.

The Davies condition forces the boundary values of u, v, θ, r, and π towards externally-specified values, although the model's internally defined tendencies are still fully used in the model integration. In comparison, only a weighted percentage of the internally-defined tendencies are used in a Perkey and Kreitzberg (1976) sponge-type boundary condition. The Davies condition results in less computational noise (and need for strong damping) at the lateral boundaries, while still forcing the lateral boundaries towards the externally-specified values (Davies and Turner, 1977; Davies, 1976; Davies, 1983).

The equation that defines the Davies boundary condition is

$$\frac{\partial \chi}{\partial t} = \left.\frac{\partial \chi}{\partial t}\right|_I + \alpha * \frac{\chi E - \chi I}{\Delta t}, \tag{2}$$

where χ is the variable being forced, χ_E is the externally-defined χ, χ_I is the internally-defined χ, Δt is the model timestep, α is a weight between 0. and 1., and $\left.\frac{\partial \chi}{\partial t}\right|_I$ is the internally-defined tendency. The forcing occurs across a zone whose width and weights (the αs) are specified by the user. Several sensitivity experiments were also completed to determine the optimal boundary zone width and weights. A nonlinear variation of the weights across the boundary zone was found to work best. The zone used in this study was 5 grid points wide and the weights (from the outside in) were: .75, .56, .32, .10, .01.

4.2.12 Top boundary condition/Rayleigh friction

The only choice for the top boundary condition in a non-hydrostatic, variable initialization simulation in RAMS 2A is the "wall on top". This is a reflective boundary condition, so because of the potential importance of vertically and horizontally propagating gravity waves, an alternative had to be developed (Halliday and Resnick, 1966; Israeli and Orszag, 1981; Kirkwood and Derome, 1977; Boville and Cheng, 1988; Klemp and Lilly, 1978; Mechoso *et al.*, 1982). Several options were considered: a radiative type condition, a very high model top, a viscous layer, and a modified Rayleigh friction. Radiative type conditions have been developed and tested for horizontally-homogeneous models (Klemp

and Durran, 1983; Bougeault, 1983). However, radiative-type boundary conditions for nonhorizontally-homogeneous models are very complicated and involve many simplifying assumptions to make them solvable (Rasch, 1986; Beland, 1976; Charney and Drazin, 1961; Dickenson, 1969). A very high model top is computationally very expensive, and even then may not solve the problem of spurious reflection of vertically-traveling waves (Boville and Cheng, 1988; Kirkwood and Derome, 1977; Mechoso *et al.*, 1982; and Klemp and Lilly, 1978). The choices of a viscous layers or some sort of Rayleigh friction are both sensitive to the vertical profiles of the smoothing or diffusion, and both are sensitive to the depth of the layer (Klemp and Lilly, 1978; Boville, 1986; Durran and Klemp, 1983; Houghton and Jones, 1969; Nickerson *et al.*, 1986). A modified form of Rayleigh friction was developed and chosen over a viscous layer because of its ability to control the scale of the diffusion. This form of Rayleigh friction relaxes the model variables towards a spatial moving-average value. The equation that describes this form of Rayleigh friction is:

$$\left.\frac{\partial \chi}{\partial t}\right|_{NEW} = \left.\frac{\partial \chi}{\partial t}\right|_{IM} + \frac{(\chi - \chi_0)}{\tau}$$

where χ is the variable being relaxed, χ_0 is the value that it is being relaxed towards, and τ is the time scale of the relaxation. $\left.\frac{\partial \chi}{\partial t}\right|_{IM}$ is the internal, model-generated tendency of that variable and $\left.\frac{\partial \chi}{\partial t}\right|_{NEW}$ is the Rayleigh friction-modified tendency. χ_0 is calculated by taking a spatial average of the variable. Several sensitivity experiments were run to determine the best values for τ and for the scale of the averaging for χ_0. For the scales used in these simulations τ was set to 5 times the timestep and χ_0 was calculated by averaging outwards 4 grid points in each horizontal direction from each χ. Vertical variations in θ along the terrain-following coordinate surfaces are taken into account. The vertical variations in horizontal wind component and mixing ratio are not considered. The Rayleigh friction layer in these simulations is applied at a very high level in the model (15-20 km in this instance) where mixing ratios are negligible and the terrain-following surfaces are almost flat (see Fig. 5.2). In addition, for computational purposes, as few calculations as possible are done in the Rayleigh friction computations as they are invoked every timestep.

The basic model options used in the simulations described in this study have been described in this chapter. The specific domains and variations between simulations for the various experiments will be described in the next chapter.

Chapter 5

BASIC SENSITIVITY EXPERIMENTS AND ANALYSIS OF SQUALL LINE PROPAGATION MECHANISM

The basic coarse grid (80 km grid spacing) and nested grid (20 km grid spacing) simulations will be described in this chapter. The different model domains and resolutions for the simulations are briefly outlined in the first section. The varying options between simulations described in this chapter are also outlined in Section 5.1. The initial fields for all the simulations are described in Section 5.2. The results from the different simulations are then described and analyzed in the following sections.

5.1 Simulation Parameter Descriptions

The simulations that will be described in this chapter all had the same coarse and fine mesh domains, but differed in their inclusions of the explicit microphysics and the cumulus parameterization scheme. Those differences will be discussed in the following sections with the simulation results. The large scale areas covered 50° × 30° with a grid spacing of 1.°× .75° (approximately 80 km at 40°N), or 50 × 41 points in the horizontal. There were 32 vertical grid levels. The vertical grid spacing varied from 250 m at the surface to 800 m at the top of the model (approximately 20 km). A Rayleigh friction layer extended from 15 to 20 km. A large timestep of 120 seconds was used. The model terrain and horizontal domain are shown in Fig. 5.1 and a cross section showing the vertical terrain-following levels is shown in Fig. 5.2. The horizontal line in Fig. 5.1 is the location for all vertical cross sections shown in this chapter, except for Fig. 5.2.

The nested grid in these simulations has a ratio of 1:4 (20 km grid spacing) over an area that covers about half of the north-south extent of the squall line (20°× 13°, 80 × 52

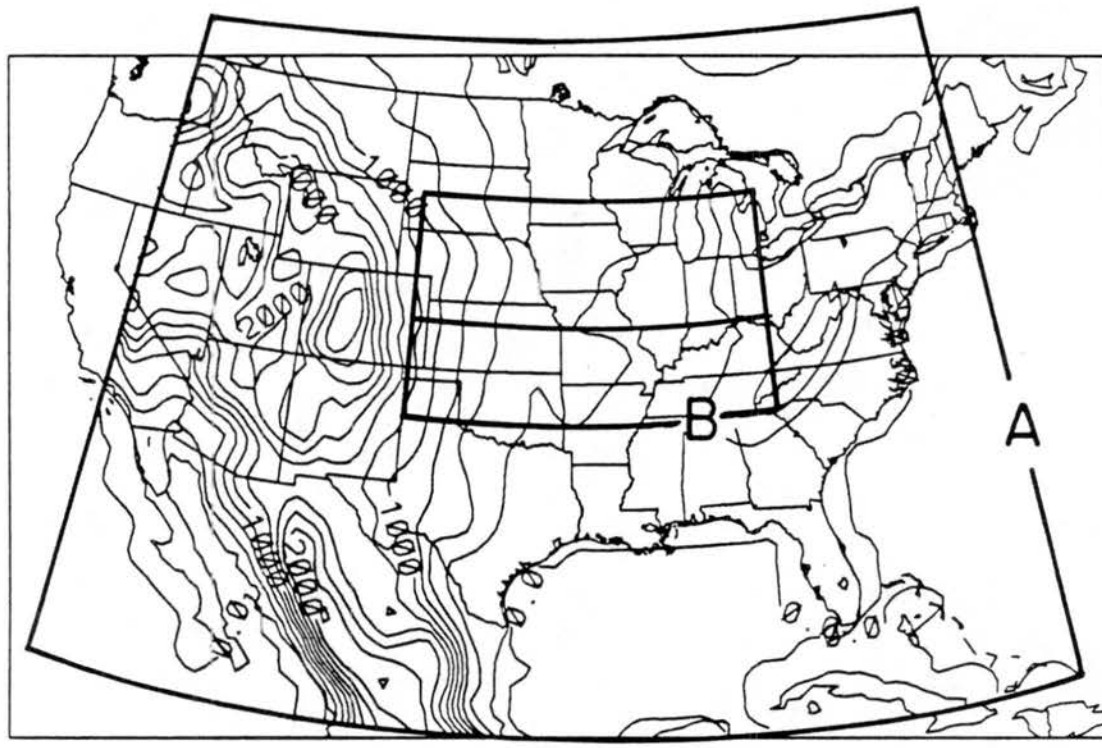

Figure 5.1: Model terrain and horizontal domains of coarse (Box A) and fine (Box B) mesh grids. The horizontal line through Box B is the location for all vertical cross sections shown in this chapter, except for Fig. 5.2.

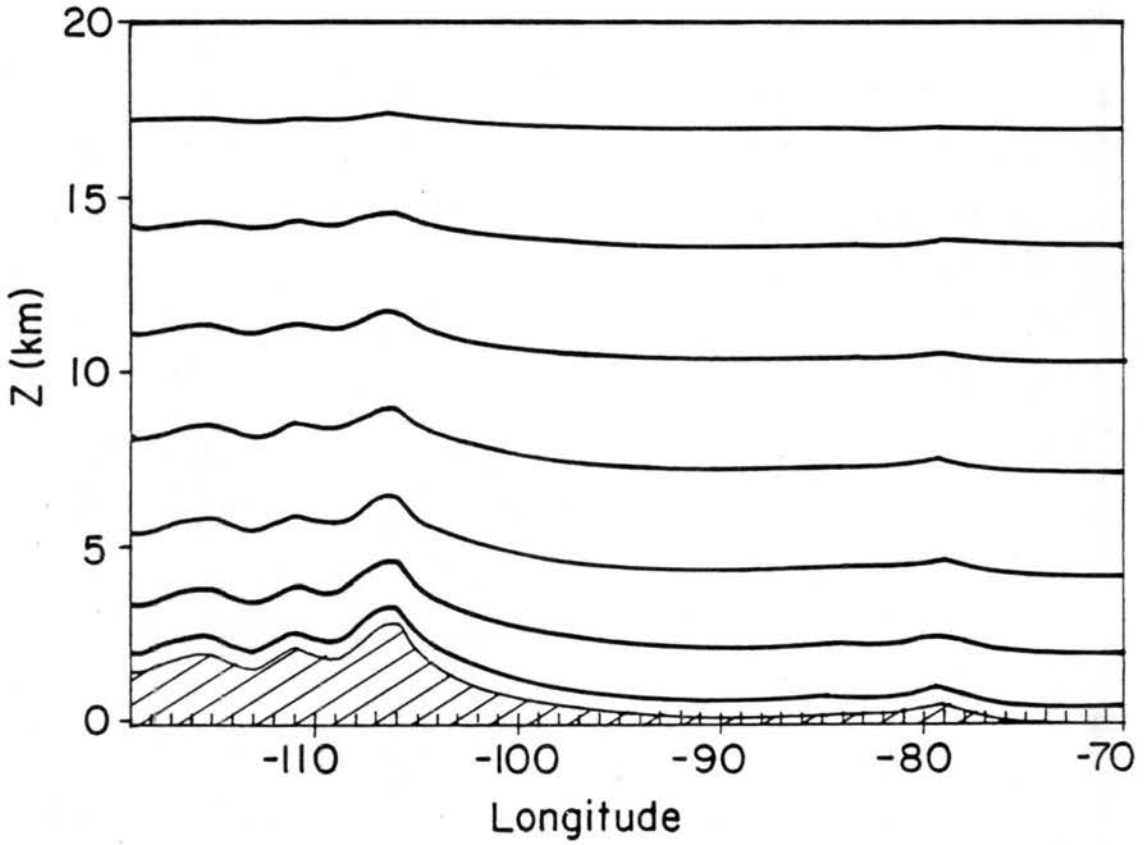

Figure 5.2: Cross section (location shown in Fig. 3.22) showing terrain-following vertical levels. Every fourth level (out of a total of 32) is shown.

horizontal grid points). The vertical spacing is the same as on the large scale (32 points). The nested domain is also shown in Fig. 5.1.

5.2 Initial Fields

The initial fields for these simulations (on the 80 km grid) were obtained by using the analysis scheme described in Section 4.1.2. The NMC spectral model data was reanalyzed to include the available surface data and rawinsonde soundings. Various parameters (discussed in Section 4.1.2) control the "strength" of the weighting of the surface and rawinsonde data in the final analysis. Strong weighting results in much noisier analyses, while weaker weighting results in smoother, but less closely matched to the input data, analyses. There is no initial adjustment done to the analyzed fields in RAMS, so the model adjusts to the analysis "noise" in the initial part of the simulation. The inclusion of the available surface data and rawinsonde soundings were found to be critical in defining the low-level stable, prefrontal environment which was necessary for the proper simulation of the squall line development; consequently a strong "weighting" was used for the analysis of the initial data. The resulting analyses were initially very "noisy" but result in much more realistic simulations. The fields shown in this section for the initial analyses are after 1.0 hour of simulation time on the 80 km grid, when the model has had some time to adjust to the initial imbalances. However, some "noise" is still evident. The fields shown are from a dry simulation, with no microphysics or cumulus parameterization included, although they are very similar to the fields at the same time for other simulations that did include those processes. The cumulus parameterization scheme is not "turned on" before 7200 seconds of simulation time, and the horizontal grid increment of this part of all the simulations was 80 km, so the effects of the microphysical processes on these scales were very small. The initial fields for all of the simulations in this chapter were the same.

Figure 5.3 shows the surface analyses of wind vectors, temperature, MSLP, and mixing ratio. Some noise is still evident in the surface wind vector field but disappears by 1500 UTC (3 hours of simulation time). The front (defined by the wind-shift line, strong

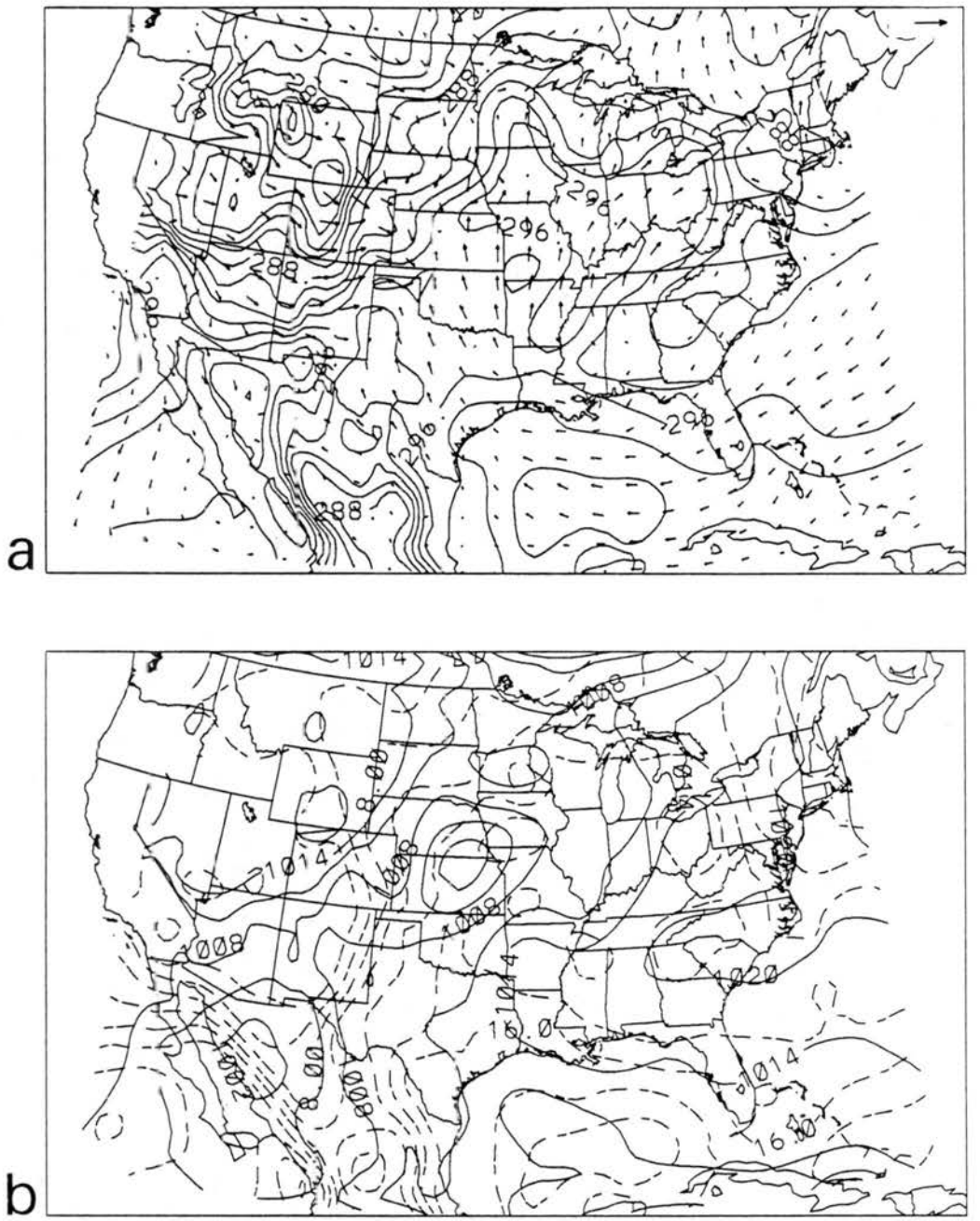

Figure 5.3: Surface analyses from model simulation at 1300 UTC 17 June 1978 of (a) wind vectors and temperature (K, contour interval is 2 K); and (b) MSLP (mb, solid lines, contour interval is 3 mb) and mixing ratio (g/kg, dashed line, contour interval is 2 g/kg). The lengths of the vectors in (a) are proportional to the wind speed: the vector in the upper right corner of (a) is 20 m s^{-1}.

temperature gradient, and moisture gradient) can be seen to stretch from the Oklahoma panhandle northeastwards through northern Iowa.

Figure 5.4 shows the pressure and temperature fields at 3.1, 5.0, and 10.5 km. The low-level trough to the west of the frontal zone that was evident in the synoptic scale upper air analyses (Section 3.6) is stronger in these analyses. A divergent flow around southern Minnesota and northern Wisconsin can also be seen at all levels. This flow is probably realistic as it appears to diverge around the area of MCC development apparent in the radar summary charts (Fig. 3.7) and satellite pictures (Fig. 3.6). As in the previously discussed synoptic analyses there is warm advection occurring ahead of the front all the way up to 5.0 km.

5.3 Comparison of Effects of Inclusion of Microphysics and Cumulus Parameterization

The first four simulations to be discussed differed only in their inclusions of explicit microphysics and the cumulus parameterization scheme. They will be referred to as:

DRY: Included neither cumulus parameterization nor explicit microphysics, and no latent heating effects.

MIC: Included explicit microphysics but no cumulus parameterization.

CU: Included cumulus parameterization but no explicit microphysics. Latent heat is released with grid-scale condensation and production of cloud water.

ALL: Included both cumulus parameterization and explicit microphysics.

All of the figures and discussion in the the following section will be concerned with the simulations on the 20 km grid interval nested grid. The DRY simulation will be described first, followed by brief comparisons of the MIC, CU, and ALL simulations. The separation of the squall line from the front, and the mechanism of the squall propagation will then be analyzed in more detail in Section 5.4.

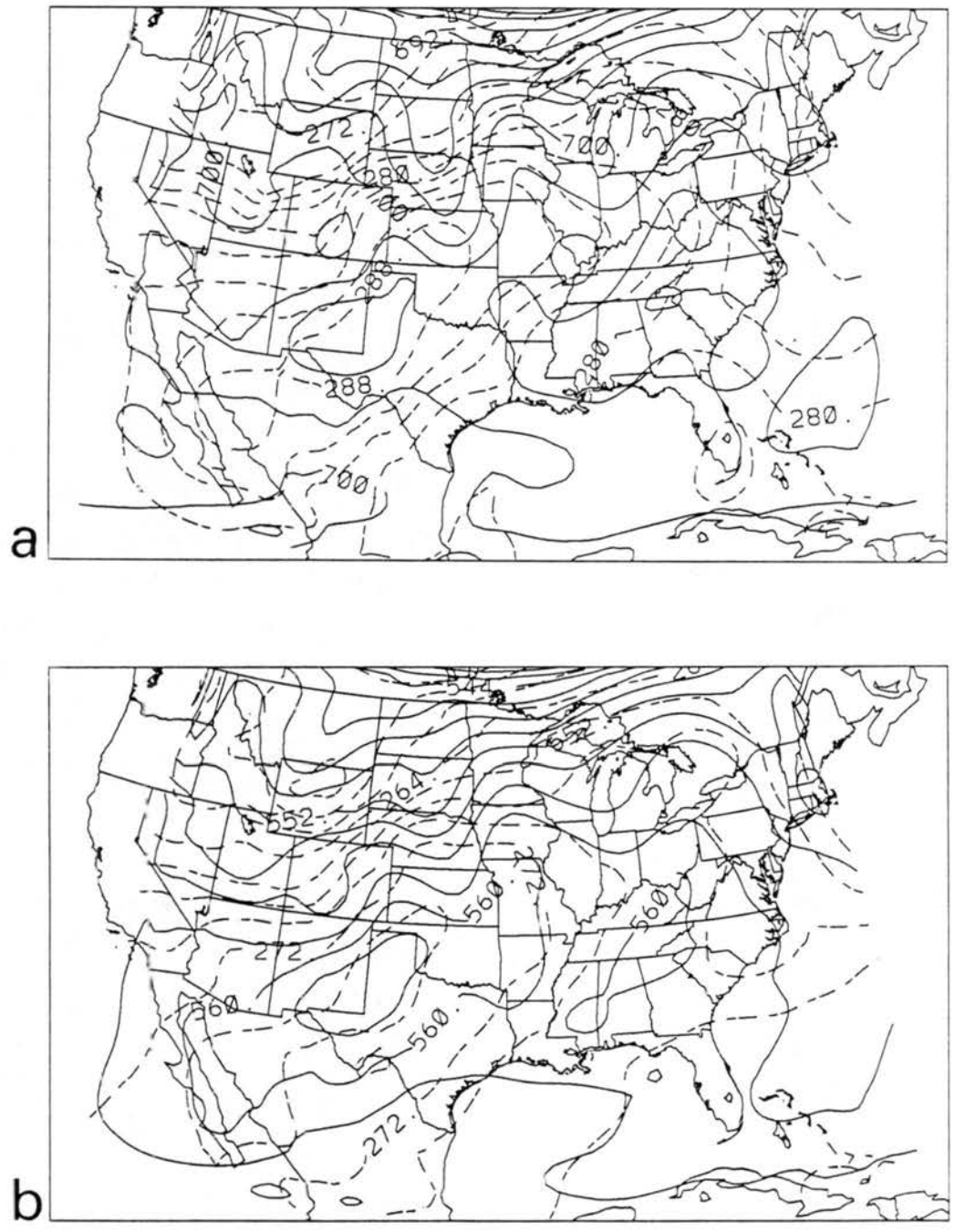

Figure 5.4: Upper air analyses from model simulation at 1300 UTC 17 June 1978 of (a) 3.1 km pressure (mb, solid lines, contour interval is 2 mb) and temperature (K, dashed lines, contour interval is 2 K); and (b) 5.0 km pressure (mb, solid lines, contour interval is 2 mb) and temperature (K, dashed lines, contour interval is 2 K).

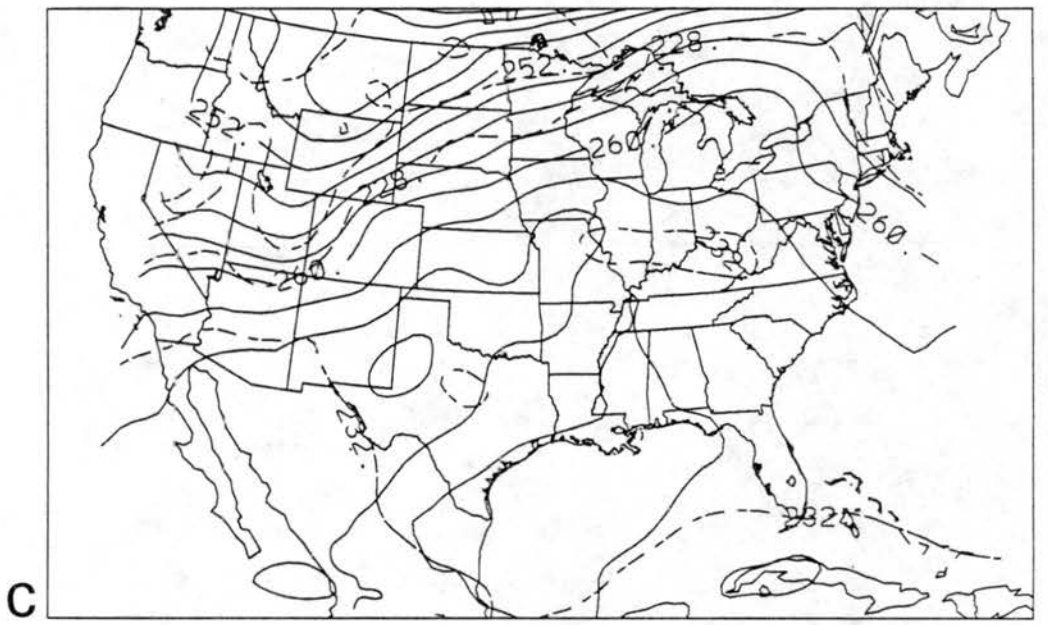

Figure 5.4: Continued: (c) 10.5 km pressure (mb, solid lines, contour interval is 2 mb) and temperature (K, dashed lines, contour interval is 2 K).

5.3.1 DRY simulation

The results from the DRY simulation will be discussed in this section. This simulation did not have any latent heating effects, or any sort of cumulus parameterization or microphysical processes. Figures 5.5-5.8 show the surface analyses from the DRY simulation of horizontal winds, horizontal divergence, reduced MSLP, and temperature at 2100 UTC 17 June, and 0000 UTC, 0300 UTC, and 0600 UTC 18 June. The position of the surface front is superimposed on the wind analyses. There is an area of divergent flow in central Kansas at 2100 UTC associated with the weakly defined front in that region at the time. At 0000 UTC strong northwesterly winds pushing down from Nebraska are increasing the gradients across the frontal zone, and by 0300 UTC there is an extremely narrow, continuous frontal zone extending from northern Illinois to the Texas panhandle. From 2100 UTC through 0000 UTC the surface trough deepens and narrows, and then from 0000 UTC through 0300 UTC the trough continues to narrow, but fills slightly. Between 0300 and 0600 UTC the well-defined narrow frontal zone continues to move southeastward at approximately 10 m s^{-1}, slightly less than the surface wind speeds just behind the front of approximately 12 m s^{-1}. Comparing Figs. 5.5-5.8 to the observed surface analyses in Figs. 3.13, 3.16, 3.19, and 3.20, the DRY simulated winds at the surface are higher than the observed simulated winds (12-16 m s^{-1} compared to 8-10 m s^{-1}). The frontal movement in the DRY simulation is slightly faster than observed (8-12 m s^{-1} vs. 5-8 m s^{-1}) and the initial area of frontogenesis over central Kansas is not evident in the observations. Figures 5.9-5.12 show vertical cross sections through the domain (cross section location shown in Fig. 5.1) of vertical motion w and equivalent potential temperature θ_e. By 0000 UTC the vertical motion associated with the diffuse area of surface frontal convergence can be seen at approximately 97°W. By 0300 UTC the area of strong vertical motion has concentrated and moved eastward (eastward in the east-west cross section, southeastward overall), and increased in strength to 56 cm s^{-1}. The upward vertical mixing of the low-level stable layer by this concentrated tongue of vertical motion can be seen in the cross section of θ_e. By 0600 UTC the area of strong vertical motion has continued to move eastward but

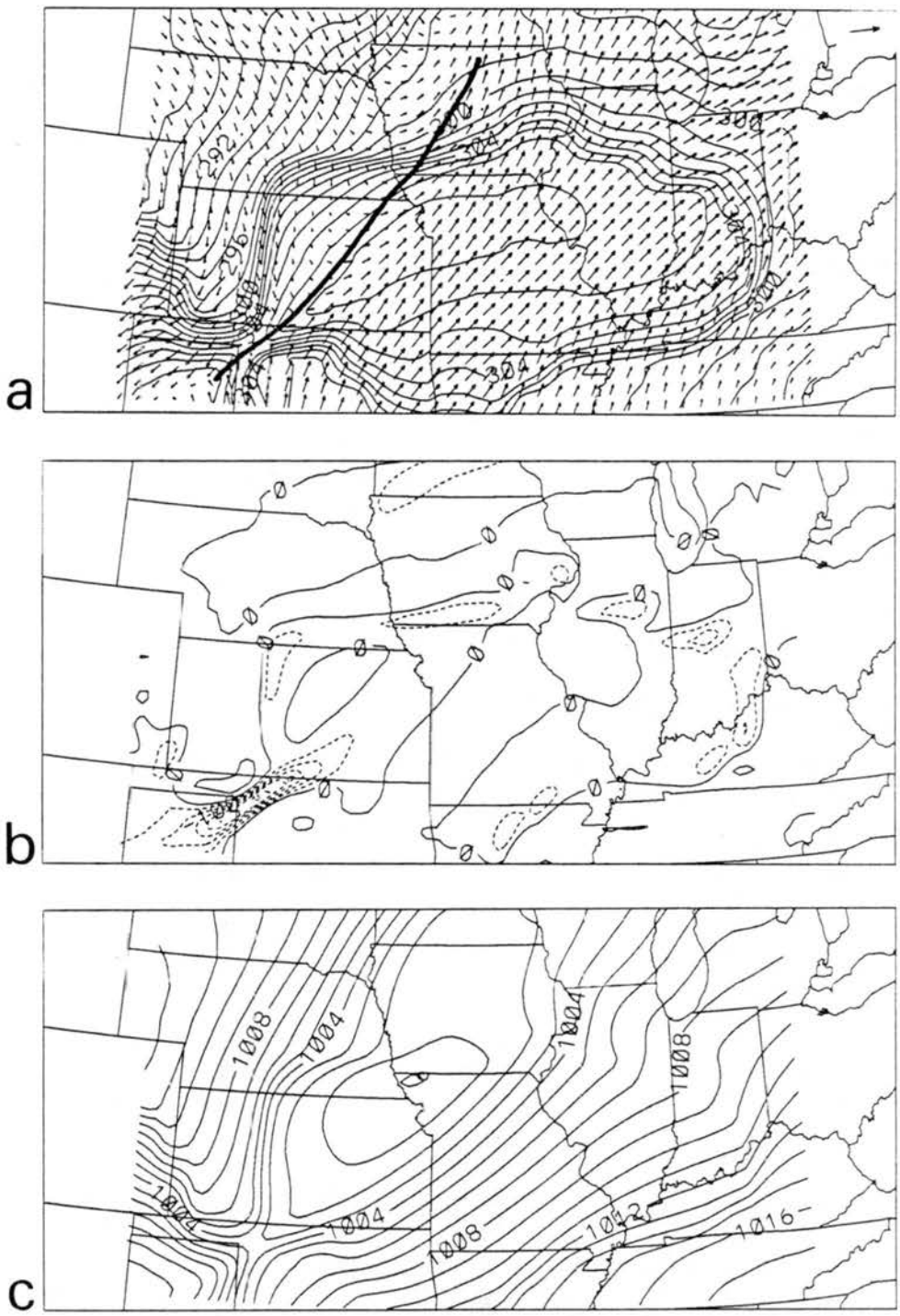

Figure 5.5: Surface analyses from DRY simulation at 2100 UTC 17 June 1978 of (a) horizontal winds and temperature (K, contour interval is 1 K); (b) horizontal divergence (s^{-1}, contour interval is .00005, dashed lines are negative value contours); and (c) reduced MSLP (mb, contour interval is 1 mb). The lengths of the vectors in (a) are proportional to the speed: the vector in the upper right corner of (a) is 20 m s^{-1}. The frontal position is superimposed on (a).

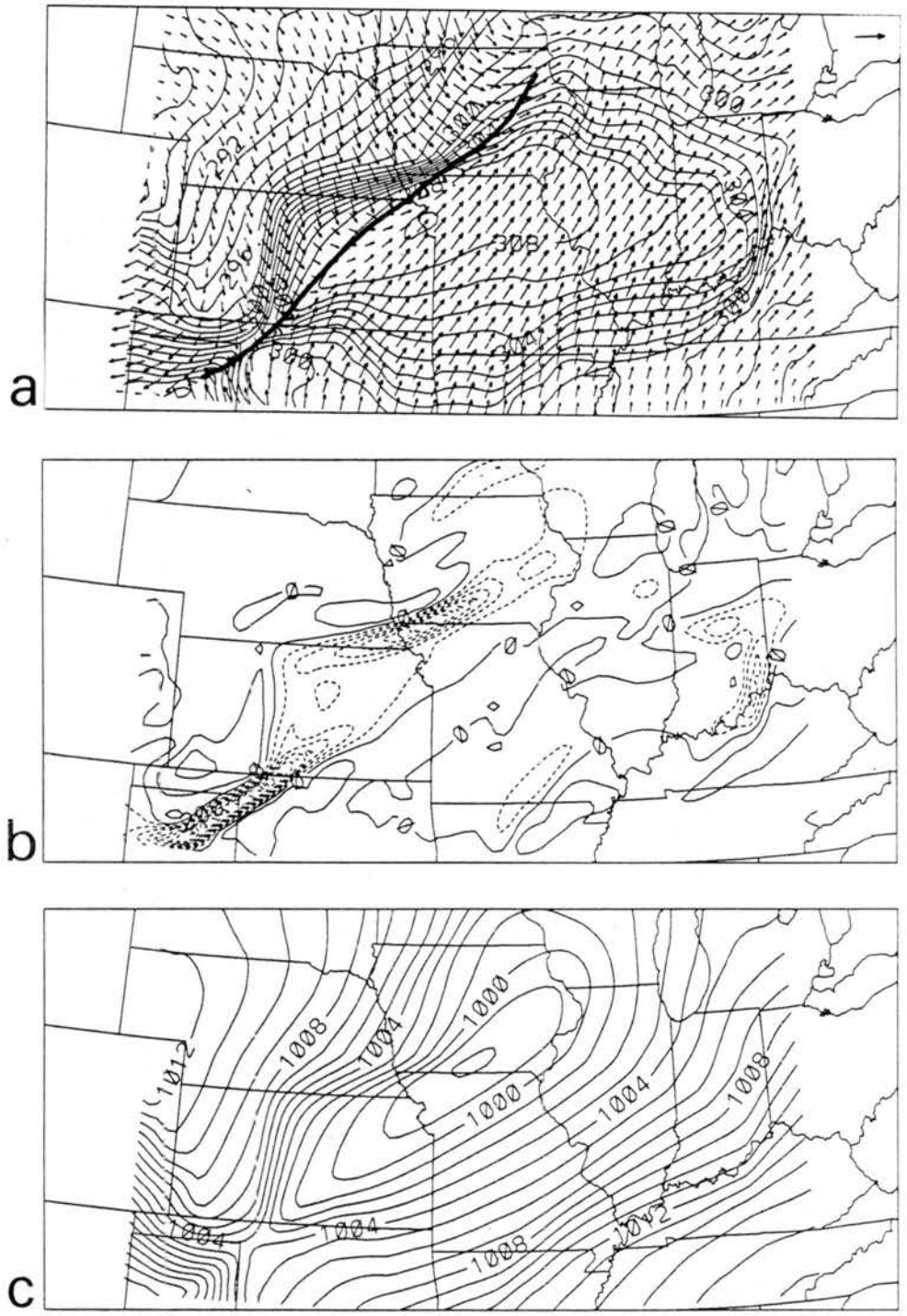

Figure 5.6: Surface analyses from DRY simulation at 0000 UTC 18 June 1978 of (a) horizontal winds and temperature (K, contour interval is 1 K); (b) horizontal divergence (s^{-1}, contour interval is .00005, dashed lines are negative value contours); and (c) reduced MSLP (mb, contour interval is 1 mb). The lengths of the vectors in (a) are proportional to the speed: the vector in the upper right corner of (a) is 20 m s^{-1}. The frontal position is superimposed on (a).

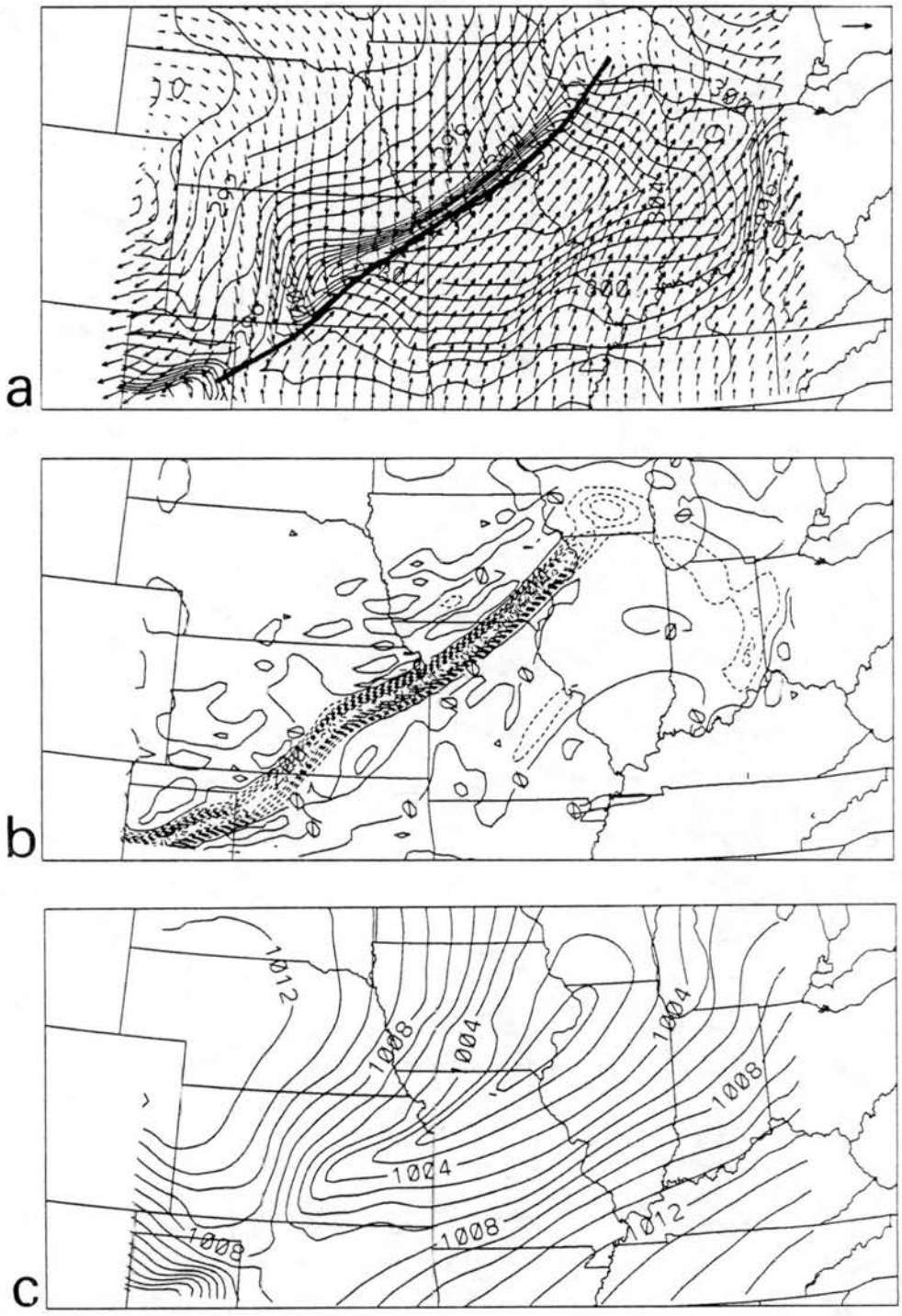

Figure 5.7: Surface analyses from DRY simulation at 0300 UTC 18 June 1978 of (a) horizontal winds and temperature (K, contour interval is 1 K); (b) horizontal divergence (s^{-1}, contour interval is .00005, dashed lines are negative value contours); and (c) reduced MSLP (mb, contour interval is 1 mb). The lengths of the vectors in (a) are proportional to the speed: the vector in the upper right corner of (a) is 20 m s^{-1}. The frontal position is superimposed on (a).

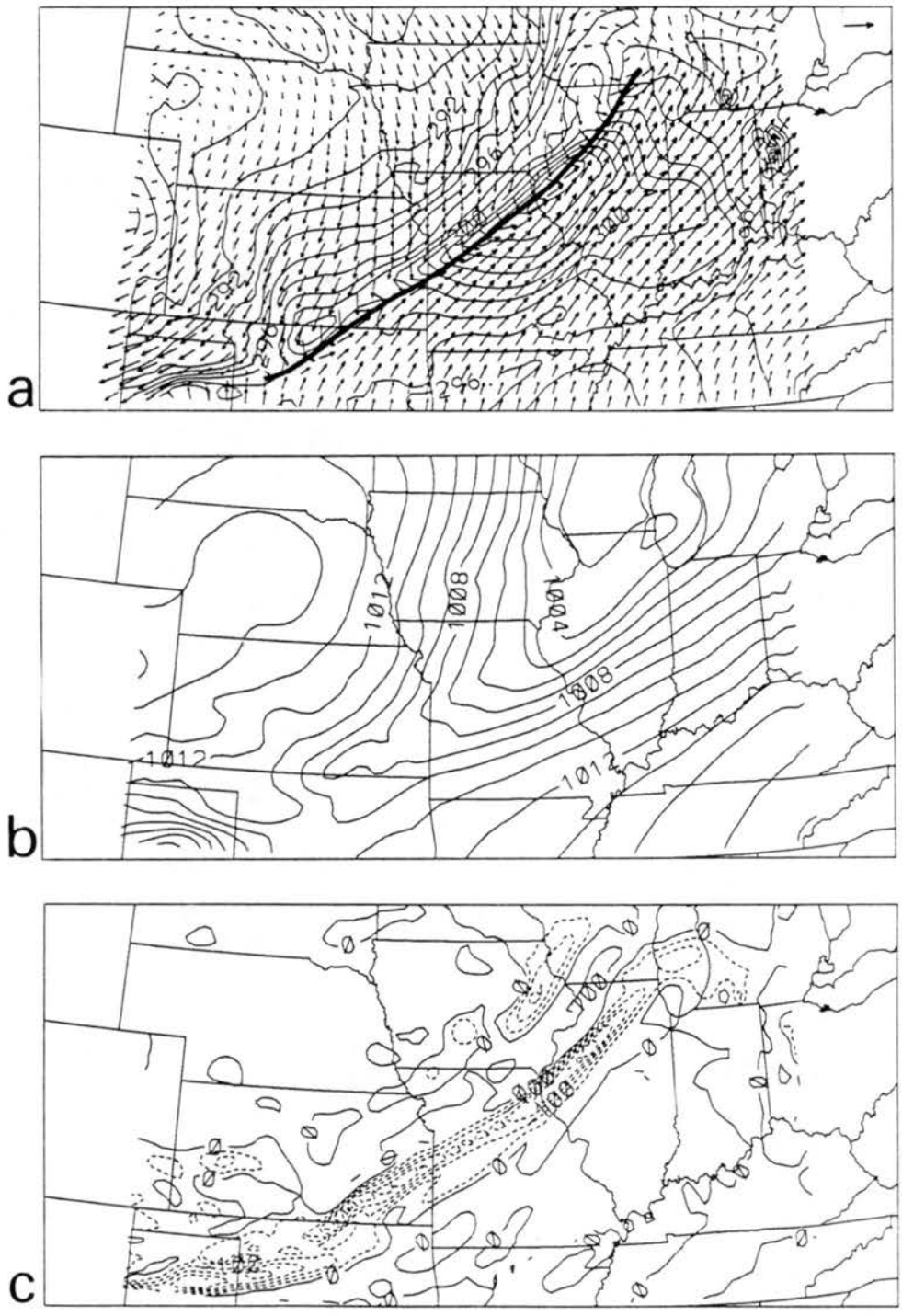

Figure 5.8: Surface analyses from DRY simulation at 0600 UTC 18 June 1978 of (a) horizontal winds and temperature (K, contour interval is 1 K); (b) horizontal divergence (s^{-1}, contour interval is .00005, dashed lines are negative value contours); and (c) reduced MSLP (mb, contour interval is 1 mb). The lengths of the vectors in (a) are proportional to the speed: the vector in the upper right corner of (a) is 20 m s^{-1}. The frontal position is superimposed on (a).

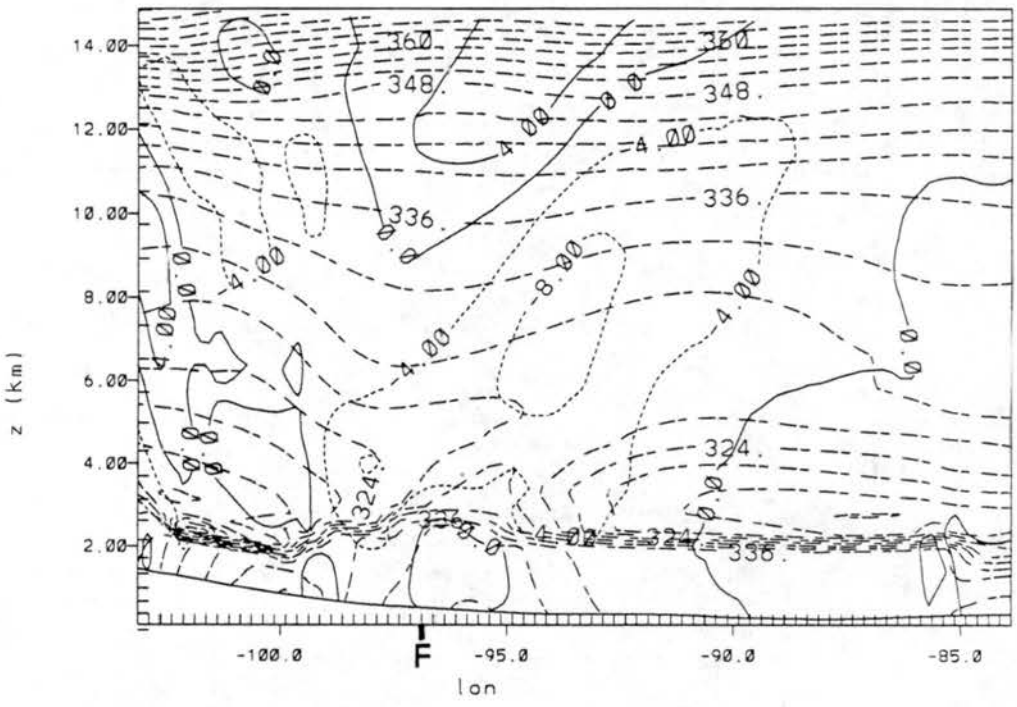

Figure 5.9: Vertical cross section from the DRY simulation at 2100 UTC 17 June 1978 of vertical motion w (cm s^{-1}, contour interval is 4 cm s^{-1}, solid lines are contours of positive values and short-dashed lines are contours of negative values) and equivalent potential temperature θ_e (K, long-dashed lines, contour interval is 3 K). The surface front location is marked by F.

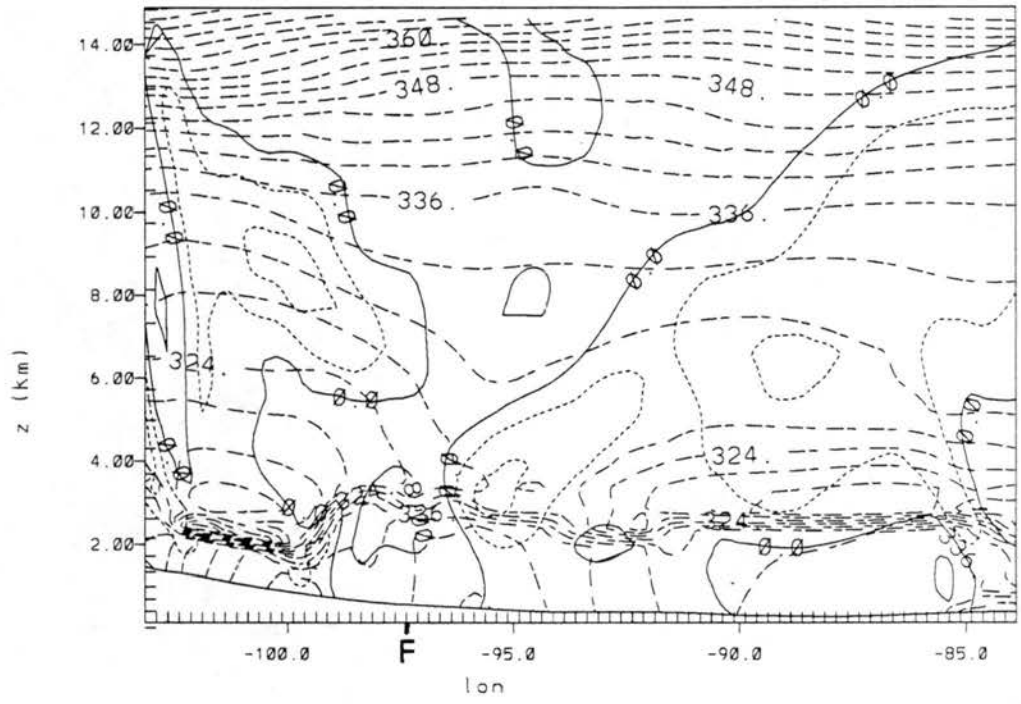

Figure 5.10: Vertical cross section from the DRY simulation at 0000 UTC 18 June 1978 of vertical motion w (cm s^{-1}, contour interval is 4 cm s^{-1}, solid lines are contours of positive values and short-dashed lines are contours of negative values) and equivalent potential temperature θ_e (K, long-dashed lines, contour interval is 3 K). The surface front location is marked by F.

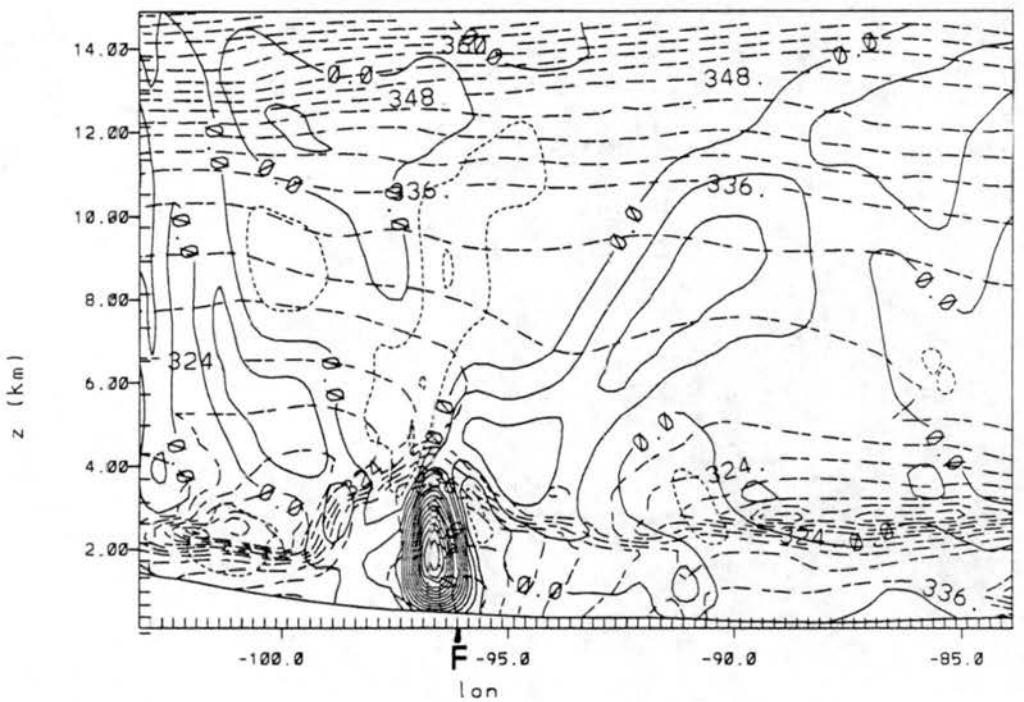

Figure 5.11: Vertical cross section from the DRY simulation at 0300 UTC 18 June 1978 of vertical motion w (cm s^{-1}, contour interval is 4 cm s^{-1}, solid lines are contours of positive values and short-dashed lines are contours of negative values) and equivalent potential temperature θ_e (K, long-dashed lines, contour interval is 3 K). The surface front location is marked by F.

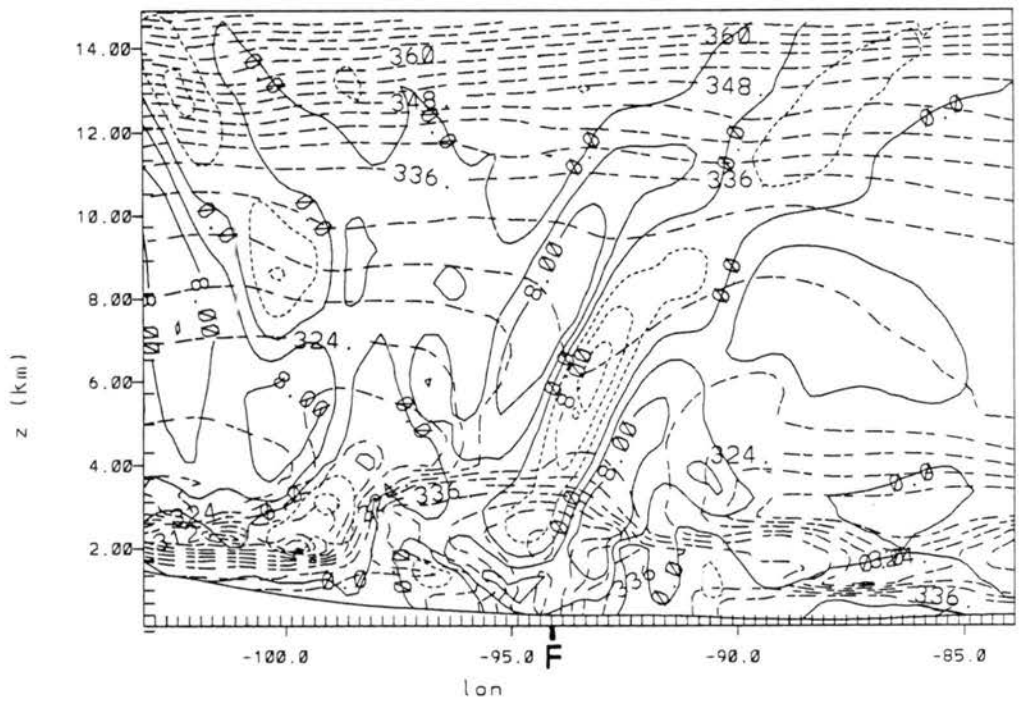

Figure 5.12: Vertical cross section from the DRY simulation at 0600 UTC 18 June 1978 of vertical motion w (cm s^{-1}, contour interval is 4 cm s^{-1}, solid lines are contours of positive values and short-dashed lines are contours of negative values) and equivalent potential temperature θ_e (K, long-dashed lines, contour interval is 3 K). The surface front location is marked by F

weakened, in accordance with the decrease in horizontal convergence at that time shown in Figs. 5.7b and 5.8b. A vertically propagating gravity wave is also evident at 0600 UTC, apparently forced by the "blocking effect" of the low-level tongue of high θ_e air. This simulation had no latent heating effects or any way of releasing the convective instability that the frontal convergence is forcing. The frontal movement in the DRY simulation will be summarized and compared to that in the observations and other simulations in Section 5.3.5.

5.3.2 MIC simulation

The MIC simulation will be discussed only very briefly as the results were very similar to the DRY simulation. This simulation differed from the DRY simulation in that explicit microphysical processes were allowed to occur, but the cumulus parameterization scheme was not included. The microphysical formulation is briefly discussed in Section 4.2. Overall, the frontal convergence on this scale (20 km grid spacing) was not enough to explicitly force the release of the convective instability. Figure 5.13 shows the vertical cross sections of w, θ_e, and total condensate mixing ratio at 0300 UTC 18 June in the MIC simulation (cross section location shown in Fig. 5.1). At this point the vertical motion is just barely pushing through the low-level stable layer and a very thin column (only one grid point wide) of positive vertical motion extends up to the tropopause where the instability has been released. The production of a very small "cloud" can be seen at 4-5 km just above where the vertical motion has pushed through the lower stable layer. The deep vertical motion and the small "cloud" are only very transient however, and seem to occur only at the point in time and space where the frontally-forced vertical motion is at its greatest. Figure 5.14 shows the accumulated total precipitation on the 20 km grid at 0600 UTC 18 June (accumulated from 1800 UTC 17 June) in the MIC simulation. The precipitation associated with the frontal forcing is negligible. There are two areas where there is significant precipitation. One is associated with the MCC circulation over Minnesota and Wisconsin, and the other is associated with an MCC-like circulation over northern Indiana. Dynamical and thermodynamical perturbations associated with

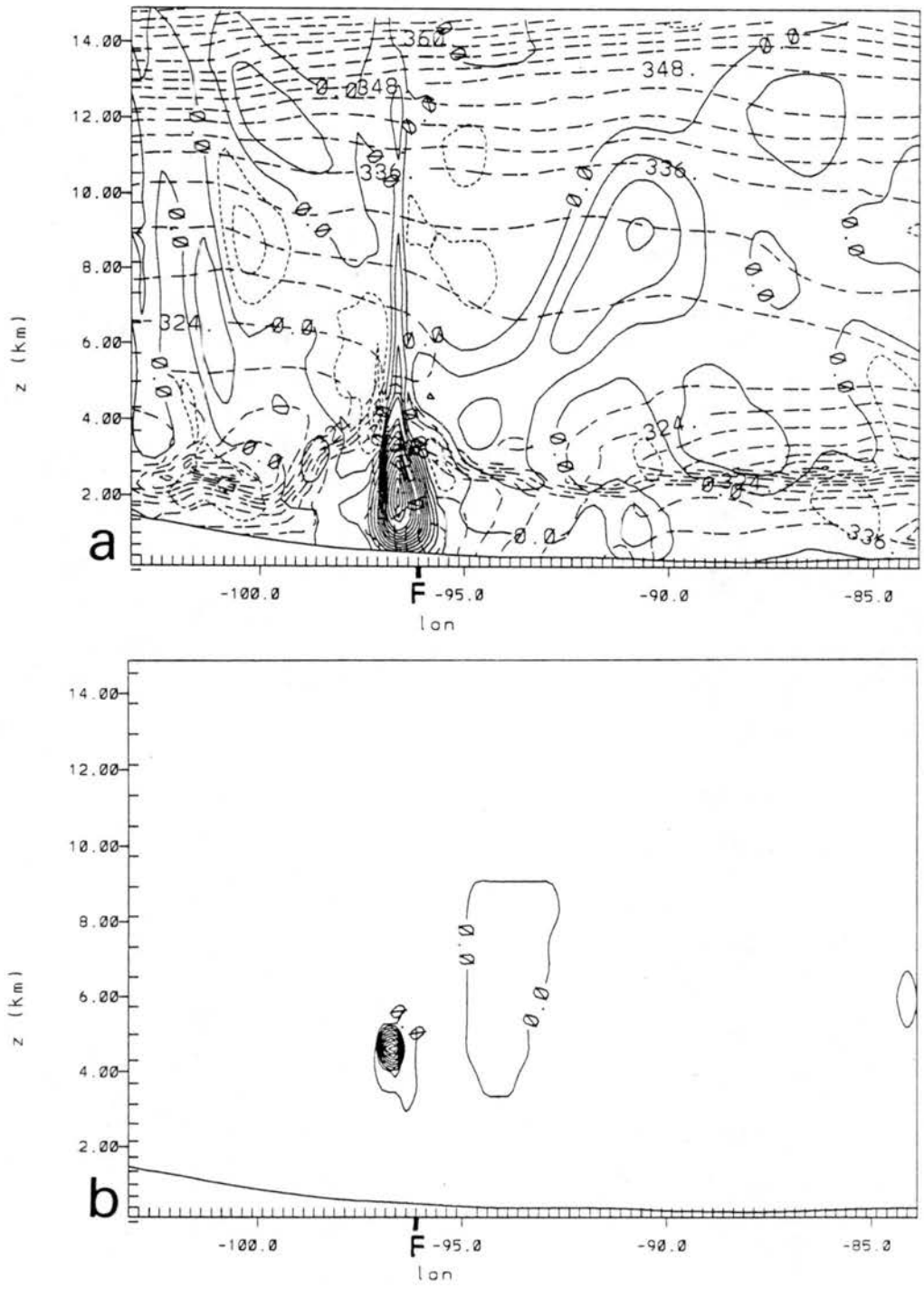

Figure 5.13: Vertical cross sections from the MIC simulation at 0300 UTC 18 June 1978 of (a) vertical motion w (cm s^{-1}, contour interval is 4 cm s^{-1}, solid lines are contours of positive values and short-dashed lines are contours of negative values) and equivalent potential temperature θ_e (K, long-dashed lines, contour interval is 3 K); and (b) condensate mixing ratio (g/kg, contour interval is 0.1 g/kg). The surface front location is marked by F.

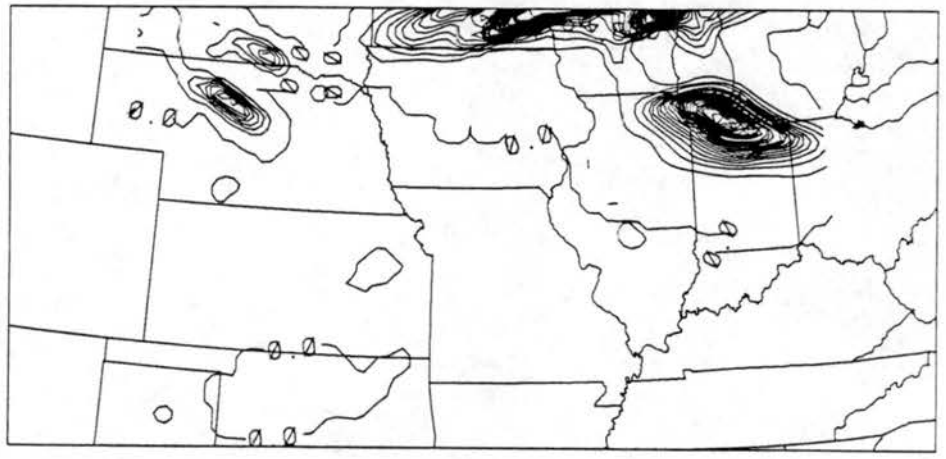

Figure 5.14: Explicit microphysically-produced precipitation in the MIC simulation accumulated from 1800 UTC 17 June to 0600 UTC 18 June 1978 (cm, contour interval is 0.2 cm).

these circulations do show up in the MIC simulation, but are not shown here as they were apparently unrelated to the frontal convergence and squall line. The development of significant microphysical processes in those two areas seemed to occur because they were relatively stationary and long-lived (compared to the line of frontal convergence), and a positive feedback mechanism occurred between the microphysical development and dynamical forcing. The region of strong frontal forcing was continuously moving along at approximately 5-10 m s^{-1}, and was not strong enough on that scale to continuously release the instability, and moving too fast to result in any sort of positive feedback. Again, the frontal movement in this simulation will be summarized and compared to that in the observations and other simulations in Section 5.3.5.

5.3.3 CU simulation

The formulation of simulation CU included the Kuo-type cumulus parameterization (discussed in Section 4.2) and grid-scale condensational heating and production of cloud water, although no explicit microphysical processes were included. Figures 5.15-5.18 show

the surface analyses of horizontal winds, horizontal divergence, MSLP, temperature, and convective precipitation rate at 2100 UTC 17 June and 0000, 0300, and 0600 UTC 18 June 1978. The frontal and squall line positions are superimposed on the wind analyses. The frontal position is defined based on the surface wind shift line and temperature analyses, and the leading edge of the squall line is defined as the leading edge of the convective precipitation. At 2100 UTC the CU simulation (Fig. 5.15) is very similar to the DRY simulation (Fig. 5.5) except for a few perturbations associated with the local areas of frontally-forced convection over east-central Kansas and western Oklahoma. By 0000 UTC 18 June the differences between the CU and DRY simulations become more apparent. At 0000 UTC the surface front over Kansas is still disorganized and diffuse in the DRY simulation (Fig. 5.6) but has concentrated into a narrow line in the CU simulation (Fig. 5.16), approximately 3 hours earlier than in the DRY simulation. At this time the cumulus parameterization has been activated all along that line, resulting in a continuous "squall line" from eastern Iowa and northern Illinois to the Texas panhandle. The convection is aligned exactly along the front at this time. By 0300 UTC (Fig. 5.17) the front edge of the convective line has moved approximately 300 km southeastward and is now located about 150 km ahead of the surface frontal location. The front is generally moving at 8-12 m s^{-1} at this time and the leading edge of the squall line is moving at $\sim$20 m s^{-1}, although that does not mean that individual "cells" are moving that fast. The area between the frontal zone and the leading edge of the convection has become more diffuse, especially as compared to the sharply-defined frontal zone in the DRY simulation at this time (Fig. 5.7). The trough in the MSLP analysis from the CU simulation has widened and deepened, with the front edge of the trough aligned with the leading edge of the convection and the back edge aligned with the frontal zone. The MSLP analysis, and the frontal and convective line locations, all compare well with the observed analyses discussed in Chapter 3. At 0600 UTC the frontal zone in the CU simulation (Fig. 5.18) is oriented just slightly ahead of its position in the DRY simulation, but the winds behind the front are substantially less than in the DRY simulation, and more in accordance

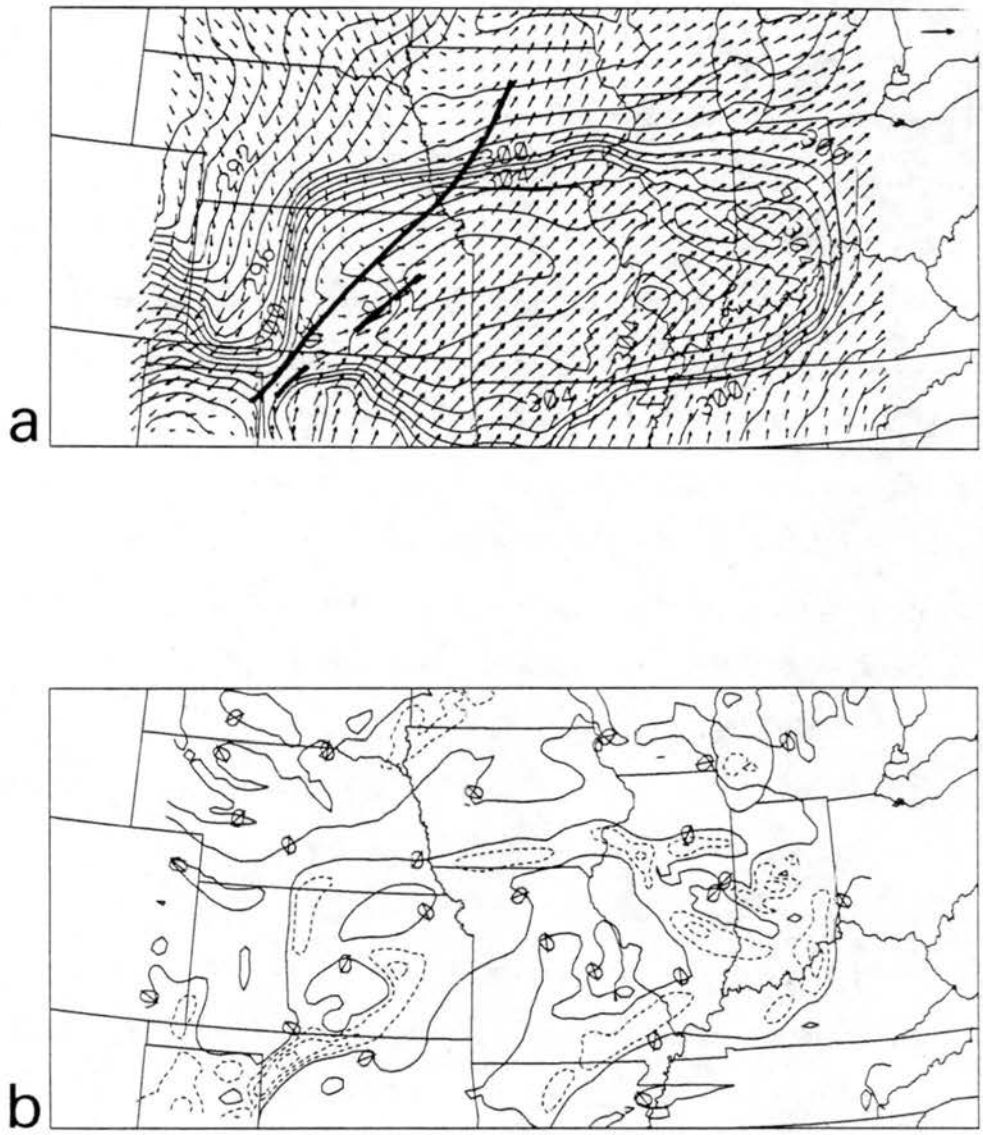

Figure 5.15: Surface analyses from CU simulation at 2100 UTC 17 June 1978 of (a) horizontal winds and temperature (K, contour interval is 1 K); and (b) horizontal divergence (s^{-1}, contour interval is .00005, dashed lines are negative value contours). The lengths of the vectors in (a) are proportional to the speed: the vector in the upper right corner of (a) is 20 m s^{-1}. The frontal (farther northwest) and squall line (farther southeast) positions are superimposed on (a).

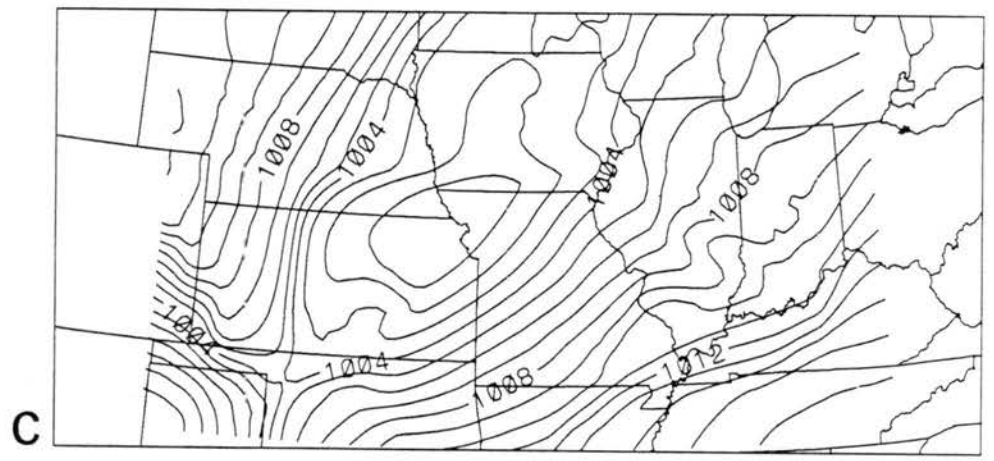

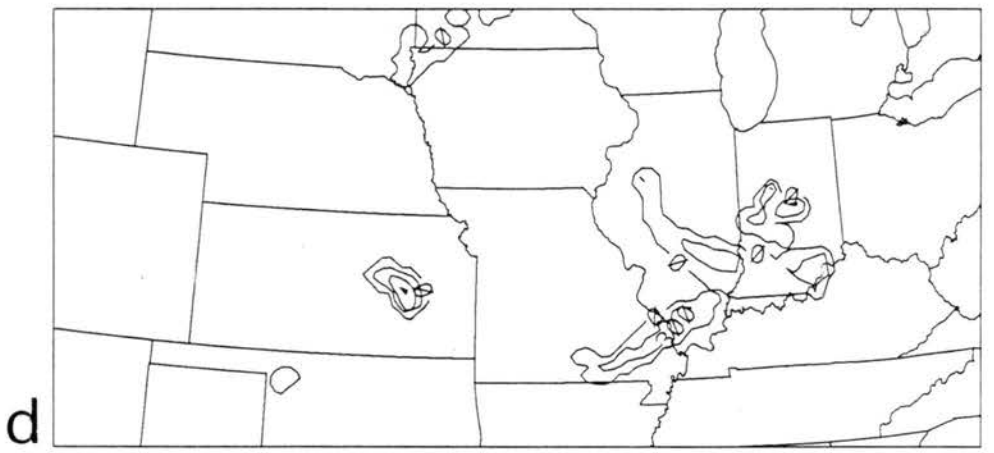

Figure 5.15: Continued: (c) reduced MSLP (mb, contour interval is 1 mb); and (d) convective precipitation rate (mm/s, contour interval is .0003).

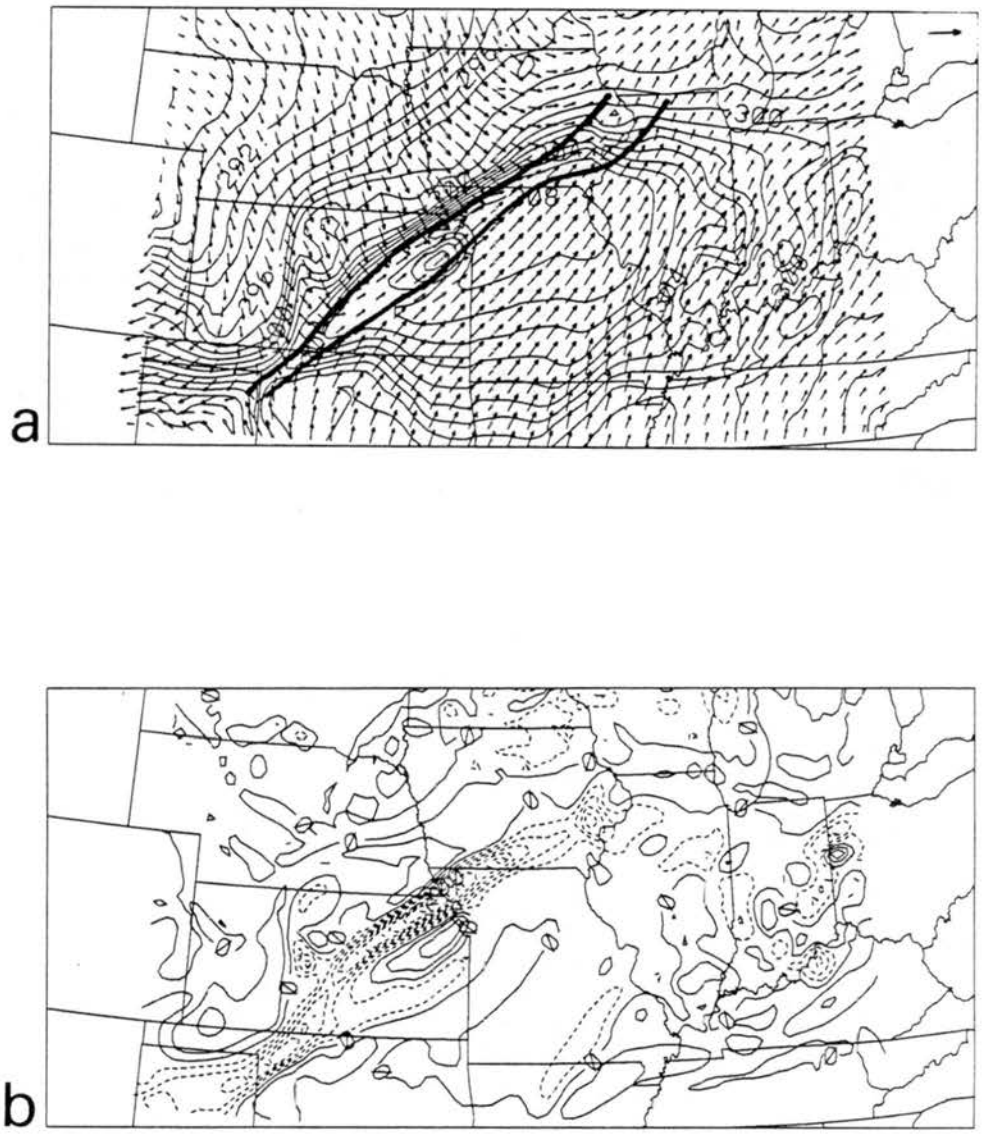

Figure 5.16: Surface analyses from CU simulation at 0000 UTC 18 June 1978 of (a) horizontal winds and temperature (K, contour interval is 1 K); and (b) horizontal divergence (s^{-1}, contour interval is .00005, dashed lines are negative value contours). The lengths of the vectors in (a) are proportional to the speed: the vector in the upper right corner of (a) is 20 m s^{-1}. The frontal (farther northwest) and squall line (farther southeast) positions are superimposed on (a).

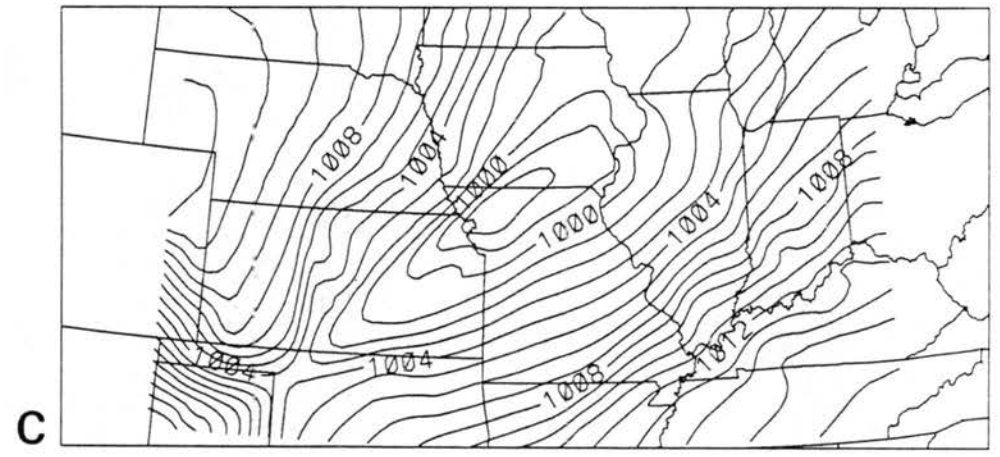

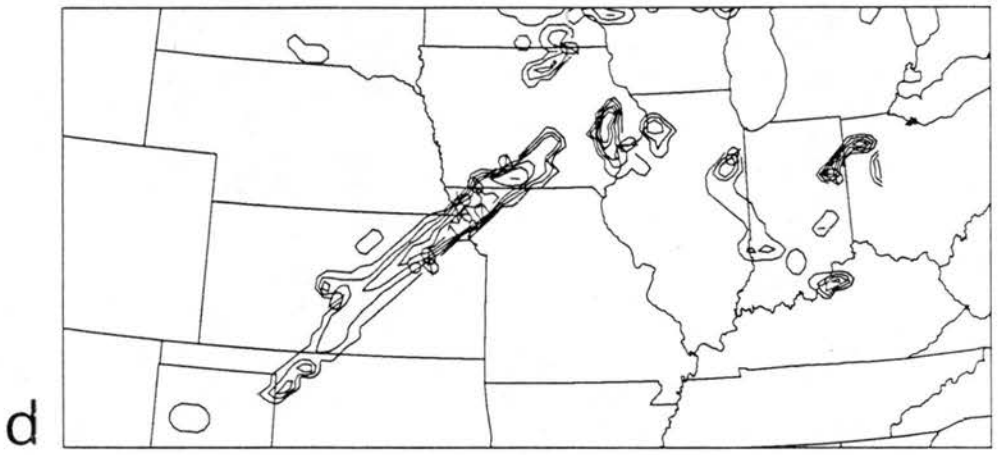

Figure 5.13: Continued: (c) reduced MSLP (mb, contour interval is 1 mb); and (d) convective precipitation rate (mm/s, contour interval is .0003).

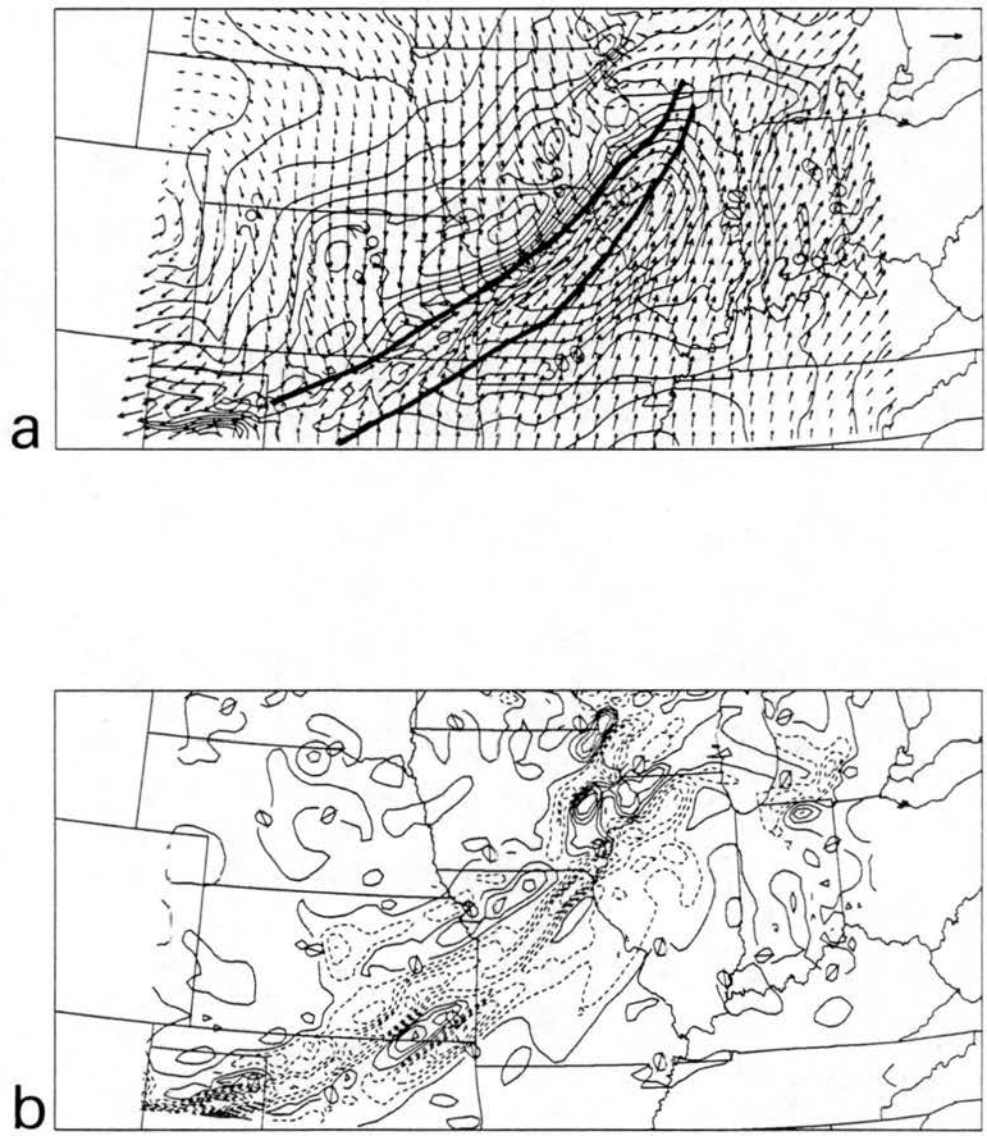

Figure 5.17: Surface analyses from CU simulation at 0300 UTC 18 June 1978 of (a) horizontal winds and temperature (K, contour interval is 1 K); and (b) horizontal divergence (s^{-1}, contour interval is .00005, dashed lines are negative value contours). The lengths of the vectors in (a) are proportional to the speed: the vector in the upper right corner of (a) is 20 m s^{-1}. The frontal (farther northwest) and squall line (farther southeast) positions are superimposed on (a).

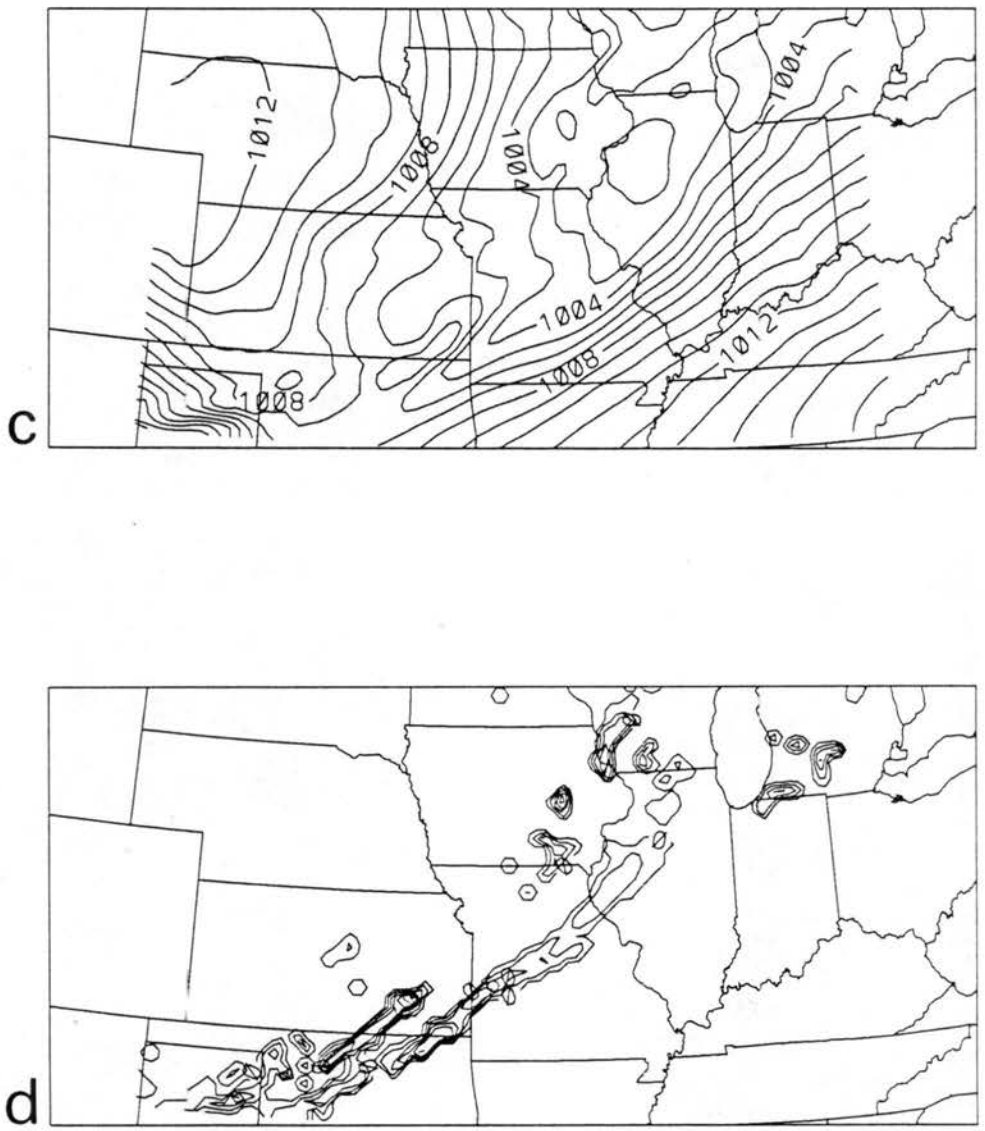

Figure 5.17: Continued: (c) reduced MSLP (mb, contour interval is 1 mb); and (d) convective precipitation rate (mm/s, contour interval is .0003).

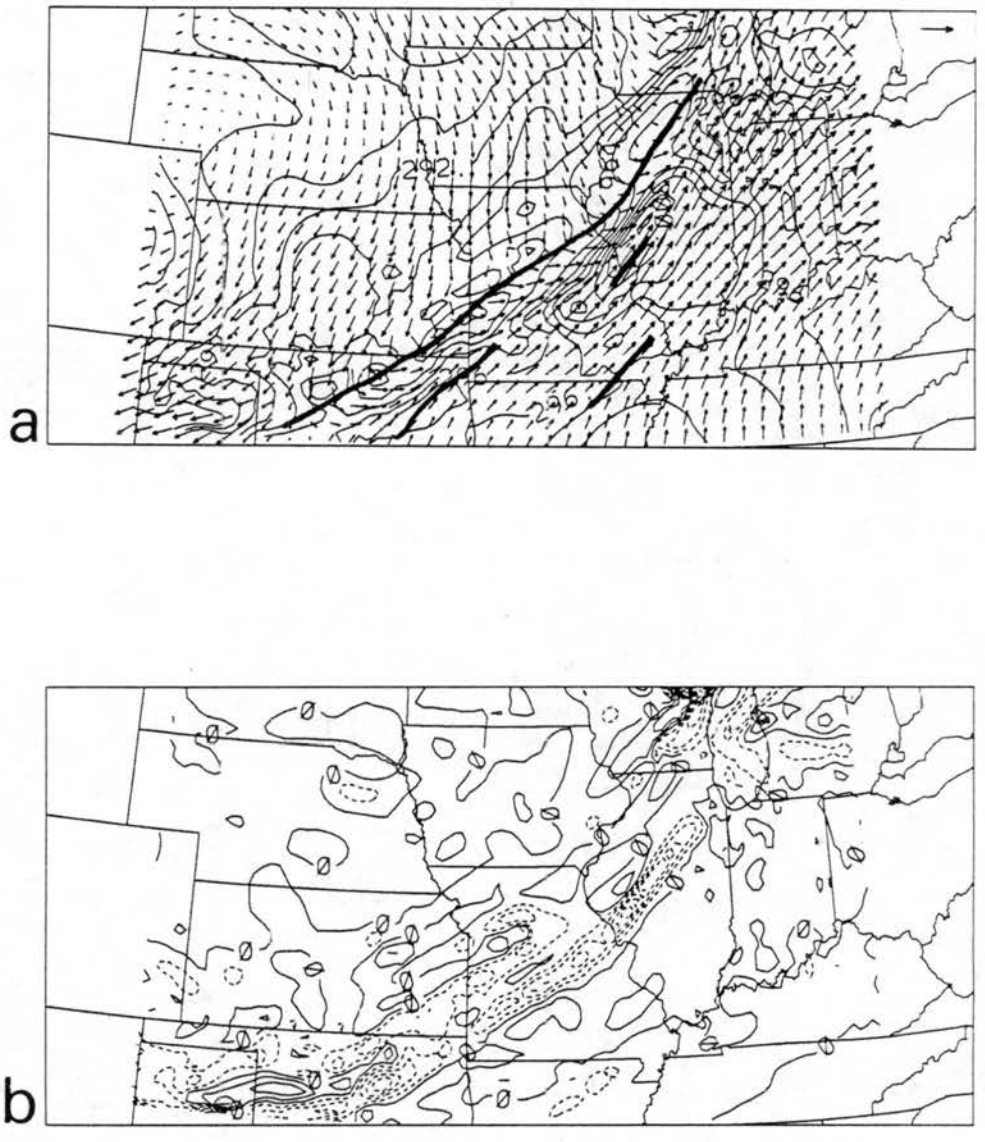

Figure 5.18: Surface analyses from CU simulation at 0600 UTC 18 June 1978 of (a) horizontal winds and temperature (K, contour interval is 1 K); and (b) horizontal divergence (s^{-1}, contour interval is .00005, dashed lines are negative value contours). The lengths of the vectors in (a) are proportional to the speed: the vector in the upper right corner of (a) is 20 m s^{-1}. The frontal (farther northwest) and squall line (farther southeast) positions are superimposed on (a).

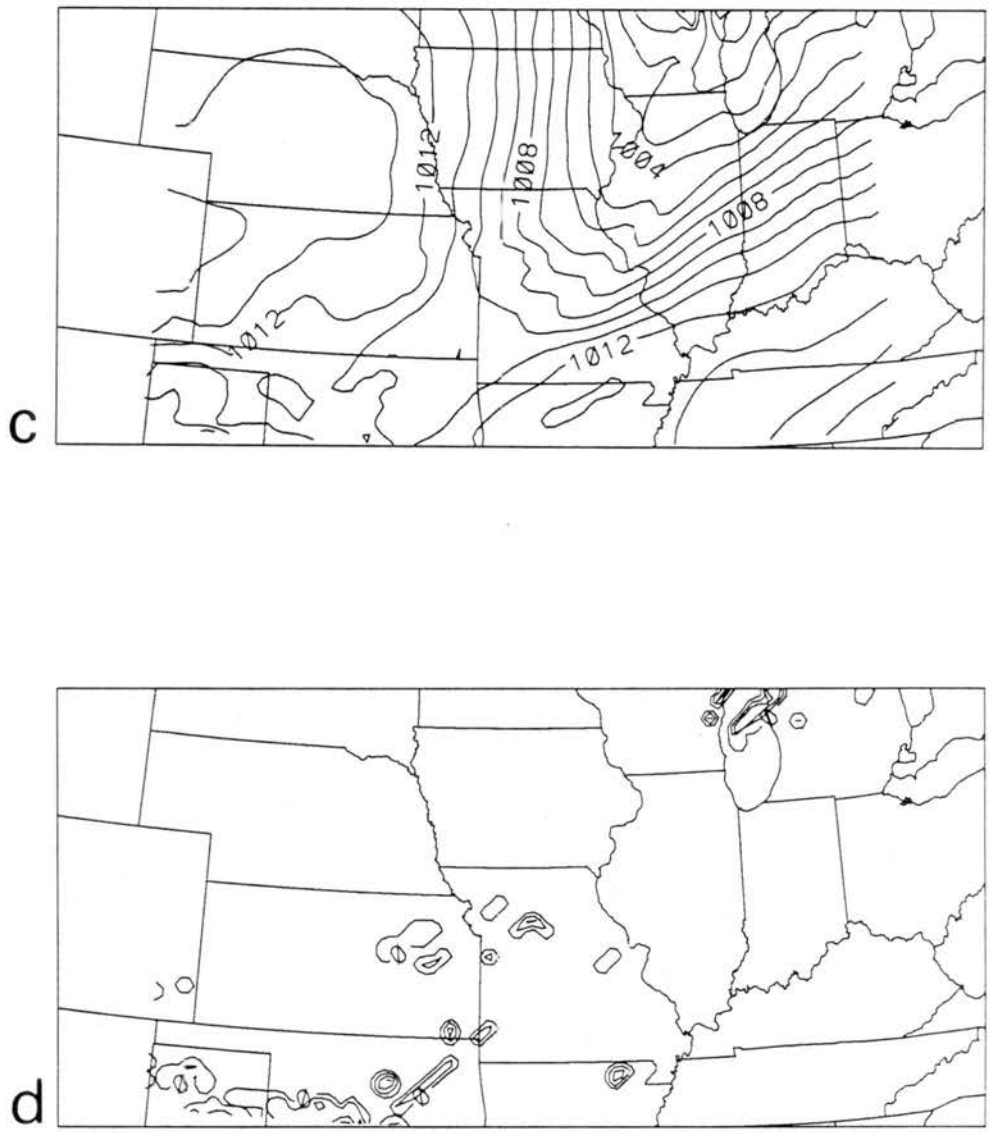

Figure 5.18: Continued: (c) reduced MSLP (mb, contour interval is 1 mb); and (d) convective precipitation rate (mm/s, contour interval is .0003).

with the observed surface wind analysis. The frontal zone and convective line in the CU simulation have both weakened considerably by 0600 UTC, but the front is still oriented along the back edge of the trough and the convective line along the front edge. Figure 5.18d shows the convective precipitation rate at 0600 UTC. The convective precipitation rate is just an instantaneous "snapshot" so it does not necessarily accurately depict the leading edge of the convection at this time, when the active convection has become more spotty. The farthest southeastward edge is in northeastern Arkansas at this time. Figure 5.19 shows the precipitation produced by the convective parameterization between 1800 UTC 17 June and 0600 UTC 18 June. Most of the precipitation fell between 0000 and

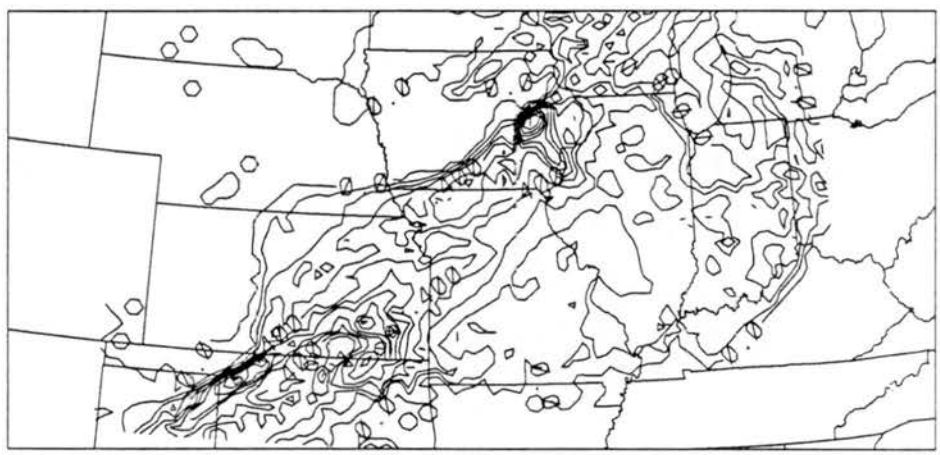

Figure 5.19: Precipitation produced by the cumulus parameterization scheme in the CU simulation between 1800 UTC 17 June and 0600 UTC 18 June (cm, contour interval is 0.1 cm).

0300 UTC 18 June. The amounts are about one-half of that of the observed precipitation shown in Fig. 3.22, although the periods of coverage do not compare exactly.

The vertical cross sections of vertical motion and equivalent potential temperature for the CU simulation are shown in Figs. 5.20-5.23 (cross section location shown in Fig. 5.1). The mixing ratio of cloud water is also shown in Figs. 5.22 and 5.23. The vertical motion fields in these figures are noisy, but they do show the areas of deep vertical motion

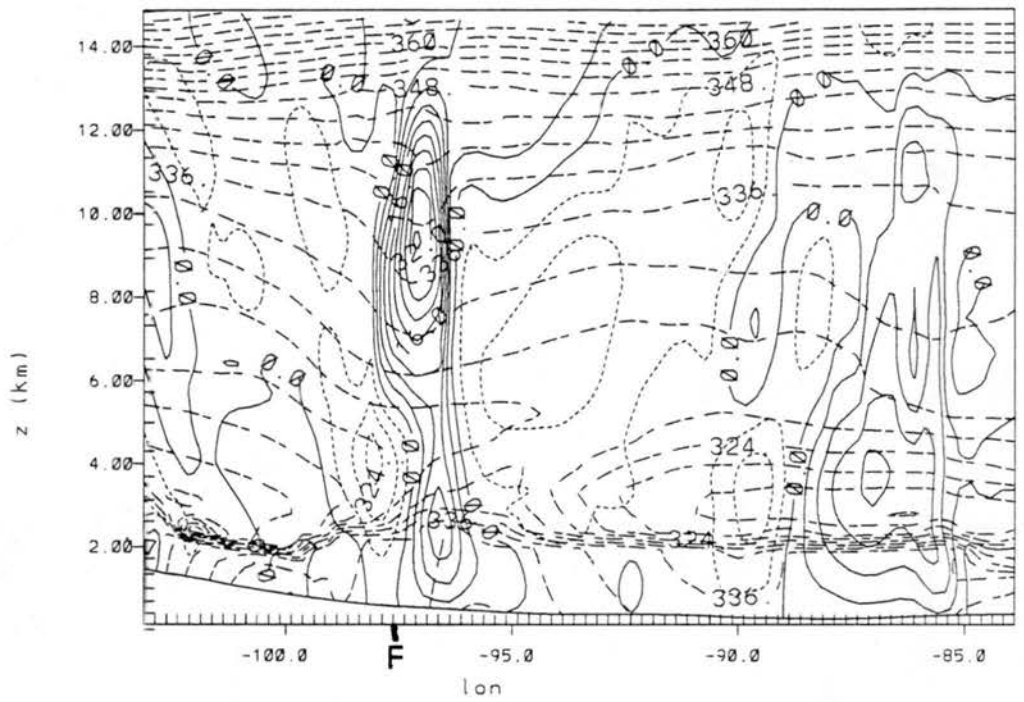

Figure 5.20: Vertical cross section from the CU simulation at 2100 UTC 17 June 1978 of vertical motion w (cm s^{-1}, contour interval is 4 cm s^{-1}, solid lines are contours of positive values and short-dashed lines are contours of negative values) and equivalent potential temperature θ_e (K, long-dashed lines, contour interval is 3 K). The surface front location is marked by F and the squall line position (leading edge of convective precipitation) by S.

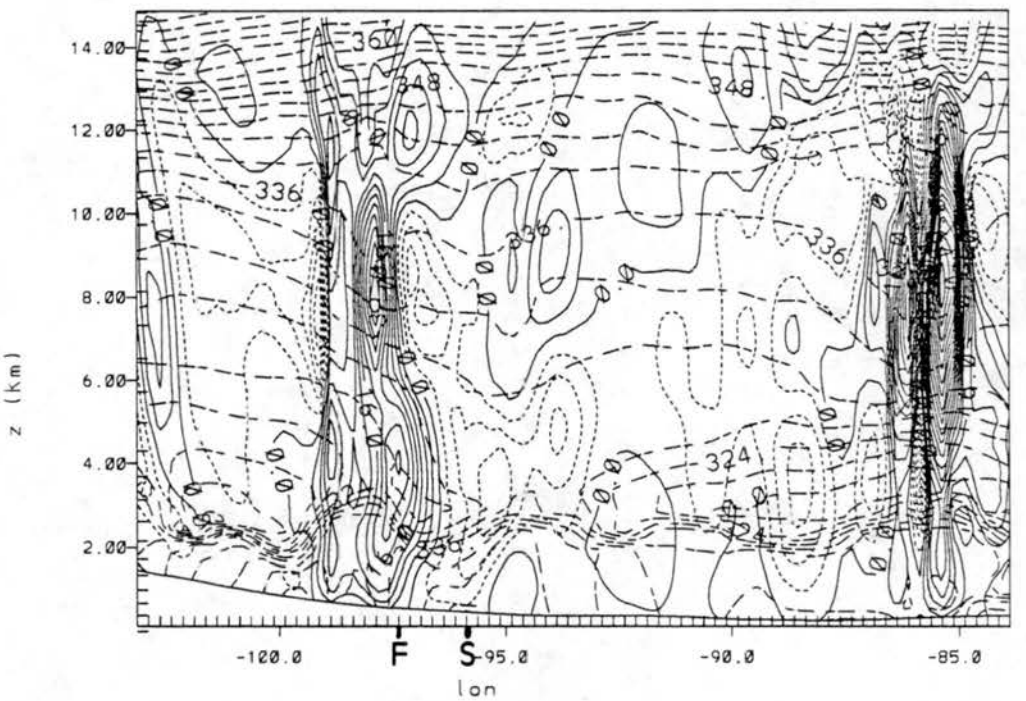

Figure 5.21: Vertical cross section from the CU simulation at 0000 UTC 18 June 1978 of vertical motion w (cm s^{-1}, contour interval is 4 cm s^{-1}, solid lines are contours of positive values and short-dashed lines are contours of negative values) and equivalent potential temperature θ_e (K, long-dashed lines, contour interval is 3 K). The surface front location is marked by F and the squall line position (leading edge of convective precipitation) by S.

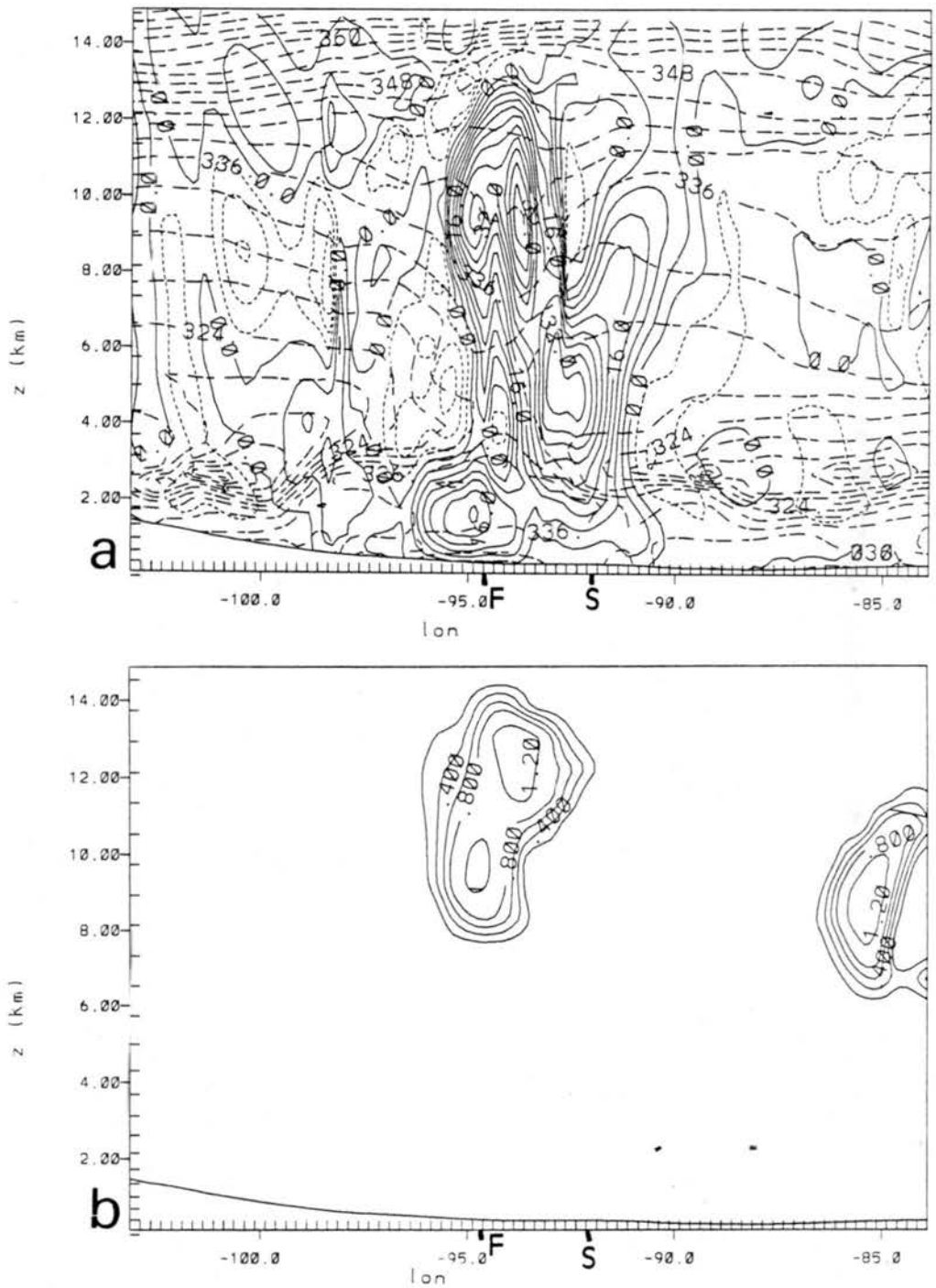

Figure 5.22: Vertical cross sections from the CU simulation at 0300 UTC 18 June 1978 of (a) vertical motion w (cm s^{-1}, contour interval is 4 cm s^{-1}, solid lines are contours of positive values and short-dashed lines are contours of negative values) and equivalent potential temperature θ_e (K, long-dashed lines, contour interval is 3 K); and (b) cloud water mixing ratio (g/kg, contour interval is 0.2 g/kg). The surface front location is marked by F and the squall line position (leading edge of convective precipitation) by S.

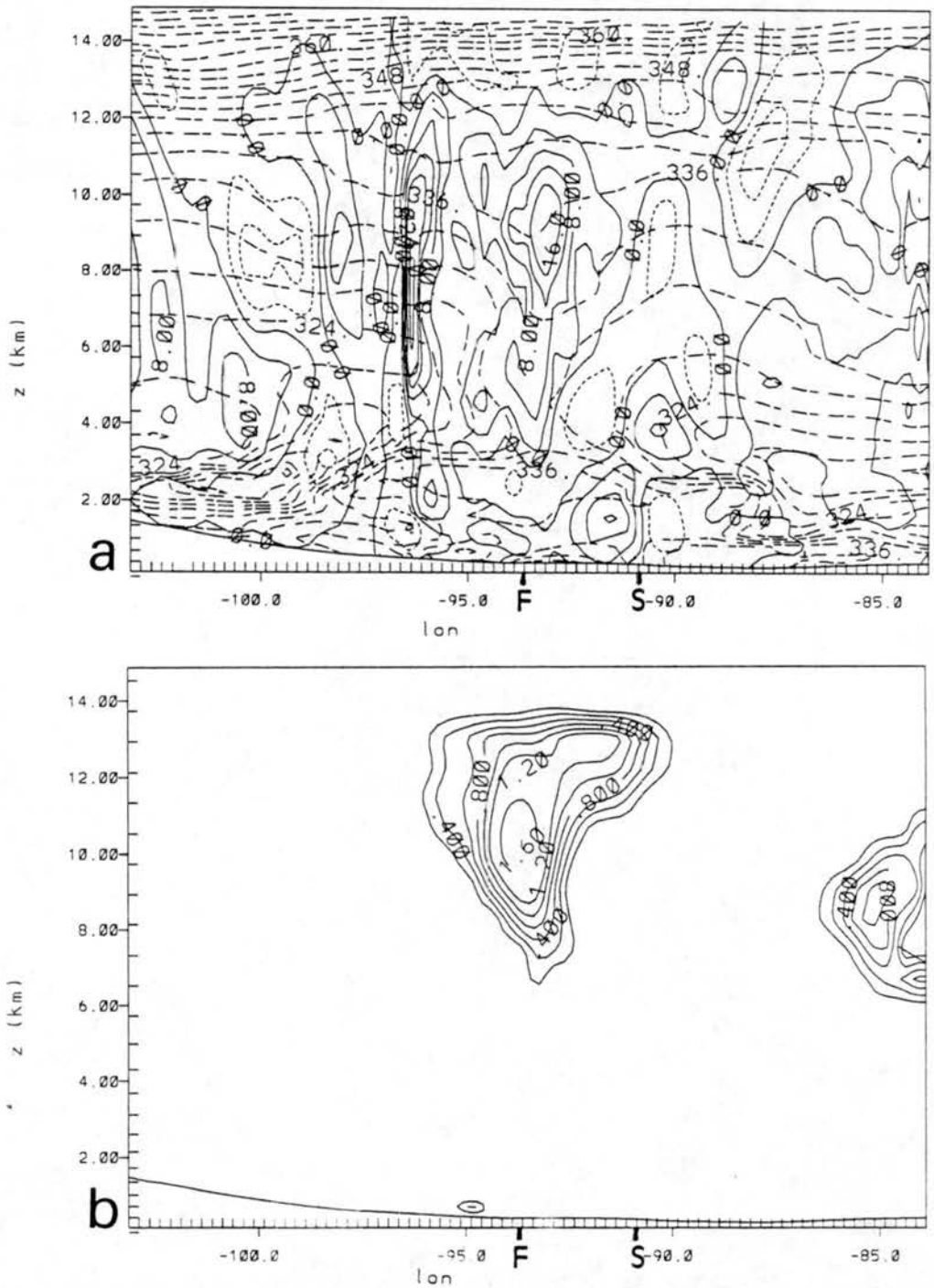

Figure 5.23: Vertical cross sections from the CU simulation at 0600 UTC 18 June 1978 of (a) vertical motion w (cm s^{-1}, contour interval is 4 cm s^{-1}, solid lines are contours of positive values and short-dashed lines are contours of negative values) and equivalent potential temperature θ_e (K, long-dashed lines, contour interval is 3 K); and (b) cloud water mixing ratio (g/kg, contour interval is 0.2 g/kg). The surface front location is marked by F and the squall line position (leading edge of convective precipitation) by S.

associated with the cumulus parameterization, and their relation to the area of shallow, frontally-forced vertical motion. At 2100 UTC the vertical motion forced by the frontal convergence is located in approximately the same place in both the CU (Fig. 5.20) and DRY (Fig. 5.9) simulations, but there is an area of deep vertical motion extending to the tropopause slightly rearward of that in the CU simulation. At 0000 UTC (Fig. 5.21) the area of deep vertical motion is located in the approximately the same place as it was 3 hours earlier. This is because the cross section passes through one of the first cells that developed at 2100 UTC (see Fig. 5.15e) and then the whole line develops by 0000 UTC (Fig. 5.16e) but has not moved substantially. By 0300 UTC (Fig. 5.22) the difference between the frontal and leading-convective-edge positions is clear in the vertical motion field, and by 0600 UTC (Fig. 5.23) the weakening of the convective organization is also apparent. Figures 5.20-5.23 also show a decrease in the vertical gradient of θ_e caused by the convection, resulting primarily from an increase in the θ_e minimum at mid-levels (3-8 km) and a substantial decrease in the high θ_e at low levels. The cross sections of cloud water at 0300 and 0600 UTC (5.22b and 5.23b) show the maximum in cloud water mixing ratio associated with the vertical motion maximum produced by the convective scheme.

The results from the CU simulation compare well with the observations. The frontal and convective line movements agree well with the observed motions, and the separation of the squall line from the front also appears to be accurately simulated. The separation of the squall line from the front will be analyzed in more detail after the following discussion of the ALL simulation. The frontal and squall line movements in the CU simulation are summarized and compared to the observations and other movements in Section 5.3.5.

5.3.4 ALL simulation

The ALL simulation included both the cumulus parameterization scheme and the explicit microphysics. Figures 5.24-5.27 show the surface fields of horizontal winds, horizontal divergence, MSLP, temperature, and convective precipitation rate for the ALL simulation at 2100 UTC 17 June, and 0000 UTC, 0300 UTC, and 0600 UTC 18 June 1978. At 2100 UTC the ALL fields (Fig. 5.24) are very similar to the CU fields (Fig. 5.15)

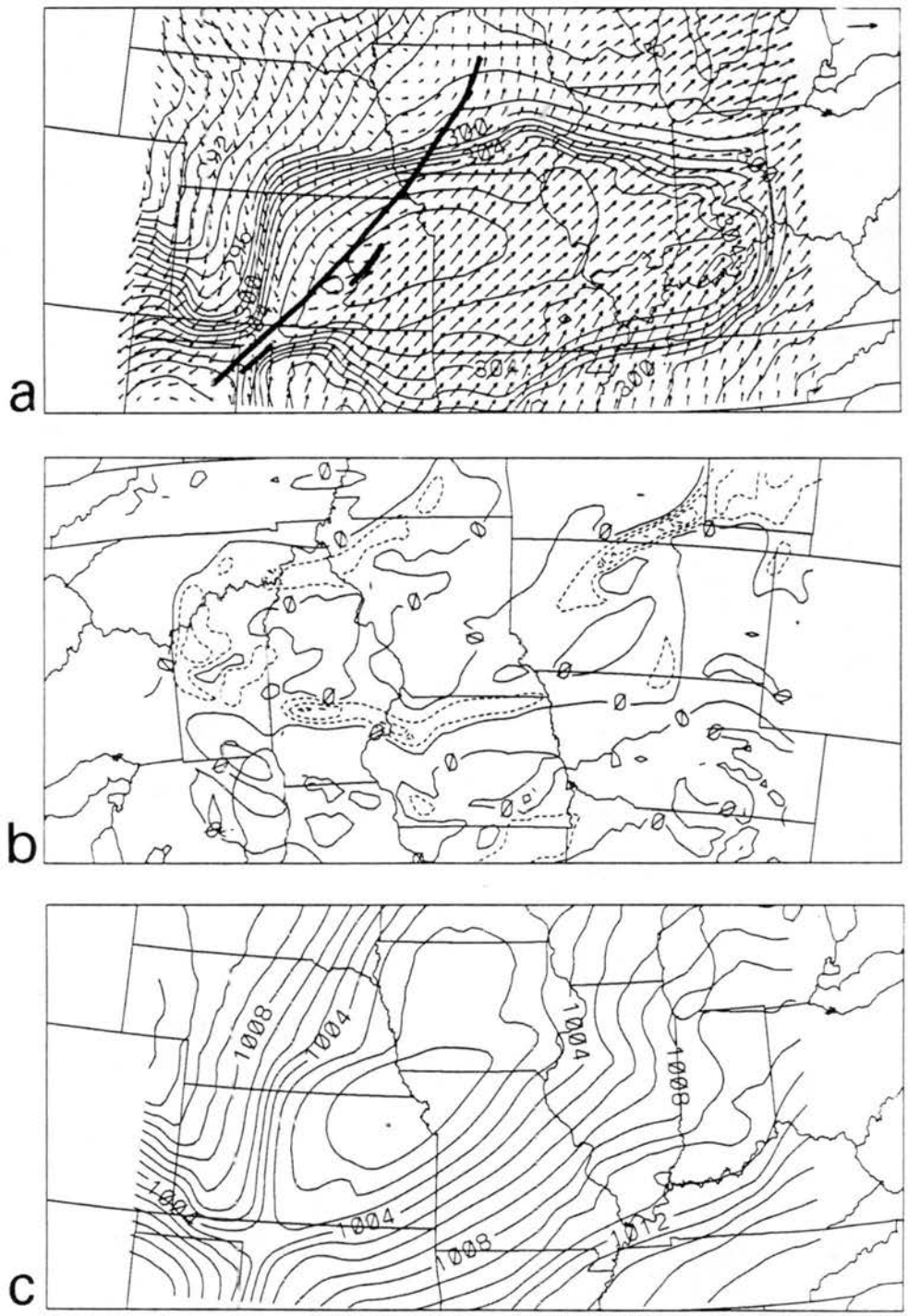

Figure 5.24: Analyses from ALL simulation at 2100 UTC 17 June 1978 of (a) surface horizontal winds and temperature (K, contour interval is 1 K); (b) surface horizontal divergence (s^{-1}, contour interval is .00005, dashed lines are negative value contours); and (c) reduced MSLP (mb, contour interval is 1 mb). The lengths of the vectors in (a) are proportional to the speed: the vector in the upper right corner of (a) is 20 m s^{-1}. The frontal (farther northwest) and squall line (farther southeast) positions are superimposed on (a).

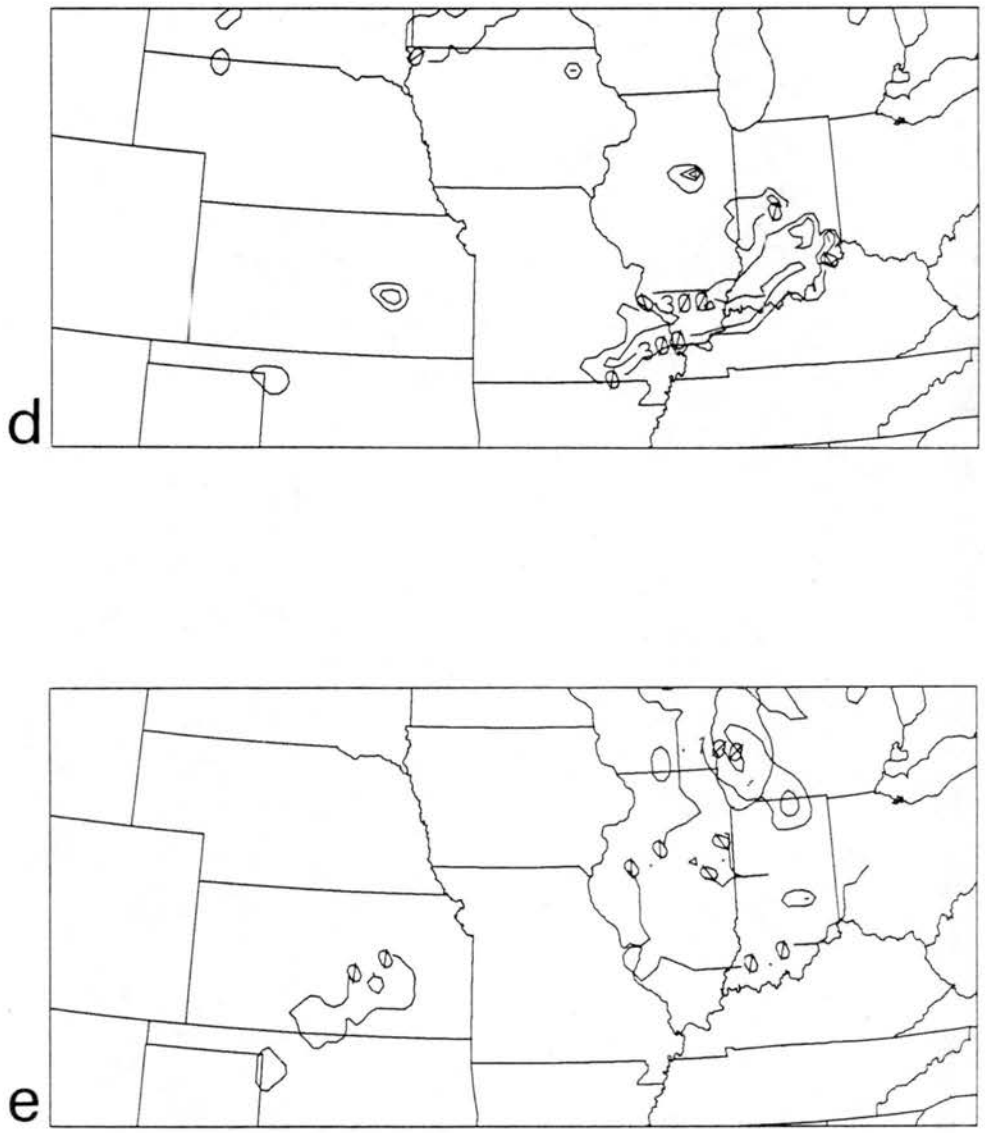

Figure 5.24: Continued: (d) convective precipitation rate (mm/s, contour interval is .0003); and (e) condensate mixing ratio at 9.7 km (g/kg, contour interval is 0.1 g/kg).

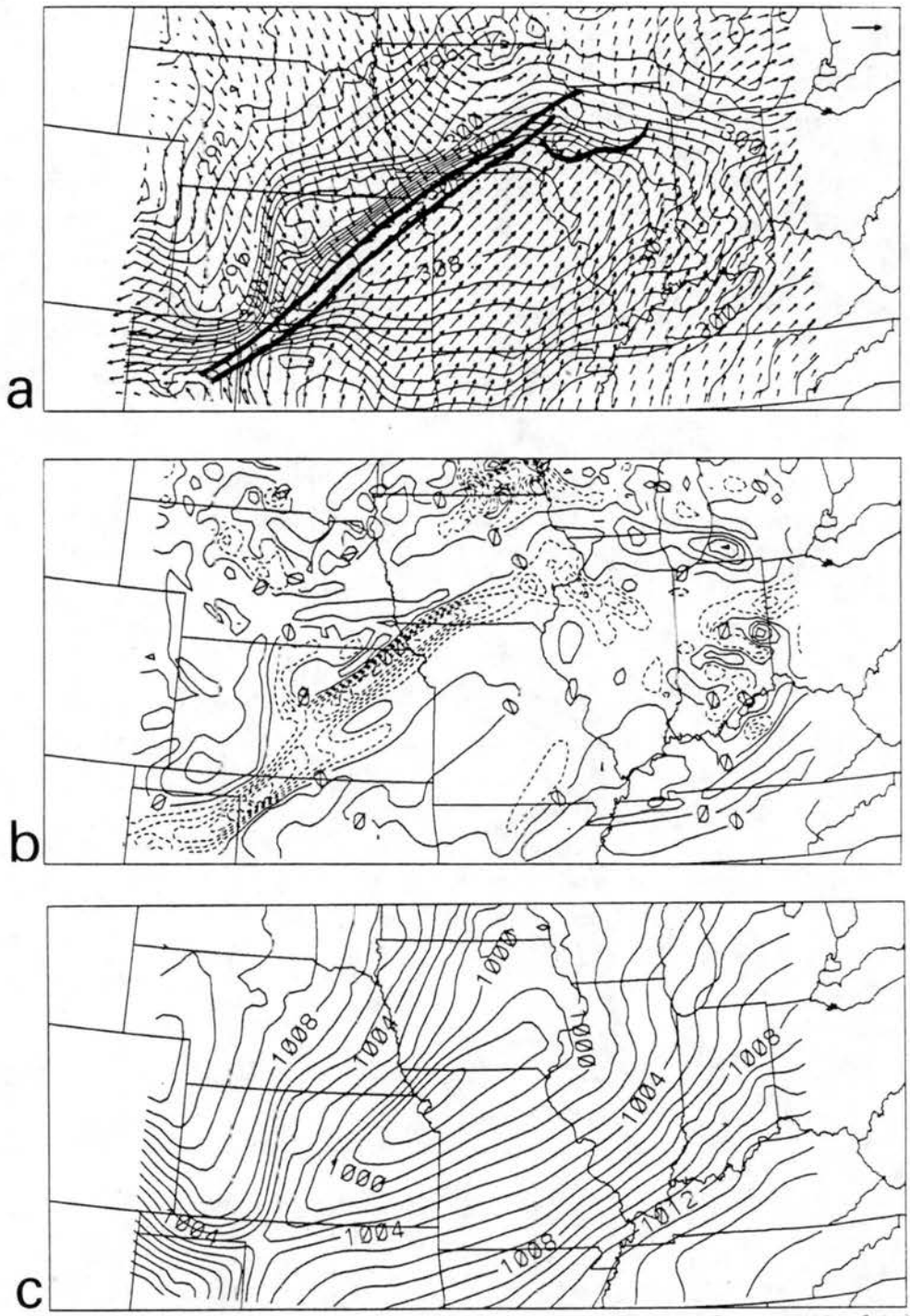

Figure 5.25: Analyses from ALL simulation at 0000 UTC 18 June 1978 of (a) surface horizontal winds and temperature (K, contour interval is 1 K); (b) surface horizontal divergence (s^{-1}, contour interval is .00005, dashed lines are negative value contours); and (c) reduced MSLP (mb, contour interval is 1 mb). The lengths of the vectors in (a) are proportional to the speed: the vector in the upper right corner of (a) is 20 m s^{-1}. The frontal (farther northwest) and squall line (farther southeast) positions are superimposed on (a).

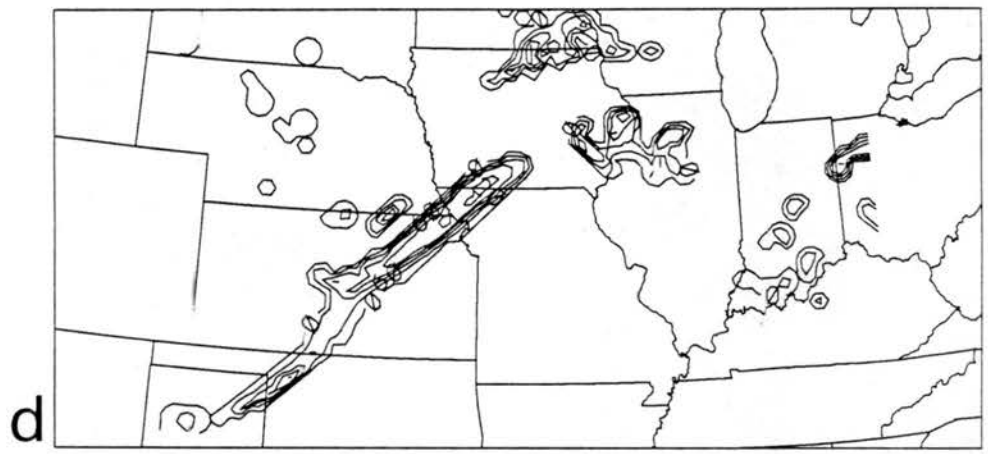

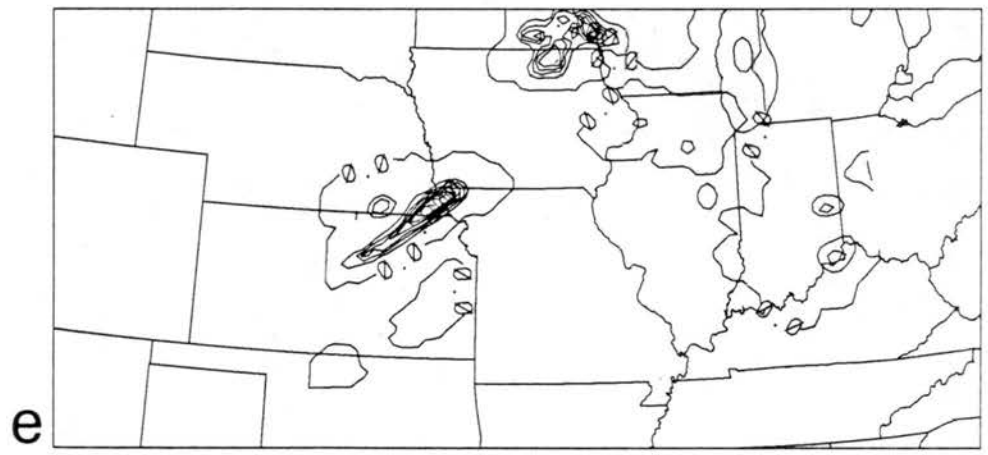

Figure 5.25: Continued: (d) convective precipitation rate (mm/s, contour interval is .0003); and (e) condensate mixing ratio at 9.7 km (g/kg, contour interval is 0.1 g/kg).

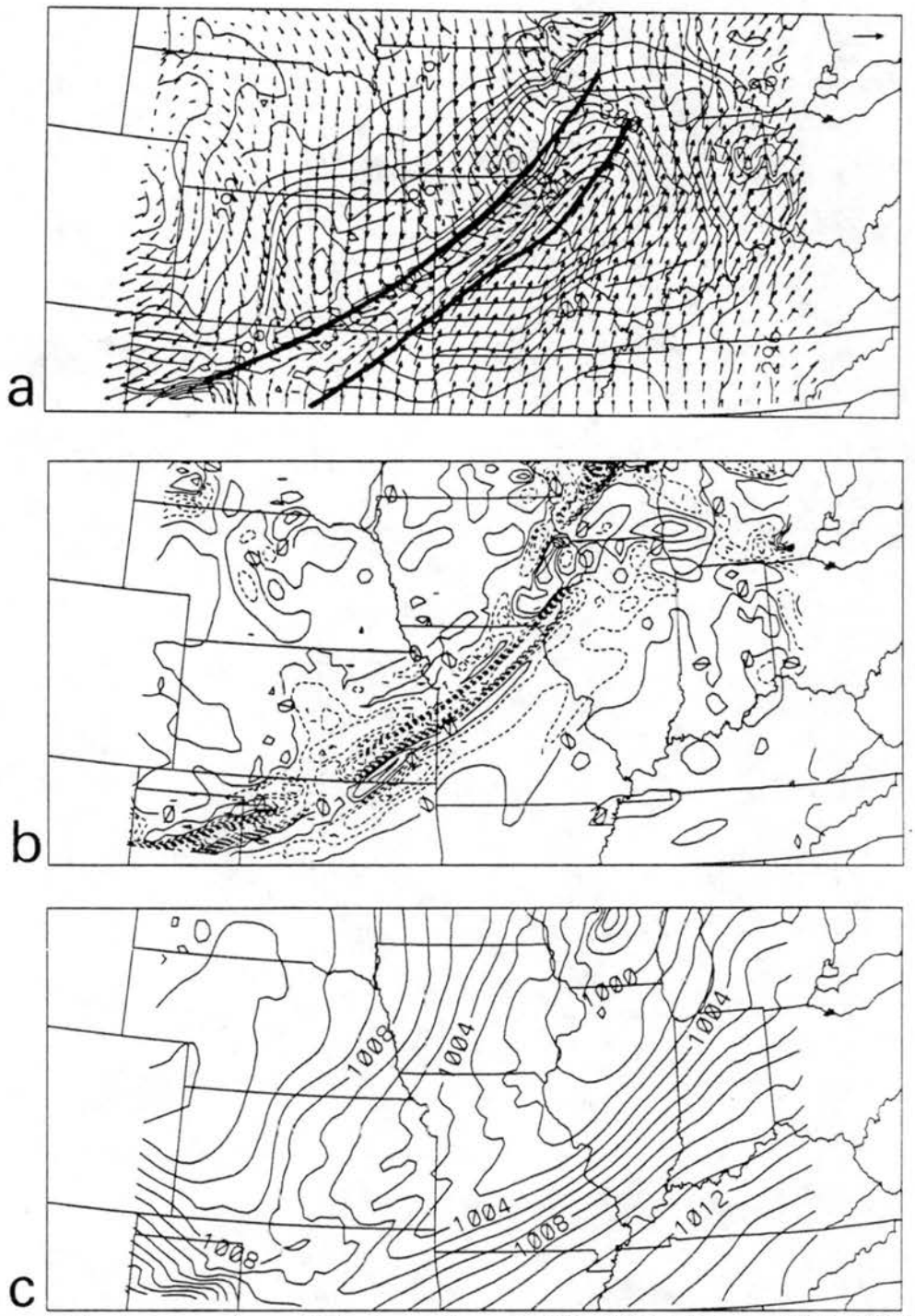

Figure 5.26: Analyses from ALL simulation at 0300 UTC 18 June 1978 of (a) surface horizontal winds and temperature (K, contour interval is 1 K); (b) surface horizontal divergence (s^{-1}, contour interval is .00005, dashed lines are negative value contours); and (c) reduced MSLP (mb, contour interval is 1 mb). The lengths of the vectors in (a) are proportional to the speed: the vector in the upper right corner of (a) is 20 m s^{-1}. The frontal (farther northwest) and squall line (farther southeast) positions are superimposed on (a).

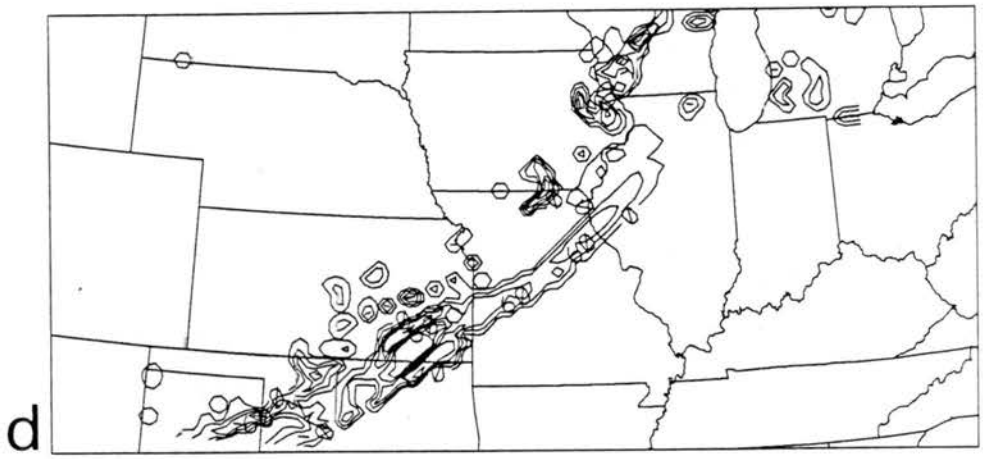

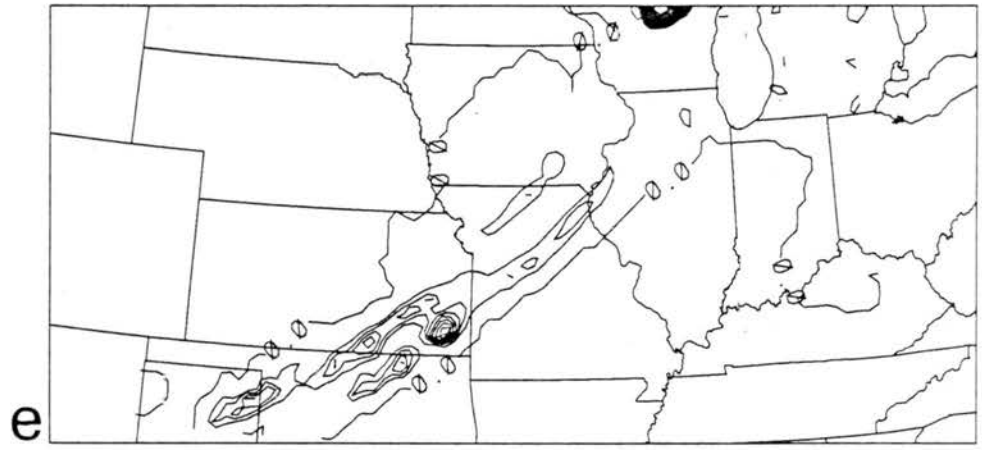

Figure 5.26: Continued: (d) convective precipitation rate (mm/s, contour interval is .0003); and (e) condensate mixing ratio at 9.7 km (g/kg, contour interval is 0.1 g/kg).

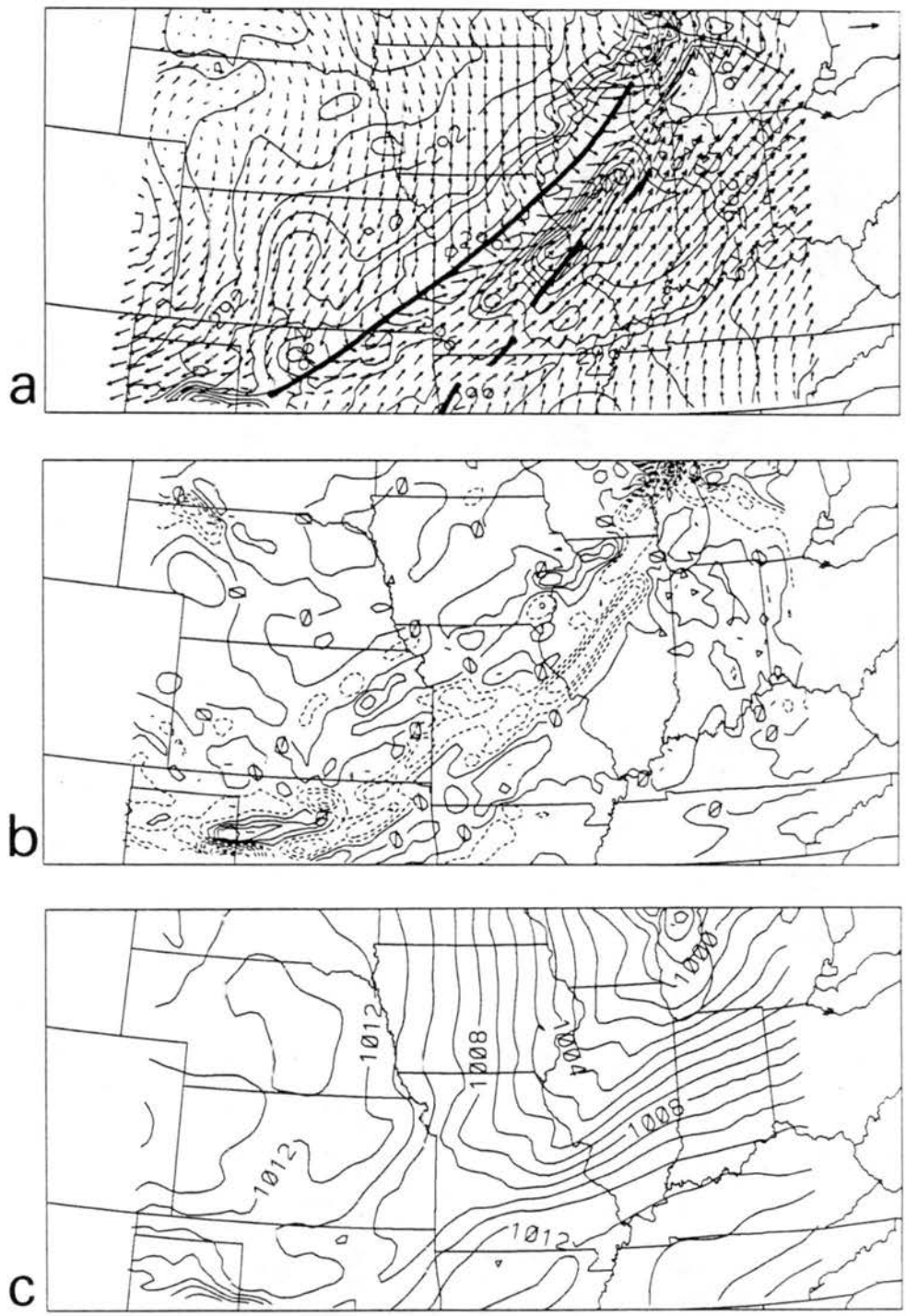

Figure 5.27: Analyses from ALL simulation at 0600 UTC 18 June 1978 of (a) surface horizontal winds and temperature (K, contour interval is 1 K); (b) surface horizontal divergence (s^{-1}, contour interval is .00005, dashed lines are negative value contours); and (c) reduced MSLP (mb, contour interval is 1 mb). The lengths of the vectors in (a) are proportional to the speed: the vector in the upper right corner of (a) is 20 m s^{-1}. The frontal (farther northwest) and squall line (farther southeast) positions are superimposed on (a).

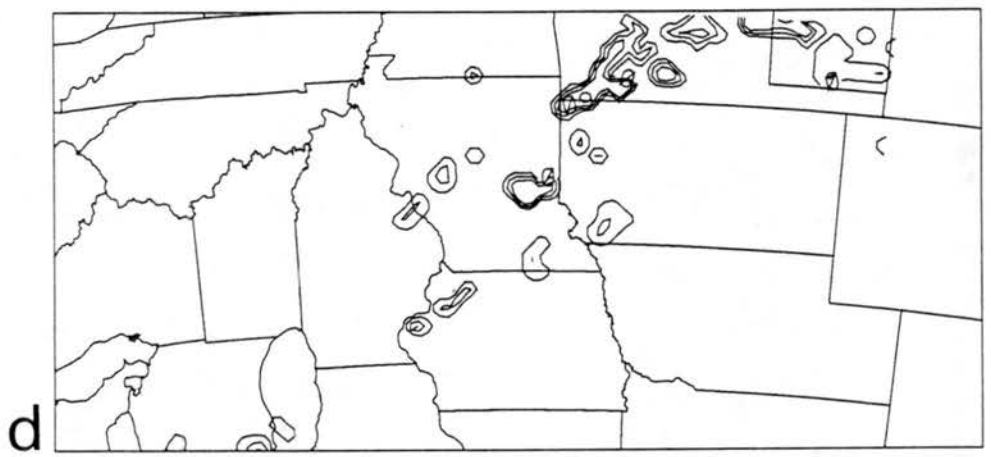

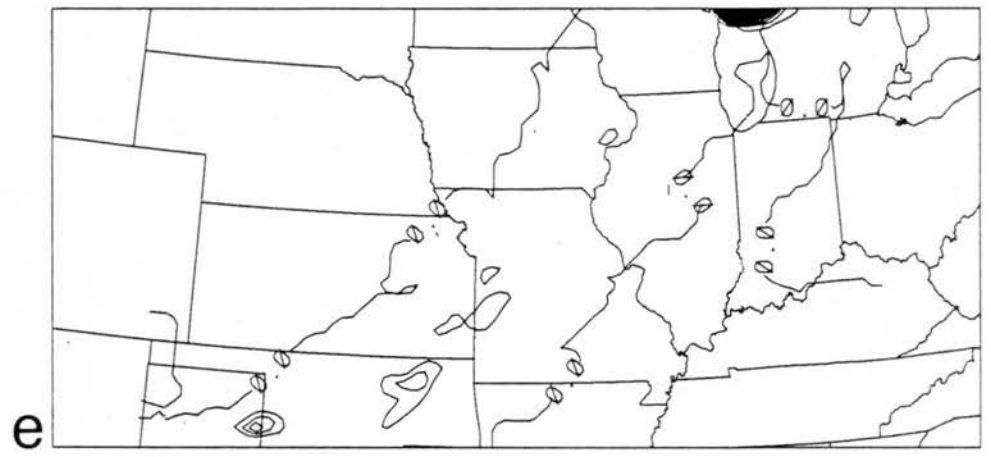

Figure 5.27: Continued: (d) convective precipitation rate (mm/s, contour interval is .0003); and (e) condensate mixing ratio at 9.7 km (g/kg, contour interval is 0.1 g/kg).

except in the area over northern Illinois and Wisconsin where the semi-stationary MCC-like feature has been affected by the explicit microphysical processes in the model. The convection along the squall line, just beginning to show up in the figures of convective precipitation rate at 2100 UTC, is very similar between the CU and ALL simulations. There is a small area of condensate at 9.73 km around the "cell" just starting to grow in central Kansas. At 0000 UTC the CU and ALL simulations are still very similar. The squall line convection shows up clearly in the plots of convective precipitation rate at 0000 UTC (Fig. 5.25e). There are a few more differences between the CU and ALL simulations at 0300 UTC, although the basic motion of the squall line (defined as the leading edge of the convective precipitation rate plot) is the same between the two simulations. By 0300 UTC, the ALL simulation has developed an anvil-like area of condensate mixing ratio at 9.7 km (Fig. 5.26e) extending back from the leading edge of the convective precipitation rate. The area of coverage of the condensate appears to correlate well with the anvil area of the squall line, but the simulated condensate mixing ratios are much smaller than they should be in this region. The simulated total mixing ratios are less than 0.1 g/kg in the anvil region. Rutledge and Houze (1987) and Fan *et al.* (1988) found stratiform anvil mixing ratios on the order of 0.5-2.0 g/kg. The model does not seem to produce significant levels of condensate on this scale unless the system is semi-stationary and has time to "spin up", as it did in the region of the MCC that moves eastward across Wisconsin in the model simulations. The outline of the condensate may be interpreted as the region where the relative advection of moisture is occurring backwards from the convective cores, but any significant anvil region latent heating effects are probably not occurring as the condensate mixing ratios are negligible (generally less than 0.1 g/kg). This lack of upper level condensate may be due to the fact that the cumulus parameterization scheme only transports moisture upwards, and does not produce or transport any form of condensate.

The same situation is true at 0600 UTC, with the CU and ALL simulations essentially very similar in the vicinity of the squall line (Figs. 5.18 and 5.27 respectively). Figures 5.28 and 5.29 show the precipitation accumulated from 1800 UTC 17 June to 0600 UTC 18

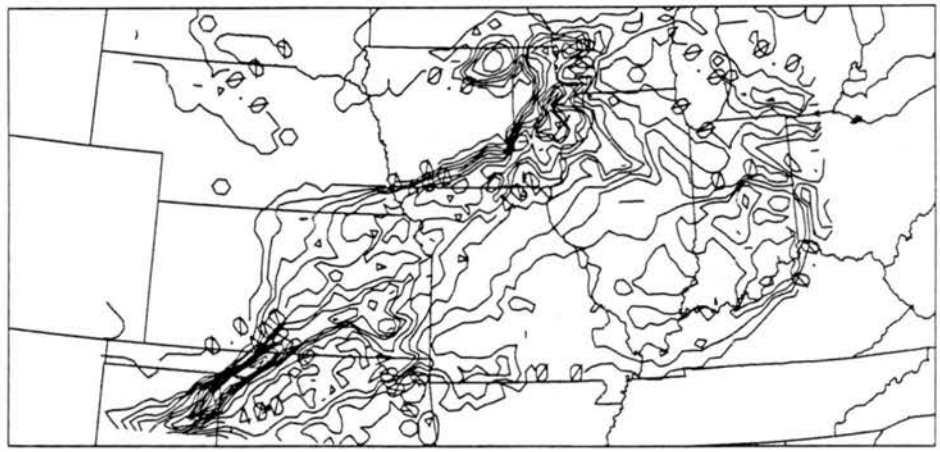

Figure 5.28: Precipitation produced by the convective parameterization scheme in the ALL simulation accumulated from 1800 UTC 17 June to 0600 UTC 18 June 1978 (cm, contour interval is 0.1 cm).

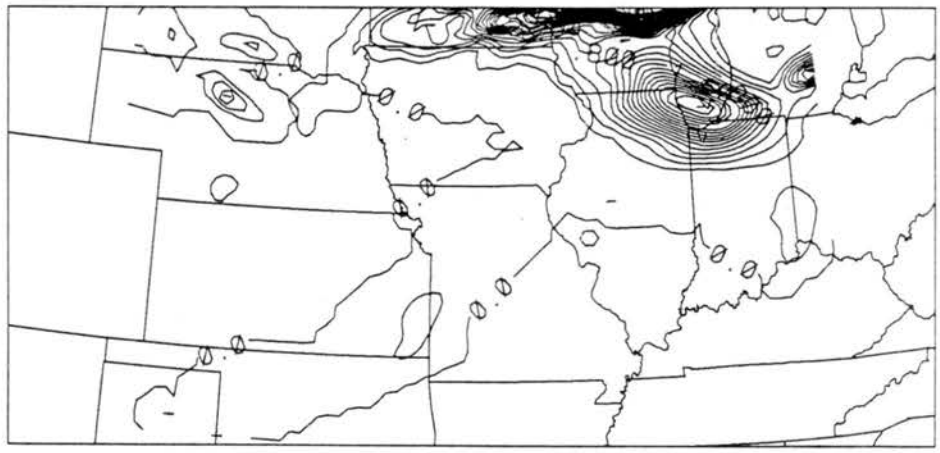

Figure 5.29: Explicit microphysically-produced precipitation from the ALL simulation accumulated from 1800 UTC 17 June to 0600 UTC 18 June 1978 (cm, contour interval is 0.2 cm).

June from the convective parameterization and from the explicit microphysical processes. The total amount of convective precipitation from the ALL simulation is more than that for the CU simulation (Fig. 5.19), but the area of coverage is very similar. Likewise, the area of coverage of the microphysically-produced precipitation from the ALL simulation is very similar to that from the MIC simulation (Fig. 5.14).

The vertical cross sections of vertical motion and equivalent potential temperature for the ALL simulation at 2100 UTC 17 June and 0000, 0300, and 0600 UTC 18 June are shown in Figs. 5.30-5.33 (cross section location shown in Fig. 5.1). The cross sections of total condensate mixing ratio produced by the explicit microphysics at 0300 and 0600 UTC are also shown in Figs. 5.32b and 5.33b. The CU and ALL simulations are again very similar at 2100 and 0000 UTC. The cross section of total condensate mixing ratio at 0300 UTC shows the maximum production of condensate at 6-7 km. The outline "looks like" a cross section through a squall line, but in this simulation the leading edge of the squall line is best defined by the leading edge of the convective precipitation rate, slightly ahead of the area of condensate mixing ratio. The lack of significant condensate means that the latent heating effects from the explicit microphysical processes are very small, and thus there is no mechanism to force anvil circulations such as the rear inflow jet. The maximum of the condensate produced in the ALL simulation is near 6 km, significantly lower than the maximum in cloud water in the CU simulation at 10-12 km.

Overall, the ALL simulation is very similar to the CU simulation. The outline of upper level total condensate in the ALL simulation is representative of the area of anvil coverage, but the mixing ratios of the condensate in the anvil region are extremely small, mostly less than 0.1 g/kg. Other studies (Rutledge and Houze, 1987; Fan *et al.*, 1988) have found anvil mixing ratios of 0.5-2.0 g/kg. This result is consistent with the comparison of the DRY and MIC simulations, where the explicit microphysical processes only seemed to become significant where a "spin-up" or feedback mechanism existed, as in the MCC development over Wisconsin. The leading edge of the squall line, represented well by the cumulus parameterization scheme, was moving too fast for any feedbacks to develop to

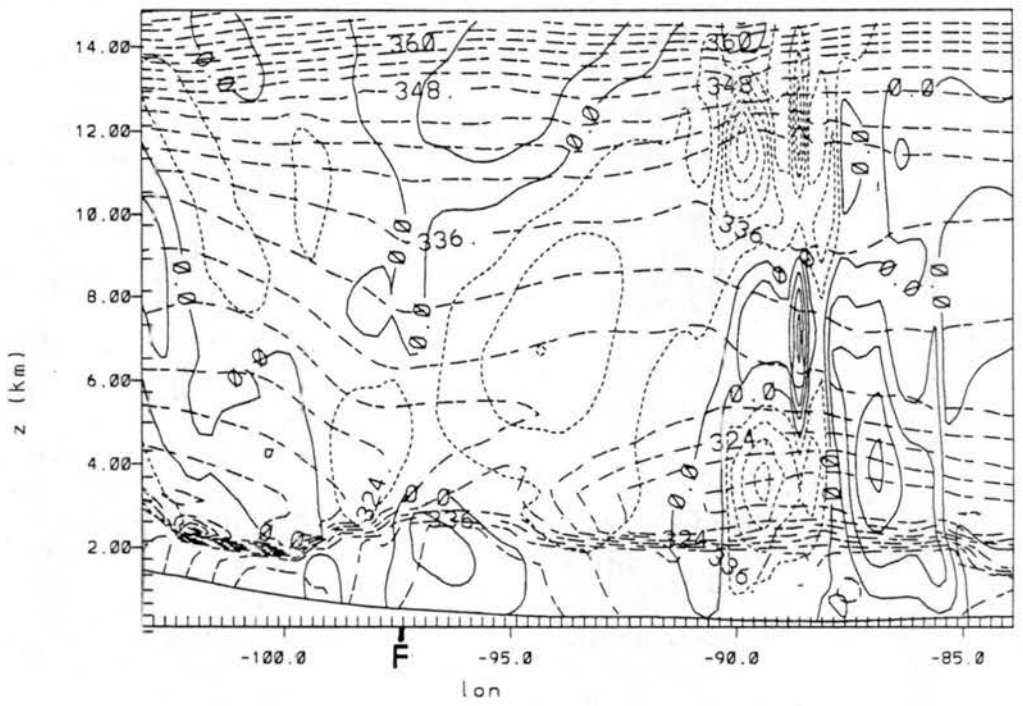

Figure 5.30: Vertical cross section from the ALL simulation at 2100 UTC 17 June 1978 of vertical motion w (cm s^{-1}, contour interval is 4 cm s^{-1}, solid lines are contours of positive values and short-dashed lines are contours of negative values) and equivalent potential temperature θ_e (K, long-dashed lines, contour interval is 3 K). The surface front location is marked by F and the squall line position (leading edge of convective precipitation) by S.

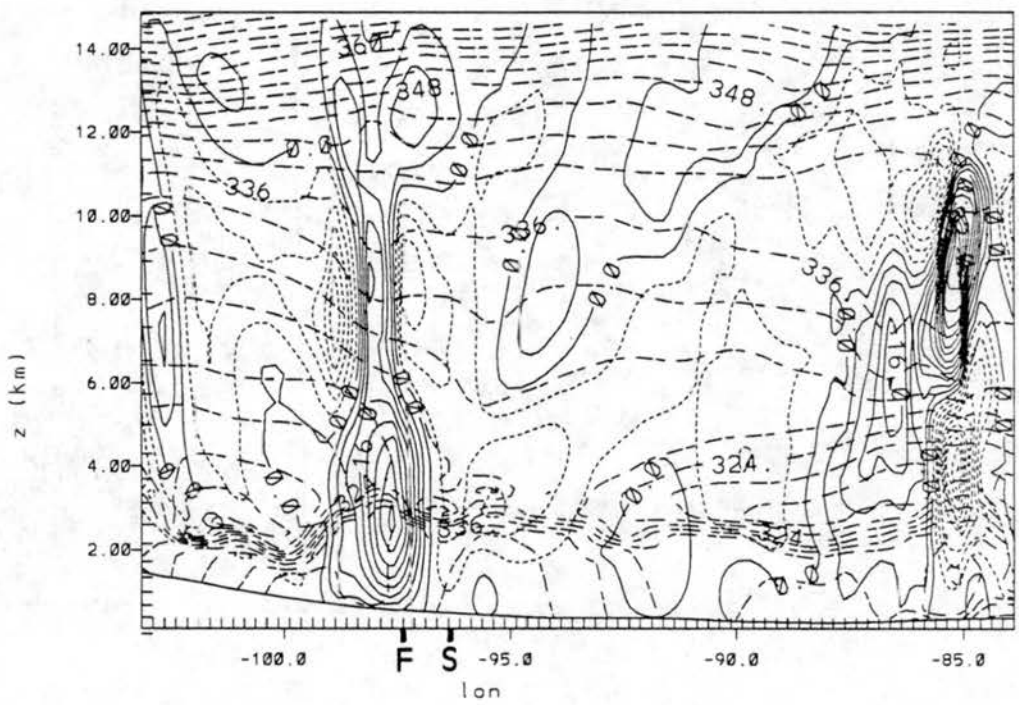

Figure 5.31: Vertical cross section from the ALL simulation at 0000 UTC 18 June 1978 of vertical motion w (cm s^{-1}, contour interval is 4 cm s^{-1}, solid lines are contours of positive values and short-dashed lines are contours of negative values) and equivalent potential temperature θ_e (K, long-dashed lines, contour interval is 3 K). The surface front location is marked by F and the squall line position (leading edge of convective precipitation) by S.

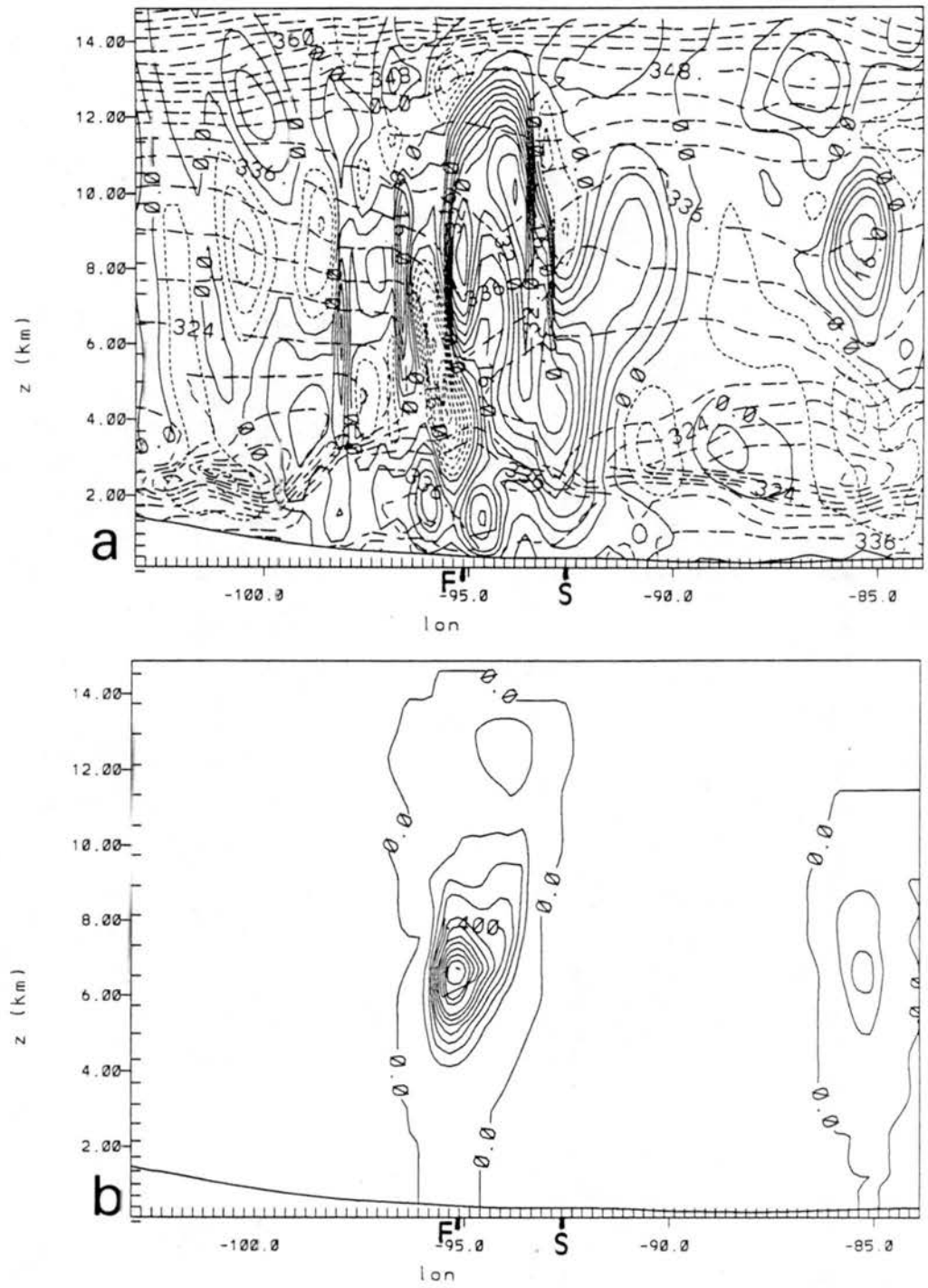

Figure 5.32: Vertical cross sections from the ALL simulation at 0300 UTC 18 June 1978 of (a) vertical motion w (cm s^{-1}, contour interval is 4 cm s^{-1}, solid lines are contours of positive values and short-dashed lines are contours of negative values) and equivalent potential temperature θ_e (K, long-dashed lines, contour interval is 3 K); and (b) condensate mixing ratio (g/kg, contour interval is 0.1 g/kg). The surface front location is marked by F and the squall line position (leading edge of convective precipitation) by S.

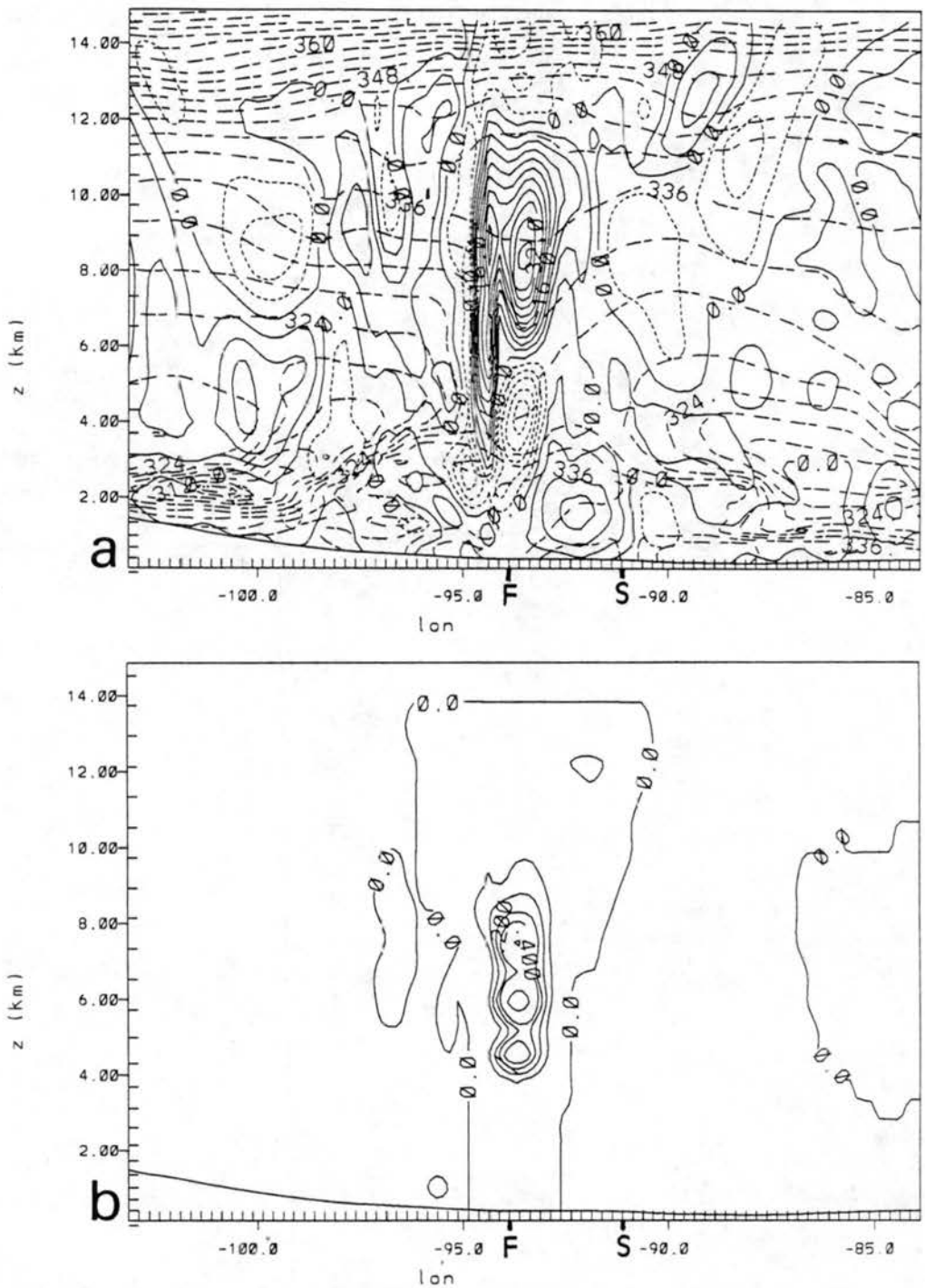

Figure 5.33: Vertical cross sections from the ALL simulation at 0600 UTC 18 June 1978 of (a) vertical motion w (cm s^{-1}, contour interval is 4 cm s^{-1}, solid lines are contours of positive values and short-dashed lines are contours of negative values) and equivalent potential temperature θ_e (K, long-dashed lines, contour interval is 3 K); and (b) condensate mixing ratio (g/kg, contour interval is 0.1 g/kg). The surface front location is marked by F and the squall line position (leading edge of convective precipitation) by S.

reinforce the microphysical processes. As the squall line moved equally fast in nature, and apparently did develop an anvil, the problem in the model is perhaps due to a deficiency in the cumulus parameterization scheme. The convective cores in nature act to explicitly produce and transport condensate upwards. The cumulus parameterization scheme does not produce or transport condensate at all, only moisture. The frontal and squall line movements in the ALL simulation are summarized and compared to the observations and other simulations in the next section.

5.3.5 Summary of frontal and squall line movements in basic four simulations

The above simulations showed that the cumulus parameterization scheme was necessary to simulate the squall line development and propagation when the 20 km grid increment was used. The convergence produced on that scale was not enough to explicitly initiate convection, but the cumulus parameterization scheme did appear to very accurately simulate the squall line movement. Figure 5.34 summarizes the relative positions of the front and squall line for the observations and the four basic simulations described in this chapter. Table 5.1 summarizes the speeds of the front and squall line from the observations and for the same four simulations. The CU and ALL simulations compare very

Table 5.1: Speeds (m s^{-1}) of front and squall line for three hourly periods from the observations and four basic simulations. The speeds in parentheses are the speeds in the region across northern Missouri, and are representative of the average speeds of the squall line and front.

Time Period	Frontal Speeds			Squall Line Speeds		
(Hours)	21-00	00-03	03-06	21-00	00-03	03-06
OBSERVED	3-11 (8)	3-8 (8)	3-5(4)		12-21 (12-20)	3-16
DRY	0-11 (5)	1-12 (12)	6-8 (7)			
MIC	0-11 (5)	1-12 (11)	6-8 (8)			
CU	0-11 (7)	5-12 (11)	4-8 (7)	0-5	16-20 (18)	5-24
ALL	3-11 (5)	3-11 (11)	6-8 (7)	0-3	14-20 (18)	5-22

well with the observations. In both simulations, and in the observations, the squall line convection initially develops along the surface frontal convergence line, and then moves

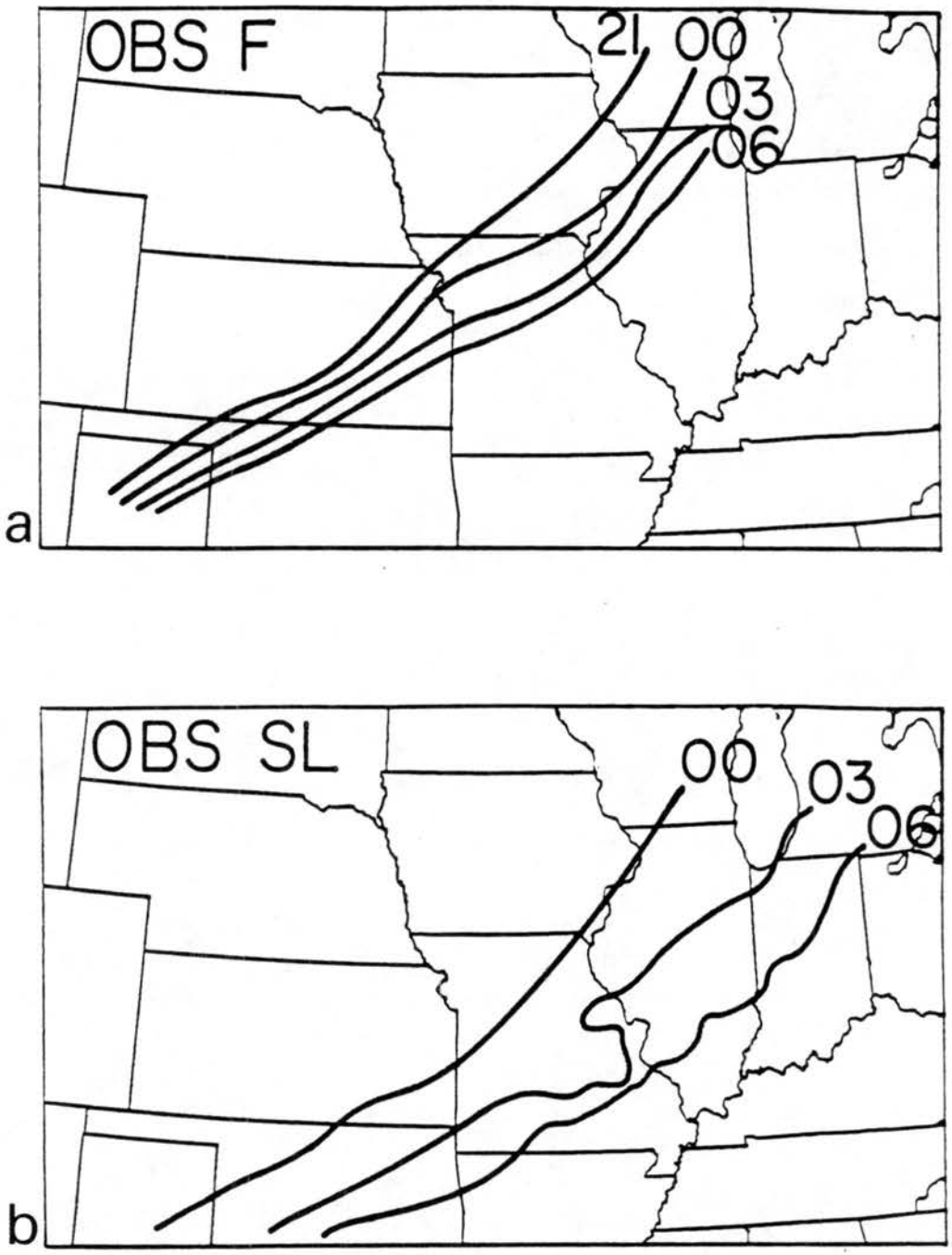

Figure 5.34: Three-hourly positions of front and squall line for (a) Observed front; and (b) observed squall line (leading edge of radar echoes).

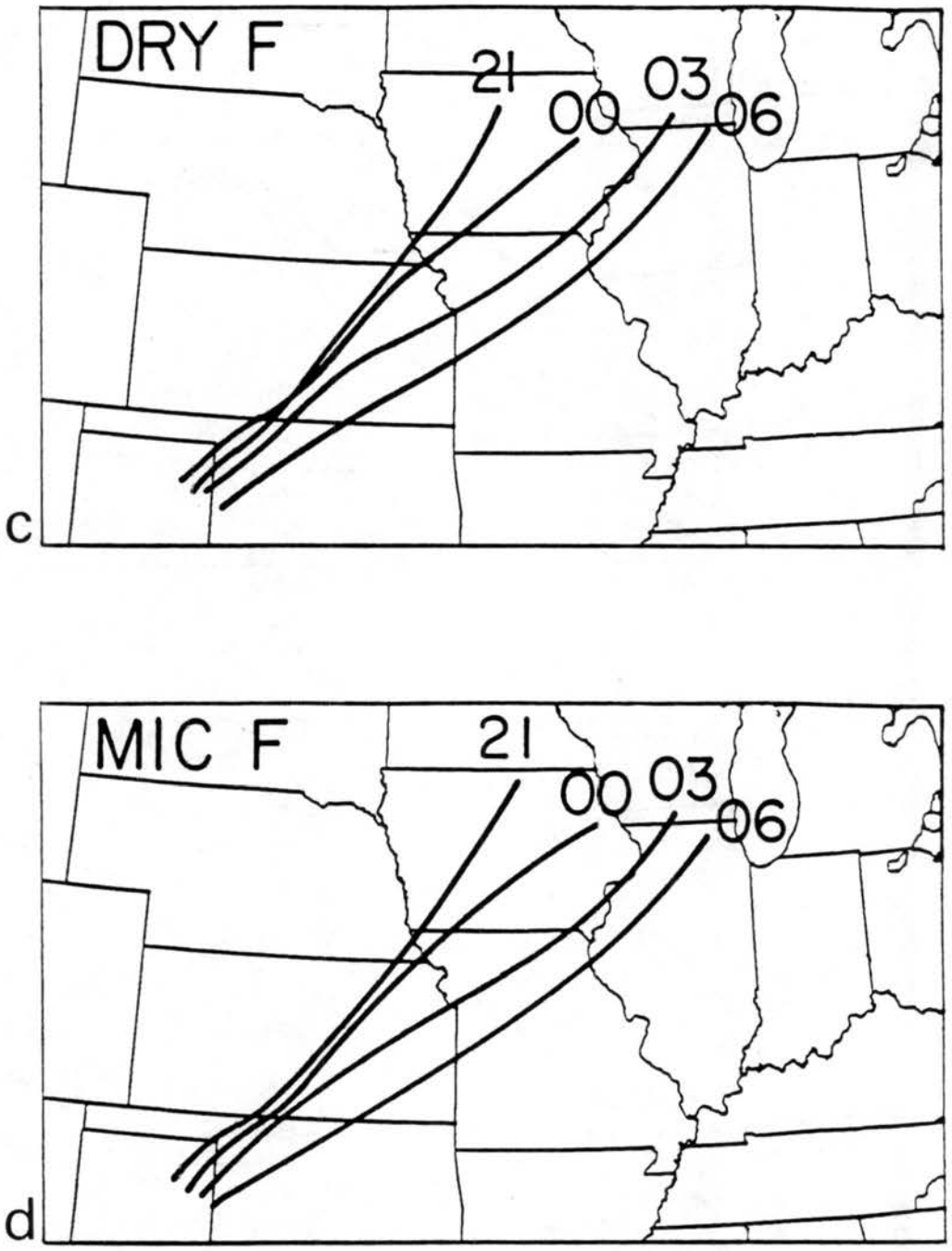

Figure 5.34: Continued: (c) DRY front; and (d) MIC front.

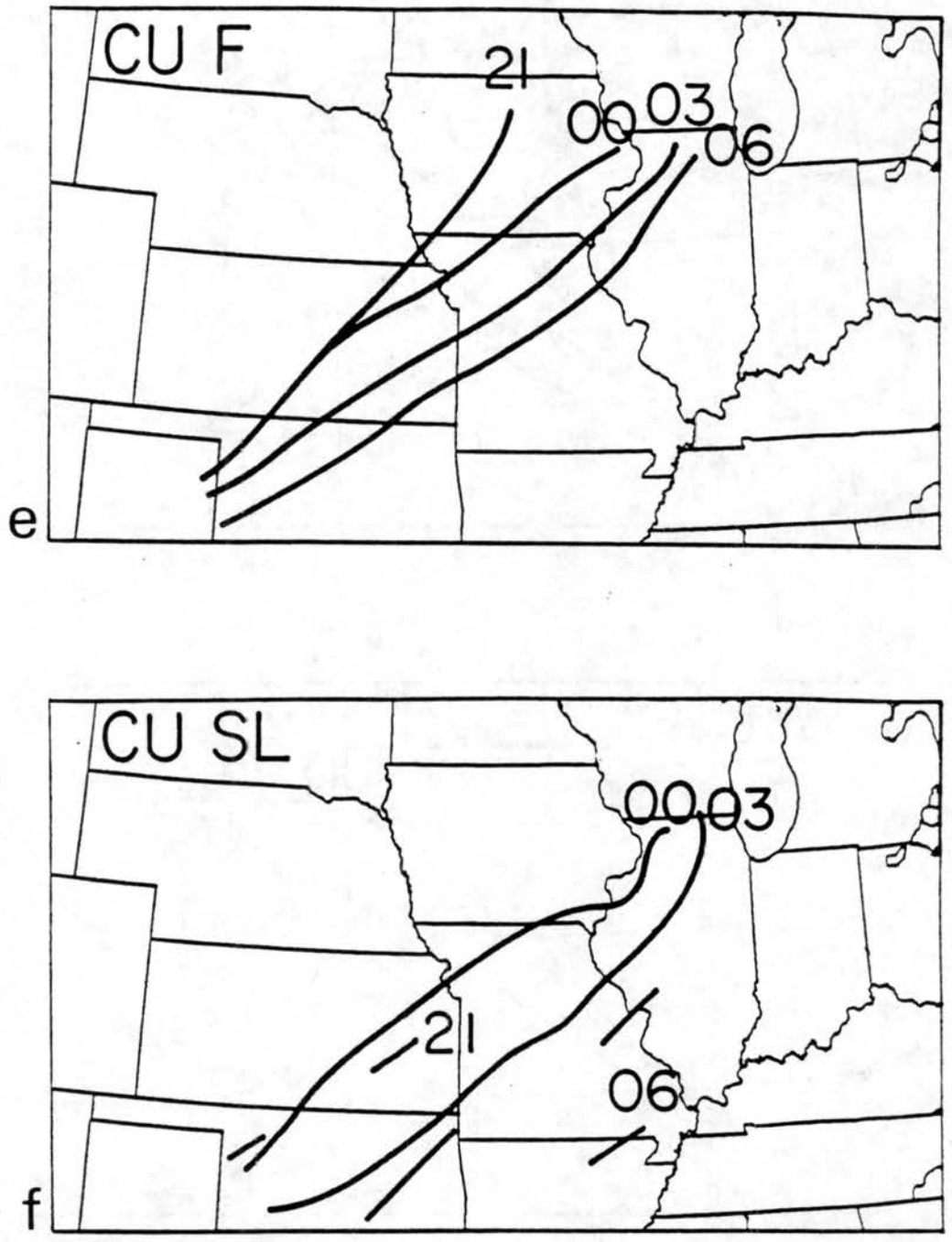

Figure 5.34: Continued: (e) CU front; and (f) CU squall line (leading edge of convective precipitation).

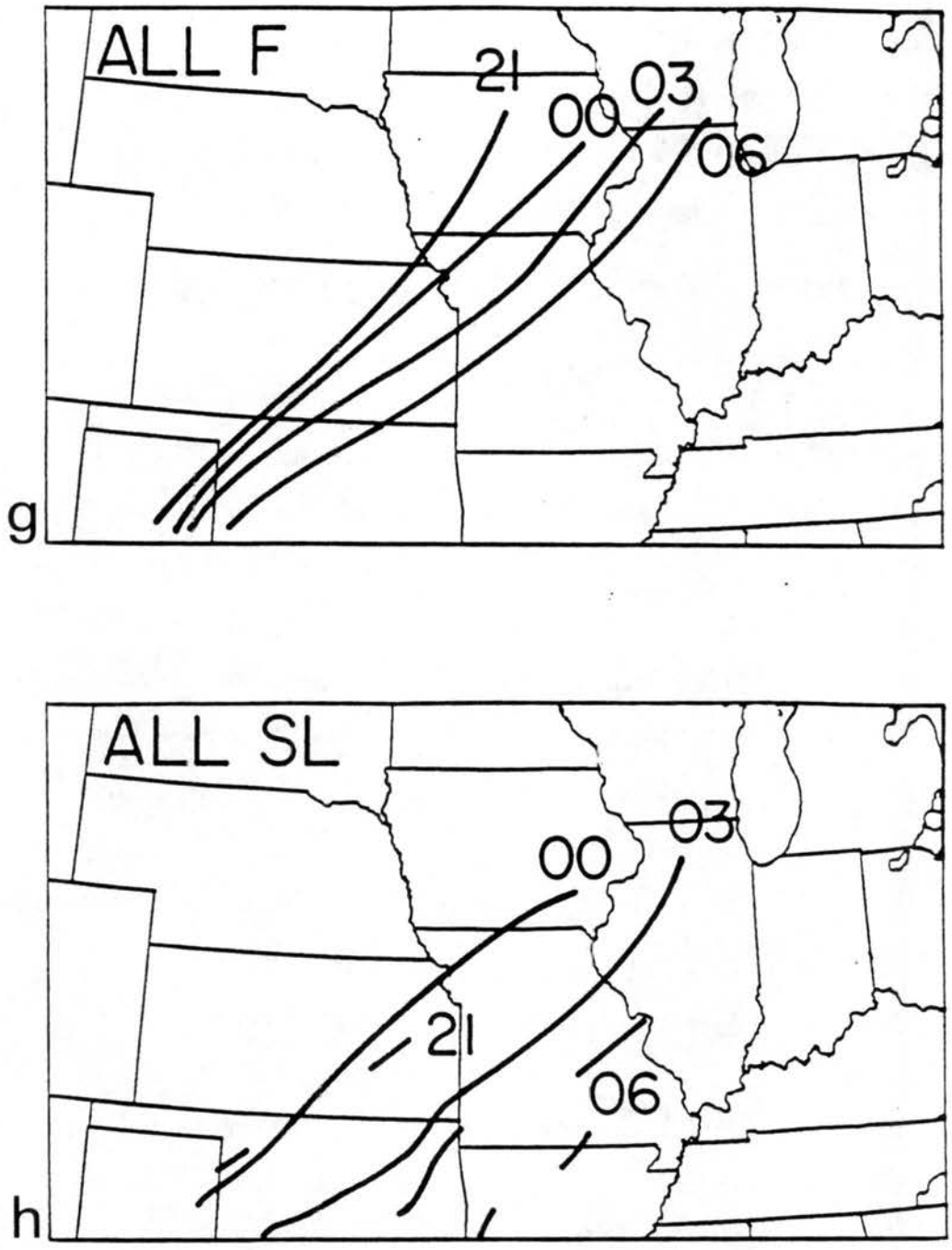

Figure 5.34: Continued: (g) ALL front; and (h) ALL squall line (leading edge of convective precipitation).

out ahead of the front between 0000 and 0600 UTC. By 0600 UTC the frontal/squall line separation is 300-400 km.

The mechanism of the squall line propagation and the frontal/squall line separation will be examined in the next section. The ALL simulation will be analyzed, although the results apply equally to both the ALL and CU simulations.

5.4 Analysis and Discussion of Squall Line/Frontal Separation and Squall Line Propagation

The squall line was initially triggered along the frontal convergence zone, but then moved southeastward faster than the front between 0000 and 0300 UTC, resulting in a squall line/front separation of approximately 300 km after 3 hours. The most commonly cited mechanism for squall line propagation in the current literature is the forcing of new cells by the gust front or cold air outflow convergence (Moncrieff and Miller, 1976; Houze, 1977; Ogura and Liou, 1980; Thorpe *et al.*, 1982; Smull and Houze, 1985, 1987; Kessinger *et al.*, 1987; Rotunno *et al.*, 1988; Johnson and Hamilton, 1988; Zhang and Gao, 1989). In the model simulations, the squall line propagated equally fast in both the CU and ALL simulations, which implies that the explicit microphysical processes and precipitation effects in the ALL simulation did not play a significant role in the propagation. The modified version of the Kuo-type cumulus parameterization scheme does include an option for downdrafts in the cloud model (discussed in Section 4.2.6 and Tremback, 1990), which was used in both the CU and ALL simulations. An additional sensitivity experiment was completed to test the effects of not using the downdraft model, and the overall squall line propagation and squall/line frontal separation was similar to the results of the CU and ALL simulations. Cross sectional analyses of temperature and wind fields showed no indication of low-level cold air outflow or that the "new convection", i.e. the leading edge of the activation of the cumulus parameterization scheme, was initiated by any sort of gust front.

The second possible mechanism considered for the squall line propagation was advection by the upper level winds, or the existence of a steering level (Newton, 1950; Moncrieff,

1978; Bluestein and Jain; 1985). The squall line translated southeastward at 15-22 m s^{-1}. If individual elements of the line were actually moving eastward, with the same total translation of the line, the eastward propagation speed would be 21-31 m s^{-1}. Figures 5.35 and 5.36 are vertical east-west cross sections (cross section location shown in Fig. 5.5) through the squall line from the ALL simulation at 0000 UTC of eastward and southeastward wind components respectively. Both figures are east-west cross sections, but the squall line was oriented northeast-southwest. The wind speeds in Fig. 5.35 are thus for the component towards the right in the figure, but towards $-45°$ with respect to the squall line propagation (if 0° is towards the southeast), while the wind speeds in Fig. 5.36 are for the component perpendicular to the squall line but at an angle to the figure. Both figures show that the squall line movement was significantly faster than the environmental winds in the model.

A third option considered to explain the squall line movement was the propagation of gravity waves. It is hypothesized in this study that, in the model simulations, the squall line propagated away from the front as a vertically trapped gravity wave in a wave-CISK-like process. The gravity wave was forced by the vertical profile of the heating associated with the convection, and the circulations associated with the wave served to maintain the convection and heating. The wave extended vertically throughout most of the troposphere and was reflected from above mostly by the difference in stratification across the tropopause and from below by a layer in which the Scorer parameter decreased to zero. The possibility of over-reflection and resonance of the wave will also be discussed in section 5.4.2. The wave traveled horizontally at about 18 m s^{-1} and was in phase with the convection from about 0000 to 0300 UTC, resulting in the squall line/frontal separation. After that time the wave dissipated and did not serve to reinforce the propagating convection, which then decreased in intensity and slowed down significantly. The structure and movement of the wave will be discussed in Section 5.4.1. It will be shown in that section that the phase relations of the model variables are consistent with gravity wave motion.

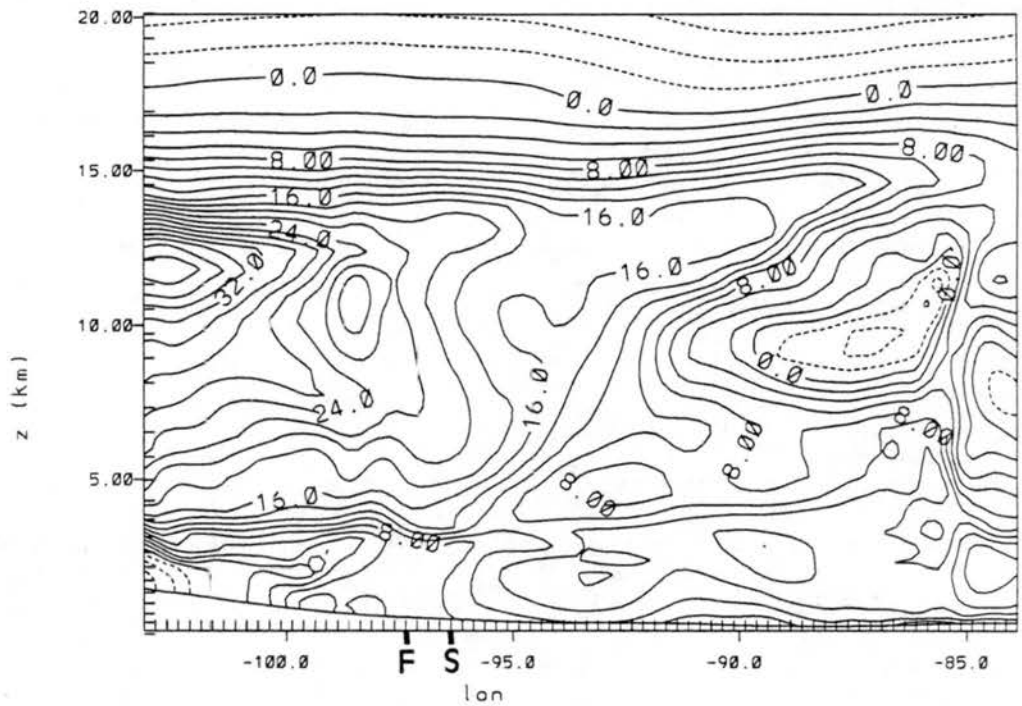

Figure 5.35: Vertical east-west cross section of wind speed (m s^{-1}) component towards the east in the ALL simulation at 0000 UTC 18 June. The surface front position is marked with an F and the squall line position (leading edge of convective precipitation rate) is marked with an S.

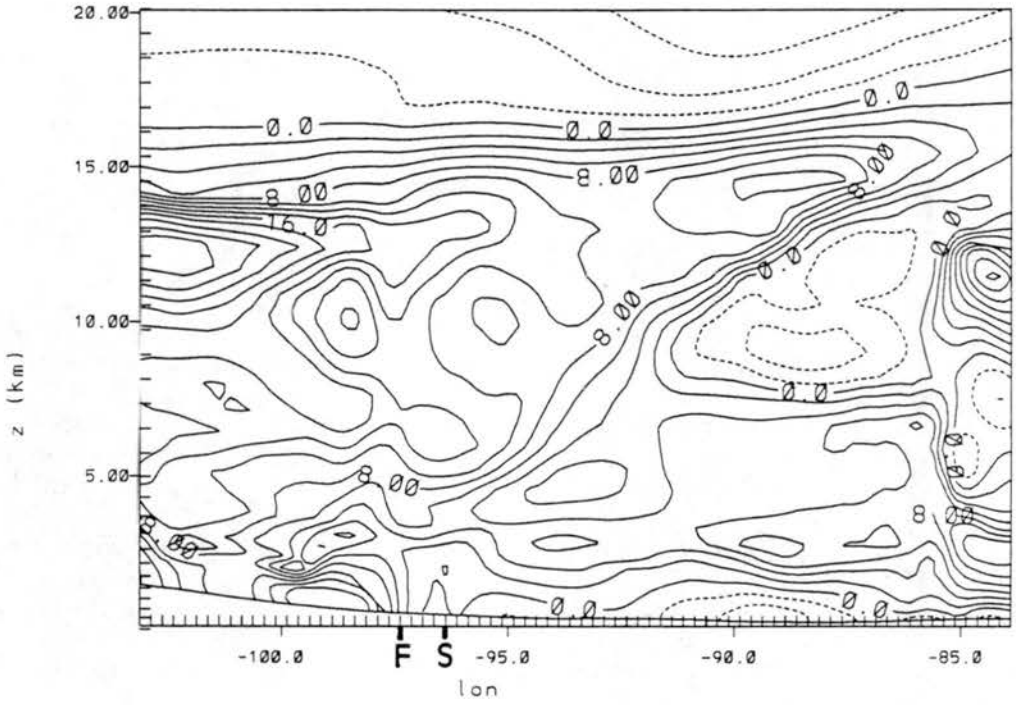

Figure 5.36: Vertical east-west cross section of wind speed (m s^{-1}) component towards the southeast in the ALL simulation at 0000 UTC 18 June. The surface front position is marked with an F and the squall line position (leading edge of convective precipitation rate) is marked with an S.

The mechanisms for the wave maintenance, propagation, and eventual demise in the ALL simulation will be further analyzed in Section 5.4.2.

5.4.1 The identification of the gravity wave

Figure 5.37 is a schematic of the hypothesized gravity wave motion associated with the squall line. Simple gravity wave theory was reviewed in Section 2.3. Figures 5.38 and 5.39 (cross section location shown in Fig. 5.1) are hourly east-west cross sections through the squall line of vertical motion, wind component perpendicular to the squall line, and potential temperature from 0000 through 0300 UTC 18 June. The hypothesized gravity wave motion is superimposed on these figures. Although, of course, there are many scales of motion occurring at the same time in the model simulation, the relations of the perturbations of horizontal and vertical motion, and the slopes of the θ surfaces, are consistent with gravity wave motions. The leading edge of the front and squall line are also indicated in each figure. The leading edge of the squall line is the leading edge of the active cumulus parameterization scheme, and thus also the leading edge (but not the maximum) of the heating. Figure 5.40 is a typical vertical profile of the heating associated with the cumulus parameterization scheme. The heating maximum was generally located at 7-9 km above the ground, which corresponds well to the center of the upper rear wave cell, as it should in gravity wave theory. The point of maximum heating in the horizontal can be identified from the vertical cross sections of potential temperature. At a given vertical level, the pressure surfaces are relatively flat, which implies that the variation of θ along a z surface is mostly due to temperature perturbations. Thus the θ surfaces bulge most through the centers of the cells while the pressure surfaces bulge at the tops and bottoms of the cells (Fig. 5.37). The slopes of the θ surfaces in Fig. 5.38 indicate that the areas of heating and cooling are consistent with the gravity wave structure in Fig. 5.37.

Figure 5.41 shows horizontal cross sections of vertical motion and pressure at 3.1 km at hourly intervals. The hourly plots of convective precipitation rate shown in Fig. 5.42 correspond closely to the areas of positive vertical motion at 3.1 km. The vertical motion at low levels is "turning on" the cumulus parameterization scheme, but the actual heating

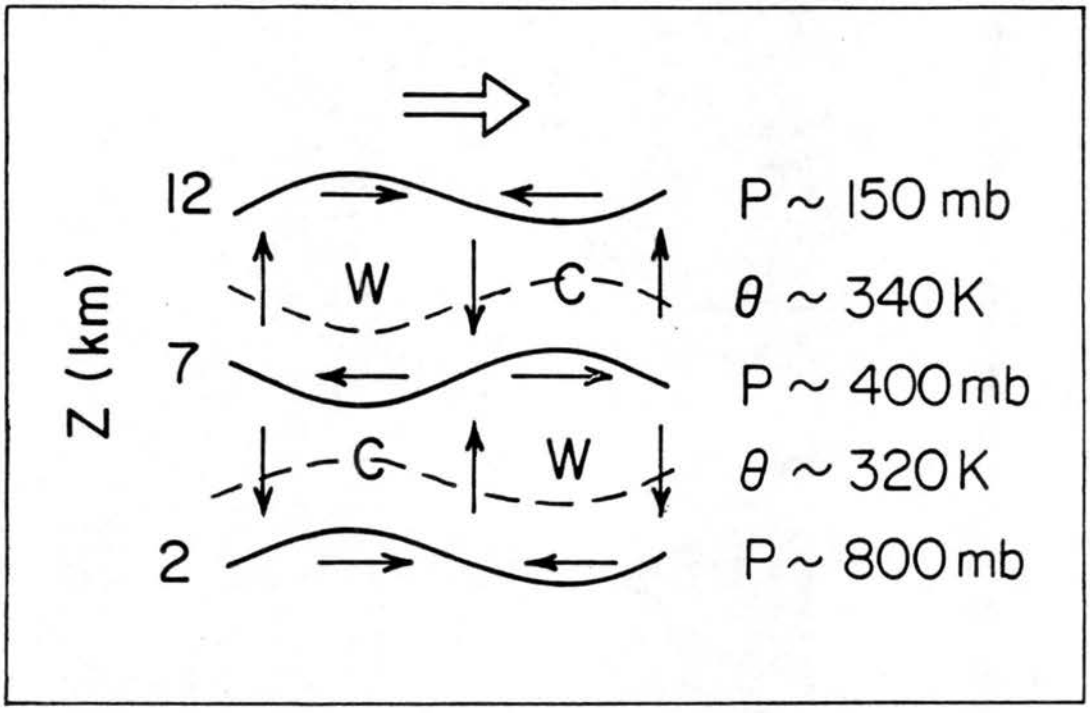

Figure 5.37: Schematic of hypothesized gravity wave motion associated with squall line.

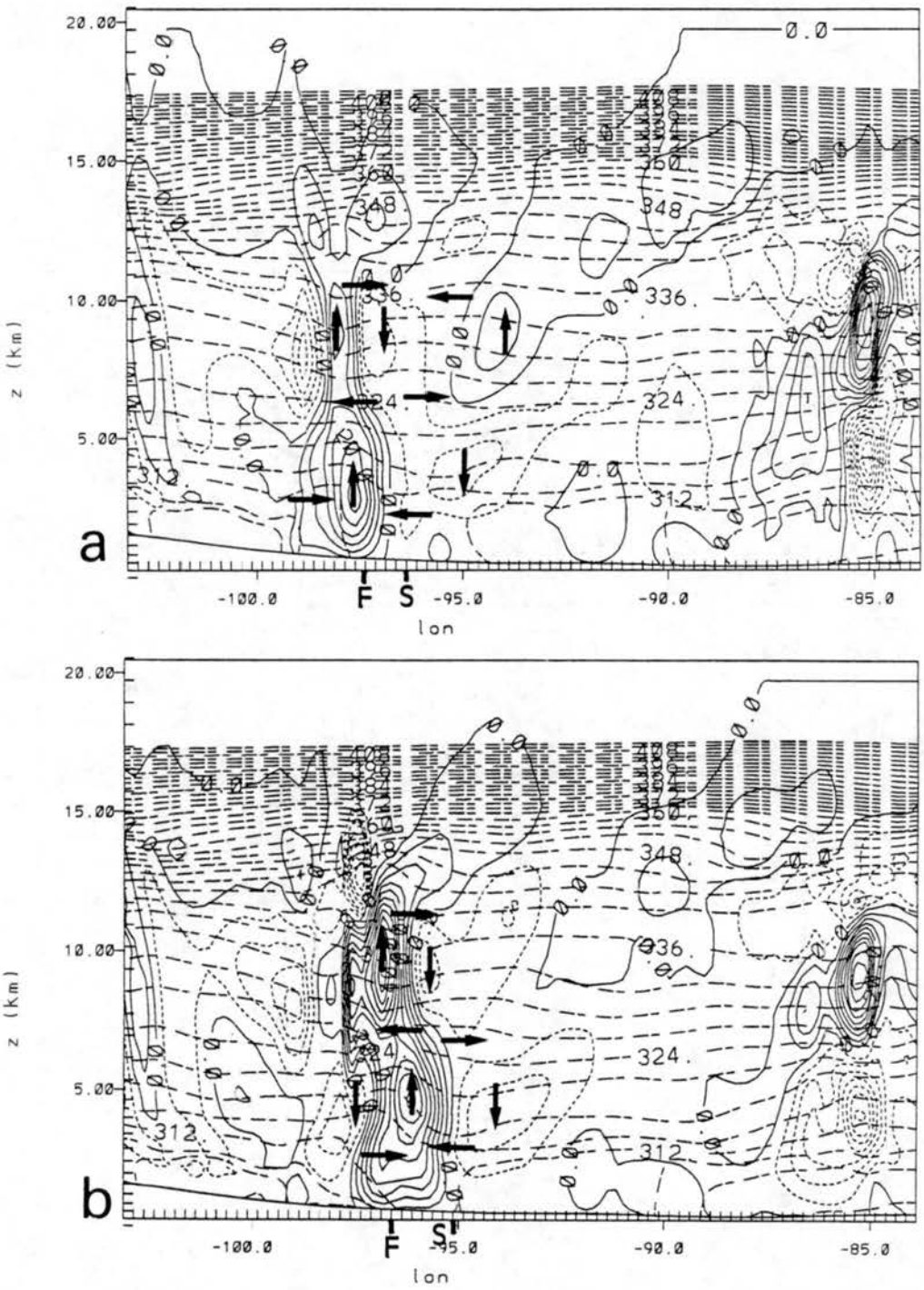

Figure 5.38: Vertical east-west cross sections of vertical motion w (m s^{-1}, contour interval is 4 cm s^{-1}, solid lines are positive value contours, short-dashed lines are negative value contours) and potential temperature θ (K, long-dashed lines, contour interval is 3 K, contours stop at 417 K) in the ALL simulation at (a) 0000 UTC; (b) 0100 UTC. Arrows are hypothesized gravity wave motions.

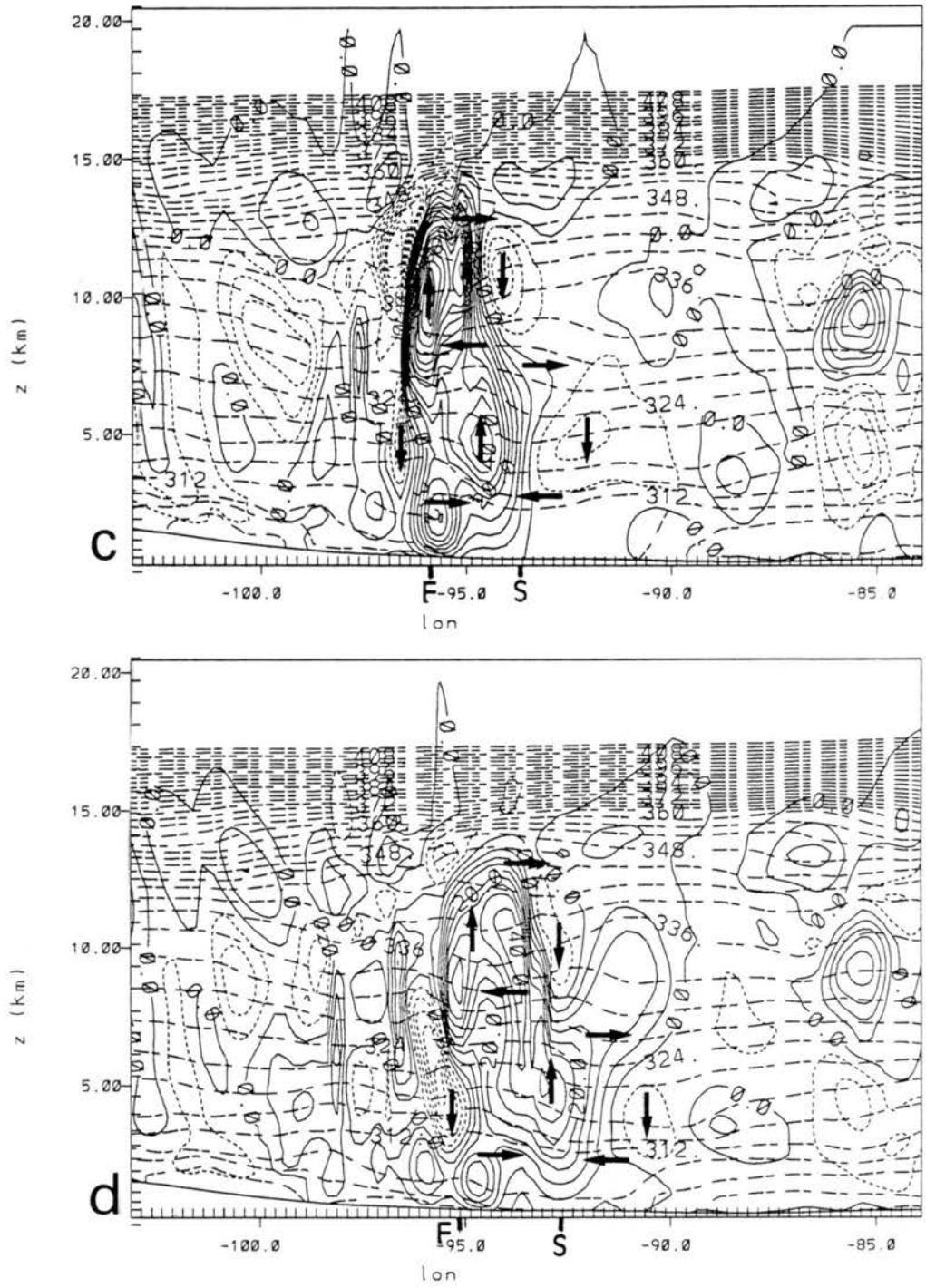

Figure 5.38: Continued: (c) 0200 UTC; and (d) 0300 UTC. Arrows are hypothesized gravity wave motions.

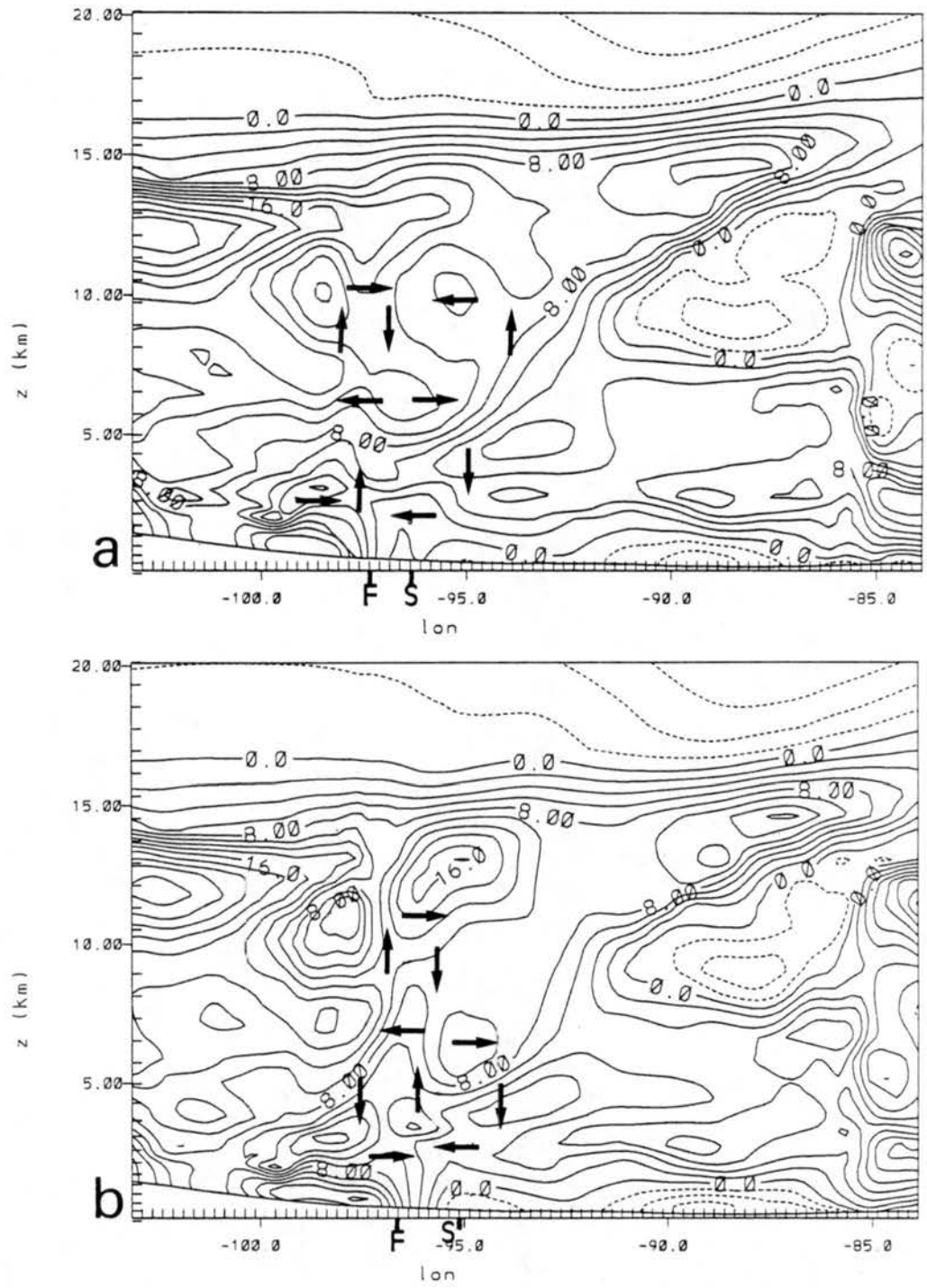

Figure 5.39: Vertical east-west cross sections of southeastward component of horizontal winds (m s^{-1}, contour interval is 2 m s^{-1}, dashed lines are negative value contours) in the ALL simulation at (a) 0000 UTC; (b) 0100 UTC. Arrows are hypothesized gravity wave motions.

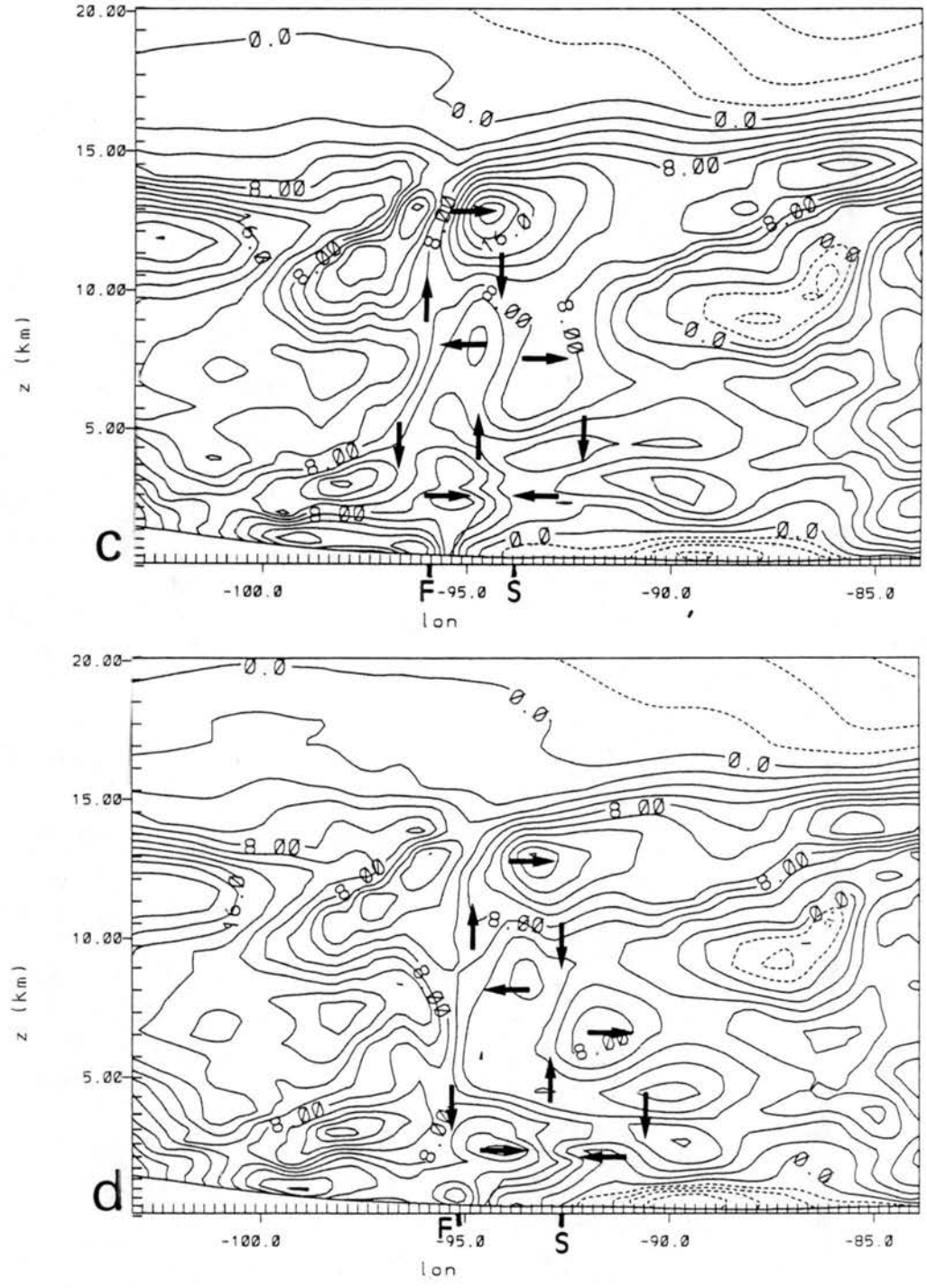

Figure 5.39: Continued: (c) 0200 UTC; and (d) 0300 UTC. Arrows are hypothesized gravity wave motions.

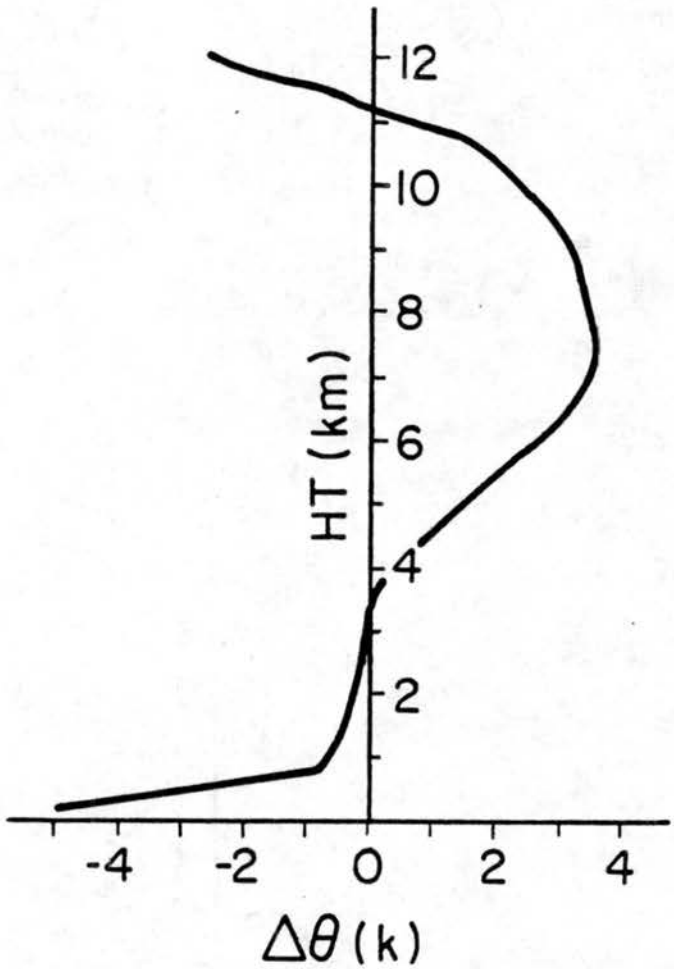

Figure 5.40: Typical heating profile (degrees K of heating per 1200 s) in the cumulus parameterization scheme as a function of height (km).

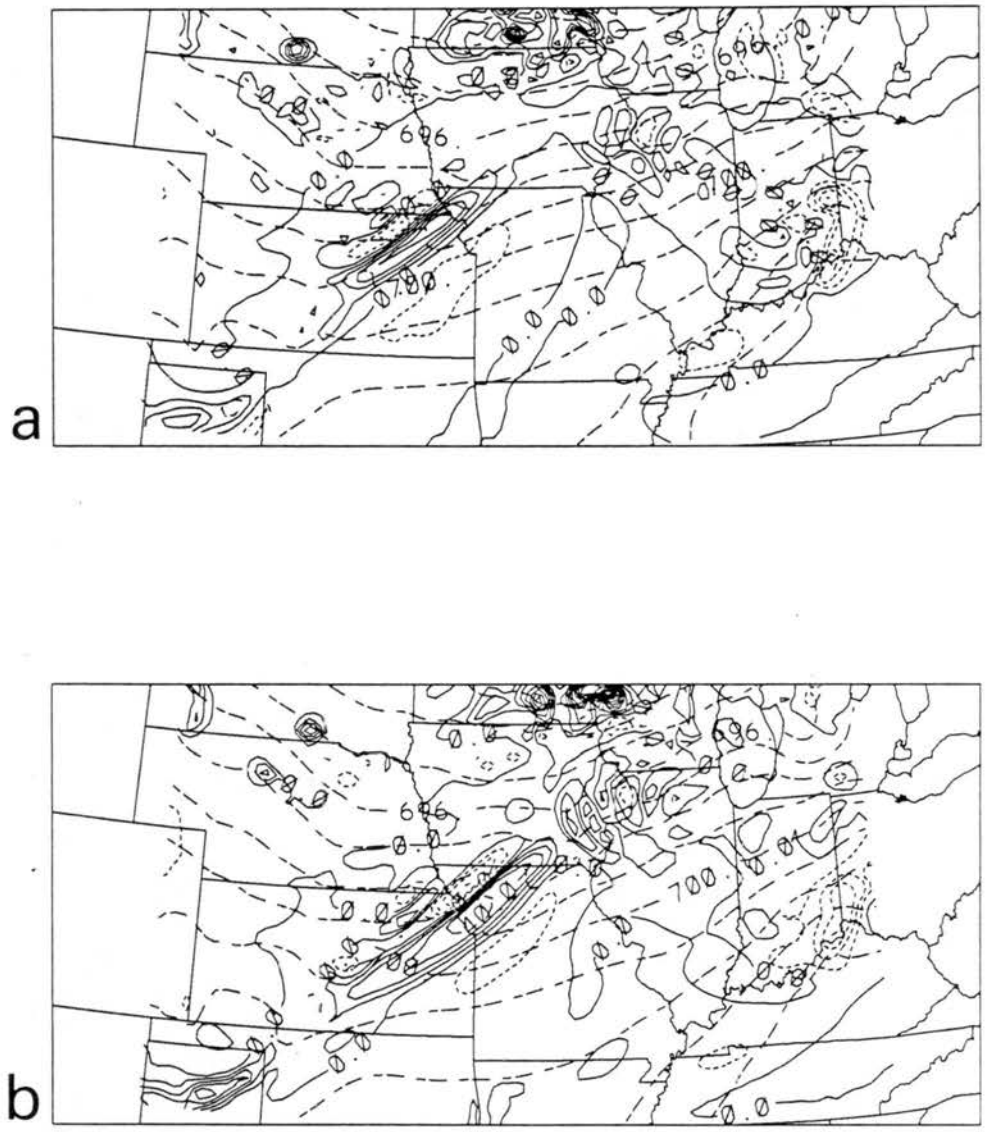

Figure 5.41: Horizontal cross sections at 3.1 km of vertical motion w (cm s^{-1}, contour interval is 10 cm s^{-1}, thin-dashed lines are contours for negative values, solid lines are contours for positive values) and pressure (mb, long-dashed lines, contour interval is 1 mb) in the ALL simulation at (a) 0000 UTC; (b) 0100 UTC.

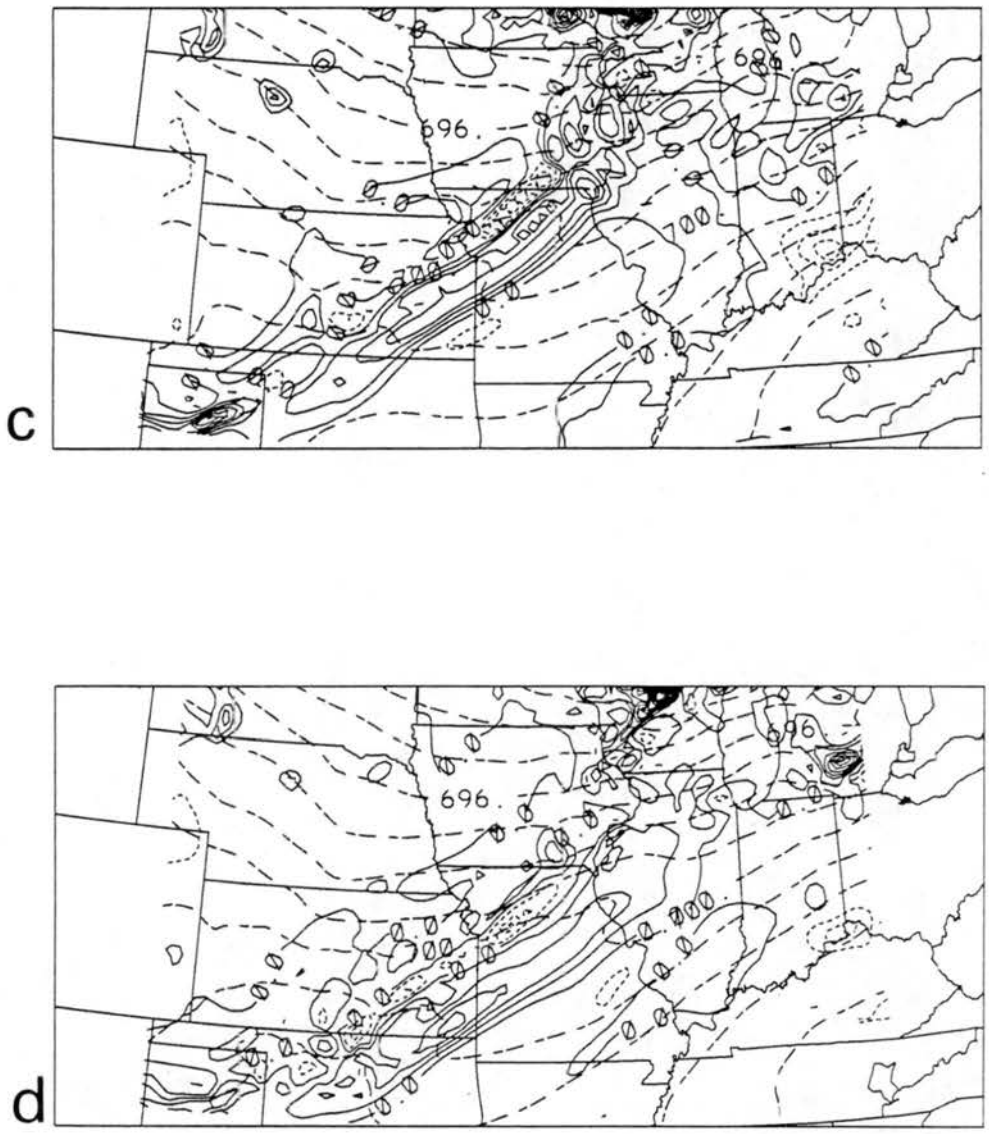

Figure 5.41: Continued: (c) 0200 UTC; and (d) 0300 UTC.

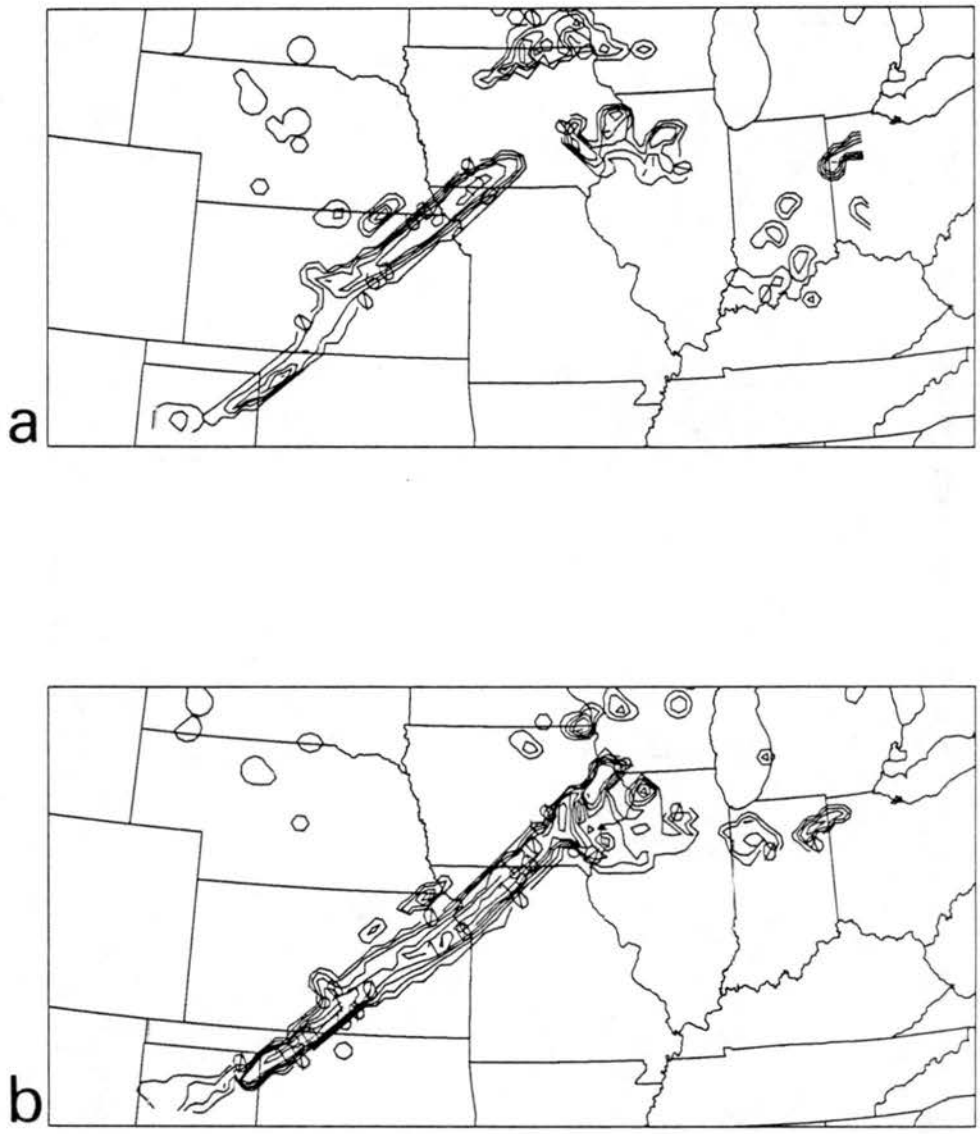

Figure 5.42: Convective precipitation rate (mm/s, contour interval is .0003) in the ALL simulation at (a) 0000 UTC; and (b) 0100 UTC.

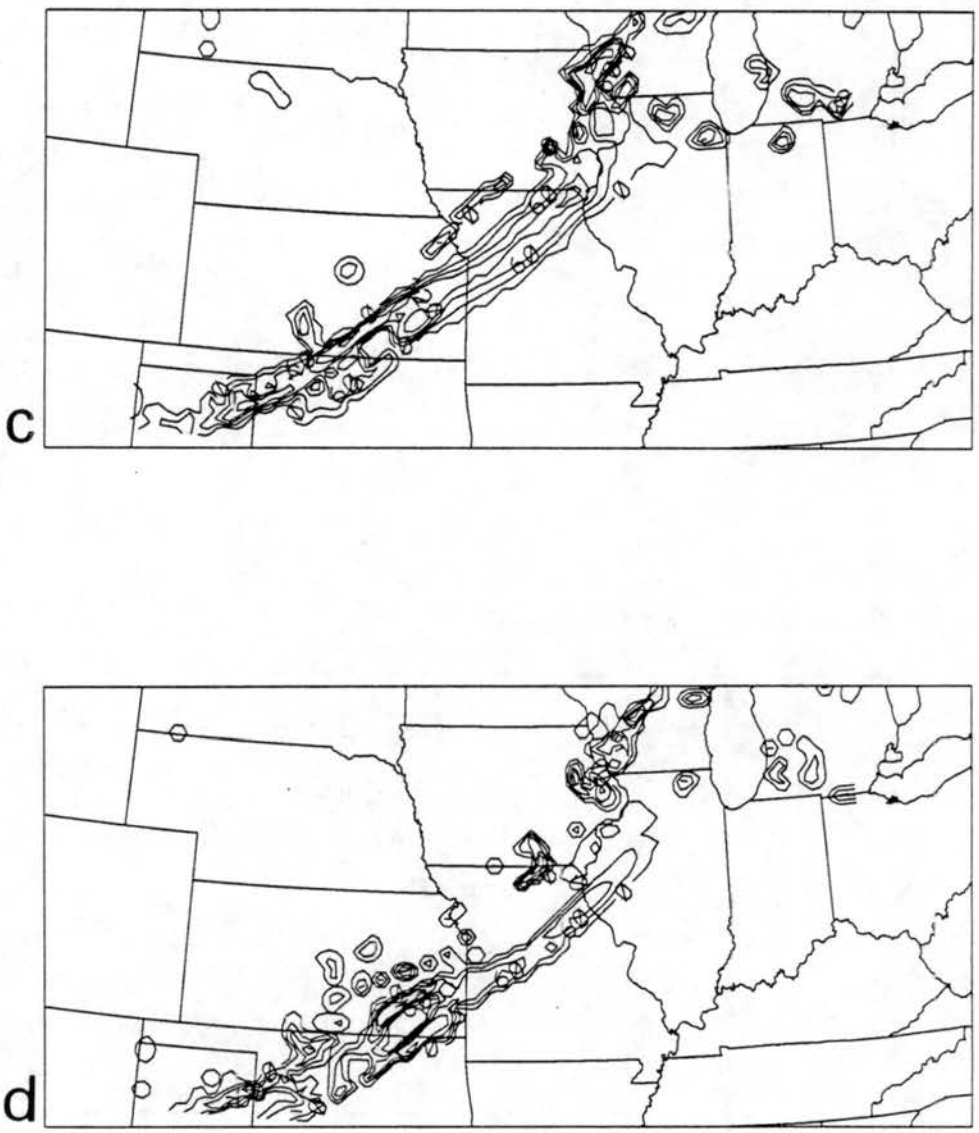

Figure 5.42: Continued: (c) 0200 UTC; and (d) 0300 UTC.

produced by the scheme is concentrated at higher levels. The "turning on" of the convective parameterization scheme does not necessarily correlate with the maximum in heating in the horizontal as there is a time lag built into the parameterization. The convective parameterization scheme is only "turned on" at finite intervals (representative of the time scale of the clouds) by checking whether a grid box meets certain criteria, but its effects then extend through that next interval. The interval in this case was 20 minutes. The area of upper level maximum heating is best diagnosed from the θ surfaces in Fig. 5.38, and is located approximately 1/4 of a horizontal wavelength behind the maximum upward motion at low levels. The lowest point of the leading trough corresponds closely to the boundary between downwards and upwards vertical motion, as it should in a gravity wave. The top of the ridge corresponds less clearly to the rear edge of the vertical motion, as there also seem to be smaller scale waves propagating rearwards relative to the squall line, superimposed upon the larger, squall line-scale gravity waves.

The propagation of the squall line as a gravity wave has been shown in this section. As this is not a horizontally-homogeneous simulation, the model fields contain many differing scales of motion, even at the initial time. It is not always possible to differentiate the scales and unequivocably determine which motions and which scales are associated with the gravity waves. However, there is a very time-coherent vertical motion profile associated with the squall line that agrees well with the simple four cell gravity wave schematic proposed in Fig. 5.37. The horizontal motion perturbations and the potential temperature perturbations also agree well with the schematic. The rearward two cells are the strongest, and correspond to the heating by the cumulus parameterization scheme. The forward two cells are weaker, although the lower cell can be consistently found in the analyses. The gravity wave structure of the squall line is very similar to the structure of the wave in the wave-CISK model of Xu and Clark (1984) (discussed in Section 2.4). The mechanism of the gravity wave development and propagation in the ALL simulation will be summarized in Section 5.4.2.

5.4.2 The maintenance and propagation of the gravity wave in the ALL simulation

Specific characteristics of the gravity wave described in Section 5.4.1 will be compared to theory in this section. The horizontal wavelength and speed, the vertical wavelength, the trapping mechanism, the initial forcing, and the lifetime of the wave will be discussed in relation to the gravity wave discussion in Section 2.3, and the Xu and Clark (1984) model discussed in Section 2.4.

Horizontal wavelength

The wavelength of the diagnosed wave in the ALL simulation is ~200-300 km. The width of the low-level upward motion shown in Fig. 5.41 was on the order of 100-150 km, and corresponds to one half of the total horizontal wavelength. The width of the active convection is also on the order of 100-200 km. The horizontal grid spacing in the ALL simulation was 20 km so the waves are adequately resolved at this scale. As discussed in Section 2.3, Lindzen and Tung (1976) suggested that the wave could be forced by the time scale of convection. A time scale of 1800 seconds (one-half hour) implies a horizontal wavelength of 200 km, defined by Eq. (2.13). Xu and Clark found a horizontal wavelength of 114 km in their wave-CISK model for their specific situation. However, they point out that the wavelength of the maximum instability will increase as the time scale of the cloud life-cycle increases (very similar to Lindzen and Tung's calculation). They used a time scale of 2000 seconds. Both of these results are consistent with the results from the ALL simulation.

Horizontal wave velocity

The speed of the wave in the ALL simulation is near 18 m s^{-1}, although it does vary between 15 and 22 m s^{-1}. The environmental winds vary both in the horizontal and vertical, with the average speed perpendicular to the squall line on the order of 5-10 m s^{-1}. Lindzen and Tung (1976) estimated the horizontal speed of a mode in a duct with Eq. (2.10) (discussed in Section 2.3). Substituting $N = 0.8 \times 10^{-2}$ s^{-1}, $H = 10$ km,

for the $n = 1$ mode ($n = 1$ in Lindzen and Tung's equation is equivalent to $n = 2$ in Xu and Clark's formulation), then $c = 17$ m s^{-1}. Xu and Clark (1984) found a wave speed of 16.7 m s^{-1} for their 114 km wave, and noted that as k decreases, c will increase. Using Fig. 2.30a (from Xu and Clark, 1984), if k decreases from 5.5 to 3 (or the wavelength increases from 114 to 200 km), then c will increase from 16.7 to 18 m s^{-1}. Again, both of these results are consistent with the results from the ALL simulation.

Wave/disturbance direction

Nehrkorn (1986) did a series of sensitivity experiments with a wave-CISK model and showed that the orientation of the disturbance axis (axis of the squall line) relative to the symmetric axis (axis of the wind shear) was sensitive to the form of the vertical heating profile. Nehrkorn found that a mid-tropospheric level of maximum heating resulted in the disturbance axis being rotated 20-30° from the symmetric axis, implying upshear propagation, while for higher levels of maximum heating the disturbance is more nearly aligned with the shear vector, or perpendicular to the baroclinic axis. However, Nehrkorn's atmosphere was very simple in that the wind shear was constant throughout the troposphere, and thus the axis of baroclinicity was the same at all levels. In this case (17-18 June 1978) the squall line axis is oriented perpendicular to the surface baroclinic axis (Figs. 5.25a and 5.26a) and the convective heating maximum is in the upper troposphere, at about 8 km (Fig. 5.40), in agreement with Nehrkorn's findings.

Vertical wavelength

According to Xu and Clark (1984) the vertical wavelength in their wave-CISK model is forced by the convective heating profile. That also appears to be the case here. The vertical wavelength in this case is approximately 10 km and in Xu and Clark's results it is approximately 8 km. The wave in the ALL simulation extends from 2-3 km to ~12 km. Figure 5.40 showed a typical heating profile associated with the convective parameterization in the ALL simulation, and it is very similar to Xu and Clark's profile (Fig. 2.28). Xu and Clark noted that minor changes in the profile did not strongly affect

the results. The level of maximum heating in Fig. 5.40 is at approximately 7-8 km above the ground which is at about 8-9 km elevation in the model, at the center of the upper cell. The height of "cloud base", or the level at which the heating profile becomes positive, is at 3.5 km in Fig. 5.40, or at .30 of the nondimensional height, again very similar to Xu and Clark's normalized level of 0.34.

Vertical trapping and reflection of the wave

The wave in Xu and Clark's model is reflected from the ground at the bottom and from the discontinuity in stability at the tropopause at the top. In the ALL simulation the wave appears to be reflected from the top by the change in stability, with an additional possible effect of a critical layer. The wave in the ALL simulation does not extend to the ground, and appears to be reflected from downward propagation by a low-level layer where the Scorer parameter decreases to zero (see Section 2.3 for a discussion of the Scorer parameter and wave trapping). The stability in the stratosphere was 3-5 times the stability in the troposphere in the ALL simulation, leading to a reflection coefficient of .50-.66, again similar to Xu and Clark's results. In addition, forward moving outflow from the top of the "convective clouds" and from the forward moving top branch of the gravity wave seemed to produce local areas of a possible critical level (see Section 2.3 for a discussion of the critical level). Figure 5.43 shows east-west cross sections (location shown in Fig. 5.1) at 0200 UTC (at the peak of the squall line) of the squared Brúnt Väisäla frequency, vertical wind component, wind component perpendicular and relative to the squall line (assuming the squall line was moving at 18 m s^{-1}), and the Scorer parameter (defined as $m^2 = \frac{N^2}{(U-c)^2}$, where N^2 and U are the locally defined values and $c = 18$ m s^{-1}). The plot of the relative horizontal wind component (Fig. 5.43c) shows that it decreases to zero just at the top and forward edge of the wave. The cross section of vertical motion in Fig. 5.43b shows that the main part of the wave does indeed extend from approximately 2-12 km. The upward motion at the surface behind the leading edge of the wave is forced by the frontal convergence and not a part of the main gravity wave. Figure 5.43d shows the layer where the Scorer parameter is close to zero extending from

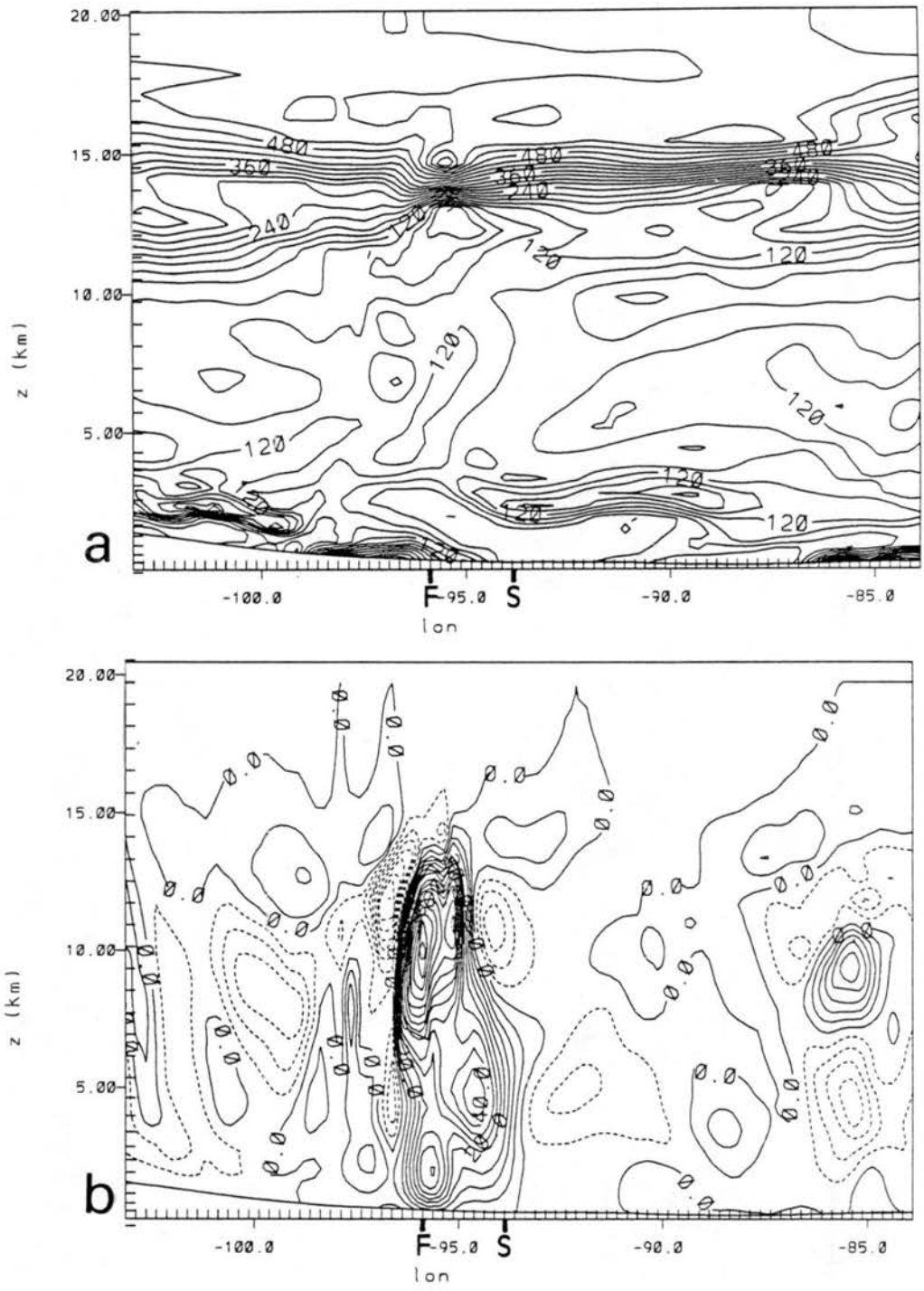

Figure 5.43: East-west cross sections at 0200 UTC of (a) the Brúnt Väisäla frequency (s^{-2}, contour interval is .00003); and (b) vertical wind component w (cm s^{-1}, contour interval is 5 cm s^{-1}, dashed lines are negative value contours, solid lines are positive value contours).

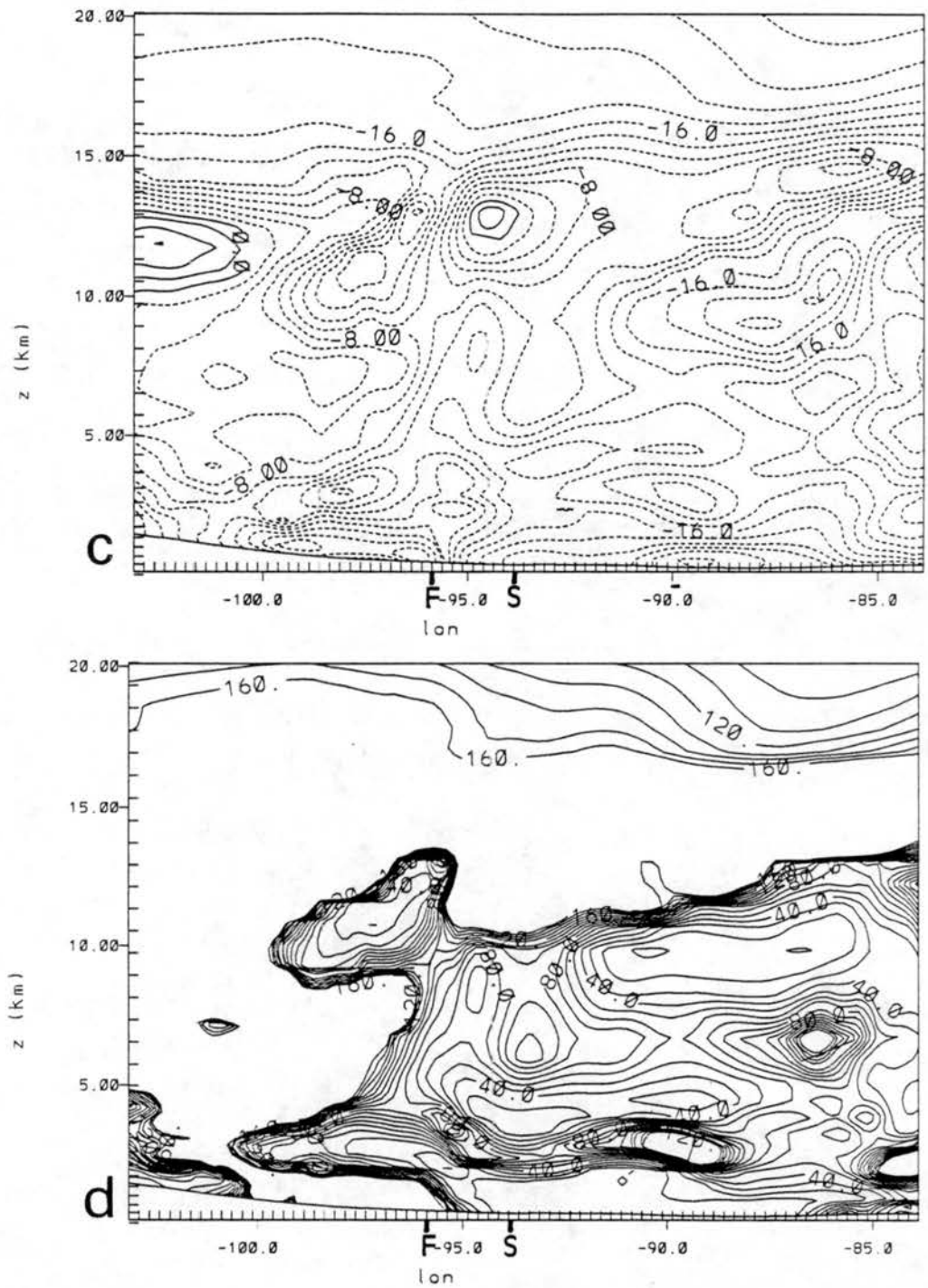

Figure 5.43: Continued: (c) wind component perpendicular and relative to the squall line (m s^{-1}, wind component in southeast direction minus 18 m s^{-1}), contour interval is 2 m s^{-1}, dashed lines are negative value contours); and (d) Scorer parameter (m^{-2}, contour interval is 10, contour upper limit is 160).

the surface to approximately 2 km. This seems to be a result of the very large increase at that level in the low-level wind speeds relative to the wave movement.

An additional possible mechanism for the wave-trapping could be cloud-top radiative cooling. The radiation scheme used in these simulations does not explicitly account for cloud top radiative cooling. Tripoli and Cotton (1989a,b) found that upper level cloud-top cooling produced an adiabatic layer which trapped a meso-α scale gravity wave beneath it. An additional simulation of this case was performed using the Chen and Cotton (1983a,b) radiation parameterization, but otherwise the same as the ALL simulation. The Chen and Cotton radiation parameterization was briefly described in Section 4.2.10 and does allow for radiative cooling from clouds. The results from that simulation were very similar to those from the ALL simulation. Although the Chen and Cotton scheme does account for cloud-top cooling, the very low concentrations of condensate produced in these simulations would therefore result in very little cooling.

The possibility that the wave could be incorrectly trapped or reflected by the model top also needs to be considered. The model top in these simulations was at 20 km, with a modified Rayleigh friction layer extending from 15-20 km (discussed in Section 4.2.12). There is no evidence in the vertical cross sections shown in Figs. 5.38, 5.39, or 5.43 of the wave extending above the tropopause or up into the Rayleigh friction layer.

Initial forcing of the wave

The wave hypothesized in Fig. 5.37 is two cells wide in the horizontal (over one horizontal wavelength) and two cells deep in the vertical. The forward two cells are much weaker than the rearward two cells in the simulation, but the forward lower cell is consistently found in the analyses. The rearward two cells are forced by the heating profile in the convective parameterization scheme, as in Xu and Clark's model. The maximum in the heating is at 8-9 km elevation in the model which corresponds to the center of the upper cell, with its horizontal maximum located in the center of the cell (as indicated by the potential temperature cross sections in Fig. 5.38).

The initial forcing for the forward two cells is less obvious. They are ahead of the heating-forced rearward two cells so they cannot have been directly forced by that heating profile. It is possible that the circulation forced by the rearward two cells could force the forward two cells. The cumulus parameterization is initially forced by the low-level upward motion between the lower two cells. The heating then extends back from the low-level upward motion and forces the rearward two cells. The circulations between the forward and rearward cells are interconnected, so if the forward cells are forced by the rearward cells, it would be consistent that the forward cell circulations are much weaker.

Lifetime of the wave

The motions of the gravity wave and of the squall line are most coherent from 0000-0300 UTC. The squall line convection does not get fully organized until almost 0000 UTC in both the observations and ALL simulation. Between 0300 and 0600 UTC, the convective line structure in both the ALL simulation and observations weakens and becomes much less organized. The gravity wave perturbations in the ALL simulation are most readily identifiable between 0000 and 0300 UTC. As stated previously, the initial forcing of the gravity wave is directly tied to the line of frontal convergence. As the gravity wave propagates from 0000 through 0300 UTC, the upper rear cell of the wave (where the heating is occurring) gradually rises and widens. Several possible mechanisms are outlined below that can help explain how this occurrence led to the demise of the wave.

The first mechanism is that the heating maximum widens with time (as the squall line widens and weakens in both the simulations and observations) and the 90° phase lags between the low-level upward motion, the upper level heating maximum, and the upper level upward motion are gradually lost. Once the phase lags between the upward motion and heating maximum are gone, the gravity wave structure and wave-CISK feedback mechanism are destroyed and the wave can no longer maintain itself.

The second mechanism is that as the heating maximum rises and widens, the structure of the gravity wave changes and the reflection/resonance process becomes less efficient. The resonance process works most constructively when the heating maximum is 1/4

wavelength from the tropopause stratification discontinuity and 3/4 wavelength from the bottom reflective surface. As the heating maximum rises, it may lose those 1/4 wavelength intervals and thus lose the positive resonant effect.

A third mechanism is that the convective outflow produces a critical layer (a layer in which the wind velocity is equal to the wave speed) within the duct which then interferes destructively with the wave reflection and resonance. The critical layer gradually develops over time from 0000 through 0300 UTC (Fig. 5.39) and is strongest at 0300 UTC. It was suggested previously that the critical layer could help in the reflection of the vertically-propagating wave energy. However, Lindzen and Tung (1976) pointed out that a critical layer within the wave will absorb the wave energy. If the critical layer is above the wave generation region (the level of maximum heating) it may also reflect the wave energy downwards but in a destructively resonant manner, as in the above discussion of the second mechanism.

Another possible mechanism for wave trapping is that adiabatic cooling by ascent above the level of maximum heating could create an adiabatic layer that would trap the wave below it. There is some indication of the development of a more unstable layer in the θ field above the region of maximum upper level ascent in Figs. 5.38a-d. However, the unstable layer only exists directly above the region of strong vertical motion, and thus would only serve to reflect that portion of the wave. This could help account for the stronger rearward half of the wave.

All of these mechanisms are plausible in this situation and help explain why the wave in the ALL simulation rapidly disappeared after 0300 UTC. Although the leading edge of the radar echoes does continue to propagate southeastward between 0300 and 0600 UTC (Figs. 3.7 and 5.34b), the echoes become weaker and there is evidence of a less linear propagation. The total propagation of the squall line in the ALL simulation did not stop at 0300 UTC, but its linear structure did weaken after that.

The analyses in this section first established that the relative motions and perturbations associated with the squall line propagation between 0000 and 0300 UTC were

consistent with gravity wave structure. Very similar results were found in a wave-CISK model by Xu and Clark (1984) (discussed in Section 2.4). Specific aspects of the modelled gravity wave were compared to theory, and the scales and time periods of the modelled motion were found to be realistic.

5.5 Comparison of Modelled Squall Line Structure to Other Studies

In this section, the structure of the squall line in the ALL simulation will be briefly compared to some of the observed and modelled structures described in Chapter 2. Figure 5.44 is a vertical cross section (location shown in Fig. 5.1) of the two-dimensional streamline field through the squall line from the ALL simulation at 0100 UTC. The cross section is along the same east-west axis as the previous cross sections, and the streamlines are calculated from the vertical motion and the horizontal motion relative to and perpendicular to the squall line. The squall line is assumed to be moving at 18 ms^{-1} in the southeastward direction. The horizontal wind component (in the southeastward direction) is adjusted to account for the fact that the streamline calculation requires the wind component and horizontal Δx to be in the same vertical plane (i.e., the wind component is multiplied by sec (45°) to account for its rotation vs. the east-west plane). As the squall line is moving faster than the environmental winds at all levels (discussed in previous section) the relative motion is all through the line from front-to-back. The streamline field is very similar to those shown in Figs. 2.7, 2.19, and 2.20 (from Ogura and Liou ,1980; Thorpe *et al.*, 1982; and Raymond, 1984) except that there is no return circulation at upper levels ahead of the squall line.

The time series of the MSLP analyses for the ALL simulation (Figs. 5.24-5.27) showed an initial pressure fall at the leading edge of the squall line with a relative pressure rise between the passage of the squall line and the front. The increase in pressure in the region between the front and squall line is consistent with observations of the surface mesohigh (Fujita, 1955; Zipser, 1977; Johnson and Hamilton, 1988). The pressure drop just ahead of the area of active convection in the ALL simulation may be construed as the presquall mesolow, but it is due to the subsidence in the propagating internal gravity wave in this

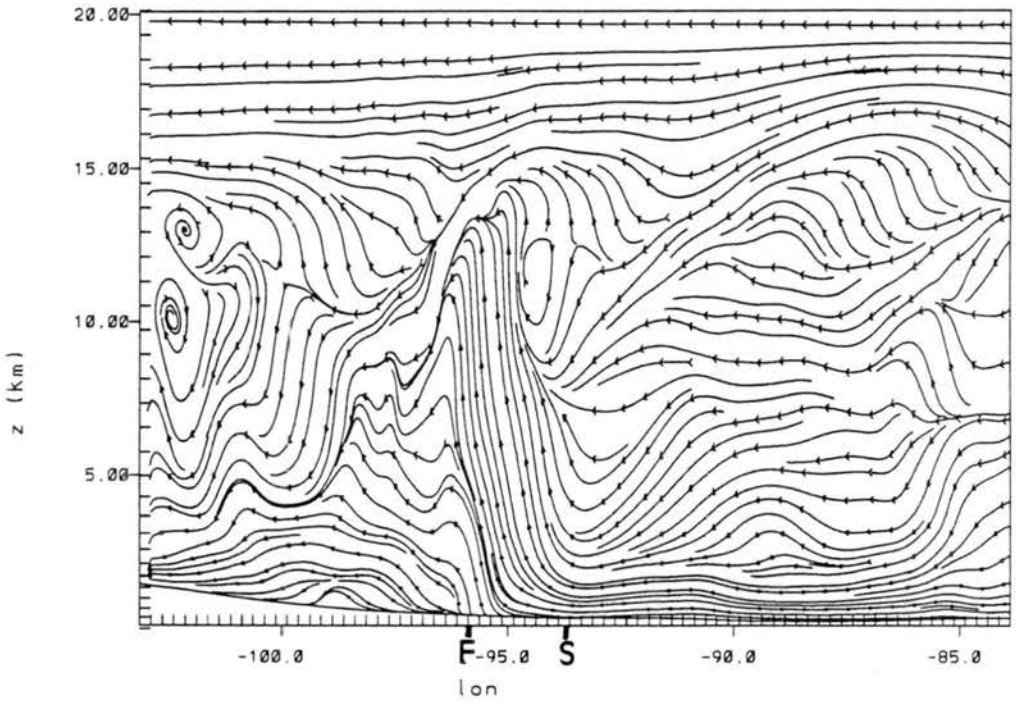

Figure 5.44: East-west cross section at 0100 UTC of the two-dimensional streamline field relative to the squall line motion, assuming the squall line is moving southeastward at 18 m s^{-1}.

case, not the preline subsidence warming postulated by Hoxit *et al.*, (1976). Zhang and Fritsch (1986, 1988a,b) and Hoxit *et al.* (1978) also found a similar offset of the convection from the trough axis for the 1977 Johnstown flood case. Zhang and Fritsch (1988b) showed that the trough in that case was due to subsidence at the leading edge of a propagating internal gravity wave. The surface pressure in the ALL simulation is at its lowest just at the edge where the convection is activated in the model, and the presquall mesolow is about 50-100 km wide.

There is not any indication in the ALL analyses of a consistent wake low region. The wake low is generally thought to be due to subsidence warming in the rear-to-front jet below the anvil region (Smull and Houze, 1987; Johnson and Hamilton, 1988). The subsidence may be initiated by evaporation from the anvil region (Zipser, 1977), or a manifestation of the subsiding rear inflow jet (Brown, 1979; Johnson and Hamilton, 1988). The lack of the wake low in the ALL simulation is probably due to the lack of any significant explicit microphysical effects in the anvil region. The outline of total condensate at 9.7 km in Figs. 5.26 and 5.27 is representative of the anvil produced only as a result of advective processes. The mixing ratios at this level (and at lower levels behind the leading "convective cores") are almost all less than 0.1 g/kg and thus indicate that any anvil latent heat production is small. Rutledge and Houze (1987) and Fan *et al.* (1988) found anvil condensate mixing ratios of 0.5-2.0 g/kg. Srivastava *et al.* (1986) did a Doppler radar study of the anvil region of the squall line on this date, but the anvil region that they studied was semi-steady and almost completely detached from the main squall line. They found reflectivities within the anvil region of 20-40 dBZ. According to Rogers (1979), these correspond to precipitation rates of 1-10 mm h^{-1}. Rutledge and Houze (1987) diagnosed anvil regions with reflectivities of 10-30 dBZ as having condensate mixing ratios of 0.4-1.0 g/kg. The maximum condensate mixing ratios in these simulations were mostly less than 0.1 g/kg.

The ALL simulation does not produce any significant cold air outflow or gust front associated with the squall line. The convective scheme used in these simulations does

have a modification for cold downdraft effects (Section 4.2.6), which show up in the profile of convective heating from the convective scheme (Fig. 5.40) as cooling below 3.5 km. As stated in Section 4.2.6, the intensity of the convective cooling is somewhat arbitrary below cloud base. A deeper or colder layer of cooling might result in a more persistent cold pool or gust front. Although cold air outflow undoubtedly occurred along portions of the squall line in reality, it was not entirely responsible for the observed squall line propagation (see Sections 3.1, 3.2). The failure of the model to produce any consistent cold downdrafts is probably due to the 20 km grid interval (and thus its dependence on the cumulus parameterization) and the lack of any significant grid-scale microphysical processes or anvil production.

Zhang and Gao (1989) modelled a squall line using a 25 km grid interval and claimed to have successfully modelled the formation of a gust front, presquall mesolow, mesohigh, wake low, and rear inflow jet. Zhang and Fritsch (1986, 1988a,b) also successfully modelled many of the meso-β scale aspects of the 1977 Johnstown flood case. The squall line in Zhang and Gao's case propagated at 14.5 ms $^{-1}$, slightly slower than the 18 m s^{-1} in this case, but in a similar environment of relatively weak shear aloft. The gravity waves simulated by Zhang and Fritsch (1988b) moved at 25-30 m s^{-1} and were coupled with the convection for a brief period. One difference in those simulations is that they used a version of the Fritsch and Chappell (1980a) cumulus parameterization scheme (hereafter referred to as FC), which has a more explicit calculation of downdraft effects than the scheme used in this study. Features such as the gust front, wake low, and rear inflow jet are all directly caused (in a model) by the successful modelling of downdraft effects and anvil processes such as mesoscale subsidence. However, Tremback (1990) has also pointed out that the FC cumulus parameterization produces unrealistically large heating rates, with the heating maximum at a very high level. Tremback found that the FC heating rates (from Fritsch and Chappell, 1980b) were 2-3 times those from the observations of Lewis (1975) (and 2-3 times the rates shown in Fig. 5.40). Zhang and Fritsch (1986) modified the FC scheme slightly for the Johnstown flood case to have smaller heating rates, but their

level of maximum heating was still very high, near 200 mb. Zack *et al.* (1985) found that the FC scheme initiated convection much more quickly than other schemes, and that the large magnitude and high level of the parameterized heating in the FC scheme initiated mesoscale ascent and saturation at low-to-mid levels. This then resulted in a much greater interaction between grid scale and parameterized heating effects. The FC scheme appears to initiate grid scale convergence, and low-to-mid level ascent and saturation, because it over-specifies the amount and level of the mid-to-upper level convective heating effects.

The failure of the model to produce an "anvil" behind the squall line probably has several causes. First of all, the grid interval in these simulations was 20 km, and the squall line was only near 200 km wide at its peak, in both the observations and simulations. The 20 km simulations also depend on a cumulus parameterization scheme to simulate the deep convection, while the explicit microphysics package is included to simulate any grid-scale condensational processes. It is not clear that there is as much interaction between the cumulus parameterization scheme and the microphysical processes as there should be. The cumulus parameterization scheme is parameterizing the overall effects of convection on the temperature and mixing ratio fields. The moisture fluxes produced by the convective parameterization may not be as strong as they need to be to maintain the grid-scale anvil microphysical processes, and they may not be consistent with the ice phase processes that occur in the explicit microphysics package. The cumulus parameterization scheme only transports moisture upwards, not condensate. Any condensate must then be explicitly produced by the grid-scale microphysical processes.

The time series of equivalent potential temperature, θ_e, shown in Figs. 5.30-5.33 are consistent with the analyses of other investigators. There is a minimum of θ_e ahead of the squall line at a height of about 3-4 km. The strong minimum is consistent with the results found by Barnes and Seickman (1984) for fast-moving lines. The vertical θ_e gradient behind the squall line is also decreased, with lower values of θ_e at the surface and an increase in the mid-level θ_e, consistent with the results of Ogura and Liou (1980).

Potential vorticity (PV) is another variable that is modified by the passage of a squall line. Hertenstein and Schubert (1990) analyzed data from the PRE-STORM experiment and also used a simple semi-geostrophic analytic model to show that a squall line leaves a positive PV anomaly at low-to-mid levels and a negative anomaly aloft. The positive anomaly is located below the level of the maximum heating. Figure 5.45 shows the PV analyses for the CU and ALL simulations at 0600 UTC in the same vertical cross section as all previous figures (shown in Fig. 5.1). The potential vorticity was defined as:

$$PV = \left(f + \frac{\partial v}{\partial x} - \frac{\partial u}{\partial y}\right)\frac{\partial \theta}{\partial z}\frac{1}{\rho g} - \frac{\partial v}{\partial z}\frac{\partial \theta}{\partial x}\frac{1}{\rho g} + \frac{\partial u}{\partial z}\frac{\partial \theta}{\partial y}\frac{1}{\rho g} \tag{5.2}$$

where f is the coriolis force, u and v are the horizontal velocities in the x and y directions respectively, ρ is the density, and g is the gravitational constant. A general increase in PV below about 5 km and a decrease above that is apparent behind the squall line, as well as a local maximum at a height of about 7-8 km. The maximum at 7-8 km is located behind the leading convective region, and is stronger in the ALL simulation. The increase in the strength of the PV anomaly in the ALL simulation is probably due to the additional latent heating provided by the explicit microphysical processes. Although the anvil latent heating effects were generally very small (mixing ratios less than 0.1 g/kg), maximum condensate mixing ratios in the convective cores were on the order of 0.5-1.0 g/kg. Figure 5.33c shows the maximum condensate extending from 5-8 km and aligned just ahead of the PV maximum. However, the PV maximum must be mostly a result of the heating produced by the cumulus parameterization scheme as it is also evident in the CU simulation. The level of maximum heating at 0300 UTC can be deduced to be at approximately 10 km from the gravity wave structure diagnosed in Fig. 5.40d, and if it is assumed to be at approximately the same level, or slightly higher as discussed in Section 5.4.3, at 0600 UTC (even though the gravity wave itself is not evident at that time), then the positive PV anomaly is located just below it, as predicted by theory.

To summarize, the structure of the squall line and its effects on the environment in the ALL simulation compare well to observed structures, and to those hypothesized and

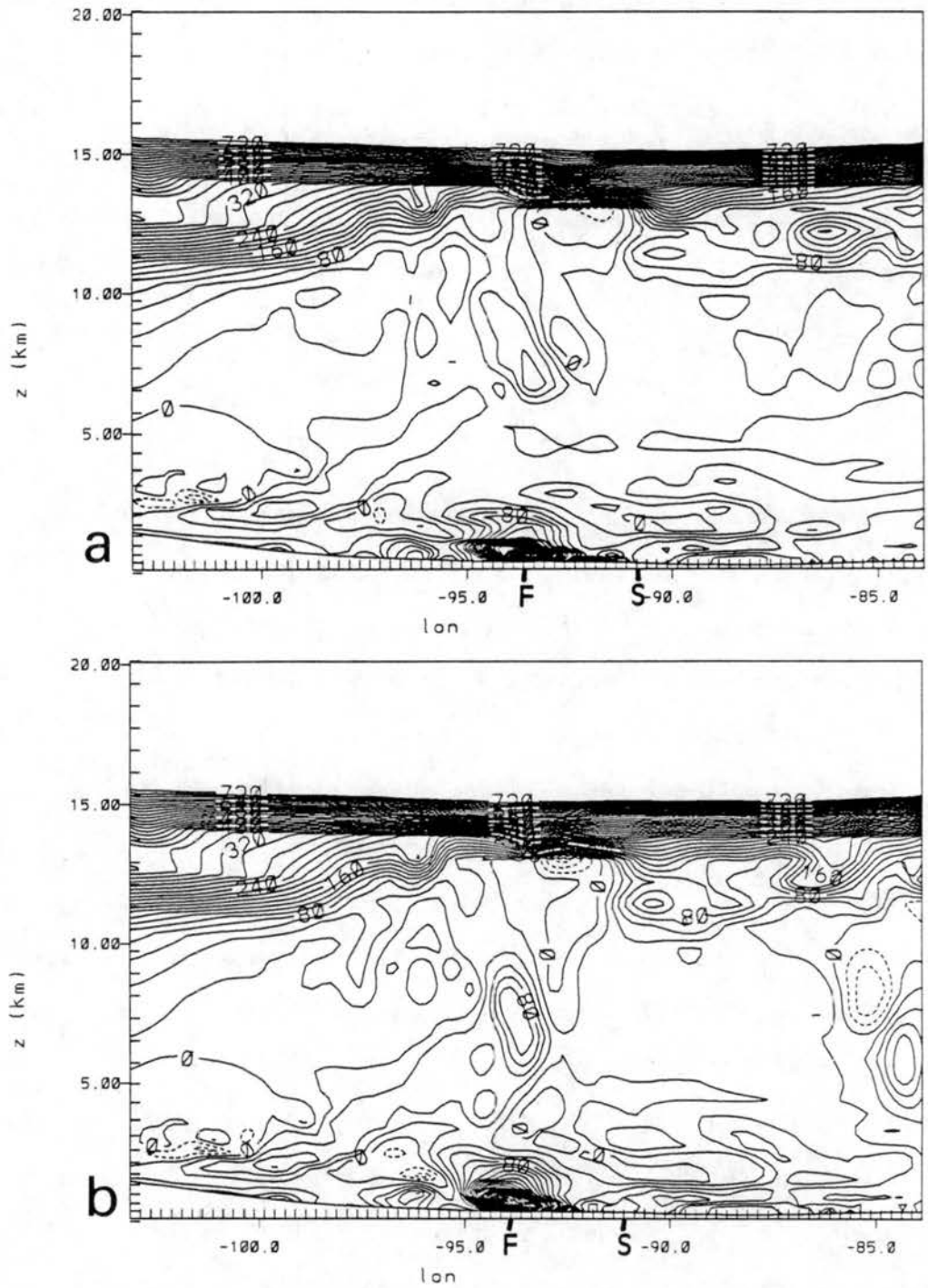

Figure 5.45: East-west cross section at 0600 UTC of potential vorticity (K s m g^{-1}, contour interval is .00000002, dashed lines are negative value contours) in (a) the CU simulation; and (b) the ALL simulation.

observed in other studies on meso-β and α scales, with the exception of the anvil and downdraft processes. The ALL simulation failed to produce any strong anvil microphysical or dynamical effects, and it is not clear whether this is due to a deficiency in the microphysical package or cumulus parameterization scheme, or to not properly modelling the interactions between the microphysical processes and the cumulus parameterization scheme. The extent and strength of the anvil processes in the observed squall line for this case are really not known either. Despite the lack of production of an anvil region in these modelling simulations, the overall structure and propagation speed of the squall line was well simulated. The propagation of the squall line in the model is hypothesized to be due to a wave-CISK-like internal gravity wave, and the mass and momentum perturbations in the model were shown to be consistent with gravity wave theory.

Chapter 6

SENSITIVITY TO VARIABLE SURFACE CONDITIONS

The simulations described in this chapter investigate the effects of a non-horizontally-homogeneous initialization of soil moisture and land surface characteristics on the simulated squall line. This simulation was the same as simulation ALL, except that it was initialized with horizontally varying values of soil type, roughness length, and soil moisture. The soil type and roughness length were calculated from the data set described in Section 4.1.1 and are shown in Figs. 4.8 and 4.9. The initial soil moisture was calculated from the analysis of the previous 24 hours of precipitation data shown in Figs. 6.1 and 6.2. If the previous 24 hours precipitation was greater than 0.5 in (1.27 cm) then the soil moisture was set to 0.90 of saturation for the particular soil type, and the soil temperature was set to T_s-1°C (1°C colder than the surface temperature). Otherwise, the soil surface temperature and percentage of saturation varied linearly from T_s-4°C to T_s-1°C and from 0.50 to 0.90, respectively. If there was no precipitation in the last 24 hours, the soil surface temperature was specified as described in Section 4.2.8 (T_s-4°C) and the soil relative humidity was set to the surface air relative humidity. The simulation described in this chapter will be referred to as the SFC simulation.

6.1 SFC Simulation Results and Comparison to ALL Results

Figures 6.3-6.6 show the surface fields of horizontal winds, horizontal divergence, MSLP, temperature, and convective precipitation rate for the SFC simulation at 2100 UTC 17 June, and 0000, 0300, and 0600 UTC 18 June 1978. At 2100 UTC the SFC fields (Fig. 6.3) are generally similar to the ALL fields (Fig. 5.24) except to the east of the squall line generation region where the surface temperature gradients are different. The regions

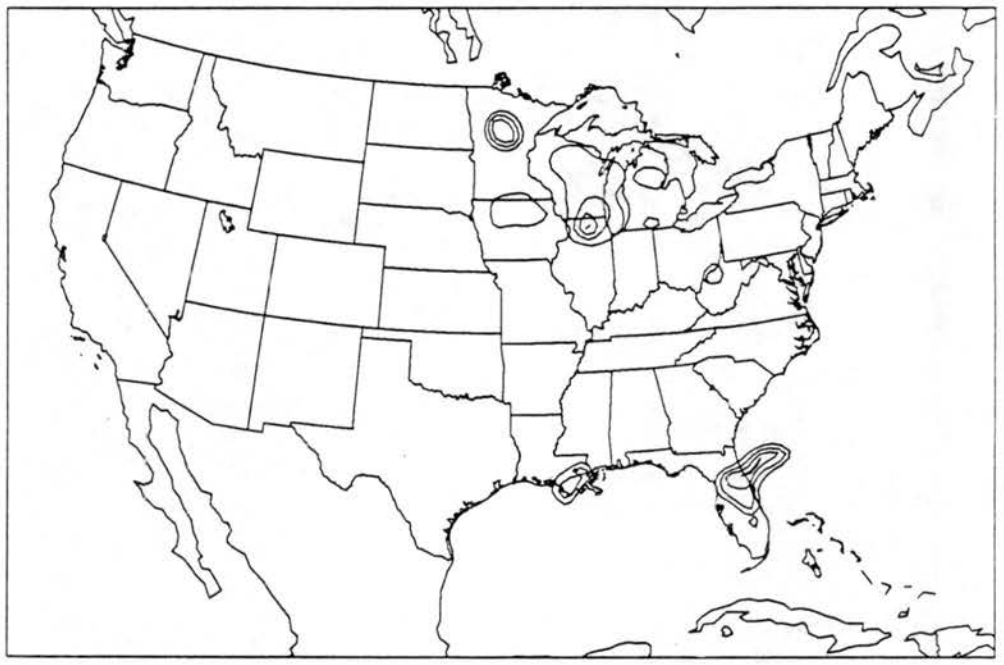

Figure 6.1: Observed precipitation from 1200 UTC 16 June 1978 through 0000 UTC 17 June 1978 (cm, contour interval is 0.5 cm).

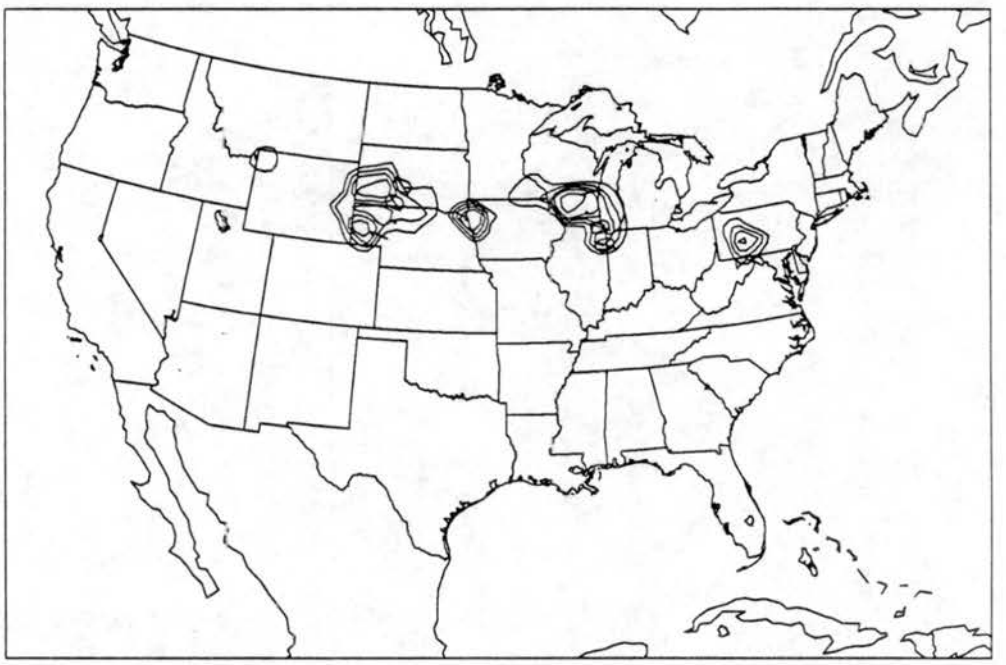

Figure 6.2: Observed precipitation from 0000 UTC 17 June 1978 through 1200 UTC 17 June 1978 (cm, contour interval is 0.5 cm).

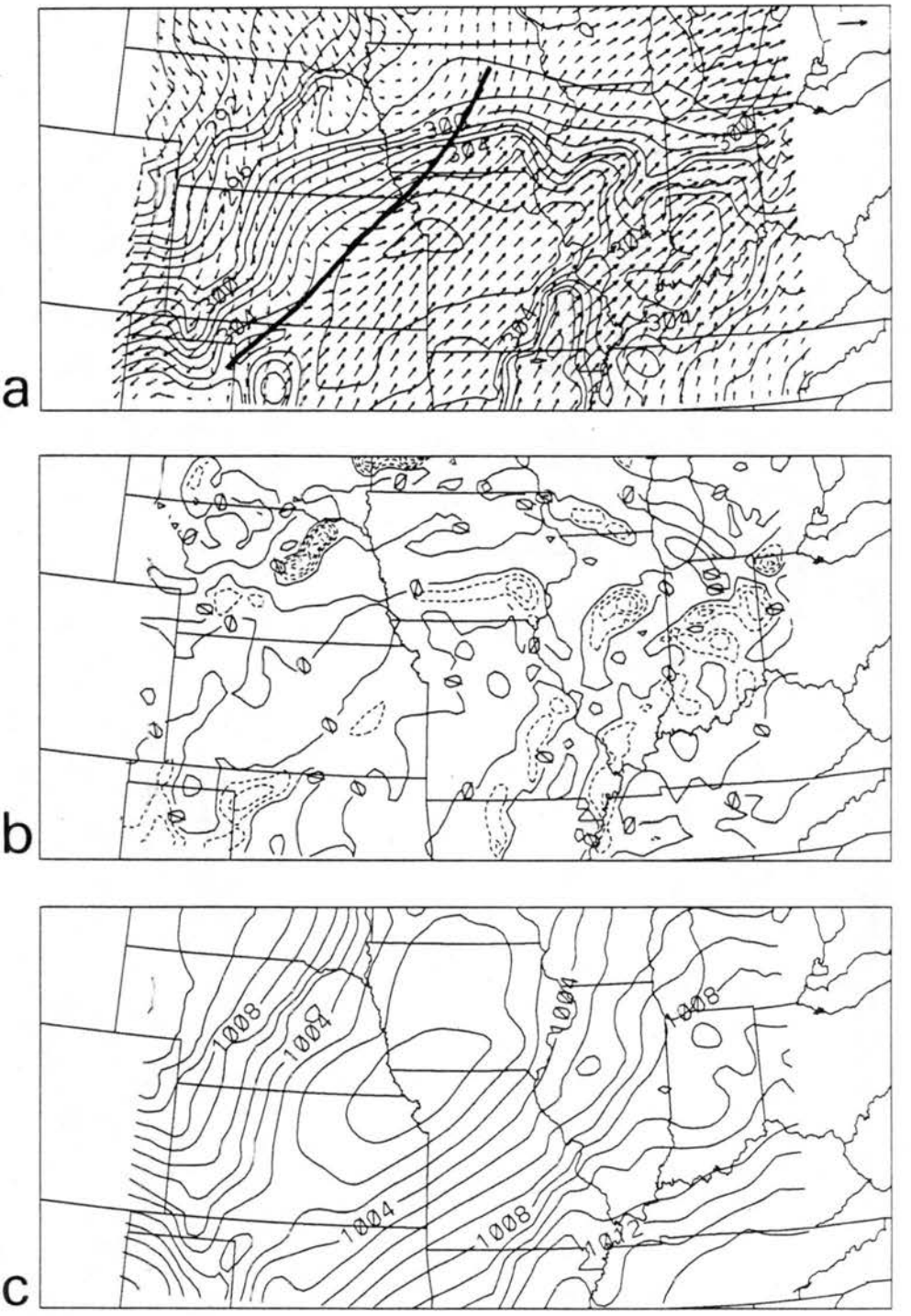

Figure 6.3: Analyses from SFC simulation at 2100 UTC 17 June 1978 of (a) surface horizontal winds and temperature (K, contour interval is 1 K); (b) surface horizontal divergence (s^{-1}, contour interval is .00005, dashed lines are negative value contours); and (c) reduced MSLP (mb, contour interval is 1 mb). The length of the vectors in (a) is proportional to their speed: the vector in the upper right corner of (a) is 20 m s^{-1}.

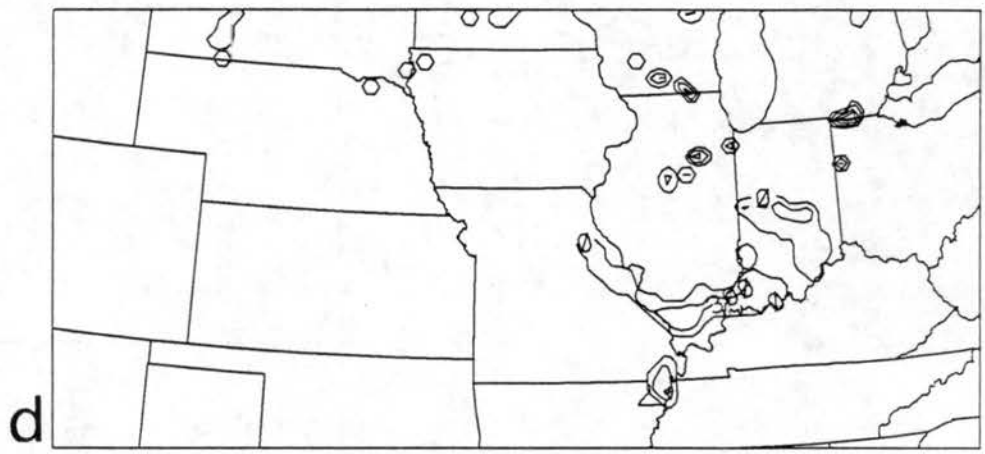

d

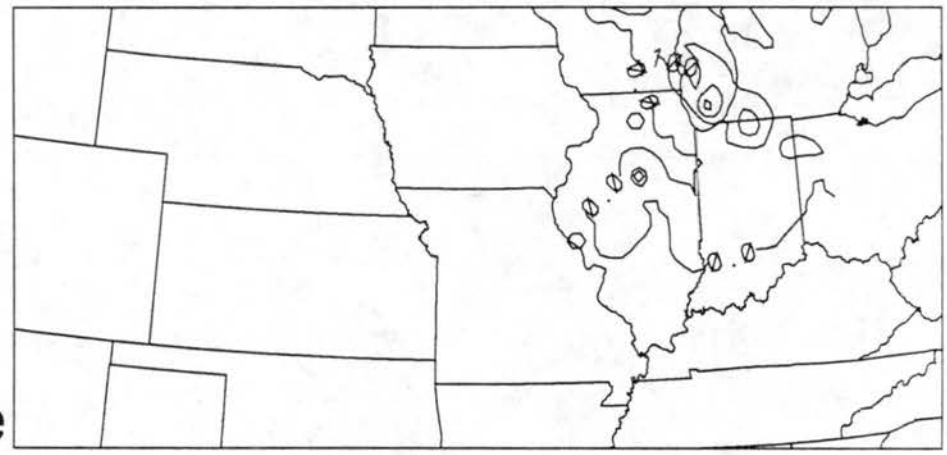

e

Figure 6.3: Continued: (d) convective precipitation rate (mm/s, contour interval is .0003); and (e) 9.7 km condensate mixing ratio (g/kg, contour interval is 0.1 g/kg).

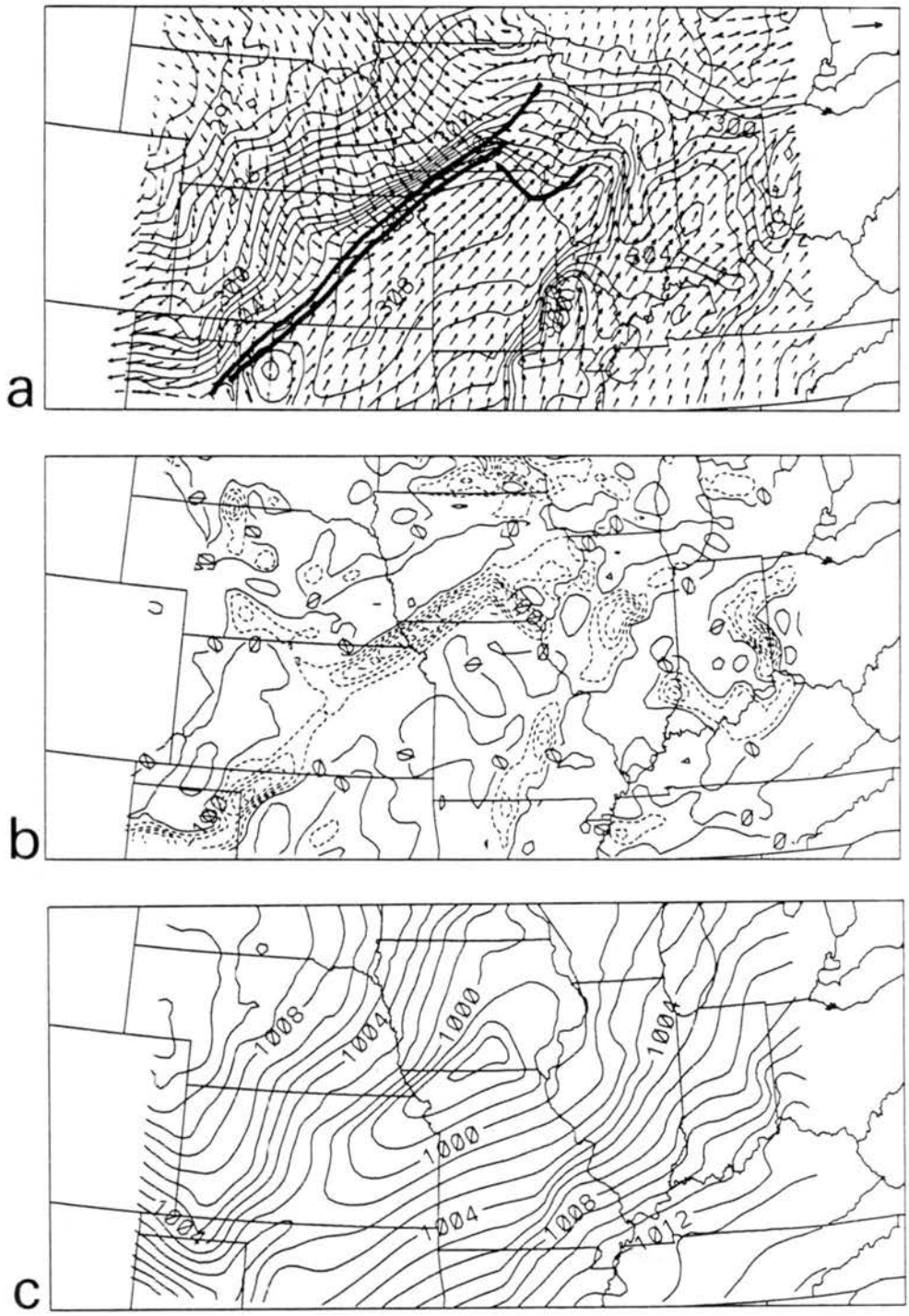

Figure 6.4: Analyses from SFC simulation at 0000 UTC 18 June 1978 of (a) surface horizontal winds and temperature (K, contour interval is 1 K); (b) surface horizontal divergence (s^{-1}, contour interval is .00005, dashed lines are negative value contours); and (c) reduced MSLP (mb, contour interval is 1 mb). The length of the vectors in (a) is proportional to their speed: the vector in the upper right corner of (a) is 20 m s^{-1}.

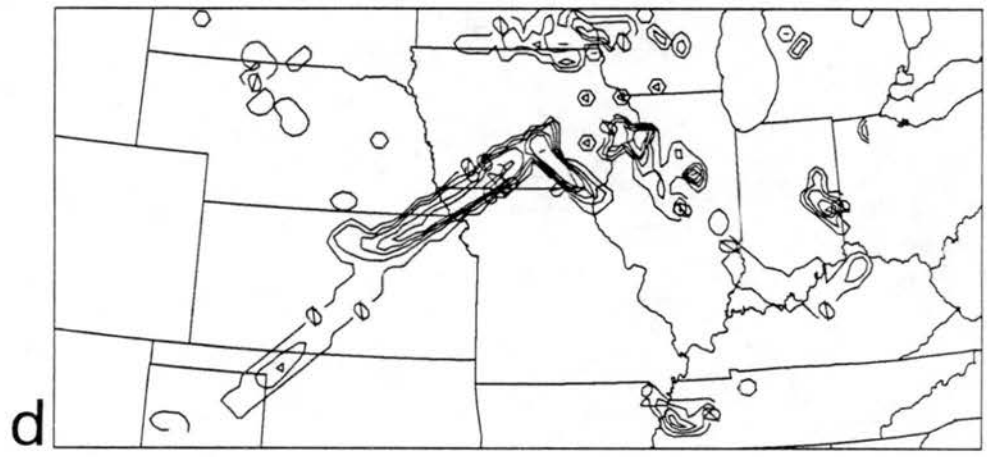

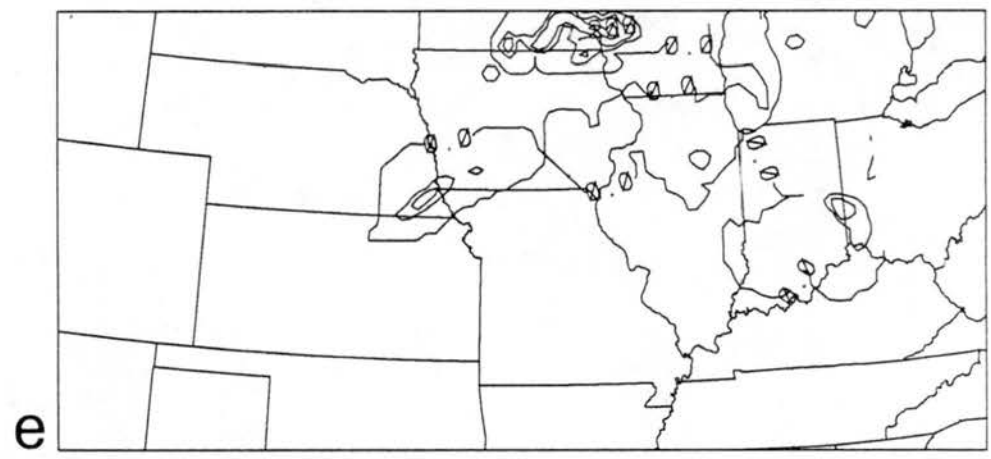

Figure 6.4: Continued: (d) convective precipitation rate (mm/s, contour interval is .0003); and (e) 9.7 km condensate mixing ratio (g/kg, contour interval is 0.1 g/kg).

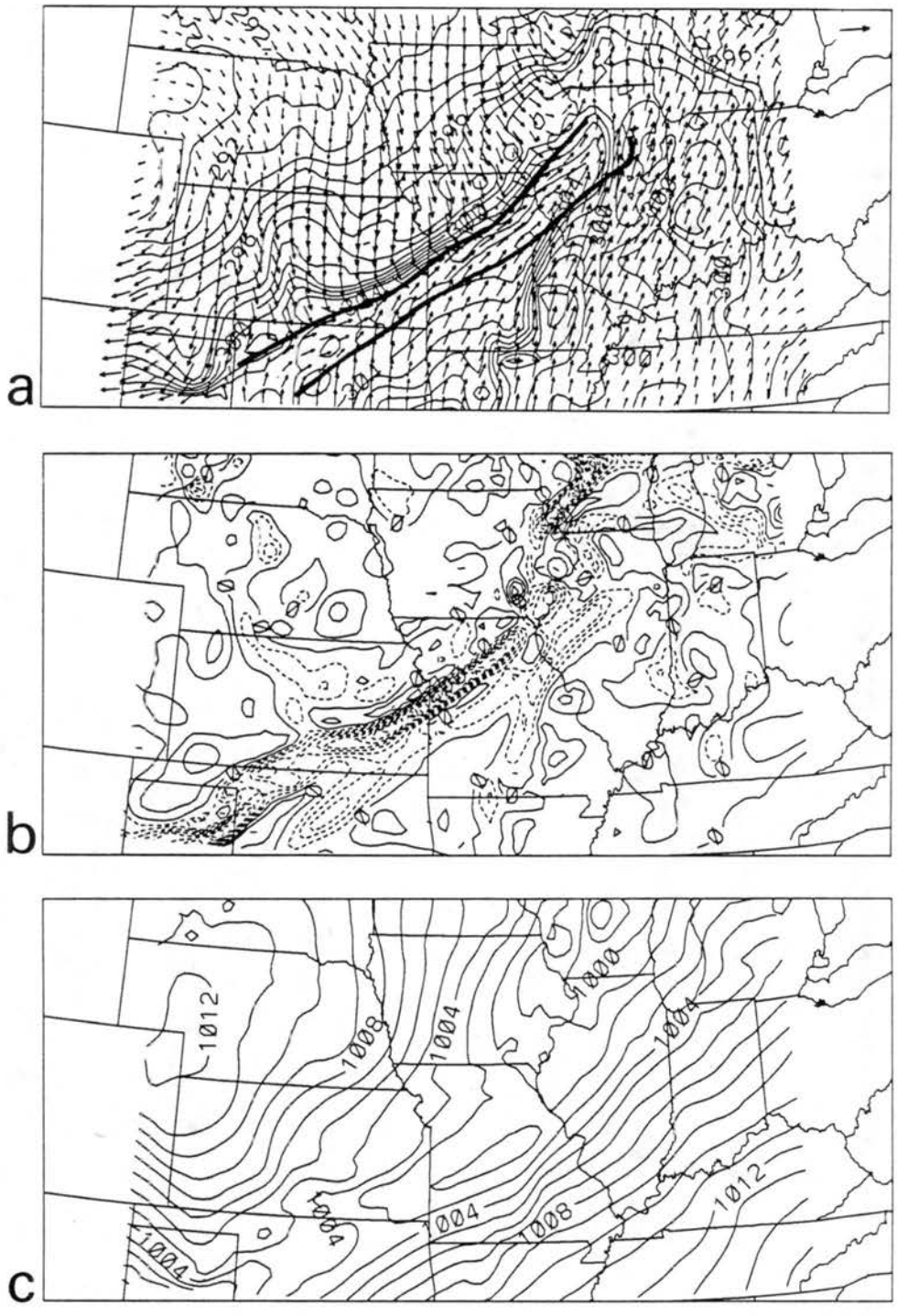

Figure 6.5: Analyses from SFC simulation at 0300 UTC 18 June 1978 of (a) surface horizontal winds and temperature (K, contour interval is 1 K); (b) surface horizontal divergence (s^{-1}, contour interval is .00005, dashed lines are negative value contours); and (c) reduced MSLP (mb, contour interval is 1 mb). The length of the vectors in (a) is proportional to their speed: the vector in the upper right corner of (a) is 20 m s^{-1}.

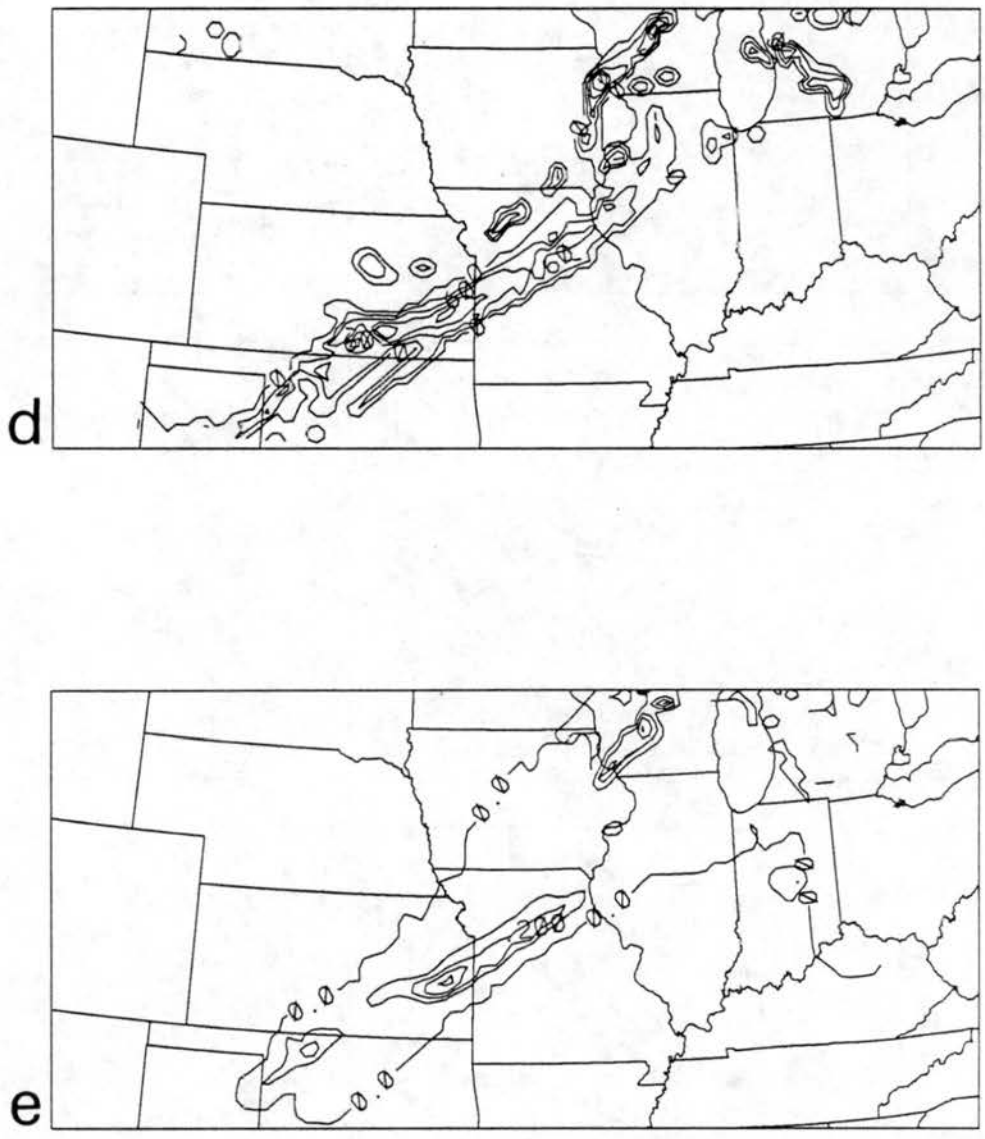

Figure 6.5: Continued: (d) convective precipitation rate (mm/s, contour interval is .0003); and (e) 9.7 km condensate mixing ratio (g/kg, contour interval is 0.1 g/kg).

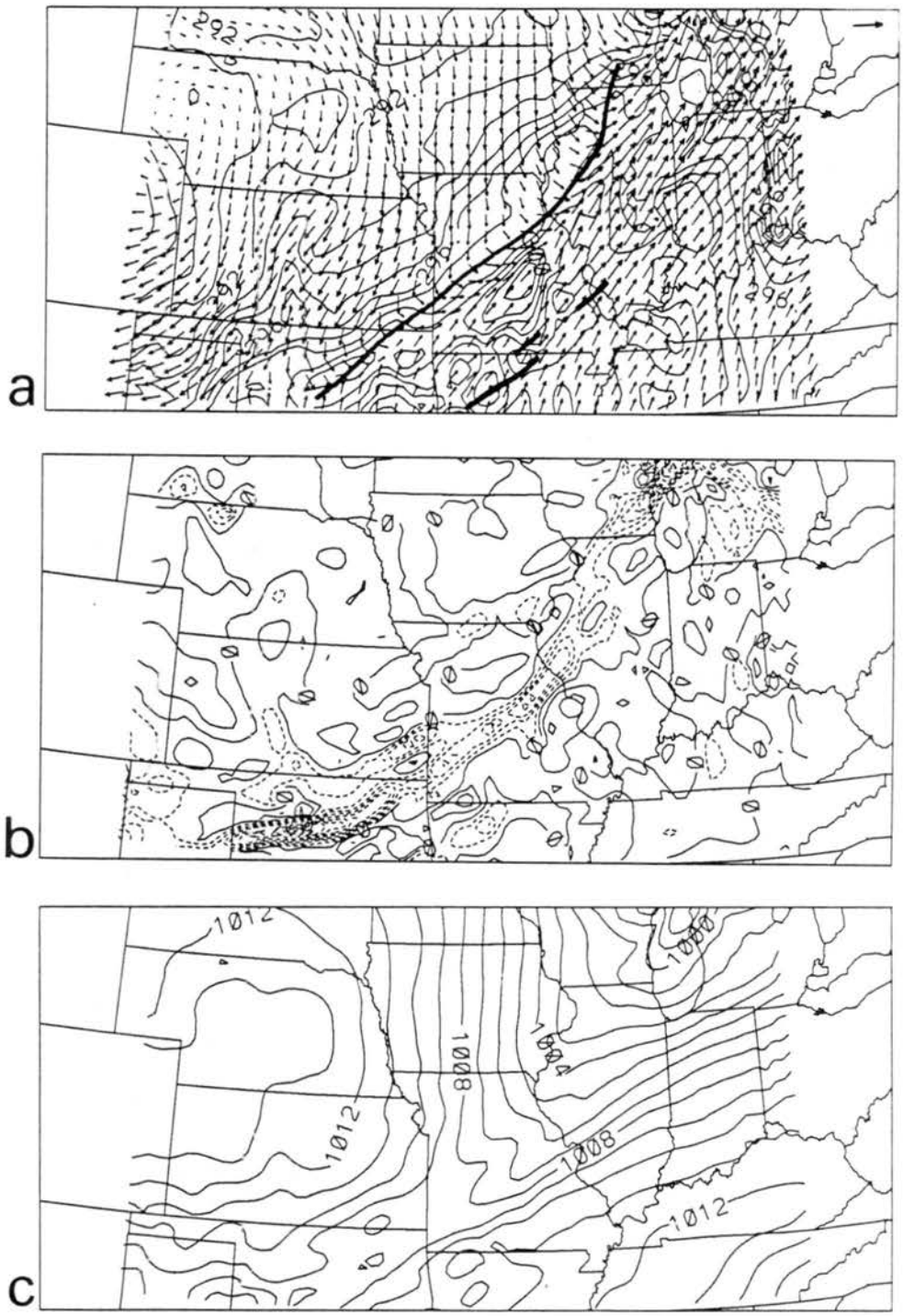

Figure 6.6: Analyses from SFC simulation at 0600 UTC 18 June 1978 of (a) surface horizontal winds and temperature (K, contour interval is 1 K); (b) surface horizontal divergence (s^{-1}, contour interval is .00005, dashed lines are negative value contours); and (c) reduced MSLP (mb, contour interval is 1 mb). The length of the vectors in (a) is proportional to their speed: the vector in the upper right corner of (a) is 20 m s^{-1}.

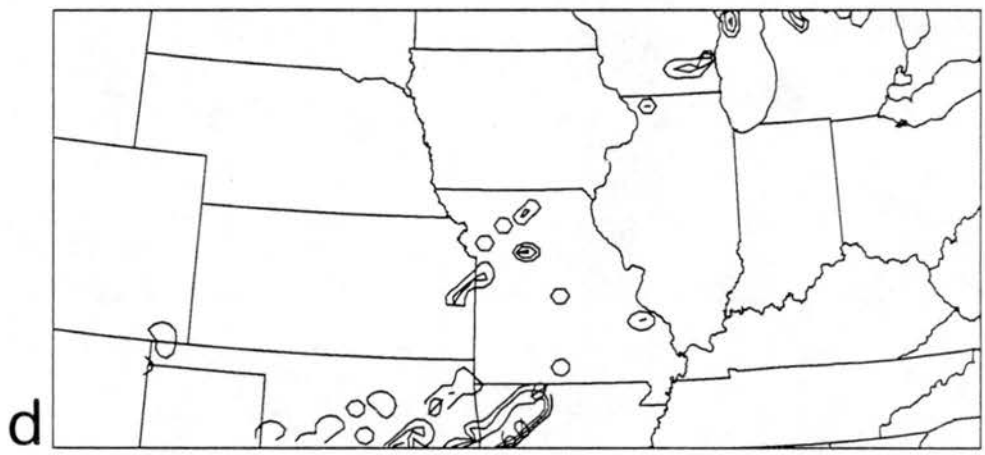

d

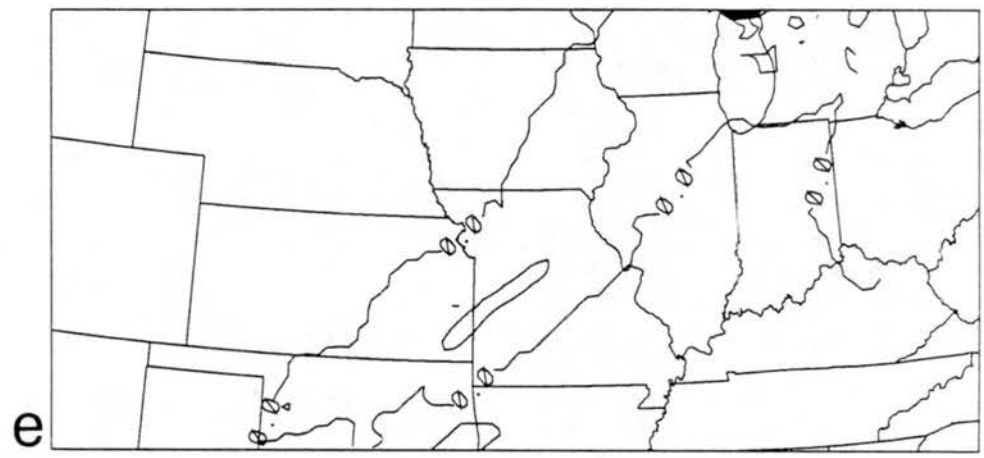

e

Figure 6.6: Continued: (d) convective precipitation rate (mm/s, contour interval is .0003); and (e) 9.7 km condensate mixing ratio (g/kg, contour interval is 0.1 g/kg).

of convective precipitation rate to the east of the squall line generation region are also slightly different between the SFC and ALL simulations. At 0000 UTC the convergence along the frontal zone is less intense in the SFC simulation and the trough is slightly wider, although the intensity and coverage of convective precipitation rate (where the the squall line is located) is similar to that in the ALL simulation. At 0300 UTC the convergence along the frontal zone is now stronger in the SFC simulation and the trough is significantly narrower, but the frontal and squall line positions are still similar to those in the ALL simulation. Finally, at 0600 UTC, there are only minor differences between the SFC and ALL simulations. Figures 6.7 and 6.8 show the precipitation accumulated from 1800

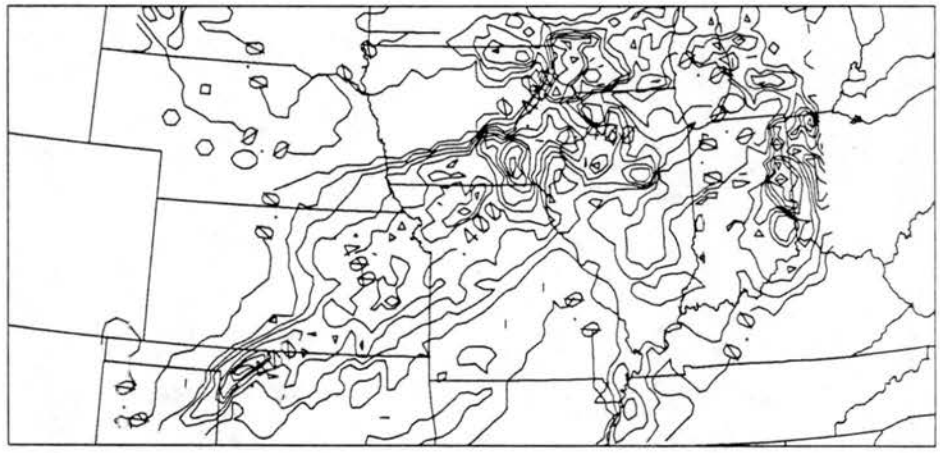

Figure 6.7: Precipitation produced by the convective parameterization scheme in the SFC simulation accumulated from 1800 UTC 17 June to 0600 UTC 18 June 1978 (cm, contour interval is 0.1 cm).

UTC 17 June to 0600 UTC 18 June from the convective parameterization and from the explicit microphysical processes. The maximums in convective precipitation from the SFC simulation are slightly less than those for the ALL simulation (Fig. 5.28), but the areas of coverage are very similar. Likewise, the area of coverage of the microphysically-produced

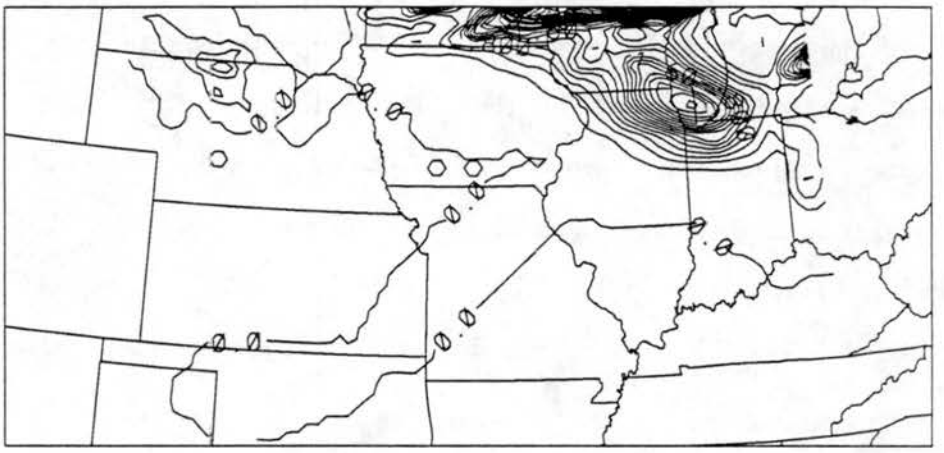

Figure 6.8: Explicit microphysically-produced precipitation in the SFC simulation accumulated from 1800 UTC 17 June to 0600 UTC 18 June 1978 (cm, contour interval is 0.2 cm).

precipitation from the SFC simulation is very similar to that from the ALL simulation (Fig. 5.29).

The vertical cross sections of vertical motion and equivalent potential temperature for the SFC simulation at 2100 UTC 17 June and 0000, 0300, and 0600 UTC 18 June are shown in Figs. 6.9-6.12. The cross sections of total condensate mixing ratio produced by the explicit microphysics at 0300 and 0600 UTC are also shown in Figs. 6.11b and 6.12b. The SFC and ALL simulations are similar at 2100 and 0000 UTC although the area of low-level frontal convergence at 2100 UTC is narrower in the SFC simulation and the squall-line-associated deep vertical motion at 0000 UTC is significantly weaker. By 0300 UTC the deep vertical motion associated with the squall line is stronger in the SFC simulation, which is consistent with the evolution of the surface convergence between 0000 and 0300 UTC. Finally, at 0600 UTC the SFC and ALL fields are again basically similar.

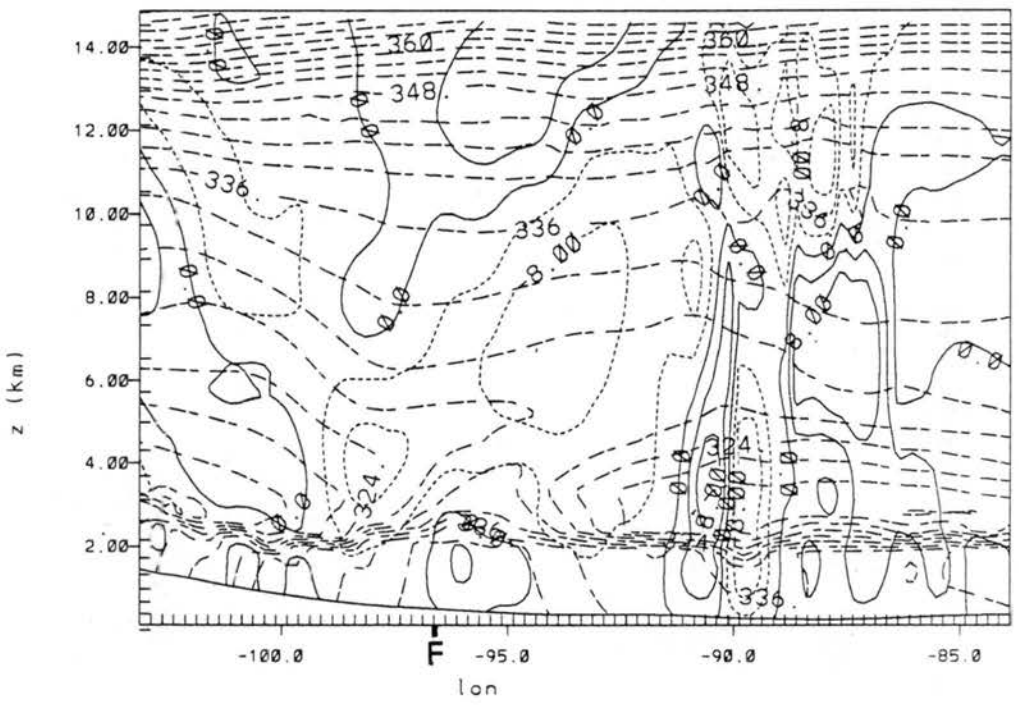

Figure 6.9: Vertical cross section for the SFC simulation at 2100 UTC 17 June 1978 of vertical motion w (cm s^{-1}, contour interval is 4, solid lines are positive value contours, short-dashed lines are negative value contours) and equivalent potential temperature θ_e (K, long-dashed lines, contour interval is 3).

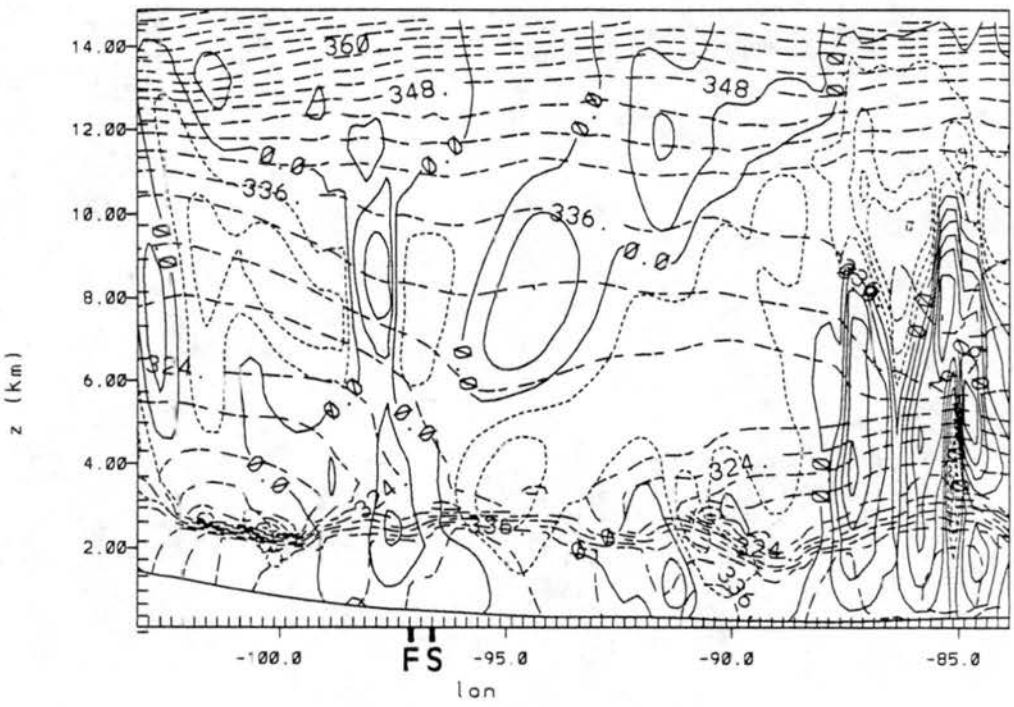

Figure 6.10: Vertical cross section for the SFC simulation at 0000 UTC 18 June 1978 of vertical motion w (cm s^{-1}, contour interval is 4, solid lines are positive value contours, short-dashed lines are negative value contours) and equivalent potential temperature θ_e (K, long-dashed lines, contour interval is 3).

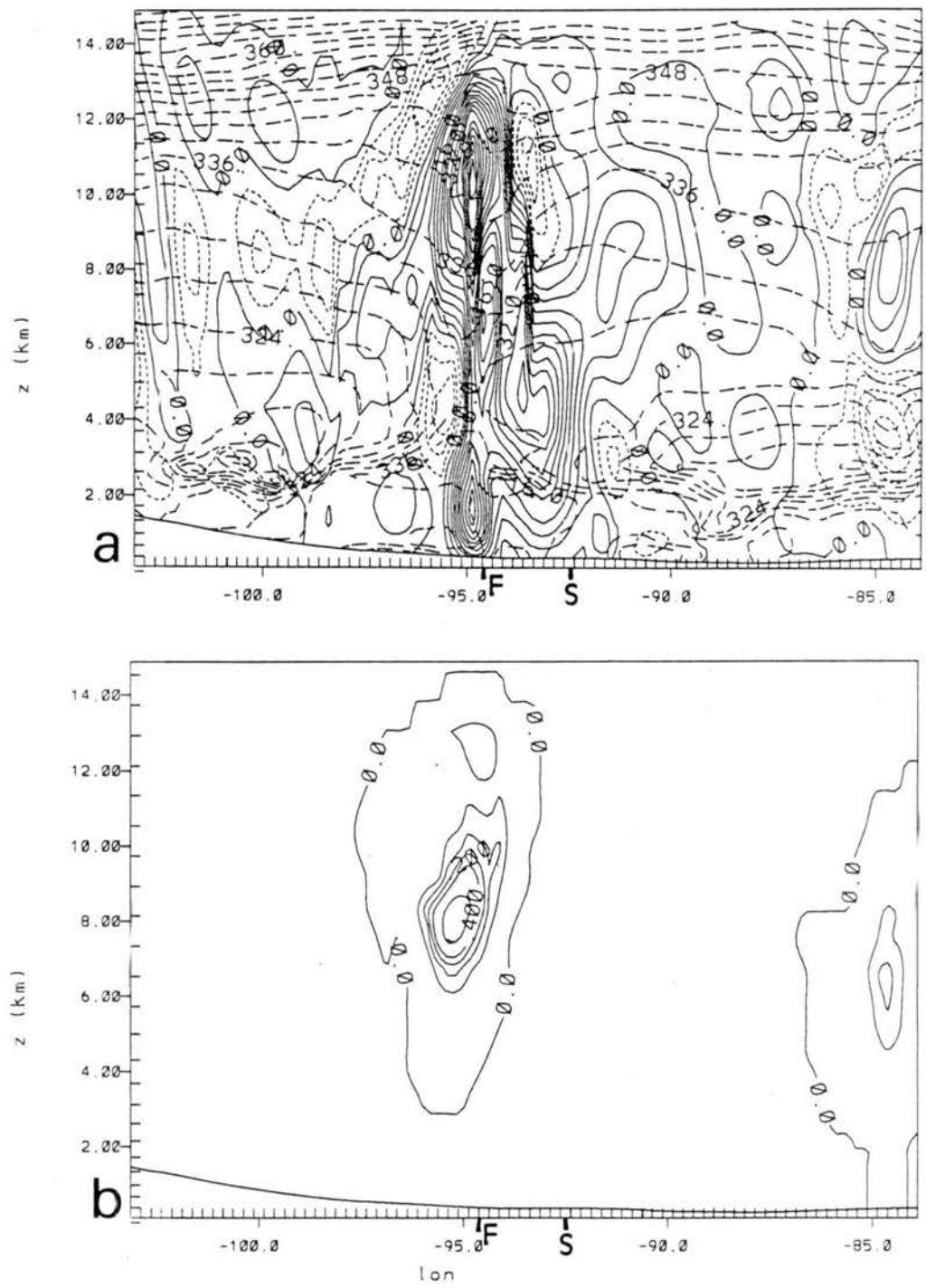

Figure 6.11: Vertical cross section for the SFC simulation at 0300 UTC 18 June 1978 of (a) vertical motion w (cm s^{-1}, contour interval is 4, solid lines are positive value contours, short-dashed lines are negative value contours) and equivalent potential temperature θ_e (K, long-dashed lines, contour interval is 3); and (b) condensate mixing ratio (g/kg, contour interval is 0.1).

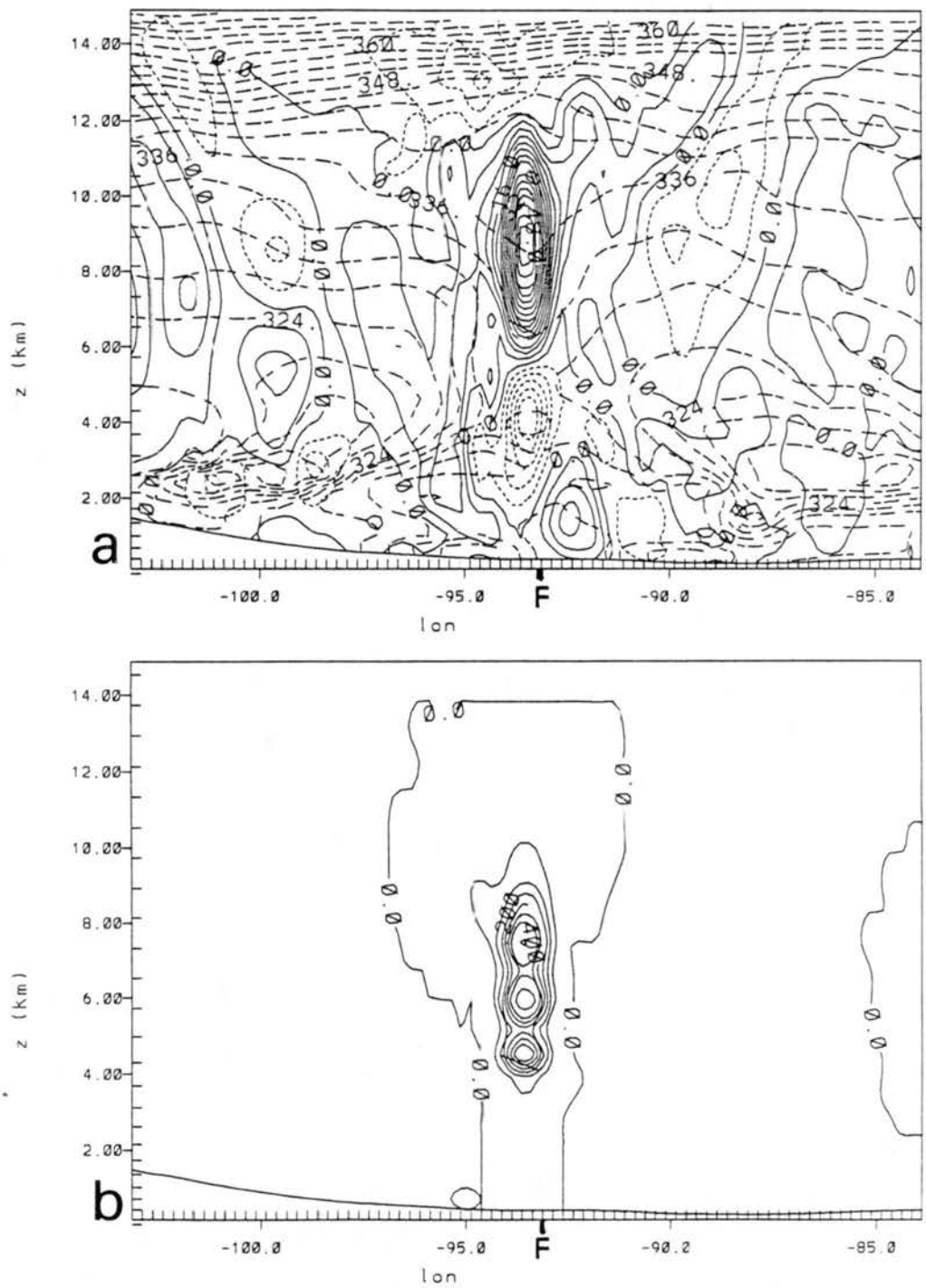

Figure 6.12: Vertical cross section for the SFC simulation at 0600 UTC 18 June 1978 of (a) vertical motion w (cm s^{-1}, contour interval is 4, solid lines are positive value contours, short-dashed lines are negative value contours) and equivalent potential temperature θ_e (K, long-dashed lines, contour interval is 3); and (b) condensate mixing ratio (g/kg, contour interval is 0.1).

6.2 Discussion of SFC Results

Overall, the evolution of the front and squall line in the SFC and ALL simulations was very similar. There were minor differences in the strengths of the frontal convergence between the simulations, but they were not large enough differences to affect the timing or areal coverage of the squall line development, although the convection does seem to be slightly less intense in the SFC simulation. The squall line convection was essentially triggered by the strong frontal convergence, and although the variations in surface characteristics affected the magnitude and timing of the convergence, those effects were relatively minor for the squall line.

The largest differences in the areas and intensity of convective precipitation were to the east of the squall line where the dynamical forcing was much weaker. Figures 6.13a-b show the soil moisture specification on the second grid in the ALL and SFC simulations at 1800 UTC, when it was initialized from the larger grid. The soil moisture is shown as the percentage of saturation for the specific soil type. The soil type was constant in the ALL simulation (sandy clay loam) and horizontally-varying in the SFC simulation (Fig. 4.8). Thus, gradients in soil moisture can be a result of either gradients in water content or gradients in soil type. The soil moistures by this time (1800 UTC) have been slightly modified by precipitation occurring in the model between 1200 and 1800 UTC. The pocket of relatively dry soils extending from Kansas to Illinois in the ALL simulation (Fig. 6.13a) is directly related to the warmer surface temperatures in that region (Fig. 5.24a). In the ALL simulation, the initial soil moisture (at 1200 UTC 17 June 1978) was calculated as directly proportional to the air relative humidity (which was lower where the temperatures were higher). In the SFC simulation, the initial soil moisture was calculated as proportional to the previous 24 hours precipitation, if there was any. If there was not any precipitation in the previous 24 hours, it was again calculated as proportional to the air humidity, but also as a function of the horizontally-varying soil type. Different types of soil become saturated with different amounts of moisture in the model. It can be seen that the areas of increased precipitation to the east of the squall line

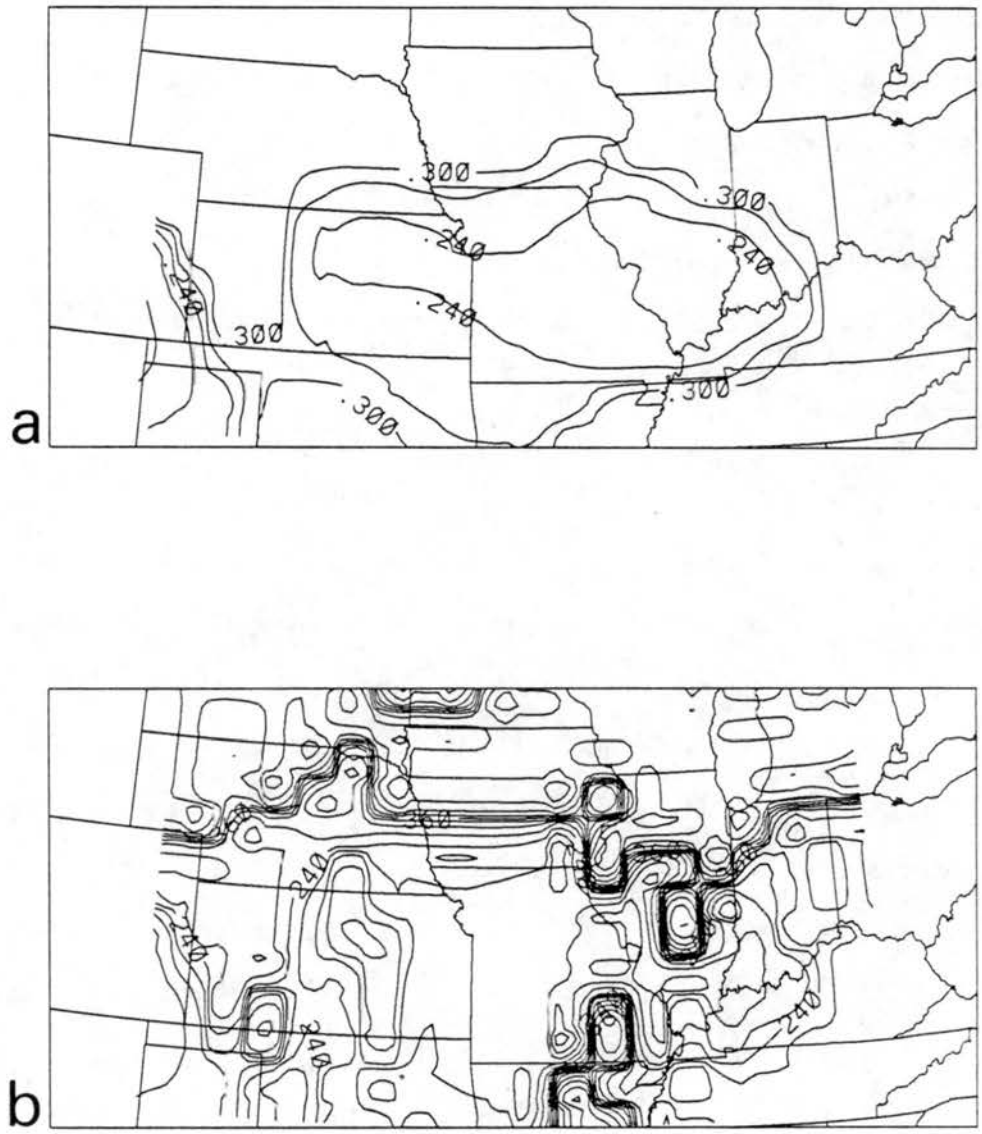

Figure 6.13: Soil moisture specification (percentage of saturation for the specified soil type, contour interval is .03) at 1800 on the 20 km grids in the (a) ALL simulation; and (b) SFC simulation.

in the SFC simulation are mostly related to increased gradients in soil moisture, which in turn is related to both the precipitation record and the specification of soil type. Other studies that have found similar sensitivities to soil moisture specification include those of Physick (1980), McCumber (1980), McCumber and Pielke (1981), Coats *et al.* (1984), and Tremback (1990).

It is also possible that the soil type (and soil roughness) variations in the SFC simulation were too "noisy" for coherent circulations to develop. The 20 km grid values of soil type and surface roughness length are simply the same values as on the 80 km analyses; the value for each of the 16 different 20 km square fine grid boxes that compose an 80 km square coarse grid box is simply the same as the single value for that one coarse grid box. The coarse grid analyses of soil texture are integer values, and need to remain as integers on the fine grid. Also, if two adjacent coarse grid boxes have soil texture values of 1 and 5 for example, all of their fine grid "sub-boxes" also should have values of 1 or 5; it would not be correct to introduce an intermediate number such as 3. The same argument also applies to the analyses of surface roughness length. If two adjacent coarse grid boxes have z_0 values of 0.01 and 20 cm, then the only known values for the fine grid "sub-boxes" are 0.01 and 20 cm. Again, it would not be correct to introduce an intermediate value of 10 cm. Unfortunately, as is evident in Figs. 6.13a-b, this type of interpolation procedure results in noisy, "boxy-looking" analyses. The problem of designing a smoother interpolation procedure for these variables needs to be considered in future research.

Chapter 7

FINE RESOLUTION EXPERIMENTS

Several simulations with three grids and grid spacings down to 5 km were completed in an attempt to simulate the squall line using the explicit microphysical processes only, without the cumulus parameterization scheme. Various problems associated with the domain and initialization of the 5 km grid were encountered in properly resolving the frontal convergence on that scale. It also became apparent that the convergence on that scale was still not strong enough to explicitly force the triggering of the convection through the low-level stable layer. Several of the existing options to the parameterization of turbulent mixing were tested, and a modification that allowed for increased vertical mixing dependent upon the vertical velocity was developed, very similar to that used by Ross and Orlanski (1982). The convection did develop on the 5 km scale with the increased vertical mixing, but several hours later than observed, and also much later than in the 20 km simulations with the convective parameterization. The squall line never developed properly on the 5 km scale or showed the separation from the front as in the 20 km simulations or in the observations.

7.1 Description of Simulation Parameters

The simulations described in this chapter all used two telescoping nests (a total of 3 grids) to nest down to a 5 km grid spacing. Full microphysics were used on all 3 grids, but no cumulus parameterization in the finest nest (5 km grid spacing). The two coarsest grids had the same parameters and horizontal domain and resolution as the ALL simulation described in Chapter 5. The finest scale nested grid was at a ratio of 1:4 (5 km) to the 20 km grid spacing, over an area 9° × 3° or 144 × 64 points. The nested domains

are shown in Fig. 7.1. These simulations did differ from the simulations described in Chapters 5 and 6 in that an increased vertical resolution (43 grid points in the vertical) was used on all 3 grids (vs. 32 grid points in the simulations described in Chapters 5 and 6). In these simulations the vertical grid spacing varied from 250 m at the surface

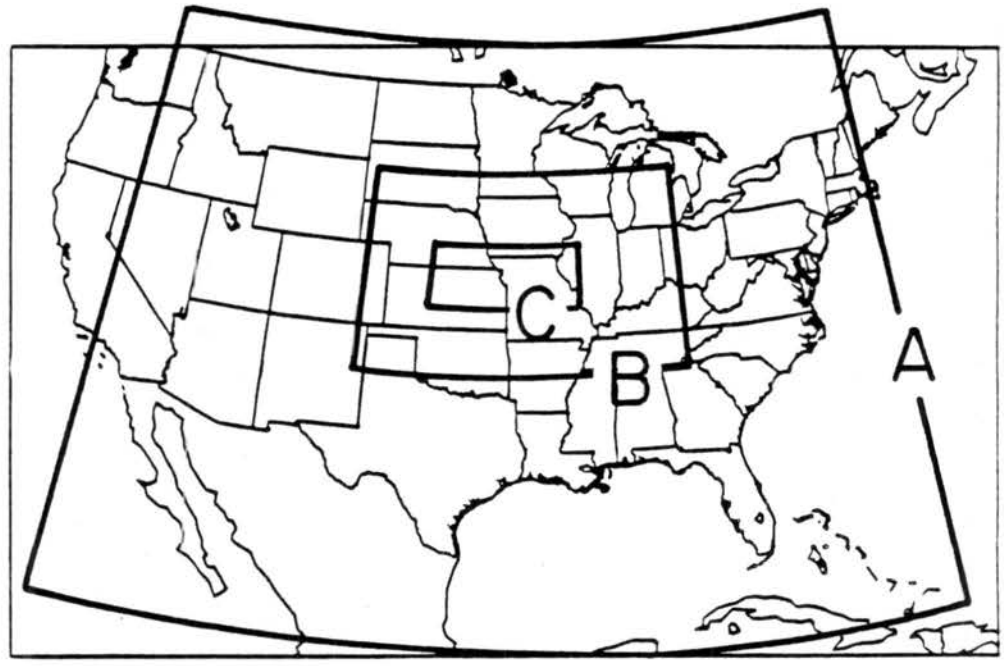

Figure 7.1: Domains of 80 km, 20 km, and 5 km grids. Domain boxes are labelled A, B, and C, respectively.

to 500 m at the model top. The model top was still at 20 km and the Rayleigh friction layer extended from 15 to 20 km. The increased vertical resolution was chosen for these simulations because of the potential importance of the explicit simulation and resolution of vertically-propagating gravity waves.

The cumulus parameterization scheme was used used on the 80 and 20 km grids, but not on the 5 km grid. The explicit microphysical processes were activated on all three grids, as described in Section 4.2.7. The 5 km grid spacing was thought to be too small to satisfy the assumptions in the cumulus parameterization scheme, and other investigators have had successes in using only grid-scale condensate processes with larger grid spacings.

For example, Rosenthal (1978) used a 20 km grid spacing, with explicit heating processes only, to simulate the development of a tropical cyclone. Ross and Orlanski (1982) and Orlanski and Ross (1984) used a 61.5 km grid, again with explicit heating only, to simulate the development of a cold front and associated squall line convection.

The 80 km simulation was started at 1200 UTC 17 June 1978 from the same initial fields as described in Section 5.2. The 20 km grid was activated at 1800 UTC, the same as in the previously described simulations. The simulation on the 5 km grid was found to be very sensitive to the time at which it was initialized. Ideally, the 5 km simulation would be initialized previous to any of the convective development along the squall line. However, it was found that when that grid was initialized at 1800 or 2100 UTC, the increase of convergence along the frontal zone between 1800 UTC 17 June and 0000 UTC 18 June was not properly simulated. The discussion of the DRY and CU simulations in Sections 5.3.1 and 5.3.3 briefly mentioned the area of divergence to the west of the front in central Kansas, with bands of increased convergence to the west and north of that. These bands merged with the main frontal zone by 0000 UTC in the CU and ALL simulations (20 km grid spacing) and increased the temperature gradient and convergence along the front. An important factor in the frontogenesis was the strong low-level winds from the north and northwest entering northern and western Kansas. The increased convergence along the front then triggered the squall line by 0000 UTC on the 20 km scale. The triggering of convection of the 5 km scale is even more dependent on the resolved frontal convergence because the vertical motion must explicitly force a convective cell, and explicitly overcome the effects of the low-level stable layer. The failure of the development of the region of strong frontal convergence on the 5 km scale (when initialized at 1800 or 2100 UTC) is linked to the areal coverage of the 5 km grid spacing domain and the boundary placement. Again, the ideal simulation would have a 5 km grid spacing (or even smaller grid spacings) over a very large domain. That is not computationally feasible so nested grids are used. In this case the 5 km nested grid was very large (144 × 64) points, but still only covered an area of 9° × 3°. The frontogenetic development between 1800 and 0000 UTC was not

correctly simulated because the strong low-level winds entering Kansas from the north and northwest were not properly resolved on the 5 km grid. It may be necessary to move the western and northern boundaries of the 5 km grid significantly outward in order to simulate the initial frontogenesis, but that was not computationally feasible in these simulations. It was thus decided to initiate the 5 km grid at 0000 UTC 18 June. The convergence along the frontal zone was at its peak on the 20 km scale at that time. The cumulus parameterization had been activated on the 20 km scale, but the results from the smaller scale grids "overwrite" the larger grids on their interiors, so there is no feedback from the effects of the parameterization scheme on the larger grids to the 5 km grid except at its initialization and from its lateral boundaries. The primary interest in the 5 km simulations was the propagation of the squall line, not its initial development. However, even with the initialization of the 5 km grid at 0000 UTC, difficulties were encountered in triggering the convection explicitly on that scale. A modification to the vertical mixing in the turbulence parameterization was developed to minimize that problem and is described in Section 7.2.

An additional problem was encountered in the specification of the minimum value of the horizontal eddy viscosity coefficient. A variable in the model input namelist, AKMIN, is the ratio of the minimum value of the horizontal eddy viscosity coefficient to that of a typical deformation K-based calculation. A typical "small" value of AKMIN would be 0.1 or 0.2, which does not result in any effective increase in the horizontal diffusion over that calculated by the deformation K scheme. A "large" value of AKMIN would be 1.0 or 2.0 which does substantially increase the horizontal diffusion. An argument can be made that AKMIN should be increased on the smallest scales (successive nested grids) to reduce the $2\Delta x$ noise on that scale. The value of AKMIN used in the 80 km and 20 km simulations was 0.2. The simulations described in Section 7.3 also used AKMIN=0.2 on the 5 km grid, but the 5 km results were much "noisier" than on the larger scale grids. A simulation with AKMIN=2.0 on the 5 km grid (and AKMIN=0.2 on the 80 km and 20 km grids) was completed, but the additional diffusion on the 5 km grid reduced the convergence-forced

vertical motion (even with the modifications described in Section 7.2) which was then not strong enough to trigger the squall line convection.

7.2 Modification to Turbulent Mixing

The turbulence parameterization used in all the model simulations described in this study is a deformation K type scheme, and was briefly described in Section 4.2.9. The vertical mixing coefficient is defined by:

$$K_M = \ell^2 \times |D| \times \left(1 - \frac{K_H}{K_M} Ri\right)^{1/2}. \tag{7.1}$$

ℓ is the vertical scale length, defined as the vertical grid spacing in this case. D is the deformation or rate-of-strain tensor, defined as $D = D_{ij} + D_{ik} + D_{jk}$, and $D_{ij} = \frac{\partial u_i}{\partial x_j} + \frac{\partial u_j}{\partial x_i}$. The ratio of $\frac{K_H}{K_M}$, the inverse eddy Prandtl number, is set equal to 3, as suggested by Deardorff (1972). Ri is the gradient Richardson number, defined as $Ri = \frac{N^2}{D_{ik}+D_{jk}}$. The denominator in the definition of Ri thus has four terms, although two of them, $\frac{\partial u_k}{\partial x_i}$ and $\frac{\partial u_k}{\partial x_j}$, are negligible on the scales used in these simulations. The last term in Eq. (7.1) is thus a Richardson-number-dependent modification to the vertical mixing. If the Richardson number is less than zero, i.e., unstable, then the mixing will be increased, while if the Richardson number is greater than zero the mixing will be decreased. The factor of the increase or decrease is limited to be between 0. and 10.

As mentioned previously, the convergence was not strong enough to explicitly initiate the convection on the 5 km scale. A boundary layer of high mixing ratios existed from the surface to approximately 2 km which resulted in the θ_e profile being nearly constant with height up to 2 km and then decreasing strongly in the next 1-2 km. The vertical motion produced by the low-level convergence advected and mixed the boundary layer air upwards, but was not strong enough to "break through" the top of the boundary layer into the layer where θ_e decreased with height. A simple modification to the vertical mixing in the deformation K scheme was developed to increase the vertical mixing dependent upon the vertical velocity. This modification was based on a very similar scheme described by

Ross and Orlanski (1982). Ross and Orlanski (1982), and Orlanski and Ross (1984) used a model with a 61.5 km grid spacing and no cumulus parameterization (grid scale moist convective processes only) to simulate the development of a front and squall line. It is hypothesized that they were able to simulate the convection through grid-scale processes because of their use of an enhancement to the turbulent mixing dependent upon a critical vertical velocity. For this case, a critical vertical velocity, w_c, was defined, and, subject to certain restrictions, Eq. (7.1) was replaced by

$$K_M = \ell^2 \times |D| \times \left(1 + C\frac{w_{max}}{w_c}\right)^{1/2}. \tag{7.2}$$

w_c is set to 40 cm s^{-1} and C is an arbitrary scaling, set to 25. w_{max} is the maximum vertical velocity defined at a point i, j, k for the column extending from $k-4$ to $k+4$, i.e., in a column approximately 2500 to 4000 meters deep. Equation (7.2) was only used for the definition of K_M if $w_{max} > w_c$ and the location of w_{max} was at a height less than 6500 m. Otherwise, Eq. (7.1) was used. The increased vertical mixing is acting to parameterize the sub-grid scale increased mixing that occurs because of the lifting of convectively unstable air. The lifting on the 5 km scale is not quite enough to initiate the instability. The increased mixing is acting as a cumulus parameterization scheme in its initiation of the convection, but once the instability is triggered the heating and moistening effects are explicitly modelled.

7.3 Simulation Description

The simulation described in this chapter, with three grids and a finest grid horizontal spacing of 5 km, will be referred to as the GRD3 simulation, for comparison purposes with the other simulations. The frontal convergence was initialized on the 5 km grid from the 20 km grid at 0000 UTC. By 0100 UTC the convergence had concentrated down to the 20 km scale, and the explicitly forced squall line convection (deep convection) was evident by 0200 UTC in the simulation. However, this is more than 2 hours after the squall line had developed in actuality. Figure 7.2 compares the hourly positions of the front and

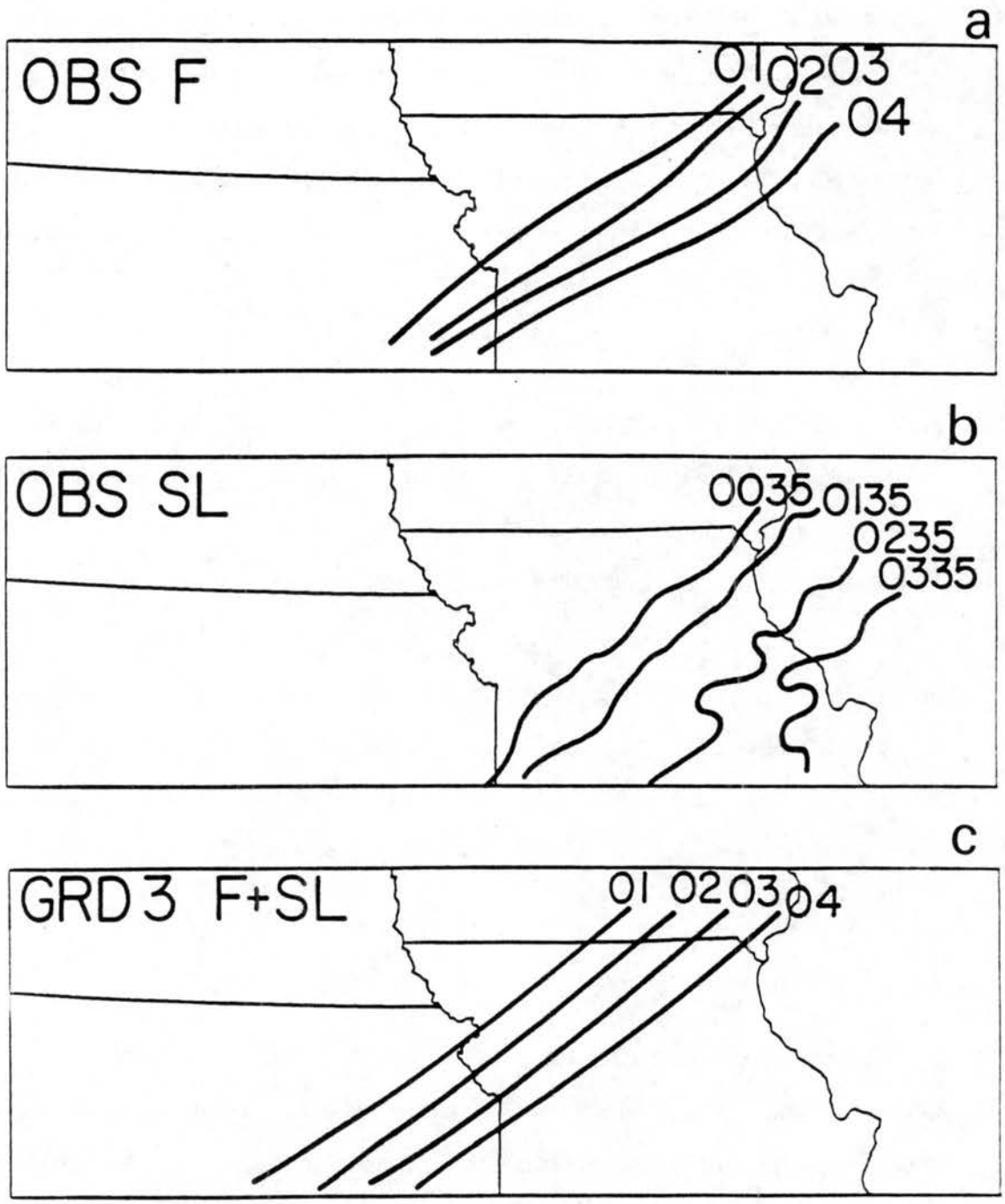

Figure 7.2: Hourly positions from 0100-0400 UTC of the (a) observed front; (b) observed squall line (leading edge of radar echoes); and (c) GRD3 simulated front and squall line.

squall line in the GRD3 simulation and observations from 0100-0400 UTC. The leading edge of the squall line and the front were identical in the GRD3 simulation; there was not any indication of the separation of the squall line from the front as in the ALL and CU simulations. The speed of the observed front is about 8-10 m s^{-1}, and the speed of the front and squall line in the GRD3 simulation is 9 m s^{-1}. Figure 7.3 shows the surface wind, temperature, and accumulated precipitation analyses at 0400 UTC. The surface wind shift line at this time is still located along the leading edge of the squall line (as determined from the leading edge of the precipitation). In the ALL and CU simulations, and in the observations, the surface wind shift line was associated with the front which was approximately 200 km behind the leading edge of the squall line at 0400 UTC. By 0400 UTC there are perturbations associated with the convection in the GRD3 simulation apparent in the surface analyses of wind speed, wind direction, and temperature, but the front is still clearly located at the wind shift line and leading edge of the convection. The squall line is propagating along with the front in this simulation, and is being directly forced by the frontal convergence. There do not seem to be any independent propagation mechanisms for the squall line in this simulation.

Figures 7.4-7.7 are vertical cross sections at half-hourly intervals from 0200-0330 UTC of potential temperature θ, vertical motion w, motion perpendicular to the squall line (i.e., towards the southeast), and total condensate mixing ratio. The cross section location is shown in Fig. 7.1. The vertical motion is only contoured up 50 cm s^{-1} to better indicate the weaker gravity wave motions. The maximum vertical velocities in these cross sections were 3.6, 2.1, 3.3, and 19.0 ms $^{-1}$ at 0200, 0230, 0300, and 0330 UTC respectively. The hypothesized gravity wave motions are superimposed on the figures, and the outline of total condensate (where the squall line "cloud" is) is superimposed on the potential temperature figures. There is an indication of a gravity wave that is being forced by the convection and moving slightly faster than the front and squall line, at about 12 m s^{-1} and with a horizontal wavelength of approximately 120 km. The gravity wave motions that are superimposed on each analysis show that the motions and temperature perturbations

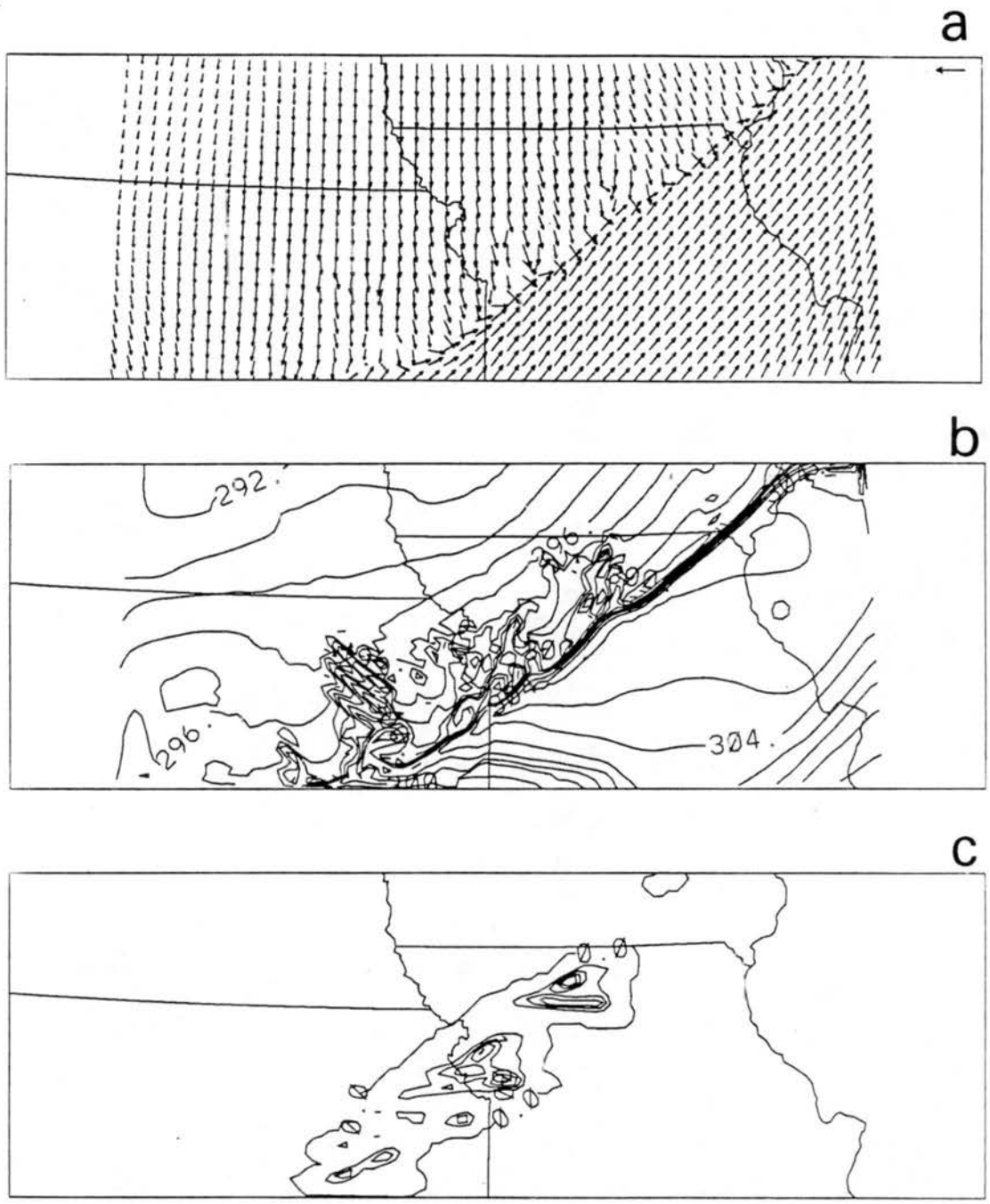

Figure 7.3: Surface analyses at 0400 UTC in the GRD3 simulation of (a) scaled wind vectors (the vector in the upper right corner corresponds to 25 m s^{-1}); (b) temperature (K, contour interval is 1 K); and (c) precipitation accumulated from 0000-0400 UTC (cm, contour interval is 0.5 cm s^{-1}).

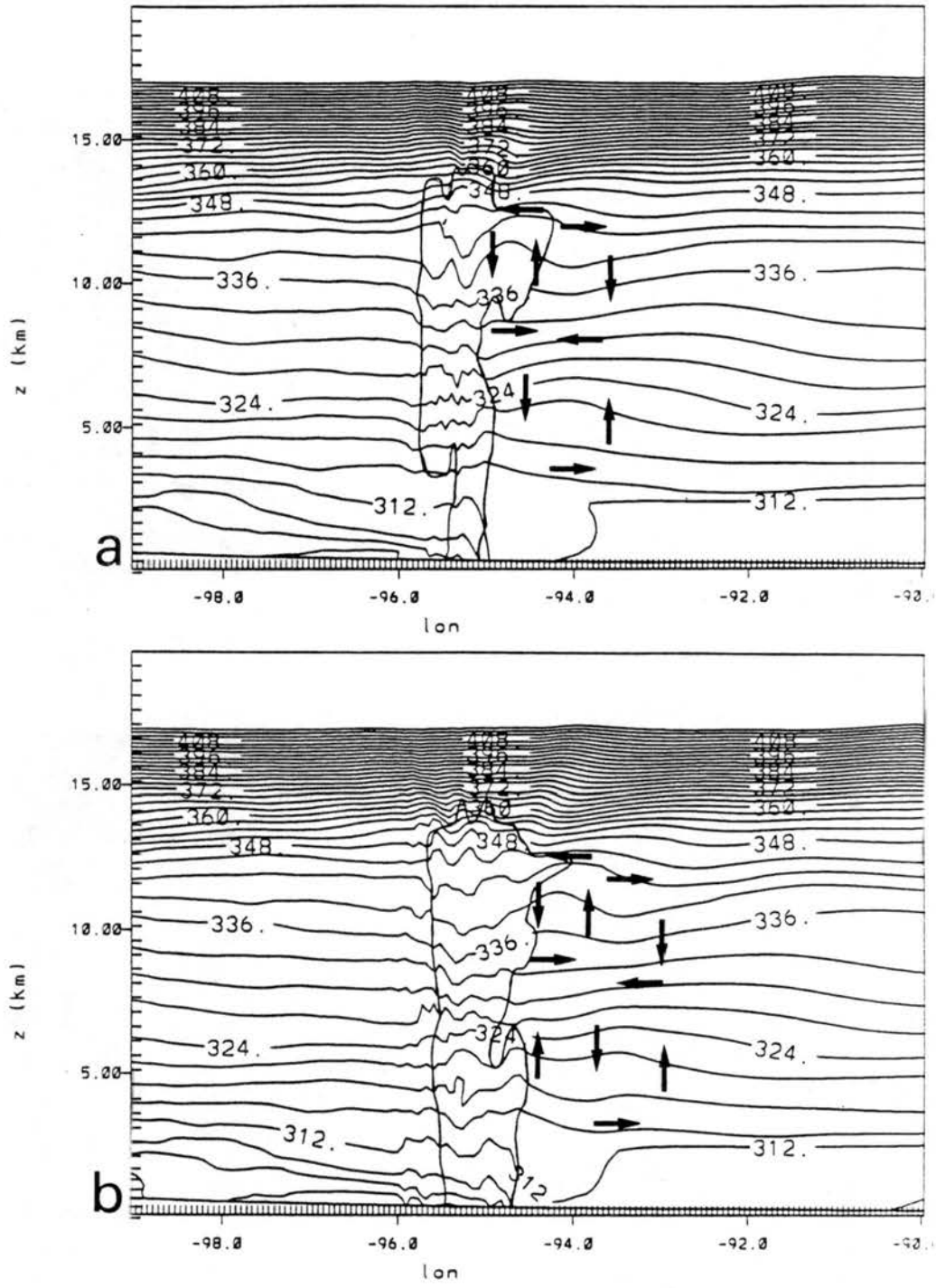

Figure 7.4: Cross sectional analyses of potential temperature θ (K, contour interval is 3 K) at (a) 0200 UTC; and (b) 0230 UTC. The potential temperature is contoured only to 417 K. The hypothesized gravity wave motions and outline of the total condensate are superimposed on the figures.

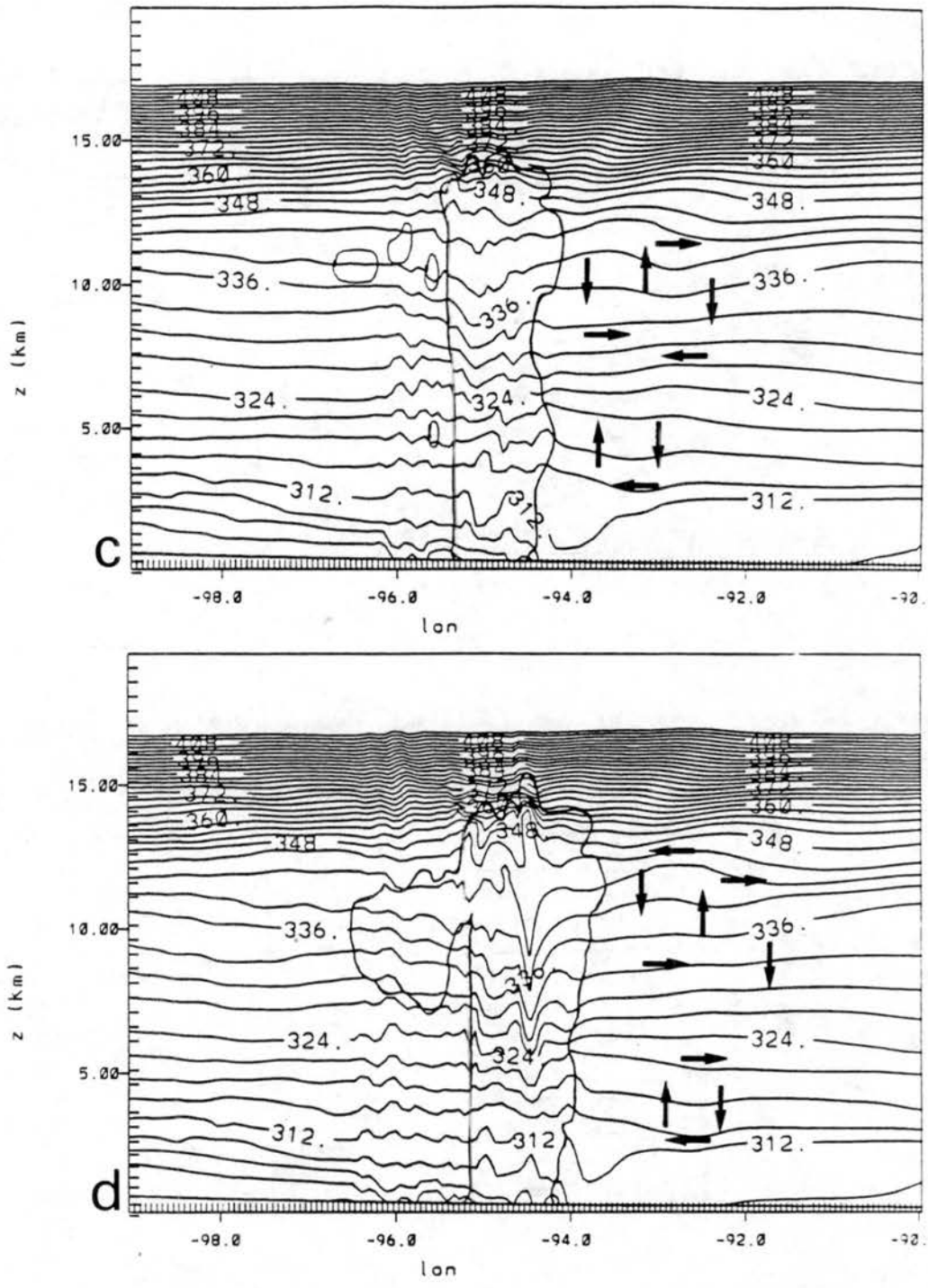

Figure 7.4: Continued: (c) 0300 UTC; and (d) 0330 UTC. The potential temperature is contoured only to 417 K. The hypothesized gravity wave motions and outline of the total condensate are superimposed on the figures.

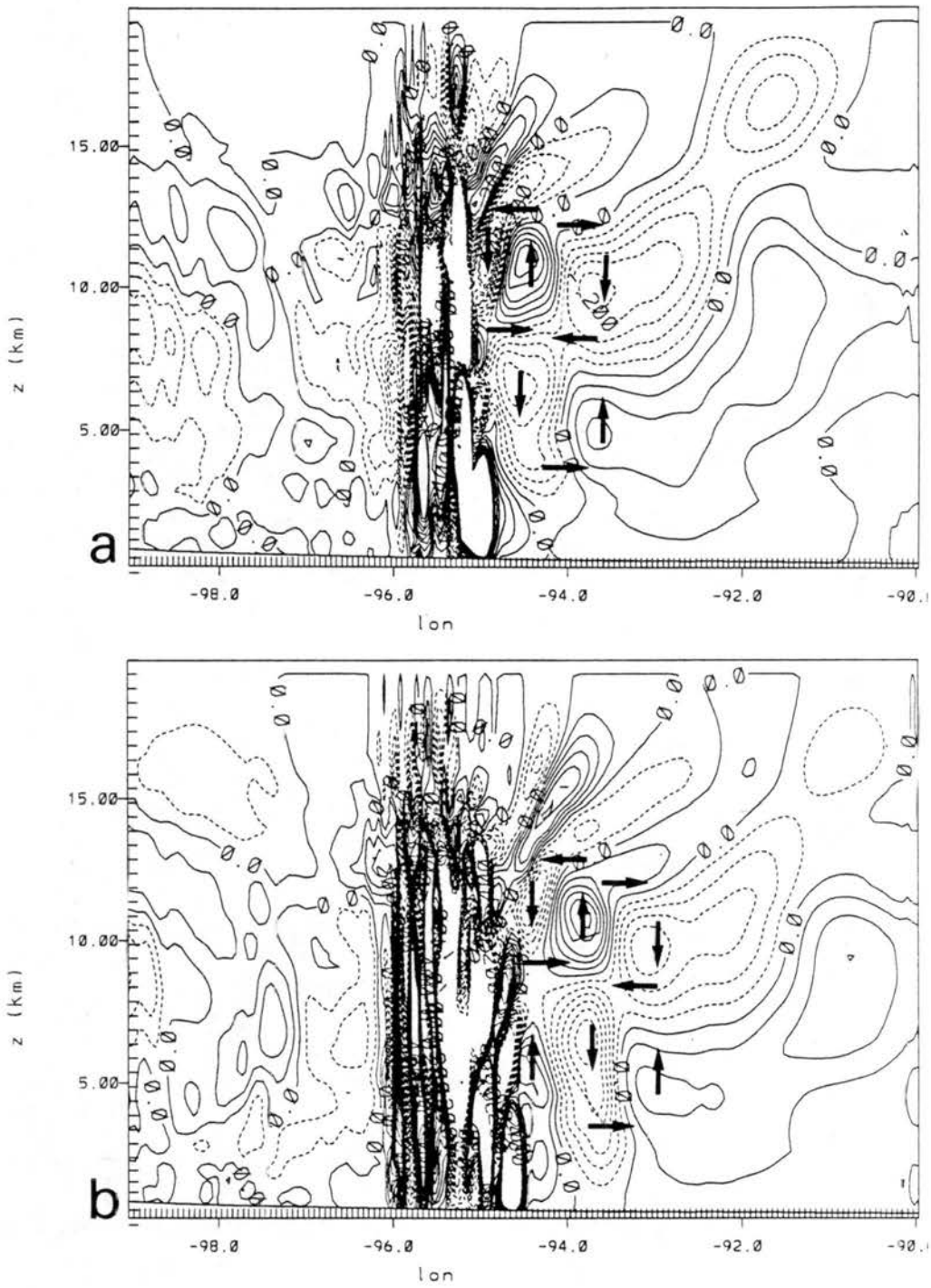

Figure 7.5: Cross sectional analyses of vertical motion w (m s^{-1}, contour interval is .05 m s^{-1}) at (a) 0200 UTC; and (b) 0230 UTC. The vertical motion is only contoured between -50 and +50 cm s^{-1}. The hypothesized gravity wave motions are superimposed on the figures.

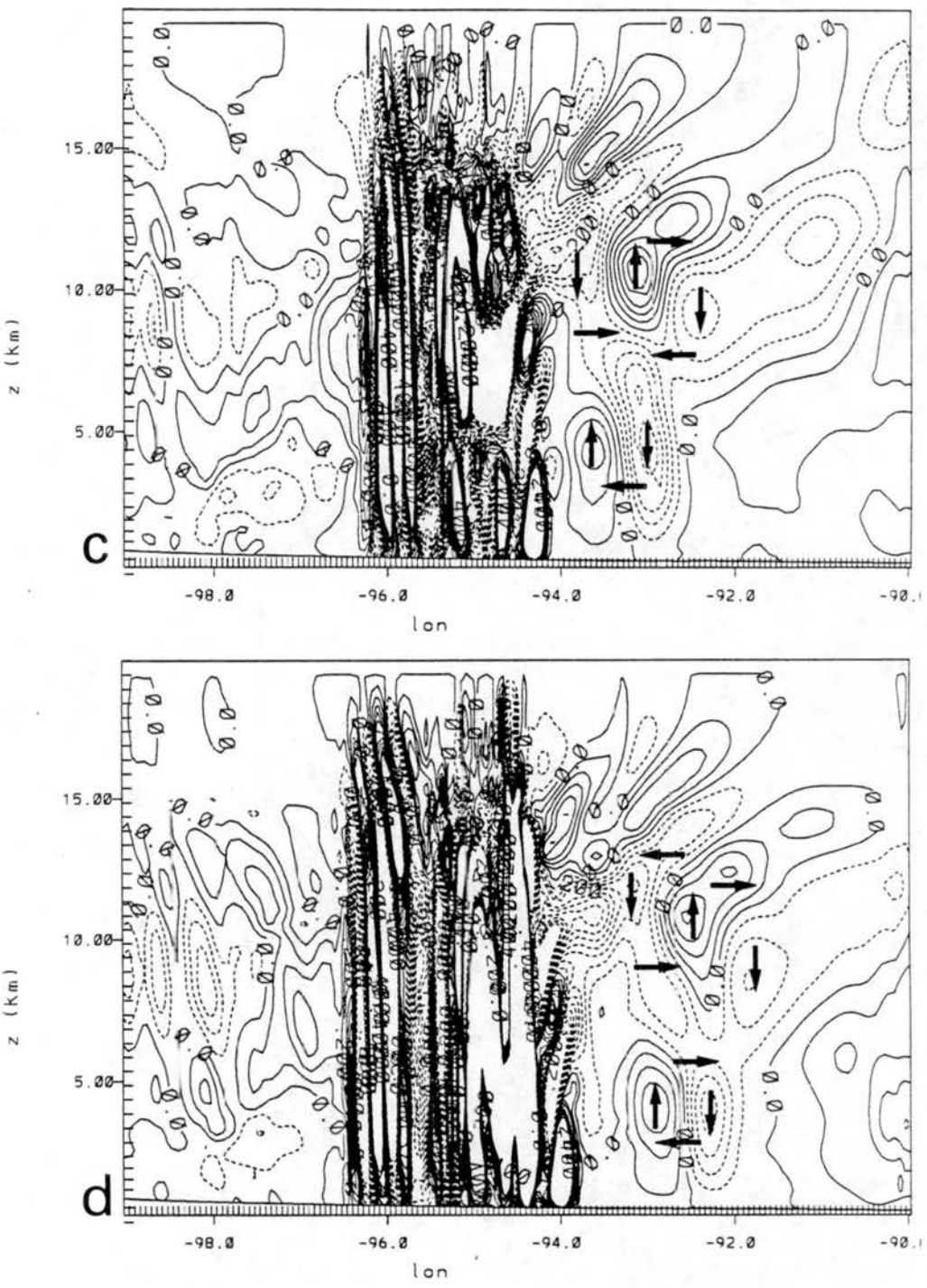

Figure 7.5: Continued: (c) 0300 UTC; and (d) 0330 UTC. The vertical motion is only contoured between -50 and +50 cm s^{-1}. The hypothesized gravity wave motions are superimposed on the figures.

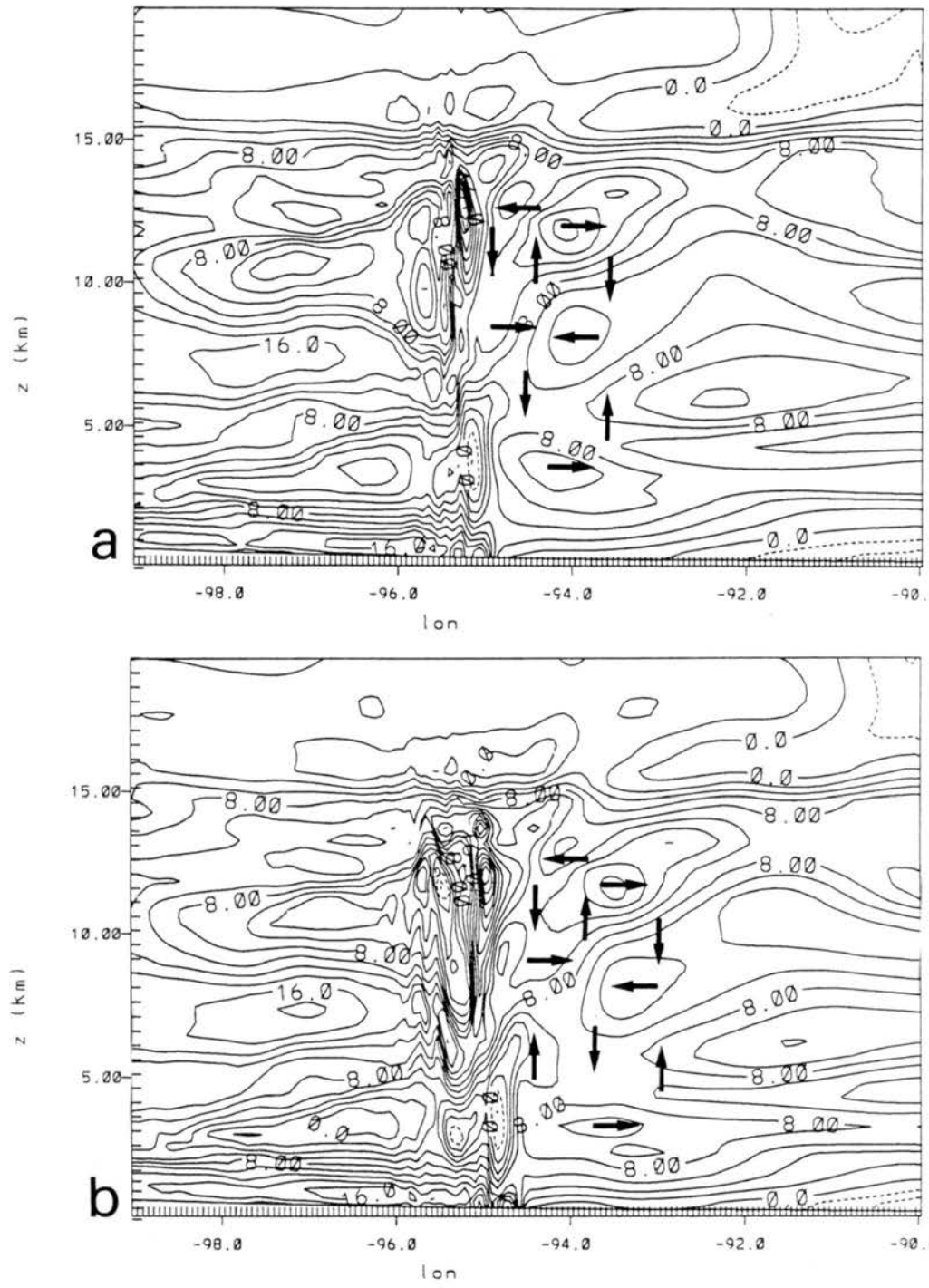

Figure 7.6: Cross sectional analyses of horizontal wind component (m s^{-1}) in the southeastward direction, i.e., perpendicular to the squall line, at (a) 0200 UTC; and (b) 0230 UTC. The hypothesized gravity wave motions are superimposed on the figures.

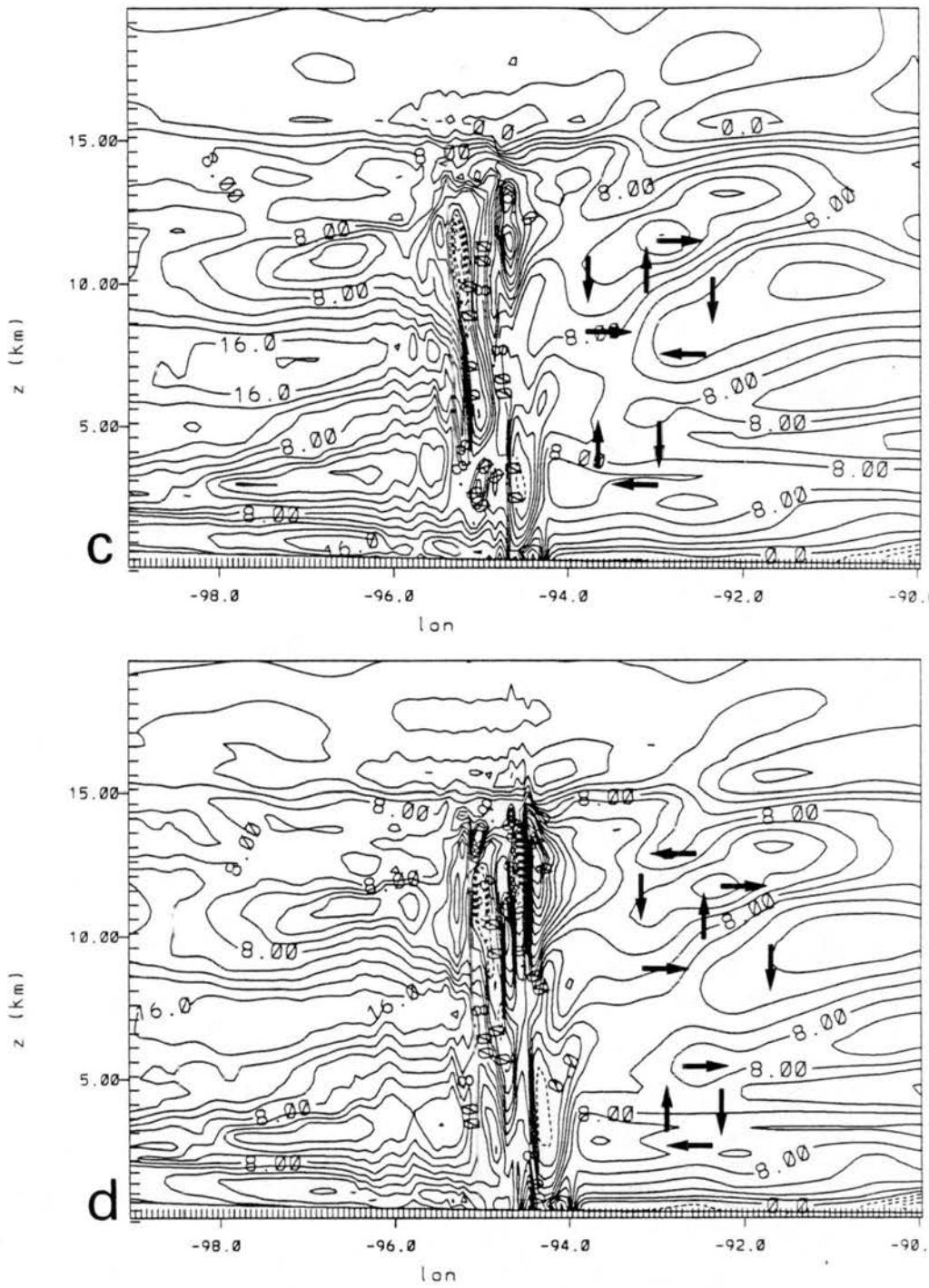

Figure 7.6: Continued: (c) 0300 UTC; and (d) 0330 UTC. The hypothesized gravity wave motions are superimposed on the figures.

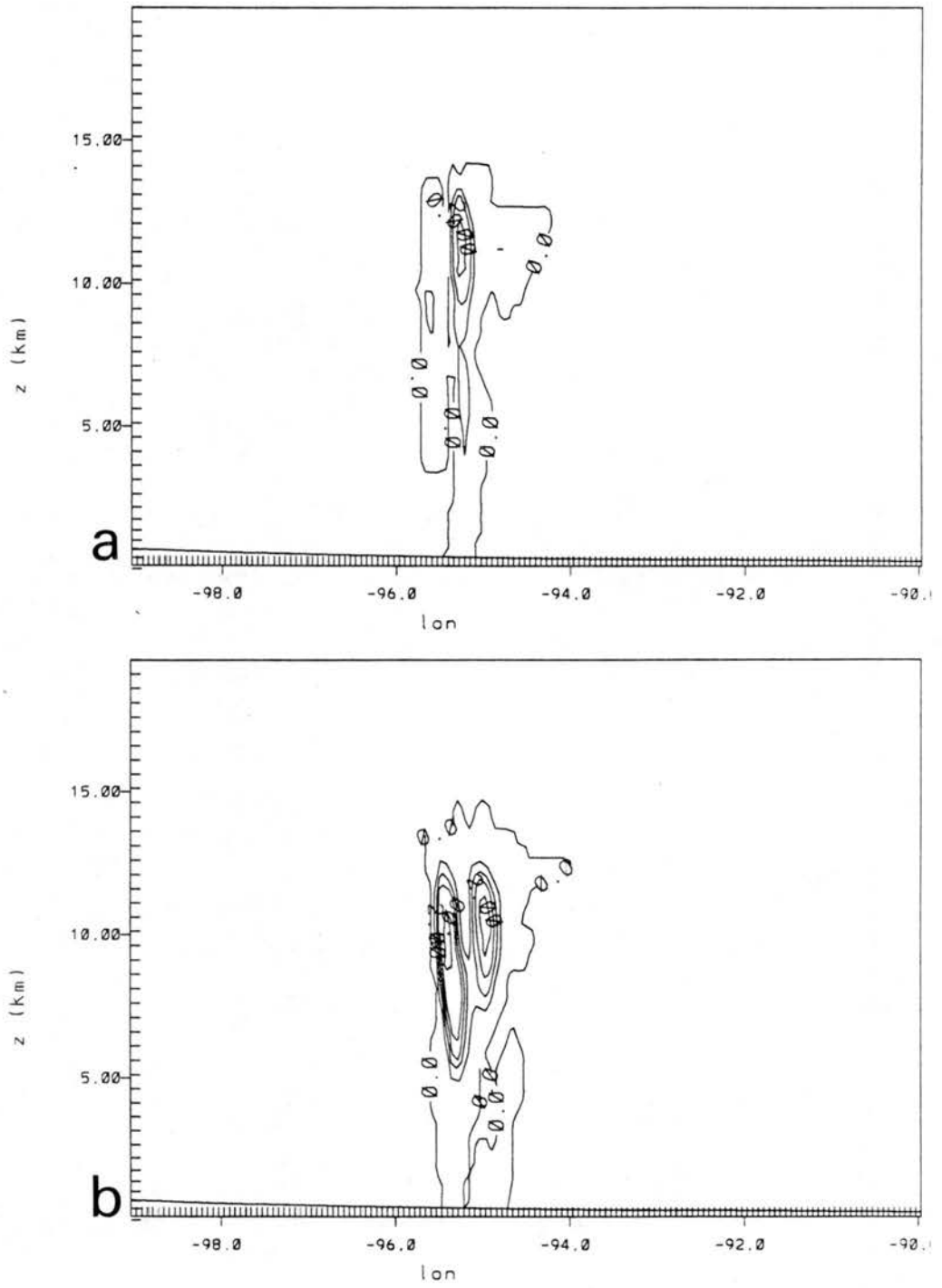

Figure 7.7: Cross sectional analyses of total condensate mixing ratio (g/kg, contour interval is 1.0 g/kg) at (a) 0200 UTC; and (b) 0230 UTC.

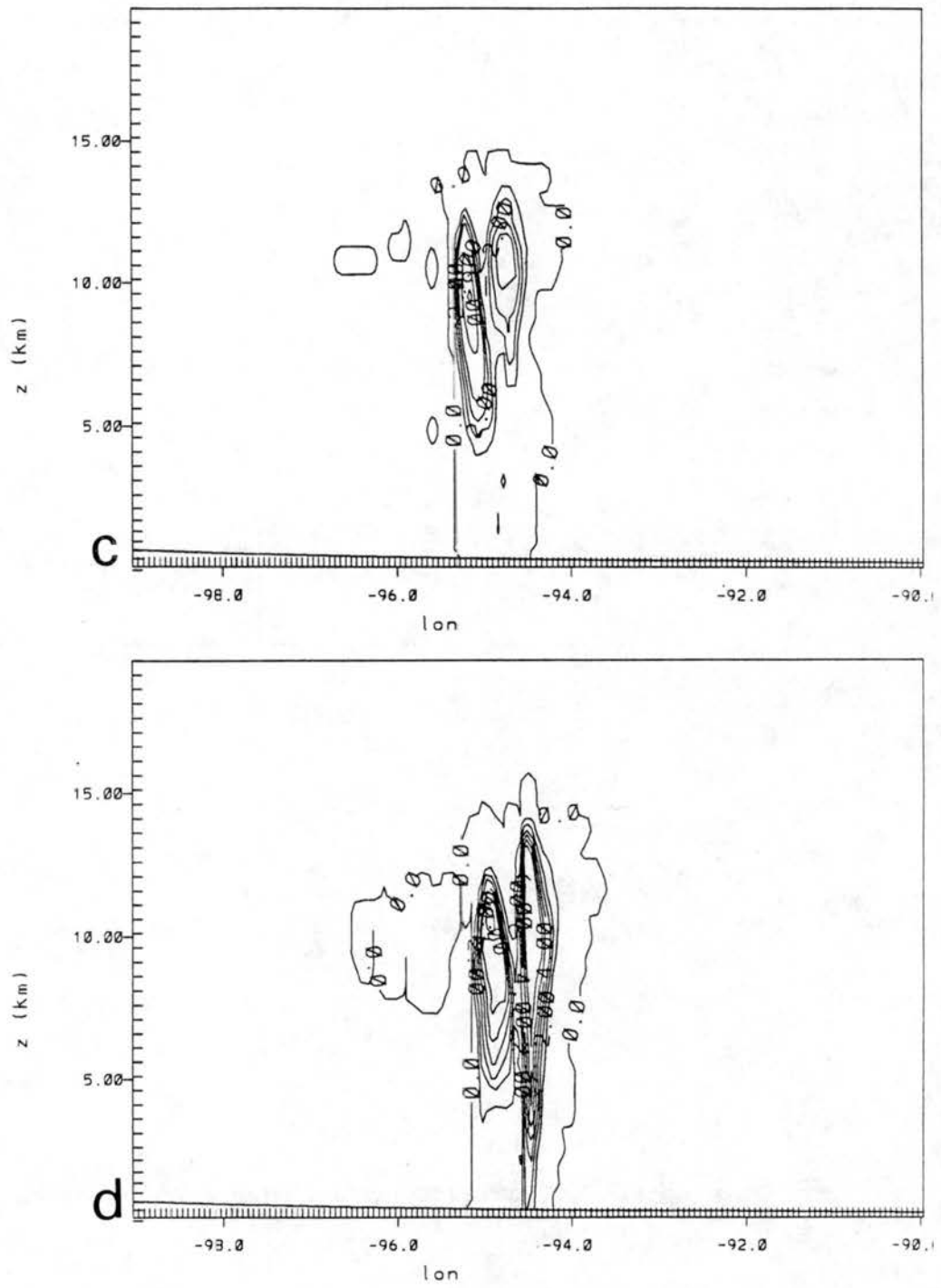

Figure 7.7: Continued: (c) 0300 UTC; and (d) 0330 UTC.

are consistent with gravity wave theory as discussed in Section 2.3. The gravity wave structure at 0200 UTC is similar to that shown in the schematic in Fig. 5.37 for the ALL simulation, but the perturbations in the GRD3 simulation are weaker, the horizontal wavelength is slightly less, and the wave is moving more slowly. Parts of the wave can be followed through the analyses from 0200 through 0330 UTC, but are lost after that. *The convection does not couple with the gravity wave in the GRD3 simulation as it did in the ALL simulation.*

7.4 Discussion/Summary of GRD3 Simulation

The GRD3 simulation was formulated as an attempt to model the squall line development and propagation away from the front without the dependence on the cumulus parameterization scheme. However, several problems were encountered in explicitly modelling the squall line convection. The first problem involved the initialization of the 5 km grid and the proper development of the frontal convergence. The line of horizontal convergence along the front did not develop properly when the 5 km grid was initialized prior to 0000 UTC. The problem with initializing the third grid at 0000 UTC was that the squall line had already developed at that time on the first two grids (by around 2200 UTC). However, it was deemed more important to develop the strong frontal convergence on the 5 km scale than to simulate the initial development of the squall line. Actually, the squall line would not even develop on the 5 km scale without the strong frontal convergence. Another problem was that the convergence on the 5 km scale was apparently not strong enough to explicitly initiate the convection and "break through" the neutral-to-stable boundary layer. A modification to the deformation K-based turbulence parameterization was developed to enhance the vertical mixing where the vertical velocity was above a specified critical value. Convection did then develop with this modification, although still 1-2 hours after that grid was initialized at 0000 UTC. Both of these problems point to the conclusion that the 5 km scale was still not small enough to successfully model the explicit convection processes associated with this squall line. Most cumulus parameterization schemes are written for scales on the order of 50 km or greater, but other investigators

(Zhang and Fritsch, 1987, 1988a,b; Zhang *et al.*, 1988) have found some sort of cumulus parameterization scheme to be necessary even with grid spacings of 10-20 km. However, most explicit simulations of squall line convection have grid spacings of 1-2 km, or even smaller. 5 km may therefore still be to large to explicitly model convective processes, although it is also too small to satisfy the closure assumptions inherent in most cumulus parameterization schemes.

Some investigators have had success in explicitly modelling convection with grid scales of 20-60 km (Rosenthal, 1978; Ross and Orlanski, 1984; Orlanski and Ross, 1986) while others have shown the need for convective parameterizations on those scales (Molinari and Corsetti, 1985; Molinari and Dudek, 1986; Kalb, 1987; Zhang *et al.*, 1988). Cotton and Anthes (1989) point out that the successes occurred in situations where the convection was strongly forced by external conditions. Molinari and Corsetti were unsuccessful in trying to simulate a more weakly forced MCC using only grid-scale condensation processes. The case described here (17-18 June 1978) was forced by strong surface frontal convergence, however there was no additional strong upper level forcing. Both Zhang *et al.* (1988), and Tripoli and Cotton (1989a) also point out that explicitly resolved convection on larger scales may be delayed in its initiation, as was the case here.

The GRD3 simulation was formulated in an attempt to test whether the gravity wave and squall line propagation were fortuitously, but incorrectly, modelled in the ALL simulation. The coupling of the gravity wave and squall line in the ALL simulation resulted in the movement of the squall line away from the front. The convection in the GRD3 simulation was forced by the frontal convergence, and never decoupled from it. There were indications of a gravity wave with the same structure, but much weaker, being forced by the convection in the GRD3 simulation, but the wave moved out ahead of and away from the convection and then dissipated. Tripoli and Cotton (1989a,b) found a similar sensitivity of grid scale to the coupling of gravity waves and convection. They were able to successfully simulate the genesis and propagation of a mesoscale convective system using only explicit, grid-scale, condensational processes on a 1.08 km grid. The

convection on that scale excited transient gravity waves that propagated outwards, away from the convection. When a cumulus parameterization scheme was introduced with a 14 km grid spacing, the convection and gravity wave propagation were incorrectly coupled, and the convection moved much faster than observed. Cotton and Anthes (1989) point out that the cumulus parameterization approach may not be as well-posed on meso-β scales as is on meso-α scales; there is a less distinct scale separation on the meso-β scales between the scales of heating and the resolved scales of forcing.

It is difficult to pinpoint the causes of the failure of the GRD3 simulation. As previously mentioned, there were problems in the initialization of the 5 km grid and the proper development of the frontal convergence and initial convection. The convection finally developed in the GRD3 simulation between 0100 and 0200 UTC, 3-4 hours later than observed or in the ALL simulation. The decoupling of the front and squall line in the ALL simulation mostly occurred between 0000 and 0300 UTC. Another cause of the failure of the GRD3 simulation may be that the convection was not properly represented by the 5 km grid spacing, and thus did not develop the proper vertical profiles of heating and cooling. The gravity wave in the ALL simulation that was coupled with the squall line movement was forced by the vertical profile of heating in the cumulus parameterization scheme. The maximum condensate mixing ratio in the cross-section at 0330 UTC (Fig. 7.7d) is 9 g/kg, which is a reasonable value for the main convective core. There does not appear to be any development of a stratiform region or any steady convective downdrafts and outflow. Those structures were not apparent in the ALL simulation either. However, the insignificant effect of the explicit microphysical processes on the squall line in the ALL simulation was attributed to the larger scale (20 km) and deficiencies in the modelled interactions between the cumulus parameterization scheme and explicitly resolved microphysical processes.

It is also likely that the increased vertical diffusion that was required to initiate the convection on the 5 km scale (and that was dependent upon the vertical velocity) may have anchored the convection to the region of strong frontal convergence. The increased

diffusion may have forced the continued coupling between the strong frontal convergence and the convection, thus never allowing the decoupling of the convection with the frontal convergence and subsequent coupling with the gravity wave. The increased diffusion may also have acted to destroy the vertical and horizontal coherence of the developing gravity wave.

Overall, the failure of the GRD3 simulation to properly simulate the squall line is probably attributable to both the problems in the initialization of the frontal convergence and convection (and thus the need to incorporate the increased vertical diffusion), and that the 5 km grid spacing was not small enough to accurately simulate the explicit microphysical processes.

Chapter 8

SUMMARY

The study results are summarized in this chapter. Section 8.1 is a brief discussion of the observed aspects of the squall line that occurred on 17-18 June 1978. The modelling results are briefly reviewed and discussed in Section 8.2. The propagation of the squall line as an internal gravity wave is discussed in Section 8.3, and Section 8.4 is a brief summary of possible related topics for future work.

8.1 Observed Squall Line

The squall line that is the subject of this investigation occurred on 17-18 June 1978 and was described in Chapter 3. Srivastava *et al.* (1986) did a Doppler radar study of part of the anvil region at the northern end of the squall line. This squall line developed very explosively between 2100 UTC 17 June and 0000 UTC 18 June 1978, with a narrow, continuous line of convection extending from Illinois to the Texas panhandle by 0000 UTC. The squall line was initially triggered by the strong convergence across a surface cold front, but then moved out ahead of and away from the cold front between 0000 and 0600 UTC. The strongest convection in the lifetime of the squall line occurred before 0300 UTC. The separation between the front and squall line was about 200 km by 0300 UTC and 300-400 km by 0600 UTC. Both Srivastava *at al.* and Thomas Matejka (personal communication, discussed in Section 3.2) noted that the squall line propagated discretely, with new convection forming 25-100 km ahead of the gust front, and hypothesized that some sort of gravity wave motion might be responsible for the non-gust-front type of propagation. This squall line is described as prefrontal, which it is in the sense that it

separated from the cold front, but it is not the same as the prefrontal squall lines that initially develop several hundred kilometers ahead of the cold front.

8.2 Modelling Results

The CSU RAMS model was used for the modelling simulations described in this study, and was described in Section 4.2. A non-hydrostatic version of the model was used, with nested grid spacings down to 20 km and 5 km. The primary simulations used a coarse grid spacing of 80 km and a fine grid spacing of 20 km. The model simulations were all initialized at 1200 UTC 17 June 1978 from an analysis of the NMC spectral model data and available rawinsonde and surface observations. Four different simulations were completed in an attempt to isolate the effects of the cumulus parameterization scheme (a modified Kuo-type scheme) and the grid scale microphysical processes:

DRY: no cumulus parameterization, no latent heating, and no grid-scale microphysical processes.

MIC: no cumulus parameterization, but grid-scale microphysical processes were included.

CU: cumulus parameterization, grid-scale latent heating and cloud water production from condensation, but no grid-scale microphysical processes.

ALL: cumulus parameterization, grid-scale microphysical processes.

Another simulation (referred to as SFC) was also completed with varying initial fields of surface roughness z_0, soil texture, and soil moisture. A final simulation with a third grid that had a spacing of 5 km was completed in an attempt to explicitly model the squall line, without the convective parameterization.

8.2.1 Basic simulations

The simulation of the squall line in the ALL and CU simulations (with 20 km grid intervals) compared well with the observed squall line movements. Both simulations used

a modified Kuo-type cumulus parameterization scheme, and the ALL simulation also included the grid scale microphysical processes. The CU simulation included grid-scale latent heating effects and production of cloud water, but no parameterization of microphysical or grid-scale precipitation processes. The squall line in the ALL and CU simulations initially developed in the zone of strong surface frontal convergence between 2100 and 0000 UTC. By 0000 UTC the squall line was evident in the model as a solid line of convection extending from Iowa to the Texas panhandle. Between 0000 and 0600 UTC the squall line separated from the front in the ALL and CU simulations, moving approximately 200 km ahead of the front by 0300 UTC and 300-400 km ahead of the front by 0600 UTC. The positions of the simulated squall line and front in the CU and ALL simulations compared well with the observed positions of the squall line and front, as summarized in Fig. 5.34. The squall line convection did not form in the MIC simulation at all, where only the grid-scale microphysical processes were represented. A cumulus parameterization scheme was necessary to simulate the effects of deep cumulus convection with the 20 km grid spacing.

Some aspects of the meso-α and β scale structure of the squall line in the CU and ALL simulations compared very well to observed squall line structures while other aspects did not. The presquall mesolow and convective mesohigh regions were consistent in the model analyses, but there was no indication of a wake low region, rear inflow jet, or gust front processes. The lack of a wake low region and rear inflow jet are due to the failure of the model to produce any significant heating or microphysical processes in the anvil region. It is not clear whether this is due to a deficiency in the model microphysical processes or cumulus parameterization scheme, or to an otherwise improper simulation that then inhibited the anvil formation. The squall line moved at approximately 18 m s^{-1} in the model simulations, and was moving too fast (in the model) for any anvil-related heating processes to consolidate. The grid-scale microphysical processes in the model simulations were only significant in regions of strong upward motion (along the convective core region of the squall line), or in semi-stationary regions where the heating and precipitation processes had a positive feedback effect (similar to conventional CISK). The cumulus parameteri-

zation scheme may be deficient in that it does not produce or transport condensate, only moisture. The lack of the production of a gust front or consistent cold downdraft processes is also tied to the apparent lack of significant grid-scale microphysical processes. The cumulus parameterization scheme used in these simulations does have a modification for cold downdraft effects, but their effects were insignificant in these simulations.

Zhang and Fritsch (1986, 1988a,b), Zhang *et al* (1989), and Zhang and Gao (1989) were apparently able to simulate the rear inflow, wake low region, and cold downdrafts and gust front in a squall line simulation with a fine grid interval of 25 km. They used a version of the Fritsch and Chappell (1980a,b) (FC) cumulus parameterization on their fine grid which has a more explicit calculation of downdraft effects. However, Tremback (1990) has pointed out that the FC scheme is very dependent on several arbitrary parameters, and thus subject to much "tweaking" for different simulations. As previously discussed, the FC scheme produces excessive amounts of heating, and at levels too high (compared with observations). The excessive heating apparently induces low-to-mid level ascent and saturation. The FC scheme is thus effectively parameterizing aspects of both the convective and stratiform heating, although in the above cases it was also used in addition to the grid-scale condensational processes.

8.2.2 SFC simulation

The SFC simulation (discussed in Chapter 6) was different from the ALL simulation in that horizontally-varying values of surface roughness length z_0 and soil texture were specified, and the initial soil moisture profile was modified by the past 24 hours precipitation. The results from the SFC simulation were generally very similar to those of the ALL simulation, especially in the vicinity of the squall line as it was dynamically forced by the large-scale baroclinicity and associated frontal convergence. The differences between the ALL and SFC simulation were most apparent to the east of the squall line where the baroclinicity was weak and the convection was more of the "air mass" type. Although there was not any precipitation in the previous 24 hours over most of the region where the squall line developed (and also to its east), most of the differences between the ALL and

SFC simulations appeared to be due to soil moisture differences. The initial specification of soil moisture in the SFC simulation was altered by the soil texture distribution, as different types of soil can hold different amount of moisture.

8.2.3 5 km grid spacing simulation

The simulation with 5 km grid spacing attempted to explicitly model the squall line convection without any dependence on the cumulus parameterization, and was discussed in Chapter 7. Difficulties were encountered in properly simulating the frontal convergence on that scale, and initially triggering the convection. A modification to the vertical mixing in the turbulence parameterization was introduced, similar to that used by Ross and Orlanski (1982). The modification specified increased vertical mixing dependent upon a critical vertical velocity, and did result in the convection then developing in the model, although much later than observed. However, the convection never did couple with the gravity wave and separate from the front. It thus moved much more slowly than in the ALL and CU simulations and in the observations.

A few other investigators have had some success in explicitly modelling convection on much larger scales (Rosenthal, 1978; Ross and Orlanski, 1982; Orlanski and Ross, 1984) although many others have found cumulus parameterization schemes necessary on grid spacings down to 10 km (Molinari and Corsetti, 1985; Molinari and Dudek, 1986; Kalb, 1987; Zhang *et al.*, 1988). Although the squall line in this case was strongly forced by the surface frontal convergence, there was not any strong forcing aloft, and the squall line developed and propagated in a low-level neutral-to-stable environment (slightly stable with respect to θ_e). The existence of the stable air ahead of the front and squall line was found to be critical to the proper initiation and development of the squall line convection, as it inhibited premature convection. The successes with explicit convection with larger horizontal grid spacings apparently occurred in cases with strong external forcing and limited model vertical resolutions. A low level stable layer does not exist in either of the two cases listed above, nor would it be resolvable in their vertical resolutions. It is also possible that the increased vertical mixing (although it is only allowed to occur below

6500 m) destroyed the vertical and horizontal coherence necessary for the convection and gravity wave to couple properly.

The convection in the 5 km simulation also did not develop a large or strong anvil region. The failure of the separation of the front from the squall line in this simulation was probably partly due to the timing of the development of the convection (much later than in the CU and ALL simulation), and probably also again due to the improper simulation of the microphysical processes on this scale, as only features with a horizontal size of 20 km or greater can be reasonably resolved in this model integration.

8.2.4 Issue of predictability

The issue of the predictability of meso-α and β scale features in models from standard synoptic information has been posed by Anthes *et al.* (1982). As mentioned above, Zhang and Fritsch (1986, 1988a,b), Zhang *et al.* (1989), and Zhang and Gao (1989) were able to simulate many of the meso-β scale features associated with a squall line in a model with a fine grid interval of 25 km. Several of the meso-β scale features of the squall line were also simulated in the model results described in this work, such as the presquall mesolow and mesohigh. These results, and those mentioned above, are promising in that they imply that smaller scale features and structures associated with convection can indeed be modelled even when only meso-α and synoptic scale information is available for model initialization. However, Zhang and Fritsch pointed out that the predictability of these features will be better in situations where the system is more strongly forced by the environmental dynamics than the thermodynamics. Such was the case for the 17 June 1978 squall line.

The issue of predictability is also related to the availability of initial analysis data. Soil moisture and soil texture are variables that are not usually considered, nor easily available, for model initial analyses. The results in this case were not particularly sensitive to the initial soil moisture specification, although that may again have been due to the fact that the squall line was very strongly forced by the frontal convergence. There did appear to

be more sensitivity to the soil moisture specification in regions of weaker baroclinicity, to the east of the squall line.

8.3 Propagation of the Squall Line as an Internal Gravity Wave

The 17-18 June 1978 squall line was initially triggered along the frontal zone but then moved southeastward faster than the front, resulting in a separation of 300-400 km by 0600 UTC. The primary movement of the squall line in the modelled simulations was hypothesized in Chapter 5 to be due to the propagation of a deep tropospheric internal gravity wave. The perturbations of pressure, potential temperature θ, and of the velocity components were shown to be consistent with gravity wave motions. The wave was forced by the upper level heating maximum associated with the convective parameterization, in a wave-CISK-like process. Very similar results were found by Xu and Clark (1984) in a wave-CISK model. The structure of the hypothesized wave was illustrated in Fig. 5.37. The wave had a horizontal wavelength of $\sim$200 km and traveled towards the southeast at 18 m s^{-1}. The vertical wavelength of the wave was 10 km. The wave retained most of its energy as it propagated southeastward because of constructive reflection of the wave from the discontinuity in stability across the tropopause and from a low-level layer where the Scorer parameter was very small. The wave was strongest between 0000 and 0300 UTC and became much less coherent after 0300 UTC. In Section 5.4 it was hypothesized that the mechanism of the positive reinforcement of the wave was destroyed as the heating maximum associated with the convective parameterization gradually widened and rose with time. There are also indications that a critical layer formed around 0300 UTC, which would absorb the wave energy. The squall line did continue to propagate southeastward between 0300 and 0600 UTC, although not as quickly or coherently.

Although the propagation of the squall line as an internal gravity wave in the model has been established, that does not necessarily mean that the squall line propagated that way in reality. The most prevalent mechanism in the current literature for squall line propagation is by the low-level convergence forced ahead of the gust front (Moncrieff and Miller; 1976; Houze, 1977; Ogura and Liou, 1980; Thorpe *et al.*, 1982; Smull and Houze,

1985, 1987; Kessinger *et al.*, 1987; Rotunno *et al.*, 1988; Johnson and Hamilton, 1988; Zhang and Gao, 1989). Some of the studies that propose gravity-wave related mechanisms for squall line propagation include Ley and Peltier (1978), Raymond (1975, 1976, 1983, 1984), Xu and Clark (1984), Orlanski and Ross (1984, 1986), Nehrkorn (1986), and Schmidt and Cotton (1990). Observational studies will be biased towards the gust front mechanism as the surface cold pool and convergence are easily observable. In addition, the upper level perturbations associated with gravity wave motions may be significantly weaker than other perturbations associated with strong convection and thus hard to observe. Many modelling studies are also biased towards gust front propagation as they may be unable to force or simulate larger scale perturbations. Most modelling studies of squall line structure and maintenance have grid spacings on the order 1-2 km and are initialized from one sounding, i.e., a horizontally-homogeneous environment. The convection in those simulations is triggered by an artificial "warm bubble" or area of convergence. The scales of motion, and structure of the system, are then independent of any initial meso-α or synoptic scale variations in the real atmosphere that might tend to favor certain scales or propagation processes. Crook and Moncrieff (1988) point out that large scale convergence can significantly alter squall line environments and triggering mechanisms.

Both Srivastava *et al* (1986) and Thomas Matejka (personal communication) noted that this squall line did not always propagate as a result of gust front convergence, as new convection systematically formed 25-100 km ahead of the gust front. It does not seem likely that the propagation of the 17-18 June 1978 squall line (or any squall line) can be entirely due to gravity wave motions, or entirely without any propagation due to gust front convergence. Instead, there is probably a spectrum of motions responsible for the squall line propagation, and the dominance of one particular scale of motion or mechanism is dependent upon the forcing scales and environmental conditions. The gravity wave mechanism was predominant in these simulations because of the particular thermodynamic and shear environment. The heating profile produced by the cumulus parameterization scheme was also inherent to the gravity wave generation. The effects of stronger downdraft and

anvil processes in the model would perhaps be to "mix", and also to mask the propagation mechanisms.

A major concern in interpreting the results of these simulations was whether the gravity wave was simply numerically forced in the model, as a result of improper boundary specifications or dependences upon the parameterizations. A modified form of Rayleigh friction was formulated to work with the "wall" top boundary condition to minimize the possibility of improper reflections from the top of the model. The Rayleigh friction layer extended from 15-20 km in the model, and thus did not even start until several kilometers above the top of the gravity wave. As discussed in Chapter 5, the semi-resonance of the wave implies partial reflection from the stability discontinuity at the tropopause, still below the layer of Rayleigh friction. The other concern was the use of the cumulus parameterization scheme, which is inherently coupled to the generation of the gravity wave through its upper level heating profile. Cumulus parameterization schemes are designed to accurately model the effects of convection on scales that are too large to explicitly model the convection, and the upper level heating profile is considered realistic in an average, grid-scale sense. However, the 5 km grid spacing simulation was formulated as an attempt to explicitly model the squall line convection and its separation from the front without the dependence on the cumulus parameterization. Unfortunately, that simulation was unsuccessful in that the convection developed much later than observed and then did not move away from the front. It was necessary to introduce an increased vertical mixing on the 5 km scale in order to initiate the convection, but the increased mixing may have also acted to destroy any vertical and horizontal coherence necessary for the convection and gravity wave coupling. Tripoli and Cotton (1989a) used a two-dimensional model with a 1 km horizontal grid spacing to simulate the formation and movement of an orogenically-forced mesoscale convective system. They found that the use of a cumulus parameterization scheme on a coarser grid (14 km grid spacing) improperly coupled the occurrence of convection in their simulations with a propagating meso-β scale wave. However, other studies have shown an apparently reasonable coupling of convection with meso-β scale gravity

wave propagation, including the wave-CISK studies of Raymond (1984) and Xu and Clark (1984). The good agreement between the observed and simulated squall line movements in this case lends credence to the gravity wave mechanism of propagation.

8.4 Future Research

Several suggestions for future research and study that became apparent during the course of this work are outlined in this section. The first area of study is that of cumulus parameterization schemes. The problems associated with cumulus parameterization schemes were discussed by Frank (1983) and do not seem to have been solved yet. An infinite number of sensitivity experiments could be done with the simple modified-Kuo-type scheme used in this work, such as increasing the downdraft intensity. Other researchers have had apparent success with the Fritsch and Chappell (1980a) (FC) scheme (Zhang and Fritsch, 1986, 1988a,b; Zhang *et al.*, 1988; Zhang and Gao, 1989), but as Tremback (1990) points out, the adjustments of the many arbitrary parameters in that scheme are very case-dependent, excessive heating is produced by the scheme, and the heating maximum is generally too high.

A second area of future research would be to again attempt to model this squall line with explicitly-resolved convective processes. The 5 km grid spacing simulations discussed in Chapter 7 were unsuccessful both because of the failure of the frontal convergence to develop properly on the 5 km grid, and then because the convergence on that scale was not quite strong enough to trigger the convection. A modification was developed (and discussed in Chapter 7) to increase the vertical mixing, but the convection still developed too late. The problem with the proper development of the initial frontal convergence in the time period from 1800 UTC 17 June through 0000 UTC 18 June may be solved by increasing the domain area of the finest mesh grid. The problem with the convergence strength may be solved by decreasing the horizontal grid interval (perhaps to 2 km). Together these requirements necessitate very large computer memories, but would perhaps be possible on a CRAY-2 computer (with job memory limits on the order of 100-200

megawords). A movable fine-grid was developed for version 2B of the RAMS model and would help decrease domain size requirements.

The third area of possible research related to this work, and perhaps the most realistic, would be to do a series of two-dimensional simulations with very small grid resolutions. It would be interesting to see if the deep tropospheric internal gravity wave could be simulated with explicit convection processes, as was attempted in the three-dimensional simulations described in Chapter 7. Two-dimensional, fine-scale simulations may also help to clarify the possible different mechanisms of the squall line propagation in this case. One possible mechanism, not investigated in this study, would be that the discrete squall line convection was forced by a low-level internal gravity wave traveling ahead of the squall line (and gust front if there was one), along the more stable, presquall, boundary layer as an internal undular bore. Similar mechanisms have been proposed by Nicholls (1987), Crook *et al.* (1990), and Carbone *et al.* (1990).

Finally, the problem of the interpolation of coarse grid values of soil texture and surface roughness length to a fine grid needs to be addressed. The simplistic type of interpolation procedure used for the simulations described in Chapter 6 results in noisy, "boxy-looking" analyses. The value of soil texture and surface roughness length for each of the 16 different 20 km square fine grid boxes composing an 80 km square coarse grid box is simply the same as the single value for that one coarse grid box. As mentioned previously, the coarse grid analyses of soil texture are integer values, and need to remain as integers on the fine grid. It is also not evident that it would be correct to introduce new integers (and thus soil texture types) as intermediate values in the interpolation procedure. The same argument also applies to the analyses of surface roughness length. Even though the values of z_0 are real numbers, the values of z_0 are not linearly related to vegetation height, and it is not obvious how to interpolate between two different values of z_0. For example, it might be more accurate to do an interpolation or analysis as a function of $\sqrt{z_0}$. The problem of designing a smoother interpolation procedure for these variables needs to be considered in future research.

REFERENCES

Alexander, R.C., and R.L. Mobley, 1974: Monthly average sea-surface temperatures and ice-pack limits on a 1° global grid. DARPA report R-1310-ARPA, ARPA order NO. 189-1, 30 pp.

Anthes, R.A. and D. Keyser, 1979: Tests of a fine-mesh model over Europe and the United States. *Mon. Wea. Rev.*, **107**, 963-984.

Anthes, R.A., Y.-H. Kuo, S.G. Benjamin, and Y.-F. Li, 1982: The evolution of the mesoscale environment of severe local storms: Preliminary modelling results. *Mon. Wea. Rev.*, **110**, 1187-1213.

Arakawa, A. and V.R. Lamb, 1981: A potential enstrophy and energy conserving scheme for the shallow water equations. *Mon. Wea. Rev.*, **109**, 18-36.

Barnes, G.M. and K. Sieckman, 1984: The environment of fast- and slow-moving tropical mesoscale convective cloud line. *Mon. Wea. Rev.*, **112**, 1782-1294.

Barnes, S.L., 1964: A technique for maximizing details in numerical weather map analysis. *J. Appl. Meteor.*, **3**, 396-409.

Barnes, S.L., 1973: Mesoscale objective map analysis using weighted time-series observations. NOAA Technical Memorandum ERL NSSL-62, National Severe Storms Laboratory, Norman, OK, 38 pp.

Beland, M., 1976: Numerical study of the nonlinear Rossby wave critical level development in a barotropic zonal flow. *J. Atmos. Sci.*, **33**, 2066-2078.

Bleck, R. and P.L. Haagenson, 1968: Objective analysis on isentropic surfaces. NCAR Technical Note TN-39. December 1968.

Bluestein, H.B. and M.H. Jain, 1985: Formation of mesoscale lines of precipitation: Severe squall lines in Oklahoma during the spring. *J. Atmos. Sci.*, **42**, 1711-1732.

Blumen, W., 1972: Geostrophic adjustment. *Rev. Geophys. Space Phys.*, **10**, 485-528.

Bolton, D., 1980: Application of the Miles theorem to forced linear perturbations. *J. Atmos. Sci.*, **37**, 1639-1642.

Bolton, D., 1984: Generation and propagation of African squall lines. *Quart. J. Roy. Meteor. Soc.*, **110**, 695-721.

Bosart. L.F., and J.P. Cussen, Jr., 1973: Gravity wave phenomena accompanying east coast cyclogenesis. *Mon. Wea. Rev.*, **101**, 446-454.

Bosart, L.F., and F. Sanders, 1986: Mesoscale structure in the megalopolitan snowstorm of 11-12 February 1983. Part III: A large-amplitude gravity wave. *J. Atmos. Sci.*, **43**, 924-939.

Bosart, L.F., and A. Seimon, 1988: A case study of an unusually intense atmospheric gravity wave. *Mon. Wea. Rev.*, **116**, 1857-1886.

Bougeault, P., 1983: A non-reflective upper boundary condition for limited-height hydrostatic models. *Mon. Wea. Rev.*, **111**, 420-429.

Boville, B.A., 1986: Wave-mean flow interactions in a general circulation model of the troposphere and stratosphere. *J. Atmos. Sci.*, **43**, 1711-1725.

Boville, B.A., and X. Cheng, 1988: Upper boundary effects in a general circulation model. *J. Atmos. Sci.*, **45**, 2591-2606.

Bretherton, C., 1988: Group velocity and the linear response of stratified fluids to internal heat or mass sources. *J. Atmos. Sci.*, **45**, 81-93.

Brown, J.M., 1979: Mesoscale unsaturated downdrafts driven by rainfall evaporation: A numerical study. *J. Atmos. Sci.*, **36**, 313-338.

Browning, K.A., 1964: Airflow and precipitation trajectories within severe local storms which travel to the right of the winds. *J. Atmos. Sci.*, **21**, 634-639.

Cahn, A., 1945: An investigation of the free oscillations of a simple current system. *J. Meteor.*, **2**, 113-119.

Carbone, R.E., J.W. Conway, N.A. Crook, and M.W. Moncrieff, 1990: The generation and propagation of a nocturnal squall line. Part I: Observations and implications for mesoscale predictability. *Mon. Wea. Rev.*, **118**, 26-49.

Chang, C.P., J.E. Millard, and G.T.J. Chen, 1983: Gravitational character of cold surges during Winter MONEX. *Mon. Wea. Rev.*, **111**, 293-307.

Chang, C.B., D.J. Perkey, and C.W. Kreitzberg, 1981: A numerical case study of the squall line of 6 May 1975. *J. Atmos. Sci.*, **38**, 1601-1615.

Charney, J.G. and P.G. Drazin, 1961: Propagation of planetary-scale disturbances from the lower into the upper atmosphere. *J. Geophys. Res.*, **66**, 83-109.

Charney, J.G., and A. Eliassen, 1964: On the growth of the hurricane depression. *J. Atmos. Sci.*, **21**, 68-75.

Chen, C. and W.R. Cotton, 1983a: A one-dimensional simulation of the stratocumulus-capped mixed layer. *Bound.-Layer Meteor.*, **25**, 289-321.

Chen, C. and W.R. Cotton, 1983b: Numerical experiments with a one-dimensional higher order turbulence model: Simulation of the Wangara Day 33 case. *Bound.-Layer Meteor.*, **25**, 375-404.

Chimonas, S.G. and J.R. Grant, 1984: Shear excitation of gravity waves. Part II: Upscale scattering from Kelvin-Helmholtz waves. *J. Atmos. Sci.*, **41**, 2278-2288.

Clark, T.L., 1977: A small-scale dynamic model using a terrain-following coordinate transformation. *J. Comput. Phys.*, **24**, 186-215.

Clark, T.L. and R.D. Farley, 1984: Severe downslope windstorm calculations in two and three spatial dimensions using anelastic interactive grid nesting: A possible mechanism for gustiness. *J. Atmos. Sci.*, **41**, 329-350.

Clark, T.C., T. Hauf, and J.P. Kuettner, 1986: Convectively forced internal gravity waves: Results from two-dimensional numerical experiments. *Quart. J. Roy. Meteor. Soc.*, **112**, 899-925.

Coats, G.D., V.C. Wong, J.W. Zack, and M.L. Kaplan, 1984: A numerical investigation of the effect of soil moisture gradients on the regional severe storm environment. *Preprints of Tenth Conference on Weather Forecasting and Analysis*, Clearwater Beach, FL, 506-512.

Cotton, W.R. and R.A. Anthes, 1989: *Storm and Cloud Dynamics.* Academic Press, 883 pp.

Cotton, W.R. and G.J. Tripoli, 1978: Cumulus convection in shear flow – Three-dimensional numerical experiments. *J. Atmos. Sci.*, **35**, 1503-1521.

Cotton, W.R., M.A. Stephens, T. Nehrkorn, and G.J. Tripoli, 1982: The Colorado State University cloud/mesoscale model-1982. Part II: An ice phase parameterization. *J. Rech. Atmos.*, **16**, 295-320.

Cotton, W.R., C.J. Tremback, and R.L. Walko, 1988: CSU RAMS - A cloud model goes regional. *Proc. NCAR Workshop on Limited-Area Modeling Intercomparison*, Nov. 15-18, NCAR, Boulder, CO, 202-211.

Crook, N.A., 1988: Trapping of low-level internal gravity waves. *J. Atmos. Sci.*, **45**, 1533-1541.

Crook, N.A. and M.W. Moncrieff, 1988: The effect of large-scale convergence on the generation and maintenance of deep moist convection. *J. Atmos. Sci.*, **45**, 3606-3624.

Crook, N.A., R.E. Carbone, M.W. Moncrieff, and J.W. Conway, 1990: The generation and propagation of a nocturnal squall line. Part II: Numerical simulations. *Mon. Wea. Rev.*, **118**, 50-65.

Davies, H.C., 1976: A lateral boundary formulation for multi-level prediction models. *Tellus*, **102**, 405-418.

Davies, H.C., 1979: Phase-lagged wave-CISK. *Quart. J. Roy. Meteor. Soc.*, **105**, 325-353.

Davies, H.C., 1983: Limitations of some common lateral boundary schemes used in regional NWP models. *Mon. Wea. Rev.*, **111**, 1002-1012.

Davies, H.C., and R.E. Turner, 1977: Updating prediction models by dynamical relaxation: an examination of the technique. *Quart. J. Roy. Meteor. Soc.*, **103**, 225-245.

Deardorff, J.W., 1972: Parameterization of the planetary boundary layer for use in general circulation models. *Mon. Wea. Rev.*, **100**, 93-106.

Dey, C.H., P.A. Phoebus, R.E. Kistler, A.J. Desmarais, J.J. Tuccillo, B.A. Ballish, 1985: 1984 Summary of NMC Operational Global Analyses. Medium-Range Modeling Branch Paper No. 5, National Meteorological Center, U.S. Department of Commerce, N.O.A.A., Rockville, Md. 20852, 11 pp.

Dickenson, R.E., 1969: Vertical propagation of planetary Rossby waves through an atmosphere with Newtonian cooling. *J. Geophys. Res.*, **74**, 929-938.

Dirks, K., 1969: A theoretical investigation of convective patterns in the lee of the Colorado Rockies. Atmospheric Science Paper No. 145, Dept. of Atmospheric Science, Colorado State University, Ft. Collins, CO, 80523, 291 pp.

Dorian, P.B., S.E. Koch, and W. C. Skillman, 1988: The relationship between satellite-inferred frontogenesis and squall line formation. *Wea. and Forecast.*, **3**, 319-342.

Durran, D.R. and J.B. Klemp, 1983: A compressible model for the simulation of moist mountain waves. *Mon. Wea. Rev.*, **111**, 2341-2361.

Einaudi, F., W.L. Clark, D. Fua, J.L. Green, and T.E. Van Zandt, 1987: Gravity waves and convection in Colorado during July 1983. *J. Atmos. Sci.*, **44**, 1534-1553.

Emanuel, K.A., 1982: Inertial instability and mesoscale convective systems. Part II: Symmetric CISK in a baroclinic flow. *J. Atmos. Sci.*, **39**, 1080-1097.

Eom, J.K., 1975: Analysis of the internal gravity wave occurrence of 19 April 1970 in the midwest. *Mon. Wea. Rev.*, **103**, 217-226.

Fan, B.-F., J.-D. Yeh, and W.R. Cotton, 1988: Microphysics in a deep convective cloud system associated with a mesoscale convective complex – Numerical simulation. *Preprints, Tenth International Cloud Physics Conference*, Bad Homburg, FRG.

Fankhauser, J.C., 1974: The derivation of consistent fields of wind and geopotential height from mesoscale rawinsonde data. *J. Appl. Meteor.*, **13**, 637-646.

Flatau, P.J., G.J. Tripoli, J. Verlinde, and W.R. Cotton, 1989: The CSU-RAMS cloud microphysics module: General theory and code documentation. Atmospheric Science Paper No. 451, Colorado State University, Dept. of Atmospheric Science, Fort Collins, CO 80523.

Frank, W.M., 1983: The cumulus parameterization problem. *Mon. Wea. Rev.*, **111**, 1859-1871.

Fritsch, J.M. and C.F. Chappell, 1980a: Numerical prediction of convectively driven mesoscale pressure systems. Part I: Convective parameterization. *J. Atmos. Sci.*, **37**, 1722-1733.

Fritsch, J.M. and C.F. Chappell, 1980b: Numerical prediction of convectively driven mesoscale pressure systems. Part II: Mesoscale model. *J. Atmos. Sci.*, **37**, 1734-1762.

Fujita, T.T., 1955: Results of detailed synoptic studies of squall lines. *Tellus VII*, 4, 405-436.

Fujita, T.T., 1979: Objectives, operation and results of project NIMROD. *Preprints, 11th Conf. on Severe Local Storms.* Kansas City, Amer. Meteor. Soc., 259-266.

Fujita, T.T., 1981: Tornadoes and downbursts in the context of generalized planetary scales. *J. Atmos. Sci.*, **38**, 1511-1534.

Gal-Chen, T. and R.C.J. Somerville, 1975a: On the use of a coordinate transformation for the solution of the Navier-Stokes Equations. *J. Comput. Phys.*, **17**, 209-228.

Gal-Chen, T. and R.C.J. Somerville, 1975b: Numerical solution of the Navier-Stokes equations with topography. *J. Comput. Phys.*, **17**, 276-310.

Gamache, J.F. and R.A. Houze, Jr., 1982: Mesoscale air motions associated with a tropical squall line. *Mon. Wea. Rev.*, **110**, 118-135.

Garstang, M., N.E. LaSeur, K.L. Warsh, R. Hadlock, and J.R. Peterson, 1970: Atmospheric-ocean observations in the tropics. *Amer. Sci.*, **58**, 482-495.

Gedzelman, S.D. and R.A. Rilling, 1978: Short-period atmospheric gravity waves: A study of their dynamic and synoptic features. *Mon. Wea. Rev.*, **106**, 196-210.

Gill, A.E., 1982: *Atmosphere-Ocean Dynamics.* Academic Press, Inc. Orlando, Florida, 662 pp.

Halliday, D. and R. Resnick, 1966: Chapter 19: Waves in elastic media. *Physics. Part I.*, John Wiley and Sons, Inc., 463-491.

Hane, C.E., 1973: The squall line thunderstorm: Numerical experimentation. *J. Atmos. Sci.*, **30**, 1672-1690.

Hane, C.E., C.J. Kessinger, and P.S. Ray, 1987: The Oklahoma squall line of 19 May 1977. Part II: Mechanisms for maintenance of the region of strong convection. *J. Atmos. Sci.*, **44**, 2866-2883.

Hayashi, Y., 1970: A theory of large-scale equatorial waves generated by condensation heat and accelerating the zonal wind. *J. Meteor. Soc. Japan*, **48**, 140-160.

Henderson-Sellers, A., M.F. Wilson, G.Thomas, and R.E. Dickenson, 1986: Current global land-surface data sets for use in climate-related studies. NCAR Technical Note TN-272, National Center for Atmospheric Research, Boulder, CO, 110 pp.

Hertenstein, R.F.A. and W.H. Schubert, 1990: Potential vorticity anomalies associated with squall lines. *submitted to Mon. Wea. Rev.*.

Heymsfield, G.M. and S. Schotz, 1985: Structure and evolution of a severe squall line over Oklahoma. *Mon. Wea. Rev.*, **113**, 1563-1589.

Hill, G.E., 1974: Factors controlling the size and spacing of cumulus clouds as revealed by numerical experiments. *J. Atmos. Sci.*, **31**, 646-673.

Houghton, D.D. and W.L. Jones, 1969: A numerical model for linearized gravity and acoustic waves. *J. Comput. Phys.*, **3**, 339-357.

Houze, R.A., Jr., 1977: Structure and dynamics of a tropical squall line system. *Mon. Wea. Rev.*, **105**, 1540-1567.

Hoxit, L.R., C.F. Chappell, and J.M. Fritsch, 1976: Formation of mesolows and pressure troughs in advance of cumulonimbus clouds. *Mon. Wea. Rev.*, **104**, 1419-1428.

Hoxit, L.R., R.A. Maddox, C.F. Chappell, F.L. Zuckerberg, H.M. Mogul, J. Jones, D.R. Greene, R.E. Saffle, and R.A. Scofield, 1978: Meteorological analysis of the Johnstown, Pennsylvania flash flood, 19-20 July 1977. NOAA Tech. Rep. ERL 401-APCL43, 71 pp.

Israeli, M. and S.A. Orszag, 1981: Approximation of radiation boundary conditions. *J. Comput. Phys.*, **41**, 115-135.

Jenne, R., 1987: Data Availability at NCAR. National Center for Atmospheric Research, SCD, Data Support Section, P.O. Box 3000, Boulder, CO 80307, 21 pp.

Johnson, R.H. and P.J. Hamilton, 1988: The relation of surface pressure features to the precipitation and air flow structure of an intense mid-latitude squall line. *Mon. Wea. Rev.*, **116**, 1444-1472.

Kalb, M.W., 1987: The role of convective parameterization in the simulation of a Gulf Coast precipitating system. *Mon. Wea. Rev.*, **115**, 214-234.

Kessinger, C.J., P.S. Ray, and C.E. Hane, 1987: The Oklahoma squall line of 19 May 1977. Part I: A multiple doppler analysis of convective and stratiform structure. *J. Atmos. Sci.*, 44, 2840-64.

Kirkwood, E., and J. Derome, 1977: Some effects of the upper boundary condition and vertical resolution on modeling forced stationary planetary waves. *Mon. Wea. Rev.*, **105**, 1239-1993.

Kistler, R.E. and D.F. Parrish, 1982: Evolution of the NMC Data Assimilation System: September 1978-January 1982. *Mon. Wea. Rev.*, **110**, 1335-1346.

Klemp, J.B. and D.R. Durran, 1983: An upper boundary condition permitting internal gravity wave radiation in numerical mesoscale models. *Mon. Wea. Rev.*, **111**, 430-444.

Klemp, J.B. and D.K. Lilly, 1978: Numerical simulation of hydrostatic mountain waves. *J. Atmos. Sci.*, **35**, 78-107.

Klemp, J.B. and R.B. Wilhelmson, 1978a: The simulation of three-dimensional convective storm dynamics. *J. Atmos. Sci.*, **35**, 1070-1096.

Klemp, J.B. and R.B. Wilhelmson, 1978b: Simulations of right- and left-moving storms produced through storm-splitting. *J. Atmos. Sci.*, **35**, 1097-1110.

Koch, S.E., 1984: The role of an apparent mesoscale frontogenetic circulation in squall line formation. *Mon. Wea. Rev.*, **112**, 2090-2111.

Koch, S.E., and P.B. Dorian, 1988: A mesoscale gravity wave event observed during CCOPE. Part III: Wave environment and possible source mechanisms. *Mon. Wea. Rev.*, **116**, 2570-91.

Koch, S.E., and R.E. Golus, 1988: A mesoscale gravity wave event observed during CCOPE. Part I: Multiscale statistical analysis of wave characteristics. *Mon. Wea. Rev.*, **116**, 2527-44.

Koch, S.E., R.E. Golus, and P.B. Dorian, 1988: A mesoscale gravity wave event observed during CCOPE. Part II: Interactions between mesoscale convective systems and antecedent waves. *Mon. Wea. Rev.*, **116**, 2545-69.

Kohnke, H., 1968: *Soil Physics.* Mcgraw-Hill Book Company, 224 pp.

Kuo, H.L., 1965: On the formation and intensification of tropical cyclones through latent heat release by cumulus convection. *J. Atmos. Sci.*, **22**, 40-63.

Kuo, H.L., 1974: Further studies of the parameterization of the influence of cumulus convection on the large-scale flow. *J. Atmos. Sci.*, **31**, 1232-1240.

Lafore, J.P. and M.W. Moncrieff, 1989: A numerical investigation of the organization and interaction of the convective and stratiform regions of a tropical squall line. *J. Atmos. Sci.*, **46**, 521-544.

Lafore, J.P. and M.W. Moncrieff, 1990: Reply. *J. Atmos. Sci.*, **47**, 1034-1035.

Lalas, D.P. and F. Einaudi, 1976: On the characteristics of gravity waves generated by atmospheric shear layers. *J. Atmos. Sci.*, **33**, 1248-1259.

LeMone, M.A., 1983: Momentum transport by a line of cumulonimbus. *J. Atmos. Sci.*, **40**, 1815-1834.

LeMone, M.A., G.M. Barnes, and E.J. Zipser, 1984: Momentum flux by lines of cumulonimbus over the tropical oceans. *J. Atmos. Sci.*, **41**, 1914-1932.

Lewis, J.M., 1975: Test of the Ogura-Cho model on a pre-frontal squall line case. *Mon. Wea. Rev.*, **103**, 764-778.

Ley, B.E. and W.R. Peltier, 1978: Wave generation and frontal collapse, *J. Atmos. Sci.*, **35**, 3-17.

Lilly, D.K., 1962: On the numerical simulation of buoyant convection. *Tellus*, **14**, 148-172.

Lim, H. and C.P. Chang, 1981: A theory for midlatitude forcing of tropical motions during the winter monsoons. *J. Atmos. Sci.*, **38**, 2377-2392.

Lin, Y.L. and R.C. Goff, 1988: A study of a mesoscale solitary wave in the atmosphere originating near a region of deep convection. *J. Atmos. Sci.*, **45**, 194-202.

Lin, Y.L., and S. Li, 1988: Three-dimensional response of a shear flow to elevated heating. *J. Atmos. Sci.*, **45**, 2987-3002.

Lin, Y.L. and R.B. Smith, 1986: Transient dynamics of airflow near a local heat source. *J. Atmos. Sci.*, **43**, 40-49.

Lindzen, R.S. and K.K. Tung, 1976: Banded convective activity and ducted gravity waves. *Mon. Wea. Rev.*, **104**, 1602-1617.

Maddox, R.A., 1980: Mesoscale convective complexes. *Bull. Amer. Meteor. Soc.*, **61**, 1374-1387. 0

Mahrer, Y. and R.A. Pielke, 1977: A numerical study of the airflow over irregular terrain. *Beitr. Phys. Atmos.*, **50**, 98-113.

McCumber, M.C., 1980: A numerical simulation of the influence of heat and moisture fluxes upon mesoscale circulations. Ph.D. Dissertation, University of Virginia, Charlottesville, VA.

McCumber, M.C., and R.A. Pielke, 1981: Simulation of the effects of surface fluxes of heat and moisture in a mesoscale numerical model – Part 1. Soil layer. *J. Geophys. Res.*, **86**, 9929-9938.

McNider, R.T., and R.A. Pielke, 1981: Diurnal boundary-layer development over sloping terrain. *J. Atmos. Sci.*, **38**, 2198-2212.

Mechoso, C.R., M.J. Suarez, K. Yamazaki, J.A. Spahr, and A. Arakawa, 1982: A study of the sensitivity of numerical forecasts to an upper boundary in the lower stratosphere. *Mon. Wea. Rev.*, **110**, 1984-1993.

Miller, D.M., and F. Sanders, 1980: Mesoscale conditions for the severe convection of 3 April 1974 in the east-central United States. *J. Atmos. Sci.*, **37**, 1041-55.

Molinari, J., 1985: A general form of Kuo's cumulus parameterization. *Mon. Wea. Rev.*, **113**, 1411-1416.

Molinari, J. and T. Corsetti, 1985: Incorporation of cloud-scale and mesoscale downdrafts into a cumulus parameterization: Results of one- and three-dimensional integrations. *Mon. Wea. Rev.*, **113**, 485-501.

Molinari, J. and M. Dudek, 1986: Implicit vs. explicit convective heating in numerical weather prediction models. *Mon. Wea. Rev.*, **114**, 1822-31.

Moncrieff, M.W., 1978: The dynamical structure of two-dimensional steady convection in constant vertical wind shear. *Quart. J. Roy. Meteor. Soc.*, **104**, 543-567.

Moncrieff, M.W. and M.J. Miller, 1976: The dynamics and simulation of tropical cumulonimbus and squall lines. *Quart. J. Roy. Meteor. Soc.*, **102**, 373-394.

NMC ON 84, 1979: NMC 360/195 Packed data fields. National Meteorological Center, U.S. Department of Commerce, N.O.A.A., Rockville, MD 20852, 29 pp.

Nehrkorn, T., 1986: Wave-CISK in a baroclinic base state. *J. Atmos. Sci.*, **43**, 2773-2791.

Newton, C.W., 1950: Structure and mechanism of the pre-frontal squall line. *J. Meteor.*, **7**, 210-222.

Nicholls, M.E., 1987: A comparison of the results of a two-dimensional numerical simulation of a tropical squall line with observations. *Mon. Wea. Rev.*, **115**, 3055-3077.

Nicholls, M.E., and M.J. Weissbluth, 1988: A comparison of two-dimensional and quasi three-dimensional simulations of a tropical squall line. *Mon. Wea. Rev.*, **116**, 2437-2452.

Nicholls, M.E., R.H. Johnson, and W.R. Cotton, 1988: The sensitivity of 2D simulations of tropical squall lines to environmental profiles, *J. Atmos. Sci.*, **45**, 3625-3649.

Nickerson, E.C., E. Richard, R. Rosset, and D.R. Smith, 1986: The numerical simulation of clouds, rain, and airflow over the Vosges and Black Forest Mountains: A meso-β model with parameterized microphysics. *Mon. Wea. Rev.*, **114**, 398-414.

Ogura, Y. and M.-T. Liou, 1980: The structure of a mid-latitude squall line: A case study. *J. Atmos. Sci.*, **37**, 553-567.

Orlanski, J. and B.B. Ross, 1977: The circulation associated with a cold front. Part I: Numerical simulation. *J. Atmos. Sci.*, **34**, 1619-1633.

Orlanski, J. and B.B. Ross, 1984: The evolution of an observed cold front. Part II: Mesoscale dynamics. *J. Atmos. Sci.*, **41**, 1669-1703.

Orlanski, J. and B.B. Ross, 1986: Low-level updrafts in stable layers forced by convection. *J. Atmos. Sci.*, **43**, 997-1005.

Pecnick, M.J. and J.A. Young, 1984: Mechanisms of a strong subsynoptic gravity wave deduced from satellite and surface observations. *J. Atmos. Sci.*, **41**, 1850-62.

Perkey, D.J. and C.W. Kreitzberg, 1976: A time-dependent lateral boundary scheme for limited-area primitive equation models. *Mon. Wea. Rev.*, **104**, 744-755.

Physick, W.C., 1980: Numerical experiments on the inland penetration of the sea breeze. *Quart. J. Roy. Meteor. Soc.*, **106**, 735-746.

Pielke, R.A., 1974: A three-dimensional numerical model of the sea breezes over south Florida. *Mon. Wea. Rev.*, **102**, 115-134.

Pielke, R.A., 1984: *Mesoscale Meteorological Modeling*, Academic Press, 612 pp.

Pielke, R.A., A. Song, P.J. Michaels, W.A. Lyons, and R.W. Arritt, 1990: The prediction of sea-breeze generated thunderstorms. *Accepted for publication in Atmosfera.*

Rasch, P.J., 1986: Toward atmospheres without tops: Absorbing upper boundary conditions for numerical models. *Quart. J. Roy. Meteor. Soc.*, **112**, 1195-1218.

Raymond, D.J., 1975: A model for predicting the movement of continuously propagating storms. *J. Atmos. Sci.*, **32**, 1308-1317.

Raymond, D.J., 1976: Wave-CISK and convective mesosystems. *J. Atmos. Sci.*, **33**, 2392-2398.

Raymond, D.J., 1983: Wave-CISK in mass flux form. *J. Atmos. Sci.*, **40**, 2561-2572.

Raymond, D.J., 1984: A wave-CISK model of squall lines. *J. Atmos. Sci.*, **41**, 1946-1958.

Rogers, R.R., 1979: *A Short Course in Cloud Physics, second edition.* Pergamon Press, 235 pp.

Rosenthal, S.L., 1978: Numerical simulation of tropical cyclone development with latent heat release by the resolvable scales. I: Model description and preliminary results. *J. Atmos. Sci.*, **35**, 258-71.

Ross, B.B. and J. Orlanski, 1982: The evolution of an observed cold front. Part I: Numerical simulation. *J. Atmos. Sci.*, **39**, 296-327.

Rossby, C.G., 1938: On the mutual adjustment of pressure and velocity distributions in certain simple current systems. II. *J. Marine Res.*, **7**, 239-263.

Rotunno, R., J.B. Klemp, and M.L. Weisman, 1988: A theory for strong, long-level squall lines. *J. Atmos. Sci.*, **45**, 463-485.

Roux, F., 1988: The west African squall line observed on 23 June 1981 during COPT81: Kinematics and thermodynamics of the convective region. *J. Atmos. Sci.*, **45**, 406-426.

Rutledge, S.A. and R.A. Houze, Jr., 1987: A diagnostic modelling study of the trailing stratiform region of a midlatitude squall line. *J. Atmos. Sci.*, **44**, 2640-2656.

Rutledge, S.A., R.A. Houze, Jr., M.I. Biggerstaff, and T. Matejka, 1988: The Oklahoma-Kansas mesoscale convective system of 10-11 June 1985: Precipitation structure and single-Doppler radar analysis. *Mon. Wea. Rev.*, **116**, 1409-1430.

Schmidt, J.M. and W.R. Cotton, 1989: A high plains squall line associated with severe surface winds. *J. Atmos. Sci.*, **46**, 281-302.

Schmidt, J.M. and W.R. Cotton, 1990: Interactions between upper and lower tropospheric gravity waves on squall line structure and maintenance. *J. Atmos. Sci.*, **47**, 1205-1222.

Seitter, K.L. and H.-L. Kuo, 1983: The dynamical structure of squall-line type thunderstorms. *J. Atmos. Sci.*, **40**, 2831-2854.

Simpson, J.E., 1987: *Gravity Currents: In the Environment and the Laboratory.* John Wiley and Sons, New York, NY, 244 pp.

Smagorinsky, J., 1963: General circulation experiments with the primitive equations. I. The basic experiment. *Mon. Wea. Rev.*, **91**, 99-164.

Smith, R.B., 1979: The influence of mountains on the atmosphere. *Adv. Geophys.*, **26**, 87-230.

Smull, B.F. and R.A. Houze, Jr., 1985: A midlatitude squall line with a trailing region of stratiform rain: Radar and satellite observations. *Mon. Wea. Rev.*, **113**, 117-133.

Smull, B.F. and R.A. Houze, Jr., 1987: Rear inflow in squall lines with stratiform precipitation. *Mon. Wea. Rev.*, **115**, 2869-2889.

Srivastava, R.C., T.J. Matejka and T.J. Lorello, 1986: Doppler radar study of the trailing anvil region associated with a squall line. *J. Atmos. Sci.*, **43**, 356-377.

Stobie, J.G., F. Einaudi, and L.W. Uccellini, 1983: A case study of gravity waves-convective storms interaction: 9 May 1979. *J. Atmos. Sci.*, **40**, 2804-2830.

Takeda, T., 1971: Numerical simulation of a precipitating convective cloud: The formation of a "long-lasting" cloud. *J. Atmos. Sci.*, **28**, 350-376.

Tapp, M.C. and P.W. White, 1976: A non-hydrostatic mesoscale model. *Quart. J. Roy. Meteor. Soc.*, **102**, 277-296.

Tepper, M., 1950: A proposed mechanism of squall lines: The pressure jump line. *J. Meteor.*, **7**, 21-29.

Tepper, M., 1951: On the desiccation of a cloud bank by a propagated pressure wave. *Mon. Wea. Rev.*, **79**, 61-70.

Thorpe, A.J., M.J. Miller, and M.W. Moncrieff, 1982: Two-dimensional convection in non-constant shear: A model of mid-latitude squall lines. *Quart. J. Roy. Meteor. Soc.*, **108**, 739-762.

Tremback, C.J., 1990: Numerical simulation of a mesoscale convective complex: model development and numerical results. Ph.D. Dissertation. Dept. of Atmospheric Science, Colorado State University, Ft. Collins, CO, 247 pp.

Tremback, C.J. and R. Kessler, 1985: A surface temperature and moisture parameterization for use in mesoscale numerical models. *Proc. 7th AMS Conf. on Numerical Weather Prediction*, June 17-20, Montreal, Quebec, American Meteorological Society, Boston, 355-358.

Tremback, C.J., G.J. Tripoli, and W.R. Cotton, 1985: A regional scale atmospheric numerical model including explicit moist physics and a hydrostatic time-split scheme. *Proc. 7th AMS Conf. on Numerical Weather Prediction*, June 17-20, Montreal, Quebec, American Meteorological Society, Boston, 433-434.

Tremback, C.J., G.J. Tripoli, R. Arritt, W.R. Cotton, and R.A. Pielke, 1986: The Regional Atmospheric Modelling System. *Proc. Inter. Conf. Development and Application of Computer Techniques to Environmental Studies*, November, Los Angeles, California, P. Zannetti, Ed., Computational Mechanics Publications, Boston, 601-607.

Tripoli, G.J., 1988: A numerical investigation of an orogenic mesoscale convective system. Ph.D. Dissertation. Dept. of Atmospheric Science, Colorado State University, Ft. Collins, CO, 290 pp.

Tripoli, G.J. and W.R. Cotton, 1980: A numerical investigation of several factors leading to the observed variable intensity of deep convection over South Florida. *J. Appl. Meteor.*, **19**, 1037-1063.

Tripoli, G.J. and W.R. Cotton, 1982: The Colorado State University three-dimensional cloud/mesoscale model-1982. Part I: General theoretical framework and sensitivity experiments. *J. Rech. Atmos.*, **16**, 185-220.

Tripoli, G.J. and W.R. Cotton, 1989a: Numerical study of an observed orogenic mesoscale convective system. Part 1: Simulated genesis and comparison with observations. *Mon. Wea. Rev.*, **117**, 273-304.

Tripoli, G.J. and W.R. Cotton, 1989b: Numerical study of an observed orogenic mesoscale convective system. Part 2. Analysis of governing dynamics. *Mon. Wea. Rev.*, **117**, 305-328.

Uccellini, L.W., 1975: A case study of apparent gravity wave initiation of severe convective storms. *Mon. Wea. Rev.*, **103**, 497-513.

Uccellini, L.W. and S.E. Koch, 1987: The synoptic setting and possible energy sources for mesoscale wave disturbances. *Mon. Wea. Rev.*, **115**, 721-729.

Wilson, M.F. and A. Henderson-Sellers, 1985: A global archive of land cover and soils data for use in general circulation climate models. *J. Climatology*, **5**, 119-143.

Xu, Q. and J.H.E. Clark, 1984: Wave CISK and mesoscale convective systems. *J. Atmos. Sci.*, **41**, 2089-2107.

Zack, J.W., M.L. Kaplan, and V.C. Wong, 1985: A comparison of the prognostic performance of several cumulus parameterizations in mesoscale simulations of the 10 april 1979 Sesame I case. *Preprints, Seventh Conference on Numerical Weather Prediction*, Montreal, 415-422.

Zhang, D.-L. and J.M. Fritsch, 1986: Numerical simulation of the meso-β scale structure and evolution of the 1977 Johnstown flood. Part I: Model description and verification. *J. Atmos. Sci.*, **43**, 1913-1943.

Zhang, D.-L. and J.M. Fritsch, 1987: Numerical simulation of the meso-β structure and evolution of the 1977 Johnstown flood. Part II: Inertially stable warm-core vortex and the mesoscale convective complex. *J. Atmos. Sci.*, **44**, 2593-2612.

Zhang, D.-L. and J.M. Fritsch, 1988a: Numerical sensitivity experiments of varying model physics on the structure, evolution, and dynamics of two mesoscale convective systems. *J. Atmos. Sci.*, **45**, 261-293.

Zhang, D.-L. and J.M. Fritsch, 1988b: Numerical simulation of the meso-β scale structure and evolution of the 1977 Johnstown Flood. Part III: Internal gravity waves and the squall line. *J. Atmos. Sci.*, **45**, 1252-1268.

Zhang, D.-L. and K. Gao, 1989: Numerical simulations of an intense squall line during 10-11 June 1985 PRE-STORM. Part II: Review of surface pressure perturbations and stratiform precipitation. *Mon. Wea. Rev.*, **117**, 2067-2094.

Zhang, D.-L., E.-Y. Hsie, and M.W. Moncrieff, 1988: A comparison of explicit and implicit predictions of convective and stratiform precipitating weather systems with a meso-β scale numerical model. *Quart. J. Roy. Meteor. Soc.*, **114**, 31-60.

Zhang, D.-L., K. Gao, and D.B. Parsons, 1989: Numerical simulations of an intense squall line during 10-11 June 1985 PRE-STORM. Part I: Model verification. *Mon. Wea. Rev.*, **117**, 960-994.

Zipser, E.J., 1977: Mesoscale and convective-scale downbursts as distinct components of squall line structure. *Mon. Wea. Rev.*, **105**, 1568-1589.